TO BIND OR NOT TO BIND – DISSOCIATION EQUILIBRIA STUDIED BY PULSE DIPOLAR EPR

Joshua Wort

A Thesis Submitted for the Degree of PhD
at the
University of St Andrews

2022

Identifiers to use to cite or link to this thesis:

DOI: https://doi.org/10.17630/sta/466
http://hdl.handle.net/10023/27615

To Bind or Not to Bind - Dissociation Equilibria Studied by Pulse Dipolar EPR

Joshua Wort

University of
St Andrews

This thesis is submitted in partial fulfilment for the degree of

Doctor of Philosophy (PhD)

at the University of St Andrews

March 2021

Candidate's declaration

I, Joshua Wort, do hereby certify that this thesis, submitted for the degree of PhD, which is approximately 75,000 words in length, has been written by me, and that it is the record of work carried out by me, or principally by myself in collaboration with others as acknowledged, and that it has not been submitted in any previous application for any degree. I confirm that any appendices included in my thesis contain only material permitted by the 'Assessment of Postgraduate Research Students' policy.

I was admitted as a research student at the University of St Andrews in September 2016.

I received funding from an organisation or institution and have acknowledged the funder(s) in the full text of my thesis.

Date 26/09/2021 Signature of candidate

Supervisor's declaration

I hereby certify that the candidate has fulfilled the conditions of the Resolution and Regulations appropriate for the degree of PhD in the University of St Andrews and that the candidate is qualified to submit this thesis in application for that degree. I confirm that any appendices included in the thesis contain only material permitted by the 'Assessment of Postgraduate Research Students' policy.

Date 26/09/21 Signature of supervisor

Permission for publication

In submitting this thesis to the University of St Andrews we understand that we are giving permission for it to be made available for use in accordance with the regulations of the University Library for the time being in force, subject to any copyright vested in the work not being affected thereby. We also understand, unless exempt by an award of an embargo as requested below, that the title and the abstract will be published, and that a copy of the work may be made and supplied to any bona fide library or research worker, that this thesis will be electronically accessible for personal or research use and that the library has the right to migrate this thesis into new electronic forms as required to ensure continued access to the thesis.

I, Joshua Wort, confirm that my thesis does not contain any third-party material that requires copyright clearance.

The following is an agreed request by candidate and supervisor regarding the publication of this thesis:

Printed copy

No embargo on print copy.

Electronic copy

No embargo on electronic copy.

Date 26/09/2021 Signature of candidate

Date 26/09/2021 Signature of supervisor

Underpinning Research Data or Digital Outputs

Candidate's declaration

I, Joshua Wort, understand that by declaring that I have original research data or digital outputs, I should make every effort in meeting the University's and research funders' requirements on the deposit and sharing of research data or research digital outputs.

Date 26/09/2021 Signature of candidate

Permission for publication of underpinning research data or digital outputs

We understand that for any original research data or digital outputs which are deposited, we are giving permission for them to be made available for use in accordance with the requirements of the University and research funders, for the time being in force.

We also understand that the title and the description will be published, and that the underpinning research data or digital outputs will be electronically accessible for use in accordance with the license specified at the point of deposit, unless exempt by award of an embargo as requested below.

The following is an agreed request by candidate and supervisor regarding the publication of underpinning research data or digital outputs:

No embargo on underpinning research data or digital outputs.

Date 26/09/2021 Signature of candidate

Date 26/09/2021 Signature of supervisor

Abstract

Pulse dipolar EPR is an appealing strategy for structural characterisation of complex systems in solution that complements other biophysical techniques. Significantly, the emergence of genetically encoded self-assembling spin labels exploiting exogenously introduced double-histidine motifs in conjunction with Cu^{II}-chelates offers high precision distance determination in systems non-permissive to thiol-directed spin labelling. However, the non-covalent Cu^{II} coordination approach is vulnerable to low binding-affinity. Here, an approach is outlined where dissociation constants (K_D) are investigated directly from the modulation depths of relaxation-induced dipolar modulation enhancement (RIDME) EPR experiments applied to the model protein *Streptococcus sp.* group G. protein G, B1 domain (GB1). This reveals low- to sub-μM Cu^{II}-chelate K_Ds under RIDME conditions at cryogenic temperatures. We show the feasibility of exploiting the double-histidine motif for EPR applications even at sub-μM protein concentrations in orthogonally labelled Cu^{II}–nitroxide systems.

Additionally, modulation depth quantitation in Cu^{II}–Cu^{II} RIDME to simultaneously estimate a pair of non-identical independent K_Ds is addressed. Furthermore, we develop a general speciation model to optimise Cu^{II} labelling efficiency, depending upon pairs of identical or disparate K_Ds and total label concentration. We find the K_D estimates are in excellent agreement with previously determined values. We also investigated the vulnerability of binding to both competition from adventitious divalent metal ions, and pH sensitivity. A combination of room-temperature isothermal titration calorimetry (ITC) and Cu^{II}-nitroxide RIDME measurements are applied to GB1. Results demonstrate double-histidine spin labelling using Cu^{II}-nitrilotriacetic acid (Cu^{II}-NTA) is robust against the competitor ligand Zn^{II}-NTA at >1000-fold excess, and high nM binding affinity is retained at acidic and basic pH, despite room-temperature behaviour suggesting a stronger dependence.

Table of Contents

Acknowledgments

First and foremost, I would like to acknowledge my supervisor, Dr Bela E. Bode. I am very grateful for his moral and academic support throughout my PhD, and for giving me the opportunity to study as a part of his group. His vast knowledge and insight were essential to my development as a researcher, and his guidance and advice are very much appreciated. I thank him for fruitful discussions of my results, as well as for introducing me to advanced EPR methods and investing his time to train me at the EPR spectrometer. I also take this opportunity to thank Dr David Norman at the University of Dundee for his support at the beginning of my PhD, and for assisting with some of the molecular dynamics simulations throughout this thesis.

I also acknowledge all the past and present members of the Bode lab. The work environment was very pleasant and engendered a team spirit and comradery. I would like to especially thank Dr Katrin Ackermann for her help with the molecular biology aspects of my PhD, fruitful discussions of my results, and her patience and understanding in training me to prepare the EPR pseudo-titration series that proved so valuable to the completion of my PhD. I would also like to thank Dr Maria Oranges, and Antoine Schuller for their moral support, especially throughout the latter part of my PhD, and for their contributions to scientific discussions of my results.

I am deeply grateful to Dr Alan Stewart, Dr Siavash Khazaipoul, and Dr Swati Arya for allowing me to use their ITC equipment, and for assisting me with many of the measurements shown throughout this thesis. I would especially like to thank Swati, for her patience while training me at the ITC, and for providing moral support throughout the latter part of my PhD, at numerous coffee mornings in the School of Medicine. I also take this opportunity to thank Professor Malcolm White, and all members of his group for allowing me to use group equipment during a largely seamless and comfortable transition from Dundee University School of Life Sciences, to the BSRC at the University of St Andrews. I also acknowledge Professor Sunil Saxena for providing the initial I6H/N8H/K28H/Q32H GB1 construct DNA.

I would like to thank the University of St Andrews Mass Spectrometry Facility, and in particular Dr Sally Shirran, Dr Catherine Botting, and Dr Sylvia Synowsky for their support in measuring and analysing many, many mass spectrometry samples over the course of my PhD, and for always being available to answer any of my questions. Additionally, I would like to thank Dr Hassane El Mkami, and Dr Robert Hunter in the group of Professor Graham Smith, for keeping the Q-band spectrometer functioning, and for assisting me when I did not know how to proceed in-front of the spectrometer.

On a more personal note, I would like to acknowledge my partner Agnieszka Malina, for her tireless motivation throughout my time at St Andrews, and indeed prior, as well as my family and my friends for their unconditional love and support. Especially, I would like to thank my parents, without whom none of this would have been possible.

I gratefully acknowledge the BBSRC Eastbio DTP, and the School of Chemistry St Andrews for their financial support. Specifically, the work shown in this thesis was supported by the Biotechnology and Biological Sciences Research Council (BBSRC).

Research data underpinning this thesis are available at: https://doi.org/10.17630/ced80b64-fa40-4d15-8f17-78bb4f06562f (chapter 3), https://doi.org/10.17630/d591aa48-7239-40b0-afef-9f63dac86e9c (chapter 4), and https://doi.org/10.17630/d7138874-55dd-4874-a2e8-c026fbc0b67f (chapter 5).

Chapter 1: Introduction

The literature review section of this chapter has the following contributions. Dr Katrin Ackermann and Dr Maria Oranges assisted with collation of literature. JLW performed the literature review and wrote the chapter, with input and assistance from Dr Bela Bode. This chapter has been published in similar form: J. L., Wort, M. Oranges, K. Ackermann, and B. E., Bode, 'Advanced EPR Spectroscopy for Investigation of Biomolecular Binding Events', *Electron Paramag. Reson.,* 2021, **27**, 47-73. DOI https://doi.org/10.1039/9781839162534-00047.

1.1 *The Structure-Function Paradigm*

The emergence of systems biology in the post-genomic era has led to investigating increasingly complex macromolecular assemblies, emphasising holistic approaches in structural biology. This changing philosophy is prefaced on the understanding that pathologies often arise from dysregulation of interactions between multiple components within wider biological networks. However, while accurate characterisation of such biomolecular interactions in a biologically valid context is important, this significantly increases the experimental complexity. In this purview, electron paramagnetic resonance (EPR) is particularly appealing because it is one of few techniques not overwhelmed by the increasing complexity of biomacromolecules in their native context or supramolecular networks. In a variety of ways EPR can additionally detect and quantify non-covalent interactions, intimately coupling structural information and binding events within the biological context.

For more than sixty years the paradigm of structure and function in biomolecules (i.e., that all biomolecular function is encoded by structure) has been successfully explored, providing great insight largely by means of X-ray crystallographic structure determination. The structure-function paradigm has become a central dogma of structural biology.[1,2] The development of systems biology[3] over the last decades has heralded a transformative change in how this structure-function relationship is investigated. As more and more examples have emerged where interactions in multi-component systems can lead to emergent properties, it has become evident that the reductionist approach of studying isolated biomolecules can be sub-optimal. This has propelled integrative biochemical and biophysical strategies which preserve biological validity under experimental conditions and facilitate measurement within biological context. Furthermore, acknowledgement of the interplay between the cellular environment[4] and machinery makes measurement *in situ* or *in vivo* especially appealing.

1.2 *The Contribution of EPR to Structural Biology*

The role of modern EPR in structural biology and investigating structure-function relationships is profound. Let us begin by providing a brief historical footing of EPR applications in structural biology.

The first applications of EPR to biomolecules may be traced back to the mid-1950s, where continuous wave (CW-EPR) spectra of irradiated amino acids were recorded, to study the local environment of free radicals within proteins,[5,6] and later free radicals occurring in freeze-dried bacterial cells.[7] In 1964, the first nitroxide-based radicals for labelling appeared,[8] and by 1982, a stable methanethiosulfonate nitroxide radical (MTSL) had been developed.[9] Concomitantly, the emergence of sophisticated pulse sequences to isolate dipolar couplings[10,11] facilitated distance measurements in the regime of 2-10 nm, and the commercialisation of higher field and frequency EPR spectrometers fostered further interest in EPR applications throughout the 1980s. By the early 1990s, the advent of thiol-based site-directed spin-labelling (SDSL)[12,13] allowed selective introduction of paramagnets into otherwise diamagnetic biomolecules and enhanced the scope of EPR for targeted structural characterisation.[14,15] By the mid 2000s, development of additional pulse sequences,[16–19] coupled soon-after with data processing methods such as Tikhonov regularisation,[20,21] (see chapter 2.9) and Hermite polynomial interpolation[22] allowed extraction of distance distributions and provided information on conformational sub-ensembles in frozen solution.[23]

In the ~15 years since this time, EPR has become an established technique in the wider toolbox of structural biology. Indeed, CW-EPR has been applied extensively in membrane protein structural elucidation,[24–28] as well as backbone and conformational dynamics,[29–33] reduction potentials of reaction centres,[34–36] and determination of oligomerisation degree.[37,38] This is leveraged by sensitivity of the spectral lineshape to the local environment of the unpaired electron, and dipolar broadening by spins in proximity, allowing measurement of distances up to 2 nm.[39] Hence, CW-EPR can provide insight into the local structure of biomolecules, but measurements beyond 2 nm become increasingly taxing,[40,41] limiting the scope of applications to investigate larger-scale global conformational transitions. In such cases, pulse dipolar EPR (PD-EPR) has proven especially fruitful, as it complements many other biophysical techniques, including X-ray crystallography, cryo-electron microscopy (cryo-EM), nuclear magnetic resonance (NMR), and Förster resonance energy transfer (FRET). For instance, sparse PD-EPR distance constraints have been applied in conjunction with various NMR constraints, including residual dipolar couplings,[42] nuclear Overhauser effects (NOEs),[43,44] and paramagnetic relaxation enhancement data,[45] to refine structural solution-state models. Additionally, FRET and PD-EPR are increasingly combined to corroborate large-scale conformational transitions in multi-domain, complex biomolecules.[46–48]

More generally, as a solution-state approach PD-EPR is well-positioned to access structural and dynamic information in biomolecules such as proteins[49–55] and nucleic acids,[44,56–58] and has contributed to conformational studies,[59–61] disentangling competing structural models,[62,63] and provided insights into the mechanisms of complex biomolecular machinery.[64–66] Furthermore, PD-EPR has been used to monitor complexation,[67–69] determine solution-state protein–ligand binding equilibria,[70–73] and study oligomerisation-degree.[74–77] Excitingly, recent advances in method development such as the improvement of measurement sensitivity through the increased adoption of arbitrary waveform generators (AWGs), and design of redox-stable spin labels[78–80] also highlight the possibility of in cell applications.[81,82] Thus, the contribution of PD-EPR to structural biology is extensive and multifaceted, and several excellent reviews exist,[41,83–87] with the importance of advanced EPR methods likely to continue to increase in the future, where biomolecules can be studied in the native cellular environment.

Both CW- and pulse-EPR will be discussed in greater detail, particularly regarding the investigation of non-covalent binding interactions in the subsequent sections.

1.3 Physical Techniques to Couple Structural and Thermodynamic Information

Perhaps the best-known example of an emergent property is the cooperativity of oxygen binding afforded by Haemoglobin quaternary structure.[88] More generally, non-covalent interactions are crucial in modulating reversible, tuneable responses to stimuli and environmental stressors. The scope of these non-covalent interactions is ubiquitous and their significance in human health and disease is exemplified by dysregulation causing neurodegenerative amyloidogenic pathologies. Select examples include: α-synuclein, and amyloid-β (Aβ) aggregate formation in Parkinson's,[89] and Alzheimer's diseases,[90] respectively, and Huntingtin misfolding in Huntington's disease.[91] Many of these interactions make ideal therapeutic targets for small-molecule drug design, which reinforces the need to characterise their binding equilibria.

Techniques commonly used to study non-covalent interactions include isothermal titration calorimetry (ITC), surface plasmon resonance (SPR), and biolayer interferometry (BLI). ITC is label-free and performed in solution, but is calorimetric which can limit sensitivity, and makes detection of low-affinity interactions difficult. Analysis of complex binding equilibria by ITC is vulnerable to overfitting, though this is being addressed in the field.[92] SPR is also label-free, can be used for thermodynamic and kinetic[93] characterisation with higher sensitivity[94] than ITC, but requires immobilisation. Similarly, BLI requires ligand immobilisation, has lower accuracy and reproducibility than SPR, but is easily adapted to a 384-well plate format facilitating high throughput.[95,96] An important consideration is that none of these methods provide any structural information.

Size exclusion chromatography mass spectrometry (SEC-MS) is also appealing as a high-throughput method used in ligand-screening,[97] and ion-mobility mass spectrometry (IMMS) has been used in conjunction with infrared spectroscopy to report coarse aggregate structure.[98,99] Indirect structural information can be inferred using Hydrogen–Deuterium exchange mass spectrometry (HDX-MS),[100,101] which has been coupled with NMR and SPR to validate protein-ligand[102] and protein–protein interactions,[103] respectively. Native mass spectrometry techniques such as laser induced liquid bead ion desorption (LILBID)[104,105] allow non-covalent interactions to be studied directly, though structural information is limited to oligomeric state.[106] Furthermore, mass spectrometry methods require measurement in the gas-phase. Alternatives which provide information about quaternary structure and can inform binding equilibria in solution-state include small-angle X-ray scattering (SAXS),[107] sedimentation velocity analytical ultracentrifugation (SV-AUC),[108] and dynamic light scattering (DLS).[109] Circular dichroism (CD) is sensitive to secondary structural changes upon ligand or protein binding,[110] which can report sub-populations in binding equilibria.[111] For instance, combinative approaches of CD and CW-EPR have been used extensively to determine the affinity and coordination environment of $\mathrm{Cu^{II}}$-binding in prion protein.[112–114] However, it should be appreciated that this is not always possible if the ligand binding event is not coupled to a structural change, in which case it can be complemented by differential scanning fluorimetry (DSF).[115,116]

In recent years, techniques such as NMR,[117] cryo-EM,[118] and FRET[119] have found increasing utility as methods for investigating macromolecular binding events.[120–125] The combination of atomistic structural constraints and binding information is especially useful to provide mechanistic insight.[126–128] Solid state NMR (ssNMR) is useful for studying large systems in a native context, isotope labelling can provide insight of individual components within a complex, without concerns of size-limitation.[129] However, owing to the incomplete averaging of anisotropies ssNMR has broader linewidths than liquid-state NMR. The latter is more frequently used in a biological context. Nevertheless, the opportunity to enhance solid-state NMR signals via dynamic nuclear polarisation (DNP) allows interrogation of systems of tremendous complexity.[130]

Cryo-EM is increasingly used to study biomolecular assemblies that are non-permissive to crystallisation. Generating an ensemble of three-dimensional structures, cryo-EM has utility in characterising heterogeneous sub-populations, which is often not possible using X-ray crystallography. Additionally, sample preparation on a shorter timescale than crystallisation provides greater sensitivity to weak non-covalent interactions between molecules. A recent example involved the trapping of the $\alpha_2\beta_2$ ribonucleotide reductase holo-complex,[125] where slowing the dissociation rate to the minute time-scale allowed detection of the complex via cryo-EM. However, the required technical expertise and access to facilities can be limiting.

FRET is appealing in complex systems with multiple components, as ‘multi-colour’ approaches using different fluorophore labels for the components of heteromultimers mean interactions between specific partners can be followed *in vivo*.[131,132] Even so, FRET is commonly limited to pairwise distances, but can provide long-range distance constraints with single molecule sensitivity at ambient conditions.[48] However, FRET requires the use of pairs of large labels, which can perturb native structure and binding interactions and gives rise to uncertainties in the orientation factor needed for accurate distance extraction. One technique which has developed very promising methodologies for the study of biomolecular binding and interactions is EPR spectroscopy.

As discussed above, EPR is a methodology exclusively and exquisitely sensitive to paramagnetic centres with unpaired electron spins. Especially the more recent pulse techniques are ideally suited to bridge the disconnect between local atomistic structural information and lower resolution topologies. Particularly, PD-EPR can provide longer range distance information than typically accessible by NMR, in favourable cases exceeding 100 Å.[133] While the sensitivity of PD-EPR is not yet comparable to optical methods, the often-required labelling is commonly less structurally perturbative than in FRET; spin labels are significantly smaller than comparable fluorophores. In this purview, PD-EPR is useful for coupling structural information and binding events. Here, the state-of-the-field of EPR applied specifically to non-covalent interactions and associated binding equilibria is discussed.

1.4 EPR Methods to Characterise Non-Covalent Binding Equilibria

1.4.1 Continuous Wave EPR

Continuous-wave EPR is sensitive to binding equilibria through changes in spectral line-shape. Broadly, this manifests by three main mechanisms: i) altered molecular dynamics (i.e., changes in the rotational correlation time, τ_c) or relaxation behaviour upon complexation, resulting in inhomogeneous or homogeneous line broadening, respectively, (figure 1.4.1.1) ii) introduction of new interactions (often dipolar coupling of unpaired electron spins), leading to line splitting or broadening, (figure 1.4.1.2) and iii) structural changes inducing altered spin Hamiltonian parameters, yielding differential spectral line-shapes amongst bound and unbound subpopulations (figure 1.4.1.3). One should bear in mind that these methods are indirect reporters of macromolecular interactions; the spectral line-shape is a convolution of homogenous and inhomogeneous line-broadening and accurate analysis relies on components being separable.[39]

Changes in τ_c have been used to monitor binding events between protein monomers[134] and between nucleic acids and small molecules.[135,136] This method allows interactions to be followed under native conditions,[137] *in vivo*[138] and in real-time to provide insight into kinetics.[139,140] It was possible to extract quantitative kinetics in the cyanobacterial circadian clock *in vitro* in a real-time CW-EPR assay over several days,[141] studying the circadian assembly and disassembly of its components based on changes in τ_c. Quantifying τ_c is useful in spin-labelled systems interacting with a diamagnetic partner (where the effects of potential dipolar broadening are absent), and in epitope mapping[142] when coupled with mutational analysis. However, labels with high intrinsic flexibility are insensitive probes to monitor changes in molecular backbone dynamics. Introducing artificial amino acids with paramagnetic moieties rigidly fixed to their backbone structure can improve sensitivity,[143] although it can be impracticable in large peptides. Furthermore, this method is dependent on both the paramagnetic species, and the chosen frequency-band; spin labels with greater anisotropy can provide sensitivity to faster timescales when measured at higher frequencies.[144] Solution-state nitroxide-based CW-EPR performed at X-band is typically sensitive to rotational correlation times on the scale of 10^{-11}-10^{-7} seconds, before being well into the isotropic and rigid limits, respectively.

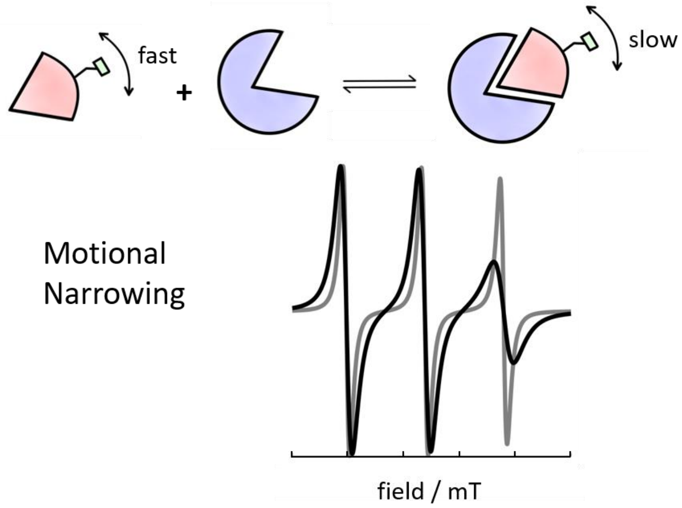

Figure 1.4.1.1: Monitoring of interactions *via* motional narrowing. The minor circular sector represents a monovalent ligand, the major circular sector represents a protein, and the square tag represents a paramagnetic spin label. The left-hand side of the reaction scheme is represented by the grey EPR spectrum, while the right-hand side of the reaction scheme is represented by the black EPR spectrum.

Dipolar line-broadening is another method to monitor binding interactions via CW-EPR,[145] particularly between multiple spin-labelled or paramagnetic species, and occurs in systems where electron spins are coupled through space. Thus, dipolar line-broadening is appealing in monitoring oligomerisation,[37,38,146] or in systems with known conformational changes upon ligand binding, that bring spin labels into a distance range between 8 and 25 Å. However, this approach requires measurement of both coupled and uncoupled spin systems to accurately assess the dipolar line-broadening, which requires control samples and can be practically difficult in homo-multimers. When monomeric subunits cannot be measured in isolation, appropriate diamagnetic spin dilution can provide a statistical label distribution and facilitate measurement of the singly labelled homo-multimer.[147]

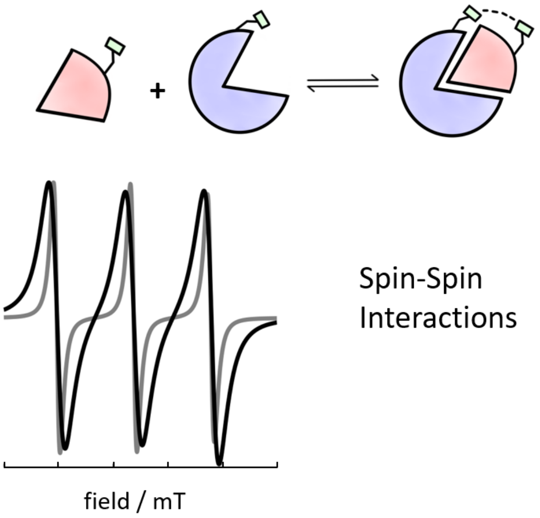

Figure 1.4.1.2: Monitoring of interactions *via* spin-spin interactions. The minor circular sector represents a monovalent ligand, the major circular sector represents a protein, and the square tag represents a paramagnetic spin label. The left-hand side of the reaction scheme is represented by the grey EPR spectrum, while the right-hand side of the reaction scheme is represented by the black EPR spectrum.

The Spin Hamiltonian parameters provide a phenomenological means to monitor structural and electronic changes, manifest as altered system parameters since they describe all the interaction energies in a spin system. More broadly, simulation of distinct spectral components is a powerful method to quantitatively assess linear weighted contributions of sub-populations to composite spectra; this approach has been used extensively to monitor metal ion binding within proteins.[148] Furthermore, dissociation constants have been determined for both protein–protein[149] and protein–ligand[150] interactions based upon spectral changes, by deconvolution of experimental spectra into bound and unbound populations.

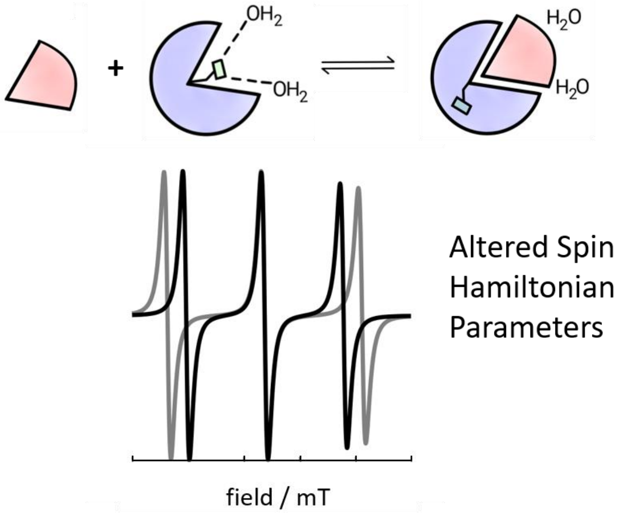

Figure 1.4.1.3: Monitoring of interactions *via* altered Spin Hamiltonian parameters. The minor circular sector represents a monovalent ligand, the major circular sector represents a protein, and the square tag represents a paramagnetic spin label. The left-hand side of the reaction scheme is represented by the grey EPR spectrum, while the right-hand side of the reaction scheme is represented by the black EPR spectrum.

A common electronic structural change is altered ligand field symmetry; the increased zero-field splitting of Mn^{II} upon coordination by MnxG was used to monitor kinetics of binding.[151] Changes in spectral parameters are especially useful reporters of interactions if coupled with robust multi-frequency simulations.[152] However, this methodology can be vulnerable to overfitting, therefore in systems with more than two components, additional biophysical techniques may be necessary to validate spectral simulations.[153] In the extreme case, charge transfer processes can remove paramagnetic centres and thus abolish the spin Hamiltonian altogether, resulting in a quenching of the spectral line. This has proved instructive in elucidating mechanistic understanding in protein redox chemistry.[154,155] While dipolar coupling is often analysed *via* convolution with a dipolar broadening function with a different susceptibility to experimental noise than direct superposition of spectral components, the robustness of all three approaches will greatly improve given spectral differences between bound and unbound components are sufficiently large to be resolved. In cases where this is ill met there is a potential risk of overfitting.

In conclusion, CW-EPR is a valuable method to probe biomolecular interactions, and can provide structural, kinetic and thermodynamic insight. However, in most cases CW-EPR only allows indirect measurement of binding events. Furthermore, quantitative analysis of CW-EPR spectra is often constrained by parametric models and thus relies on a priori knowledge of the system. This is a significant limitation, particularly because observing binding directly removes dependence on such parametric models and is more robust and facile than indirect detection; pulse EPR methods have subsequently found increased appeal as additional tools for investigating binding events.

1.4.2 Pulse EPR

Pulse EPR spectroscopic methods allow direct measurement of binding events by isolating specific terms in the spin Hamiltonian. This typically involves two spin coupling regimes: i) hyperfine couplings arising from electron–nuclear interactions, and ii) dipolar couplings arising from electron–electron interactions. Hyperfine spectroscopy methods may provide direct evidence of binding events in the frequency domain by virtue of nuclear Larmor precession, and the relative intensities of the frequency peaks, (figure 1.4.2.1.1). On the other hand, dipolar spectroscopy can provide direct evidence of binding in the time domain, manifesting in the modulation depth (Δ) (i.e., the percentage of electron spins coupled through space contributing to the signal), (figure 1.4.2.2.1.1). Additionally, dipolar spectroscopy can also give indirect evidence of interactions in the distance domain, via a conformational change coupled to the binding event (figure 1.4.2.2.2.1).

1.4.2.1 Electron Nuclear Spin Coupling

Electron–nuclear interactions can provide valuable insight into ligand binding environment and ternary complex formation *via* fingerprinting of the coordinating nuclei. This hyperfine coupling is typically probed by two main strategies: i) electron spin echo envelope modulation (ESEEM)[156,157] that is most sensitive for weak coupling interactions to quadrupolar nuclei and at low fields owed to reliance on forbidden transitions, and ii) electron-nuclear double resonance (ENDOR)[158,159] for strongly coupled nuclei often attractive at higher frequency due to dispersion of nuclear frequencies. Therefore, ESEEM and ENDOR offer complementary information in different regimes of hyperfine couplings. An additional technique is electron-electron double resonance (ELDOR)-detected NMR (EDNMR),[160,161] which is also sensitive to strong-coupling interactions but has improved sensitivity compared to ENDOR.[162]

ESEEM has been used extensively to characterise metal ion binding within proteins, particularly Cu^{II}-binding to proteins involved in amyloidogenic disorders.[163–167] Notably, integrated Fourier Transform ESEEM spectra were used to count backbone and imidazole nitrogen atoms coordinating Cu^{II} in amyloid-β, and demonstrated component II contains single histidine coordination, with histidine residues 13 and 14 favoured as equatorial ligands compared to histidine residue 6.[168] Another study using ESEEM and CW-EPR to investigate Cu^{II}-coordination in the human copper transporter CTR1 showcased the role of histidine residues 5 and 6, by comparing reduced ^{14}N ESEEM oscillations in H5A and H6A mutants with WT peptide.[169] Additionally, the nitrogen ESEEM modulation depth quantified the binding affinity of Cu^{II}-iminodiacetic acid (IDA) for α-helical and β-sheet double-histidine motifs in *Streptococcus sp. G.* protein G, B1 domain (GB1) and confirmed double histidine coordination.[170] Furthermore, a combination of ESEEM and hyperfine sub-level correlation (HYSCORE) spectroscopy was used to investigate the influence of pH upon Cu^{II}-binding to the active site of D. *melanogaster* Lysyl Oxidase (LOX).[171] Results indicated that under high pH conditions (pH 9.3) the Cu^{II} is uniformly coordinated in an environment containing a single histidine residue, but under physiological pH (pH 7.5), the Cu^{II} is instead coordinated in two equivalently populated environments containing one and three histidine residues, respectively. A novel Mn^{II} binding site in human Calprotectin, coordinated by six histidine residues was characterised using two-, three- and four-pulse ESEEM.[172] Quantification of the ^{15}N four-pulse ESEEM combination peak showed that the Mn^{II} binding equilibrium could be shifted from multiple lower affinity sites to the high-affinity hexa-histidine site, upon addition of Ca^{II}.

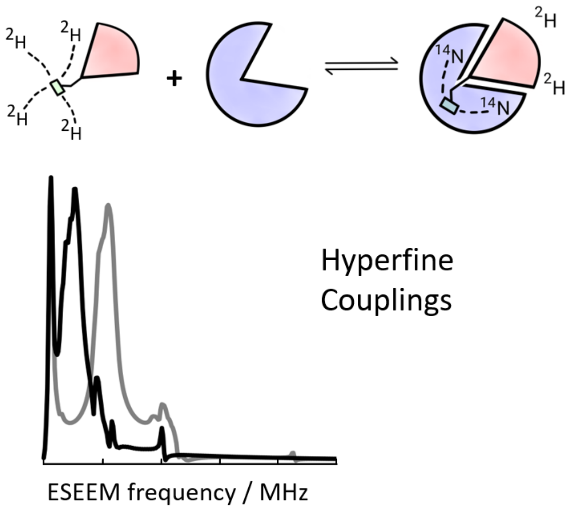

Figure 1.4.2.1.1: Monitoring of interactions *via* hyperfine couplings. The minor circular sector represents a monovalent ligand, the major circular sector represents a protein, and the square tag represents a paramagnetic spin label. The left-hand side of the reaction scheme is represented by the grey EPR spectrum, while the right-hand side of the reaction scheme is represented by the black EPR spectrum.

Conversely, ENDOR is an appealing strategy to investigate interactions within nucleotides, especially at Q- and W-band frequencies where the coupling originating from ^{31}P in the phosphate backbone is too large to be detectable by routine ESEEM measurements. ENDOR is also increasingly combined with EDNMR because of improved sensitivity, and an absence of blind spots in the EDNMR spectrum. Additionally, quantitation of peak intensities is more straightforward when compared to both ENDOR and ESEEM, and therefore EDNMR is a powerful tool that has been appropriated to directly quantify equilibrium sub-populations.[173] However, while EDNMR is useful in the study of interactions with low-γ quadrupolar nuclei, the improved sensitivity compared to ENDOR is compromised by a loss in the line-shape information and subsequent resolution (i.e., the central hole can mask signals manifesting from low frequencies).

Notably, ^{31}P hyperfine couplings can provide insight into the catalytic cycles of systems with ATPase activity, particularly those amenable to substitution of diamagnetic divalent metal cofactors with paramagnetic analogues. For example, substituting a Mg^{II} cofactor for paramagnetic Mn^{II} in the chaperone Heat Shock Protein 90 (Hsp90)[174] allowed investigation of the ATP hydrolytic cycle using ^{31}P ENDOR. While the ATP-bound state had been studied extensively, the ADP-bound (post-hydrolytic) state has been identified to be involved in recruitment and chaperoning of client proteins, and was found to be in a 'compact' configuration in solution. This approach has been suggested as broadly applicable to other systems utilising Mg^{II} cofactors and driven by ATP-hydrolysis. In another study, a combination of ENDOR and EDNMR allowed identification of different nucleotides coordinated to a Mn^{II} cofactor in the nucleotide binding site of a pair of ABC exporters, homodimeric MsbA and heterodimeric BmrCD, and revealed how their ATP turnover kinetics differed.[175] These results support the postulated mechanistic divergence of ABC exporters in dependence of their nucleotide-binding domains with slower sequential ATP-hydrolysis in heterodimeric exporters, compared to homo-dimeric exporters. 2D EDNMR was used to correlate ^{31}P and ^{13}C cross-peaks,[176] combined with ^{13}C ENDOR to detect a ternary complex of a synthetic tetracycline (TC) RNA aptamer, TC and Mn^{II}.

1.4.2.2 Electron Electron Spin Coupling

1.4.2.2.1 Direct Measurement of Binding Affinity

It was recognized as early as 1984 that PD-EPR could principally be used to assess multimerization via spin-counting.[177] Here, we can define the modulation depth[178] (Δ) mathematically and relate this to the number of coupled electron spins (N):

$$\Delta = 1 - (1 - f\lambda)^{N-1} \tag{1.4.2.2.1.1}$$

where λ and f are the inversion efficiency of the pump microwave pulse, and the labelling efficiency, respectively. Importantly, for a constant labelling efficiency, as inversion efficiency increases (e.g., in the RIDME experiment,[179,180] where $\lambda_{max} = 0.5$, for $S = 1/2$ systems) modulation depths become non-linear. Furthermore, it should be noted that while this relationship is conceptually valid for all PD-EPR experiments, it has only been empirically validated for the 4-pulse pulse electron–electron double resonance (PELDOR) experiment.[181]

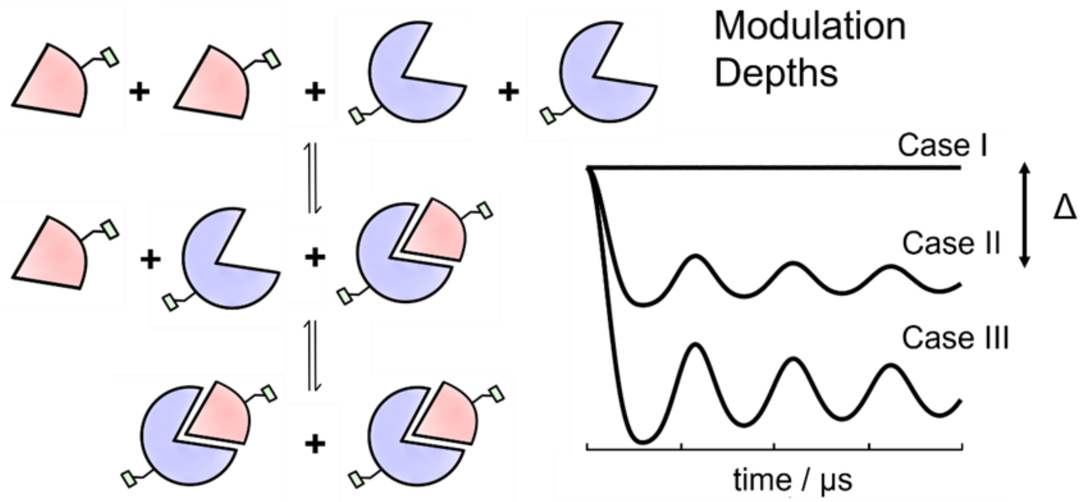

Figure 1.4.2.2.1.1: Monitoring of interactions directly *via* modulation depths. The minor circular sector represents a monovalent ligand, the major circular sector represents a protein, and the square tag represents a paramagnetic spin label. Each row of the reaction corresponds to each row of the background corrected dipolar evolution function of simulated PELDOR data. The modulation depth parameter (Δ) is indicated.

Since this time, PD-EPR has been used to disentangle competing structural models,[63,182] metal–ligand binding,[67,70] and cooperativity of binding.[68,69] Modulation depth quantification is arguably the most direct way to investigate binding equilibria via PD-EPR, and one of the most sensitive. Considering a binary interaction between quantitatively labelled macromolecules that each contain identical paramagnetic moieties, only dipolar-coupled electron spins (i.e., the fraction of molecules that form an intermolecular complex) will modulate the detected echo, representing the weighted contributions of signals arising from macromolecules in the free and intermolecularly bound states. This fraction is reported by the modulation depth. By systematically titrating the binding partners (e.g., ligand against a fixed protein concentration) the equilibrium can be characterised. There are several examples of using PELDOR modulation depths to determine association constants in monomer-dimer, or more complex equilibria,[77,183–187] or to infer respective affinities.[188] PELDOR has also been used to investigate stoichiometry of binding,[189] and the stability of nucleic acid complexes.[190]

The strengths of this approach to investigate macromolecular interactions directly, compared with indirect methods are multifaceted. Modulation depth quantification is more robust than quantification of populations from PD-EPR distance distributions because it is not predicated on detectable conformational changes upon ligand binding. Perhaps more significantly, the probability of false-positive errors (i.e., modulation of the detected echo when interaction does not occur) can be minimised by measuring negative control samples where the interaction is knocked out. However, false-positive errors are feasible as the result of sub-optimal estimation of the background function; the necessity for high-quality time domain data is therefore crucially important in modulation depth quantitation. Additionally, from a simply qualitative perspective modulation depth can provide a Boolean assessment of interactions in the system under investigation. This is rarely possible using indirect methods such as CW-EPR, outside of charge transfer or quenching reactions (see Section 1.4.1).

The potential of modulation depths to report equilibrium populations is broadly leveraged on two factors: i) accurate background correction to faithfully separate the modulated and unmodulated components of the detected echo from the echo decay and ii) to robustly separate and quantify the modulated and unmodulated contributions neither should be vanishingly small as the sensitivity to changes would diminish within experimental noise. While the PELDOR background is best understood, achievable modulation depths are frequently constrained by low inversion efficiency (λ) of rectangular microwave pulses, particularly in paramagnetic centres with broad spectral lines such as many metal ions. This is frequently remedied through application of shaped-pulses and AWGs.[191,192] Nevertheless, single-frequency techniques such as RIDME,[179,180] double quantum coherence (DQC) filtered EPR[18] and single-frequency technique for refocusing (SIFTER)[19] can yield significantly improved sensitivity. Although this has not been shown comprehensively for all methods discussed, conceptually all signals will be superpositions of modulated and unmodulated echoes, representing bound and unbound components. Thus, there is significant scope to increase sensitivity to weak binding events by single-frequency methods.

A potential caveat of quantifying modulation depths to monitor macromolecular interactions is that both interacting species must contain a paramagnetic moiety, otherwise the modulation depth will remain constant. Particularly in the case of small molecule effectors, introducing paramagnetic moieties or using analogues can risk structural perturbation and disrupt the interaction. Additionally, in multibody systems modulation depths may not resolve all distinct pairs of interacting species. It may then be desirable to correlate modulation depths between individual sets of spin-pairs, which can be accomplished through spin labelling with spectroscopically orthogonal paramagnetic moieties. These spin labels have distinct spectroscopic properties, such as not fully overlapping EPR spectra, or different relaxation behaviours. Such orthogonality allows each type of spin label to be addressed selectively, and their respective contributions to a modulated signal can be separated by an appropriate choice of experiment parameters. However, this is often a laborious process, and may require additional sample preparation and control measurements. Instead, in favourable cases[71,193] all permutations of the interacting species yield unique and detectable distances, and sub-populations can be quantified in the distance domain without the need for spectroscopically orthogonal labels.

1.4.2.2.2 Indirect Measurement of Binding Affinity

PD-EPR can also be used to monitor binding equilibria indirectly in the distance domain. The dipolar evolution function can be transformed into a distance distribution by regularisation procedures and shifts in peak intensities can provide a proxy for direct detection of free and bound sub-populations. Of course, this presupposes that the interaction under investigation is coupled to a conformational or structural transition on a scale detectable by PD-EPR, which is a dichotomous problem; differences between conformational sub-ensembles should be as large as possible but not outside the range of reliable distance detection. In favourable cases it will be possible to extract orientation information in addition to the distances.[194,195] The coupling of conformational transitions with ligand binding or protein–protein interactions is a common motif in evolution to modulate binding affinity.

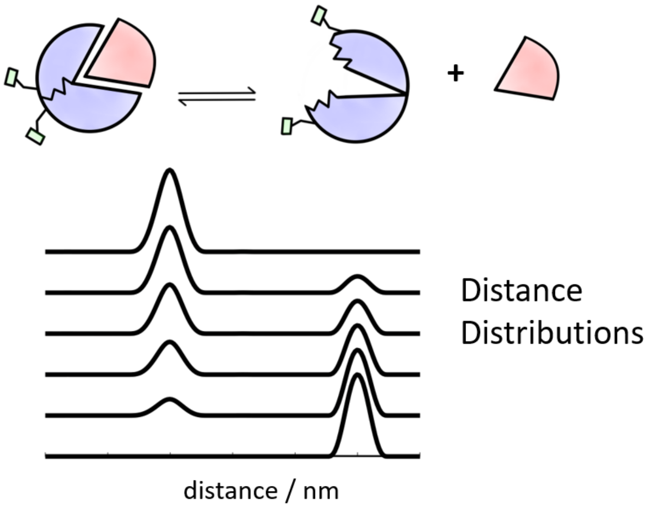

Figure 1.4.2.2.2.1: Monitoring of interactions indirectly *via* distance distributions. The minor circular sector represents a monovalent ligand, the major circular sector represents a protein, and the square tag represents a paramagnetic spin label. The left- and right-hand sides of the reaction scheme are represented by the left and right peaks in the distance distribution.

For the modulation depth to be a sensitive reporter of binding interactions, they must involve (at least) pairs of species; otherwise, the modulation depth remains constant. Therefore, shifts in distance distribution peaks can be advantageous in monitoring diamagnetic ligand or metal ion binding events, where the modulation depth is otherwise unchanged. Several studies have successfully interpreted conformational equilibrium populations from integrated distance distribution peaks in synthetic model systems,[196] globular proteins,[197] transmembrane ion transporters,[71,72,198,199] and signal transduction proteins.[200,201] An additional benefit of this approach is that it can be used to quantify populations of multiple conformational states from a single series of measurements. Furthermore, monitoring binding equilibria in the distance domain affords structural insight, while modulation depth alone does not.

For N-degree singly spin-labelled homo-multimers, this yields at least N-fold coupled unpaired electron spins and causes deviations from the spin-pair approximation in the standard Tikhonov regularisation kernel of DeerAnalysis,[21] a commonly used software in the processing of PD-EPR data. Multi-spin effects manifest from this interaction as sum and difference combination frequencies[202] being mapped to the distance domain. Significantly, these peaks do not correspond to distances between spin labels in physical space, and so are referred to as ghost peaks.[203] This phenomenon can often complicate distance distribution analysis owing to an artificial peak broadening and suppression, particularly at longer distances.[75] This is problematic in both systems with multiple conformational states and where structural models are not available.

Several strategies have been developed to suppress multi-spin effects at the level of sample preparation,[54,204] data acquisition,[205–207] and in post-processing.[203] However, ghost peaks can also be diagnostic of complex formation in the distance domain, as was demonstrated for ternary complexes of metal ions and nitroxide terpyridine ligands.[69] Furthermore, the oligomeric state of the *Anabaena*

Sensory Rhodopsin (ASR) was confirmed as trimeric[208] by comparing experimental and simulated dipolar evolution functions with N coupled electron spins (*vide supra*, regarding spin-counting *via* PD-EPR). Very recently oligomerisation degree could be derived by multi-quantum counting in trityl labelled model multimers.[209]

However, quantification of distance distribution peaks is often less stable than direct analysis of time-domain data, owing to the need for a subjective regularisation step. Additionally, arbitrary selection of integration boundaries of distance peaks is likely to compound this problem and may result in confirmation bias by the user. In this case, model-free multi-Gaussian fitting is a viable option to circumvent the need for a regularisation step.[210–213] Furthermore, several recent studies have concerned how to streamline dipolar EPR data processing and optimise the regularisation parameter.[214–216] As mentioned above, high-quality time-domain data is necessary to ensure distance distribution peaks can be integrated reliably, and quantification is predicated on the assumption that binding events are coupled to detectable conformational transitions, a condition not well met for all systems.

1.5 Examples of EPR Applications to Study Binding Equilibria

1.5.1 Altered CW-EPR Spectral Lineshape

A particularly significant branch of non-covalent interactions involves the study of protein misfolding events and pathological protein fibrillation; understanding the structural alterations that accompany these deleterious transitions is of paramount importance in developing targeted therapeutic drugs. In this regard, CW-EPR has proved especially useful as a tool to probe the associated kinetic and dynamic processes with individual monomer resolution. For instance, aggregation kinetics of Δ*tau*-187 were investigated using rotational correlation times, and linear combinations of mobile, immobile, and spin-exchanged components.[146] Importantly, the spin-exchanged component was absent for residues 400C and 404C throughout the aggregation process indicating that the C-terminal region of the protein remains flexible. In another study, three-component simulations of CW-EPR spectra suggested the proliferation of amyloid-β plaques is mediated by the concentration of sodium-dodecyl sulphate (SDS), indicating incorporation of detergent molecules into the aggregates.[217]

Spin labels with high intrinsic flexibility can be ill-suited to report changes in molecular backbone dynamics upon binding or oligomerisation. Indeed, this emphasizes the need for highly rigid spin labels with short tethers, where motion is not dominated by rotation about bonds linking the paramagnetic moiety to the protein backbone. An example is the artificial amino acid 2,2,6,6-tetramethyl-N-oxyl-4-amino-4-carboxylic acid (TOAC) quantitatively incorporated into amyloid aggregates using solid phase peptide synthesis (SPPS) to approximate the number of monomers in the aggregates by monitoring a respective increase in the rotational correlation time and spectral simulation.[143] Importantly, in this example the model peptide was only 13 amino acids long and therefore TOAC could be directly incorporated during synthesis. This strategy is not amenable to all systems and genetically encoded spin-labels that self-assemble are sometimes preferable to improve labelling efficiency in larger peptides, however these often cannot compete with TOAC rigidity. Genetically encoding a motif for self-assembling spin-labelling was initially demonstrated for Cu^{II} binding to a double histidine motif in nitroxide-labelled T4 lysozyme,[218] and later in the membrane protein Lactose Permease to confirm the α-helical packing structure.[219]

An illustrative example of how CW-EPR has also been appropriated for the optimisation of genetically encoded double-histidine based spin labels is a study by Lawless *et al*.[170] Here, the formation of the Cu^{II}-IDA chelate for labelling of engineered double-histidine motifs was monitored by shifts in the $A_{\parallel}$ and $g_{\parallel}$ components between the free Cu^{II} and Cu^{II}-IDA complex. The authors could show that adding a stoichiometric amount of IDA only resulted in ~65% complexation, even at 500 µM Cu^{II} concentration. Instead, complexation of ~80% could be achieved by adding 2 molar equivalents of IDA, and complexation formation plateaued at higher equivalents. CW-EPR has also been used in the characterisation of protein–protein[38,134,138] and protein–nucleic acid interactions,[140] small molecule binding events,[137,139,150,220] the validation of predicted in silico trends in affinity based on structural modelling,[142] and determination of Michaelis constants.[221] Development of a bifunctional spin label also allows immobilisation and surface-ligand binding studies in proteins.[222]

Importantly, Lawless *et al*. could show that while formation of bis-IDA complex was favoured at excess IDA concentrations, in presence of another coordinating ligand such as imidazole, formation of the bis-complex was inhibited. This is significant because only the mono-complex of Cu^{II}-IDA can effectively coordinate to double-histidine motifs, while the bis-complex has all four equatorial coordination sites occupied and free Cu^{II} will bind the conjugate bases of acidic amino-acid residues non-discriminately. The authors also estimated apparent dissociation constant (K_D) values from CW-EPR for the interaction between Cu^{II}-IDA and two configurations of double histidine motifs. However, it should be noted that all measurements were performed at 500 µM protein concentration, meaning these apparent K_D values are likely only lower-bound estimates of affinity. This emphasizes the need for caution when using CW-EPR to determine K_D in the absence of other complementary approaches that can yield more complete thermodynamic information. An example of using a combination of CW-EPR, ENDOR and UV–vis spectroscopies to determine both kinetic and dissociation constants is a recent study of the cytochrome P450 enzyme CYP121.[223]

1.5.2 Quantification of Hyperfine Couplings

Hyperfine spectroscopy is a particularly valuable toolbox in characterising the binding environment of small molecule effectors and can yield insight into both inner and outer coordination-sphere interactions of paramagnetic metal ions. Significantly, this allows hyperfine spectroscopy to bridge the local and long-range structural information provided by CW-EPR and PD-EPR methods, respectively. For instance, a combination of ESEEM and CW-EPR was used to investigate the Mn^{II}/Mn^{IV} redox cycle of the multi-copper oxidase MnxG protein.[151] Here, three populations of Mn^{II}-containing species were detectable in the reaction mixture, and quantification of ^{14}N and ^{2}H ESEEM modulation depths calibrated against other systems with known coordination environments allowed counting of the nitrogenous and solvent coordinating ligands, respectively. The multi-copper oxidase complex performs a two-electron oxidation of Mn^{II} to Mn^{IV} and assistance of the binding site in tuning the Mn^{II} redox potential is postulated. The coordination environment of Mn^{II} in the MnxG protein was shown to contain two solvent water molecules and one histidine residue. Additionally, the observation of a weakly exchange-coupled Mn^{II}-Mn^{II} dimer by CW-EPR allowed proposing mechanistic details for Mn^{II} binding and oxidation.

Another example of quantifying ESEEM and ENDOR to determine distinct binding environments for sub-populations in frozen solution was shown by Gagnon *et al*.[172] Here, the human Mn^{II}-sequestering protein Calprotectin was shown to coordinate Mn^{II} *via* a novel hexa-histidine high-affinity binding site. Residues H103 and H105 of the C-terminal tail were speculated to be mechanistically significant in the exclusion of solvent water from the binding site, and quantification of ^{2}H ESEEM modulation depths indicated one or two inner-sphere deuterons in H105A and H103A constructs, respectively. Therefore, this study demonstrates the power of hyperfine spectroscopy and EPR more broadly to intimately couple structural and thermodynamic insight. Hyperfine spectroscopy has been used extensively in many other systems to investigate non-covalent interactions.[171,173–176]

Additionally, Calprotectin is a heterodimer of S100A8 and S100A9 subunits and isotopic enrichment with ^{15}N eliminated the quadrupolar interaction inherent for naturally abundant ^{14}N; this allowed quantitative determination of the number of coordinating nitrogenous ligands based on the intensity of the ^{15}N combination peak in 4-pulse ESEEM. 4-pulse ESEEM was also used to monitor Mn^{II}-Calprotectin speciation in the absence of Ca^{II}; interestingly Mn^{II} binding became promiscuous: the ^{15}N combination peak intensity corresponded to coordination by 2.6 nitrogen ligands, as opposed to 6 nitrogen ligands in presence of Ca^{II}, suggesting approximately 50% occupancy of the high-affinity hexa-histidine site. Furthermore, ^{2}H ESEEM modulation depths in the absence of Ca^{II} could be fitted as a linear combination of ESEEM signals from hexaaqua-Mn^{II} and of Mn^{II}-Calprotectin in presence of Ca^{II}, and so the authors concluded that Ca^{II} was necessary to promote specific and high-affinity Mn^{II}-binding and sequestration.

1.5.3 Quantification of Modulation Depths

Hetero- and homo-oligomerisation events represent another class of non-covalent interactions that are encountered frequently across all domains of life.[224] These interactions are crucially important in the evolution of novel functionality and activity in complex multicomponent systems[225] and the cellular machinery.[226] Membrane ion channels are a notable example where oligomerisation has facilitated incredible diversification of protein function and are particularly interesting as potential drug targets. Indeed, over 60% of all current therapeutics target membrane protein interactions.[227] Determination of the oligomeric state of a system can therefore provide mechanistic insight and is accessible through modulation depth quantitation and spin-counting using PD-EPR. For instance, three-pulse PELDOR indicated that the peptaibol Alamethicin exists in equilibrium between monomers, dimers and pentamers;[228] this oligomeric polydispersity facilitates formation of differently sized ion channels in bacterial membranes, causing lethal ion permeation. An inhibitor-based spin label was used to investigate the dimerisation mode of the receptor tyrosine kinase epidermal growth factor receptor.[229] The protein was predicted to form asymmetric (active) and symmetric (inactive) dimers in solution, based on crystallographic data. Results suggested that interface mutations inhibited formation of the active dimer, and caused adoption of a monomeric state, as opposed to the predicted symmetric dimers.

Another illustrative demonstration of quantifying modulation depths to directly determine the mechanism of oligomerisation in an ion channel protein is a study by Georgieva *et al*.[184] Here, Influenza A M2 transmembrane domain (TMD) was shown to exist in an equilibrium of tightly interacting dimers, and weakly interacting functional tetramers (as dimers-of-dimers). The efficiency of the TMD self-association was shown to be influenced by the protein-to-lipid ratio; increasing this ratio led to monotonically increasing PELDOR modulation depths. However, at all protein-lipid ratios the observed modulation depths were consistently lower than predicted for complete tetramerisation, instead indicating polydispersity with dimeric species dominating at very low protein-to-lipid ratios. Modulation depth quantification has been applied successfully to study many other complex protein[77,183,185,186,230,231] and nucleic acid[188,190] conformational and thermodynamic equilibria.

Importantly, this study also showcases the utility of modulation depth quantification for studying subtle changes in equilibrium populations under disparate sample conditions, namely at pH 5.5 compared with pH 8.0. The authors performed a global fit of both pH series and could therefore differentiate between the proposed monomer-to-tetramer kinetic scheme, and a tandem model in which a monomer-to-dimer transition is followed by a consecutive dimer-to-tetramer transition. More recently, the hydrolytic cycle of Hsp90 was also investigated by modulation depth quantitation in presence of ATP (pre-hydrolysis state), ATP and Vanadate (trapped high-energy state), and ADP (post-hydrolysis state). The authors could nicely reconcile increasing modulation depths throughout the cycle with K_D values taken from literature.[174]

Lastly, one advantage of using modulation depth quantitation compared to ITC, SPR and other more established techniques to monitor complex equilibria is the additional distance information allowing to assign the quantitative interaction to structure, as well as the potential for obtaining multiple modulation depths from a single sample when using orthogonal labelling. In contrast, ITC and SPR typically provide only a single observable into which all interactions are subsumed which requires careful experiment design to prevent over-fitting. Introducing the dipolar interaction through a spin label that is not contributing to the detected echo (*e.g.,* in RIDME or PELDOR with orthogonal labels) can provide information on practically non-saturable or nonspecific binding events, which can be notoriously difficult and expensive to analyse using other techniques.

1.5.4 Quantification of Distance Distribution Peaks

Small molecule effectors are ubiquitous throughout nature, modulating the relationship between macromolecular structure and function. From a thermodynamic perspective enthalpically unfavourable ligand binding can achieve net free-energy gain through coupling with a structural transition that increases the entropic component of the free-energy landscape, and *vice versa*. Therefore, PD-EPR is well-suited to monitor such binding events in the distance domain. For instance, a thermophilic cytochrome P450 family protein (CYP119) undergoes a disordered-to-ordered transition upon binding of lauric acid, which could be followed as changes in the PELDOR distance distribution.[232] Along the same concept, the influence of preventing lipid penetration into nano-pockets of the mechanosensitive ion channel MscL was investigated by PELDOR through sulfhydryl modification, and the channel conformation was monitored. Results suggested that lipids behave as negative allosteric modulators, wherein their absence within the nano-pockets lowers the activation energy to channel opening.[65]

Disordered-to-ordered transitions are also common motifs in nucleic acid interactions, as the tertiary structure of the synthetic tetracycline RNA riboswitch was shown to be stabilised in presence of $\mathrm{Mg^{II}}$ using PELDOR, independent of the tetracycline ligand.[176] The distribution width decreased with increasing $\mathrm{Mg^{II}}$ concentration, indicating transition from an ensemble of metastable states to a global energy minimum. A similar reduction in conformational flexibility was monitored by PELDOR in the DNA cocaine aptamer upon ligand binding.[233] Another example for quantifying equilibrium populations from the distance domain is a study by Glaenzer *et al*. Here, neuraminic acid binding to a tripartite ATP-independent periplasmic (TRAP) transporter protein was shown to trigger the open-to-closed transition of the channel.[71] A K_D was determined for the interaction from integration of PELDOR distance distribution peaks, which was consistent with previous ITC data. Notably, the time-domain data could also be fitted as a linear combination of free and ligand bound states and could show the resulting simulations agreed nicely with experiment.

Importantly, this circumvented the Tikhonov regularisation step; the authors note that for the same time-domain data, this processing influences distribution shape and width in dependence of the selected regularisation parameter (a). By fitting the time-domain data directly, this removed the dependence of the calculated integrals upon the regularisation parameter, and additionally indicated no intermediate states in the energy landscape. Analysis of distance distribution peaks from PD-EPR has been used successfully to investigate conformational and binding equilibria in protein systems,[197–200,210,234–236] as well as in protein–nucleic acid,[59,237–239] and ligand–nucleic acid[240] interactions.

Perhaps most significantly for this study is that previous ITC studies had not detected any binding of neuraminic acid for a R125A construct. However, PELDOR was sufficiently sensitive to detect weak ligand binding. This suggests that PD-EPR may be especially suited to monitor weak binding interactions in concentration regimes where ITC is insensitive or impractical. An additional consideration beyond the scope of the initial study is the influence of temperature upon binding equilibria; this is most likely relevant for diffusion-limited high-affinity interactions, since even under snap-freezing conditions, the cooling rate is still comparatively slow. A recent study illustrated this point by comparing dissociation constants estimated from PD-EPR measurements in frozen solution and ITC measurements at room-temperature.[70] Results indicated the affinities reconciled if the ITC-derived value was extrapolated to cryogenic temperatures, 50–60 K below room-temperature where chemical dynamics freeze out. A further implication is that endothermic reactions may not be accessible under cryogenic EPR conditions, though this consideration could be overcome by measuring at ambient temperature (by altering the matrix composition or using different spin labels).

It is also worth noting that this strategy is often leveraged on the availability of high resolution cryo-EM or X-ray crystal structures to inform construct design. More broadly, the approach is also limited by the ability to resolve distinct conformers in the distance distribution in dependence of the rotameric freedom of the attached spin labels and is particularly challenging in systems with subtle conformational transitions.[66] The development of highly rigid genetically encoded double-histidine motifs to coordinate Cu^{II}-chelate labels has been shown to dramatically improve precision of distance determination in proteins and can potentially ameliorate this resolution issue.[241]

1.6 Aims and Motivation

In the context elaborated above, the main aims of this thesis involve the benchmarking of methodologies and development of mathematical descriptions to quantitatively characterise non-covalent binding equilibria. Specifically, this is achieved by quantifying Cu^{II}-nitroxide and Cu^{II}-Cu^{II} RIDME modulation depths. Indeed, previous publications have established that RIDME modulation depths reported complexation, and used qualitative descriptions to rationalise observed trends.[67,68] However, quantification of binding constants in this way is highly promising because it accesses this information with greater concentration sensitivity compared with other techniques, such as ITC, and so is especially appealing in cases where material is limiting. Therefore, this also motivated a systematic investigation of the concentration sensitivity of Cu^{II}-nitroxide and Cu^{II}-Cu^{II} RIDME. An additional aim was further characterisation of an emerging non-covalent spin labelling strategy using double-histidine motifs and Cu^{II}-chelates. The approach affords significantly enhanced precision and accuracy in the distance domain when compared with nitroxide-based spin labels, such as MTSL, making it tremendously useful to resolve subtle conformational changes and equilibria.[237,242]

Coupling these two aims, we found that not only is Cu^{II}-chelate coordination at double-histidine motifs an appealing spin labelling strategy, but also provides a tractable biological model of a non-covalent binding equilibrium, with modular complexity that is ideal for study by PD-EPR. However, it should be noted that the value of Cu^{II}-based double histidine motif spin labelling is leveraged upon high binding affinity under cryogenic conditions, which becomes particularly relevant for optimising Cu^{II}-Cu^{II} dipolar EPR measurements. In this purview, we were also motivated to develop a general mathematical description to optimise labelling efficiency in systems containing pairs of double-histidine motifs, which would allow the identification of predicted sensitivity optima in dependence of binding affinity prior to sample preparation and measurement. An additional aim was to further generalise this model to an arbitrary number of binding sites (nominally grouped into high- and low-affinity sites described by a pair of dissociation constants) to allow appropriation to more complex systems with >2 sites.

Additionally, while buffer conditions have recently been optimised,[243] the robustness of Cu^{II}-chelate binding at double-histidine motifs with regards to both fluctuations in buffer pH and the presence of adventitious divalent metal centres has not been shown in the literature, and so are investigated here under different temperature regimes, using Zn^{II} nitrilotriacetic acid (NTA) as a model competitor ligand. Application of Cu^{II}-nitroxide RIDME modulation depths to remotely study diamagnetic competitor binding kinetics at high concentration sensitivity is appealing for several reasons: i) it has potential to ameliorate economic and safety concerns regarding radiolabelled material used in conventional competitive binding assays, ii) it provides a potential avenue to investigate kinetics *via* dipolar EPR in systems where paramagnetic analogues of competitor ligands are unavailable or cause significant structural perturbation, and iii) it allows characterisation of competitor ligand binding interactions with much lesser material than by other methods, such as ITC.

1.7 Outline of Thesis Chapters

This section is intended to serve as a roadmap for the layout of the thesis.

In chapter 2 fundamental EPR theory is outlined. Contributions to phenomenological relaxation processes (section 2.3) and the Spin Hamiltonian (section 2.4) are described. The contributions to the pulse dipolar EPR signal are described analytically for PELDOR and RIDME experiments, (section 2.6) and the corresponding pulse sequences are discussed. Post-processing workflows of pulse dipolar EPR data are also outlined (section 2.7-9). Finally, analytical descriptions of the binding models used throughout this thesis are given (section 2.10).

In chapter 3, a quantitative single-site binding model is applied to describe Cu^{II}-nitroxide RIDME modulation depths and fit a dissociation constant. A model protein (GB1) with exogenously introduced double histidine motifs is used to benchmark the method. Pseudo-titration series (a titration with discrete samples prepared for each data point) measured at 75, 25 and 0.5 µM protein concentration are presented (section 3.3.11) and the measured binding affinity is in the high nM concentration regime for Cu^{II}-NTA at the α-helical double-histidine site. Exquisite concentration sensitivity of hundreds of nM, and numerical agreement within a factor 2 between ITC- and EPR-determined dissociation constants is also observed (section 3.3.11). Additionally, methods of data analysis are discussed, and the mathematical model is extended to two independent ligand-binding sites.

In chapter 4, the extended description of a two-site independent binding model is applied to describe Cu^{II}-Cu^{II} RIDME modulation depths and fit a pair of dissociation constants. GB1 containing two disparate double-histidine motifs is used to benchmark the method. Strong numerical agreement between the Cu^{II}-Cu^{II} and Cu^{II}-nitroxide RIDME-determined dissociation constants is observed and recapitulates an order of magnitude difference in affinity between α-helical and β-sheet double-histidine motifs (section 4.3.4) for Cu^{II}-NTA. The mathematical description is further generalised to arbitrary numbers of sites, governed by two dissociation constants. The model is applied to optimise sensitivity of Cu^{II}-Cu^{II} RIDME measurements, and limitations of the methodology are discussed (section 4.3.5).

In chapter 5, the influence of pH and the presence of a diamagnetic model competitor ligand on the labelling efficiency of double-histidine motifs is investigated using a combinative approach of room-temperature ITC and Cu^{II}-nitroxide RIDME measurements. A quantitative competitive binding model is applied to determine the dissociation constant of the diamagnetic ligand Zn^{II}-NTA from Cu^{II}-nitroxide RIDME modulation depths, where excellent numerical agreement of a factor 2 between ITC- and RIDME-determined dissociation constants is observed (section 5.3.4). Surprisingly, binding affinity in the high nM concentration regime is conserved at pH 6.4 and 8.4, with results suggesting there is a compensatory effect on binding affinity at low temperature, as the protonation of histidine residues is endothermic (section 5.3.4).

In chapter 6, conclusions and future directions are outlined. Pulse dipolar EPR is well suited to the quantitative investigation of non-covalent binding equilibria. Modulation depths of different pulse dipolar EPR experiments may present opportunities to study more complex binding equilibria, particularly in conjunction with orthogonal labelling. Prospectively, this may increase the accessible information content from a single measurement series, comparing favourably to ITC and SPR where multiple interactions may be subsumed into a single calorimetric or sensorgram output, respectively. In this purview, an analytical cooperative binding model (in which nitroxide-nitroxide PELDOR modulation depths inform metal-templated dimerisation, and Cu^{II}-nitroxide RIDME modulation depths informs the initial metal-binding step) is discussed.

CHAPTER 2: EPR Theory

This section is intended as a brief overview of semi-classical EPR theory, particularly of electron-electron dipolar coupling and the PELDOR and RIDME experiments. Additionally, modulation depths will be defined analytically and contextualised within a framework of non-covalent binding models derived from first principles. The EPR theory described herein can be found in several textbooks[244–246] and review articles.[40,85,247,248] Similarly, the binding models described herein are largely adapted from previous publications.[249–254]

2.1 The Magnetic Dipole Moment

From a macroscopic vantage, it is perhaps trivially observed that any body with angular momentum and non-zero electric charge will yield a magnetic moment. From the Stern-Gerlach experiment[255,256] (wherein magnetic momentum was first shown to be quantised), it is known that electrons possess an intrinsic angular momentum, $\boldsymbol{S}$, arising from the quantum property, spin. The corresponding magnetic moment of a particle, μ_i, with charge q and mass m can then be defined:

$$\mu = \frac{q}{2m}\hbar\boldsymbol{S} \tag{2.1.1}$$

Similarly, for an electron with charge, $-e$, and mass, m_e, the magnetic moment, μ_e, can be expressed as:

$$\mu = -g\beta_e\boldsymbol{S} \tag{2.1.2}$$

where: g is a factor that takes account of deviations arising from assuming a quantum object behaves as a classical charged particle. It is called the g-factor, and for the free electron is one of the most precisely determined physical constants. β_e is the Bohr magneton defined as:

$$\beta_e = \frac{e\hbar}{2m_e} \tag{2.1.3}$$

where: $\hbar$, e, and m_e are defined above.

The spin quantum number (i.e., the z-component of the spin angular momentum) of the electron, m_s, has a value of ± 0.5, such that we define two spin states: i) α ($m_s = 0.5$), and ii) β ($m_s = -0.5$), which for a single unpaired electron, ($S = 0.5$), are degenerate in the absence of an external magnetic field. In the presence of an external magnetic field, $\boldsymbol{B}$, the degeneracy of the α and β spin manifolds is removed, such that they align antiparallel or parallel to $\boldsymbol{B}$, with higher or lower energy, respectively. This interaction of the electron magnetic moment with the external magnetic field is called the Zeeman interaction, and for $S = 0.5$ systems under the high-field approximation is usually the dominant contribution to the spin Hamiltonian (see section 2.4). The splitting of energy levels for each spin manifold is given:

$$\Delta E = h\nu = g\beta_e B \tag{2.1.4}$$

This is the resonance condition, wherein irradiation of the system with energy quanta ΔE results in a transition from the β to the α spin manifold. This is at the heart of all EPR spectroscopy,[257] and underpins many subsequent experiments.[11,258–260]

2.2 The Magnetisation Vector and Hahn Echo

In the absence of an external magnetic field, the individual magnetic moments, μ_i, of each electron spin are randomly oriented in space. When an external magnetic field ($\boldsymbol{B_0}$) is applied, the magnetic moments will begin to precess on a cone around $\boldsymbol{B_0}$, by the Larmor frequency, ω_s. The detected quantity is the macroscopic magnetisation, M_0, (i.e., the net magnetic moment per unit volume), which for N spins at thermal equilibrium is defined:

$$M_0 = \frac{1}{V}\sum_{i=1}^{N} \mu_i \tag{2.2.1}$$

while the Larmor frequency is defined:

$$\omega_s = \frac{g_e \beta_e B_0}{\hbar} \tag{2.2.2}$$

where: g_e is the gyromagnetic ratio for a free electron spin, and β_e is the Bohr magneton, $\boldsymbol{B_0}$ is the external magnetic field, and ħ is the reduced Planck constant. This is the case for a static magnetic field, wherein the macroscopic magnetisation vector will either align parallel or antiparallel to the magnetic field, depending on the electron spin quantum number, m_s. At thermal equilibrium, the electron spins aligned parallel to the magnetic field will have lower energy, and will have a greater population, in accordance with the Boltzmann distribution. Therefore, the macroscopic magnetisation vector, M_0, will align parallel to $\boldsymbol{B_0}$ in the laboratory frame.

Detection of pulse dipolar EPR signals requires that the macroscopic magnetisation vector be perturbed away from the thermal equilibrium state (i.e., parallel to the external magnetic field). This requires the addition of a time-dependent linearly polarised magnetic field, $\boldsymbol{B_1}$, which has the components: $\boldsymbol{B_1}\, cos(\omega_{mw} t)$, $\boldsymbol{B_1}\, sin(\omega_{mw} t)$, and 0, along with x, y, and z dimensions, respectively. Since it is more convenient to consider a frame in which $\boldsymbol{B_1}$ is time-independent, we now consider the rotating frame, rotating with frequency ω_{mw}. The precession frequency is then described by:

$$\Omega_s = \omega_s - \omega_{mw} \tag{2.2.3}$$

where: Ω_s is the resonance offset, and the $\boldsymbol{B_1}$ field has frequency, ω_{mw}, and is perpendicular to the $\boldsymbol{B_0}$ field. This is explained because in presence of the $\boldsymbol{B_1}$ field there is an additional precession, ω_1, defined analogously to above:

$$\omega_1 = \frac{g_e \beta_e \boldsymbol{B_1}}{\hbar} \tag{2.2.4}$$

which leads to a superposition of both precessions, and subsequently a nutation about an effective field, described by:

$$\omega_{eff} = \sqrt{{\Omega_s}^2 + {\omega_1}^2} \tag{2.2.5}$$

Consider being in the resonance condition, that is where $\omega_s = \omega_{mw}$, in which case the magnetisation vector is invariant in the z-principal axis; meaning the $\boldsymbol{B_1}$ field must be aligned perpendicular to the $\boldsymbol{B_0}$ field for magnetisation to be detected. Magnetisation will then precess for even small values of ω_1, with the axis of the effective field at an incline, θ, from the z-principal axis defined by:

$$\theta = \tan^{-1}\left(\frac{\omega_1}{\Omega_s}\right) \tag{2.2.6}$$

In the opposite case, where $\Omega_s \gg \omega_1$, then the motion of M_0 is largely unperturbed since θ will tend to 0, and $\omega_{eff} = \Omega_s$, representing off-resonance irradiation. Let us now consider how the magnetisation vector, M_0, behaves when exposed to a strong microwave pulse of length t_p, where $\omega_1 \gg \Omega_s$, such that the incline of the effective field, θ is perpendicular to the z-principal axis (e.g., along the x-principal axis of the rotating frame). The magnetisation vector will be rotated by a flip angle, β, away from the equilibrium magnetization, according to:

$$\beta = \omega_1 t_p \tag{2.2.7}$$

after which the macroscopic magnetisation vector instead undergoes precession about the z-principal axis, by the resonance offset frequency, Ω_s, in the transverse (xy)-plane. A microwave pulse with a flip angle of π/2-radians rotates M_0 out of the z-principal axis and into the (xy)-plane without changing the spin populations. An 'inversion' microwave pulse (i.e., with a flip angle of π-radians) rotates M_0 into the -z dimension, and causes a change of the spin quantum number, such that the spin populations invert.

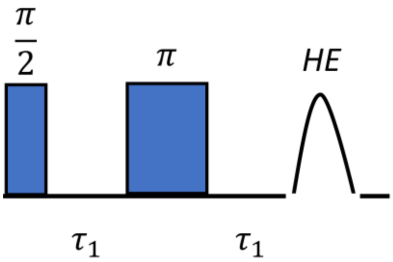

Figure 2.2.1: The Hahn echo pulse sequence. This is the observer subsequence used in many other pulse EPR experiments.

Microwave pulses can be applied in sequence to manipulate the magnetisation vector, and a simple example is the Hahn echo sequence (shown in figure 2.2.1). Herein a (π/2-τ_1-π) pulse sequence is used (i.e., the observer subsequence used in more complex modern experiments), which generates a Hahn echo at time $2\tau_1$. This is contextualised by considering that since the $\boldsymbol{B_1}$ microwave pulse is of finite length, immediately after the pulse, M_0 will begin to relax back towards thermal equilibrium (i.e., with the net magnetisation aligned parallel to the $\boldsymbol{B_0}$ field). Additionally, M_0 is a summation of quantum objects (discrete electron spins), such that for each individual electron spin there are local inhomogeneities in Ω_s, that cause electron spin packets to dephase and for the coherence to decay. These processes are forms of longitudinal and transverse relaxation and will be discussed in the next section. Owing to these local inhomogeneities, the spin packets will undergo a random phase shift, described by:

$$\Delta\varphi = (\Omega_s \pm \delta\Omega_s)t \tag{2.2.8}$$

However, this coherence can be recovered by applying a resonant π-pulse along the same dimension, and at time τ_1 after the first pulse. This causes an inversion of the phase shift, so that at time $2\tau_1$, local inhomogeneities in Ω_s have been refocussed and a spin echo (a Hahn echo) is formed.

2.3 Longitudinal and Transverse Relaxation Processes

Phenomenological relaxation can be discussed in a classical model of EPR spectroscopy; however, several mechanisms are neglected here, being beyond the scope of this thesis. As mentioned in the previous section, immediately following a resonant microwave pulse, macroscopic magnetisation deviates from thermal equilibrium by a flip angle, assumed subsequently to be a rotation of π/2 radians. After the microwave pulse, electron spin magnetisation will eventually decay back to thermal equilibrium, *via* longitudinal relaxation (and with the time-constant T_1). Concomitantly, as discussed, spin packets will each precess with individual Larmor frequencies leading to a random phase shift and loss of coherence in the (xy)-plane, *via* transverse relaxation (and with the time-constant T_2). Both longitudinal and transverse relaxation are first order processes and are ideally described by mono-exponential functions, in accordance with Redfield theory. However, distributions of rotational correlation times associated with librational motion can lead to deviations from mono-exponential behaviour, as commonly observed in polymers and glasses.

Longitudinal relaxation requires energy exchange between electron spins and the surroundings, (i.e., the solvent bath lattice). Therefore, longitudinal relaxation is also sometimes called ‘spin-lattice’ relaxation, and is commonly driven by thermal motion and vibrations, resulting in phonon emission and absorption within the lattice. Longitudinal relaxation typically proceeds *via* i) the single-phonon direct process (a phonon with frequency ω_s is absorbed or emitted by the spin system), and ii) a two-phonon Raman process (one phonon is absorbed by the spin system, promoting transition to a virtual energy level, and then a second phonon is emitted promoting a transition to ground-state of a spin state). At low temperatures, the direct process dominates the relaxation behaviour, but at higher temperatures the Raman process increasingly contributes. In solids, a major source of longitudinal relaxation is modulation of the spin-orbit coupling by lattice vibrations; T_1 is typically 10^{-3} seconds, and 10^{-6} seconds for nitroxide and low spin transition metal radicals at 50 K, respectively. Additionally, enhanced electron spin relaxation may be induced through dipolar coupling between spins.[261] The component of non-equilibrium magnetisation that has relaxed to thermal equilibrium at time t after a microwave pulse can be described:

$$M_z(t) = M_0\left(1 - \exp\left(\frac{-t}{T_1}\right)\right) \tag{2.3.1}$$

Unlike spin-lattice relaxation the corresponding transverse relaxation, spin-spin relaxation, does not require energy exchange with the surroundings. Despite this, typical mechanisms for spin-spin relaxation involve the solvent matrix and nuclear flip-flop interactions[262] (i.e., decay of coherence manifests through dipolar coupling of electrons with surrounding nuclei, and spontaneous nuclear spin flips cause a change at the local magnetic field of the electron spin. Per-deuteration is a strategy to prolong the lifetime of electron coherence in the transverse plane, T_m, because deuterium has a significantly weaker magnetic moment, μ_i, than protons resulting in weaker perturbations of the local magnetic field. Methyl protons can strongly influence electron spin echo dephasing behaviour.[263,264] More precisely, the coherence decay of transverse magnetisation at time t after a microwave pulse can be described:

$$M_x(t) = M_0 \sin(\omega_{AB} t) \exp\left(\frac{-t}{T_2}\right) \tag{2.3.2}$$

$$M_y(t) = M_0 \cos(\omega_{AB} t) \exp\left(\frac{-t}{T_2}\right) \tag{2.3.3}$$

Another phenomenon which manifests as a relaxation process is that of electron-electron and electron-nuclear spectral diffusion, that arises when detected spin magnetisation is transferred to surrounding electron or nuclear spins that are outside the excitation bandwidth of the microwave pulses. This results in spin packets with non-equilibrium magnetization being replaced by spin packets with magnetization at thermal equilibrium and appears to an observer of the detected spins as longitudinal relaxation. However, it is important to clarify between longitudinal relaxation (i.e., where magnetisation has returned to equilibrium and is thus irreversibly lost) and spectral diffusion (i.e., where non-equilibrium magnetisation is still observable in other parts of the spectrum). Usually, contributions from spectral diffusion are easily separable from longitudinal relaxation, and often manifest as a 'fast' relaxation component in the bi-exponential approximation of T_1, in inversion recovery measurements. This was demonstrated for the stable L-alanine radical (SAR1), which has strongly non-exponential T_1 relaxation behaviour, partially attributed to strong spectral diffusion contributions arising from neighbouring NH_3 and CH_3 groups.[265] Saturation recovery measurements using a 'picket fence' sequence $(\pi/2)_n$ or a high-turning angle (HTA) pulse can suppress spectral diffusion contributions.

2.4 The Spin Hamiltonian

The Spin Hamiltonian describes all the energies present in a paramagnetic spin system, reflecting the contributions to a detected EPR line. Commonly, the spin Hamiltonian, $\mathcal{H}_0$, is described:[266]

$$\mathcal{H}_0 = \mathcal{H}_{EZ} + \mathcal{H}_{ZFS} + \mathcal{H}_{HF} + \mathcal{H}_{NZ} + \mathcal{H}_{NQ} + \mathcal{H}_{NN} + \mathcal{H}_{EX} + \mathcal{H}_{DD} \tag{2.4.1}$$

where: $\mathcal{H}_{EZ}$ is the electron Zeeman interaction term (defined in section 2.1). $\mathcal{H}_{ZFS}$ is the zero-field splitting term arising from interactions between multiple unpaired electron spins ($S > 0.5$). $\mathcal{H}_{HF}$ is the hyperfine coupling term and describes the interaction between an electron and nuclei (with nuclear spin $I \neq 0$). $\mathcal{H}_{NZ}$ is the nuclear Zeeman interaction term. $\mathcal{H}_{NQ}$ is the nuclear quadrupolar interaction term, describing interaction between electrons and nuclei (with nuclear spin $I \geq 1$). $\mathcal{H}_{NN}$ describes the dipole-dipole interaction between pairs of nuclei. $\mathcal{H}_{EX}$ is the Heisenberg exchange coupling term and describes a through-bond interaction between unpaired electron spins. $\mathcal{H}_{DD}$ is the dipole-dipole interaction term and describes a through-space interaction between unpaired electron spins. The exchange coupling and dipole-dipole interaction terms will be discussed in more detail in section 2.5.

For simplicity, an arbitrary spin system containing a single unpaired electron, ($S = 0.5$), coupled to a nucleus, ($I = 0.5$), can be defined such that only the electron Zeeman interaction and the hyperfine interaction contribute to the spin Hamiltonian. This can be reframed as:

$$\mathcal{H}_0 = \frac{\beta_e \boldsymbol{B}.\boldsymbol{g}.\boldsymbol{S}}{\hbar} + \mathbf{S}.\mathbf{A}.\mathbf{I} \qquad (2.4.2)$$

where: $\boldsymbol{S}$ and $\boldsymbol{I}$ are the electron and nuclei spin angular momenta, $\boldsymbol{g}$ is the g-tensor, and $\boldsymbol{A}$ is the hyperfine coupling tensor. Both $\boldsymbol{g}$ and $\boldsymbol{A}$ are second-rank tensors that depend on the orientation of the external magnetic field with respect to the molecular axis frame. However, it should be made clear that the hyperfine coupling is independent of the magnitude of the external magnetic field. The two-level energy system previously defined in section 2.1, with the α and β spin manifolds arising from the electron Zeeman interaction, will now be perturbed, and further split by the hyperfine coupling interaction. The nuclear spin states, m_I, can take integer values from $-I$, to $+I$, resulting in two additional energy levels within each spin manifold.

The energy level splitting is now defined as:

$$\Delta E = g\beta_e B_0 + A_{zz} m_I \qquad (2.4.3)$$

The selection rules: $\Delta m_s \pm 1$ and $\Delta m_I = 0$ mean that there are two allowed transitions, resulting in two resonances in the resultant EPR spectrum. It should be noted that forbidden transitions ($\Delta m_I \neq 0$) are the source of ESEEM phenomena in pulse EPR. The intensity of ESEEM is therefore dependent on the external magnetic field strength, since the quanta of energy required to transition between electron spin manifolds will be larger and so the probability of a given forbidden transition will reduce.

2.5 The Dipole-Dipole Interaction and Exchange Coupling

For systems that have weakly coupled interacting electron spins, additional contributions to the spin Hamiltonian, $\mathcal{H}_0$ manifest as exchange coupling, and dipole-dipole interaction, given $\mathcal{H}_{EX}$ and $\mathcal{H}_{DD}$, respectively in [2.4]. In the simple case of an isolated spin pair ($S = 0.5$):

$$\mathcal{H}_0(S_1, S_2) = \mathcal{H}_0(S_1) + \mathcal{H}_0(S_2) + S_1 \boldsymbol{J} S_2 + S_1 \boldsymbol{D} S_2 \qquad (2.5.1)$$

where: $\mathcal{H}_0(S_A)$ and $\mathcal{H}_0(S_B)$ are the individual spin Hamiltonians for each spin, respectively, while $\boldsymbol{J}$ and $\boldsymbol{D}$ correspond to the exchange coupling and dipole-dipole tensors, respectively. Here, the exchange coupling is significant in solids when spins are separated by less than ~1.5 nm, or where spins are delocalised such that there is considerable overlap of occupied orbitals, manifesting in systems with extensive conjugated rings. Since excitation bandwidth limitations impose a lower detection limit on the measurable distance by pulse dipolar EPR methods of ~1.5 nm, the exchange coupling term is precluded from further consideration. The dipole-dipole interaction term can be defined:

$$\mathcal{H}_{DD} = \frac{1}{{r_{AB}}^3}\frac{\mu_0}{4\pi\hbar}\boldsymbol{g_A g_B}{\mu_B}^2\left[{\boldsymbol{S}_A}^{\boldsymbol{T}}\boldsymbol{S}_B - \frac{3}{{r_{AB}}^2}\left({\boldsymbol{S}_A}^{\boldsymbol{T}}\boldsymbol{r}_{AB}\right)\left({\boldsymbol{S}_B}^{\boldsymbol{T}}\boldsymbol{r}_{AB}\right)\right] \tag{2.5.2}$$

where: $\boldsymbol{r}_{AB}$ is the vector that connects spins A and B, $r_{AB} = |\boldsymbol{r}_{AB}|$, μ_0 is the vacuum permeability constant, β_e is the Bohr magneton, and g_A and g_B are the corresponding g-tensors of the spins A and B, respectively. If the g-tensors are isotropic, and the high-field approximation is valid (i.e., all other contributions to the spin Hamiltonian are, to first order, perturbations of the electron Zeeman interaction), then the dipolar coupling tensor can be written in the principal axis frame as:

$$\boldsymbol{D} = \frac{\mu_0}{4\pi\hbar}\frac{g_A g_B {\mu_B}^2}{{r_{AB}}^3}\begin{pmatrix} -1 & 0 & 0 \\ 0 & -1 & 0 \\ 0 & 0 & 2 \end{pmatrix} \tag{2.5.3}$$

which results in the correspondences: $-\omega_{dd}$, $-\omega_{dd}$, and $2\omega_{dd}$, in the x-, y- and z-principal axes, where ω_{dd} is the dipolar coupling frequency. Equation (2.5.2) is usually then transformed into[83]:

$$\mathcal{H}_{DD} = \frac{\mu_0}{4\pi\hbar}\frac{g_A g_B {\mu_B}^2}{{r_{AB}}^3}\left\{\hat{A} + \hat{B} + \hat{C} + \hat{D} + \hat{E} + \hat{F}\right\} \tag{2.5.4}$$

where: $\hat{A}$ and $\hat{B}$ can be expressed as:

$$\hat{A} = \hat{S}_{Z,A}\hat{S}_{Z,B}(1 - 3\cos^2(\theta)) \tag{2.5.5}$$

$$\hat{B} = \frac{1}{4}\left(\hat{S}_{A,+}\hat{S}_{B,-} + \hat{S}_{A,-}\hat{S}_{B,+}\right)(1 - 3\cos^2(\theta)) \tag{2.5.6}$$

Here: $\hat{S}_{Z,A}$ and $\hat{S}_{Z,B}$ are the z-spin operators, θ is the angle between the interspin vector, r_{AB}, and the external magnetic field, $\boldsymbol{B_0}$, and $\hat{S}_{\pm}$ are the raising and lowering operators defined: $\hat{S}_{\pm} = \hat{S}_x \pm i\hat{S}_y$. The operators $\hat{C} - \hat{F}$ have been defined previously,[41] and are precluded from discussion here. Under the high-field approximation, only the secular term (A) and the pseudo-secular term (B) contribute to the dipole-dipole interaction, such that the Hamiltonian has the form:

$$\mathcal{H}_{DD} = \omega_{dd}\hat{S}_{Z,A}\hat{S}_{Z,B} - \frac{1}{4}\omega_{dd}\hat{S}_{A,+}\hat{S}_{B,-} + \hat{S}_{A,-}\hat{S}_{B,+} \tag{2.5.7}$$

If the weak-coupling approximation is well met (i.e., the dipolar coupling frequency, ω_{dd}, is much less than the difference in the Larmor frequencies of spin packets A and B, ω_A and ω_B, respectively. $\omega_{dd} \ll (\omega_B - \omega_A)$) then the pseudo-secular term may also be neglected, see figure 2.5.1. Then the electron-electron coupling, ω_{ee} has the form:

$$\omega_{ee} = \frac{\mu_0 g_A g_B {\mu_B}^2}{4\hbar {r_{AB}}^3}(1 - 3\cos^2\theta_{AB}) + J = \omega_{dd} + J \tag{2.5.8}$$

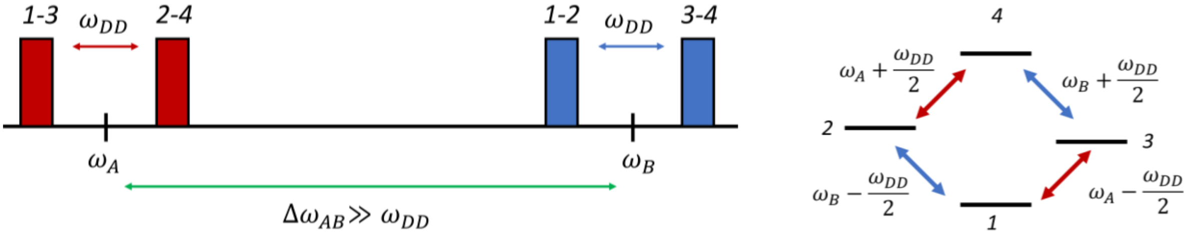

Figure 2.5.1: left panel) The weak-coupling approximation, with the dipolar splitting of the A- and B-spins around their respective Larmor frequencies, indicated in red and blue, respectively. right panel) The corresponding energy level diagram, with the corresponding transition energies indicated.

For reasons discussed above, the exchange coupling term, J, can be neglected for $r_{AB} >$ 1.5 nm. As stated above, in a powder sample or in the case of frozen solution, all random molecular orientations are present, so that the frequency response yields a Pake pattern. Phenomenologically, this response arises because the corresponding intensities of the orientations are weighted by $\sin\theta$, and so orientations perpendicular ($\theta_\perp$) to $\boldsymbol{B_0}$ dominate the Pake pattern, with a splitting corresponding to $\nu_\perp$, see figure 2.5.2. Singularities are also present at orientations parallel ($\theta_\parallel$) to $\boldsymbol{B_0}$, with a splitting corresponding to $\nu_\parallel$, which is often referred to as the 'double frequency component', since $\nu_\parallel = 2\nu_\perp$. This arises from the correspondences given in equation (2.5.3).

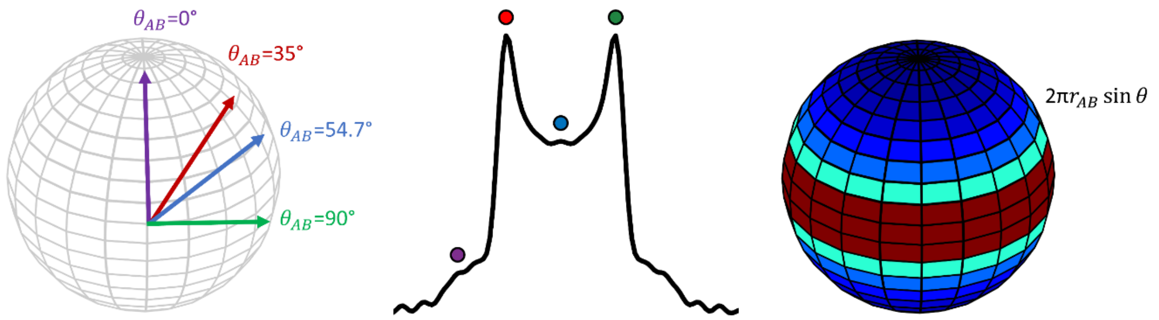

Figure 2.5.2: left panel) A unit sphere indicating the angle θ_{AB} between the magnetic field (**B**$_1$) and the distance vector (r_{AB}). centre panel) A typical Pake pattern frequency response, indicating the singularities corresponding to different values of θ_{AB} (shown as dots). Colour scheme is consistent for both the left and centre panels. right panel) The unit sphere with a heat-map to indicate the relative intensities of given conformations; weighted with $\sin\theta_{AB}$, there is greater intensity at the equator than at the poles of the sphere, reflected by the frequency response.

2.6 The Four-Pulse PELDOR and Five-Pulse RIDME Experiments

Let us now consider in detail two pulse dipolar EPR pulse sequences: the four-pulse PELDOR and five-pulse RIDME experiments.

The four-pulse PELDOR experiment[16,17] (figure 2.6.1) is a dead-time free version of the three-pulse PELDOR experiment[11] (figure 2.6.2), wherein the initial π/2-pulse is replaced by the sub-sequence (π/2-τ_1-π-τ_1), which forms a Hahn echo at time $2\tau_1$. The π-pulse at the second frequency can then be applied at $t \leq 2\tau_1$, so that the pulse position is incremented through the maximum of the PELDOR signal, to accurately determine the zero-time. In the 3-pulse analogue experiment, pulse overlap results in a dead-time (i.e., no data are recorded). A final π-pulse is applied at the detection frequency at time τ_2, causing a refocused echo to form at time $2\tau_2$. The π-pulse at the second frequency is on-resonance with a spin packet B and inverts the magnetisation of these spins resulting in a perturbation of the local magnetic field of another spin packet A (which is on-resonance with the detection pulses at the first frequency). This process leads to a shift in Ω_s, whereby the perturbed A-spins will no longer refocus at time $2\tau_2$, as their precession frequency is shifted by $\pm\omega_{dd}$. The perturbed A-spins accumulate phase $\Delta\varphi = \omega_{AB}(\tau_2 - t) - \omega_{AB}\tau_2$, which results in the detected echo being modulated by $\cos(\omega_{dd}t)$.

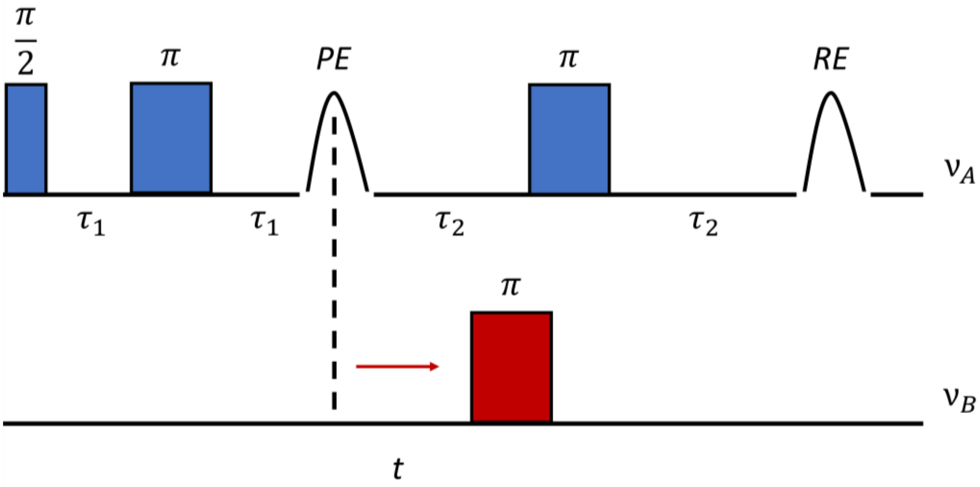

Figure 2.6.1: 4-pulse dead-time free PELDOR pulse sequence. Observer pulses at the first frequency are shown in blue, and the inversion pulse at the second frequency is shown in red. PE and RE correspond to primary echo and refocused echo, respectively.

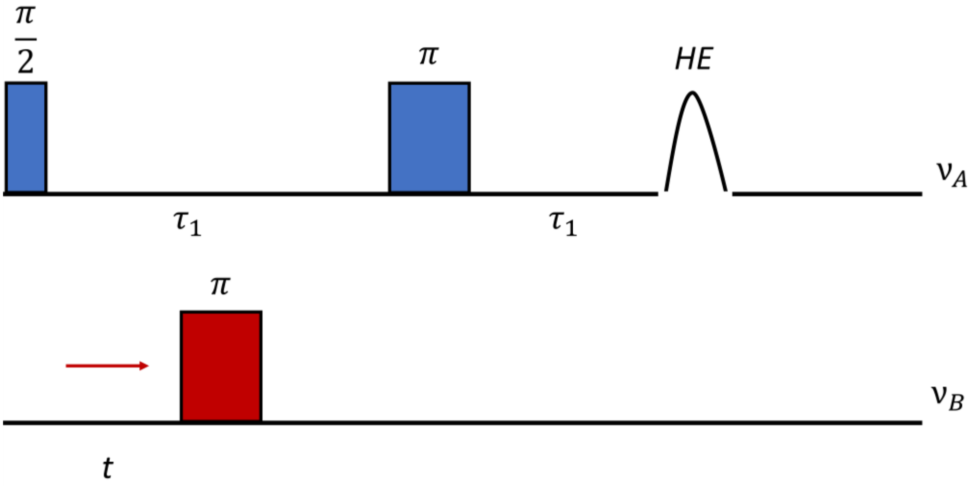

Figure 2.6.2: 3-pulse PELDOR pulse sequence. Observer pulses at the first frequency are shown in blue, and the inversion pulse at the second frequency is shown in red. HE corresponds to a Hahn echo.

The five-pulse RIDME experiment[180] (figure 2.6.3) is a dead-time free version of the three-pulse RIDME experiment,[179] wherein akin to the four-pulse PELDOR experiment, an initial π/2 pulse is replaced by the sub-sequence (π/2-τ_1-π-τ_1) again forming a Hahn echo at time $2\tau_1$. The inversion π-pulse used in PELDOR is replaced by a 'mixing block' subsequence (π/2-T_{mix}-π/2), which causes longitudinal-relaxation driven spontaneous spin flips of non-resonant 'pump-spins' so that $\Delta m_s \neq 0$. During the mixing block the A-spin magnetization is stored parallel to $\boldsymbol{B_0}$, (i.e., there is no phase accumulation) and the second π/2-pulse is a polarisation grating that restores $\leq 50\%$ of the A-spin magnetisation to the transverse plane. Analogously to PELDOR, a coherence transfer to resonant (detected) spins, causes their precession frequency to shift by $\pm\omega_{dd}\Delta m_s$. This is significant for high-spin systems ($S > 0.5$) where Δm_s is not bounded by ± 1, and can therefore yield higher-order harmonic frequencies.[267,268] The position of the mixing block is incremented, before a final π-pulse at time $(t_2 - t)$ generates a refocussed echo modulated by $\cos(\omega_{dd} t)$.

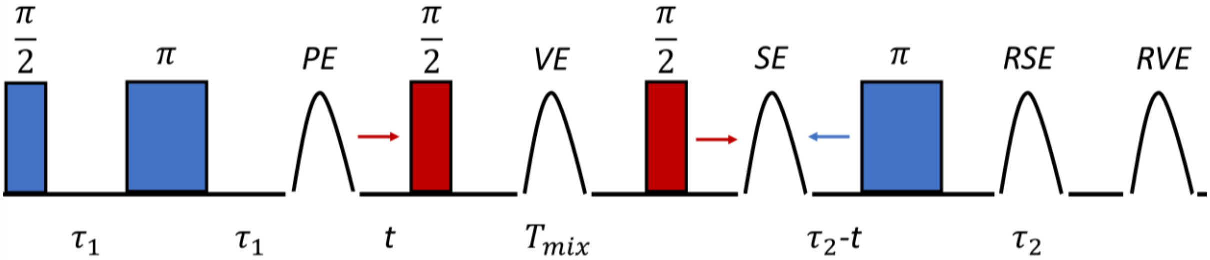

Figure 2.6.3: 5-pulse dead-time free RIDME pulse sequence. Observer pulses are shown in blue, and mixing block pulses are shown in red. The mixing block is incremented with *t*, while the interval for the final observer pulse is decremented to maintain a constant-time experiment. PE, VE, SE, RSE and RVE correspond to primary echo, virtual echo, stimulated echo, refocused stimulated echo and refocused virtual echo, respectively.

2.7 Background Correction

The detected signal of both the PELDOR and RIDME experiments (and all pulse dipolar EPR methods) has contributions that arise from the intramolecular couplings of electron spin pairs, V_{intra}, and an intermolecular component from couplings of electron spins on discrete macromolecules, V_{inter}, as given in equation (2.7.1). Since the dipole-dipole coupling frequency information is encoded only by V_{intra}, the intermolecular component must be suppressed to expedite downstream processing.

$$V_{signal} = V_{intra} \times V_{inter} \tag{2.7.1}$$

The intramolecular component of the detected signal is given by the quotient of the detected signal, and the intermolecular component. This encapsulates the importance of appropriate background correction in pulse dipolar EPR data processing, since if the background function cannot be adequately approximated, the intramolecular component of interest cannot be isolated. In the PELDOR experiment, this intermolecular signal component is approximated as a stretched exponential background function, given by equation (2.7.2):

$$B(t) = \exp\left(-kt^{\frac{d}{3}}\right) \tag{2.7.2}$$

where *k* is the decay rate-constant, and *d* is the fractional dimension, where spins are assumed to be homogenously distributed in a glassy frozen solution. Soluble proteins and macromolecules are homogenously distributed in three dimensions ($d = 3$), while membrane proteins are homogenously distributed in the plane of the membrane (i.e., in two dimensions) ($d = 2$). Linear polymers following a 'beads-on-a-string' structure can result in homogenous distribution in a single dimension, ($d = 1$), along the length of the chain.

The intermolecular decay in the detected RIDME signal is dominated by electron-electron and electron-nuclear spectral diffusion. These spectral diffusion processes manifest largely during the mixing block interval since it is often on the µs timescale, and result in RIDME background decay often being considerably steeper than PELDOR traces measured with the same dipolar evolution period. Before the development of an analytical description for the RIDME background,[269] second order polynomials were used to approximate the decay empirically.[195,270] While it is sufficient to describe the RIDME background function as a stretched exponential with dimensions between three and six, a full derivation is beyond the scope of this thesis.

Let us begin by considering an isolated spin pair (where $S_A = S_B = 0.5$), such that the detected RIDME signal, V_{signal}, can be defined:

$$V_{signal} = \exp\left[\int_0^{t_{RVE}} i\omega_{dd}(t)dt\right] \tag{2.7.3}$$

where ω_{dd} is the dipole-dipole coupling frequency defined in section 2.5, and the signal is detected at the time of refocussed virtual echo formation, t_{RVE}. Additionally, a sign factor of the phase accumulation during the dipolar evolution time, $s(t)$, is necessary and can be assigned $+1$ after the first π/2 pulse. The sign of the accumulated phase is then inverted at each subsequent π-pulse, being 0 during the mixing block, where the detected magnetisation is stored along the z-principal axis. Furthermore, B-spin flips can occur at any time, t', during the transverse evolution of the detected spins, and so is described by the factor $h(t, t')$, which can be assigned $+1$ at the beginning of the dipolar evolution time, and changes sign each time a B-spin flips. In this case, equation (2.7.3) can be rewritten:

$$V_{signal}(t) = \exp\left[i\omega_{dd}\int_0^{t_{RVE}} s(t')h(t,t')dt'\right] \tag{2.7.4}$$

For a macroscopic ensemble of k spins, (i.e., having averaged over all spatial positions of the k B-spins, and all possible outcomes of the $h(t)$ process), this can be described:

$$V_{signal}(t) = \prod_{i=1}^{k} \langle\langle \exp\left[i{\omega_{dd}}^{k}(r_k, \theta_k)\int_0^{t_{RVE}} s(t')h(t,t')dt'\right]\rangle_h\rangle_{r,\theta} \tag{2.7.5}$$

The probability of a B-spin flip during the transverse evolution time is assumed to be small since the inequality, $T_{m,A} < T_{1,B}$, is usually satisfied. This can be approximated by a Poisson distribution law, where the 'expected rate' of the B-spin flips during the transverse evolution of detected spins, $\lambda_{poisson}$, can be considered as the product of the B-spin flip rate, W, and the period during which a B-spin flip can occur (i.e., the total length of dipolar evolution, t_{max}). Considering that $W = 1/2T_{1,B}$, and $t_{max} = (2\tau_1 + 2\tau_2)$, $\lambda_{poisson}$ can then be defined:

$$\lambda_{poisson} = \frac{(2\tau_1 + 2\tau_2)}{2T_{1,B}} \tag{2.7.6}$$

where the probability of k spin-flip events, $P(k)$, can be defined:

$$P_B(k) = \exp(-\lambda)\frac{\lambda^k}{k!} \tag{2.7.7}$$

This allows for $k \geq 2$ to be neglected, such that only single B-spin flips during the transverse evolution time need to be considered. The probabilities of no B-spin flips during the transverse evolution interval, q, and the probability of one B-spin flip, p, are defined:

$$q = \frac{1}{1+\lambda} \tag{2.7.8}$$

$$p = \frac{\lambda}{1+\lambda} \tag{2.7.9}$$

With the probabilities of B-spins during the transverse evolution time of the detected spins determined, let us now consider the mixing block interval, T_{mix}, where an arbitrary number of B-spin flips occurs. The probability of an even number of spin flips during the mixing block, q_m, and the probability of an odd number of spin-flips, p_m, are defined:

$$q_m = \frac{\left(1 + \exp\left(\frac{-T_{mix}}{T_{1B}}\right)\right)}{2} \tag{2.7.10}$$

$$p_m = \frac{\left(1 - \exp\left(\frac{-T_{mix}}{T_{1B}}\right)\right)}{2} \tag{2.7.11}$$

Consider also that the first interval $2\tau_1$, it is assumed that there are no B-spin flips, so that the spin flips can only occur during the interval $2\tau_2$. There are then four cases that need consideration: i) no B-spin flips occur during the transverse evolution time, and an even number of spin flips occur during the mixing block, with probability $P_1 = qq_m$, defined as:

$$P_1 = \frac{\left(1 + \exp\left(\frac{-T_{mix}}{T_{1,B}}\right)\right) 2T_{1,B}}{2\left(2T_{1,B} + 2\tau_2\right)} \tag{2.7.12}$$

ii) no B-spin flips during the transverse evolution period, and an odd number of spin flips occur during the mixing block, with probability $P_2 = qp_m$, defined as:

$$P_2 = \frac{\left(1 - \exp\left(\frac{-T_{mix}}{T_{1,B}}\right)\right) 2T_{1,B}}{2\left(2T_{1,B} + 2\tau_2\right)} \tag{2.7.13}$$

iii) one B-spin flip during the transverse evolution period, and an even number of spin flips occur during the mixing block, with probability $P_3 = pq_m$, defined as:

$$P_3 = \frac{\left(1 + \exp\left(\frac{-T_{mix}}{T_{1,B}}\right)\right) 2\tau_2}{2\left(2T_{1,B} + 2\tau_2\right)} \tag{2.7.14}$$

iv) one B-spin flip during the transverse evolution period, and an odd number of spin flips occur during the mixing block, with probability $P_4 = pp_m$, defined as:

$$P_4 = \frac{\left(1 - \exp\left(\frac{-T_{mix}}{T_{1,B}}\right)\right) 2\tau_2}{2\left(2T_{1,B} + 2\tau_2\right)} \tag{2.7.15}$$

Then the trajectory integrals for each of the four cases listed (i.e., if a B-spin flip occurs, then it occurs at time t'') must be calculated and result in the correspondences: $I_1 = 0$, $I_2 = 2t$, $I_3 = \tau_2$, and $I_4 = \tau_2(1 - 2t/\tau_2 + \ 2t^2/{\tau_2}^2)$. For many B-spins, N, the average number of spins evolving according to case l, N_l, can be calculated as $P_l N_l$, and so equation (2.7.5) can be reframed:

$$V_{signal}(t) = \prod_{l=1}^{4} \left[\langle\langle \exp\left[i{\omega_{dd}}^k(r_k, \theta_k) \int_0^{t_{RVE}} s(t')h(t,t')dt' \right] \rangle_h \rangle_{r,\theta} \right]^{N_l} \tag{2.7.16}$$

Finally, for sufficiently large N, we arrive at the form:

$$V_{signal}(t) = \exp\left[-\Delta\omega_{1/2}\sum_{l=1}^{4} P_l I_l\right] \tag{2.7.17}$$

where the average dipolar frequency between detected and B-spins, $\Delta\omega_{1/2}$, is defined:

$$\Delta\omega_{1/2} = \frac{\mu_0}{4\pi}\frac{4\pi^2 g_A g_B \beta_A \beta_B}{9\sqrt{3}\hbar}\frac{N}{V} \tag{2.7.18}$$

where: μ_0 is the vacuum permeability constant, g_A and g_B are the g-factors of the detected and B-spins, β_A and β_B are the different electron or nuclear magnetons of the detected and B-spins, and N/V is the spin concentration, related to the inverse cube of the distance r_{AB}.

Once this expression is expanded, it can be factorised into terms that depend on the position of the mixing block, t, and those that are independent of t, representing a constant attenuation term, F_0, and can be expressed as a stretched exponential:

$$V_{signal}(t) = F_0 \exp\left(-\Delta\omega_{1/2}(\alpha t + \beta t^2)\right) \tag{2.7.19}$$

where the constant attenuation term, F_0, and the coefficients, α and β, are defined:

$$F_0 = \exp\left(-\Delta\omega_{\frac{1}{2}}\frac{{\tau_2}^2}{T_{1,B}}\right) \tag{2.7.20}$$

$$\alpha = \frac{T_{1,B} - \tau_2}{T_{1,B} + \tau_2}\left(1 - \exp\left(\frac{-T_{mix}}{T_{1,B}}\right)\right) \tag{2.7.21}$$

$$\beta = \frac{\left(1 - \exp\left(\frac{-T_{mix}}{T_{1,B}}\right)\right)}{T_{1,B} + \tau_2} \tag{2.7.22}$$

It should be noted that F_0 is assumed not to vary in the regime $\tau_2 \ll T_{1,B}$, and this is well met for most constant-time RIDME measurements. Additionally, this definition of the coefficients, α and β, does not account for the initial pulse sub-sequence, namely the time $2\tau_1$ in the transverse evolution time for B-spin flips to occur.

2.8 Modulation Depth Build-up in PELDOR and RIDME

After this background correction procedure, the intramolecular contribution to the detected signal from an isolated spin pair, V_{pair}, and with a single orientation, θ_{AB}, can be expressed according to equation (2.8.1):[85]

$$V_{pair}(t) = V_0(1 - \lambda + \lambda\cos(\omega_{AB}t)) \tag{2.8.1}$$

where: V_0 is the signal intensity at $t = 0$, $V_{pair}(t)$ is the intramolecular signal from the isolated spin pair, ω_{AB} is the dipole-dipole coupling frequency between A- and B-spin pair, and λ is the fraction of B-spin packets that are inverted at the ‘pump’ frequency. Consider that in a frozen solution, anisotropy is not averaged by molecular motion, so that the detected signal will be a weighted summation of all molecular orientations with respect to the external magnetic field. Powder averaging then allows equation (2.8.1) to be reframed for all orientations:

$$V(t) = V_0 \int_0^{2\pi} \int_0^{\pi} (1 - \lambda(\theta) + \lambda(\theta) cos(\omega_{AB}(\theta)t) \sin\theta \, d\theta \qquad (2.8.2)$$

where $V(t)$ is now the intramolecular signal from all spin pairs. For systems that have significant backbone flexibility, orientational correlations between the interspin vector and the molecular axis are averaged, since the conformational sampling space is sufficiently large. Additionally, the orientational dependence of λ can then be neglected. This approximation yields a Pake pattern in the frequency domain, see figure 2.8.1, and is assumed to be well-met for the remainder of this thesis, unless otherwise stated.

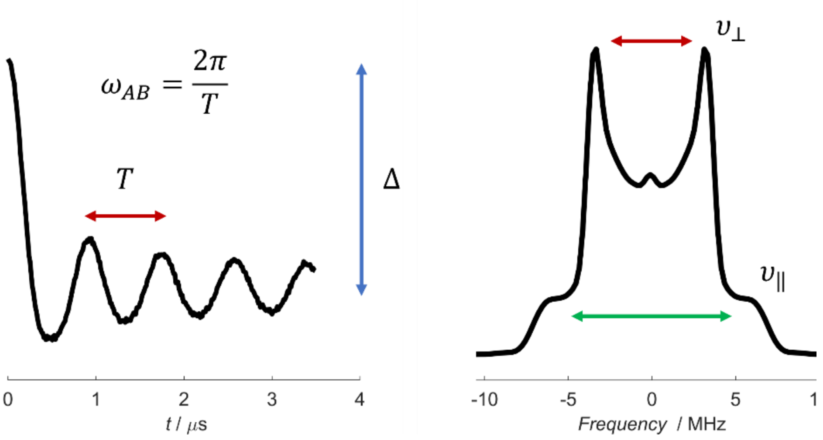

Figure 2.8.1: left panel) Simulated time-domain signal, indicating the period (T) and the relation to dipolar coupling frequency (ω_{AB}), as well as the modulation depth (Δ) information. right panel) The corresponding frequency response after Fourier Transformation of the time-domain signal. The singularities corresponding to perpendicular ($\upsilon_{\perp}$) and parallel ($\upsilon_{||}$) components are indicated.

For PELDOR, in the absence of orientational correlations, λ_{PELDOR} is often well approximated as the ratio of the mw pulse excitation bandwidth to the spectral width of the pumped species. Whereas in the RIDME experiment, λ_{RIDME} is independent of the spectral width of the B-spin, where broadband B-spin excitation is limited by longitudinal relaxation anisotropy as opposed to excitation bandwidth of a 'pump' pulse. The implication is two-fold: i) sensitivity can be improved in systems with prohibitively broad spectral width, and ii) sensitivity to orientational correlations is reduced, since in the limit of isotropic longitudinal relaxation spin-flips occur uniformly over the entire B-spin spectral width. This has led to RIDME being applied in systems containing transition or lanthanide metals, or in orthogonally labelled systems.

Consider also from equation (2.8.1), that in the limiting case $t \rightarrow \infty$, and specifically for a spin pair, the normalised background corrected signal decays to a non-zero value, $(1 - \lambda)$, and can be defined as a 'residual offset', at which point the modulated component is completely damped. This residual offset is an unmodulated contribution to $V(t)$, and will depend on the number of coupled spins in the system. A further parameter, the modulation depth (Δ), describes the difference between the signal intensity at $t = 0$ (normalised to 1) and the residual offset, according to equation (2.8.3):[178,181]

$$\Delta_{PELDOR} = 1 - (1 - f\lambda_{PELDOR})^{N-1} \tag{2.8.3}$$

where: f is defined as the fractional labelling efficiency with a paramagnetic moiety, λ is the fraction of spins on resonance with the PELDOR pump pulse, and *N* describes the number of intramolecularly coupled electron spins.

It should be noted that while equation (2.8.3) is conceptually valid for all pulse dipolar EPR experiments, it has only been empirically verified for PELDOR,[181] wherein spin counting was performed for a series of synthetic model systems. In the case of an obligate spin pair, under conditions of 100% spin labelling efficiency, $\Delta_{PELDOR} = \lambda_{PELDOR}$. The modulation depth build up kinetics in RIDME has previously been described using a Poisson stochastic flipping process,[271,272] where only B-spins that undergo an odd number of spin flips contributing to the modulation depth. Δ_{RIDME} is proportional to $P_{odd}(T_{mix})$, where P_{odd} is the probability of an odd number of spin flips after time T_{mix}, defined by equation (2.8.4):[273]

$$P_{odd} = \frac{(1 - \exp(-2WT_{mix}))}{2} \tag{2.8.4}$$

where: $2W$, see [2.7], is a rate defined as $1/T_{1B}$, the longitudinal relaxation time-constant of the B-spins. This results in the familiar expression for Δ_{RIDME}, and reiterated in equation (2.8.5):

$$\Delta_{RIDME} = \frac{\left(1 - \exp\left(\frac{-T_{mix}}{T_{1B}}\right)\right)}{2} \tag{2.8.5}$$

Equation (2.8.5) describes the asymptotic limit of RIDME modulation depth, for a given ratio of T_{mix} and T_{1B}. From this point forward, this asymptotic modulation depth is defined as Δ_{Tmix}, and empirical RIDME modulation depths are defined as Δ_{RIDME}. Akin to PELDOR, in the case of an obligate spin pair, under conditions of 100% spin labelling efficiency, $\Delta_{RIDME} = \Delta_{Tmix}$.

2.9 Tikhonov Regularisation

The background corrected time-domain signal can be mapped to the distance domain to yield structural information. However, this step requires the solution to an ill-posed inverse problem. This can be expressed as a Fredholm integral of the first kind:

$$S(t) = \int_0^\infty K(r,t)P(r)dr \tag{2.9.1}$$

where: $K(r,t)$ is a kernel function and for a spin-pair ($S = 1/2$), without orientational correlations, is defined as:

$$K(t,r) = \int_0^{\frac{\pi}{2}} \sin\theta \cos\left((1 - 3\cos^2\theta) \frac{\mu_0 {\mu_B}^2 g_A g_B}{4\pi\hbar {r_{AB}}^3} \right) d\theta \qquad (2.9.2)$$

and the integral transformation is described by $S = KP$. The inverse problem is to determine the distance probability density distribution $P(r)$ from the time-domain signal $S(t)$, but owing to the ill-posed nature of the problem, $P(r)$ is highly sensitive to small noise fluctuations in the time domain data, or indeed minor violations of the spin-pair approximation, where the kernel function is no longer valid. Significantly, processing of data with strong orientational correlations will yield erroneous results. Orientational correlations result in deviations from the assumption of the DeerAnalysis kernel (i.e., that all orientations contribute to the frequency response and form a Pake pattern). In such cases, bespoke software packages such as Dipfit[274] are preferable for analysis.

To stabilise the solution of $P(r)$, regularisation methods are required, as first demonstrated by Tikhonov.[275] Tikhonov regularisation has since become common place in the analysis of pulse dipolar EPR data. Other methods of model-free solutions to this ill-posed problem include: Mellin transformation,[276] single-value decomposition (SVD), approximate Pake transformation, and maximum entropy.[277] Generally, regularisation takes the form of a least-squares minimisation coupled with a penalty term, defined in equation (2.9.3):

$$P_{reg}(r) = ||V(t) - S(t)||^2 + \alpha^2 R[LP] \qquad (2.9.3)$$

where: $P_{reg}(r)$ is the regularised solution, $V(t)$ is the corresponding fit to the experimental time domain data, $S(t)$, $R[LP]$ is the penalty functional, with L being the regularisation matrix, and α is the regularisation parameter which weights the penalty term. The first term describes the square deviation between the experimental data and the solution, corresponding to the quality of fit, and the second term describes the weighting and criterion for penalisation of the solution. While the regularisation matrix can have varying structures, in Tikhonov regularisation it takes the form of a second order differential operator:

$$L = \frac{d^2}{dR^2} \qquad (2.9.4)$$

This penalises steep turning points in the distance distribution, (i.e., jagged edges arising from sharp peaks). Therefore, the penalty is minimised for smooth distributions, which physically manifest where sufficiently many molecular orientations are sampled (as for powders and glassy frozen solutions). In fact, other regularisation matrices also enforce smoothness, for instance when L is a first order differential operator (as in the Huber and Total Variation functionals), this also penalises steep slopes.

Further stabilisation of the solution can manifest as a non-negativity constraint ($P \geq 0$) since it describes a probability density distribution. Having defined the equation to be minimised:

$$P_{reg}(r) = ||V(t) - S(t)||^2 + \alpha \left\| \frac{d^2}{dR^2} P(r) \right\|^2 \qquad (2.9.5)$$

The weighting of the penalty term, α, which best fits the experimental data, while also ensuring the corresponding solution is smooth needs to be found. Consider the following regimes: i) when α is large the solution will be over-smoothed, and the error will be dominated by deviation between the fit solution and experiment, and ii) when α is small the solution will be under-smoothed and the experimental data will be overfitted by the solution. There is an assortment of methods to find the optimal regularisation parameter, including the L-curve, Akaike information and Bayesian information criteria, and these selection methods have recently been optimised systematically using a synthetic dataset.[214] From this study, the authors concluded that the Akaike information criterion and generalised cross validation methods were preferable for their relative simplicity and robust nature. Furthermore, additional studies have concerned how to streamline dipolar EPR data processing and optimisation of the regularisation parameter.[215,216,278] In cases where distribution peaks are quantified, it may be preferable to circumvent the regularisation step altogether; multi-Gaussian fitting is then a viable option.[210–213]

Here, the L-curve criterion for α selection is briefly described, as this is the method used in the DeerAnalysis software, commonly applied to analyse PD-EPR data. Firstly, the L-curve criterion is so called because of the 'L-shape' formed by the intersection of the two regimes described above (i.e., by the minimisation of the error between the fit and experiment, and the corresponding minimal 'smoothness' required by the solution). This is best visualised as a log plot of the two right-hand side terms in equation (2.9.6), where $\rho = \|V(t) - S(t)\|^2$ and $\eta = \alpha \left\| \frac{d^2}{dR^2} P(r) \right\|^2$ are the abscissa and ordinate, respectively. As the regularisation parameter first increases ($\alpha \ll \alpha_{opt}$), smoothness rapidly increases with small changes in α (comprising the vertical arm of the L-curve), before eventually plateauing for further large increases in α ($\alpha \gg \alpha_{opt}$) (comprising the horizontal arm of the L-curve). Hence, α_{opt} should occur at approximately the intersection of these two arms, see figure 2.9.1.

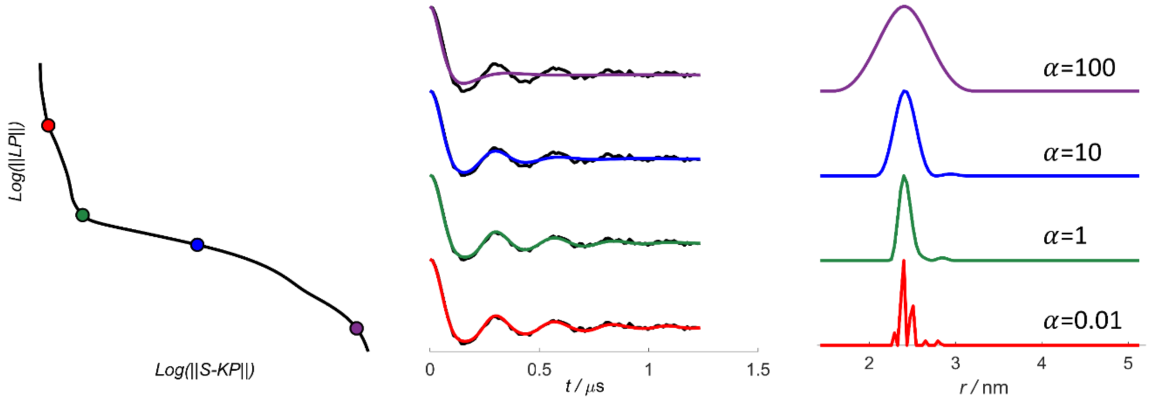

Figure 2.9.1: left panel) L-curve for optimisation of the regularisation parameter (α) in Tikhonov regularisation. centre panel) time-domain data and corresponding fits for different regularisation parameters. right panel) distance distributions corresponding to each dipolar evolution function, with the regularisation parameter indicated. Colour scheme is consistent across all panels.

2.10 Analytical Binding Models

Now that both Δ_{PELDOR} and Δ_{RIDME} have been defined analytically, the subsequent section describes how modulation depths can be applied to quantify non-covalent binding interactions, in terms of binding affinities, and equilibrium concentrations, starting from first principles. In the following derivations, all solutions are assumed to be sufficiently dilute such that activity can be approximated by concentrations. These models are then used in the analysis and simulation of the pseudo-titration data in the respective results chapters.

2.10.1 One-site Langmuir Isotherm Binding Model

Let us begin by considering a simple reaction scheme between a nitroxide-labelled protein (P) and a monovalent, paramagnetic ligand (L):

$$PL \overset{K_D}{\rightleftharpoons} P + L \tag{2.10.1.1}$$

The dissociation constant (K_D) can be written in terms of the equilibrium concentrations of protein, ligand, and protein-ligand complex, given as $[P]$, $[L]$ and $[PL]$ respectively:

$$K_D = \frac{[P][L]}{[PL]} \tag{2.10.1.2}$$

The equilibrium concentration of protein can be rewritten in terms of total protein, and protein-ligand complex, given as $[P]_0$ and $[PL]$, respectively:

$$[P] = ([P]_0 - [PL]) \tag{2.10.1.3}$$

Substitution of (2.10.1.3) into (2.10.1.2) yields (2.10.1.4):

$$K_D = \frac{([P]_0 - [PL])[L]}{[PL]} \tag{2.10.1.4}$$

Here, rearranging for total protein, $[P]_0$ yields the following expression:

$$[P]_0 = \frac{K_D[PL] + [PL][L]}{[L]} \tag{2.10.1.5}$$

Finally, isolating the concentration of protein-ligand complex, $[PL]$ is given in (2.10.1.6):

$$[PL] = \frac{[P]_0[L]}{K_D + [L]} \tag{2.10.1.6}$$

Furthermore, the fractional saturation can be given in terms of total protein and ligand concentrations, respectively, by substituting $[L]$ in equation (2.10.1.4), (in analogous fashion to equation (2.10.1.3)). After rearrangement, the fractional saturation is given in equation (2.10.1.7):

$$\frac{[PL]}{[P]_0} = \theta_{PL} = \frac{([L]_0 + [P]_0 + K_D) - \sqrt{([L]_0 + [P]_0 + K_D)^2 - 4[P]_0[L]_0}}{2[P]_0} \tag{2.10.1.7}$$

Now, we can relate this back to the RIDME modulation depths by considering three assumptions: i) nitroxide spin labelling is quantitative, ii) there is negligible free nitroxide spin label in frozen solution (i.e., all protein macromolecules have a nitroxide label, and all detected nitroxide spins are bound to protein molecules), and iii) the paramagnetic ligand is spectroscopically orthogonal to the detected spin (i.e., excitation of the paramagnetic ligand by detection pulses is negligible). The detected echo will be the weighted sum of signals from proteins which either have the paramagnetic ligand bound (in which case it will contribute to the modulation depth), or that do not have the ligand bound (in which case it will not contribute to the modulation depth). In the limiting cases of i) no ligand binding, ($\theta_{PL} = 0$), $\Delta_{RIDME} = 0$, and ii) complete ligand binding, ($\theta_{PL} = 1$), all detected spins will be intramolecularly coupled to the paramagnetic ligand, such that $\Delta_{RIDME} = \Delta_{Tmix}$. Here, Δ_{Tmix} can be defined as the asymptotic value of modulation depth for a given ratio of T_{mix} and T_1, such that $\Delta_{RIDME} = \Delta_{Tmix}$ when all detected spins are intramolecularly coupled to Cu^{II}-spins. Finally, we can define Δ_{RIDME} in terms of Δ_{Tmix}, binding affinity, and total protein and ligand concentrations according to equation (2.10.1.8):

$$\frac{\Delta_{RIDME}}{\Delta_{Tmix}} = \frac{([L]_0 + [P]_0 + K_D) - \sqrt{([L]_0 + [P]_0 + K_D)^2 - 4[P]_0[L]_0}}{2[P]_0} \qquad (2.10.1.8)$$

It should be noted that this expression is only valid for a single binding-site model. As such, this mathematical model is used in the analysis of Cu^{II}-nitroxide RIDME modulation depths for the pseudo-titration series shown in chapter 3.

2.10.2 Competitive One-site Binding Model

This formalism can also be extended to a one-site competitive binding model (i.e., we can treat the binding equilibrium in presence of a competitor ligand). Let us again consider the scheme given above, in presence of the competitor ligand (A)

$$PL + A \overset{K_{DL}}{\rightleftharpoons} P + L + A \quad \bigcup \quad PA + L \overset{K_{DA}}{\rightleftharpoons} P + L + A \qquad (2.10.2.1)$$

The following three assumptions are made: i) the binding of (L) and (A) to (P) is mutually exclusive, ii) the competitor (A) binds to (P) weakly with respect to (L), and iii) the competitor (A) is diamagnetic, while the ligand (L) is paramagnetic. Dissociation constants for both the ligand (K_{DL}) and for the competitor (K_{DA}), can be defined as given in (2.10.2.1) and (2.10.2.2) respectively:

$$K_{DL} = \frac{[P][L]}{[PL]} \qquad (2.10.2.1)$$

$$K_{DA} = \frac{[P][A]}{[PA]} \qquad (2.10.2.2)$$

Rearranging (2.10.2.1) and (2.10.2.2) for equilibrium concentrations of protein and protein-competitor complex, given as $[P]$ and $[PA]$ respectively, yields (2.10.2.3) and (2.10.2.4):

$$[P] = \frac{K_{DL}[PL]}{[L]} \tag{2.10.2.3}$$

$$[PA] = \frac{[P][A]}{K_{DA}} \tag{2.10.2.4}$$

Here, an expression for total protein, $[P]_0$, can be defined:

$$[P]_0 = [P] + [PL] + [PA] \tag{2.10.2.5}$$

Substitution of (2.10.2.3) and (2.10.2.4) into (2.10.2.5) yields (2.10.2.6):

$$[P]_0 = \frac{K_{DL}[PL]}{[L]} + [PL] + \frac{K_{DL}[PL][A]}{[L]K_{DA}} \tag{2.10.2.6}$$

Symbolic substitution and rearrangement of (2.10.2.6) to solve for $[PL]$ yields (2.10.2.7):

$$[PL] = \frac{[P]_0[L]}{[L] + K_{DL}\left(1 + \frac{[A]}{K_{DA}}\right)} \tag{2.10.2.7}$$

Hence the effect of the competitor ligand can be subsumed into an apparent dissociation constant defined as[252]:

$$K_{DLAPP} = K_{DL}\left(1 + \frac{[A]}{K_{DA}}\right) \tag{2.10.2.8}$$

Owing to assumption ii) (that the competitor ligand (A) binds to protein (P) weakly with respect to ligand (L)), in (2.10.2.8) we can assume that (2.10.2.9) is also well met:

$$[A] = [A]_0 \tag{2.10.2.9}$$

Substitution of equations (2.10.2.8) and (2.10.2.9) into equation (2.10.1.7) gives an expression for the Cu^{II}-nitroxide RIDME modulation depths:

$$\frac{\Delta_{RIDME}}{\Delta_{Tmix}} = \frac{\left(K_{DL}\left(1 + \frac{[A]_0}{K_{DA}}\right) + [P]_0 + [L]_0\right) - \sqrt{\left(K_{DL}\left(1 + \frac{[A]_0}{K_{DA}}\right) + [P]_0 + [L]_0\right)^2 - 4[P]_0[L]_0}}{2[P]_0} \tag{2.10.2.10}$$

This gives an expression for modelling modulation depths as a function of total competitor concentration, in presence of fixed concentrations of protein and non-competitor ligand. Owing to assumption iii) (that the competitor ligand (A) is diamagnetic), Δ_{RIDME} is continuously decreasing as a function of total competitor ligand.

2.10.3 Two-site Langmuir Isotherm Binding Model

Let us now consider the more complex scenario of a two-site independent ligand binding model, wherein the ligand binding sites are non-identical. Here, the following two assumptions are made: i) the protein macromolecule is not nitroxide labelled, so the unbound component is EPR silent, and ii) the detected echo signal is proportional to $[L]_0$, (which may not always be true for changing speciation or differential longitudinal relaxation times between free and bound component). For such a binding model (and for any higher degree multi-ligand-binding site model) equations (2.10.1.2) and (2.10.1.5) are not well met, this is because species with a higher degree of ligand binding (PL_2, PL_3, $PL_4 \ldots PL_n$) are not accounted for. Instead in analogy to (2.10.1.2), the bound ligand, $[L]_B$ can be expressed:

$$[L]_B = [L]_0 - [L] \qquad (2.10.3.1)$$

Similarly, in analogy to (2.10.1.5) the bound ligand concentration can be expressed as a two-site Langmuir isotherm, where K_{D1} and K_{D2} are the dissociation constants at sites one and two, respectively:

$$([L]_0 - [L]) = \frac{[P]_0[L]}{K_{D1} + [L]} + \frac{[P]_0[L]}{K_{D2} + [L]} \qquad (2.10.3.2)$$

Rearrangement of (2.10.3.2) yields:

$$([L]_0 - [L])(K_{D1} + [L])(K_{D2} + [L]) = (K_{D2} + [L])[P]_0[L] + (K_{D1} + [L])[P]_0[L] \qquad (2.10.3.3)$$

Which can be expressed as a cubic equation:

$$[L]^3 + a[L]^2 + b[L] - c = 0$$

Here a, b, and c are defined in (2.10.3.4)-(2.10.3.6):

$$a = (2[P]_0 + K_{D1} + K_{D2} - [L]_0) \qquad (2.10.3.4)$$

$$b = ([P]_0K_{D1} + [P]_0K_{D2} + K_{D1}K_{D2} + (K_{D1} + K_{D2})[L]) \qquad (2.10.3.5)$$

$$c = K_{D1}K_{D2}[L]_0 \qquad (2.10.3.6)$$

After Vietta's substitution, the one real root of $[L]$ is given as:

$$[L] = -\frac{a}{3} + \frac{2}{3}\sqrt{(a^2 - 3b)}\cos\frac{\theta}{3} \qquad (2.10.3.7)$$

Here θ can be defined according to (2.10.3.8):

$$\theta = \cos^{-1}\left(\frac{-2a^3 + 9ab - 27c}{2\sqrt{(a^2 - 3b)^3}}\right) \qquad (2.10.3.8)$$

Having an analytical expression for the equilibrium ligand concentration,[250] this can be combined with a binding polynomial approach, using a partition function (Z) to calculate the fractions of each species. Let us revert to the simple reaction scheme previously defined above:

$$P + iL \overset{\beta_i}{\leftrightarrow} PL_i$$

A macroscopic association constant β_i can be defined for this scheme as:

$$\beta_i = \frac{[PL_i]}{[P][L]^i} \tag{2.10.3.9}$$

Additionally, the binding polynomial can be defined as:

$$Z = \sum_{i=0}^{n} \frac{[PL_i]}{[P]} \tag{2.10.3.10}$$

Insertion of (2.10.3.9) into (2.10.3.10) yields (2.10.3.11):

$$Z = \sum_{i=o}^{n} \beta_i [L]^i \tag{2.10.3.11}$$

For s identical ligand binding sites, the macroscopic association constant (β_i) can be expressed in terms of binomial coefficients and the microscopic association constant (K_i) as:

$$\beta_i = \binom{s}{i} K^i \tag{2.10.3.12}$$

Substitution of (2.10.3.12) into (2.10.3.11) yields (2.10.3.13):

$$Z = \sum_{i=0}^{s} \binom{s}{i} K^i [L]^i \tag{2.10.3.13}$$

By virtue of the symmetry of Pascal's triangle of binomial coefficients (2.10.3.13) can be rewritten as:

$$Z = \sum_{i=0}^{s} \binom{s}{i} K [L]^{s-i} \tag{2.10.3.14}$$

Using the binomial identity Z can be defined as a sth order polynomial in product of free ligand concentration:

$$Z = (1 + K_i [L])^s \tag{2.10.3.15}$$

In the case of non-identical ligand binding sites (where $K_1 \neq K_2$), the binding polynomial can instead be expressed as:

$$Z = \prod_{i=1}^{n} (1 + K_i [L]) \tag{2.10.3.16}$$

This is a more succinct form of the double sum operation taken from multinomial theorem, namely for two classes of s- and t-fold degenerate binding sites, with association constants K_1 and K_2, respectively:

$$Z = \sum_{i=0}^{s} \binom{s}{i} K_1 [L]^{s-i} \sum_{j=0}^{t} \binom{t}{j} K_2 [L]^{t-j} \tag{2.10.3.17}$$

A two-site independent binding model is then a simple case of this multi-site binding model formalism, where Z has the form:

$$Z = 1 + K_1[L] + K_2[L] + K_1K_2[L]^2 \tag{2.10.3.18}$$

The fractions of unbound, θ_P, singly bound, θ_{PL}, and doubly bound, θ_{PL_2}, macromolecule can then be calculated. To relate this to the RIDME modulation depths, consider that unbound, singly bound, and doubly bound ligand will contribute to the detected echo, but only the doubly bound ligand will contribute to the modulation depth. Therefore, the RIDME modulation depth can be expressed as:

$$\frac{\Delta_{RIDME}}{\Delta_{Tmix}} = \frac{[L]_{1,2}}{[L]_0} \tag{2.10.3.19}$$

where: Δ_{Tmix} is defined above, $[L]_0$ is the total ligand concentration, and $[L]_{1,2}$ is the doubly bound ligand concentration, given as:

$$[L]_{1,2} = 2[P]_0\theta_{PL_2} \tag{2.10.3.20}$$

where: $[P]_0$ is the total protein concentration, and θ_{PL_2} is the fraction of the doubly bound macromolecule, defined in equation (2.10.3.21):

$$\theta_{1,2} = \frac{(K_1K_2K_{12})[L]^2}{Z} \tag{2.10.3.21}$$

where: K_{12} is defined as the cooperativity factor, which for an independent binding model is assumed to be non-cooperative ($K_{12} = 1$). The theory of a cooperative binding model (i.e., where binding sites cannot be treated independently) is detailed subsequently.

This binding model is used in the analysis of the Cu^{II}-Cu^{II} RIDME pseudo-titration series shown in chapter 5, the analytical solution of the equilibrium ligand concentration is adapted from reference [250] and the multi-site derivation is informed by reference [253].

2.10.4 Multi-site Langmuir Isotherm Binding Model

While the focus of this thesis is mainly quantification of modulation depths from the RIDME experiment, PELDOR modulation depths can also be modelled using this approach, where equation (2.8.3) can be adapted for a weighted mixture of differentially labelled species in frozen solution. An example is the statistical labelling distribution of a multimeric macromolecule, such as a membrane protein. If there are n-fold identical labelling sites, and different species are k-fold labelled, with labelling efficiency f and relative weightings $x(k)$, Δ_{PELDOR} can be described according to equation (2.10.4.1)[204] :

$$\Delta_{PELDOR} = 1 - \frac{\sum_{k=1}^{n}\binom{n}{k}f^k(1-f)^{n-k}(1-\lambda)^{k-1}\,k\,x(k)}{\sum_{k=1}^{n}\binom{n}{k}f^k(1-f)^{n-k}k\,x(k)} \tag{2.10.4.1}$$

The denominator of the fraction normalises the residual offsets from each labelled species by their contribution to the detected signal at $t = 0$. Significantly, equation (2.10.4.1) can be adapted to model PELDOR modulation depths in dependence of an arbitrary number of non-covalent labelling sites governed by a pair of dissociation constants, using the multi-site speciation model developed above.

Here, equation (2.10.3.17) is first rearranged so that the binomial coefficients and variable terms were separated into block vectors, C and U, respectively:

$$Z = \sum_{i=0}^{s} \sum_{j=0}^{t} \binom{s}{i} \binom{t}{j} \times (K_1[L])^{s-i}(K_2[L])^{t-j} \tag{2.10.4.2}$$

Beginning with the combinatorial coefficients, one can express this product as a block vector, over all i permutations of s and j permutations of t, given in equation (2.10.4.3):

$$C = [s_1[t_1 \quad t_2 \quad \cdots t_j] \quad s_2[t_1 \quad t_2 \quad \cdots t_j] \ldots s_i[t_1 \quad t_2 \quad \cdots t_j]\,] \tag{2.10.4.3}$$

This is recognisable as the Kronecker product of two vectors containing the combinatorial coefficients, and preserves the appropriate dimensionality where each coefficient describes the weighting of the associated microscopically-bound state. Similarly, U can also be written as a block vector:

$$U = [p_1\,[q_1 \quad q_2 \quad \cdots q_{t+1}] \quad p_2[q_1 \quad q_2 \quad \cdots q_{t+1}] \ldots p_{s+1}[q_1 \quad q_2 \quad q_{t+1}]\,] \tag{2.10.4.4}$$

Where for $i = 0 \rightarrow s$ and $j = 0 \rightarrow t$:

$$p_{i+1} = {K_{A1}}^{i}[L]^{i} \tag{2.10.4.5}$$

$$q_{j+1} = {K_{A2}}^{j}[L]^{j} \tag{2.10.4.6}$$

Therefore, both C and U can be constructed as Kronecker products, and for l-macroscopically bound states, Z can be expressed as a single summation over the microscopic speciation vector D:

$$Z = \sum_{i=0}^{l} D_{i+1} \tag{2.10.4.7}$$

Where: $D_i = C_i U_i'$ and $l = (s + t) + 1$

Let us also consider that one must convert from the microscopic speciation vector D to the macroscopic speciation vector x', because of degeneracy of microscopically-bound species. By reshaping the microscopic speciation vector with dimensions $(s + 1, t + 1)$, this allows indexing of states from unbound to $(s + t)$-bound protein, and can be considered algebraically as:

(s,t)	$t-t$	$t-2$	$t-1$	t
$s-s$	$(t-t)+(s-s)$	$(t-2)+(s-s)$	$(t-1)+(s-s)$	$t+(s-s)$
$s-4$	$(t-t)+(s-4)$	$(t-2)+(s-4)$	$(t-1)+(s-4)$	$t+(s-4)$
$s-3$	$(t-t)+(s-3)$	$(t-2)+(s-3)$	$(t-1)+(s-3)$	$t+(s-3)$
$s-2$	$(t-t)+(s-2)$	$(t-2)+(s-2)$	$(t-1)+(s-2)$	$t+(s-2)$
$s-1$	$(t-t)+(s-1)$	$(t-2)+(s-1)$	$(t-1)+(s-1)$	$t+(s-1)$
s	$(t-t)+s$	$(t-2)+s$	$(t-1)+s$	$t+s$

The transformation from one element to an adjacent anti-diagonal element, if it exists, can be expressed $(D_{i,j} \rightarrow D_{i-1,j+1})$.

Here, each element in the matrix is related to the total number of ligands bound to the protein molecule, through the summation of its respective coordinates. From this transformation, the sum of coordinates along an anti-diagonal is constant. That is, the total number of ligand molecules bound to the protein molecule is constant along the anti-diagonals, representing degenerate microscopically bound states that must be summed over to give the appropriate populations of the macroscopically bound states. Finally, using $x'(k)$ as a modified weighting of the macroscopically bound states, PELDOR modulation depths can be expressed:

$$\Delta_{PELDOR} = 1 - \frac{\sum_{k=1}^{n} x'^{(k)}\,(1-\lambda)^{k-1}\,k}{\sum_{k=1}^{n} x'^{(k)}\,k} \tag{2.10.4.8}$$

where: k is the number of spins for each species, $(1-\lambda)^{k-1}$ is the residual offset of the k-fold labelled species, n is the total number of binding sites present in the macromolecule, and $x'(k)$ is the fractional weighting of the k-fold labelled species, wherein combinatorial coefficients are also subsumed. This will be discussed in more detail in chapter 6.

2.10.5 Cooperative Binding Model

So far, theoretical descriptions have been provided for varying forms of one-site, two-site and multi-site Langmuir isotherm, but in each case binding was assumed to be independent. This is not always well met, and so an analytical description of a cooperative binding model is desirable,[254] wherein sequential binding events are thermodynamically (dis)favoured depending on the cooperativity mode. Let us consider a pair of coupled equilibria, of a cooperative ligand-templated dimerisation event, described by the reaction scheme:

$$P_2L \overset{K_{D2}}{\rightleftharpoons} PL + P \overset{K_{D1}}{\rightleftharpoons} 2P + L \tag{2.10.5.1}$$

Two assumptions are made about the system: i) the ligand is bivalent and so a single ligand molecule can coordinate two protein molecules simultaneously, and ii) the modulating effects of the first binding event upon the second (i.e., effects that result in the phenomenon $K_{D1} \neq K_{D2}$) are all subsumed into a cooperativity factor α. When $\alpha < 1$, cooperativity is negative so that $K_{D1} \ll K_{D2}$, when $\alpha = 1$, cooperativity is neutral so that $K_{D1} = K_{D2}$ (i.e., sites are independent), and when $\alpha > 1$, cooperativity is positive so that $K_{D2} \ll K_{D1}$. We can then define a single K_D value for the process (since the binding sites are the same) and an α value that modulates the affinity after the initial binding event. From equation (2.10.1.2) we have an expression of K_D for a monovalent ligand, while for a bivalent ligand there are two ways to form protein-ligand complex from protein and ligand (i.e., protein can bind at either site A or site B), but only one way to dissociate into protein and ligand. This gives a statistical pre-factor of 2 for K_A and 0.5 for K_D, hence we can reframe equation (2.10.1.2) with this consideration as:

$$K_D = \frac{2[P][L]}{[PL]} \tag{2.10.5.2}$$

In the second step of the reaction scheme shown above, there is one way to form protein-ligand-protein complex from protein and protein-ligand complex (i.e., protein can only bind protein-ligand complex at the one unoccupied site), but two ways to dissociate into protein-ligand complex (leaving either site A or site B unoccupied). This gives a statistical pre-factor of 0.5 in K_A and 2 for K_D. Hence, K_D can also be expressed as:

$$K_D = \frac{\alpha[P][PL]}{2[P_2L]} \tag{2.10.5.3}$$

Rearrangement of (2.10.5.2) and (2.10.5.3) for $[PL]$ and $[P_2L]$ respectively, yields (2.10.5.4) and (2.10.5.5):

$$[PL] = \frac{2[P][L]}{K_D} \tag{2.10.5.4}$$

$$[P_2L] = \frac{\alpha[P][PL]}{2K_D} \tag{2.10.5.5}$$

After successive substitution of (2.10.5.4) into (2.10.5.5) total ligand concentration can be expressed as:

$$[L]_0 = [L] + \frac{2[P][L]}{K_D} + \frac{\alpha[L][P]^2}{{K_D}^2} \tag{2.10.5.6}$$

Factorising and rearrangement for $[L]$ yields (2.10.5.7):

$$[L] = \frac{[L]_0 {K_D}^2}{{K_D}^2 + 2[P]K_D + \alpha[P]^2} \tag{2.10.5.7}$$

Substitution of (2.10.5.7) into (2.10.5.4) and (2.10.5.5) respectively, yields (2.10.5.8) and (2.10.5.9):

$$[PL] = \frac{2[P][L]_0 K_D}{{K_D}^2 + 2[P]K_D + \alpha[P]^2} \tag{2.10.5.8}$$

$$[P_2L] = \frac{\alpha[L]_0[P]^2}{{K_D}^2 + 2[P]K_D + \alpha[P]^2} \tag{2.10.5.9}$$

Using (2.10.5.8) and (2.10.5.9) one can define total protein concentration, $[P]_0$ as follows:

$$[P]_0 = [P] + \frac{2[P][L]_0 K_D}{{K_D}^2 + 2[P]K_D + \alpha[P]^2} + \frac{2\alpha[L]_0[P]^2}{{K_D}^2 + 2[P]K_D + \alpha[P]^2} \tag{2.10.5.10}$$

This can be rearranged to yield a cubic equation in $[P]$:

$$0 = ([P]_0 - [P])\left({K_D}^2 + 2[P]K_D + \alpha[P]^2\right) - 2[P][L]_0 K_D - 2\alpha[L]_0[P]^2 \tag{2.10.5.11}$$

Solving symbolically yields the cubic equation:

$$0 = [P]^3 + a[P]^2 + b[P] + c$$

Here *a*, *b* and *c* are given in (2.10.5.12)-(2.10.5.14), respectively:

$$a = \frac{2K_D}{\alpha} + 2[L]_0 - [P]_0 \tag{2.10.5.12}$$

$$b = \frac{K_D}{\alpha}(K_D + 2[L]_0 - 2[P]_0) \tag{2.10.5.13}$$

$$c = \frac{-(K_D)^2}{\alpha}[P]_0 \tag{2.10.5.14}$$

The physically real root of this cubic equation is given in (2.10.5.15):

$$[P] = -\frac{a}{3} + \sqrt[3]{\left(R + \sqrt{Q^3 + R^2}\right)} + \sqrt[3]{\left(R - \sqrt{Q^3 + R^2}\right)} \tag{2.10.5.15}$$

Where *a* is defined as above, and *Q* and *R* are defined below as:

$$Q = \frac{3b - a^2}{9} \tag{2.10.5.16}$$

$$R = \frac{9ab - 27c - 2a^3}{54} \tag{2.10.5.17}$$

Significantly, this binding model allows the simultaneous analysis and fitting of both PELDOR and RIDME modulation depths. The derivation is adapted from reference [254]. The wider scope of this application will be explored in chapter 6.

CHAPTER 3: Sub-micromolar Affinity of Cu^{II} Labeling at Double Histidine Motifs

This chapter has the following contributions. Dr Katrin Ackermann expressed and purified the model protein and prepared the EPR samples. JLW designed the double-histidine/cysteine construct primers, purified the construct DNA, performed the EPR measurements, processed the data and performed the biochemical characterisation (i.e., circular dichroism, isothermal titration calorimetry, mass spectrometry measurements). Dr David Norman built the Cu^{II}-IDA and Cu^{II}-NTA spin labels in XPLOR-NIH for molecular dynamics simulations. Dr Angeliki Giannoulis benchmarked the synthetic model systems that preceded this work. Dr Bela Bode designed the experiments and performed the initial *in silico* simulations. The results of this chapter have been peer-reviewed and published in a similar form: J. L., Wort, K. Ackermann, A. Giannoulis, A. J., Stewart, D. G., Norman, and B. E., Bode, *Angew. Chem. Int. Ed.,* 2019, **58**, 11681-11685. DOI: https://doi.org/10.1002/anie.201904848.

3.1 Introduction

PD-EPR spectroscopy is an attractive technique for the investigation of biomolecular structures that is complementary to NMR spectroscopy, crystallography and cryo-EM, providing nanometre distance constraints. PD-EPR is a solution-based technique that is not size-limited, nor requires crystallisation, akin to FRET. It has been instrumental in the structural and dynamical elucidation of proteins and nucleic acids on a length scale of 1.5–16 nm[133,279,280]. Specific applications include characterising multi-component systems,[281,282] intermolecular domain interactions,[283] distance constraints for structural modelling,[44] and functional mechanisms.[55] Furthermore, quantitative PD-EPR allows monitoring complexation events[67–69] and thus may couple structural information to binding equilibria.[183,184,229] Typically, paramagnetic moieties, such as nitroxide radicals, are site-specifically conjugated with thiol side-chains of cysteine residues, introduced in pairs at strategic positions via site-directed mutagenesis. Covalent attachment of the common methanethiosulfonate spin label (MTSL) results in the modified amino acid, R1, bearing a spin-labelled sidechain.

Notwithstanding the broad success of nitroxide based radicals, spectroscopically orthogonal spin labels, such as transition metal ions,[284–286] lanthanides,[287–290] and triarylmethyl-based spin labels,[291,292] are frequently used in conjunction with nitroxides. This allows the accessible information content of a single multi-labelled sample to be increased.[181,202] Importantly, orthogonal site-specific labelling can become problematic when relying on conjugation to cysteine thiols,[15,293] which lead to a statistical occupancy of labelling sites. In this purview, it is sometimes desirable to introduce genetically encoded labels such as unnatural amino-acids,[294–296] though these may perturb native structure when compared with post-translational modification of canonical amino-acids, with labelling efficiency an additional complication.

Recently, genetically encoded double-histidine motifs,[218] combined with Cu^{II}-chelates, and introduced in α-helices (at residue positions *i* and *i+4*), and β-sheets (at residue positions *i* and *i+2*) have emerged as alternatives to nitroxides for PD-EPR applications.[148,170,241] Importantly, coordination *via* histidine residues is chemically orthogonal to covalent cysteine modification, and allows systems non-permissive to thiol-based labelling (i.e., with essential disulfide bridges) to be investigated. An additional benefit of these Cu^{II}-based labels is the vastly superior precision in macromolecular distance measurements,[241] borne out of reduced conformational flexibility compared to R1. This manifests from the bipedal attachment mode and a reduced number of rotatable bonds between the paramagnetic centre and the protein backbone. Taken together, Cu^{II}-based spin labels in conjunction with double-histidine motifs provide powerful means to investigate nuanced conformational equilibria,[237,242] otherwise masked by broad distributions dominated by linker flexibility, as observed with mainstay spin labels.

However, this labelling strategy is non-covalent and so the binding equilibrium is described by a dissociation constant (K_D). Low affinity of double-histidine motifs for Cu^{II}-chelates is potentially compromising in two ways: i) the labelling efficiency would be consistently low, or ii) the excess of Cu^{II}-label would be large, leading to free label dominating the signal and reducing sensitivity. The free Cu^{II}-label would contribute to the detected echo but not the modulated signal and as such the modulation depth (Δ) would decrease. In tandem, this makes reliable extraction of the component modulated by the dipolar frequency more challenging, as instrumental artefacts and background would be more severe. Another consideration is the limiting sensitivity of the PELDOR experiment[11,16,17] when applied to paramagnetic centres with broad spectral width, such as transition metals. Herein, the RIDME experiment[179,180,269] obviates sensitivity concerns. In this case, the dipolar interaction is not driven by a microwave pulse, but rather stochastic spin flips arising from longitudinal relaxation. Hence, sensitivity is significantly improved as pulse excitation bandwidth limitations are removed, and broadband B-spin excitation only restricted by anisotropic T_1 relaxation.

In the case of hetero-spin RIDME measurements (inorganic radicals and metal ions), the detection frequency is placed on the nitroxide spin. This allows for addition of excess Cu^{II} without the free component contributing to the detected signal (at Q-band frequency and above), thereby improving double-histidine motif labelling without significantly reducing sensitivity. However, in regimes where a significant excess of Cu^{II}-chelate is added, this will decrease sensitivity because the transverse dephasing time (T_m) will decrease, while the background decay becomes steeper. Binding affinities have previously been estimated for Cu^{II}-IDA and Cu^{II}-NTA complexes for the protein double histidine motifs used in this work.[148,170,241]

A tetra-histidine (double-dH) GB1 construct I6H/N8H/K28H/Q32H[241] is investigated by RIDME, having previously been measured using Cu^{II}-Cu^{II} DEER,[241] where it was observed that Δ (i.e., binding affinity at the dH motifs) was limiting. Preliminary measurements of this construct to check reproducibility failed to recapitulate the poor binding affinity and precipitated the investigation of the individual dH sites through two dH/R1 constructs with dH sites in a β-sheet (I6H/N8H/K28R1) and an α-helix (I6R1/K28H/Q32H), respectively. Subsequently, we infer a sub-μM binding affinity from 5-pulse RIDME experiments at sub-μM protein concentrations, in stark contrast to the previous literature suggesting affinities were instead in the mid-to-high μM regime.

3.2 Materials and Methods

3.2.1 Construct Design

The I6H/N8H/K28H/Q32H GB1 gene was inserted into the pET11a plasmid vector without N- or C-terminal affinity tags. Nucleotide primers were ordered and mutagenesis (QuikChange Lightning Site-Directed Mutagenesis Kit, Agilent) proceeded in two rounds. Firstly, the following two GB1 constructs were produced: I6H/N8H and K28H/Q32H, before constructs I6H/N8H/K28C and I6C/K28H/Q32H were subsequently produced. The sequences of both the primers and constructs are provided in figures 3.2.1.1 and 3.3.2.2, respectively. Following *dpn1* treatment, PCR products were transformed into XL10-Gold Ultracompetent cells (Agilent), corresponding cDNA was extracted and purified (QIAprep® Spin Miniprep Kit 250), and sequence fidelity was confirmed with DNA sequencing (Dundee University DNA Sequencing and Services).

I6H/N8H GB1 Forward Primer Sequence:
5’ GCT GCT ACC GCG GAA AAG GTT TTC AAA CAG TAC GCT AAC G 3’
I6H/N8H GB1 Reverse Primer Sequence:
5’ CGT TAG CGT ACT GTT TGA AAA CCT TTT CCG CGG TAG CAG C 3’
K28H/Q32H GB1 Forward Primer Sequence:
5’ CAG TAC AAG CTT ATC CTG AAC GGT AAA ACC CTG AAA GGT G 3’
K28H/Q32H GB1 Reverse Primer Sequence:
5’ CAC CTT TCA GGG TTT TAC CGT TCA GGA TAA GCT TGT ACT G 3’
6H/8H/K28C GB1 Forward Primer Sequence:
5’ GTC GAC GCT GCT ACC GCG GAA TGC GTT TTC AAA 3’
6H/8H/K28C GB1 Reverse Primer Sequence:
6H/8H/K28C GB1 Forward Primer Sequence:
5' TTT GAA AAC GCA TTG CGC GGT AGC AGC GTC GAC 3'
I6C/28H/32H GB1 Forward Primer Sequence:
5' GCA GTA CAA GCT TTG CCT GCA CGG TAA AAC CCT G 3'
I6C/28H/32H GB1 Reverse Primer Sequence:
5' CAG GGT TTT ACC GTG CAG GCA AAG CTT GTA CTG C 3'

Figure 3.2.1.1. Forward and reverse nucleotide primer sequences used in the mutagenesis process for each GB1 construct.

I6H/N8H/K28C GB1 Protein Sequence:

6 8 28
MQYKLHLHGKTLKGETTTEAVDAATAECVFKQYANDNGVDGEWTYDDATKTFTVTE

I6C/K28H/Q32H GB1 Protein Sequence:

6 28 32
MQYKLCLNGKTLKGETTTEAVDAATAEHVFKHYANDNGVDGEWTYDDATKTFTVTE

Figure 3.2.1.2. Full amino-acid sequence for both I6H/N8H/K28C and I6C/K28H/Q32H GB1 constructs, with the cysteine residue for R1-labelling in red, and each histidine residue of the double-histidine motifs shown in blue; and residue number indicated above the sequence in each case.

3.2.2 Protein Expression and Purification

The I6H/N8H/K28H/Q32H construct was expressed and purified as published previously.[241] The sequenced plasmid vectors for the other constructs were transformed into expression-strain BL21 (DE3) cells and grown in Luria-Bertani (LB) medium (50 µg/ml Ampicillin Sodium (Formedium™)) via incubation (37 °C, 180 rpm) until OD = 0.6-0.8, before expression was induced with 0.5 mM isopropyl-β-D-1-galactopyranoside (IPTG) (Formedium™) for 4 hours. Cultures were pelleted *via* centrifugation (45 minutes, 6,000 × g). Pellets were resuspended in lysis buffer (20 mM Tris-HCl, 5 mM NaCl, 0.1% v/v Triton X-100, 0.5 mg/mL hen-egg lysozyme (Sigma Aldrich), DNAse (Sigma Aldrich), cOmplete™ mini EDTA-free protease inhibitor cocktail (Roche), pH 8.5) and sonicated immediately. The 6C/28H/32H construct was lysed in a volume of lysis buffer corresponding to 10 × the pellet weight, for the 6H/8H/28C construct half of that volume (5 × pellet weight) was used. Cellular resuspensions were lysed via sonication (6 × 30 seconds pulsed, 30 seconds off, 12 µm amplitude), and then heat-shocked (80 °C, 10 minutes) and centrifuged (30 minutes, 48,380 × g, 4 °C). The supernatant was sterile-filtered (0.2 µm hydrophilic membrane filter, Millex®, Sigma Aldrich) before loading onto a pre-equilibrated anionic exchange column (5 mL Hi-Trap™ Q HP). The column was subsequently washed with 10 column volumes of 20 mM Tris-HCl, 5 mM NaCl, pH 8.5 (buffer A), protein was eluted via a gradient over 8 column volumes to 50% 20 mM Tris-HCl, 1M NaCl, pH 8.5 (buffer B) and fraction purity for each construct was assayed via sodium dodecyl sulfate polyacrylamide gel electrophoresis (SDS-PAGE). In case of the 6H/8H/28C construct, the majority of the protein was found in the flow-through of the HiTrap column. The flow-through was therefore diluted 1:1 with buffer A and reloaded using 2 × 5 mL Hi-Trap™ Q HP columns in tandem to avoid potential overloading. Fractions containing GB1 were pooled and subsequently concentrated via 3,000 Da MWCO (molecular weight cut-off) centrifugal concentrators (Pall Microsep™ Advance), with final sample purity being assessed via matrix-assisted laser desorption/ionisation (MALDI) time-of-flight (TOF) mass spectrometry, as shown in section 2.3, and SDS-PAGE, as shown in section 2.1, before proceeding with MTSL-labelling. All gel electrophoresis was performed with 4-12% polyacrylamide gels (NuPAGE), run at a constant 200 V for 30 minutes. As marker a broad range protein ladder (10-180 kDa) was used (PageRuler™ Pre-stained Protein Ladder) (ThermoFisher™).

3.2.3 MTSL Labelling and PD-EPR Sample Preparation

Labelling of I6C/K28H/Q32H and I6H/N8H/K28C GB1 constructs with S-[(1-oxyl-2,2,5,5-tetramethyl-2,5-dihydro-1Hpyrrol-3-yl)methyl] methanesulfonothioate (MTSL) (Santa Cruz™ Biotechnology) proceeded *via* incubation with 10 mM dithiothreitol (DTT) (Formedium™) (4 °C, 2 hours) to reduce the cysteine residues. A desalting PD10 column (Amersham Biosciences) was used to remove the reducing agent. The column was equilibrated in buffer A and protein eluted in 3.5 mL, before incubation with MTSL label (10-fold molar excess, 4 °C, 16 hours). To remove free MTSL label, material was loaded on a HiLoad 26/600 Superdex 200 pg size-exclusion chromatography column equilibrated in 42.4 mM Na_2HPO_4, 7.6 mM KH_2PO_4, 150 mM NaCl, pH 7.4 (buffer C). Spin labelling efficiency was qualitatively assessed using MALDI-TOF mass-spectrometry and quantitatively assessed using CW-EPR. Freeze-drying and redissolution of quantitatively MTSL-labelled protein into D_2O facilitated exchange into deuterated matrix. Ethylene glycol d-6 (Deutero GmbH) was used as cryoprotectant (50% v/v), and ensured samples formed a glass upon freezing, after Cu^{II}-IDA or Cu^{II}-NTA label was added. All samples had a final volume of 70 µL, unless otherwise stated, and immersion in liquid nitrogen ensured snap-freezing.

Concentrated solutions of the Cu^{II}-chelate labels were produced using anhydrous $CuCl_2$ (VWR™), IDA ($C_4H_5NO_4Na_2$, sodium iminodiacetate dibasic hydrate; Sigma Aldrich®), and NTA ($C_6H_9NO_6$; Sigma Aldrich®). 100 mM solutions of NTA and $CuCl_2$ in deionized H_2O at pH 2.0, and pH 12.0, respectively were prepared for the Cu^{II}-NTA label. Dilution of the NTA solution 1:8 parts in 42.4 mM Na_2HPO_4, 7.6 mM KH_2PO_4, 150 mM NaCl, pH 7.4, followed by dropwise addition of 1 part $CuCl_2$ solution, gave a working concentration of 10 mM Cu^{II}-NTA.[297] Dilution of 200 mM IDA solution 1:1 part in 200 mM $CuCl_2$ solution, each in deionized H_2O, yielded a working concentration of 100 mM Cu^{II}-IDA. For the Cu^{II}-labelling of the protein, Cu^{II}-IDA and Cu^{II}-NTA stock solutions were freeze-dried and redissolved in D_2O to final concentrations of 100 and 10 mM, respectively.

3.2.4 EPR Instrumentation

All pulse EPR experiments were performed using a Bruker ELEXSYS 580 pulse EPR spectrometer. Temperatures were maintained using a cryogen-free variable temperature cryostat (Cryogenic Ltd) operating in the 3.5-300 K temperature range. All measurements of the electron spin longitudinal relaxation times (T_1) of Cu^{II}-IDA and Cu^{II}-NTA, and all 5-pulse dead-time free RIDME measurements[180] were performed at 30 K, using a high-power 150 W travelling-wave tube (TWT; Applied Systems Engineering) at Q-band (34 GHz) in a critically coupled 3 mm cylindrical resonator (Bruker ER 5106QT-2w in TE012 mode). All 4-pulse dead-time free PELDOR measurements[16,17] were performed at 15 K at X-band (9.4 GHz) with a 1 kW TWT (Applied Systems Engineering) in an overcoupled 3 mm split-ring resonator (Bruker 4118X-MS3), unless otherwise stated. All CW-EPR measurements were performed using a Bruker EMX 10/12 spectrometer equipped with an ELEXSYS Super Hi-Q resonator, at X-band frequencies (9.8 GHz) and at 298 K.

3.2.5 Parameters of Relaxation Time Measurements

Longitudinal relaxation time constants, T_1, were measured using the 3-pulse inversion recovery (IR) experiment (π-T-π/2-τ-π). In all cases inversion pulses (nominal flip-angle π) were of length 12 ns, and detection pulses (π/2- and π, respectively) were of lengths 20 ns and 40 ns. Detection was consistently performed at the maximum field position of the Cu^{II} spectrum. Trace length was consistently 500 µs, the time-step increment of the interval T was 200 ns, shot repetition time (SRT) was 2 ms (unless otherwise stated), and τ was 800 ns. T_1 values were estimated using mono- and bi-exponential approximations, with traces fitted to equations 3.2.5.1 and 3.2.5.2, respectively:

$$y = M_0\left[1 - 2\lambda \times \exp\left(\frac{-t}{T_1}\right)\right] \tag{3.2.5.1}$$

$$y = M_0\left[1 - 2\lambda\left(b \times \exp\left(\frac{-t}{T_{1A}}\right) + (1-b) \times \exp\left(\frac{-t}{T_{1B}}\right)\right)\right] \tag{3.2.5.2}$$

where: M_0 is the signal intensity at $t \to \infty$, and so acts as a scaling factor, λ is the efficiency of the inversion pulse (bounded 0-1), and T_1 is the fitted longitudinal time constant. For the bi-exponential approximation, M_0 and a are defined as above, while b and $(1-b)$ are the relative contributions of the fast and slow components, given as T_{1A} and T_{1B}, respectively.

The 2-pulse (π/2-τ-π) electron spin-echo (ESE) decay experiment was applied at either the maximum field position of the nitroxide or Cu^{II}-chelate spectrum, using 16 and 32 ns π/2- and π-pulses. Traces were acquired to various time windows between 10-20 µs depending on the measurement temperature in the range 10-50 K, using a τ of 800 ns (due to dead-time in high Q mode), and was incremented in steps of 8 ns. The SRT used varied depending on the measured temperature and detected species. Raw data was fitted with a stretched-exponential function, and is given in equation 3.2.5.3, to estimate T_m:

$$y = M_0\left[\exp\left(\left(\frac{-t}{T_m}\right)^x\right)\right] \tag{3.2.5.3}$$

where x is the stretching exponent constrained between 1 and 2, M_0 is the signal intensity at $t = 0$, and T_m is the fitted phase memory time constant.

3.2.6 Parameters of PD-EPR Measurements

For the Cu^{II}-nitroxide X-band PELDOR measurements the 4-pulse experiment (π/2(υ_A)-τ_1-π(υ_A)-τ_1-t-π(υ_B)-(τ_2-t)-π(υ_A)-τ_2-echo) was used, where υ_A and υ_B indicate the pulse excitation at the observer and pump frequencies, respectively. In all cases pulses of lengths 16 and 32 and 10 ns were used for observer and pump pulses (π/2, π and π). The magnetic field and microwave frequency were adjusted for the maximum of the nitroxide spectrum to coincide with the pump pulse position, while the observer pulse was placed at 140 MHz higher frequency for detection of spins centred on copper ions and minimal overlap of pump and detection excitation bands. Due to strong ESEEM induced by deuterium nuclei a τ_1 of 470 ns was chosen, to maximise electron spin echo intensity, and thus improve the signal-to-noise ratio.

The I6H/N8H/K28R1 and I6R1/K28H/Q32H GB1 constructs were measured at concentrations of 220 and 250 μM, and at sample volumes of 15 and 25 μL, respectively, in presence of 1.5 molar equivalents of each Cu^{II}-chelate. The I6H/N8H/K28R1 Cu^{II}-chelate samples were measured with a time window of 1360 ns, a dipolar increment of 8 ns, 135 points, 50 shots-per-point and were averaged for 12 and 16 hours for Cu^{II}-IDA and Cu^{II}-NTA, respectively. The I6R1/K28H/Q32H Cu^{II}-IDA sample was measured with a time window of 1900 ns, a dipolar increment of 8 ns, 180 points, 50 shots-per-point and averaged for 3 hours. The Cu^{II}-NTA sample was measured with a time window of 1160 ns, a dipolar increment of 8 ns, 96 points, 50 shots-per-point and averaged for 3 hours.

The I6H/N8H/K28H/Q32H GB1 construct was measured using the 4-pulse PELDOR experiment at 30 K and Q-band frequency, at a concentration of 25 μM and at a sample volume of 100 μL, in presence of 2.0 molar equivalents of Cu^{II}-NTA. This was performed on a Bruker ELEXSYS 580 pulse EPR spectrometer; the Bruker ER 5106QT-2w in TE012 mode resonator was overcoupled, pulses of lengths 16 and 32 and 24 ns were used for observer and pump pulses (π/2, π and π). Magnetic field and microwave frequency were adjusted for the maximum of the Cu^{II}-NTA spectrum to coincide with the pump pulse position, while the observer pulse was placed at 80 MHz higher frequency. The sample was measured with a time window of 1280 ns, a dipolar increment of 8 ns, 122 points, 1 shot-per-point and 1 scan, for the purpose of sensitivity comparison with Cu^{II}-Cu^{II} and Cu^{II}-nitroxide RIDME.

The 5-pulse RIDME experiment ($\pi/2$-τ_1-π-τ_1-t-$\pi/2$-T_{mix}-$\pi/2$-(τ_2-t)-π-τ_2-echo) was used (figure 2.6.3). Rectangular pulses of lengths 12 and 24 ns were used (π/2 and π, respectively), consistently placing the detection frequency to the maximum of the nitroxide spectrum. All acquisitions were performed over a single scan (unless otherwise stated), with two shots-per-point, with a SRT of 30 ms, and deuterium ESEEM was suppressed via a 16-step nuclear modulation τ-averaging cycle.[298] Signal contributions from unwanted echoes were eliminated using an 8-step phase-cycle, totalling 128 steps per measurement, with the refocused virtual echo (RVE) being detected. For all samples, at least two lengths of mixing block were recorded; a short reference mixing time (T_{ref}) and a long mixing time (T_{long}) to allow suppression and observation of the dipolar coupling, respectively. The I6H/N8H/K28R1 and I6R1/K28H/Q32H GB1 constructs were measured at 5 μM, with one equivalent of each Cu^{II}-chelate, and at a sample volume of 75 µL. The RIDME traces of the pseudo-titration performed at 0.5 μM I6R1/K28H/Q32H GB1 in presence of varying Cu^{II}-NTA concentrations were also recorded in the same manner, and at a sample volume of 75 µL.

3.2.7 Sensitivity Optimisation of PD-EPR Measurements

Sensitivity optimisation of Cu^{II}-nitroxide and Cu^{II}-Cu^{II} RIDME experiments was essential before performing the 500 nM pseudo-titration series measurements. A sensitivity expression for 4-pulse PELDOR[247] was adapted to account for additional contributing factors in the 5-pulse RIDME experiment and is shown in equation (3.2.7.1):

$$\frac{S}{N_{RIDME}} \sim \frac{1}{T}\exp\left(\frac{-2t_{max}}{T_{mA}}\right)\frac{1}{\sqrt{T_{1A}}}\exp\left(\frac{-T_{mix}}{T_{1A}}\right)\left(\frac{\left(1-\exp\left(\frac{-T_{mix}}{T_{1A}}\right)\right)}{2}\right) \tag{3.2.7.1}$$

where: the subscripts A and B indicate the detected and inverted (fast-relaxing) spins, respectively. T is the temperature in Kelvin, T_1 and T_m are the longitudinal relaxation and transverse dephasing times, respectively, t_{max} is the dipolar evolution time window, and T_{mix} is the mixing block interval. Additional terms added to the literature expression describe longitudinal relaxation and subsequent loss of detected spin magnetisation, and modulation depth arising from the longitudinal relaxation of non-resonant spins, both during the interval T_{mix}. This expression was also further extended to include a stretching exponent for T_m and a bi-exponential approximation of T_1, primarily because electron spin echo decay and inversion recovery data were fitted best using a stretched exponential and bi-exponential approximation, respectively, yielding the form:

$$\frac{S}{N_{RIDME}} \sim \frac{1}{T}\exp\left(\left(\frac{-2t_{max}}{T_{mA}}\right)^{x}\right)\frac{1}{\sqrt{T_{1A}^{fast}}}\left(b\times\exp\left(\frac{-T_{mix}}{T_{1A}^{fast}}\right)+(1-b)\times\exp\left(\frac{-T_{mix}}{T_{1A}^{slow}}\right)\right)\times$$

$$\left(\frac{\left(1-\left(b\times\exp\left(\frac{-T_{mix}}{T_{1B}^{fast}}\right)+(1-b)\exp\left(\frac{-T_{mix}}{T_{1B}^{slow}}\right)\right)\right)}{2}\right) \tag{3.2.7.2}$$

For a homo-spin pair, the optimum mixing block interval (T_{mix}) can be determined by finding the maximum of the product of the longitudinal relaxation loss factor and the modulation depth build-up (since $T_{1A} = T_{1B}$):

$$f(T_{mix}) = \exp\left(\frac{-T_{mix}}{T_{1,A}}\right)\left(\frac{\left(1-\exp\left(\frac{-T_{mix}}{T_{1,B}}\right)\right)}{2}\right) \tag{3.2.7.3}$$

Thus, sensitivity is maximised when T_{mix} is approximately $0.7 \times T_1$. For $\mathrm{Cu^{II}}$-$\mathrm{Cu^{II}}$ PELDOR[241] sensitivity was estimated using the literature expression, with the stretched exponential in the transverse dephasing term, as is given in equation 3.2.7.4:

$$\frac{S}{N_{PELDOR}} \sim \frac{1}{T}\exp\left(\left(\frac{2t_{max}}{T_{m,A}}\right)^{x}\right)\frac{1}{\sqrt{T_{1,A}}} \tag{3.2.7.4}$$

The influence of multiple parameters was investigated systematically, with the corresponding sensitivity profiles discussed in greater detail in section 3.3.9.

3.2.8 RIDME Data Analysis and Processing

Nitroxide-detected 5-RIDME traces have a low frequency artefact that is caused by dynamical decoupling,[299] at time $t = \tau_1$ because the mixing block can behave as an effective π-pulse and yield a

Carr-Purcell pulse sequence: π/2-τ_1-π-2τ_1-π-echo. This leads to a refocussing of coherence decay in the transverse plane at time $t = \tau_1$. In this purview, RIDME traces were pre-processed by dividing the time domain data of the long mixing time (T_{long}) trace by the short mixing time (T_{ref}) trace, which allowed imperfections (i.e., the low frequency artefact) to be deconvoluted away. The resulting deconvoluted data could be fitted well using second-order polynomial background functions and facilitated modulation depth quantitation in DeerAnalysis2015. The RIDME background decay has recently been shown to behave as a stretched exponential with dimensions 3-6,[269] and is largely dominated by electron-electron and electron-nuclear spectral diffusion, which leads to a steeper background decay compared to PELDOR. The spectral diffusion occurs most significantly in the mixing block, as it is long with respect to the rest of the pulse sequence. Particularly for RIDME measurements acquired to short dipolar evolution times, stretched exponential background functions can be well approximated by polynomials. The error arising from background correction was minimised by using values for background start and cut-off robust against changes in modulation depth, (i.e., modulation depth was stable when background start and cut-off points were iterated. However, the pre-processing step erases some dipolar contribution such that modulation depths are underestimated, thus a re-scaling is necessary to account for the deconvolution step. This correction was performed according to equation 3.2.8.1, where $\mathit{\Delta}_{T_{long}}$ and $\mathit{\Delta}_{T_{ref}}$ are the long and short mixing-time calculated modulation depths, respectively.

$$\Delta_c = \left(1 - \frac{1 - \Delta_{T_{long}}}{1 - \Delta_{T_{ref}}}\right) \qquad (3.2.8.1)$$

where: the magnitude of Δ as a function of time T_{mix} (T_{long} or T_{ref}) and T_1 has been defined in the theory section (see chapter 2.7).

3.2.9 Mass Spectrometry

All mass spectra were collected in-house using a Sciex MALDI TOF/TOF 4800 mass-spectrometer, with samples crystallised using a matrix of α-cyano-4-hydroxycinnamic acid. Unlabelled and MTSL-labelled I6H/N8H/K28C and I6C/K28H/Q32H GB1 samples were both prepared at 20 μM concentration in 20 mM Tris-HCl, 5 mM NaCl, pH 8.5 or 42.4 mM Na_2HPO_4, 7.6 mM KH2PO4, 150 mM NaCl, pH 7.4, respectively, and mass spectra were recorded in the absence of Cu^{II}.

3.2.10 CW EPR Sample Preparation

Nominally, measurements were performed at 100 μM protein concentration, using disposable 50 μL capacity micropipettes (BlauBrand®). Labelling efficiency with MTSL was estimated from double integrals of the background corrected spectra and compared against fixed concentrations of the unbound spin label; measured labelling efficiency was consistently ≥ 95%, and negligible residual free spin label contribution was detected.

3.2.11 *Circular Dichroism and Thermal Denaturation Assay Measurements*

All measurements were performed using a MOS-500 circular dichroism spectrometer (BioLogic) with an ALX-300 Hg lamp in the far-UV range (180-260 nm). Samples were measured in a 0.1 mm quartz cuvette at a protein concentration of 50 μM, in the presence and absence of 150 μM Cu^{II}-IDA, all in 10 mM sodium phosphate, pH 7.4. Before and after each sample measurement, a blank was taken containing only 10 mM sodium phosphate, pH 7.4 (and 150 μM Cu^{II}-IDA where appropriate) to be subtracted from the raw data for baseline correction. All measurements were performed using an acquisition period of 0.5 seconds, a 0.25 nm step-size, at 298 K, and using a 2 nm bandwidth from 200-260 nm. For the thermal denaturation curves, two wavelengths (220 and 260 nm) were monitored over the temperature range 20-98 ºC using a TCU250 Peltier temperature controller. The two wavelengths reported changes in the global minimum of the spectra, and in the background signal, respectively. The thermal profile used 39 intervals of 2 ºC in the range 20-98 ºC, and a 120 second equilibration interval at each temperature prior to measurement. As above, measurements were baseline corrected with 10 mM sodium phosphate, pH 7.4 (+ 150 μM Cu^{II}-IDA where appropriate). Finally, the melting curves were fitted using a two-state unfolding model to extract the melting temperatures (T_M).

3.2.12 *Isothermal Titration Calorimetry Measurements*

All ITC experiments used a Malvern MicroCal ITC200 instrument, and were optimised and performed over 19 injections of 2 μL titrant, with an equilibration time of 150 seconds between injections, at 298 K. All samples were centrifuged immediately before measurement for degassing. All protein was measured at 75 μM concentration and titrant concentrations were either 1 or 2 mM; therefore blank conditions of buffer (42.4 mM Na_2HPO_4, 7.6 mM KH_2PO_4, 150 mM NaCl, pH 7.4) and titrated against addition of 1 or 2 mM titrant were recorded, to be subtracted from the raw data and mitigate the heat of dilution; all data analyses were performed in MicroCal Origin 7 (OriginLab, Northampton, MA) and thermodynamic parameters were derived using a single-site fitting model. To this end eq. 3.2.12.1 and 3.2.12.2 were used, given below, where: Q_i is the heat content of the solution at the point of the ith injection, K is the binding constant, n is the number of sites, $\mathit{\Delta H}$ is the molar heat of ligand binding, V_0 is the active cell volume, M_t is the total concentration of macromolecule contained in V_0, X_t is the total concentration of ligand contained in V_0 and $\mathit{\Delta Q_i}$ is the change in heat content of the solution between the (i-1)th and the ith injection and ΔV_i is the injection volume. Standard Marquardt methods are then applied to minimise the deviation between the estimated values of n, $\mathit{\Delta H}$ and K and the experimental values determined from $Q_{(1,2\ldots\mathrm{i}-1,\mathrm{i})}$.

$$Q_i = \frac{nM_t\Delta HV_0}{2}\left[1+\frac{X_t}{nM_t}+\frac{1}{nKM_t}-\sqrt{\left(1+\frac{X_t}{nM_t}+\frac{1}{nKM_t}\right)^2-\frac{4X_t}{nM_t}}\right] \tag{3.2.12.1}$$

$$\Delta Q_i = Q_i + \frac{\Delta V_i}{V_0}\left[\frac{Q_i + Q_{i-1}}{2}\right] - Q_{i-1} \tag{3.2.12.2}$$

3.2.13 *Molecular Dynamics and MMM Simulations*

At the time of writing, forcefields for molecular dynamics simulations of dH-bound $\mathrm{Cu^{II}}$-NTA and other $\mathrm{Cu^{II}}$-based spin labels were not available but have since been developed and benchmarked.[300,301] In lieu of this, the XPLOR-NIH package[302] was used to perform simplified molecular dynamics simulations, and to investigate the available conformational space of the spin labels. The force field (CHARMM19) and restraints on movement were implemented within XPLOR to allow for exploration of available geometry in the absence of electrostatics and solvation (i.e., *in vacuo*). While simple in implementation, this approach has compared favourably to other more sophisticated approaches using rotamer sampling algorithms.[303] The geometry of the chelated copper ion and surrounding ligands was constrained with a planarity constraint, while the backbone of the protein was constrained using a harmonic potential. The side chains (including those of the histidine ligands) were allowed to move freely under the influence of the simplified bond, angle and dihedral potentials. To improve reproducibility, exemplary dynamics, parameter and topology input files used in the simulations are given in appendix A. These contain details regarding planarity and harmonic constraints, bond angles, dihedrals and force-constants.

In silico mutagenesis was performed in the mutagenesis tool in PyMOL (The PyMOL Molecular Graphics System, Version 2.0 Schrödinger, LLC), and steric strain was minimised for rotamer populations before MTSL and $\mathrm{Cu^{II}}$-IDA labels were built. Models were then stabilised with iterative minimisation via Powell's conjugate direction method[304] (n = 50) and molecular motion was simulated using Verlet integration[305] at 200 K for 100 trials; between 103-105 structures were collected in the time interval of 25 ns, in steps of 0.25-2.5 ps. The molecular dynamics for the R1 label generated rotamer libraries that were compared with those from MTSSL Wizard tool in Pymol[303] and indicated reasonable agreement.

All MMM modelling was performed using MMM2018.[306–308] Here, libraries of rotamers of spin labels are calculated (i.e., yield a coarse-grain representation of the conformational space available to the label) from long trajectory molecular dynamics runs. These trajectories are performed for 100 ns at 298 or 175 K, with the spin label typically modelled onto an isolated residue using a customised form of CHARMM27 forcefield[309,310] and assuming implicit solvation,[311] before a representative set of rotamers with 'canonical' dihedrals (i.e., values around which dihedral angles taken from the molecular dynamics trajectories are clustered) is generated. The backbone atoms are constrained with a harmonic and so cannot freely move. This describes the general approach for generating spin label rotamer libraries in MMM, however further details of the parameters for molecular dynamics simulations and the MMM methodology are available in reference [307]. In the I6H/N8H/K28H/Q32H GB1 crystal structure (PDB ID: 4WH4[241]) histidine residues at positions 28 and 32 were replaced, respectively, with cysteine and glutamine residues, on chain A of the crystal structure. A $\mathrm{Cu^{II}}$-IDA label (using the 'symmetric' mode) was introduced at position 6, along with an R1 label at position 28, to simulate the I6H/N8H/28R1 GB1 construct. The process was then repeated, instead with replacement of the histidine residues at positions 6 and 8 with cysteine and asparagine, respectively, and insertion of R1 at position 6 to simulate the 6R1/K28H/Q32H construct. PELDOR traces were simulated using the ‘ambient’ temperature (298 K) option.

3.2.14 *UV-Visible Spectroscopy*

UV-visible spectroscopy quantified both Cu^{II}-IDA and Cu^{II}-NTA concentrations. A single beam Varian 50 bio UV-visible spectrophotometer with a Xe flash lamp and a wavelength resolution of 1 nm was used to record all spectra. Before measuring all experimental conditions, blanks containing only buffer were run to suppress background signal. For quantification, Cu^{II}-IDA samples of concentrations 25.4, 12.7, 5.1, and 2.5 mM and Cu^{II}-NTA samples of concentrations 10.0, 7.5, 5.0, 2.5 and 1.0 mM were prepared as described in section 3.2.3 and were respectively blanked against milliQ H_2O and corresponding buffer (42.4 mM Na_2HPO_4, 7.6 mM KH_2PO_4, 150 mM NaCl, pH 7.4). Quadruplicate repeat measurements were performed for each sample, in the range 300-800 nm, using a path-length of 10 mm and spectra were analysed and plotted using the Cary software package.

3.3 *Results and Discussion*

3.3.1 *Expression and Purification of GB1 Constructs*

To determine the efficacy of expression of the I6H/N8H/K28C and I6C/K28H/Q32H GB1 constructs, SDS-PAGE gels of the corresponding expression profiles are shown in the left and right panels of figure 3.3.1.1, respectively. It should be noted that GB1 runs on SDS-PAGE gels as a ~13 kDa band. In each case, bands corresponding to GB1 are visible ~1 hour post-induction using 500 μM IPTG (Formedium™).

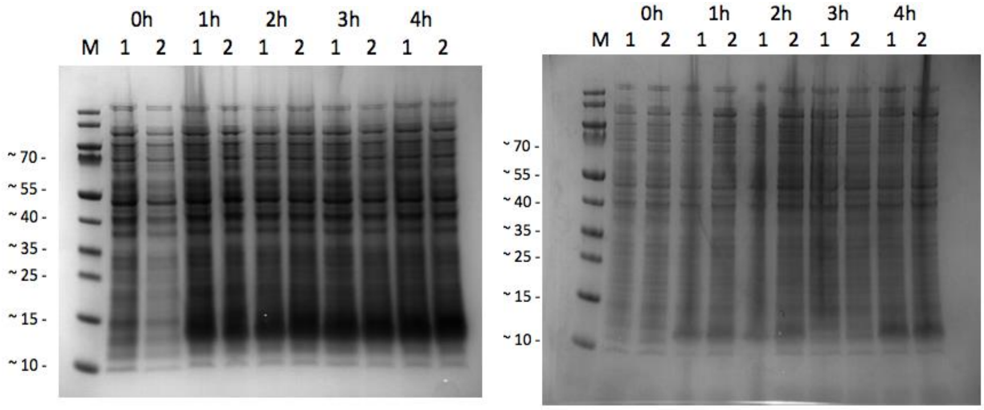

Figure 3.3.1.1. SDS-PAGE gels showing the expression profiles for the I6H/N8H/K28C and I6C/K28H/Q32H constructs, shown left and right respectively.

Protein purification then proceeded via an anionic-exchange step, and figure 3.3.1.2 shows the corresponding chromatograms and SDS-PAGE gels. For the I6H/N8H/K28C construct, after this step protein persisted in the flow-through and wash fractions (red circle on the SDS-PAGE gel shown in figure 3.3.1.2 (centre panel, right column)), indicating a large fraction of the protein failed to bind to the column. This was rationalised as an insufficient volume of lysis buffer being used to solve the cell pellet, contributing to a higher conductivity, and lower affinity for the column than expected. Upon repetition of this anionic exchange step after further dilution with buffer A to reduce conductivity, the wash and flow-through fractions were clear of any GB1 protein (bottom row of figure 3.3.1.2). Potential overloading of the resin was also minimised by using two columns in concert.

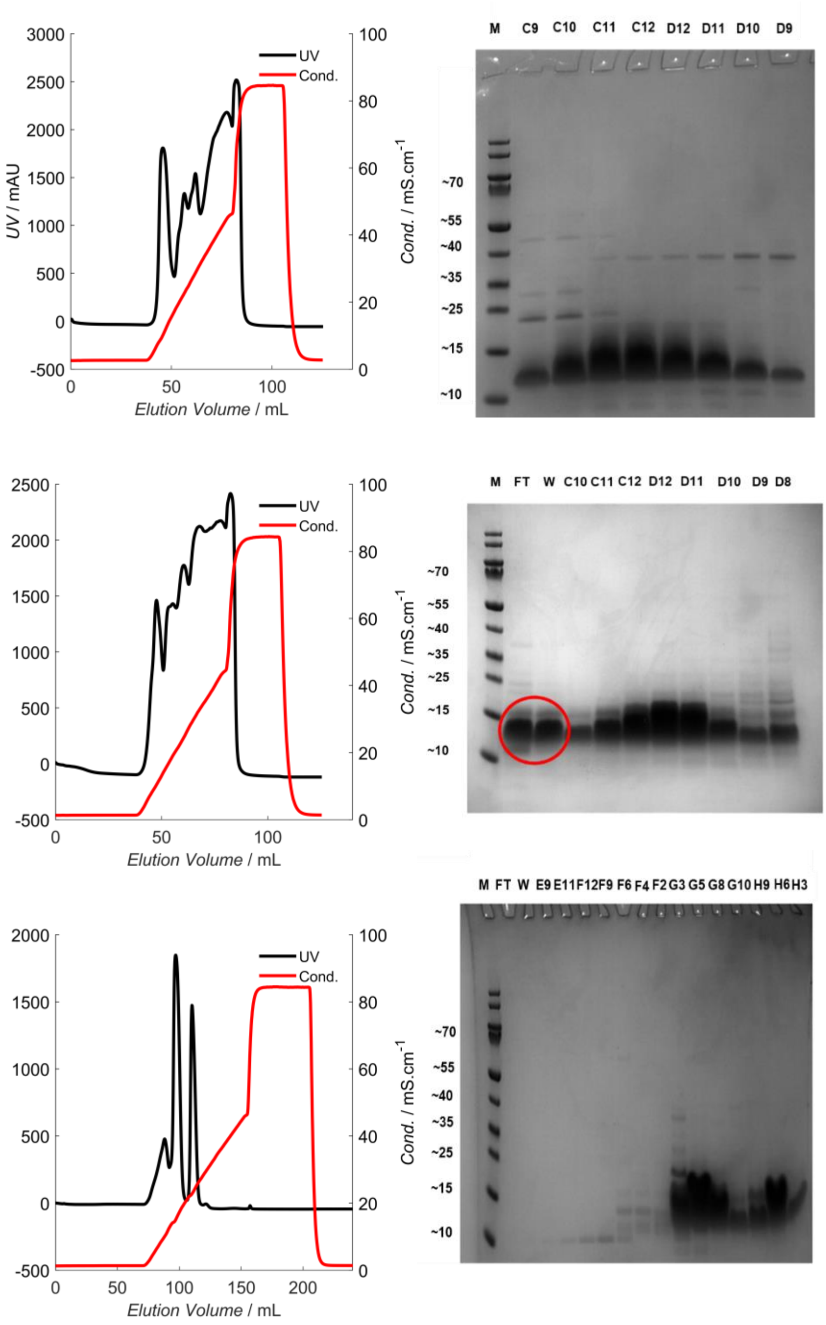

Figure 3.3.1.2: Chromatograms of the HiTrap anionic-exchange columns recorded at 280 nm, with absorbance shown in black and conductivity shown in red, and SDS-PAGE gels assessing fraction purity for the I6C/K28H/Q32H construct in the top row, and for the I6H/N8H/K28C construct in the centre and bottom rows, for the first and second HiTrap columns, respectively.

Size-exclusion chromatography was used as the final step of protein purification, and figure 3.3.1.3 shows the corresponding chromatograms and SDS-PAGE gels. This step also facilitated free spin label removal, and yielded a thorough buffer exchange before EPR sample preparation, compared to PD10 columns. As can be seen, protein purity is sufficiently high to proceed with use in subsequent experiments, with only a single peak corresponding to GB1, circled in the chromatograms. All pooled fractions were subsequently confirmed to contain pure GB1 *via* mass spectrometry.

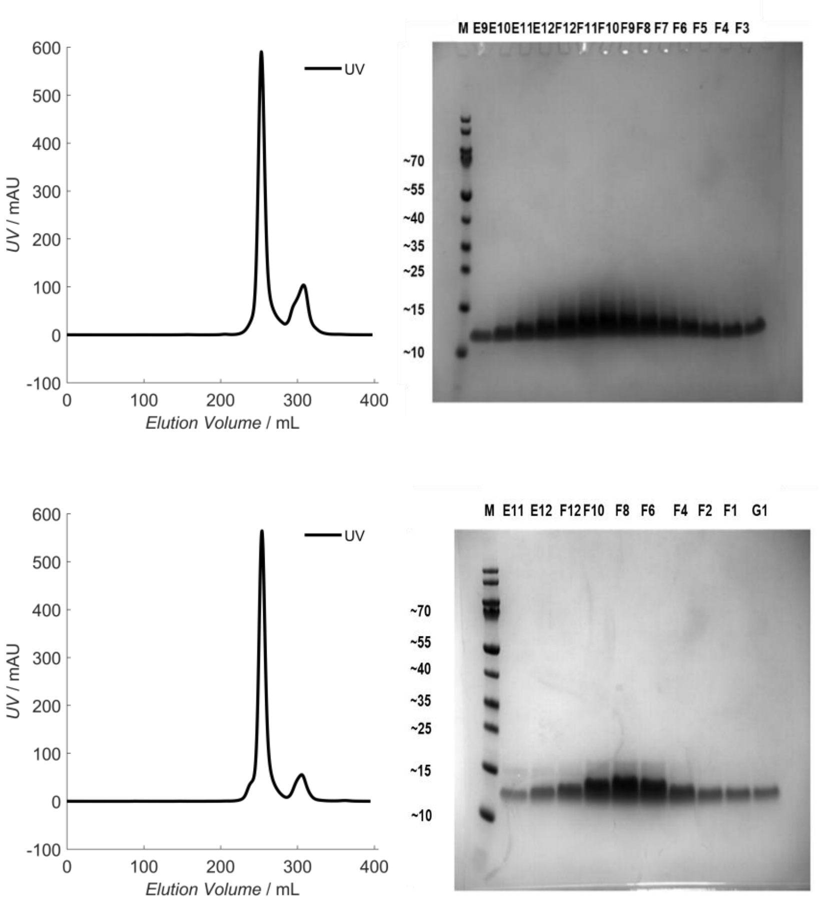

Figure 3.3.1.3: Chromatograms recorded at 280 nm, and SDS-PAGE gels assessing fraction purity for I6C/K28H/Q32H and I6H/N8H/K28C constructs, in the top and bottom rows, respectively.

3.3.2 *MTSL Spin Labelling of GB1 Constructs*

Continuous-wave EPR spectra for each GB1 construct are shown in figure 3.3.2.1 for constructs I6R1/K28H/Q32H and I6H/N8H/K28R1 GB1 and indicate an absence of free-label, lacking high mobility components in the high-field peaks. For the quantification, all samples were acquired for 10 scans; prior to integration steps, data were baseline corrected using cubic polynomial functions, and the double integrals (DI) were calculated using the Bruker™ WIN-EPR software package. The corresponding labelling efficiencies are given in table 3.3.2.1 below and indicate quantitative labelling of both constructs.

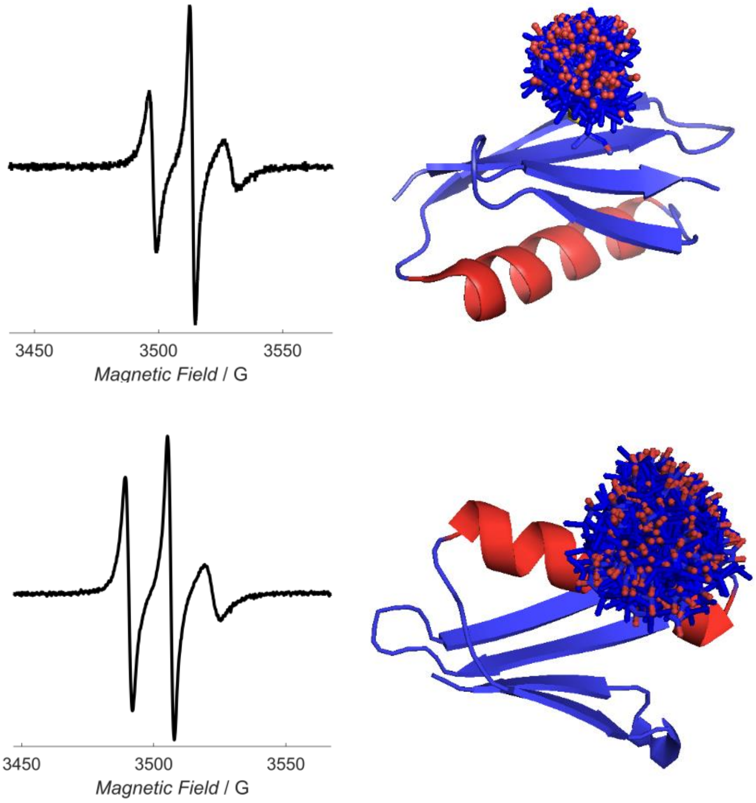

Figure 3.3.2.1: Continuous-wave EPR spectra of I6R1/K28H/Q32H and I6H/N8H/K28R1 constructs in the top and bottom left, respectively. Each construct is shown diagrammatically with the MTSL rotamer library shown at the relevant positions (top and bottom right), respectively.

Sample	Labelling Efficiency (%)
I6R1/K28H/Q32H	95±5
I6H/N8H/K28R1	97±5

Table 3.3.2.1. Labelling efficiencies for each of the GB1 constructs.

3.3.3 *Cu^{II}-Chelate Concentration Quantification by UV-Visible Spectroscopy*

The concentrations of the Cu^{II}-chelate solutions were quantified using UV-visible spectrophotometry. Cu^{II}-IDA has an extinction coefficient (ε) of 62 M^{-1}cm^{-1} at 726 nm.[312] This literature extinction coefficient was validated when A_{726nm} was plotted as a function of Cu^{II}-IDA concentration and found to be approximately linear (figure 3.3.3.1 bottom row). For this quantification, a dilution series of Cu^{II}-IDA was prepared as described in section 3.2.14 with nominal concentrations of 2.5, 5.1, 12.7, and 25.4 mM. Measurements were repeated in quadruplicate, and spectra are overlaid in the first row of figure 3.3.3.1. Cu^{II}-IDA concentrations calculated using the absorbance at 726 nm (table 3.3.3.1), show agreement within ~5% of prediction. To check there was no associated change in concentration owing to freeze-drying and redissolving Cu^{II}-IDA, an additional set of repeat measurements were performed after these steps (figure 3.3.3.2) and indicate freeze-drying is lossless as there is no concentration shift. Calculated concentrations are given in table 3.3.3.2.

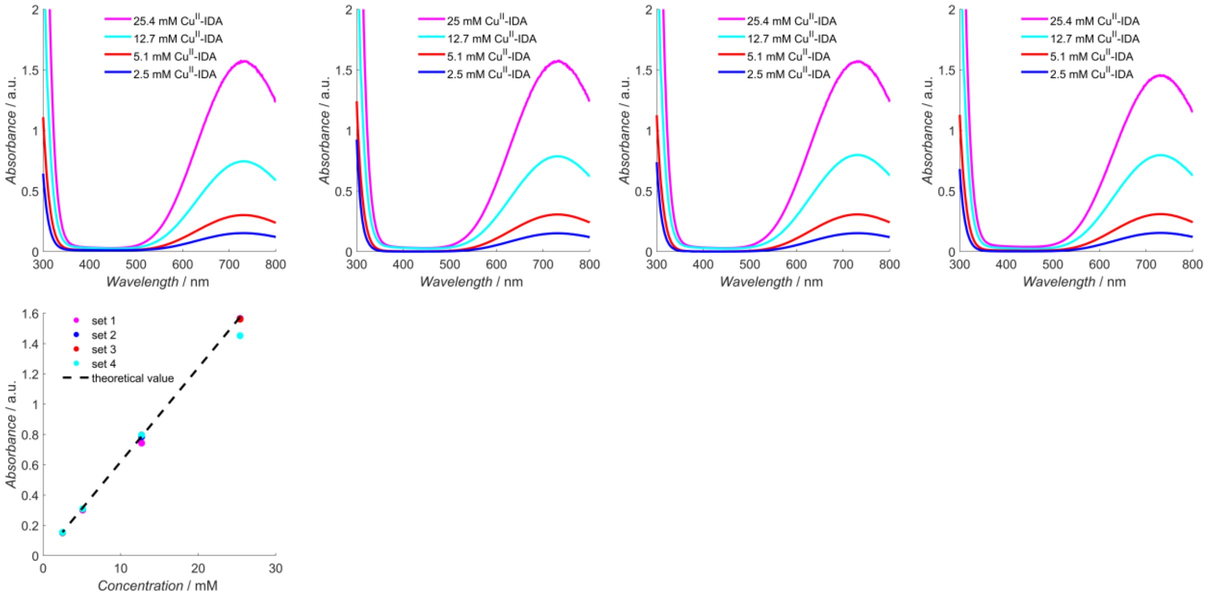

Figure 3.3.3.1: Absorbance spectra recorded for a Cu^{II}-IDA dilution series and repeated in 4 sets. In each set, the 25.4 mM stock solution is shown in magenta, the 2-fold dilution is shown in cyan, the 5-fold dilution is shown in red and the 10-fold dilution is shown in blue.

Sample	Predicted A_{726nm}	Observed A_{726nm}				Concentration [mM]			
Repeat		1	2	3	4	1	2	3	4
25.4 mM Cu^{II}-IDA	1.575	1.565	1.564	1.561	1.452	25.2	25.2	25.2	25.2
12.7 mM Cu^{II}-IDA	0.787	0.743	0.785	0.797	0.796	12.0	12.7	12.9	12.8
5.1 mM Cu^{II}-IDA	0.316	0.301	0.307	0.307	0.309	4.9	5.0	5.0	5.0
2.5 mM Cu^{II}-IDA	0.155	0.152	0.151	0.152	0.154	2.5	2.4	2.5	2.5

Table 3.3.3.1. The predicted and observed absorbance for the initial Cu^{II}-IDA dilution series, along with the calculated Cu^{II}-IDA concentrations, taken from the spectra shown in figure 3.3.3.1. The predicted absorbance is estimated using the literature extinction coefficient of 62 $M^{-1}cm^{-1}$.

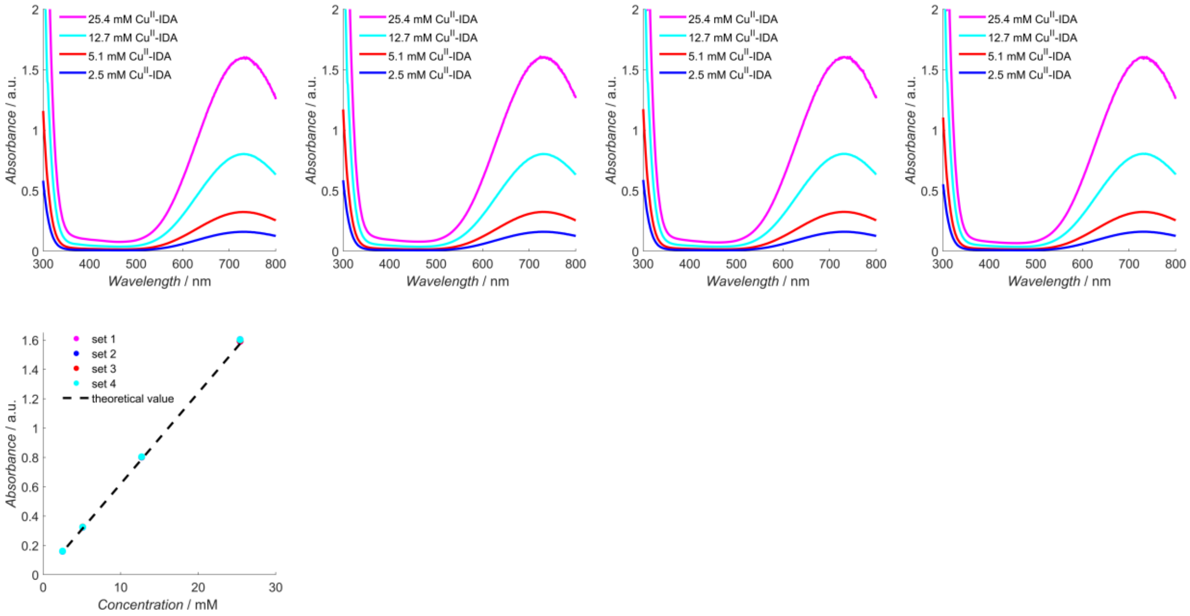

Figure 3.3.3.2: Absorbance spectra recorded for the freeze-dried Cu^{II}-IDA dilution series and repeated in 4 sets; the colour scheme is consistent with that used in figure 3.3.3.1.

Sample	Predicted A_{726nm}	Observed A_{726nm}				Concentration [mM]			
Repeat		1	2	3	4	1	2	3	4
25.4 mM Cu^{II}-IDA	1.575	1.591	1.603	1.595	1.602	25.7	25.9	25.7	25.8
12.7 mM Cu^{II}-IDA	0.787	0.802	0.802	0.803	0.804	12.9	12.9	13.0	13.0
5.1 mM Cu^{II}-IDA	0.316	0.323	0.324	0.325	0.324	5.2	5.2	5.2	5.2
2.5 mM Cu^{II}-IDA	0.155	0.160	0.160	0.161	0.161	2.6	2.6	2.6	2.6

Table 3.3.3.2. The predicted and observed absorbance for the freeze-dried Cu^{II}-IDA dilution series, along with the calculated Cu^{II}-IDA concentrations, taken from the spectra shown in figure 3.3.3.2.

For Cu^{II}-NTA no extinction coefficient could be found in published literature, so instead ε was calculated empirically using A_{800nm}, and determined to be 63 $M^{-1}cm^{-1}$ (right panel figure 3.3.3.3). For quantification of Cu^{II}-NTA concentration, a dilution series was prepared as described in section 3.2.14, with nominal concentrations of 1.0, 2.5, 5.0, 7.5 and 10 mM. Experimental spectra were recorded for two independent preparations, (left and middle panels in figure 3.3.3.3).

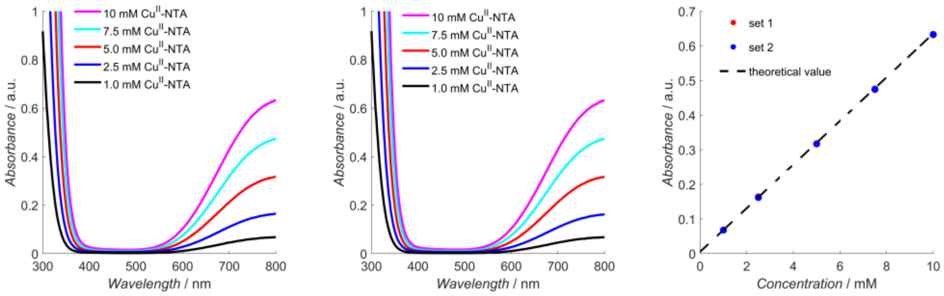

Figure 3.3.3.3: Absorbance spectra recorded for the Cu^{II}-NTA dilution series and repeated in 2 sets; the colour scheme is consistent with that used in figure 3.3.3.1, with the addition of 1 mM Cu^{II}-NTA shown in black. The theoretical value shown in dotted black in the right-most panel is calculated using an extinction coefficient of 63 $M^{-1}cm^{-1}$.

Sample	Observed A_{800nm}	
Repeat	1	2
10 mM Cu^{II}-NTA	0.632	0.633
7.5 mM Cu^{II}-NTA	0.474	0.475
5.0 mM Cu^{II}-NTA	0.317	0.317
2.5 mM Cu^{II}-NTA	0.164	0.162
1.0 mM Cu^{II}-NTA	0.068	0.068

Table 3.3.3.3. The observed absorbance for each of the Cu^{II}-NTA dilution series taken from the spectra shown in figure 3.3.3.3.

3.3.4 *Circular Dichroism Spectroscopy and Thermal Denaturation Assays*

Figure 3.3.4.1 shows circular dichroism spectra for GB1 constructs 6H/8H/28C and 6C/28H/32H GB1, in presence (blue) and absence (red) of 3 equivalents Cu^{II}-IDA, respectively. Typically in circular dichroism, α-helices yield double-lobed minima in the region 205-225 nm, while β-sheets correspond to shallower, singularly-lobed minima around 220 nm.[110] As α-helical and β-sheet secondary structural elements are both present in GB1, the resulting spectra should have contributions of each. Indeed, all spectra have a singular minimum ~220 nm and indication of a turning point around 200 nm (clearly visible for the 6C/28H/32H GB1 w/o Cu^{II}-IDA sample), fingerprinting the β-sheet motif.

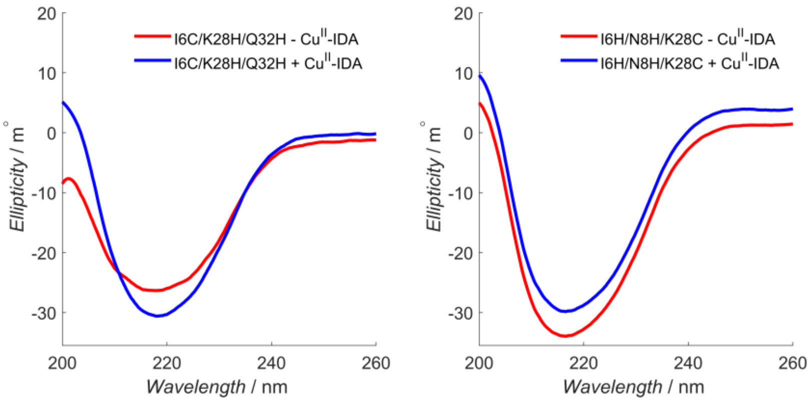

Figure 3.3.4.1: Far-UV circular dichroism spectra for 6C/28H/32H and 6H/8H/28C GB1 shown in left and right panels respectively, in presence and absence of 3 equivalents of Cu^{II}-IDA.

Interestingly, results indicate Cu^{II}-IDA has a stabilizing effect on the structure of the α-helix, because the magnitude of the minimum at ~220 nm increases, coupled with sharpening of the trough feature, which is consistent with previous literature[241,313] and furthermore supports the hypothesis that binding at the helix-site may be entropically expensive. By contrast, Cu^{II}-IDA binding at the β-sheet double-histidine site yields no observable changes in the spectrum, suggesting negligible impact on the protein secondary structure and consistent with a sterically hindered site, with low plasticity. All data agree nicely with published circular dichroism spectra for wildtype and tetra-histidine (6H/8H/28H/32H) GB1, suggesting the additional mutations do not perturb the native structure.

Thermal denaturation studies for each construct are shown in the main body (at 220 nm) or the inset (at 260 nm) of figure 3.3.4.2 (left panel). The melting curves are fitted well to a two-state unfolding model (black), and residuals are shown in figure 3.3.4.2 (right panel), with the corresponding melting temperatures T_M given in table 3.3.4.1. For 6C/28H/32H GB1 the fitted melting temperatures are 324 and 321 K in the absence and presence of Cu^{II}-IDA, respectively. While 6H/8H/28C GB1 shows the greatest thermal stability in absence of Cu^{II}-IDA, (fitted T_M is 328 K) upon binding of Cu^{II}-IDA the T_M decreases to 318 K, the lowest melting temperature of all conditions, suggesting the addition of Cu^{II}-IDA to the α-helical double-histidine site is less de-stabilising than corresponding addition to the β-sheet double-histidine site.

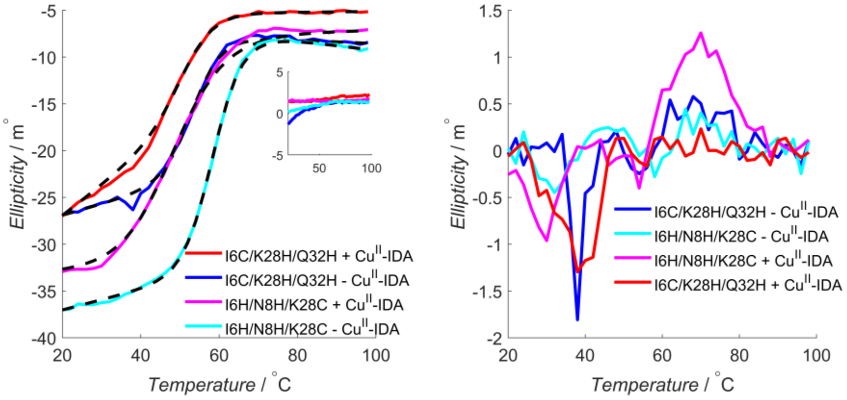

Figure 3.3.4.2: Thermal denaturation curves of GB1 constructs in presence and absence of 3 equivalents Cu^{II}-IDA, shown in the left panel. T_M fits are shown in dotted black, with I6H/N8H/K28C ± Cu^{II}-IDA shown in magenta and cyan, respectively, and I6C/K28H/Q32H ± Cu^{II}-IDA shown in red and blue, respectively. In the right panel, the residuals of each of the fits to the raw data are given, with the same colour scheme.

Sample	T_M [K]
I6C/K28H/Q32H GB1 + Cu^{II}-IDA	321
I6C/K28H/Q32H GB1 - Cu^{II}-IDA	324
I6H/N8H/K28C GB1 + Cu^{II}-IDA	318
I6H/N8H/K28C GB1 – Cu^{II}-IDA	328

Table 3.3.4.1. Melting temperatures (T_M) for each of the sample conditions

Taken together the circular dichroism spectra and thermal melting curves indicate that these GB1 constructs are free of structural perturbation owing to multiple rounds of mutagenesis, and therefore could be used in subsequent ITC and RIDME measurements.

3.3.5 *Isothermal Titration Calorimetry*

Both I6H/N8H/K28R1 and I6R1/K28H/Q32H GB1 constructs were measured at 75 µM in degassed buffer (42.4 mM Na_2HPO_4, 7.6 mM KH_2PO_4, 150 mM NaCl, pH 7.4). As titrant for the I6H/N8H/K28R1 GB1 measurements, 2000 µM Cu^{II}-NTA, and 1000 µM Cu^{II}-IDA ligand were used, while for the I6R1/K28H/Q32H GB1 measurements, 1000 µM Cu^{II}-NTA, and 2000 µM Cu^{II}-IDA ligand were used. The resulting isotherms, raw data and fits are shown in figure 3.3.5.1-2, respectively. The calculated K_D values based on these fits for the I6H/N8H/K28R1 measurements are 42 ± 2 µM and 7 ± 1 µM, for Cu^{II}-NTA and Cu^{II}-IDA, respectively. Conversely, fits for the I6R1/K28H/Q32H measurements revealed calculated K_D values of 5.0 ± 0.3 and 27.0 ± 1.8 µM for Cu^{II}-NTA and Cu^{II}-IDA, respectively. Taken together these findings are consistent with a lower affinity observed at the β-sheet site in previous literature, and the observation of low µM affinity for double-histidine motifs binding Cu^{II}.[112,314,315] It is also consistent with the expected trend for binding to a double-histidine motif on an α-helix, albeit with an affinity two orders of magnitude greater than previously reported.

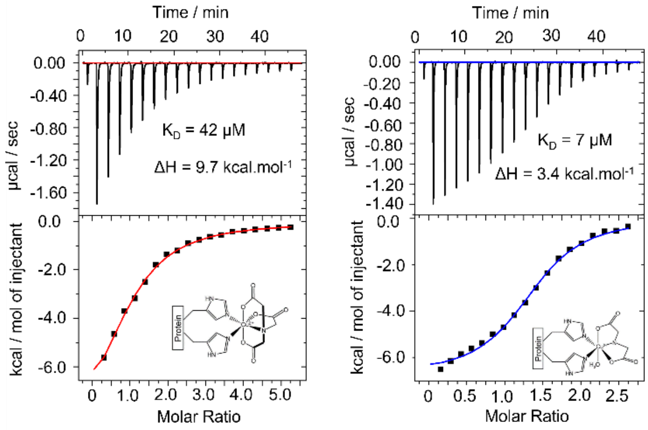

Figure 3.3.5.1: Isothermal titration calorimetry data for the I6H/N8H/K28R1 construct, titrated against Cu^{II}-NTA and Cu^{II}-IDA and shown in the left and right panels respectively, with the raw ITC traces shown at the top, and the binding isotherm at the bottom in each case.

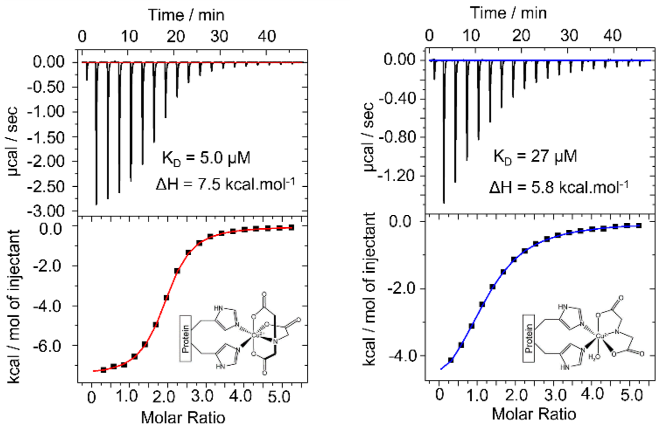

Figure 3.3.5.2: Isothermal titration calorimetry data for the I6R1/K28H/Q32H construct, titrated against Cu^{II}-NTA and Cu^{II}-IDA and shown in the left and right panels respectively, with the raw ITC traces shown at the top, and the binding isotherm at the bottom in each case.

Each Cu^{II}-chelate coordinated double-histidine motifs exothermically (as seen from the ITC-data), and the empirical enthalpy changes calculated for each construct/chelator permutation are given in table 3.3.5.1 below (ΔH values are reported as positive, as the dissociation event will be endothermic). The integrated form of van't Hoff equation is given as:

$$\ln\frac{K_2}{K_1} = \frac{-\Delta H^{\emptyset}}{R}\left(\frac{1}{T_2} - \frac{1}{T_1}\right) \tag{3.3.5.1}$$

It is apparent that for an exothermic reaction, as the temperature is decreased the affinity of binding increases, and the RIDME data shown in figures 3.3.6.1-2 suggest that K_D values estimated are consistently lower than the value from ITC at room temperature. Importantly, the increased affinity at lower temperature is assumed to be thermodynamically-driven, rather than kinetically-driven; the diffusion constant of Cu^{II}-NTA in aqueous solution is ~5.4 × 10^{-6} cm^2 s^{-1} at 293 K,[316] and for a small molecules such as Cu^{II}-NTA the K_{on} rate (i.e., rate of binding) is likely to be in the range 10^7-10^8 s$^-$

[1],[317,318] while molecules on the scale of proteins typically have K_{on} in the range 10^6 s^{-1},[319] and excepting slower large-scale molecular motions is usually diffusion limited.[320] This would suggest that thermodynamic re-equilibration would occur quickly with respect to a cooling rate of seconds. Indeed, if kinetics were slower and did not allow re-equilibration, then binding would be anticipated to get weaker (i.e., closer to room-temperature) rather than stronger. While freeze-quench methods of cooling could provide greater insight into the kinetics of binding, if the K_{on} rate is ~10^7 s^{-1}, this would equilibrate at least two orders of magnitude faster than microsecond freeze-hyperquenching is sensitive to (cooling rates of 10^{-4}-10^{-5} s),[321] this is discussed in more detail in chapter 6.

Note that the enthalpies of dissociation will instead be positive, as the dissociation event is endothermic and disfavoured at lower temperature; in figure 3.3.5.2 and table 3.3.5.1, the enthalpy is given as positive because all reaction schemes throughout this thesis are framed as dissociation reactions, rather than association reactions, despite the ITC data monitoring the association event. The difference in affinites between the ITC- and EPR-determined values is reconciled by extrapolation of K_D values to low temperature and minimising the root mean square deviation (RMSD) between the four RIDME-determined K_Ds and the ITC extrapolation as a function of temperature. Interestingly, deviation is minimal at 239 K, hence the RIDME binding constant is reflective of the ITC derived thermodynamic parameters at 239 K. Coincidentally, this agrees well with the melting point of a 1:1 water-ethylene glycol mixture at about 235 K,[322] suggesting that below this temperature the decreasing diffusional motion and increasing viscosity allow no further equilibration and the ions will be trapped in the solid matrix whether bound or unbound. It should also be noted that the Wiseman factor (c) provides a measure of the reliability of the empirical enthalpy change and K_D extracted from ITC data. It is calculated according to equation 3.3.5.2:

$$c = K_A[P]_t \tag{3.3.5.2}$$

Where: K_A is the association constant for the reaction, and $[P]_t$ is the total protein concentration. The significance of this parameter is that the shape of the ITC titration curve depends on c, with values ≥ 10 yielding a sigmoidal shape, and giving the clearest indication of the K_D value; and allowing easy saturation of the receptor in the experimental window $10 \leq c \leq 500$. While in this purview, the values of c are quite low, literature has also demonstrated that for measurements of sufficient signal-to-noise, c values as low as $c = 0.001$ can provide reliable K_D information, but that in this case, ΔH is less reliable.[323]

Therefore, disparity between ITC-derived and RIDME-derived affinity estimates manifest primarily owing to the different temperature regimes under which measurements are performed: 298 K for the ITC measurements, and at the approximate temperature where the binding equilibrium freezes out for the RIDME pseudo-titrations. Additionally, due to the exothermic binding event, this leads to much stronger binding under PD-EPR conditions, as suggested by data shown in figures 3.3.12.1-2. This is discussed with respect to the RIDME pseudo-titrations in section 3.3.12 of the chapter. Differences in concentration between ITC and EPR measurements (75 vs 5 μM) may contribute to the disparity in the

K_D estimates, however it is worth noting that not treating the thermodynamics leads to differences of two-orders of magnitude (discussed more in chapter 6), which cannot be accounted for by the concentration difference alone. Both are likely only to yield upper limits of K_D values (i.e., isotherms are poorly resolved at these concentrations with respect to a sub-μM K_D) and furthermore the wiseman factors indicate that the ITC isotherms may be interpretted reliably for all samples, suggesting the protein concentration of 75 μM does not cause significant perturbation in the K_D estimate. Indeed, measurement of ITC data at lower protein concentrations to determine the K_D value more accurately is of interest in the future, several examples in the literature showcase measurement of sub-μM K_D values,[324,325] but for our purposes an upper-bound estimate is sufficient.

ITC sample	Empirical ΔH [kcal.mol^{-1}]	Empirical ΔS [cal.mol^{-1}.deg^{-1}]	Wiseman Factor (*c*)
75 μM I6R1/K28H/Q32H GB1 + Cu^{II}-NTA	7.54 ± 0.02	-1.0	15.0
75 μM I6R1/K28H/Q32H GB1 + Cu^{II}-IDA	5.75 ± 0.05	-1.6	2.8
75 μM I6H/N8H/K28R1 GB1 + Cu^{II}-NTA	9.68 ± 0.52	-12.5	1.8
75 μM I6H/N8H/K28R1 GB1 + Cu^{II}-IDA	3.37 ± 0.05	10.8	10.7

Table 3.3.5.1: The empirical ΔH and ΔS values calculated from each ITC measurement, and the associated Wiseman factor *c*.

3.3.6 *Inversion Recovery Measurements*

3.3.6.1 T_1 of RIDME Pseudo-Titrations

The raw inversion recovery traces and the corresponding mono-exponential and bi-exponential fits are shown for the 0.5 µM pseudo-titration series, in figure 3.3.6.1.1. The T_1 values estimated from the mono- and bi-exponential fits of the raw data shown in figure 3.3.6.1.1, along with the 1/e time (the time taken for ~63% of the electron spin magnetisation to return to thermal equilibrium) are given in table 3.3.6.1.1. The relative contributions of the two decay time constants in the bi-exponential fits are given as the parameter *b* in equation 3.2.5.2 in section 3.2.5.

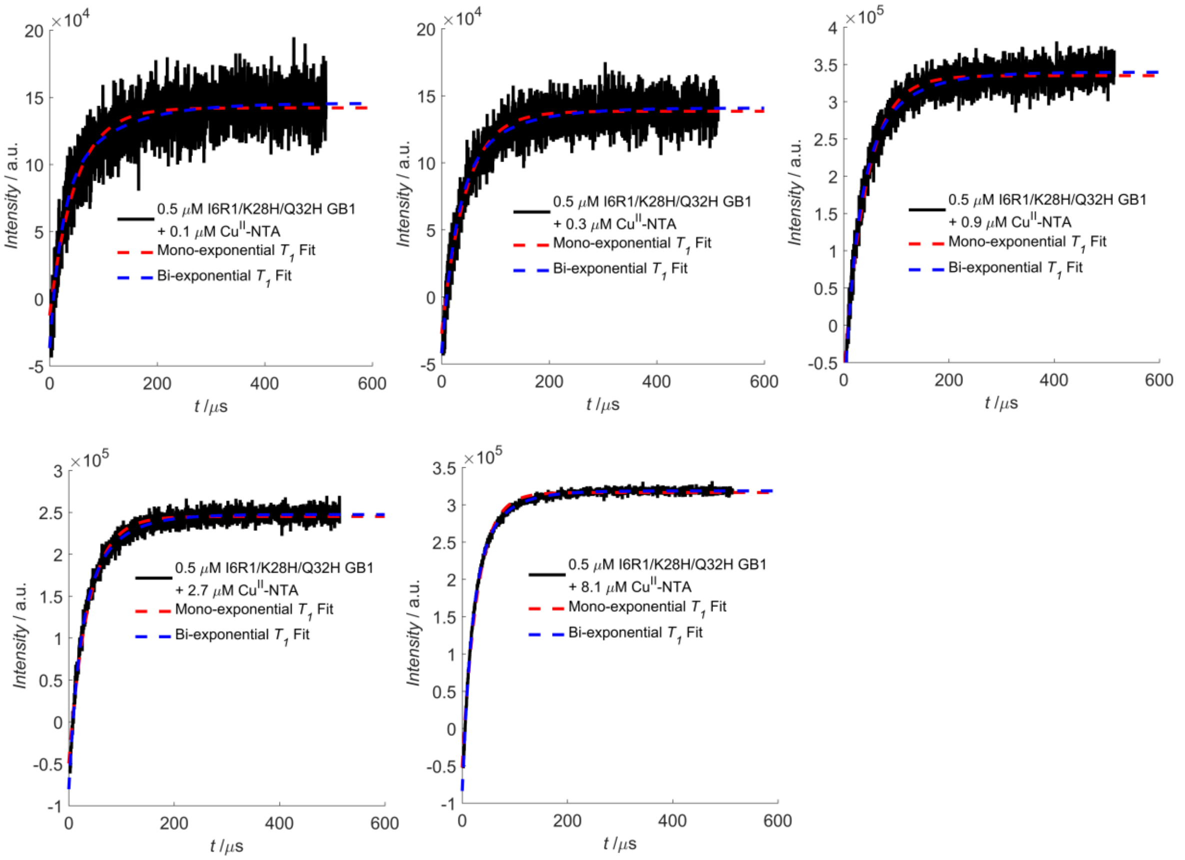

Figure 3.3.6.1.1. Inversion recovery data for 0.5 µM I6R1/K28H/Q32H, in presence of 0.1, 0.3, 0.9, 2.7 and 8.1 µM Cu^{II}-NTA, shown left-to-right, and top-to-bottom, respectively. The experimental data is shown in black, with the mono-exponential and bi-exponential fits shown as red and blue dotted lines, respectively.

Sample	Mono-exponential T_1 [μs]	Bi-exponential T_{1A} / T_{1B} [μs]	Relative Contributions	1/e time [μs]
I6R1/K28H/Q32H + 0.1 μM Cu^{II}-NTA	47.8 ± 1.92 (0.797)	21.7 / 98.9 (0.808)	0.63 : 0.37	63.4
I6R1/K28H/Q32H + 0.3 μM Cu^{II}-NTA	44.3 ± 1.26 (0.887)	26.6 / 92.0 (0.892)	0.68 : 0.32	59.4
I6R1/K28H/Q32H + 0.9 μM Cu^{II}-NTA	41.5 ± 0.69 (0.957)	24.9 / 81.1 (0.963)	0.67 : 0.33	56.6
I6R1/K28H/Q32H + 2.7 μM Cu^{II}-NTA	36.6 ± 0.46 (0.975)	18.9 / 60.6 (0.980)	0.57 : 0.43	48.8
I6R1/K28H/Q32H + 8.1 μM Cu^{II}-NTA	28.6 ± 0.21 (0.992)	17.9 / 54.3 (0.996)	0.69 : 0.31	43.8

Table 3.3.6.1.1: Mono- and bi-exponential T_1 estimates, and 1/e times for each of the RIDME 0.5 μM I6R1/K28H/Q32H pseudo-titration samples, from the inversion recovery traces shown in figure 3.3.6.1.1 above. R^2 values of each model are indicated in parentheses.

Inversion recovery traces for the 25 and 75 μM pseudo-titrations are given in the appendix, but the estimated T_1 values from the mono- and bi-exponential fits are given in tables 3.3.6.1.2-5 for I6H/N8H/K28R1 and I6R1/K28H/Q32H in presence of Cu^{II}-NTA and Cu^{II}-IDA, respectively. All mono-exponential functions fit the raw data well and do not appear to show significant contribution from spectral diffusion to the inversion recovery measurement that could lead to under-estimating the T_1. Spectral diffusion can manifest as a fast component of the inversion recovery data, and subsequently cause mono-exponential fits to under-represent longitudinal relaxation time, by overfitting the fast component. Although not performed during the present work spectral diffusion can be reduced in future measurements of T_1 by instead using the saturation recovery (SR) experiment; a train of inversion pulses will saturate both resonant electron spin transitions within the bandwidth of the detection pulse, and the transitions which can undergo magnetization exchange with this region of the spectrum, otherwise contributing to spectral diffusion.

Sample	Mono-exponential T_1 [μs]	Bi-exponential T_{1A} / T_{1B} [μs]	Relative Contributions	1/e time [μs]
I6H/N8H/K28R1 + 10 μM Cu^{II}-NTA	46.3 ± 0.20 (0.997)	31.7 / 80.1 (0.999)	0.67 : 0.33	56.4
I6H/N8H/K28R1 + 20 μM Cu^{II}-NTA	44.5 ± 0.17 (0.998)	30.5 / 74.1 (1.00)	0.65 : 0.35	55.0
I6H/N8H/K28R1 + 40 μM Cu^{II}-NTA	38.9 ± 0.19 (0.997)	25.5 / 70.9 (1.00)	0.68 : 0.32	47.0
I6H/N8H/K28R1 + 90 μM Cu^{II}-NTA	30.9 ± 0.16 (0.996)	18.9 / 55.5 (1.00)	0.66 : 0.34	35.8
I6H/N8H/K28R1 + 600 μM Cu^{II}-NTA	25.5 ± 0.14 (0.995)	16.6 / 49.9 (1.00)	0.72 : 0.28	29.6

Table 3.3.6.1.2. Mono- and bi-exponential T_1 estimates, and 1/e time for each sample of the 25 μM I6H/N8H/K28R1 + Cu^{II}-NTA RIDME pseudo-titration series. R^2 values of each model are indicated in parentheses.

Sample	Mono-exponential T_1 [μs]	Bi-exponential T_{1A} / T_{1B} [μs]	Relative Contributions	1/e time [μs]
I6H/N8H/K28R1 + 10 μM Cu^{II}-IDA	54.1 $\pm$ 0.23 (0.997)	36.0 / 93.8 (0.999)	0.64 : 0.36	63.4
I6H/N8H/K28R1 + 20 μM Cu^{II}-IDA	48.7 $\pm$ 0.20 (0.998)	32.3 / 82.1 (1.00)	0.64 : 0.36	57.8
I6H/N8H/K28R1 + 35 μM Cu^{II}-IDA	46.3 $\pm$ 0.21 (0.997)	30.3 / 82.9 (1.00)	0.66 : 0.34	55.8
I6H/N8H/K28R1 + 75 μM Cu^{II}-IDA	39.3 $\pm$ 0.17 (0.997)	26.0 / 69.4 (1.00)	0.67 : 0.33	49.0
I6H/N8H/K28R1 + 450 μM Cu^{II}-IDA	36.2 $\pm$ 0.15 (0.997)	24.2 / 64.8 (1.00)	0.68 : 0.32	43.6

Table 3.3.6.1.3. Mono- and bi-exponential T_1 estimates, and 1/e time for each sample of the 25 μM I6H/N8H/K28R1 + Cu^{II}-IDA RIDME pseudo-titration series. R^2 values of each model are indicated in parentheses.

Sample	Mono-exponential T_1 [μs]	Bi-exponential T_{1A} / T_{1B} [μs]	Relative Contributions	1/e time [μs]
I6R1/K28H/Q32H + 15 μM Cu^{II}-NTA	51.6 $\pm$ 0.19 (0.998)	35.5 / 86.0 (1.00)	0.65 : 0.35	62.8
I6R1/K28H/Q32H + 30 μM Cu^{II}-NTA	48.7 $\pm$ 0.20 (0.997)	32.3 / 85.4 (1.00)	0.66 : 0.34	59.2
I6R1/K28H/Q32H + 60 μM Cu^{II}-NTA	36.5 $\pm$ 0.20 (0.995)	21.3 / 63.2 (1.00)	0.62 : 0.38	42.0
I6R1/K28H/Q32H + 135 μM Cu^{II}-NTA	29.1 $\pm$ 0.16 (0.995)	16.9 / 50.1 (1.00)	0.63 : 0.37	33.0
I6R1/K28H/Q32H + 960 μM Cu^{II}-NTA	25.1 $\pm$ 0.13 (0.996)	15.7 / 46.0 (1.00)	0.68 : 0.32	29.0

Table 3.3.6.1.4. Mono- and bi-exponential T_1 estimates, and 1/e time for each sample of the 25 μM I6R1/K28H/Q32H + Cu^{II}-NTA RIDME pseudo-titration series. R^2 values of each model are indicated in parentheses.

Sample	Mono-exponential T_1 [μs]	Bi-exponential T_{1A} / T_{1B} [μs]	Relative Contributions	1/e time [μs]
I6R1/K28H/Q32H + 45 μM Cu^{II}-IDA	59.7 $\pm$ 0.20 (0.998)	42.0 / 102.9 (1.00)	0.66 : 0.34	73.4
I6R1/K28H/Q32H + 100 μM Cu^{II}-IDA	49.9 $\pm$ 0.19 (0.998)	32.1 / 82.5 (1.00)	0.62 : 0.38	61.6
I6R1/K28H/Q32H + 185 μM Cu^{II}-IDA	44.2 $\pm$ 0.21 (0.997)	28.1 / 79.1 (1.00)	0.65 : 0.35	52.8
I6R1/K28H/Q32H + 350 μM Cu^{II}-IDA	40.7 $\pm$ 0.20 (0.996)	26.1 / 74.8 (1.00)	0.67 : 0.33	48.0
I6R1/K28H/Q32H + 600 μM Cu^{II}-IDA	39.5 $\pm$ 0.18 (0.997)	25.6 / 70.1 (1.00)	0.66 : 0.34	46.8
I6R1/K28H/Q32H + 1750 μM Cu^{II}-IDA	36.4 $\pm$ 0.17 (0.997)	24.1 / 68.2 (1.00)	0.70 : 0.30	45.2

Table 3.3.6.1.5: Mono- and bi-exponential T_1 estimates, and 1/e time for each sample of the 75 μM I6R1/K28H/Q32H + Cu^{II}-IDA RIDME pseudo-titration series. R^2 values of each model are indicated in parentheses.

3.3.6.2 T_1 for Sensitivity Analysis

It was also necessary to perform inversion-recovery measurements at different temperatures to allow estimating the maximum sensitivity as a function of temperature for both Cu^{II}-nitroxide RIDME, and Cu^{II}-Cu^{II} RIDME and PELDOR, discussed in section 3.3.8. Therefore, inversion recovery measurements were performed on the maximum of the Cu^{II}-IDA spectrum (and the R1 nitroxide spectrum for the I6H/N8H/K28R1 construct) in the temperature range 10-50 K on samples of 75 μM I6H/N8H/K28H/Q32H GB1 in presence of 250 μM Cu^{II}-IDA, and 25 μM I6H/N8H/K28R1 GB1 in presence of 100 μM Cu^{II}-IDA. The raw inversion recovery traces and corresponding mono-exponential and bi-exponential fits are shown in figures 3.3.6.2.1-3 respectively, and the estimates of T_1 are given in tables 3.3.6.2.1-3.

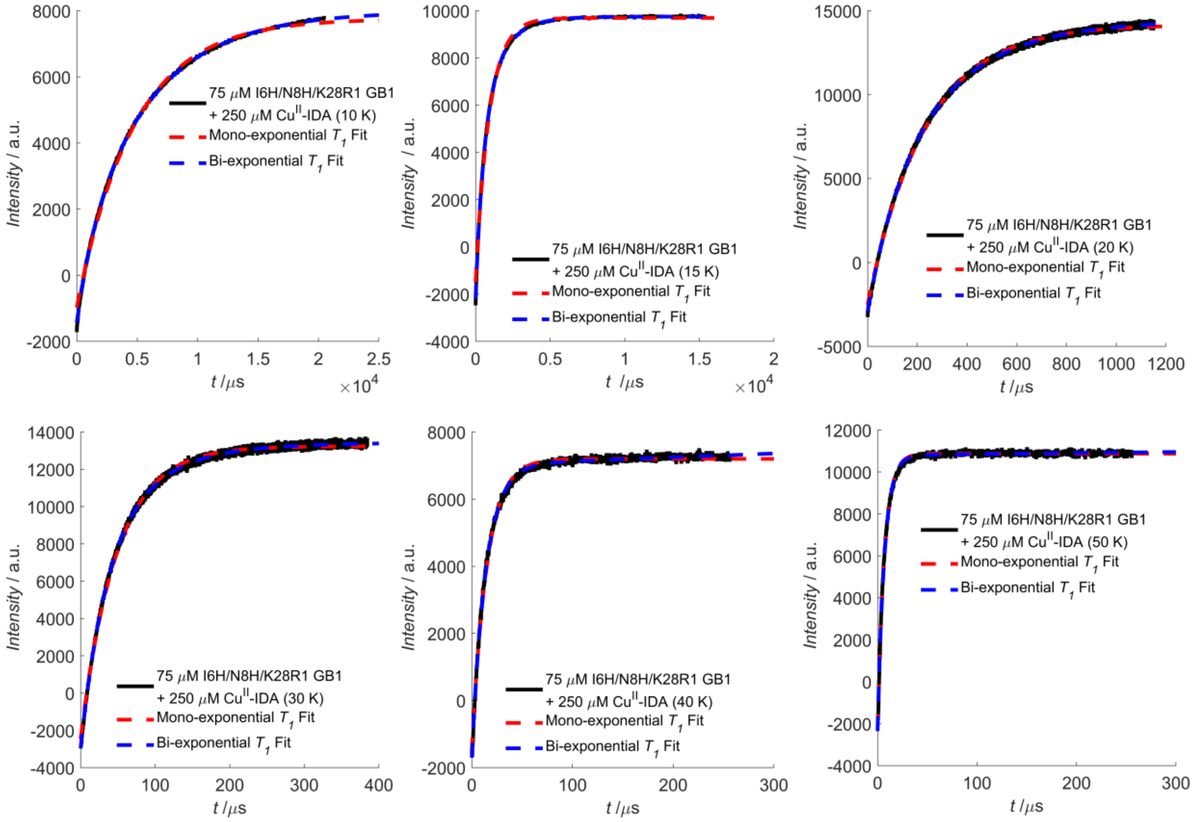

Figure 3.3.6.2.1. Inversion recovery traces for 75 μM I6H/N8H/K28H/Q32H GB1 + 250 μM Cu^{II}-IDA at various temperatures shown in black, with mono- and bi-exponential fits shown in red and blue, respectively. The corresponding estimates for T_1 are given in table 3.3.6.2.1 below.

Temperature [K]	Mono-exponential T_1 [μs]	Bi-exponential T_{1A} / T_{1B} [μs]	Relative Contributions	1/e time [μs]
10	4769 (0.998)	1510 / 5969 (1.00)	0.22 : 0.78	5601
15	912.1 (0.996)	521.8 / 1441 (1.00)	0.56 : 0.44	996.5
20	232.1 (0.998)	128.7 / 302.7 (0.998)	0.34 : 0.66	256.6
30	48.3 (0.996)	33.9 / 79.6 (0.997)	0.63 : 0.37	58.3
40	14.8 (0.994)	12.0 / 39.5 (0.997)	0.86 : 0.14	18.1
50	7.0 (0.993)	5.4 / 14.2 (0.995)	0.80 : 0.20	8.2

Table 3.3.6.2.1: Mono- and bi-exponential T_1 estimates, and 1/e time for each sample of the 75 μM I6H/N8H/K28H/Q32H GB1 + 250 μM Cu^{II}-IDA temperature series. R^2 values of each model are indicated in parentheses.

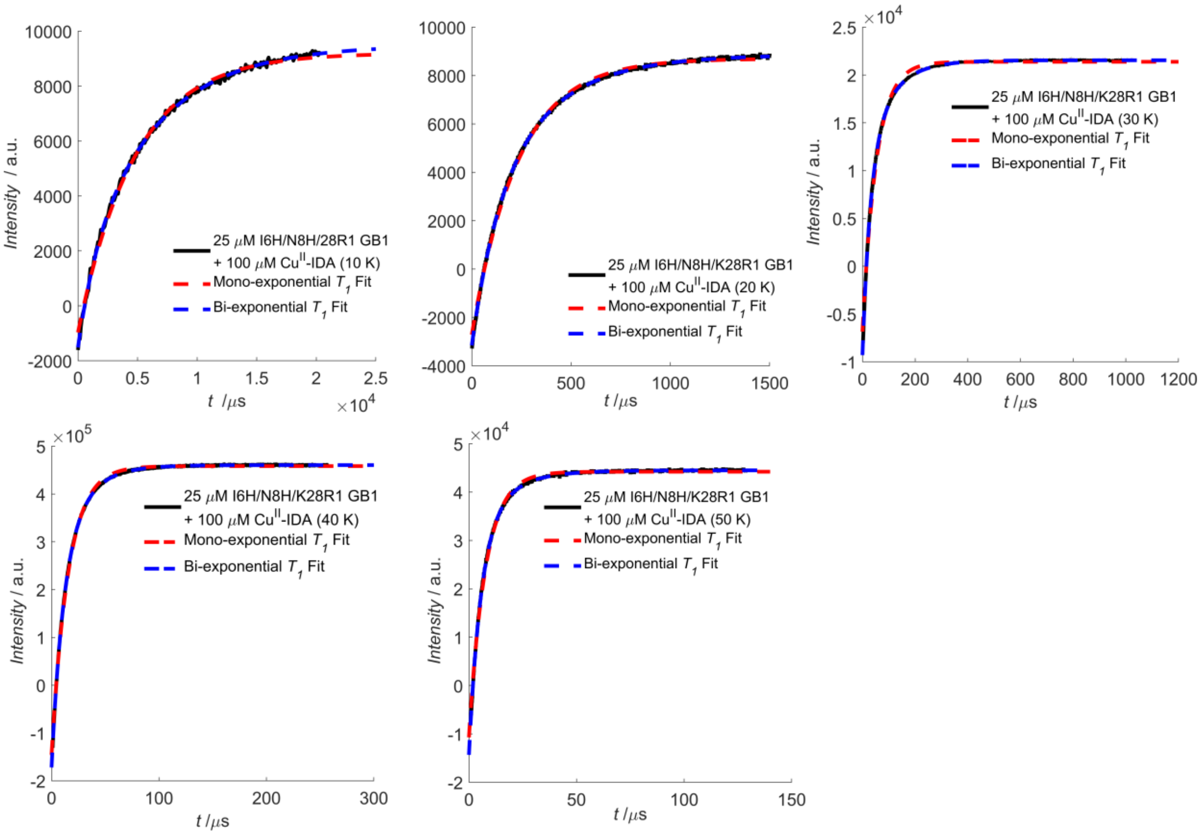

Figure 3.3.6.2.2. Inversion recovery traces of Cu^{II}-IDA for 25 μM I6H/N8H/K28R1 GB1 + 100 μM Cu^{II}-IDA at various temperatures shown in black, with mono- and bi-exponential fits shown in red and blue, respectively. The corresponding estimates for T_1 are given in table 3.3.6.2.2 below.

Temperature [K]	Mono-exponential T_1 [μs]	Bi-exponential T_{1A} / T_{1B} [μs]	Relative Contributions	1/e time [μs]
10	4800 (0.997)	1500 / 6130 (0.999)	0.23 : 0.77	5201
20	234.0 (0.998)	134.3 / 334.3 (1.00)	0.44 : 0.56	301.0
30	52.8 (0.994)	31.0 / 97.8 (1.00)	0.66 : 0.34	67.6
40	15.6 (0.999)	11.2 / 25.3 (1.00)	0.68 : 0.32	19.6
50	7.6 (0.997)	5.6 / 15.6 (1.00)	0.81 : 0.19	8.9

Table 3.3.6.2.2: Mono- and bi-exponential T_1 estimates, and 1/e time for Cu^{II}-IDA of the 25 μM I6H/N8H/K28R1 GB1 + 100 μM Cu^{II}-IDA temperature series. R^2 values of each model are indicated in parentheses.

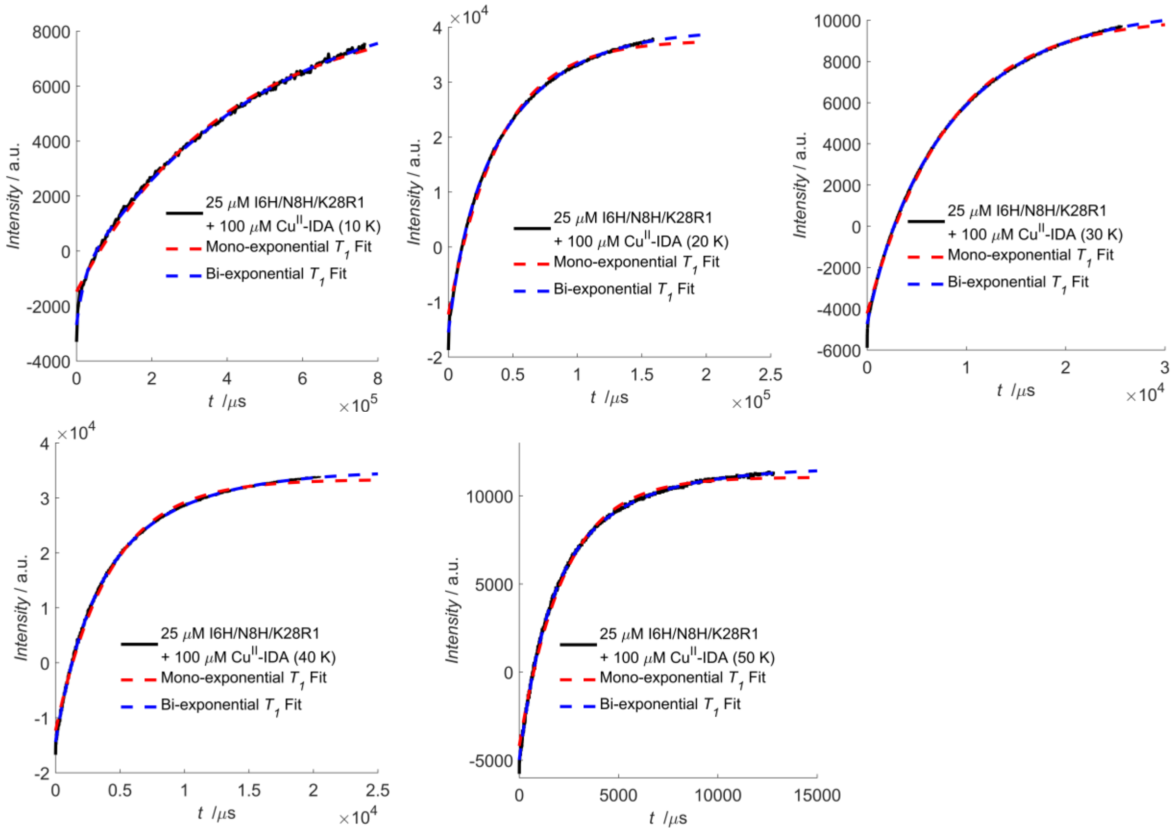

Figure 3.3.6.2.3: Inversion recovery traces of R1 nitroxide for 25 µM I6H/N8H/K28R1 GB1 + 100 µM Cu^{II}-IDA at various temperatures shown in black, with mono- and bi-exponential fits shown in red and blue, respectively. The corresponding estimates for T_1 are given in table 3.3.6.2.3 below.

Temperature [K]	Mono-exponential T_1 [ms]	Bi-exponential T$_{1A}$ / T$_{1B}$ [ms]	Relative Contributions	1/e time [ms]
10	397 (0.995)	196 / 486 (1.00)	0.14 : 0.86	387
20	39.8 (0.997)	11.7 / 53.5 (1.00)	0.25 : 0.75	52.0
30	8.1 (0.999)	2.1 / 9.6 (1.00)	0.13 : 0.87	10.4
40	4.2 (0.998)	2.1 / 6.5 (1.00)	0.42 : 0.58	5.7
50	2.2 (0.997)	1.2 / 3.9 (1.00)	0.52 : 0.48	3.1

Table 3.3.7.2.3: Mono- and bi-exponential T_1 estimates, and 1/e time for R1 nitroxide of the 25 µM I6H/N8H/K28R1 GB1 + 100 µM Cu^{II}-IDA temperature series. R^2 values of each model are indicated in parentheses.

3.3.7 *Electron Spin Echo Decay Measurements for Sensitivity Analysis*

To allow estimation of sensitivity as a function of temperature for both Cu^{II}-nitroxide RIDME, and Cu^{II}-Cu^{II} RIDME and PELDOR, discussed in section 3.3.8, it was necessary to estimate the transverse dephasing times T_m for both Cu^{II}-IDA and nitroxide. Therefore, electron spin echo decay measurements were performed on the maximum of the Cu^{II}-IDA spectrum (and the R1 nitroxide spectrum for the I6H/N8H/K28R1 construct) in the temperature range 10-50 K on samples of 75 µM I6H/N8H/K28H/Q32H GB1 in presence of 250 µM Cu^{II}-IDA, and 25 µM I6H/N8H/K28R1 GB1 in presence of 100 μM Cu^{II}-IDA. The raw electron spin echo decay traces and corresponding stretched exponential fits are shown in figures 3.3.7.1-3 respectively, and the estimates of T_m are given in tables 3.3.7.1-3, fitted according to equation 3.2.5.3 in section 3.2.5.

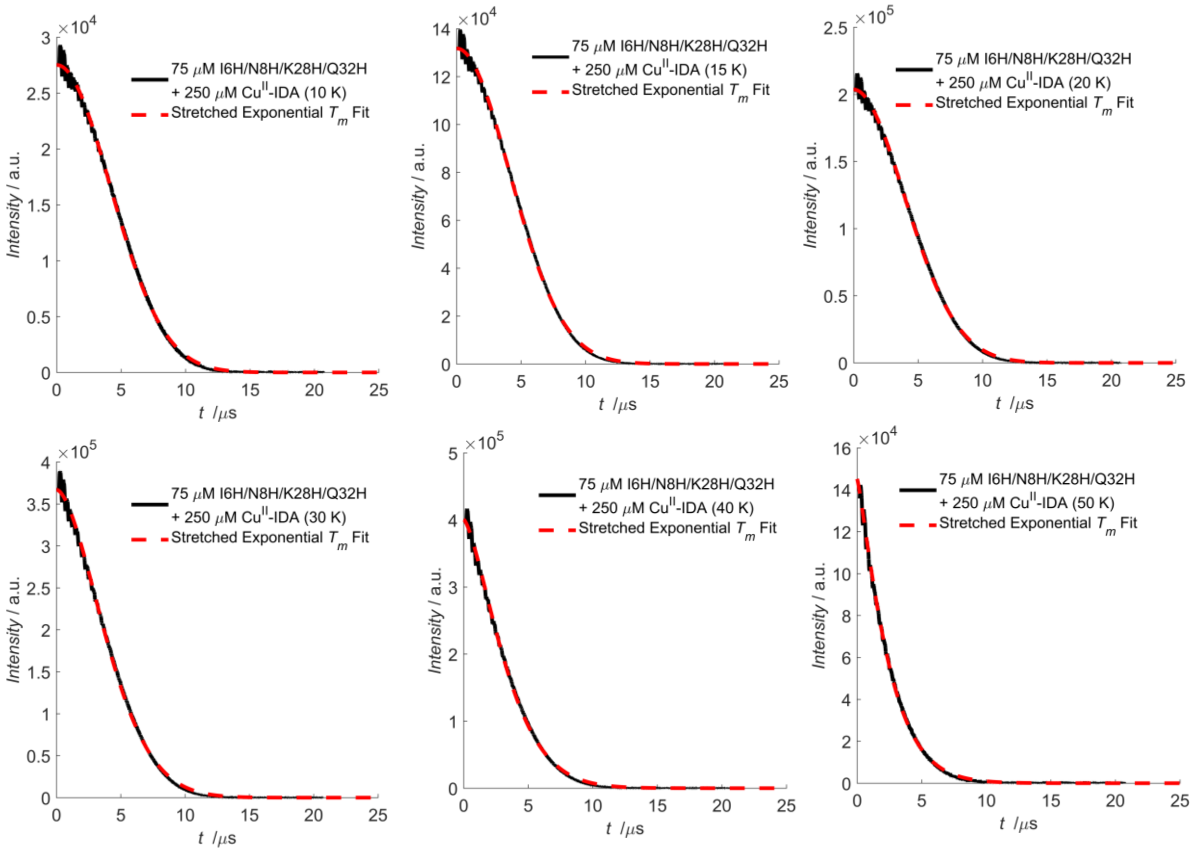

Figure 3.3.7.1: Two pulse electron spin echo traces for 75 μM I6H/N8H/K28H/Q32H GB1 + 250 μM Cu^{II}-IDA at various temperatures shown in black, with stretched exponential fits shown in red. The corresponding estimates for T_m are given in table 3.3.7.1 below.

Temperature [K]	T_m Estimate [μs]	Stretch Exponent
10	5.8	2.00
15	5.8	2.00
20	5.7	1.95
30	4.9	1.72
40	3.8	1.45
50	2.4	1.07

Table 3.3.7.1: Stretched exponential T_m estimates for the 75 μM I6H/N8H/K28H/Q32H GB1 + 250 μM Cu^{II}-IDA temperature series.

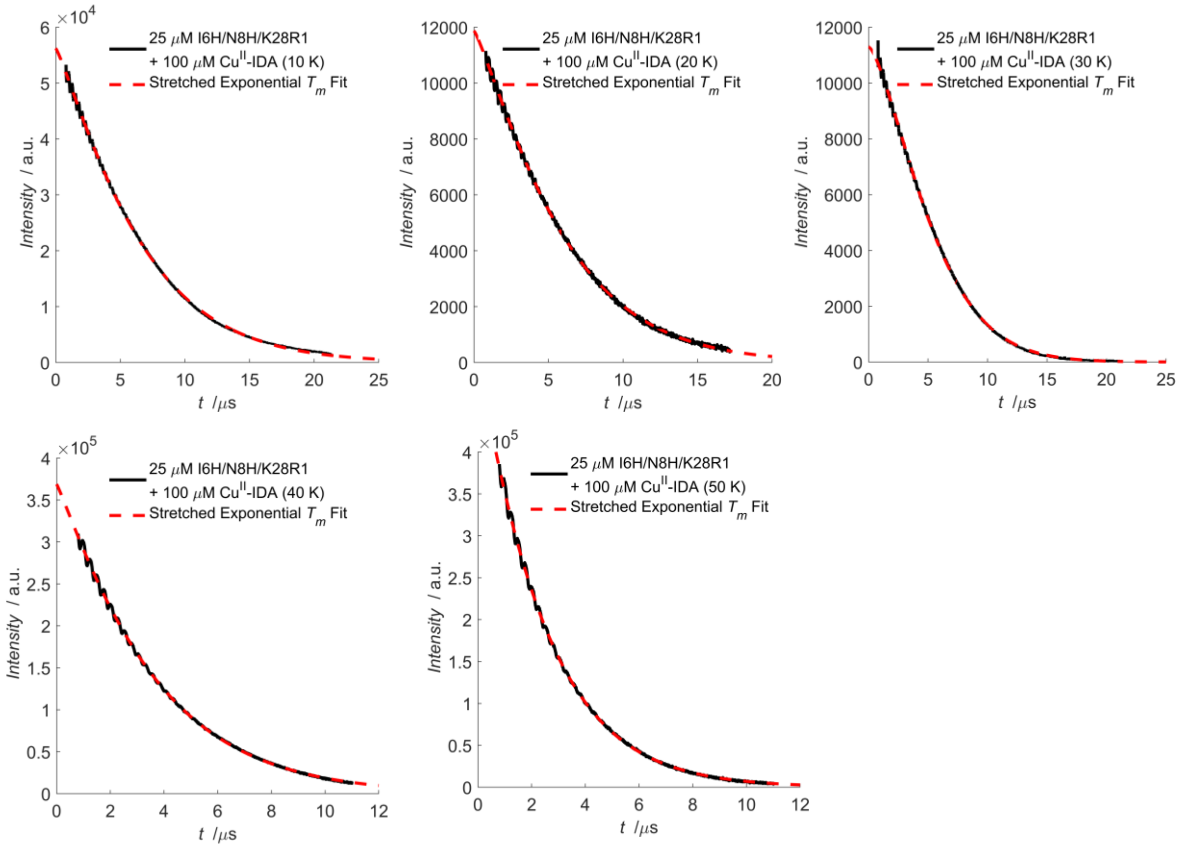

Figure 3.3.7.2: Two pulse electron spin echo traces for 25 μM I6H/N8H/K28R1 GB1 + 100 μM Cu^{II}-IDA at various temperatures shown in black, with stretched exponential fits shown in red. The corresponding estimates for T_m are given in table 3.3.7.2 below.

Temperature [K]	T_m Estimate [μs]	Stretch Exponent
10	6.8	1.17
20	6.2	1.19
30	5.9	1.45
40	3.7	1.10
50	2.6	1.07

Table 3.3.7.2: Stretched exponential T_m estimates for the 25 μM I6H/N8H/K28R1 GB1 + 100 μM Cu^{II}-IDA temperature series.

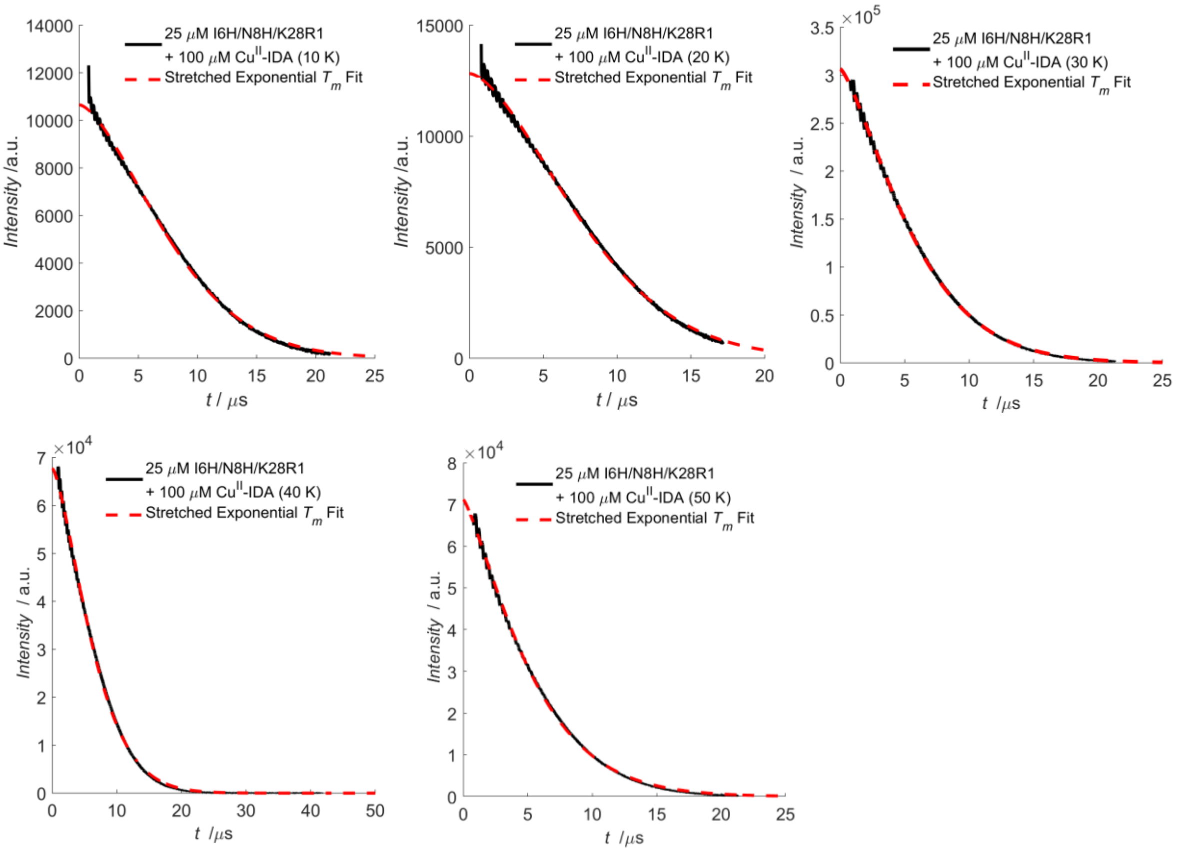

Figure 3.3.7.3: Two-pulse electron spin echo decay data of nitroxide for 25 μM I6H/N8H/K28R1 GB1 + 100 μM Cu^{II}-IDA at various temperatures shown in black, with stretched exponential fits shown in red. The corresponding estimates for T_m are given in table 3.3.7.3 below.

Temperature [K]	T_m Estimate [μs]	Stretch Exponent
10	9.1	1.58
20	9.2	1.63
30	7.0	1.23
40	7.3	1.45
50	5.8	1.26

Table 3.3.7.3: Stretched exponential T_m estimates of the nitroxide for the 25 μM I6H/N8H/K28R1 GB1 + 100 μM Cu^{II}-IDA temperature series.

3.3.8 *Sensitivity Optimisation of Cu^{II}-Cu^{II} RIDME and PELDOR Measurements*

Sensitivity in pulse dipolar EPR is given as the product of the signal-to-noise ratio of the detected echo, and the modulation depth (i.e., in accordance with equations 3.2.7.1-2). Experimental sensitivity can be normalised to a single acquisition shot, or acquisition time (as described in section 3.3.9, pg 95) however for the numerical simulations below, the plotted sensitivity is normalised arbitrarily (i.e., equivalent to acquisition over a single echo). A sensitivity profile for Cu^{II}-Cu^{II} RIDME was numerically simulated using T_1 and T_m estimates from 75 μM I6H/N8H/K28H/Q32H GB1 + 250 μM Cu^{II}-IDA relaxation data. Sensitivity was calculated according to equations 3.2.7.1 and 3.2.7.2 given in section 3.2.7.

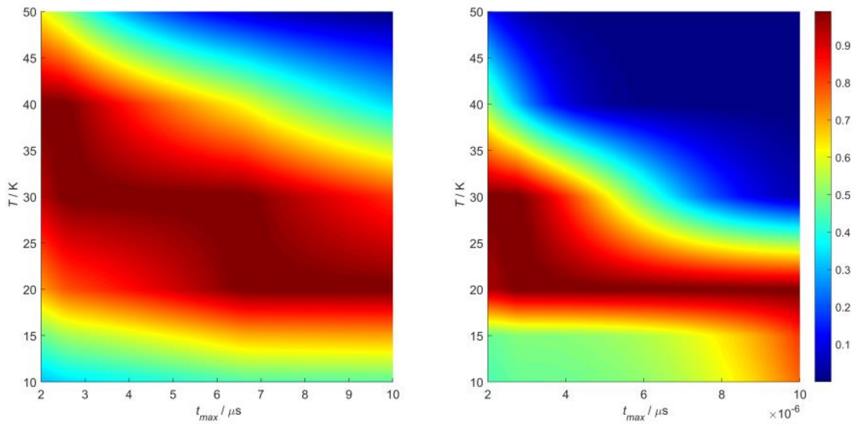

Figure 3.3.8.1: Sensitivity contour plots of the 5-pulse Cu$^{\mathrm{II}}$-Cu$^{\mathrm{II}}$ RIDME experiment, for the 75 µM I6H/N8H/K28H/Q32H + 250 µM Cu$^{\mathrm{II}}$-IDA sample, numerically simulated from equations 3.2.7.1 (left) and 3.2.7.2 (right) to investigate the influence of using a bi-exponential and stretched exponential approximation to describe the longitudinal and transverse relaxation times, respectively.

The general sensitivity profile is conserved when using a bi-exponential approximation to describe longitudinal relaxation, however the transition from 30 K to 20 K shifts to shorter t_{max} values, though for our measurements 30 K is still the optimal temperature. It is observed from the contour plots in figure 3.3.8.1 that regardless of the model used for simulation, sensitivity is maximised for Cu$^{\mathrm{II}}$-Cu$^{\mathrm{II}}$ RIDME by measuring at 30 K for $t_{max} < 4$ µs. It was also necessary to optimise parameters for the 4-pulse Cu$^{\mathrm{II}}$-Cu$^{\mathrm{II}}$ PELDOR measurements. Here, the sensitivity contour was numerically simulated according to equation 2.7.4 in the temperature range from 10 to 50 K and for t_{max} in the range from 2 to 10 µs, and is shown in figure 3.3.8.2. It is important to note that the normalised contour plots should appear numerically identical to that of the Cu$^{\mathrm{II}}$-Cu$^{\mathrm{II}}$ RIDME contour; because for a homo-spin pair the additional exponential terms in the RIDME expression are constant, under the assumption that $T_{mix} \sim 0.7 \times T_1$.

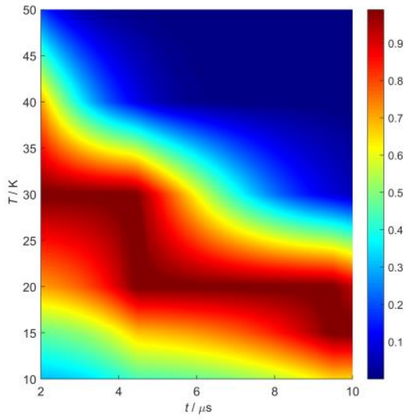

Figure 3.3.8.2: Sensitivity contour plot of the 4-pulse Cu$^{\mathrm{II}}$-Cu$^{\mathrm{II}}$ PELDOR experiment, using experimental values for the 75 µM I6H/N8H/K28H/Q32H + 250 µM Cu$^{\mathrm{II}}$-IDA sample, numerically simulated from equation 2.7.4.

Data suggest that using a mono-exponential approximation to estimate T_1 and T_m relaxation times leads to an over-estimation of the relative sensitivity at higher temperatures as seen in the left panel of figure 3.3.8.1. The use of a bi-exponential approximation to estimate T_1 leads to a reduction in the optimum temperature, as shown in the right panel of figure 3.3.8.1. It is to be expected that at longer t_{max} the optimum temperature reduces, and in this case for $t_{max} > 4$ µs measuring at 20 K is likely to be optimal. In this vein, the bi-exponential approximation and stretched exponential approximation, for estimation of T_1 and T_m respectively, are used to determine sensitivity contours, using equation 3.2.7.2.

For the Cu^{II}-nitroxide RIDME, sensitivity contour plots simulated using equations 3.2.7.1 and 3.2.7.2, for temperatures from 10 to 50 K and in the t_{max} range from 2 to 10 µs are shown in figure 3.3.8.3 below. It is seen that under the mono-exponential approximation there is a normalised sensitivity of > 0.90 at 30 K for $t_{max} \leq 4$ µs, while under the bi-exponential approximation the sensitivity profile is noticeably changed and a splitting of the sensitivity maximum is observed at both 20 and 40 K. It is important to note that this is likely artificial owing to imperfect fits of experimental ESE decay and IR data at low temperature, and particularly the behaviour of the stretching exponent in the transverse dephasing term, which does not decrease significantly with lower temperatures. Under the bi-exponential approximation normalised sensitivity at 30 K is ≥ 0.55 at $t_{max} \leq 4$ µs.

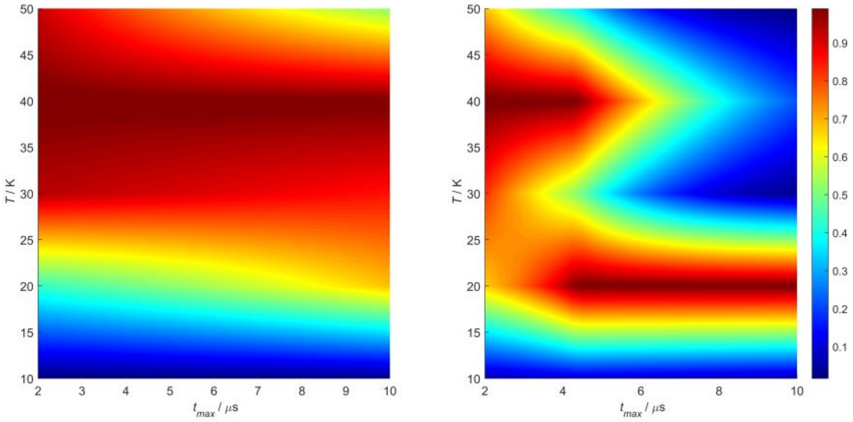

Figure 3.3.8.3: Contour plots of sensitivity calculated from equations 3.2.7.1 (left) and 3.2.7.2 (right) in the 5-pulse Cu^{II}-NO RIDME experiment, using experimental values for the 25 µM I6H/N8H/K28R1 + 100 µM Cu^{II}-IDA sample, for temperatures in the range 10-50 K, numerically simulating t_{max} in the range 2-10 µs.

To optimise the experimental T_{mix} used for Cu^{II}-nitroxide RIDME measurements, sensitivity contour plots were numerically simulated from equation 3.2.7.2 by varying the mixing block interval (T_{mix}) in the range 0-1000 µs for $t_{max} = 1.5$ µs and 4 µs, shown in figure 3.3.8.4. It is seen that for $t_{max} = 1.5$ µs a normalised sensitivity ≥ 0.90 is achieved at 30 K with a mixing time of 200 µs. At $t_{max} = 4$ µs normalised sensitivity at 30 K falls to ~0.55, but is still optimised at that temperature with a mixing time of 200 µs. This process optimises sensitivity, while also minimising the effect of spectral diffusion by keeping the mixing time short. This is significant because spectral diffusion is more prominent at longer mixing times and can lead to RIDME background functions which are fitted poorly by second-order polynomials, making background correction problematic. However, it should also be mentioned that for the quantification of

Δ and specifically the product $\Delta \times {\Delta_{Tmix}}^{-1}$, a longer mixing time can be beneficial, particularly when T_{mix} >>T_1, since in this case the product $\Delta \times {\Delta_{Tmix}}^{-1}$ is less sensitive to error in T_1 estimation, and the robustness of the approach is increased. Therefore, a mixing time of 200 µs was used for all Cu^{II}-nitroxide 5-pulse RIDME measurements.

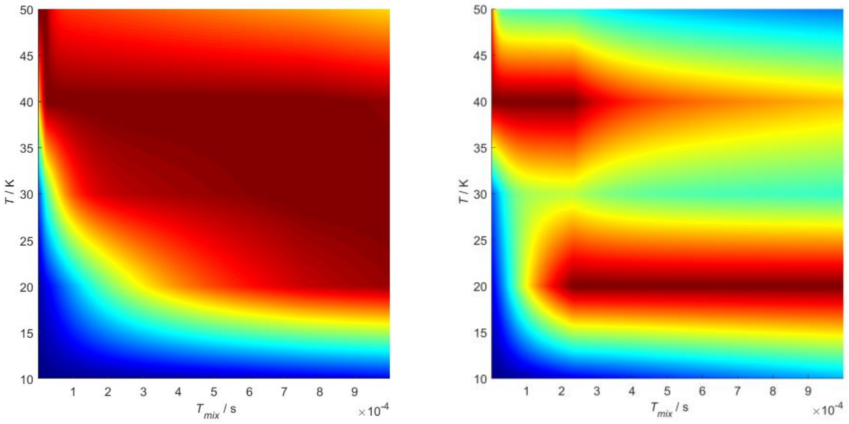

Figure 3.3.8.4: Contour plots of sensitivity calculated from equation 3.2.7.2 in the 5-pulse Cu^{II}-NO RIDME experiment, for the 25 µM I6H/N8H/K28R1 + 100 µM Cu^{II}-IDA sample, for temperatures in the range 10-50 K, numerically simulating mixing block intervals (T_{mix}) in the range 0-1000 µs, and for tmax = 1.5 µs (left) and 4 µs (right).

3.3.9 *Cu^{II}-Nitroxide RIDME Sensitivity Estimate*

The sensitivity comparison of Q-band Cu^{II}-NO RIDME and Cu^{II}-Cu^{II} RIDME and PELDOR was estimated using an approach outlined previously.[204,207] In this approach, the modulation depth of each trace is calculated in DeerAnalysis, then the noise level in each trace is estimated from the imaginary part of the phase-corrected and normalised time-trace, and the modulation depth is divided by this value, giving the sensitivity as modulation-to-noise ratio. This is then normalised for number of echoes by division with the square-root of the total echoes per point considering all averaging and phase cycles giving the sensitivity per echo (S_e). Different signal averaging rates based on different relaxation times can be taken into account by multiplying with the square root of the averaging rate to yield the sensitivity per unit time (S_t).

For a comparison of the sensitivity of Cu^{II}-Cu^{II} and Cu^{II}-nitroxide RIDME and Cu^{II}-Cu^{II} PELDOR, samples of 25 µM I6R1/K28H/Q32H GB1 + 30 µM Cu^{II}-NTA and 25 µM I6H/N8H/K28H/Q32H GB1 + 50 µM Cu^{II}-NTA were prepared (to give approximately equimolar equivalents of double-histidine motifs and Cu^{II}-NTA). Samples were measured at 30 K and 122 points, recorded with respective shot-repetition times of 1, 2, and 30 ms for Cu^{II}-Cu^{II} RIDME, PELDOR and Cu^{II}-nitroxide RIDME measurements (corresponding to rates of 1,000, 500 and 33 Hz). For the Cu^{II}-Cu^{II} and Cu^{II}-nitroxide RIDME respectively, mixing block intervals (T_{mix}) of 34 and 200 µs were used.

At this concentration, the Cu^{II}-nitroxide RIDME trace shows strong dipolar modulation even after a single scan and single shot-per-point, this was problematic for estimation of the trace noise, since the RMSD is dominated by the error in the Tikhonov fitting rather than the noise. Imperfections of the phase cycle and other artefacts dominated the imaginary part. Therefore, dummy RIDME and PELDOR traces were run, at which the respective echo was integrated multiple times at $t = 0$ and dipolar evolution was not incremented. Briefly, in these dummy measurements all interpulse delays are set to be constant, hence the entire pulse sequence is shifted by the dipolar increment. The result is a trace that is dominated only by thermal noise on the detected echo. Indeed this allows direct comparison of the noise level between measurements with different conditions or pulse sequences without contributions from any dipolar modulation. This has made nuclear modulation averaging obsolete and it was not used for dummy experiments. However, for capturing the experimental phase cycling schemes, dummy RIDME traces were recorded with one shot per point and an 8-step phase cycle (i.e., each point corresponds to 8 total echoes). To compensate for this, the dummy PELDOR trace was recorded using four shots per point and a 2-step phase cycle (i.e., each point corresponds to 8 total echoes). The resulting noise traces are shown below in figure 3.3.9.1, and the calculated RMSD is given in table 3.3.9.1. These results show that the detected echo carries the lowest noise for Cu^{II}-nitroxide RIDME whereas it is approximately a factor 3 and 15 higher for Cu^{II}-Cu^{II} RIDME and PELDOR, respectively. This does not yet consider modulation depths or signal averaging.

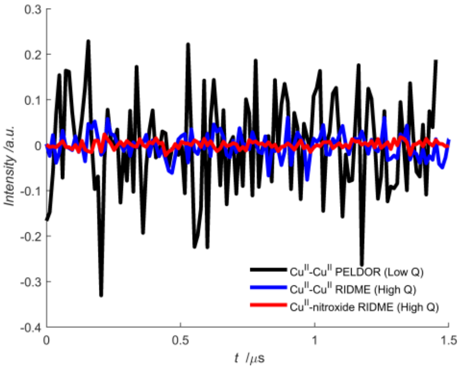

Figure 3.3.9.1: A comparison of the noise traces measured for Cu^{II}-Cu^{II} PELDOR and Cu^{II}-Cu^{II} and Cu^{II}-nitroxide RIDME experiments, shown in black, blue and red traces, respectively.

Experiment	RMS noise	Δ	S_e	Relative S_e	Averaging rate	S_t	Relative S_t
Cu^{II}-Cu^{II} PELDOR	1.38×10^{-1}	0.01	2.56×10^{-2}	1.00	660	0.658	1.00
Cu^{II}-Cu^{II} RIDME	2.93×10^{-2}	0.20	2.41	94.2	660	62.0	94.2
Cu^{II}-nitroxide RIDME	9.26×10^{-3}	0.45	17.2	671	33.3	99.1	151

Table 3.3.9.1: A comparison of the estimated RMSD of the noise traces shown in figure 3.3.9.1. Dummy measurements were run by setting the period of dipolar evolution to 0 and not incrementing t, therefore yielding traces without dipolar modulation.

In this work, Cu^{II}-Cu^{II} PELDOR modulation depths at Q-band were found to be limited to ~1%, while Cu^{II}-Cu^{II} RIDME is experimentally observed to yield 20% and Cu^{II}-nitroxide RIDME is (in practice) limited to ~45%. Experimental raw and processed RIDME and PELDOR traces are shown below in figures

3.3.9.2-4, with modulation depths and background correction parameters given in table 3.3.9.2. As only the modulated part of the signal contains the desired structural information, the modulation depths contributes linearly to the effect sensitivity. This can be expressed in the modulation-to-noise ratio (given by the modulation depth divided by the root mean square noise). For the present comparison this yields the highest sensitivity per echo (S_e) for Cu^{II}-nitroxide RIDME whereas it is factors ~7 and ~670 lower for Cu^{II}-Cu^{II} RIDME and PELDOR, respectively. This does not yet consider signal averaging.

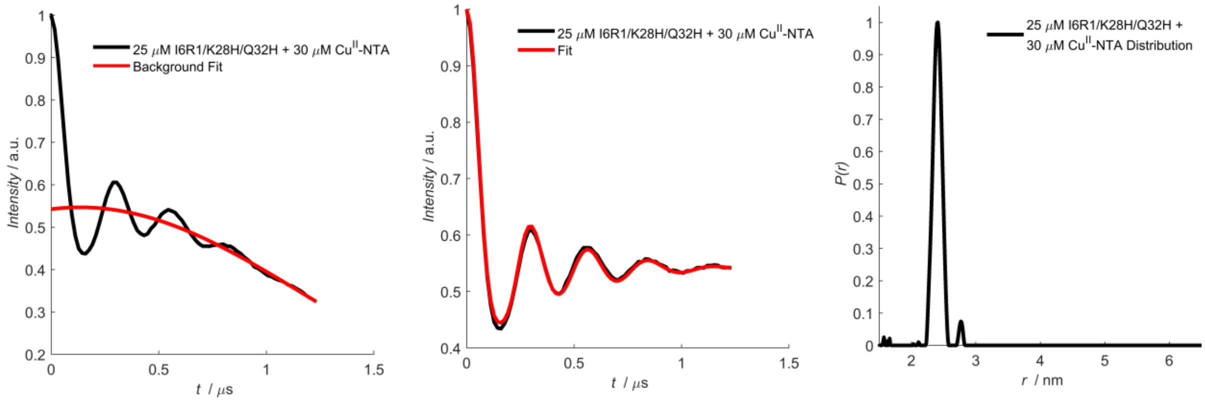

Figure 3.3.9.2: Cu^{II}-nitroxide RIDME measured for 25 µM I6R1/K28H/Q32H GB1 + 30 µM Cu^{II}-NTA, with the raw trace, background corrected trace and distance distribution shown left-to-right. Data is shown in black, and the background correction and Tikhonov fit are shown in red.

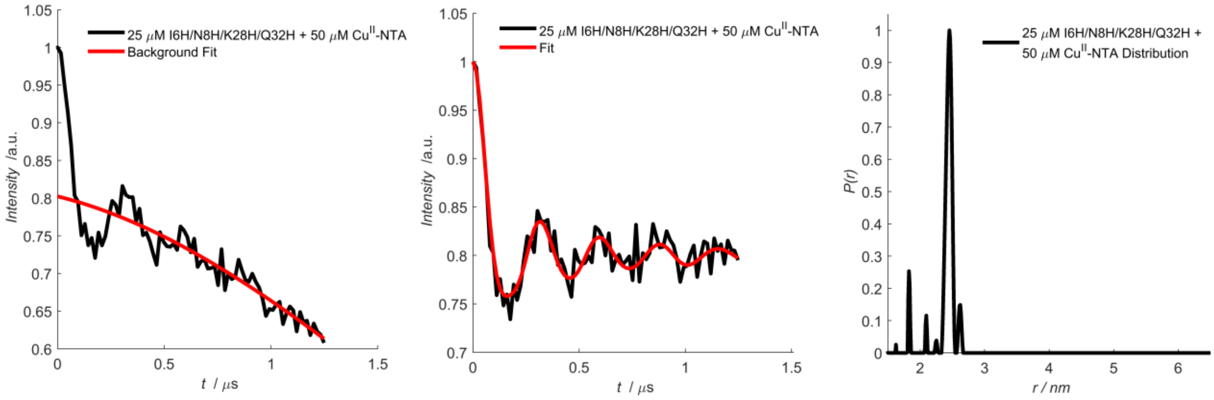

Figure 3.3.9.3: Cu^{II}-Cu^{II} RIDME measured for 25 µM I6H/N8H/K28H/Q32H GB1 + 50 µM Cu^{II}-NTA, with the raw trace, background corrected trace and distance distribution shown left-to-right. Data is shown in black, and the background correction and Tikhonov fit are shown in red.

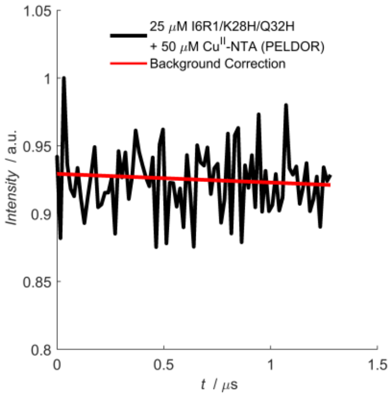

Figure 3.3.9.4: Cu^{II}-Cu^{II} PELDOR measured for 25 µM I6H/N8H/K28H/Q32H GB1 + 50 µM Cu^{II}-NTA. Data is shown in black, and the background correction is shown in red.

Experiment	Zero-time [ns]	Background start [ns]	Background cut-off [ns]	Modulation depths (Δ)
Cu^{II}-nitroxide RIDME	206	324	1232	0.45
Cu^{II}-Cu^{II} RIDME	204	216	1248	0.20
Cu^{II}-Cu^{II} PELDOR	171	320	1280	-

Table 3.3.9.2: A comparison of background correction parameters and modulation depths for traces shown in figures 3.3.9.2-4.

Both Cu^{II}-Cu^{II} PELDOR and Cu^{II}-Cu^{II} RIDME measurements are averaged faster than the Cu^{II}-nitroxide RIDME. For simplicity we consider an average enhancement of the averaging rate by a factor of 20. All factors relevant for determination of the sensitivities per echo (S_e) and per unit time (S_t) are given in table 3.3.9.3. Given that the signal-to-noise (and consequently modulation-to-noise) ratio is proportional to the square root of the number of averages, this translates to a loss in sensitivity for Cu^{II}-nitroxide RIDME due to slower averaging. The overall sensitivity gain for Cu^{II}-nitroxide and Cu^{II}-Cu^{II} RIDME over Cu^{II}-Cu^{II} PELDOR is ~150-fold and ~100-fold, respectively. It should be appreciated that these values are discussed as a non-exhaustive treatment, but are sufficient to conclude that Cu^{II}-Cu^{II} and Cu^{II}-nitroxide RIDME experiments are approximately two orders of magnitude more sensitive than Cu^{II}-Cu^{II} PELDOR at Q band frequencies.

Sample	Experiment	RMSD Estimate	Relative noise
25 µM I6H/N8H/K28H/Q32H GB1 + 50 µM Cu^{II}-NTA	Cu^{II}-Cu^{II} PELDOR	1.38×10^{-1}	14.9
25 µM I6H/N8H/K28H/Q32H GB1 + 50 µM Cu^{II}-NTA	Cu^{II}-Cu^{II} RIDME	2.93×10^{-2}	3.16
25 µM I6R1/K28H/Q32H GB1 + 30 µM Cu^{II}-NTA	Cu^{II}-nitroxide RIDME	9.26×10^{-3}	1.00

Table 3.3.9.3: Sensitivity for Cu^{II}-Cu^{II} PELDOR and RIDME and Cu^{II}-nitroxide RIDME.

3.3.10 *K_D Determination from RIDME Pseudo-Titration Series*

As mentioned above, RIDME pseudo-titrations were first performed for 75 µM and 25 µM I6R1/K28H/Q32H GB1 in presence of Cu^{II}-IDA and Cu^{II}-NTA, respectively, and for 25 µM

I6H/N8H/K28R1 in presence of Cu^{II}-IDA and Cu^{II}-NTA. Corresponding data is shown in figure 3.3.10.1 below, with K_D estimates and error bars given in table 3.3.10.1. The blue traces indicate the bivariate fitted K_D values and corresponding binding isotherms, while the black (for the I6R1/K28H/Q32H GB1 series) and cyan (for the I6H/N8H/K28R1 GB1 series) traces are simulated isotherms, that allow a crude estimation of the error in K_D by visual inspection. Initially these binding isotherms were processed and fitted using a univariate error function where only K_D could vary and Δ_{Tmix} was always 0.5. In this case the hyperbolic function was poorly resolved, and so led to adoption of a bi-variate fitting approach, which also scaled Δ_{Tmix} (this was predicated on the observation that in practice Δ_{Tmix} is closer to 0.45) and this is discussed more in-depth in section 3.3.12 of the chapter. Additionally, the poor resolution of the hyperbolic function led to a reduction of the protein concentration to 500 nM, for which another pseudo-titration series was performed, also discussed in more detail in chapter 3.3.12. Importantly, the fitted K_D values shown in figure 3.3.10.1 are calculated from deconvoluted RIDME modulation depths (deconvolution is necessary to suppress a low-frequency artefact attributed to dynamical decoupling,[273,299] and is discussed in more detail in section 3.3.11). For completeness, non-deconvoluted RIDME traces were also processed, however the fit quality of the dipolar evolution functions was significantly reduced. As anticipated the bivariate fitted K_D values using non-deconvoluted RIDME modulation depths were lower, indicating a factor ~2-3 higher binding affinity, however these values are unlikely to be reliable owing to the poor quality of fit to the dipolar evolution functions. The corresponding isotherms are given in appendix A.

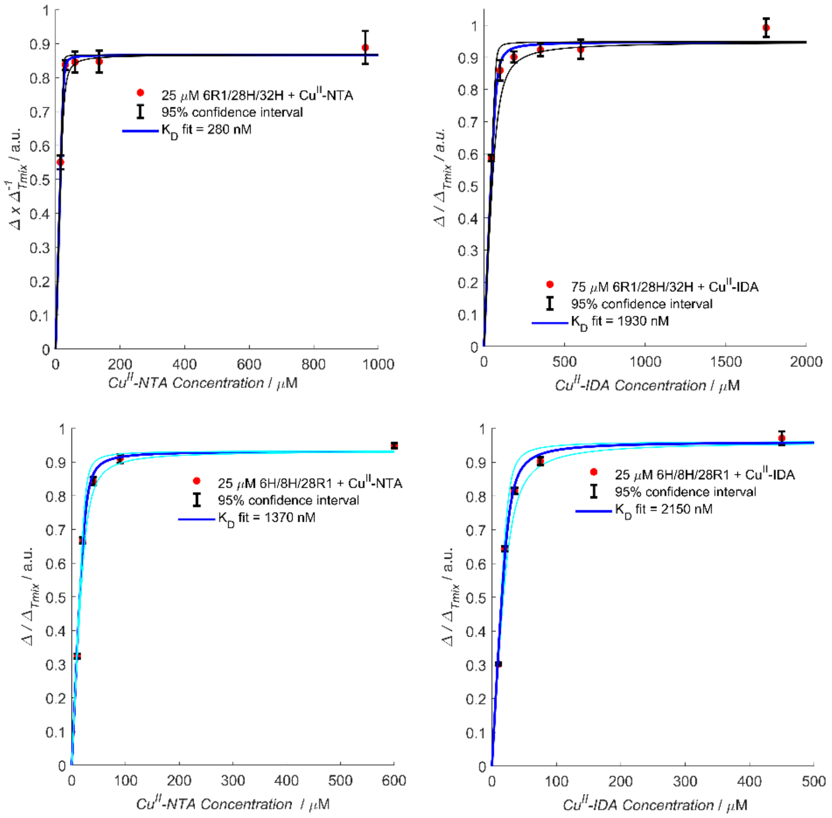

Figure 3.3.10.1: Binding isotherms of the RIDME pseudo-titrations, for 25 µM and 75 µM 6R1/28H/32H GB1 + Cu^{II}-NTA and Cu^{II}-IDA, (top right and left), respectively, and 25 µM 6H/8H/28R1 GB1 + Cu^{II}-NTA and Cu^{II}-IDA (bottom right and left), respectively. K_D values are given in table 3.3.10.1. The cyan traces show isotherms for a K_D a factor 2 higher and lower than the best fit (solid blue line). The black traces show isotherms for a K_D a factor 5 and 4 higher and lower than the best fit, for 6R1/28H/32H in presence of Cu^{II}-NTA and Cu^{II}-IDA, respectively

Pseudo-titration Series	Predicted K_D [nM]	Calculated Δ_{Tmix} from Bivariate Fit
25 µM I6R1/K28H/Q32H GB1 + Cu^{II}-NTA	280 ± 475	0.434
75 µM I6R1/K28H/Q32H GB1 + Cu^{II}-IDA	1930 ± 2375	0.490
25 µM I6H/N8H/K28R1 GB1 + Cu^{II}-NTA	1370 ± 785	0.467
25 µM I6H/N8H/K28R1 GB1 + Cu^{II}-IDA	2150 ± 1000	0.476

Table 3.3.10.1. The estimated K_D values taken from the RIDME binding isotherms given in figure 3.3.10.1, using a bi-variate fitting approach.

It can be seen from the simulated cyan traces (i.e., simulated with two-fold higher and lower K_D compared to the fitted value) that for the 6H/8H/28R1 construct, for the Cu^{II}-IDA and Cu^{II}-NTA pseudo-titration series the fitted K_D is sensitive to a factor 2 (i.e., the datapoints lie between the cyan curves within error, particularly in the curved region of the isotherm). This is also reflected by the error in K_D estimated from Gaussian fits of the one-dimensional error surfaces (given in appendix A), with 1370 ± 785 nM and 2150 ± 1000 nM, for Cu^{II}-NTA and Cu^{II}-IDA, respectively. However, as seen from the simulated black traces (i.e., simulated with four-fold higher and lower K_D compared to the fitted value) for the 6R1/28H/32H construct, the fitted K_D is sensitive to a factor 4 (i.e., the datapoints lie approximately between the black curves within error, particularly in the curved region of the isotherm). Again, this is reflected by the error bars in table 3.3.10.1, with 280 ± 475 nM and 1930 ± 2375 nM, for Cu^{II}-NTA and Cu^{II}-IDA, respectively. This posed the issue of sensitivity to low (particularly sub µM) K_D as is estimated from the 6R1/28H/32H + Cu^{II}-NTA pseudo-titration series, and so this was the motivation to measure the 500 nM pseudo-titration series with this construct. It should also be noted that the fit value of Δ_{Tmix} ranges from 0.43-0.49, whereas the theoretical limit is 0.5. A comparison of the ITC-extrapolated and RIDME-determined K_D values is given below in table 3.3.10.2, and it is seen that these differ by less than a factor 2, showing good agreement.

Construct-Chelator Permutation	K_D Estimate at 239 K [µM]	K_D Estimate from RIDME pseudo-titrations [µM]
I6R1/K28H/Q32H GB1 + Cu^{II}-NTA	0.22	0.28 ± 0.48
I6R1/K28H/Q32H GB1 + Cu^{II}-IDA	2.48	1.93 ± 2.4
I6H/N8H/K28R1 GB1 + Cu^{II}-NTA	0.75	1.37 ± 0.79
I6H/N8H/K28R1 GB1 + Cu^{II}-IDA	1.73	2.15 ± 1.0

Table 3.3.10.2: A comparison of the predicted K_D values at 239 K, using van't Hoff's equation and the thermodynamic data from ITC (section 3.3.5), with K_D values estimated from the RIDME pseudo-titrations shown in figure 3.3.10.1.

This is better visualised in figure 3.3.10.2 below, showing the behaviour of K_Ds with temperature in the range 175-300 K. The black dots indicate the temperature at which the RIDME-determined K_D values match the extrapolated ITC-determined K_D using van't Hoff's equation. For all samples, the temperature is remarkably consistent to a temperature between 230 and 240 K. This is an internal control, since all RIDME pseudo-titration samples are measured with 50% (v/v) deuterated ethylene glycol and aqueous buffer, meaning the temperatures where the dynamics are frozen-out should be similar. Most importantly, this demonstrates there is strong numerical agreement between the RIDME-determined K_D values and the room-temperature ITC-determined values once different temperature regimes are accounted for. The precise temperatures and log(K_D) values are given in table 3.3.10.3.

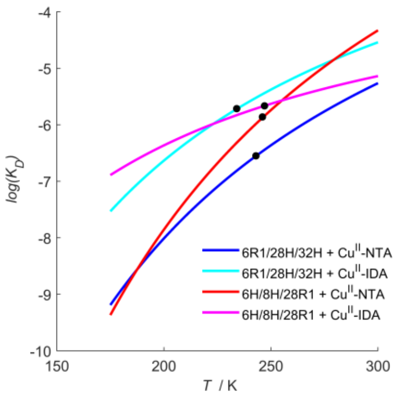

Figure 3.3.10.2: The dependence of K_D on temperature, calculated using van't Hoff's equation and the empirical ΔH values taken from ITC (section 3.3.5). Here the solid lines show the predicted behaviour of each construct/Cu^{II}-chelate dissociation constant as a function of temperature, and the black scatter indicates the temperature at which the RIDME-determined K_D intersects the predicted affinity from ITC data.

Construct-Chelator Permutation	Temperature [K]	log(K_D)
I6R1/K28H/Q32H GB1 + Cu^{II}-NTA	243	-6.55
I6R1/K28H/Q32H GB1 + Cu^{II}-IDA	234	-5.71
I6H/N8H/K28R1 GB1 + Cu^{II}-NTA	246	-5.86
I6H/N8H/K28R1 GB1 + Cu^{II}-IDA	247	-5.67

Table 3.3.10.3: A comparison of the temperature values where the RIDME-determined K_D intersects with the prediction using the van't Hoff's equation and the thermodynamic data from ITC with the corresponding log(K_D) values also given.

The 75 µM pseudo-titration of 6R1/K28H/Q32H in presence of Cu^{II}-IDA deviates from the trend observed for other pseudo-titrations. The RIDME-determined K_D intersects with the ITC prediction at a lower temperature and suggests that the deviation is the result of an over-estimation of the affinity from the RIDME pseudo-titration. This is also reflected by the RMSD of the fit which is approximately a factor 3 greater than for the other series, and so poses an interesting point of discussion regarding error analysis, which is addressed more rigorously in the next results chapter. Even so, the K_D values determined by RIDME and ITC have strong agreement, suggesting this method is robust.

3.3.11 *PD-EPR Measurements*

5-pulse RIDME traces are shown for I6R1/K28H/Q32H and I6H/N8H/K28R1 measured at 5 µM, in figures 3.3.11.1 and 3.3.11.2, respectively; the data is deconvoluted as described in section 3.2.8 and the modulation depth values (adjusted for deconvolution using equation 3.2.8.1) are given in table 3.3.11.1. For the I6R1/K28H/Q32H construct, distance distributions are mono-modal at 2.40 nm and 2.41 nm for Cu^{II}-NTA and Cu^{II}-IDA, respectively. This is relatively consistent with the 2.45 nm distance reported between Cu^{II}-IDA labels in the tetra-histidine I6H/N8H/K28H/Q32H GB1 construct by

Cunningham *et al.*,[241] and slight variation is to be anticipated given the R1-linker has a greater conformational freedom than the Cu^{II}-label.

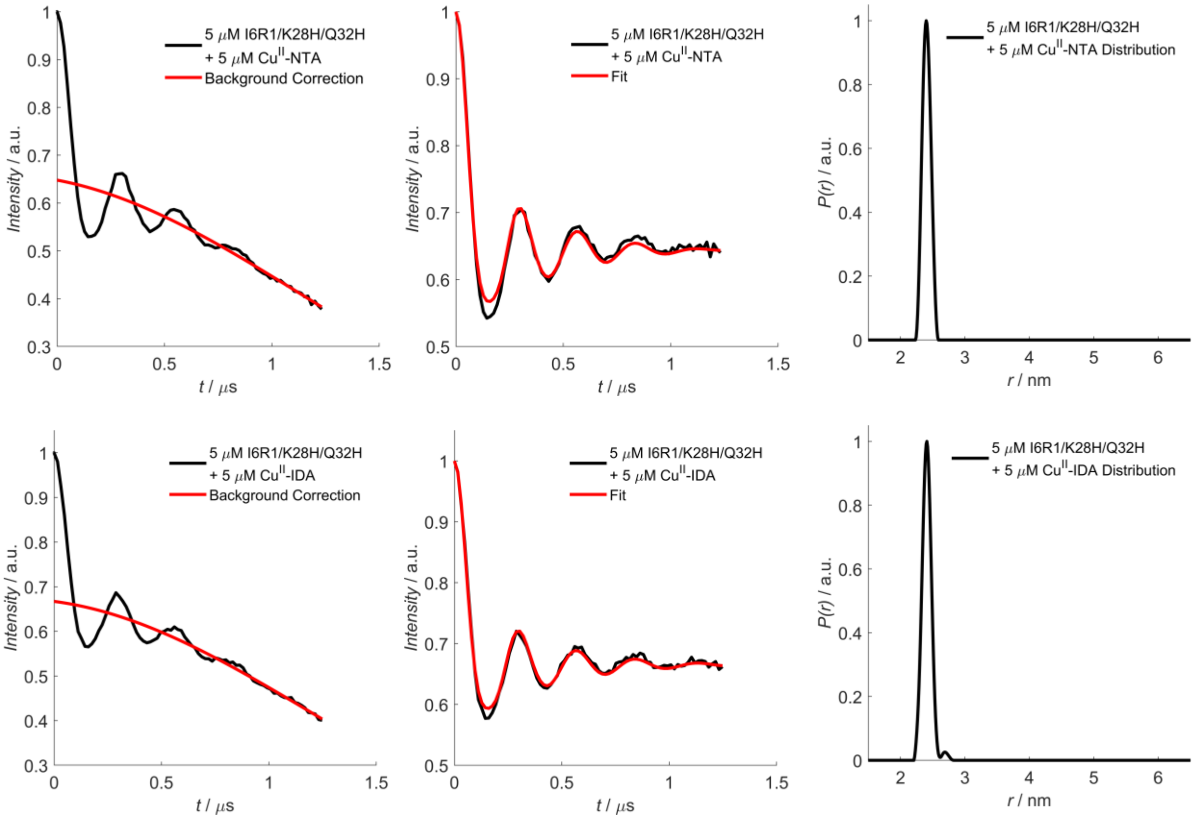

Figure 3.3.11.1. Deconvoluted RIDME data for 5 µM I6R1/K28H/Q32H, in presence of one equivalent Cu^{II}-NTA and Cu^{II}-IDA, shown in the top and bottom rows, respectively. The raw data, background corrected dipolar evolution function, and corresponding distance probability distributions P(r) are shown left-to-right. The experimental data is shown in black, with the respective background correction and fit to the dipolar evolution function shown in red.

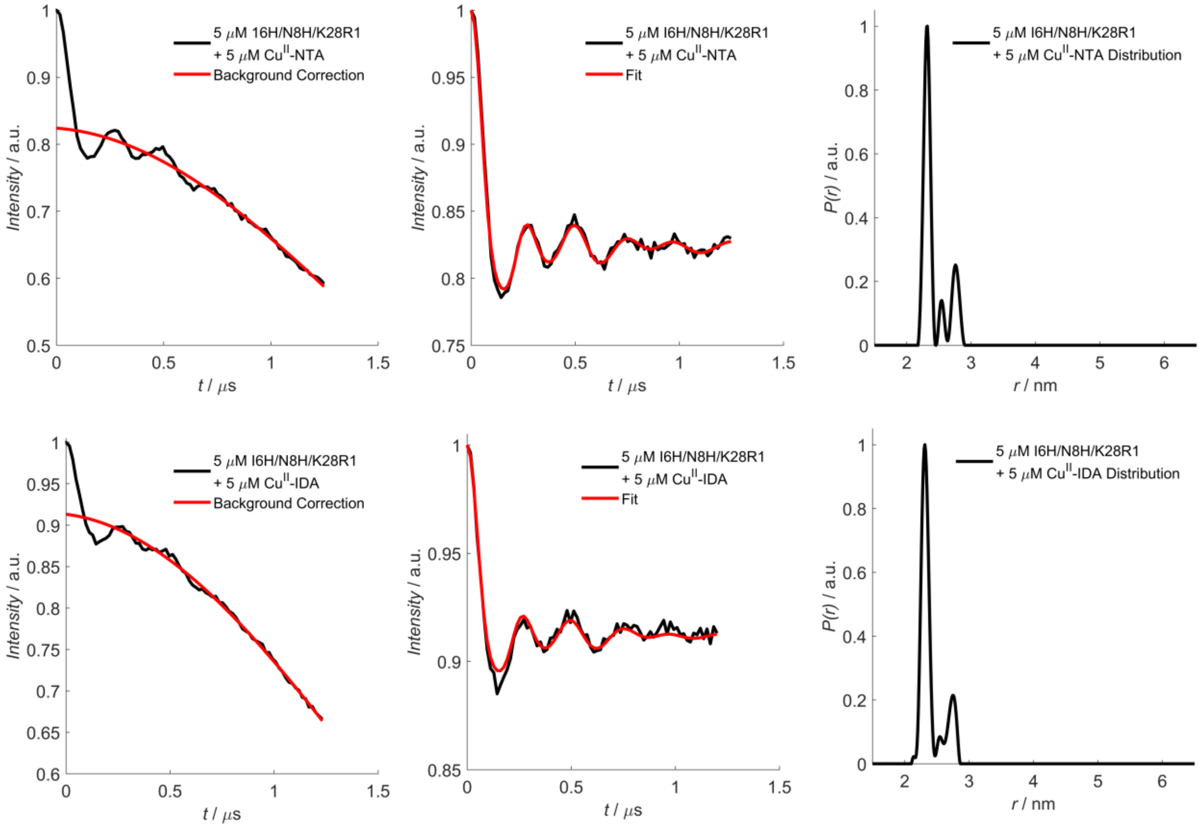

Figure 3.3.11.2. Deconvoluted RIDME data for 5 µM I6H/N8H/K28R1, in presence of one equivalent Cu^{II}-NTA and Cu^{II}-IDA, shown in the top and bottom rows, respectively. The raw data, dipolar evolution functions, and corresponding P(r) are shown left-to-right. The experimental data is shown in black, with the respective background correction and fit to the dipolar evolution function shown in red.

Sample	Modulation depth (Δ)
5 µM I6R1/K28H/Q32H + 5 µM Cu^{II}-IDA	0.35±0.01
5 µM I6R1/K28H/Q32H + 5 µM Cu^{II}-NTA	0.37±0.01
5 µM I6H/N8H/K28R1 + 5 µM Cu^{II}-IDA	0.09±0.01
5 µM I6H/N8H/K28R1 + 5 µM Cu^{II}-NTA	0.18±0.01

Table 3.3.11.1: The modulation depths of the deconvoluted RIDME traces shown above in figures 3.3.11.1 and 3.3.11.2, as adjusted according to equation 3.2.8.1, given above.

Interestingly, the RIDME data for the I6H/N8H/K28R1 construct shows a bi-modal distance distribution; with a major peak at ~2.3 nm, and a smaller shoulder peak at ~2.7 nm, possibly indicating that the nitroxide is occupying distinct conformations on the helix. It is also feasible that the emergence of a shoulder peak indicates another Cu^{II}-label binding site, though at one equivalent of Cu^{II}-label this is unlikely to arise from non-specific interactions. To clarify that a second Cu^{II}-binding site was not present, a Cu^{II}-Cu^{II} RIDME measurement was performed. This was necessary to determine that there was only one Cu^{II}-binding site, as expected, because the model used to fit the experimental data and estimate the K_D values assumed a single binding-site. However, it should be noted that a native low affinity Cu^{II}-binding site has been observed in GB1.[326] A sample of I6H/N8H/K28R1 in presence of equimolar Cu^{II}-NTA was measured by 5-pulse RIDME, with the detection pulses positioned at the maximum of the Cu^{II}-NTA spectrum and using a mixing block of ~0.7×T_1. The raw trace is shown in figure 3.3.11.3, and as can be seen there is no dipolar modulation, indicating that there are no secondary Cu^{II}-NTA binding sites.

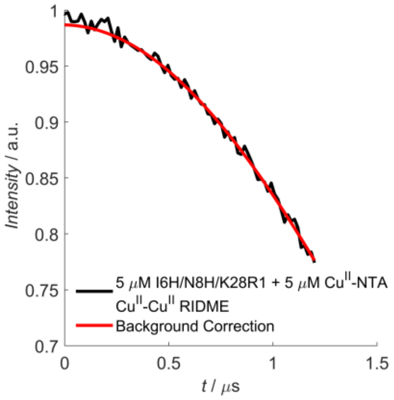

Figure 3.3.11.3: A Cu^{II}-Cu^{II} RIDME trace, measured on the I6H/N8H/K28R1 + Cu^{II}-NTA sample. Data was acquired overnight (~16 hours), using an SRT of 2 ms and a mixing-time of 30 μs, observing at the maximum field position of the Cu^{II}-NTA spectrum.

A further indication that this shoulder peak at 2.7 nm is a real feature, and not the result of improper background correction is that the dipolar evolution functions in figure 3.3.11.2 both distinctly show modulation by a second dipolar frequency. To further investigate this, X-band PELDOR traces were recorded for both constructs in presence of 1.5 equivalents of each Cu^{II}-chelate, in figures 3.3.11.4 and 3.3.11.5, respectively.

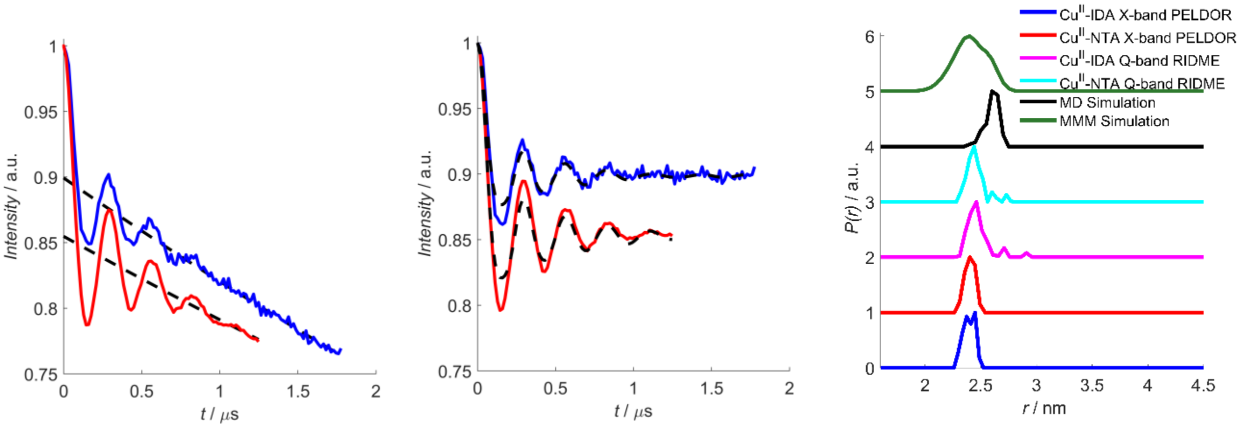

Figure 3.3.11.4. X-band PELDOR raw and processed data for I6R1/K28H/Q32H GB1 in presence of Cu^{II}-IDA and Cu^{II}-NTA shown in blue and red respectively, with the background correction, and corresponding fits in black. In the right-most panel, distance distributions are overlaid with those obtained for Q-band RIDME, in presence of Cu^{II}-IDA and Cu^{II}-NTA, and with the distribution predicted by molecular dynamics, and MMM2018 shown in magenta, cyan, black and green respectively. Distance distributions are vertically offset to aide visualisation.

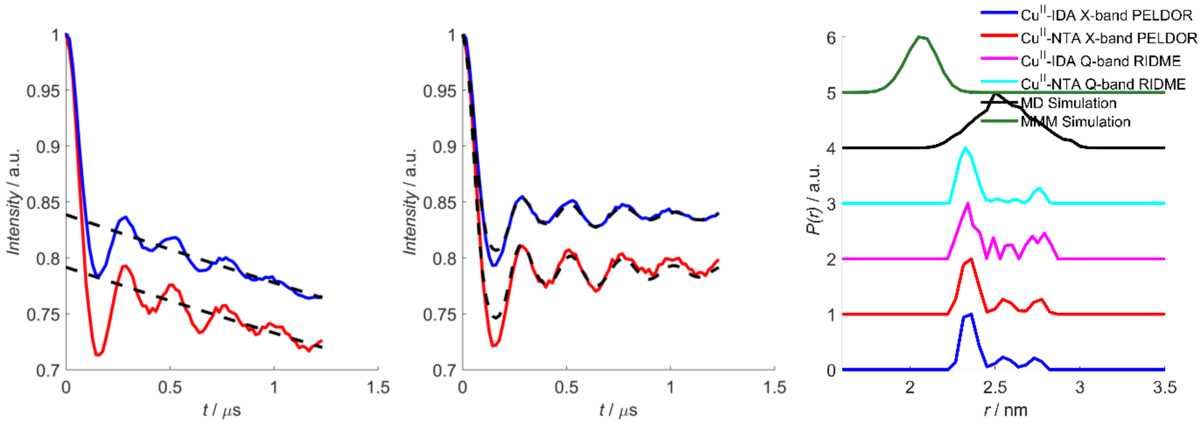

Figure 3.3.11.5. X-band PELDOR raw and processed data for I6H/N8H/K28R1 GB1 in presence of Cu^{II}-IDA and Cu^{II}-NTA shown in blue and red respectively, the corresponding background correction and fit are shown in dotted black. In the right-most panel, distance distributions are overlaid with those obtained for Q-band RIDME, in presence of Cu^{II}-IDA and Cu^{II}-NTA, and with the distribution predicted by molecular dynamics, and MMM2018, shown in magenta, cyan, black and green respectively. Distance distributions are vertically offset to aide visualisation.

Results of the 4-pulse PELDOR measurements are shown above for I6R1/K28H/Q32H and I6H/N8H/K28R1 in presence of Cu^{II}-IDA and Cu^{II}-NTA, shown in blue and red, respectively. The 5-pulse Q-band RIDME measurements for Cu^{II}-IDA and Cu^{II}-NTA, molecular dynamics simulated distributions, and the corresponding distributions simulated in MMM are also overlaid and compared for each construct, shown in magenta, cyan, black and green respectively. The X-band PELDOR measurements reproduce the distance distributions seen in the RIDME experiment for all construct-chelate permutations. This should be taken with a grain of salt, as orientational selectivity is not probed, however the high flexibility of the nitroxide label and measurement at X-band frequency make orientation selection of the detected spin unlikely. We can also exclude orientational selectivity arising from the Cu^{II}-chelate labels; while orientation selection has been observed in PELDOR at Q-band,[327] it has not been observed at X-band frequencies.[300] Since the T_1 behaviour of Cu^{II}-IDA and Cu^{II}-NTA is isotropic,[328] orientational selection in RIDME is also minimised , with all orientations contributing to spin flips during the mixing block. It is interesting to note that for the I6H/N8H/K28R1 construct the molecular dynamics simulation in XPLOR significantly outperforms MMM and agrees well with all empirical data. However, for the I6R1/K28H/Q32H construct, the molecular dynamics simulation shifts the modal distance ~0.3 nm higher than observed and fails to reproduce the exact distribution-shape, while MMM predicts both the modal distance and distribution-width more accurately. Note that these initial samples had issues with the determination of the absolute protein concentration leading to significant errors in the absolute modulation depths. Nonetheless, these measurements allow relating the distance distributions obtained by RIDME to results from the more established PELDOR method.

Importantly, the dipolar evolution functions in figure 3.3.11.1 and 3.3.11.2 indicate high affinity for both constructs in combination with both Cu^{II}-labels. These measurements directly contradict the high K_D values previously estimated for Cu^{II}-IDA[241] and Cu^{II}-NTA.[148] This could be explained by the significantly increased concentrations (approximately six-fold or more) of both protein and Cu^{II}-labels used in previous literature, relative to this work and by the different methods used for quantifying bound *versus* unbound Cu^{II} ions.

5-pulse RIDME traces for a 0.5 µM I6R1/K28H/Q32H Cu^{II}-NTA pseudo-titration series are shown in figures 3.3.11.6-10, for 0.1, 0.3, 0.9, 2.7 and 8.1 µM Cu^{II}-NTA respectively. This data is not deconvoluted. Nitroxide-detected RIDME is empirically found to lead to a pronounced first minimum of the oscillation that is not reproduced by the fitting, though this artefact is reduced by deconvolution (as described in the methods section 3.2.8). Briefly, deconvolution of the RIDME traces involves division in the time-domain of a trace recorded with a long mixing time (i.e., containing both the dipolar modulated signal component, as well as ESEEM modulations and artefact features) with a trace recorded with a short mixing time (i.e., containing only the ESEEM modulations and artefacts). Division in the time domain results in subtraction in the frequency domain; deconvolution can thus provide an efficient post-processing method to isolate the dipolar modulations of interest. However, deconvolution can also decrease the observed modulation depths, because even for short mixing times some Cu^{II} electron spins will undergo spontaneous spin-flips and contribute to a modulated signal component. Upon division in the time domain, some of this modulated signal component will be erased and thus lead to an underestimation of the modulation depth (and by extension will inflate the apparent K_D value). Deconvoluted modulation depths may still be interpreted quantitatively, however they must be corrected for deconvolution using equation 3.2.8.1. The associated modulation depths are given in table 3.3.11.2. Furthermore, the deconvoluted modulation depths for the pseudo-titration series shown and discussed in section 3.3.10, are given in tables 3.3.11.3-6 for 25 µM and 75 µM I6R1/K28H/Q32H in presence of Cu^{II}-NTA and Cu^{II}-IDA, respectively, and 25 µM I6H/N8H/K28R1 in presence of Cu^{II}-NTA and Cu^{II}-IDA. The raw and processed RIDME traces are given in the appendix.

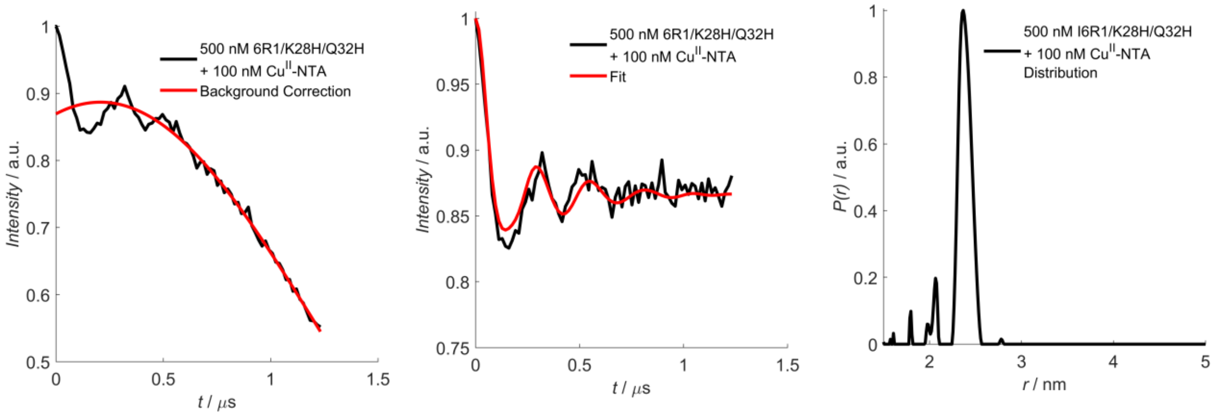

Figure 3.3.11.6: Non-deconvoluted RIDME data for 0.5 µM I6R1/K28H/Q32H, in presence of 0.1 µM Cu^{II}-NTA. The raw data, dipolar evolution function, and corresponding distance distribution are shown left-to-right. The experimental data is shown in black, with the respective background correction and fit to the dipolar evolution function shown in red.

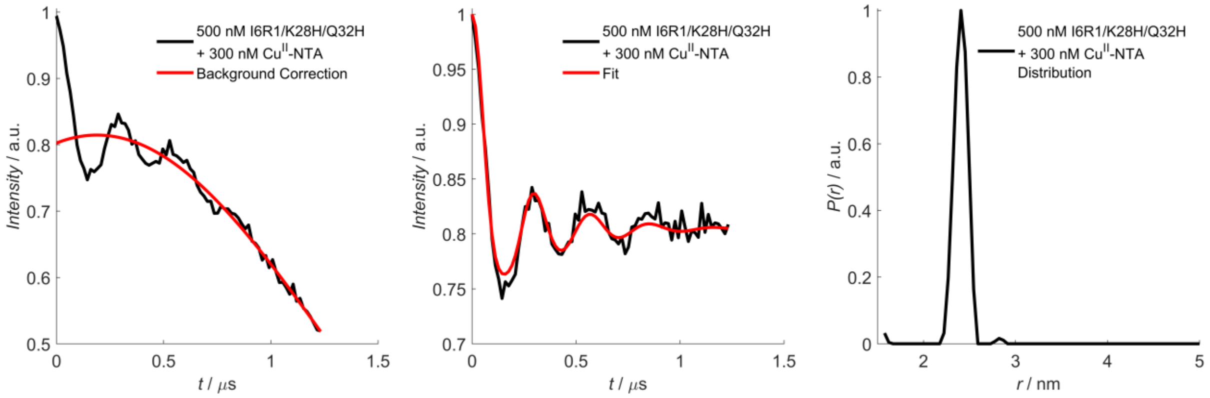

Figure 3.3.11.7: Non-deconvoluted RIDME data for 0.5 µM I6R1/K28H/Q32H, in presence of 0.3 µM Cu^{II}-NTA. The raw data, dipolar evolution function, and corresponding distance distribution are shown left-to-right. The experimental data is shown in black, with the respective background correction and fit to the dipolar evolution function shown in red.

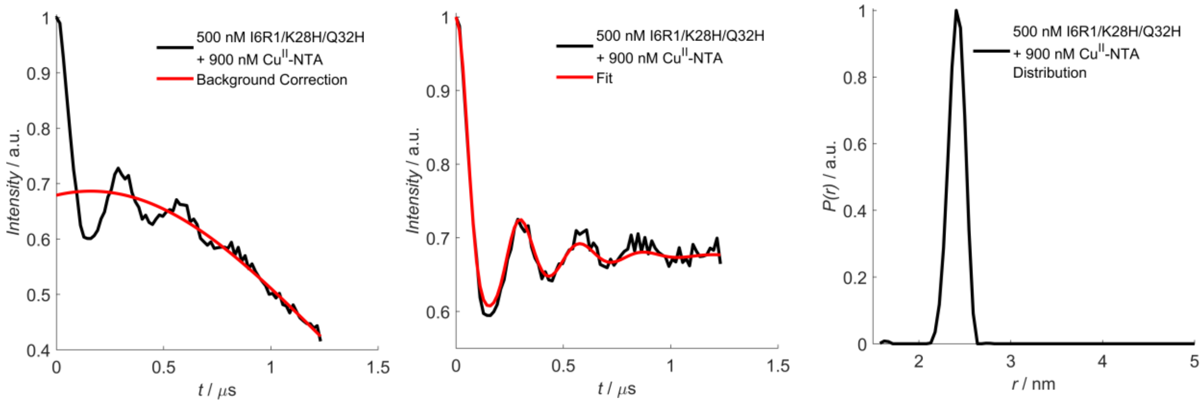

Figure 3.3.11.8: Non-deconvoluted RIDME data for 0.5 μM I6R1/K28H/Q32H, in presence of 0.9 μM Cu^{II}-NTA. The raw data, dipolar evolution function, and corresponding distance distribution are shown left-to-right. The experimental data is shown in black, with the respective background correction and fit to the dipolar evolution function shown in red.

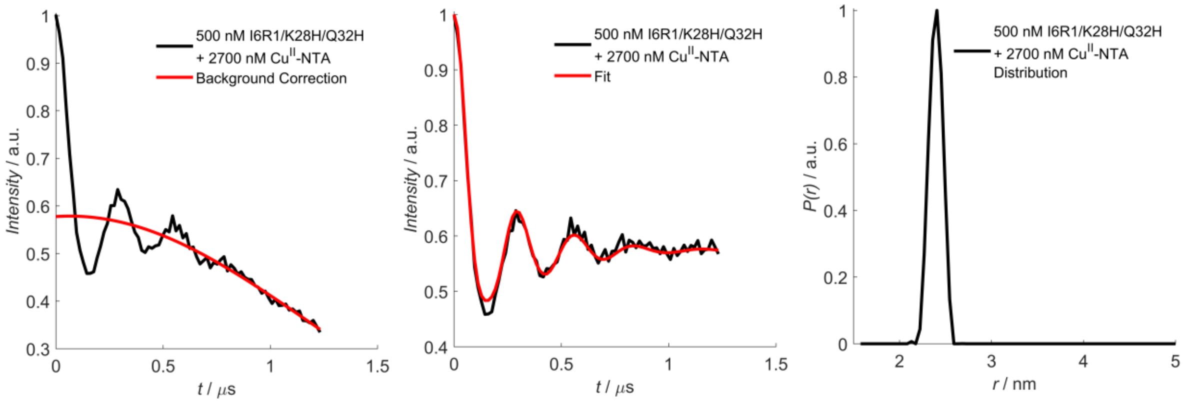

Figure 3.3.11.9. Non-deconvoluted RIDME data for 0.5 μM I6R1/K28H/Q32H, in presence of 2.7 μM Cu^{II}-NTA. The raw data, dipolar evolution function, and corresponding distance distribution are shown left-to-right. The experimental data is shown in black, with the respective background correction and fit to the dipolar evolution function shown in red.

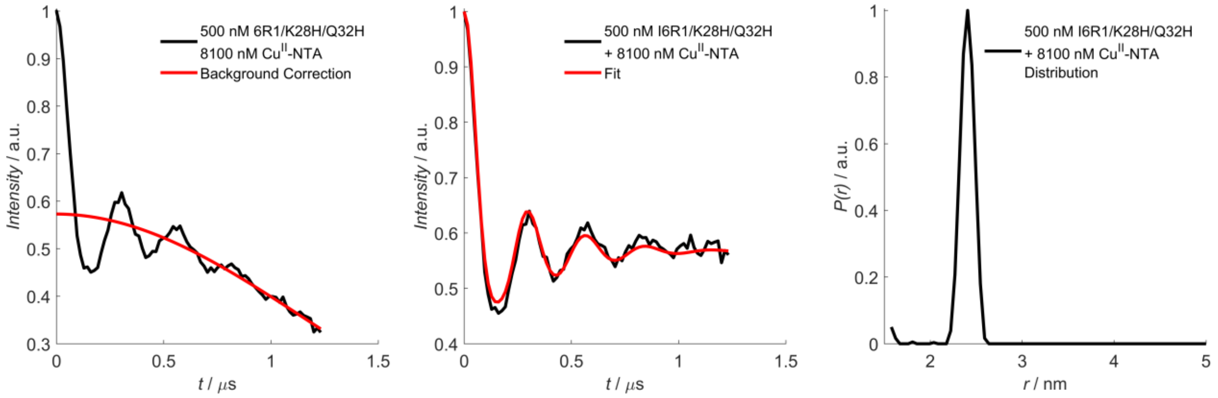

Figure 3.3.11.10. Non-deconvoluted RIDME data for 0.5 µM I6R1/K28H/Q32H, in presence of 8.1 µM Cu^{II}-NTA. The raw data, dipolar evolution function, and corresponding distance distribution are shown left-to-right. The experimental data is shown in black, with the respective background correction and fit to the dipolar evolution function shown in red.

Sample	Modulation depth (Δ)
I6R1/K28H/Q32H + 0.1 µM Cu^{II}-NTA	$0.13 \pm 8.4 \times 10^{-3}$
I6R1/K28H/Q32H + 0.3 µM Cu^{II}-NTA	$0.20 \pm 1.2 \times 10^{-2}$
I6R1/K28H/Q32H + 0.9 µM Cu^{II}-NTA	$0.32 \pm 2.1 \times 10^{-2}$
I6R1/K28H/Q32H + 2.7 µM Cu^{II}-NTA	$0.42 \pm 2.2 \times 10^{-2}$
I6R1/K28H/Q32H + 8.1 µM Cu^{II}-NTA	$0.43 \pm 2.3 \times 10^{-2}$

Table 3.3.11.2: The modulation depths of the non-deconvoluted RIDME traces shown in figures 3.3.12.6-10, given above.

Sample	Modulation depth (Δ)
25 µM I6R1/K28H/Q32H + 15 µM Cu^{II}-NTA	$0.26 \pm 9.6 \times 10^{-3}$
25 µM I6R1/K28H/Q32H + 30 µM Cu^{II}-NTA	$0.39 \pm 6.7 \times 10^{-3}$
25 µM I6R1/K28H/Q32H + 60 µM Cu^{II}-NTA	$0.39 \pm 1.4 \times 10^{-2}$
25 µM I6R1/K28H/Q32H + 135 µM Cu^{II}-NTA	$0.39 \pm 1.5 \times 10^{-2}$
25 µM I6R1/K28H/Q32H + 960 µM Cu^{II}-NTA	$0.40 \pm 2.2 \times 10^{-2}$

Table 3.3.11.3. The modulation depths of the deconvoluted 25 µM I6R1/K28H/Q32H RIDME pseudo-titration in presence of Cu^{II}-NTA.

Sample	Modulation depth (Δ)
75 µM I6R1/K28H/Q32H + 45 µM Cu^{II}-IDA	0.27 ± 4.5 × 10^{-3}
75 µM I6R1/K28H/Q32H + 100 µM Cu^{II}-IDA	0.40 ± 1.5 × 10^{-2}
75 µM I6R1/K28H/Q32H + 185 µM Cu^{II}-IDA	0.42 ± 8.2 × 10^{-3}
75 µM I6R1/K28H/Q32H + 350 µM Cu^{II}-IDA	0.43 ± 9.2 × 10^{-3}
75 µM I6R1/K28H/Q32H + 600 µM Cu^{II}-IDA	0.43 ± 1.4 × 10^{-2}
75 µM I6R1/K28H/Q32H + 1750 µM Cu^{II}-IDA	0.46 ± 1.3 × 10^{-2}

Table 3.3.11.4. The modulation depths of the deconvoluted 75 µM I6R1/K28H/Q32H RIDME pseudo-titration in presence of Cu^{II}-IDA.

Sample	Modulation depth (Δ)
25 µM I6H/N8H/K28R1+ 10 µM Cu^{II}-NTA	0.15 ± 3.2 × 10^{-3}
25 µM I6H/N8H/K28R1+ 20 µM Cu^{II}-NTA	0.31 ± 4.1 × 10^{-3}
25 µM I6H/N8H/K28R1+ 40 µM Cu^{II}-NTA	0.39 ± 5.5 × 10^{-3}
25 µM I6H/N8H/K28R1+ 90 µM Cu^{II}-NTA	0.42 ± 6.0 × 10^{-3}
25 µM I6H/N8H/K28R1+ 600 µM Cu^{II}-NTA	0.43 ± 3.5 × 10^{-3}

Table 3.3.11.5. The modulation depths of the deconvoluted 25 µM I6H/N8H/K28R1 RIDME pseudo-titration in presence of Cu^{II}-NTA.

Sample	Modulation depth (Δ)
25 µM I6H/N8H/K28R1+ 10 µM Cu^{II}-IDA	0.14 ± 1.9 × 10^{-3}
25 µM I6H/N8H/K28R1+ 20 µM Cu^{II}-IDA	0.30 ± 3.6 × 10^{-3}
25 µM I6H/N8H/K28R1+ 35 µM Cu^{II}-IDA	0.38 ± 3.9 × 10^{-3}
25 µM I6H/N8H/K28R1+ 75 µM Cu^{II}-IDA	0.42 ± 5.5 × 10^{-3}
25 µM I6H/N8H/K28R1+ 450 µM Cu^{II}-IDA	0.45 ± 9.5 × 10^{-3}

Table 3.3.11.6. The modulation depths of the deconvoluted 25 µM I6H/N8H/K28R1 RIDME pseudo-titration in presence of Cu^{II}-IDA.

It was also necessary to determine the influence of both cryoprotectant and the buffer system. 5-pulse RIDME traces for buffer and cryoprotectant controls are shown below for 50 mM phosphate or N-ethyl morpholine (NEM) buffer conditions,[241] and 50% (v/v) *d-6* ethylene glycol or 20% (v/v) *d-8* glycerol as cryo-protectants,[241] in figures 3.3.11.11 and 3.3.11.12 respectively. The data is deconvoluted and the associated modulation depths are given in table 3.3.6.7. There is ~15% variation in the Δ between the four permutations, and an apparent decreasing trend as conditions change from 50% ethylene glycol cryoprotectant and 50 mM phosphate buffer to 20% glycerol cryoprotectant and 50 mM NEM buffer.

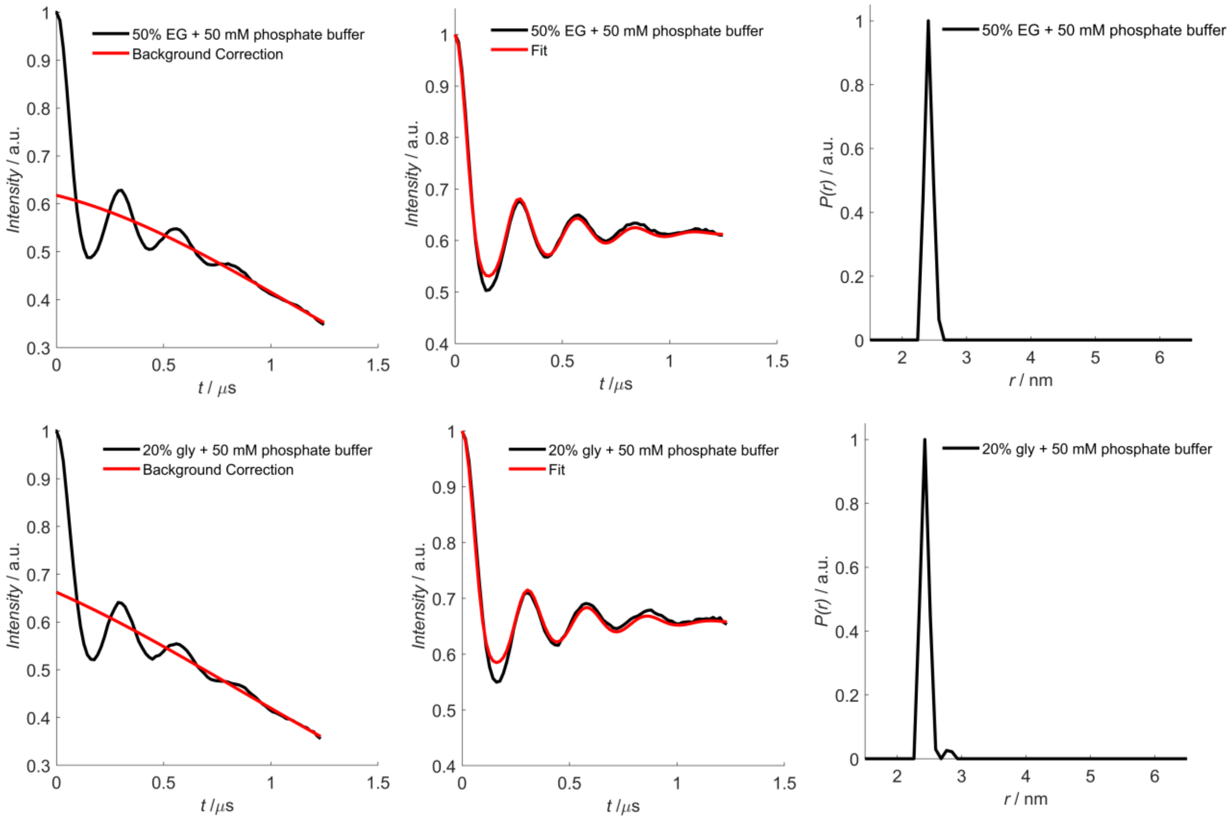

Figure 3.3.11.11: Deconvoluted RIDME data for 75 µM I6R1/K28H/Q32H, in presence of 75 µM Cu^{II}-IDA and 50 mM sodium phosphate buffer condition. The different cryoprotectant conditions, 50% ethylene glycol and 20% glycerol are shown in the top and bottom row respectively. The raw data, dipolar evolution function, and corresponding distance distribution are shown left-to-right. The experimental data is shown in black, with the respective background correction and fit to the dipolar evolution function shown in red.

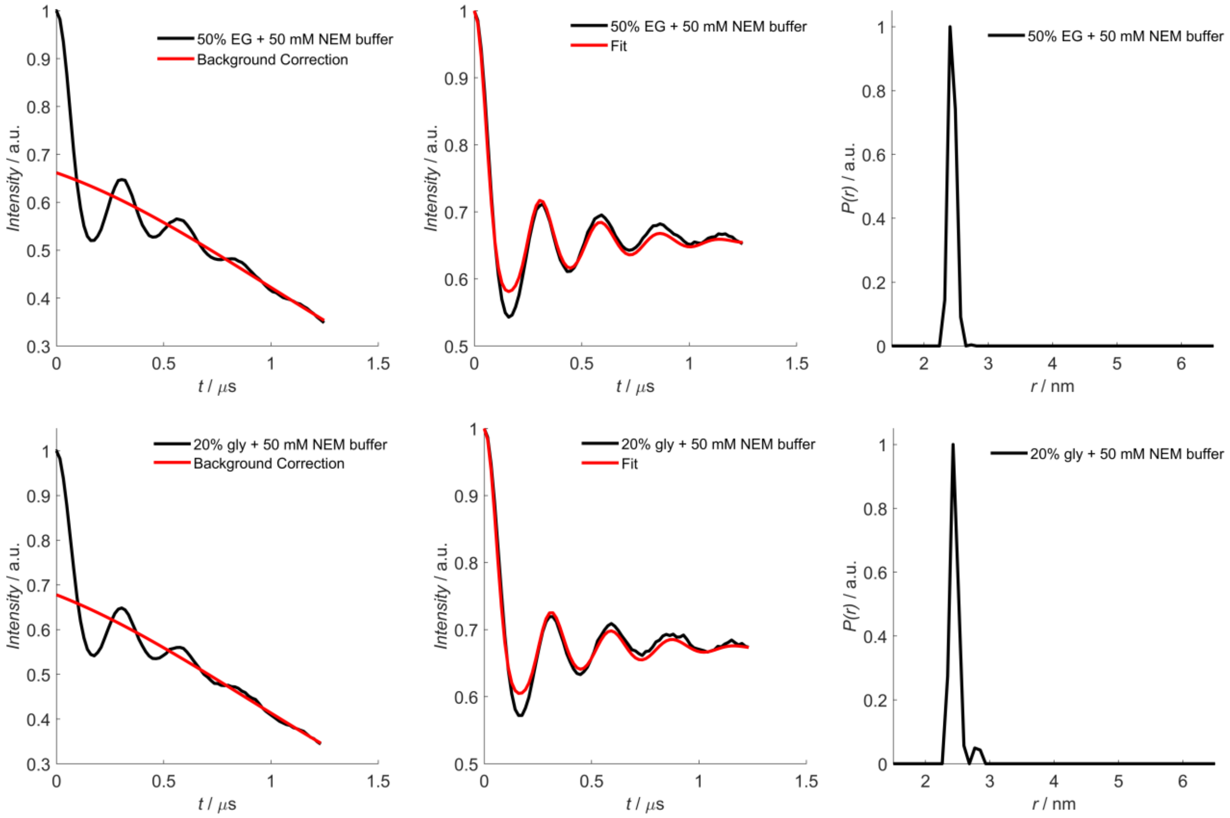

Figure 3.3.11.12: Deconvoluted RIDME data for 75 μM I6R1/K28H/Q32H, in presence of 75 μM Cu^{II}-IDA and 50 mM N-ethyl morpholine buffer condition. The different cryoprotectant conditions, 50% ethylene glycol and 20% glycerol are shown in the top and bottom row respectively. The raw data, dipolar evolution function, and corresponding distance distribution are shown left-to-right. The experimental data is shown in black, with the respective background correction and fit to the dipolar evolution function shown in red.

Sample	Modulation depth (Δ)
50 mM phosphate buffer + 50% ethylene glycol	0.38±0.01
50 mM phosphate buffer + 20% glycerol	0.34±0.01
50 mM N-ethyl morpholine + 50% ethylene glycol	0.34±0.01
50 mM N-ethyl morpholine + 20% glycerol	0.32±0.01

Table 3.3.11.7. The modulation depths of the deconvoluted RIDME traces shown in figures 3.3.11.11-12, given above.

This is speculated to occur for two reasons; the first is that a reduction in cryoprotectant will correspondingly reduce the formation of an adequate glass, and therefore contribute to regions of high local concentrations within the sample. The second reason is associated with the chosen buffer conditions; NEM can compete with the double histidine motif to co-ordinate Cu^{II}-IDA. Indeed, it was recently shown that phosphate buffer optimises the affinity of Cu^{II}-NTA for double-histidine motifs.[243] In any case, a 15% variation in the values of Δ does not account for the apparent 1000-fold increase in affinity, and therefore disparities between buffer and cryoprotectant conditions used in this work and previous literature are not the source of this observation.

3.3.12 *The Influence of T_1 and Δ_{Tmix} on K_D Estimation from Modulation Depth Quantitation*

The influence of parameters on the fitted K_D values was investigated to validate that the methodology was sufficiently robust; this was particularly relevant since K_D estimation relies on several parameters, such as T_1, Δ_{Tmix}, and assumes experimental Δ is accurately determined. In this case, the 500 nM pseudo-titration series was used for benchmarking owing to the resolution of hyperbolic function curvature. Firstly, K_D was approximated by minimising a univariate error function, shown in the top left panel in figure 3.3.12.1. Here, only the K_D varied, with T_1 being determined empirically for discrete samples in the pseudo-titration series and Δ_{Tmix} calculated according to eq. 2.8.5 in section 2.8.

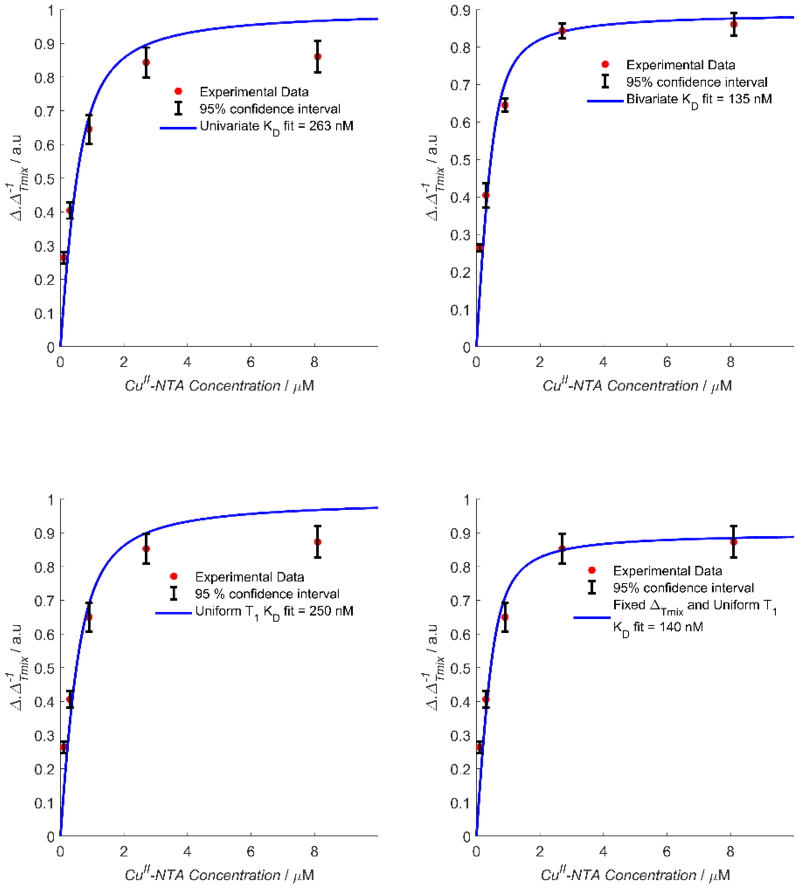

Figure 3.3.12.1: A comparison of the different fits and approaches to approximate K_D from the 0.5 µM I6R1/K28H/Q32H Cu^{II}-NTA pseudo-titration series. The experimental data, and fits are shown as red dots and solid blue, respectively. The top row shows uni-variate and bi-variate fits of K_D, (left and right, respectively) and the bottom row shows uni-variate fit of K_D with a uniform T_1 value, and with a uniform T_1 value and scaling factor for Δ_{Tmix} (left and right, respectively).

It was found that empirical modulation depths approached 0.45, and the product $\Delta \times \Delta_{Tmix}{}^{-1}$ tended towards 0.9 rather than 1.0. Therefore, Δ_{Tmix} was fitted simultaneously with K_D using a bivariate fit (top right panel of figure 3.3.12.1). This dramatically improves the fit, so the decision was made to scaledown the observed Δ. It followed that the approximated K_D from the bivariate fit should be the same if rather than fitting Δ_{Tmix}, it was fixed to a value of 0.45 instead of 0.5, and then a univariate fit was used (bottom right panel in figure 3.3.12.1).

The effect of longitudinal relaxation times on the determined K_D values was investigated by assuming a uniform value of T_1 for all pseudo-titration samples, and the K_D approximated by a uni-variate fit (bottom left panel of figure 3.3.12.1). The influence is shown to be small, evidenced by the similarity of K_D values where each sample in the pseudo-titration has an individual, or a uniform T_1. This is unsurprising because the mixing block interval (T_{mix}) is long with respect to T_1, (T_{mix} ~4×T_1) which yields greater stability in Δ_{Tmix} even with relatively significant variation in T_1. This is particularly relevant in the hetero-spin case (metal and organic radical) where T_{mix} may be considerably longer than T_1 of the fast-relaxing spin. The approximated K_D values for all fits vary by less than a factor 2 and are given in table 3.3.12.1. The corresponding Gaussian fits to estimate the error in K_D are given in appendix A.

Fitting Approach	K_D Approximation [µM]
Univariate (Individual T_1 Values)	0.26 ± 0.20
Bivariate	0.14± 0.15
Univariate (Uniform T_1 Value)	0.25 ± 0.18
Univariate (Uniform T_1 Value and Δ_{Tmix} Scaling Factor)	0.14± 0.14

Table 3.3.12.1. A comparison of the different K_D values approximated from the 0.5 µM I6R1/K28H/Q32H Cu^{II}-NTA pseudo-titration series by the different fitting approaches, shown in figure 3.3.12.1.

Significantly, the 0.5 µM Cu^{II}-nitroxide RIDME pseudo-titration series highlights two points of interest, i) the affinity of α-helical double histidine motifs for Cu^{II}-NTA is in the high nanomolar concentration regime (highly consistent with room-temperature ITC), and ii) Cu^{II}-nitroxide RIDME provides exquisite concentration sensitivity, (supported by the sensitivity comparison with Cu^{II}-Cu^{II} RIDME and PELDOR, nominally improving sensitivity by a factor of 2 and 150, respectively). This concentration sensitivity proves essential to being able to adequately resolve the curvature of the saturation function and precisely determine K_D values in the sub-µM concentration regime. This is emphasized by comparison of the error curves for each of the RIDME pseudo-titration series shown below in figure 3.3.12.2, with only the 0.5 µM pseudo-titration series giving an unambiguous global minimum.

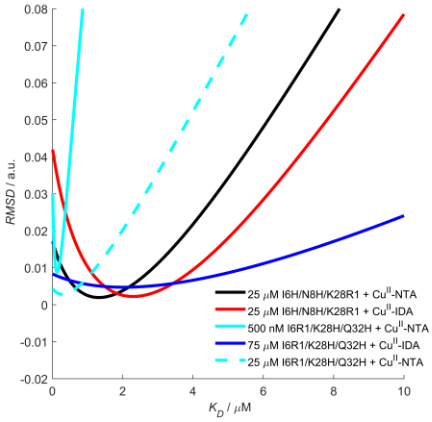

Figure 3.3.12.2: A comparison of the 1D error surfaces of the fitted pseudo-titrations performed at 0.5 µM, 25 and 75 µM GB1 protein concentrations, in presence of Cu^{II}-NTA and Cu^{II}-IDA.

3.4 Conclusion and Outlook

The novel non-covalent spin labelling strategy of exogenously introduced double-histidine motifs coupled with Cu^{II}-chelates had previously been shown to have limiting binding affinities in the mid-to-high µM concentration regime. Herein, this was investigated through a combinative approach of room-temperature ITC and cryogenic Cu^{II}-nitroxide RIDME measurements. Results demonstrate that the α-helical *i* and *i+4* double histidine motif has sub µM affinity for Cu^{II}-NTA at cryogenic EPR conditions, owing to the exothermic nature of the binding event. This has important implications for the use of Cu^{II}-chelators as spin labels, and particularly for their application to constructs containing pairs of double-histidine motifs. Furthermore, measurements revealed exquisite concentration sensitivity of Cu^{II}-nitroxide and Cu^{II}-Cu^{II} RIDME performed at Q-band frequencies. The sensitivity analysis[204] herein gives nominal sensitivity gains of ~150 and ~100 fold, when compared to Cu^{II}-Cu^{II} PELDOR. This is highly consistent with recent literature suggesting that Cu^{II}-nitroxide RIDME significantly outperformed PELDOR, even when acquired using an ultrawide bandwidth spectrometer.[273]

This concentration sensitivity makes distance measurements feasible at considerably lower protein concentrations, facilitating measurements of novel systems that were previously inaccessible, as well as new science.[326] Furthermore, application of RIDME to investigate binding equilibria, and remote determination of binding affinities *via* the dipolar interaction has been benchmarked. Importantly, this allows intimate coupling of both structural and thermodynamic information for protein-ligand interactions and could be applied to ligand-gated systems in the future. The approach is complementary to calorimetric methods such as ITC, and especially valuable for characterisation of high-affinity interactions, where other methods of structural investigation are often sensitivity-limited. In summary, double histidine affinity for Cu^{II}-chelators is not limiting in pulse dipolar spectroscopy studies, and 5-pulse RIDME data allows quantitative estimation of K_D values that are highly consistent with extrapolated ITC data.

Indeed, one of the most appealing aspects of double histidine motifs as spin labelling sites is the high precision and accuracy of distance determination, particularly in systems containing pairs of double histidine motifs. This raises additional considerations at the conclusion of this chapter: i) whether the approach can be extended to a two-site independent binding model, ii) how labelling efficiency of double histidine motifs may be optimised in dependence of K_D, and iii) systematic error analysis of pseudo-titration data to optimise the precision and accuracy of determined K_D values. These considerations form the motivation for the next results chapter.

CHAPTER 4: General Model to Optimise Cu^{II} Labeling at Double Histidine Motifs

This chapter has the following contributions. Dr Katrin Ackermann expressed and purified the model protein. JLW prepared the EPR samples and performed the Q-band EPR measurements, processed the data and adapted the speciation model. Dr David Norman built the Cu^{II}-NTA spin label in XPLOR-NIH for molecular dynamics simulations. Dr Bela Bode performed the X-band EPR measurements and designed the experiments. The results of this chapter have been peer reviewed and published in similar form: J. L., Wort, K. Ackermann, D. G., Norman, and B. E., Bode, *Phys. Chem. Chem. Phys.,* 2021, **23**, 3810-3819. DOI: https://doi.org/10.1039/D0CP06196D.

4.1 Introduction

Non-covalent spin labelling strategies are particularly appealing in the purview of PD-EPR applications,[229,329,330] as labelling sites may be genetically encoded (such as double-histidine motifs introduced in chapter 3), with labels self-assembling on short time-scales. In this way, labelling procedures are streamlined through omission of post-translational covalent modifications. Indeed, native double-histidine motifs have enabled the study of systems otherwise non-permissive to heterologous expression (and thus site-directed mutagenesis), and exogenously introduced motifs allow paramagnetic handles to be introduced for pseudo-contact shift (PCS) NMR measurements.[331] The finding that Cu^{II}-Cu^{II} RIDME sensitivity is comparable to Cu^{II}-nitroxide RIDME, while affording higher precision in the distance domain is further motivation to use this labelling strategy.[70] Cu^{II}-based spin labelling efficiency at pairs of double histidine motifs has recently been optimised through a systematic buffer screening,[243] facilitating > 60% increased loading compared to previous literature.[148] The importance of optimising Cu^{II}-based spin labelling at double histidine motifs is further crystallised by PD-EPR measurements approaching near-physiological protein concentration sensitivity,[70,78,79,332] where limiting binding affinities of non-covalent interactions become especially problematic.

Considering the simple case of a protein containing a pair of double-histidine motifs (an α-helical site and a β-sheet site) labelled with Cu^{II} spin-label, optimisation of labelling efficiency is non-trivial because each site will have a differential affinity for the label (see chapter 3), and ideally should be treated as non-identical and independent.[249,253,333] Under conditions of partial loading, all Cu^{II} species whether bound at a double-histidine motif or not can be detected, but not all species will contribute to dipolar modulation of the detected echo. This has implications for measurement sensitivity, (i.e., driving double-histidine loading to completion will not necessarily optimise sensitivity), a situation that complicates further in systems containing > 2 double-histidine sites. To achieve widespread use of double-histidine based Cu^{II}-labelling requires a general method to optimize labelling efficiency and measurement sensitivity in any given system containing pairs of double-histidine sites.

This problem has been approached previously using a probabilistic method to approximate double histidine loading in tetra-histidine (6H/8H/28H/32H) GB1,[170] in which the affinities of Cu^{II}-IDA and Cu^{II}-NTA for each double-histidine co-ordination site were treated individually. However, the approximation of independent sites not depleting the free ligand concentration is not always satisfied. Thus, a model to explicitly treat two independent double-histidine coordination sites simultaneously in a single macromolecule is currently lacking in the literature. Here, a general derivation for a multi-site binding polynomial is provided, treating a pair of binding sites with differential affinities. Numerical simulations are used to predict the optimal labelling efficiency of tetra-histidine GB1 in dependence of K_D values previously determined from extrapolated ITC and Cu^{II}-nitroxide RIDME (chapter 3). Additionally, the mathematical model is validated experimentally by measuring a six-point Cu^{II}-Cu^{II} RIDME pseudo-titration series, with a pair of K_D values being fitted. The methodology is evaluated in two aspects: i) benchmarking the theoretical treatment of modelling speciation against experiment, and ii) empirical considerations and limitations associated with the determination of binding affinities from Cu^{II}-nitroxide and Cu^{II}-Cu^{II} RIDME.

Lastly, we find the dissociation constant estimates from Cu^{II}-Cu^{II} RIDME are in excellent agreement with previously determined values, and empirical modulation depths support the proposed model. Accuracy of K_D determination generally increases with the length of the mixing block relative to T_1, and distance distribution information is still reliably extracted in the regime T_{mix} ~ 2× T_1. Significantly, by assuming double-histidine sites can be grouped into i) high affinity sites, and ii) low affinity sites, the analytical expression for equilibrium label concentration[250] is retained and allows extension of the model to systems containing > 2 double-histidine sites. The approach has since been appropriated to optimise double-histidine motif loading in Cu^{II}-Cu^{II} RIDME measurements at 500 nM protein concentration.[334]

4.2 Materials and Methods

4.2.1 Protein Purification and Pulse EPR Sample Preparation

All GB1 protein constructs (I6H/N8H/K28H/Q32H, I6R1/K28H/Q32H and I6H/N8H/K28R1) were produced, expressed, purified and spin labelled as previously reported. Cu^{II}-chelate spin labels were prepared and quantified as previously reported.[70,297] In all samples, addition of 50% (v/v) ethylene glycol d-6 (Deutero GmbH) ensured formation of a glassy frozen solution, after addition of Cu^{II}-NTA label. For Q-band RIDME samples a total volume of 70 µL was used. All material was exchanged into deuterated buffer A (42.4 mM Na2HPO4, 7.6 mM KH2PO4, 150 mM NaCl, pH 7.4) by first freeze-drying and then re-dissolving in D_2O. For X-band PELDOR samples of 6H/8H/28R1 and 6R1/28H/32H GB1 constructs, a total volume of 15 µL was used. All EPR samples were frozen by direct immersion into liquid nitrogen. Cu^{II}-IDA and Cu^{II}-NTA stock solutions were prepared as previously described in section 3.2.3; and for Cu^{II}-labelling, Cu^{II}-IDA and Cu^{II}-NTA stock solutions with nominal concentrations of 100 and 10 mM were used, respectively.

4.2.2 EPR Instrumentation

All pulse EPR experiments were performed using a Bruker ELEXSYS 580 pulse EPR spectrometer. Temperatures were maintained using a cryogen-free variable temperature cryostat (Cryogenic Ltd) operating in the 1.8-300 K temperature range. All measurements of the electron spin longitudinal relaxation times (T_1), and transverse dephasing times (T_m) of Cu^{II}-IDA and Cu^{II}-NTA, and all 5-pulse dead-time free RIDME measurements[180] were performed at 30 K, using a high-power 150 W travelling-wave tube (TWT; Applied Systems Engineering) at Q-band (34 GHz) in a critically coupled 3 mm cylindrical resonator (Bruker ER 5106QT-2w in TE012 mode). All PELDOR measurements[16,17] were performed at 10 K at X-band (9.4 GHz) with a 1 kW TWT (Applied Systems Engineering) in an over-coupled 3 mm split-ring resonator (Bruker 4118X-MS3), unless otherwise stated.

4.2.3 Mass Spectrometry

All mass spectra were collected in-house using a Sciex MALDI TOF/TOF 4800 mass-spectrometer, with samples crystallised using a matrix of α-cyano-4-hydroxycinnamic acid. I6H/N8H/K28H/Q32H GB1 samples were submitted at 20 μM in buffer A, and mass spectra were recorded in the absence of Cu^{II}-labels.

4.2.4 PD-EPR Measurement Parameters

The 5-pulse RIDME pulse sequence is shown in section [2.6, figure 2.6.3]. All RIDME measurements were performed detecting at the maximum of the Cu^{II}-NTA spectrum, with rectangular pulses of lengths 12 and 24 ns (π/2 and π, respectively). All acquisitions were performed over three scans (unless otherwise stated), with 10 shots per point, with a SRT of 2 ms, and deuterium ESEEM was suppressed *via* a 16-step nuclear modulation τ-averaging cycle.[298] Signal contributions from unwanted echoes were eliminated using an 8-step phase-cycle, totalling 128 steps per measurement (resulting in 384 echoes per point per scan), with the RVE being detected. For all samples, at least two lengths of mixing block were recorded; a short reference mixing time (T_{ref}) and a long mixing time (T_{mix}) to allow suppression and observation of the dipolar coupling, respectively. A pseudo-titration series of I6H/N8H/K28H/Q32H GB1 was measured at 100 μM protein concentration, in presence of varying Cu^{II}-NTA concentration. All RIDME data was used without division by the reference trace and background corrected using stretched exponential functions with stretching exponent bounded between 1 and 2 (unless otherwise stated).

For the Cu^{II}-detected X-band PELDOR measurements, samples of 250 and 220 μM I6R1/K28H/Q32H and I6H/N8H/K28R1 GB1, respectively, were measured either in presence of 1.5 equivalents of Cu^{II}-IDA or Cu^{II}-NTA. The 4-pulse experiment was used. In all cases monochromatic pulses of lengths 16 and 32 and 12 ns were used for observer and pump pulses (π/2, π and π). The magnetic field and microwave frequency were adjusted to the maximum of the nitroxide spectrum to coincide with the pump pulse position, while the observer pulse spectral position was varied between frequency offsets of 150 and 300 MHz depending on the measurement. Data were acquired with an SRT of 3 ms, a τ_1 of 420 ns and a τ_2 of 1260 ns were used respectively, with 50 shots-per-point and measurements averaged for 12 hours to yield sufficient signal-to-noise ratio (SNR). ^{2}H ESEEM was suppressed using a 16-step τ-averaging cycle.

4.2.5 RIDME Data Processing, Analysis and Validations

All 5-pulse RIDME traces were processed using DeerAnalysis2018,[215] and were background-corrected using either second order polynomial or stretched-exponential functions as specified. The observed modulation depth quotients were found to be robust against background correction models. The stretched exponential functions were of the form:[273]

$$y = c \times \exp\left(-(kt)^{\frac{d}{3}}\right) \tag{4.2.5}$$

where c is the initial amplitude, k is the decay constant, t is the time-point, and d is the background dimension, which is constrained between 3 and 6, in keeping with recent RIDME theory.[269] For the validations of the RIDME traces, a modified version of the Tikhonov validation functionality in DeerAnalysis2018 was used; a total of 896 trials were performed for each validation, consisting of 16 white-noise iterations (noise-level of 1.5), 8 iterations of background start position (between 5-30% of the total RIDME trace length), and 7 iterations of background dimension (between 3-6 in increments of 0.5). From each pruned validation trial (prune level = 1.15) a modulation depth (Δ) is calculated, and the standard deviation (σ) is used to approximate the modulation depth error, relevant in the propagation of errors to calculate K_D from RIDME pseudo-titration series. Bivariate fitting used in-house Matlab scripts and employed a Nelder-Mead simplex. Each K_D value was varied independently, and a least-squares bivariate error minimisation was performed. The RMSD was used as an estimate of goodness-of-fit between simulation and experiment. Fits were found to be largely stable regardless of chosen initial parameters.

It should be noted that distance distributions are based on the dipolar coupling calculated for the free electron g-value and this has not been corrected. If the distributions were analyzed and interpreted in detail the x-axes would need to be scaled by a factor 0.885.[83] Furthermore, background imperfections from using a short τ_1 were compensated by dividing by reference traces and did not hamper modulation depth analysis.[273]

4.2.6 Error Propagation for Dissociation Constants Calculated from RIDME Pseudo-Titrations

To provide an error boundary for the estimation of dissociation constants coming from RIDME pseudo-titration series, it was necessary to perform an error analysis. Here, all errors are assumed to be independent, such that all can be approximated by normal distribution functions, and correlation terms between variables are neglected in the subsequent analysis. It should be noted that here we employ two distinct approaches to estimate the error in K_D; i) it can be propagated directly, and ii) it is proportional to the bivariate fitting error, and can be approximated by a fitted Gaussian of the one-dimensional simplex error surface. Let us begin by showing how the error in K_D is propagated directly, since equation 2.10.1.7 can be rearranged to yield K_D:

$$K_D = \frac{\left(\Delta_{Tmix}{}^2 \times L_0 + \Delta^2 \times P_0 - \Delta \times \Delta_{Tmix} \times P_0\right)}{\Delta \times \Delta_{Tmix}} \tag{4.2.6.1}$$

Assuming the error in each variable can be accurately approximated, the error in K_D can then be calculated using the variance formula.[335] While this approach is suitable for error estimation in single measurements, since the K_D is calculated by fitting several measurements, it is perhaps more suitable to approximate the error in K_D using the second approach elaborated above. In this case, the respective errors in Δ and Δ_{Tmix} are assumed to dominate the error in K_D, where the error in Δ is estimated from a statistical distribution of validation trials. The error in Δ_{Tmix} is assumed to be dominated by error in estimating longitudinal relaxation time (T_1) under the mono-exponential approximation. These errors are propagated for the quotient Δ/Δ_{Tmix}, and K_D is subsequently fitted using a weighted bivariate error function, where the weighting, w, is proportional to the reciprocal of the squared error at that point. The weighted error function to be minimised is then given as:

$$rms = \sum\left(w\left(\left(\frac{P_0 + L_0 + K_D - \sqrt{(P_0 + L_0 + K_D)^2 - 4P_0L_0}}{2P_0}\right) - \beta \times \frac{\Delta}{\Delta_{Tmix}}\right)^2\right) \tag{4.2.6.2}$$

where: w is the associated weighting of each experimental point, β is the reciprocal scaling factor of Δ_{Tmix} and L_0, P_0, K_D, Δ and Δ_{Tmix} are as previously defined. This leads to a weighted 2D error surface, which after finding the optimal reciprocal scaling factor, reduces to a 1D error function in K_D. After taking the reciprocal of this weighted root mean square error, this can be approximated as a Gaussian of the form:

$$\frac{1}{rms} = \left(a \times \exp\left(-\frac{(K_D - \mu)}{\sigma}\right)^2\right) + b \tag{4.2.6.3}$$

where: rms is defined as above in equation 4.2.6.2, a is the amplitude of the Gaussian, b is a vertical offset, μ and σ are the mean and standard deviation which define the Gaussian, and K_D is the dissociation constant. The error in K_D is then approximated as σ, and can be calculated within a 95% confidence interval. However, it should be appreciated that equation 4.2.6.2 is only valid for a system containing a single ligand-binding site (n = 1).

4.3 *Results and Discussion*

4.3.1 *Exploratory Speciation and Modulation Depth Profile Simulations*

In the case of orthogonal spin labels, as for Cu^{II}-nitroxide RIDME (elaborated in chapter 3) isotherms can be measured at plateau because Cu^{II}-chelate can be added to vast excess ensuring saturation, and modulation depth increases asymptotically. This yields a hyperbolic single site saturation function as excess Cu^{II}-chelate does not contribute to the detected nitroxide echo (at Q-band frequencies and above). However, as alluded to in section 4.1, in the case of a Cu^{II}-Cu^{II} RIDME isotherm, the titrant contributes to the detected signal. This implies that for Cu^{II}-Cu^{II} RIDME, sensitivity optima are characterised as point solutions on the curve rather than a plateau, and will instead yield a log normal profile. For a $\mathrm{Cu^{II}}$ homo spin-pair ($S = ½$) this means the detected echo will be the weighted contributions of unbound, singly-bound, and doubly-bound (macromolecules with both double-histidine motifs occupied) $\mathrm{Cu^{II}}$ spin-label. However, only the doubly-bound macromolecule will modulate the detected echo signal with the dipolar frequency, and so to good approximation, the observed modulation depth is the relative quotient of $\mathrm{Cu^{II}}$-chelate which is doubly-bound against all $\mathrm{Cu^{II}}$-chelate in the sample.

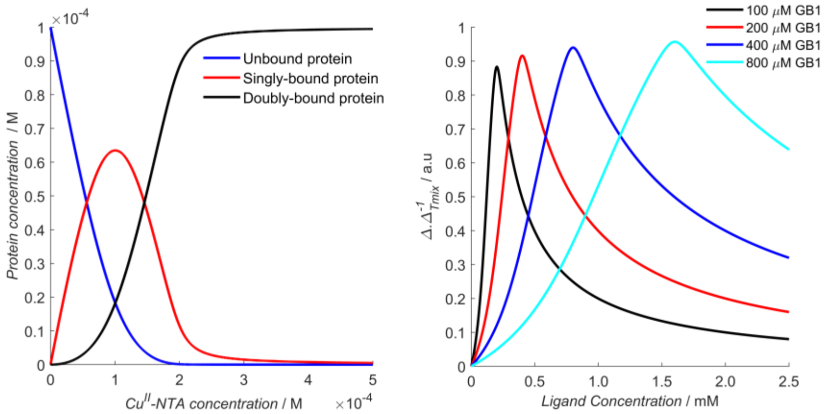

Figure 4.3.1.1: A speciation profile simulated with protein concentration of 100 µM, and K_D values of 1.4 µM and 140 nM, as a function of $\mathrm{Cu^{II}}$-NTA concentration (left), and the corresponding modulation depth profiles at different protein concentrations (right).

Using the K_D values previously determined from $\mathrm{Cu^{II}}$-nitroxide RIDME pseudo-titrations (1.4 µM and 140 nM, for the β-sheet and α-helical double histidine motifs respectively), and 100 µM protein concentrations, a simulated speciation profile (figure 4.3.1.1 left panel) was generated. This indicates that in this concentration regime double-histidine labelling efficiency is >90%, and sensitivity optima of modulation depth profiles are expected at approximately a protein-to-$\mathrm{Cu^{II}}$-NTA ratio of 1:2, for various protein concentrations (figure 4.3.1.1 right panel). To investigate the influence of protein concentration on the position of the sensitivity maximum, additional simulations were performed for a fixed pair of K_D values and varying protein concentrations. One can identify two concentration regimes; i) the protein concentration exceeds the K_D values (figure 4.3.1.2 left panel) so that as ligand becomes available, binding to double histidine sites is quantitative, or ii) the protein concentration is below the K_D values (4.3.1.2 right panel), so that ligand binding is not quantitative. This can be related back to equation 2.10.3.20 in section 2.10.3, and is reiterated below for clarity:

$$[L]_{1,2} = 2\theta_{1,2}[P]_0 \tag{4.3.1.1}$$

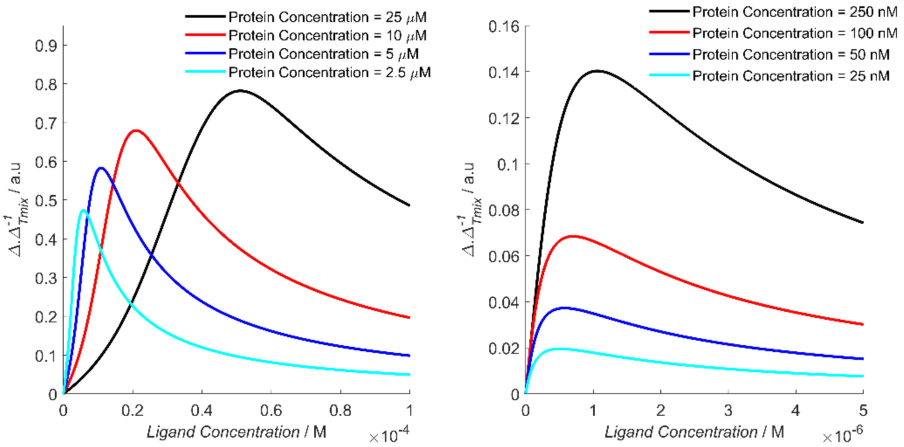

Figure 4.3.1.2: Comparative plots of modulation depth profiles simulated with varying protein concentrations (indicated in the figure legends) with K_D values of 140 nM, and 1.4 μM.

In the first case, a sensitivity optimum is predicted at approximately $[L]_0 = 2[P]_0$ because ligand concentration is sufficiently high to drive quantitative binding to the protein molecule. In this case, the following approximation holds: $\theta_{1,2} = 1$, which implies complete saturation of the double-histidine motifs. In the second case, $\theta_{1,2} \neq 1$ because when $[L]_0 = 2[P]_0$, the ligand concentration is still insufficient to drive quantitative binding to the protein molecule. It follows that in the second case, a sensitivity optimum is predicted to occur at some ligand concentration: $[L]_0 > 2[P]_0$, which maximizes $\theta_{1,2}$. Results of the simulations given below in figure 4.3.1.2 for the high (left), and low (right) protein concentration regimes, respectively. The predictions outlined above are borne-out by the simulations. The maxima of the modulation depth profiles are given in table 4.3.1.1. This suggests that this approach may be especially useful in studies where macromolecule concentrations are limiting, and where sensitivity optimisation is paramount. Indeed, recent measurements of Cu^{II}-Cu^{II} RIDME at 0.5 μM using pairs of double-histidine motifs had a predicted sensitivity maximum at $[L]_0 = 3.2[P]_0$.[334]

Protein Concentration [μM]	Label Concentration at Sensitivity Maximum [μM]
25	51
10	21
5.0	11
2.5	5.9
2.5×10^{-1}	1.1
1.0×10^{-1}	7.0×10^{-1}
5.0×10^{-2}	5.6×10^{-1}
2.5×10^{-2}	4.9×10^{-1}

Table 4.3.1.1: Comparison of sensitivity maxima positions for different simulated modulation depth profiles in figure 4.3.1.2.

To investigate the behaviour of modulation depth profiles under conditions of different concentration regimes for pairs of K_D values, exploratory simulations were performed for 100 μM protein, and K_D values of (100 μM, 100 nM), (10 μM, 100 nM), and (1 μM, 100 nM) shown in figure 4.3.1.3. This range of K_D values was chosen to demonstrate how this approach may be diagnostic of significant differences in affinity between the two sites. Notably, to the right of the maxima (the double-histidine motif saturation point) addition of further Cu^{II}-chelate will lead to a reduction in the observed modulation depth quotient simply through a dilution effect. Therefore, this region of the curves does not add information about the K_D of the binding sites, but can act as an internal control for the sample Cu^{II}-chelate and protein concentration across the pseudo-titration series. Comparatively, to the left of the maxima (especially at low Cu^{II}-chelate concentrations) is shown to be more significant as a diagnostic of the respective magnitude and relative differences between affinities; in the case of a large difference (red trace), there is a lag in the initial rise of the modulation depth profile, which is recapitulated to a lesser extent as the relative difference reduces (black and blue traces).

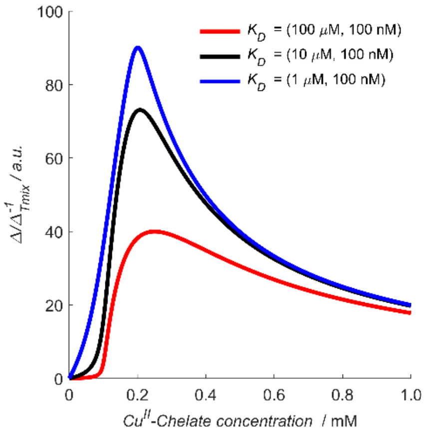

Figure 4.3.1.3: A comparative plot of modulation depth profiles simulated with 100 μM protein concentration and varying K_D values (indicated in the figure legends).

As expected, the modulation depth quotient at the maximum is highly sensitive to the respective magnitude of the K_D, and increasingly approaches unity as the overall affinity of the binding sites increases. Importantly, it should be noted that at sufficiently high affinities, the maximum of the modulation depth (under these simulated conditions) becomes the only distinguishing feature, and protein concentration should be reduced to a regime with greater sensitivity to high affinities.[336–338] This discussion indicates that these simulations may be useful in disentangling different binding modalities, given that the shape of the modulation depth profile can inform both the individual K_D values, and their relative difference in magnitude. This also explains why the error contours (shown and discussed in section 4.3.6) indicate that the pair of K_D values are not anti-correlated, because goodness-of-fit cannot be compensated by reduction of one K_D if the other increases.

4.3.2 Double-Histidine Motif Pair Pseudo-Titration with Cu^{II}-NTA

The validity and robustness of the speciation model was determined by measuring a pseudo-titration series of 100 μM I6H/N8H/K28H/Q32H GB1 in presence of 50, 70, 100, 170, 500 and 1000 μM Cu^{II}-NTA. Since the modulation depth is a function of both the extent of double-histidine motif loading and T_{mix}, RIDME measurements were performed with 3 experimental mixing times, between 0.7 and 1.9 × T_1 to determine the consistency of the modulation depth quotients. It must also be considered that for a homo-spin pair there is a trade-off between measurement sensitivity and the accuracy of the observed modulation depth quotients ($Qexp$), since relatively small errors in the approximated T_1 will become more significant at shorter mixing times. Importantly, the largest source of error will likely manifest as deviations from the mono-exponential approximation, (see section 4.3.7 for discussion).

Exemplary RIDME data recorded with a ratio of ~0.7 between mixing time and T_1 (and background corrected using a stretched exponential function) are shown in figure 4.3.2.1. Quantitatively, the trend in modulation depth is consistent with expectation: upon comparison of the dipolar evolution functions (figure 4.3.2.1 top-right panel) the modulation depths first increase towards 20% before reducing as excess Cu^{II}-NTA is added. The distance distributions (figure 4.3.2.1 bottom-left panel) at low double-histidine motif loading have greater uncertainty compared to optimal labelling conditions. This indicates the reliability of the distance distributions may be substantially reduced. Furthermore, additional distance peaks observed for the 1000 μM Cu^{II}-NTA sample (orange trace) may correspond to non-specific interactions away from the double-histidine sites. Nevertheless, in all cases reliable modulation depth information could still be extracted. This emphasizes the utility of being able to identify optimal labelling conditions for a given system, in the purview of extracting reliable, meaningful distances from Cu^{II}-Cu^{II} RIDME measurements.

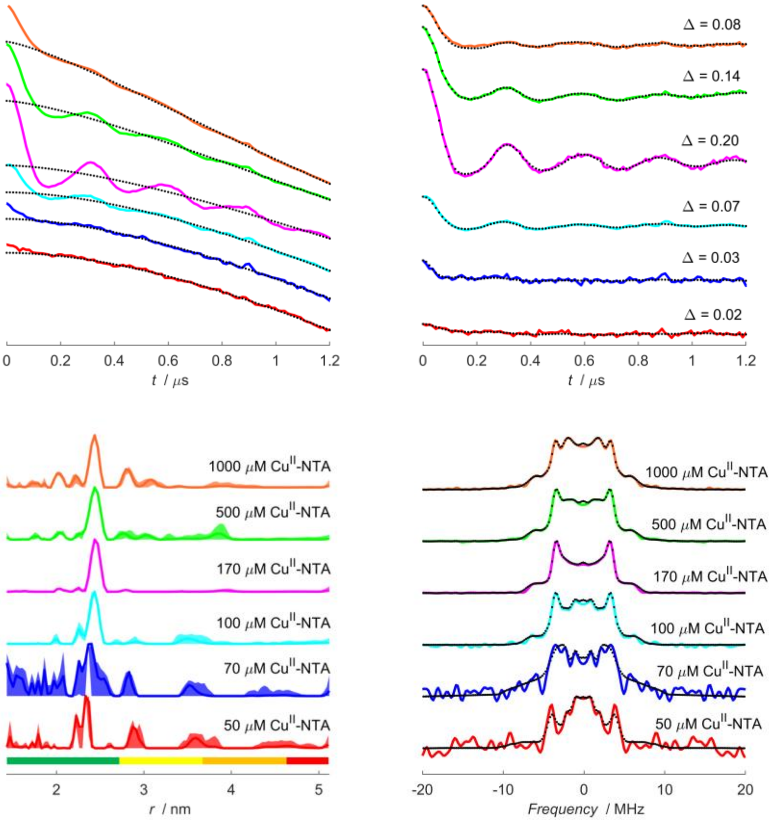

Figure 4.3.2.1. top-row left panel) A stack-plot of the raw RIDME traces for 100 μM 6H/8H/28H/32H GB1 in presence of 50 (red), 70 (blue), 100 (cyan), 170 (magenta), 500 (green) and 1000 μM Cu^{II}-NTA (orange), recorded using a ratio of Tmix to T1 of 0.7. Stretched exponential background functions are shown as black dotted lines. Data have been shifted vertically for visibility. top-row right panel) A stack plot of the background corrected data (from top-row left panel) with their fits shown as black dotted lines. bottom-row left panel) The corresponding distance distributions (from top-row right panel). The 2σ confidence intervals are shown as the shaded background for each distribution. bottom-row right panel) The dipolar spectra corresponding to the dipolar evolution functions (top row right panel).

The dipolar spectrum (figure 4.3.2.1 bottom-right panel) of the sample measured in presence of 170 μM Cu^{II}-NTA (magenta trace) gives a spectrum closely resembling a Pake pattern and indicating minimal effects from orientational correlation. However, other points in the series yield spectra with low signal-to-noise (as seen for the 50 (red trace) and 70 (blue trace) μM Cu^{II}-NTA samples) or with additional singularities (1000 μM Cu^{II}-NTA sample (orange trace)). An advantage of the 5-pulse RIDME experiment is a reduced susceptibility to orientation selection arising from broadband B-spin excitation only limited by relaxation anisotropy rather than pulse excitation bandwidth as in PELDOR.[195,268,339,340]

Orientation selection has previously been demonstrated for double dH Cu^{II}-Cu^{II} PELDOR at Q-band frequencies,[327] although it has not been observed at X-band frequencies. This is attributed to the parallel component of the g-tensor being broadly distributed, and the relative orientations of the g-tensors of the two Cu^{II} centres.[300] This mechanism of orientational selectivity suppression at X-band has also been observed in other Cu^{II}-based spin labels.[301] It should also be noted that this phenomenon may arise from the g-perpendicular component overlapping with the high-field parallel component of the A tensor at X-band, while being well separated at Q-band.

The raw 5-pulse RIDME traces (figure 4.3.2.1 top-left panel) contained an additional feature at ~900 ns in the dipolar evolution functions; particularly in samples with under-labelled double-histidine motifs. This was attributed to a standing echo artefact that can likely be suppressed through use of an extended 32-step phase-cycle.[273] Here, an 8-step phase-cycle was retained for the sake of simplicity as the presence of the artefact did not affect the downstream data analysis. Initial concern that for low signal-to-noise ratio samples, the presence of the artefact would artificially inflate the white-noise estimation in the error analysis did not manifest (see section 4.3.6 for discussion).

To quantify the modulation depth quotients for the Cu^{II}-Cu^{II} RIDME pseudo-titration series, inversion recovery measurements were performed for 100 µM I6H/N8H/K28H/Q32H GB1 in presence of 50, 70, 100, 170, 500 and 1000 µM Cu^{II}-NTA. Corresponding fitted mono- and bi-exponential functions (figure 4.3.2.2 red and blue traces, respectively), were used to estimate T_1 with reciprocal e-times (table 4.3.2.1).

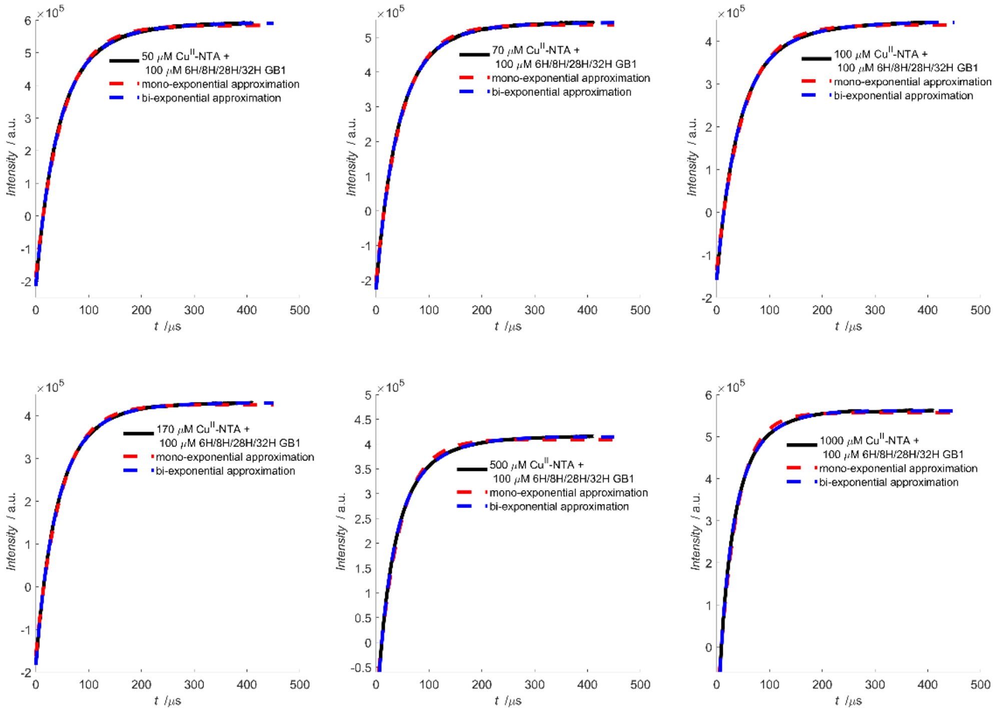

Figure 4.3.2.2: Inversion recovery data for 50, 70, 100 µM Cu^{II}-NTA (top row) and 170, 500 and 1000 µM Cu^{II}-NTA (bottom row), in presence of 100 µM I6H/N8H/K28H/Q32H GB1 shown left-to-right, respectively. The experimental data is shown in black, with the fitted mono-exponential and bi-exponential functions shown as red and blue dotted lines, respectively.

Sample	Mono-exponential T_1 [µs]	Bi-exponential T_{1A} / T [µs]	Relative Contributions	1/e time [µs]	0.5 × $(1/e)^2$ time [µs]
100 µM 6H/8H/28H/32H + 50 µM Cu^{II}-NTA	49.8 ± 0.16 (0.999)	33.6 / 76.7 (1.00)	0.57 : 0.43	63.6	60.1
100 µM 6H/8H/28H/32H + 70 µM Cu^{II}-NTA	47.1 ± 0.14 (0.990)	33.4 / 72.5 (1.00)	0.61 : 0.39	62.8	59.2
100 µM 6H/8H/28H/32H + 100 µM Cu^{II}-NTA	49.7 ± 0.18 (0.999)	34.5 / 84.2 (1.00)	0.64 : 0.36	63.6	61.5
100 µM 6H/8H/28H/32H + 170 µM Cu^{II}-NTA	46.2 ± 0.14 (0.999)	31.0 / 67.8 (1.00)	0.55 : 0.45	61.0	59.3
100 µM 6H/8H/28H/32H + 500 µM Cu^{II}-NTA	41.0 ± 0.21 (0.997)	22.8 / 64.2 (1.00)	0.53 : 0.47	51.8	52.0
100 µM 6H/8H/28H/32H + 1000 µM Cu^{II}-NTA	34.1 ± 0.18 (0.997)	17.5 / 50.2 (1.00)	0.49 : 0.51	42.6	42.9

Table 4.3.2.1. Mono- and bi-exponential T_1 estimates, and 1/e time for each sample of the series shown in figure 4.3.2.2. R^2 values of each model are indicated in parentheses.

4.3.3 Cu^{II}-Nitroxide and Cu^{II}-Cu^{II} RIDME Pseudo-Titration Validations

4.3.3.1 Cu^{II}-Nitroxide RIDME Validations

To estimate the error in RIDME modulation depths as a function of background correction parameters and noise level, it was necessary to assess the utility of the validation tool in DeerAnalysis2018 when applied to RIDME traces, to check the Tikhonov validation of the corresponding distance distributions.

For completion, the deconvoluted experimental traces, background corrected traces, validated distance distributions, and a histogram representation of the distribution of modulation depths for the validation run are shown in figures 4.3.3.1.1-5, respectively. For each histogram, a normal distribution is overlaid, and is calculated using:

$$f(x) = \frac{1}{\sqrt{2\pi\sigma^2}} exp\left(-\frac{(x-\mu)^2}{2\sigma^2}\right) \tag{4.3.3.1.1}$$

where: μ and σ are the mean and standard deviation which define the Gaussian, and x is the modulation depth calculated for each Tikhonov validation trial.

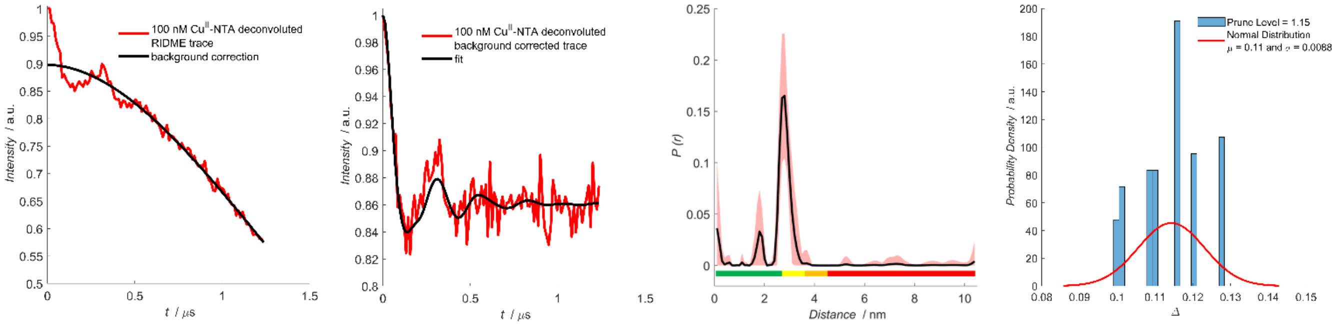

Figure 4.3.3.1.1: Plot of deconvoluted 100 nM Cu^{II}-NTA RIDME pseudo-titration data. The deconvoluted experimental trace, background corrected data, the validated distance distribution, and a histogram showing the distribution of Δ for trials within a 1.15 prune level, are shown left-to-right respectively. The mean of the distance distribution is shown as the black trace, with the 2σ confidence interval shown as the shaded region.

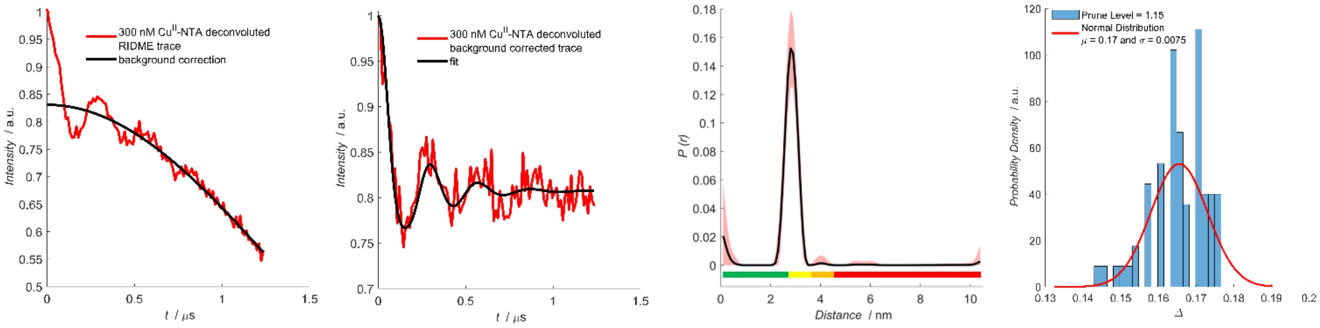

Figure 4.3.3.1.2: Plot of deconvoluted 300 nM Cu^{II}-NTA RIDME pseudo-titration data. The deconvoluted experimental trace, background corrected data, the validated distance distribution, and a histogram showing the distribution of Δ for trials within a 1.15 prune level are shown left-to-right respectively. The mean of the distance distribution is shown as the black trace, with the 2σ confidence interval shown as the shaded region.

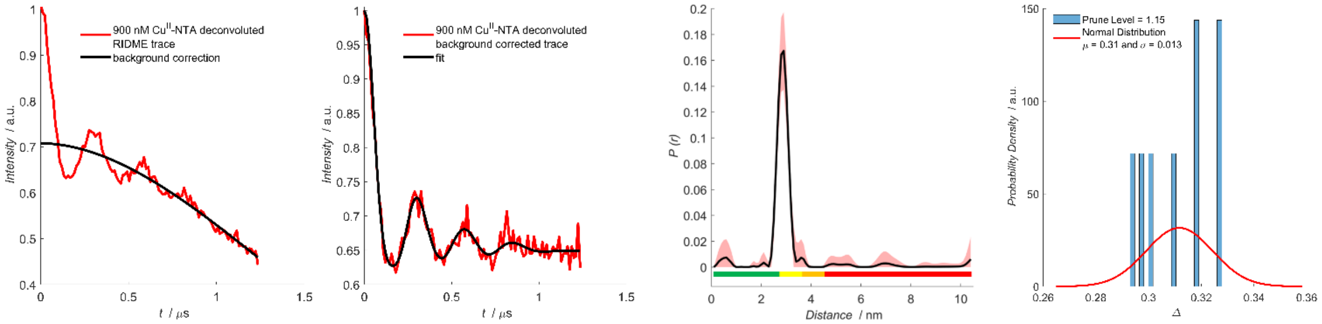

Figure 4.3.3.1.3: Plot of deconvoluted 900 nM Cu^{II}-NTA RIDME pseudo-titration data. The deconvoluted experimental trace, background corrected data, the validated distance distribution, and a histogram showing the distribution of Δ for trials within a 1.15 prune level, are shown left-to-right respectively. The mean of the distance distribution is shown as the black trace, with the 2σ confidence interval shown as the shaded region.

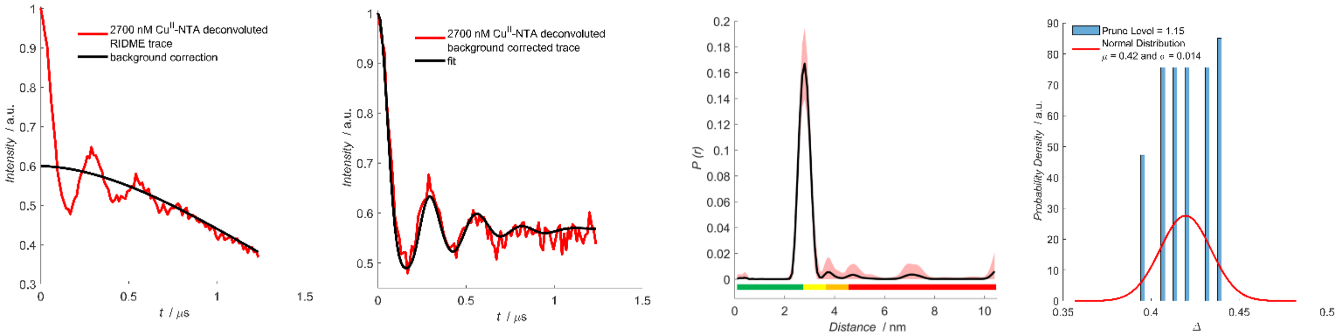

Figure 4.3.3.1.4: Plot of deconvoluted 2700 nM Cu^{II}-NTA RIDME pseudo-titration data. The deconvoluted experimental trace, background corrected data, the validated distance distribution, and a histogram showing the distribution of Δ for trials within a 1.15 prune level, are shown left-to-right respectively. The mean of the distance distribution is shown as the black trace, with the 2σ confidence interval shown as the shaded region.

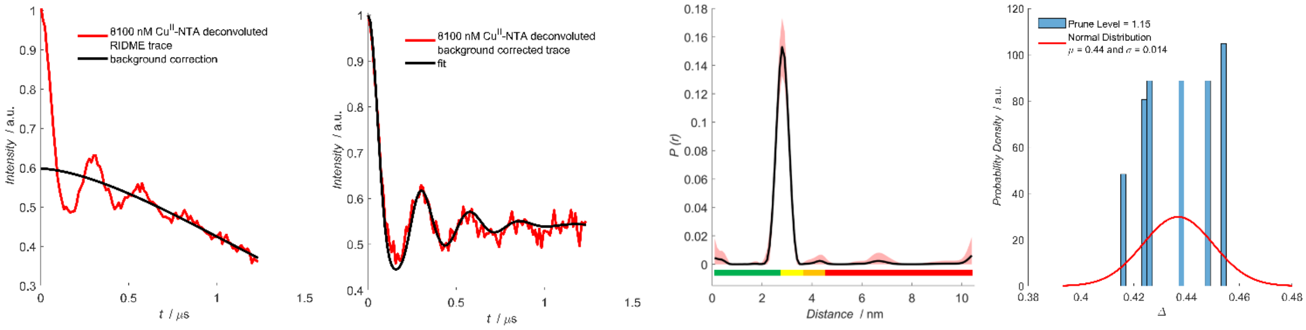

Figure 4.3.3.1.5: Plot of deconvoluted 8100 nM Cu^{II}-NTA RIDME pseudo-titration data. The deconvoluted experimental trace, background corrected data, the validated distance distribution, and a histogram showing the distribution of Δ for trials within a 1.15 prune level, are shown left-to-right respectively. The mean of the distance distribution is shown as the black trace, with the 2σ confidence interval shown as the shaded region.

Background correction parameters and modulation depths for each sample are given below in table 4.3.3.1.1.

Sample	Zero-time (ns)	Background start (ns)	Background Cut-off (ns)	Δ	Background Dimension
100 nM Cu-NTA	207	150	1232	0.102	3.0
300 nM Cu-NTA	206	239	1232	0.169	6.0
900 nM Cu-NTA	206	371	1232	0.292	3.0
2700 nM Cu-NTA	207	62	1232	0.400	3.0
8100 nM Cu-NTA	205	238	1232	0.402	3.0

Table 4.3.3.1.1: Comparison of background correction parameters for the deconvoluted RIDME traces shown in figures 4.3.3.1.1-5.

For all deconvoluted Cu^{II}-nitroxide RIDME traces, the validated distance distributions show that only the main peak observed at 2.5 nm is significant, since at all other distances, the lower estimate (shown in the unfilled space) has a probability density of 0 and therefore is within the noise floor. This is also encouraging that regardless of background correction parameter choice, the distance distribution is preserved, however the observed modulation depth is generally more sensitive to the choice of background correction parameters. Even so, all modulation depths carried forward for additional processing were found to be within ± 2 σ of the distribution mean. It is seen that all modulation depth distributions have 95% confidence intervals within ± 0.03 of the distribution mean. It should also be noted that because deconvolution suppresses the low frequency artefact, trials in which the RMSD is dominated by this feature are minimised.

4.3.3.2 Cu^{II}-Cu^{II} RIDME Validations – Stretched Exponential Background Correction

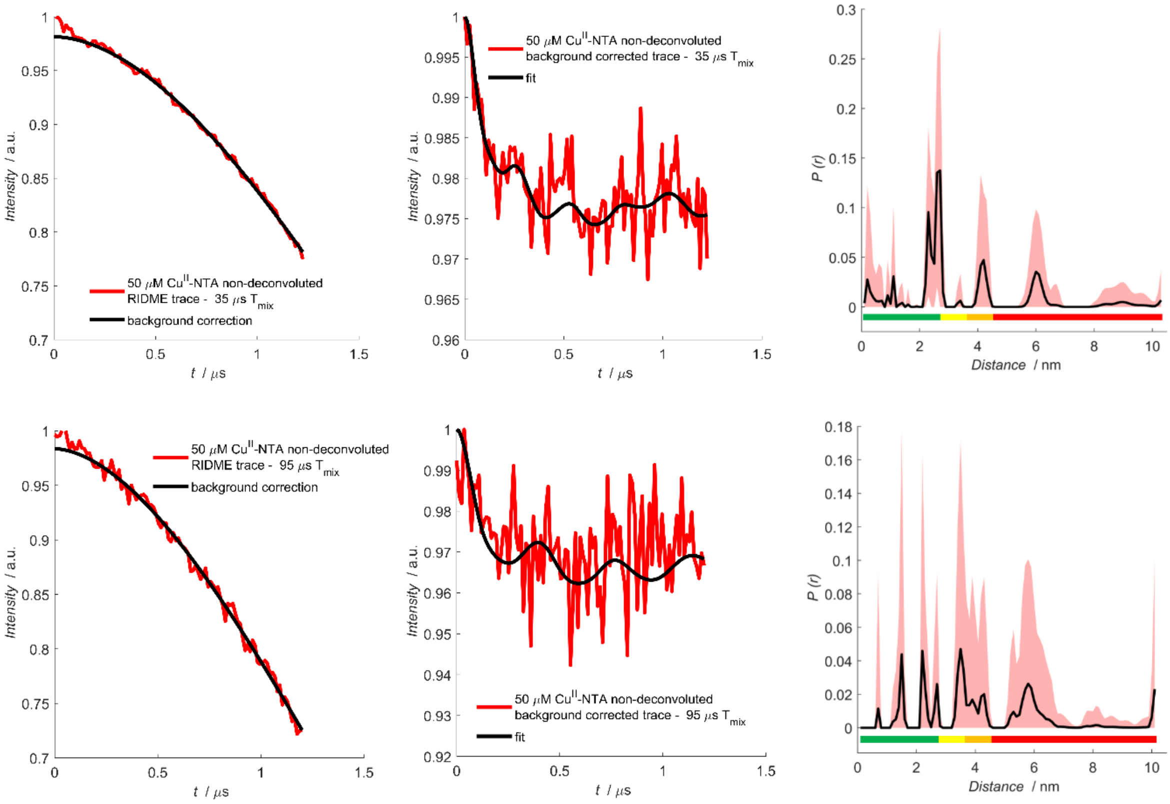

Figure 4.3.3.2.1: Plot of non-deconvoluted 50 µM Cu^{II}-NTA pseudo-titration data performed with 35 (top row) and 95 (bottom row) µs mixing times. The non-deconvoluted experimental trace, background corrected data, and the validated distance distribution, are shown left-to-right respectively. The mean of the distance distribution is shown as the black trace, with the 2σ confidence interval shown as the shaded region.

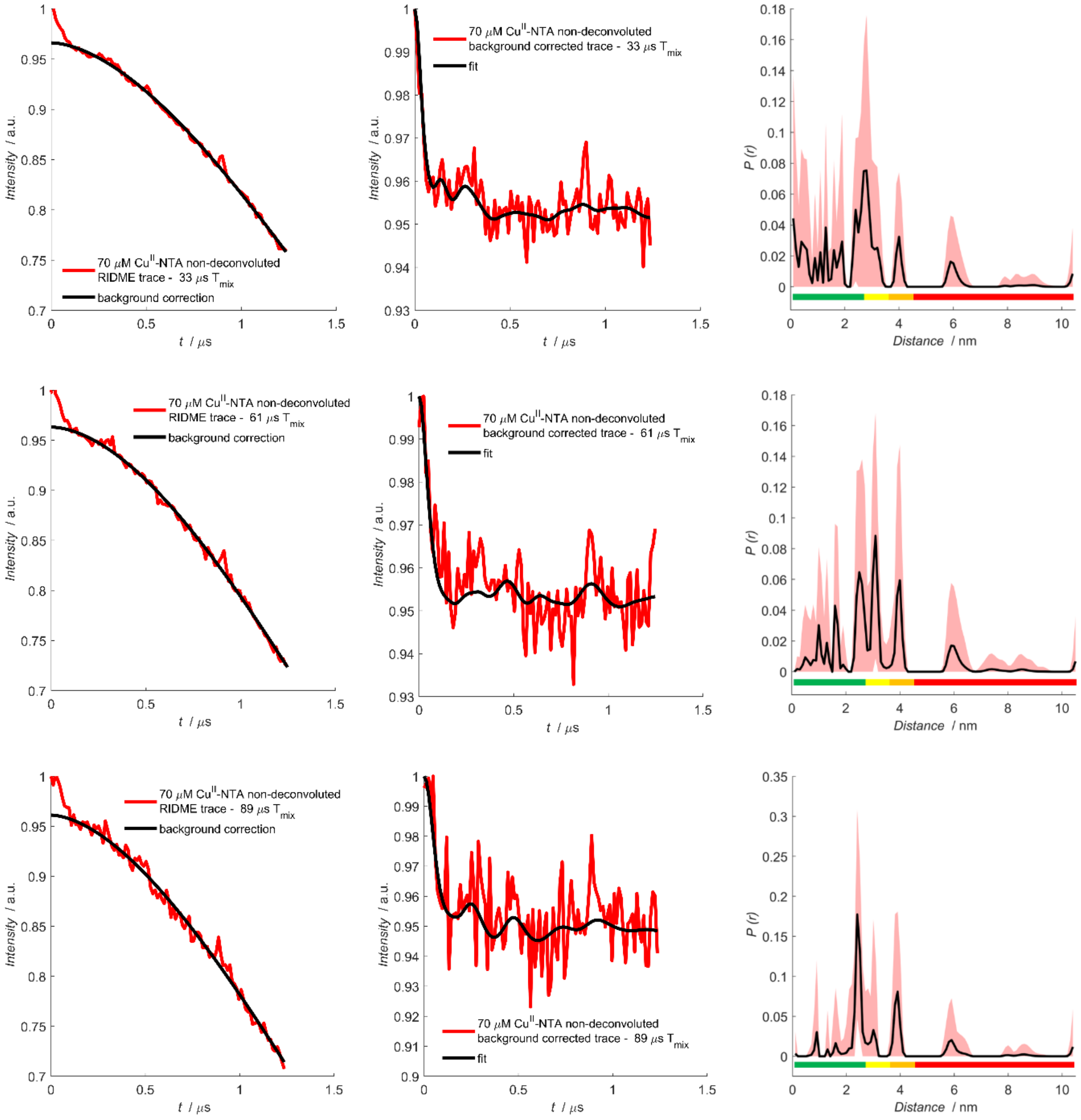

Figure 4.3.3.2.2: Plot of non-deconvoluted 70 µM Cu^{II}-NTA pseudo-titration data performed with 33 (top row), 61 (middle row) and 89 (bottom row) µs mixing times. The non-deconvoluted experimental trace, background corrected data, and the validated distance distribution, are shown left-to-right respectively. The mean of the distance distribution is shown as the black trace, with the 2σ confidence interval shown as the shaded region.

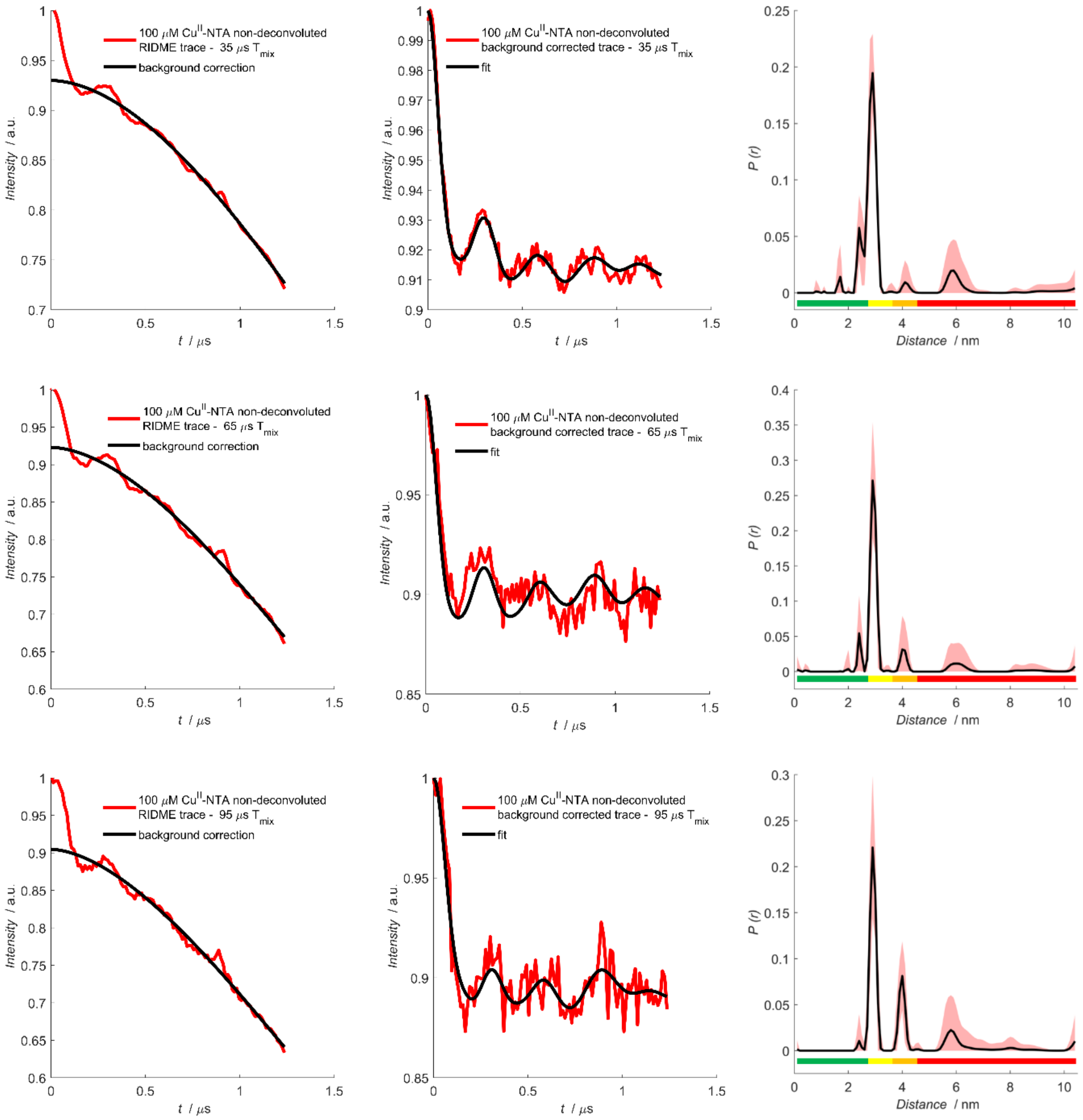

Figure 4.3.3.2.3: Plot of non-deconvoluted 100 µM Cu^{II}-NTA pseudo-titration data performed with 35 (top row), 65 (middle row) and 95 (bottom row) µs mixing times. The non-deconvoluted experimental trace, background corrected data, and the validated distance distribution, are shown left-to-right respectively. The mean of the distance distribution is shown as the black trace, with the 2σ confidence interval shown as the shaded region.

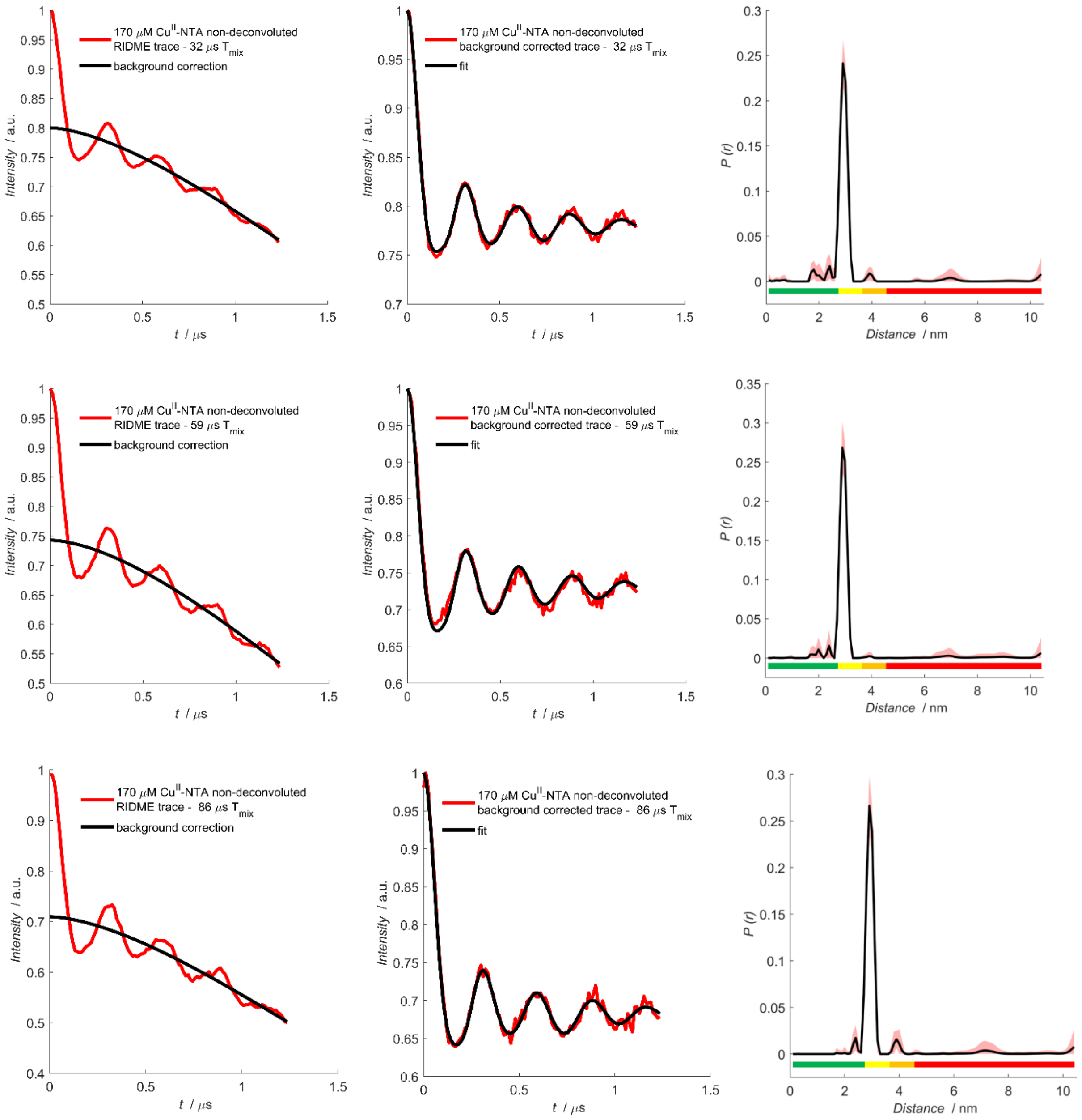

Figure 4.3.3.2.4: Plot of non-deconvoluted 170 µM Cu^{II}-NTA pseudo-titration data performed with 32 (top row), 59 (middle row) and 86 (bottom row) µs mixing times. The non-deconvoluted experimental trace, background corrected data, and the validated distance distribution, are shown left-to-right respectively. The mean of the distance distribution is shown as the black trace, with the 2σ confidence interval shown as the shaded region.

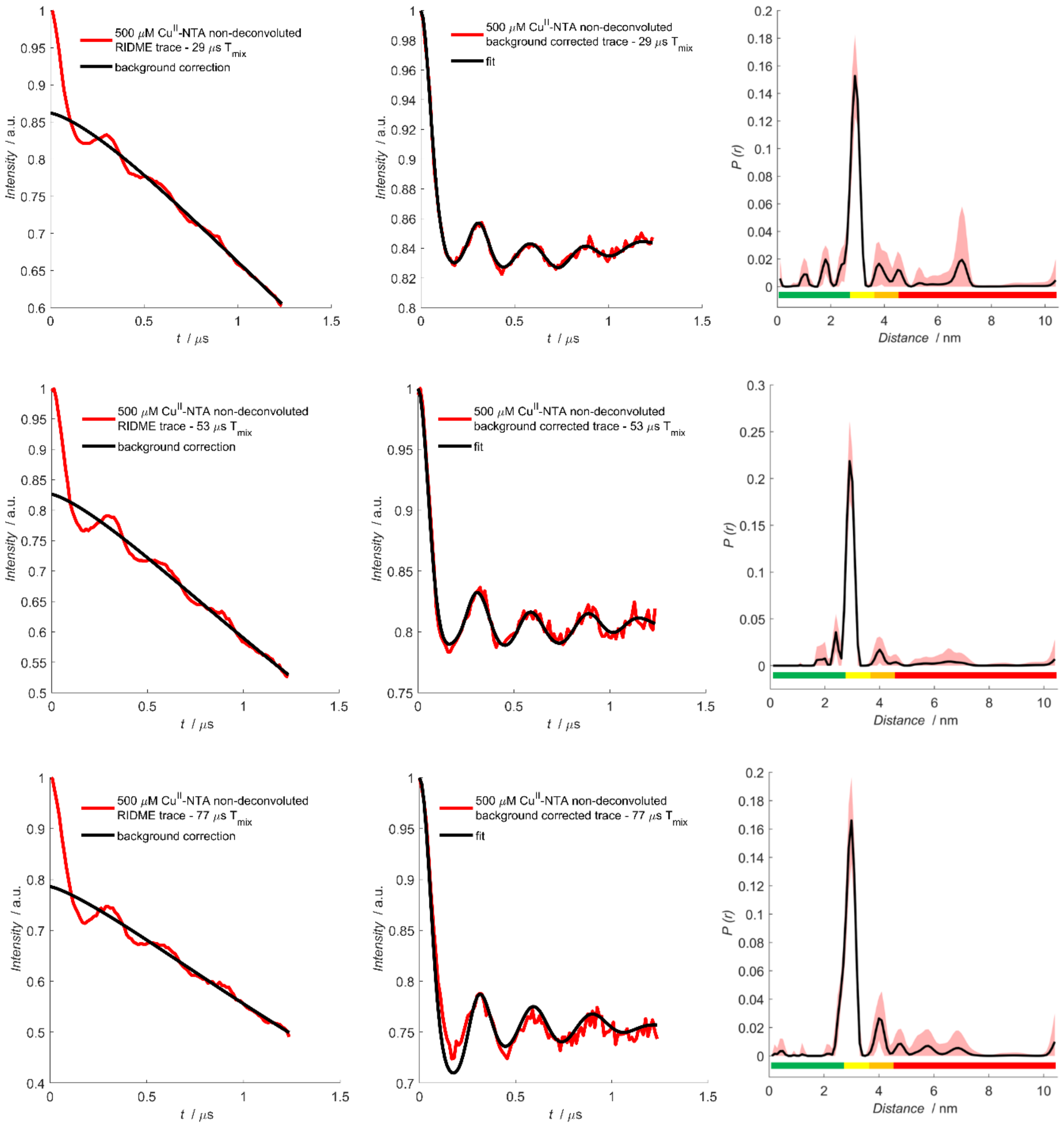

Figure 4.3.3.2.5: Plot of non-deconvoluted 500 µM Cu^{II}-NTA pseudo-titration data performed with 29 (top row), 53 (middle row) and 77 (bottom row) µs mixing times. The non-deconvoluted experimental trace, background corrected data, and the validated distance distribution, are shown left-to-right respectively. The mean of the distance distribution is shown as the black trace, with the 2σ confidence interval shown as the shaded region.

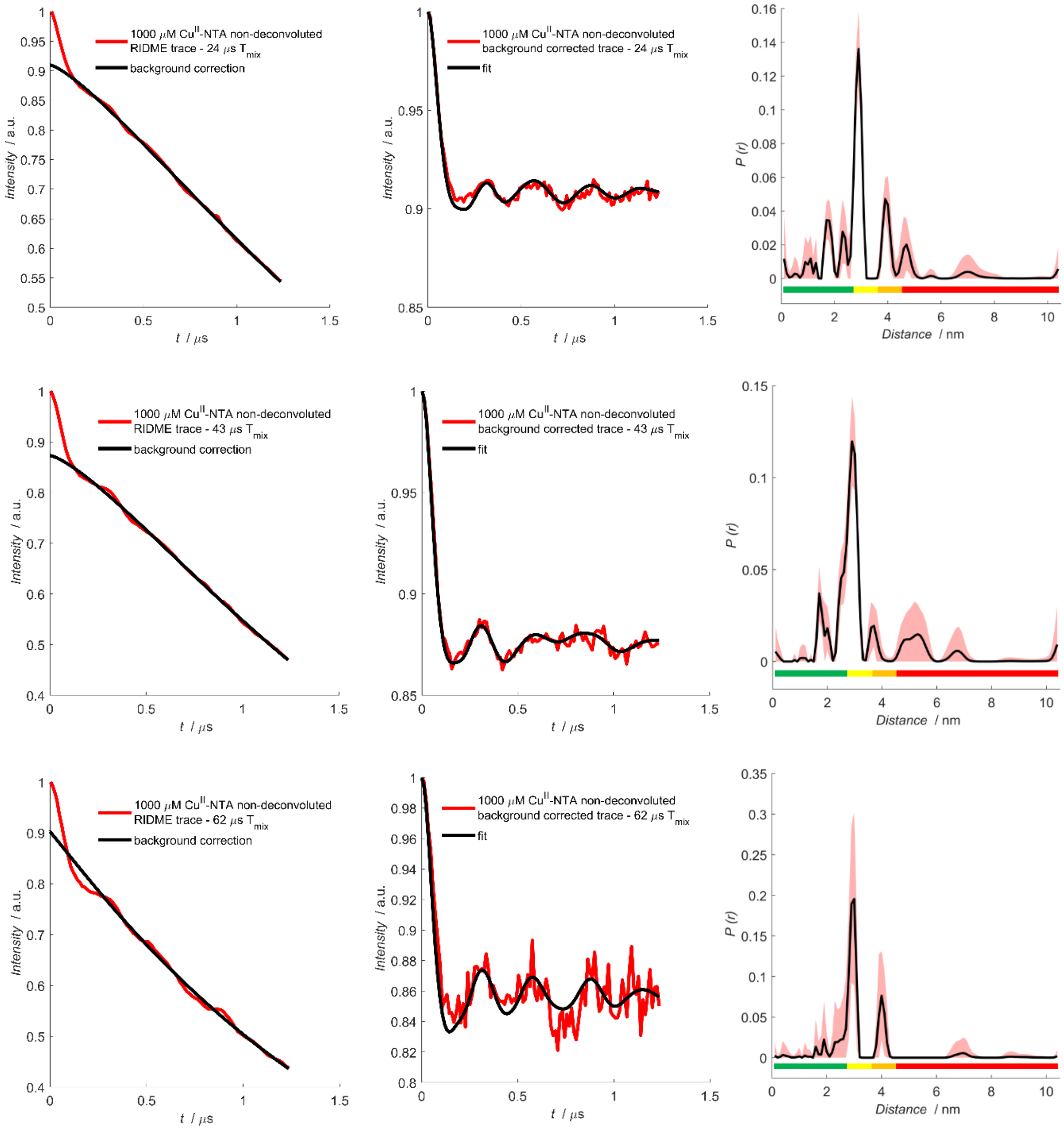

Figure 4.3.3.2.6: Plot of non-deconvoluted 1000 µM Cu^{II}-NTA pseudo-titration data performed with 24 (top row), 43 (middle row) and 62 (bottom row) µs mixing times. The non-deconvoluted experimental trace, background corrected data, and the validated distance distribution, are shown left-to-right respectively. The mean of the distance distribution is shown as the black trace, with the 2σ confidence interval shown as the shaded region.

Background correction parameters and modulation depths for each sample are given overleaf in table 4.3.3.2.1.

Sample	Mixing time [μs]			Zero-time [ns]			Background Start [ns]			Background Cut-off [ns]			Δ		
100 μM 6H/8H/28H/32H + 50 μM Cu^{II}-NTA	35	65	95	219	-	241	328	-	239	1224	-	1200	0.019 ± 4.6 x 10^{-3}	-	0.016 ± 5.8 x 10^{-3}
100 μM 6H/8H/28H/32H + 70 μM Cu^{II}-NTA	33	61	89	211	203	213	372	372	328	1236	1248	1236	0.034 ± 5.0 x 10^{-3}	0.037 ± 5.6 x 10^{-3}	0.039 ± 6.4 x 10^{-3}
100 μM 6H/8H/28H/32H + 100 μM Cu^{II}-NTA	35	65	95	211	210	216	372	284	106	1236	1236	1236	0.070 ± 1.1 x 10^{-2}	0.077 ± 1.5 x 10^{-2}	0.095 ± 1.8 x 10^{-2}
100 μM 6H/8H/28H/32H + 170 μM Cu^{II}-NTA	32	59	86	208	207	208	372	328	106	1236	1236	1236	0.200 ± 1.5 x 10^{-2}	0.257 ± 2.2 x 10^{-2}	0.290 ± 2.4 x 10^{-2}
100 μM 6H/8H/28H/32H + 500 μM Cu^{II}-NTA	29	53	77	208	207	208	283	106	283	1236	1236	1236	0.138 ± 1.8 x 10^{-2}	0.174 ± 2.6 x 10^{-2}	0.214 ± 2.6 x 10^{-2}
100 μM 6H/8H/28H/32H + 1000 μM Cu^{II}-NTA	24	43	62	210	208	207	239	239	372	1236	1236	1236	0.090 ± 8.2 x 10^{-3}	0.127 ± 1.2 x 10^{-2}	0.098 ± 2.0 x 10^{-2}

Table 4.3.3.2.1: Comparison of background correction parameters for the validated non-deconvoluted RIDME traces, using a stretched exponential background function, shown in figures 4.3.3.2.1-6. The error in modulation depth is ± 2σ.

4.3.3.3 Cu^{II}-Cu^{II} RIDME Validations – Second Order Polynomial Background Correction

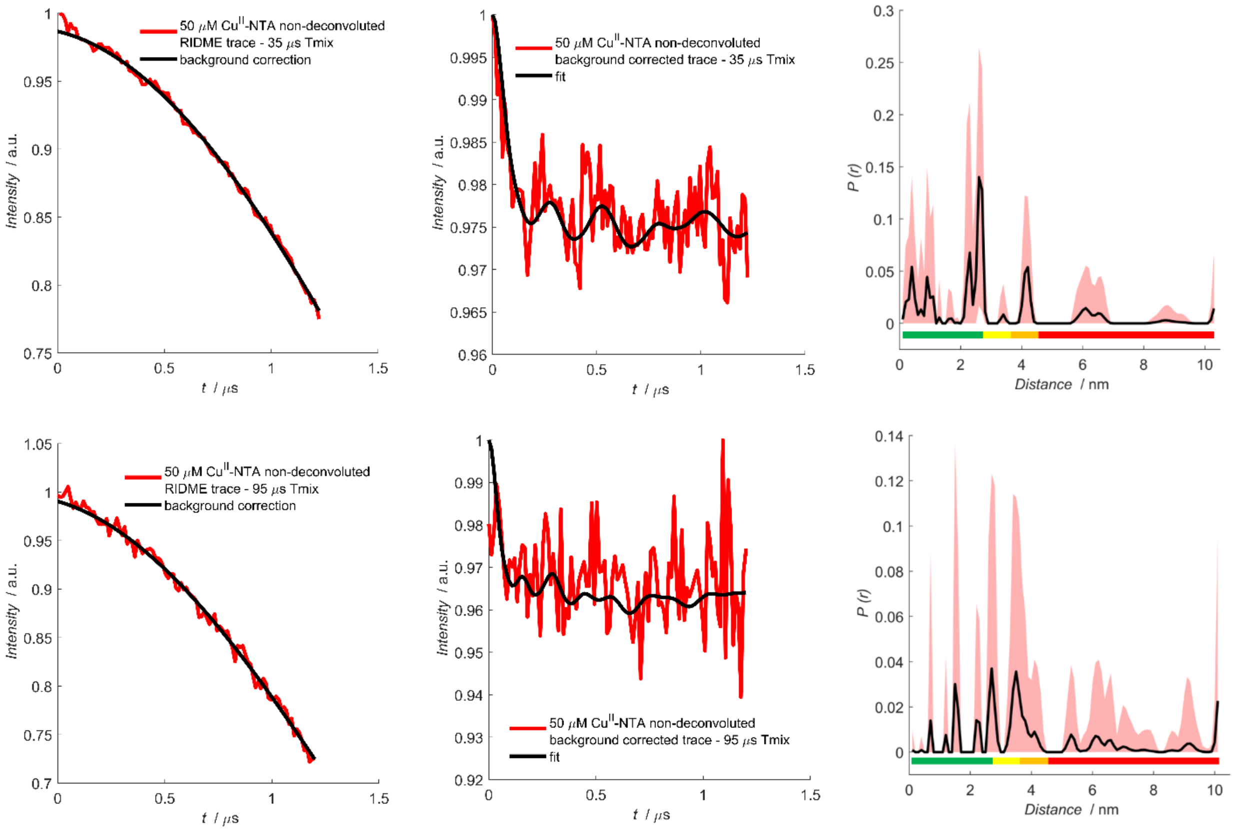

Figure 4.3.3.3.1: Plot of non-deconvoluted 50 μM Cu^{II}-NTA pseudo-titration data performed with 35 (top row) and 95 (bottom row) μs mixing times. The non-deconvoluted experimental trace, background corrected data, and the validated distance distribution, are shown left-to-right respectively. The mean of the distance distribution is shown as the black trace, with the 2σ confidence interval shown as the shaded region.

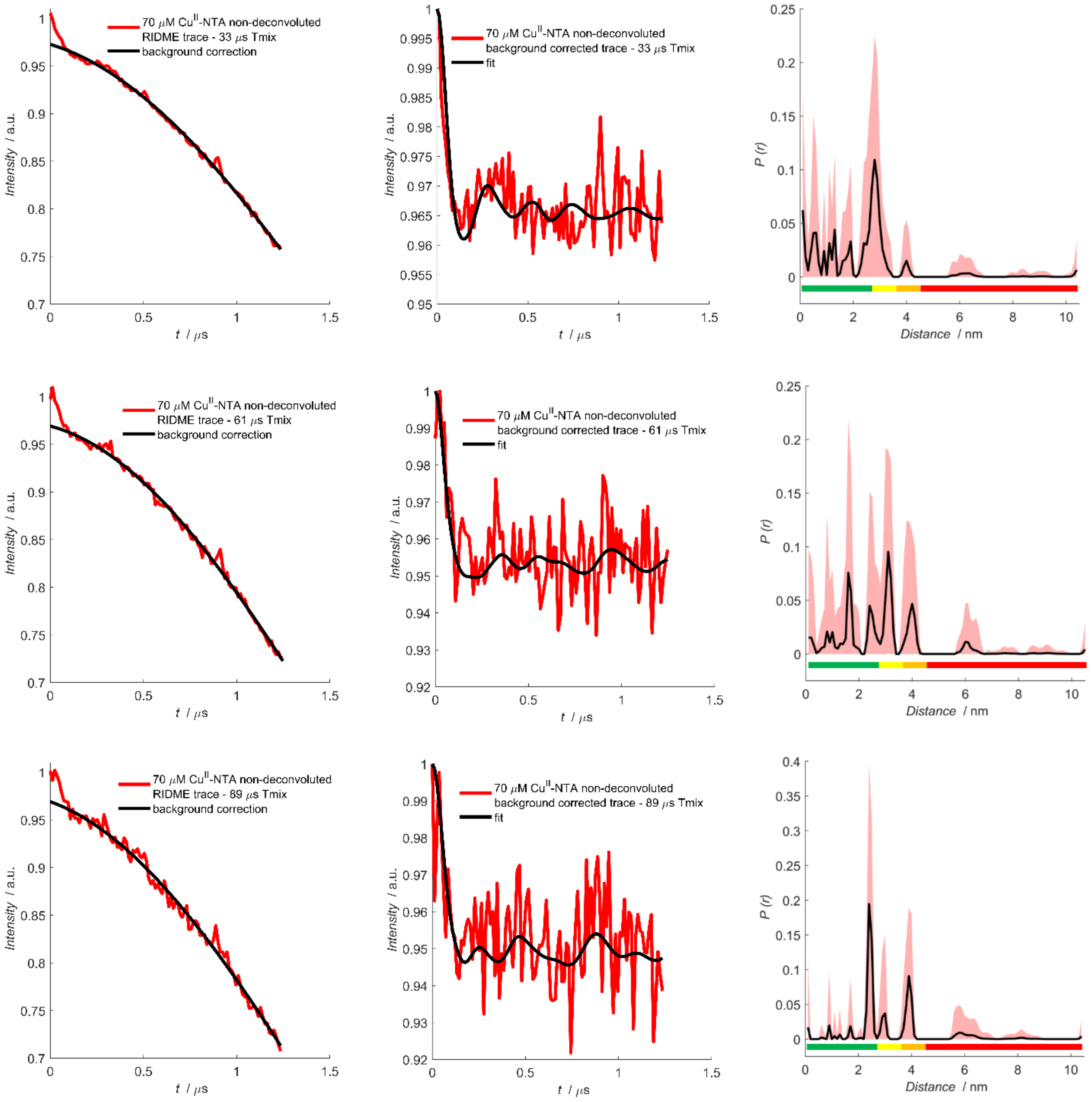

Figure 4.3.3.3.2: Plot of non-deconvoluted 70 µM Cu^{II}-NTA pseudo-titration data performed with 33 (top row), 61 (middle row) and 89 (bottom row) µs mixing times. The non-deconvoluted experimental trace, background corrected data, and the validated distance distribution, are shown left-to-right respectively. The mean of the distance distribution is shown as the black trace, with the 2σ confidence interval shown as the shaded region.

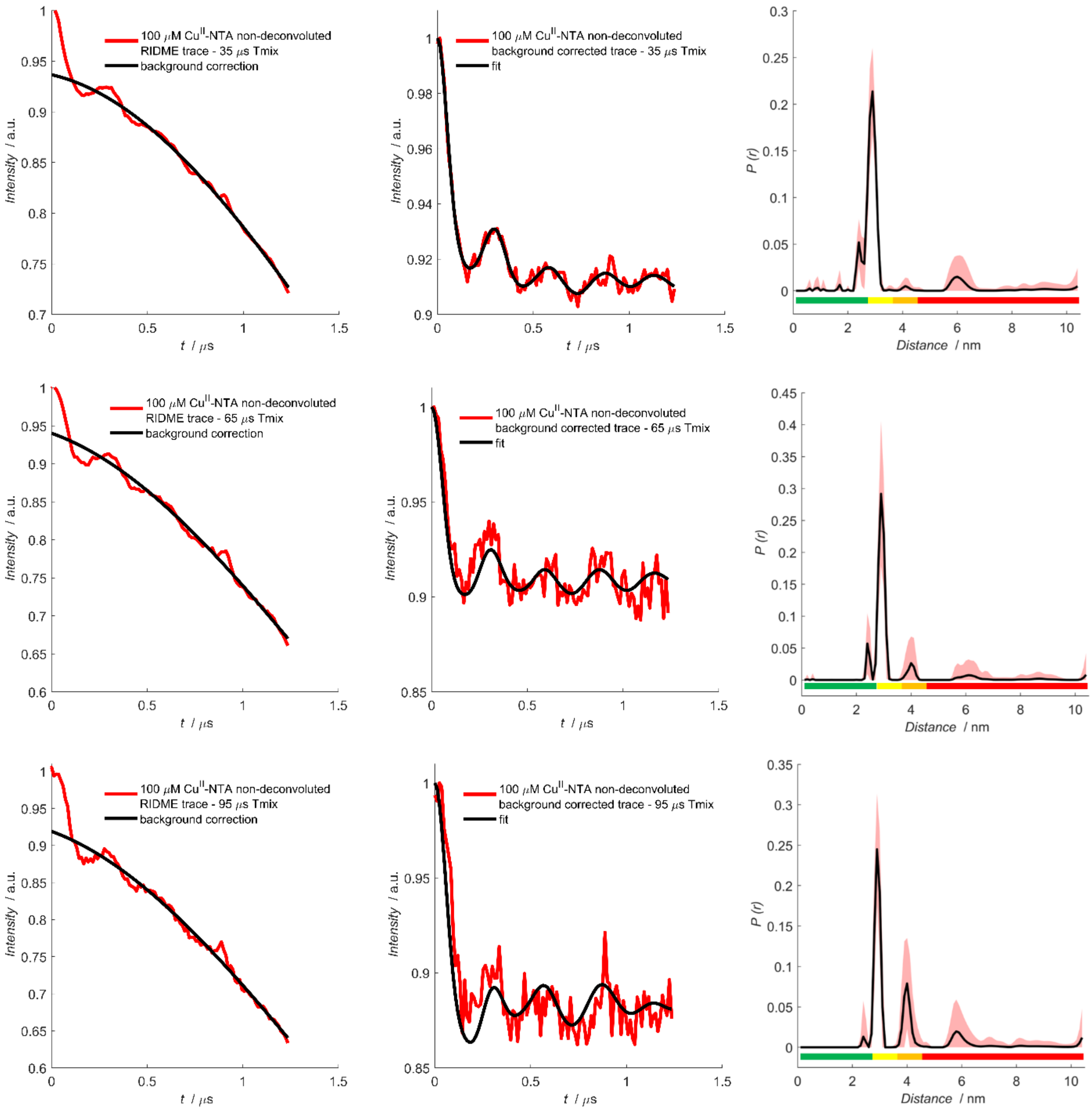

Figure 4.3.3.3.3: Plot of non-deconvoluted 100 µM Cu^{II}-NTA pseudo-titration data performed with 35 (top row), 65 (middle row) and 95 (bottom row) µs mixing times. The non-deconvoluted experimental trace, background corrected data, and the validated distance distribution, are shown left-to-right respectively. The mean of the distance distribution is shown as the black trace, with the 2σ confidence interval shown as the shaded region.

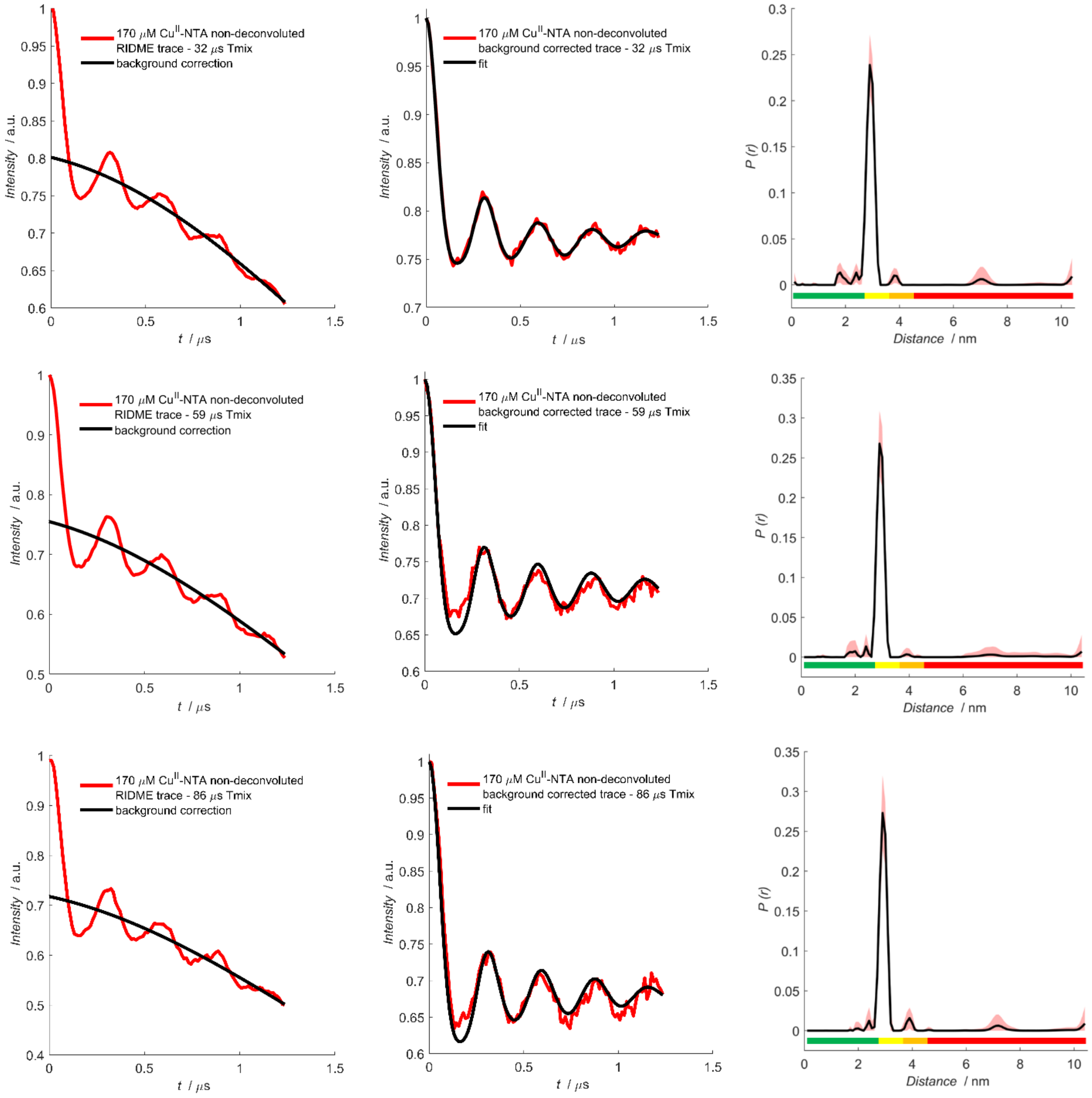

Figure 4.3.3.3.4: Plot of non-deconvoluted 170 µM Cu^{II}-NTA pseudo-titration data performed with 32 (top row), 59 (middle row) and 86 (bottom row) µs mixing times. The non-deconvoluted experimental trace, background corrected data, and the validated distance distribution, are shown left-to-right respectively. The mean of the distance distribution is shown as the black trace, with the 2σ confidence interval shown as the shaded region.

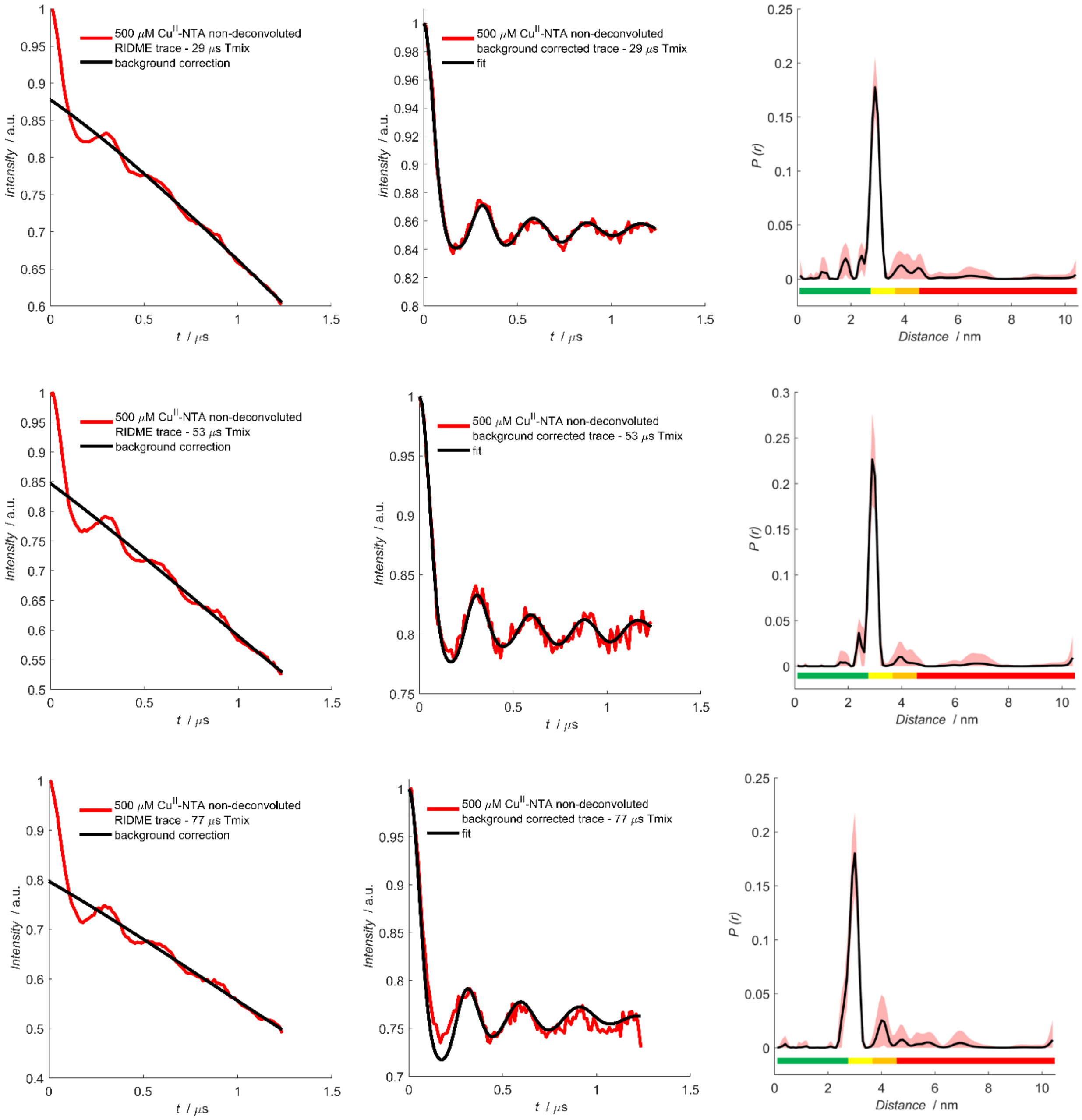

Figure 4.3.3.3.5: Plot of non-deconvoluted 500 µM Cu^{II}-NTA pseudo-titration data performed with 29 (top row), 53 (middle row) and 77 (bottom row) µs mixing times. The non-deconvoluted experimental trace, background corrected data, and the validated distance distribution, are shown left-to-right respectively. The mean of the distance distribution is shown as the black trace, with the 2σ confidence interval shown as the shaded region.

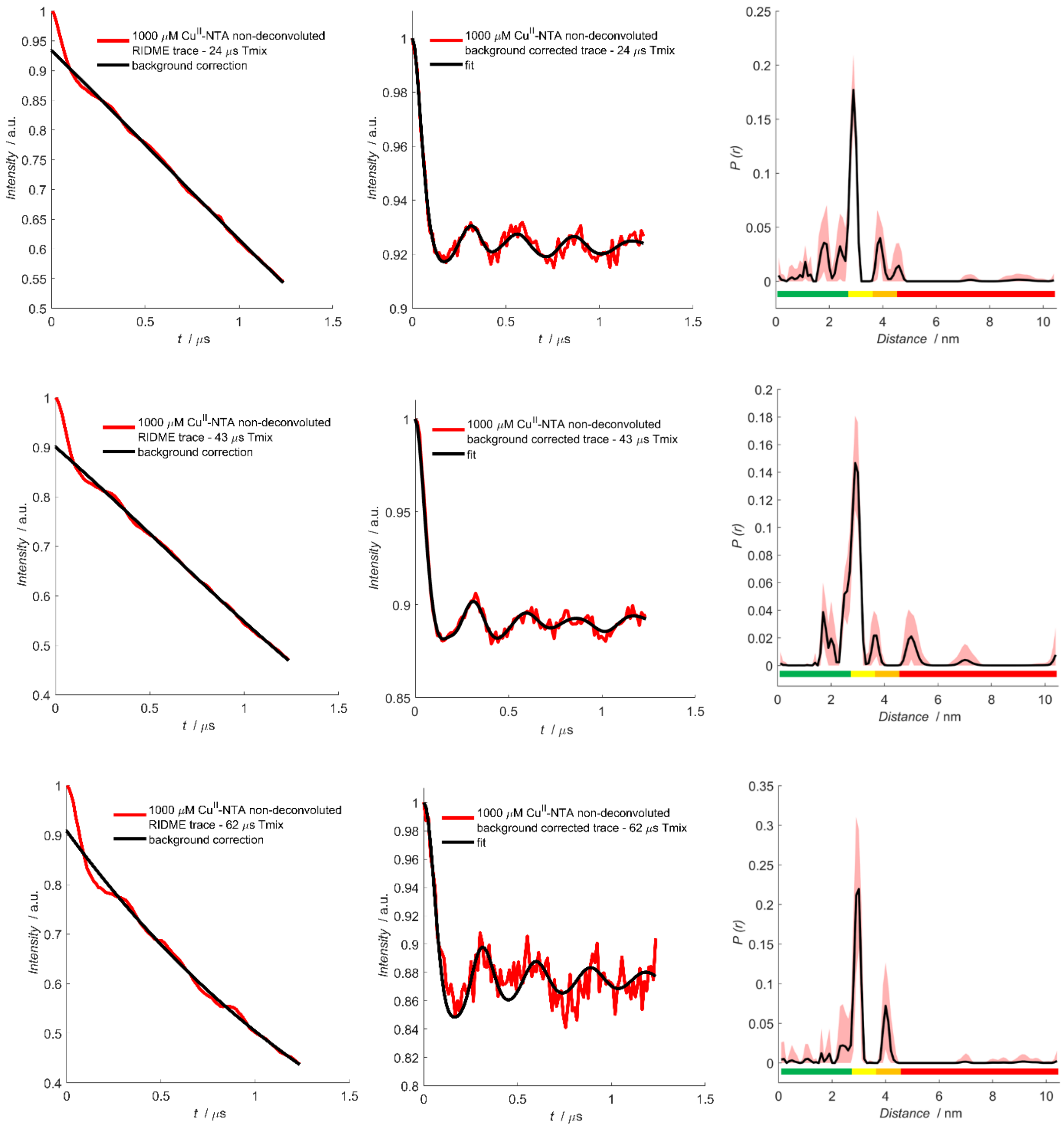

Figure 4.3.3.3.6: Plot of non-deconvoluted 1000 µM Cu^{II}-NTA pseudo-titration data performed with 24 (top row), 43 (middle row) and 62 (bottom row) µs mixing times. The non-deconvoluted experimental trace, background corrected data, and the validated distance distribution, are shown left-to-right respectively. The mean of the distance distribution is shown as the black trace, with the 2σ confidence interval shown as the shaded region.

Background correction parameters and modulation depths for each sample are given overleaf in table 4.3.3.3.1.

Sample	Mixing time [μs]			Zero-time [ns]			Background Start [ns]			Background Cut-off [ns]			Δ		
100 μM 6H/8H/28H/32H + 50 μM Cu$^{\text{II}}$-NTA	35	65	95	219	-	241	283	-	239	1224	-	1200	0.013 ± 4.8 x 10^{-3}	-	0.010 ± 6.0 x 10^{-3}
100 μM 6H/8H/28H/32H + 70 μM Cu$^{\text{II}}$-NTA	33	61	89	211	203	213	106	150	327	1236	1248	1236	0.027 ± 5.4 x 10^{-3}	0.031 ± 7.0 x 10^{-3}	0.031 ± 6.4 x 10^{-3}
100 μM 6H/8H/28H/32H + 100 μM Cu$^{\text{II}}$-NTA	35	65	95	211	210	216	371	106	62	1236	1236	1236	0.063 ± 1.6 x 10^{-2}	0.060 ± 2.0 x 10^{-2}	0.081 ± 2.0 x 10^{-2}
100 μM 6H/8H/28H/32H + 170 μM Cu$^{\text{II}}$-NTA	32	59	86	208	207	209	106	283	194	1236	1236	1236	0.199 ± 2.4 x 10^{-2}	0.245 ± 2.6 x 10^{-2}	0.282 ± 3.4 x 10^{-2}
100 μM 6H/8H/28H/32H + 500 μM Cu$^{\text{II}}$-NTA	29	53	77	208	207	208	150	150	283	1236	1236	1236	0.122 ± 1.5 x 10^{-2}	0.153 ± 2.2 x 10^{-2}	0.203 ± 2.8 x 10^{-2}
100 μM 6H/8H/28H/32H + 1000 μM Cu$^{\text{II}}$-NTA	24	43	62	210	208	207	150	150	283	1236	1236	1236	0.066 ± 7.8 x 10^{-3}	0.099 ± 1.1 x 10^{-2}	0.092 ± 1.4 x 10^{-2}

Table 4.3.3.3.1 Comparison of background correction parameters for the validated non-deconvoluted RIDME traces, using a second-order polynomial background function, shown in figures 4.3.3.3.1-6. The error in modulation depth is ± 2σ.

For the 6H/8H/28H/32H GB1 RIDME traces corrected assuming a stretched exponential background decay shown in figures 4.3.3.2.1-6, the validated distance distributions show that under conditions of low loading (50 and 70 μM Cu$^{\text{II}}$-NTA) even the main peak at ~2.5 nm is barely above the noise floor, since at all distances the lower estimate (shown as the unfilled space) has a probability density close to 0. This is also recapitulated for the RIDME traces corrected assuming a second-order polynomial background correction shown in figures 4.3.3.3.1-6. Importantly, for all higher concentrations of Cu$^{\text{II}}$-NTA (except for 170 μM Cu$^{\text{II}}$-NTA) there is a second significant peak at ~4.0 nm. This suggests that under such Cu$^{\text{II}}$-NTA labelling conditions there is a non-specific interaction away from the double-histidine motifs, or this may reflect the formation of a Cu$^{\text{II}}$-templated dimer construct. However, the feature is largely suppressed under conditions of optimal labelling but is still present in the 100 μM Cu$^{\text{II}}$-NTA sample, which is inconsistent with the peak resulting from a non-specific binding event. More likely, it is an erroneous feature arising from poor labelling efficiency or low SNR. While all samples give a significant peak at 2.5 nm, it should be apparent that only under conditions of optimal Cu$^{\text{II}}$-NTA labelling can the distance be uniquely identified. It is also interesting to note that modulation depth is consistently higher when using a stretched exponential model of background correction, compared to a second-order polynomial, but that the standard deviation of Δ is consistently larger for the latter background model.

Despite the poor reliability of the distance distributions for several of the 6H/8H/28H/32H GB1 pseudo-titration samples, all modulation depth distributions have 95% confidence intervals within ± 0.03 (to 2 decimal places) of the distribution means, suggesting modulation depth information can be extracted reliably. Furthermore, the modulation depths calculated from the validations appear largely robust against choice of background correction model. It is also worth noting that the standard deviation (σ) increases with mixing time, as expected. This trend is harder to predict for propagation of the error in the modulation depth quotient, since at longer mixing times, the error in Δ_{Tmix} will decrease, despite the increased error in the empirical modulation depth owing to reduced sensitivity.

4.3.4 Bivariate Fitting of Dissociation Constants

The pseudo-titration series (treated with a stretched exponential background function) for all ratios of T_{mix} and T_1 are shown in figure 4.3.4.1, and pairs of dissociation constants are fitted to experimental modulation depth quotients (Q_{exp}) and are given in the figure legend. Importantly, the fit demonstrates that both sites differ by an order of magnitude in affinity, in good agreement with ITC data and Cu^{II}-NTA nitroxide RIDME pseudo-titrations. Cu^{II}-nitroxide RIDME pseudo-titrations suggested K_D values of 140 nM and 1.4 μM for the α-helical and β-sheet dH motifs, respectively. Figure 4.3.4.1 (bottom-row right panel) shows the error surface corresponding to all Cu^{II}-Cu^{II} RIDME pseudo-titration data fitted simultaneously. There are two correlated troughs, with the diagonal ridge indicating the affinities are different, though all fitted solutions fall within these broad ridges. The determined affinities from the Cu^{II}-Cu^{II} RIDME pseudo-titration are in the low μM concentration regime (one site will be <10 μM, and the other will be an order of magnitude lower).

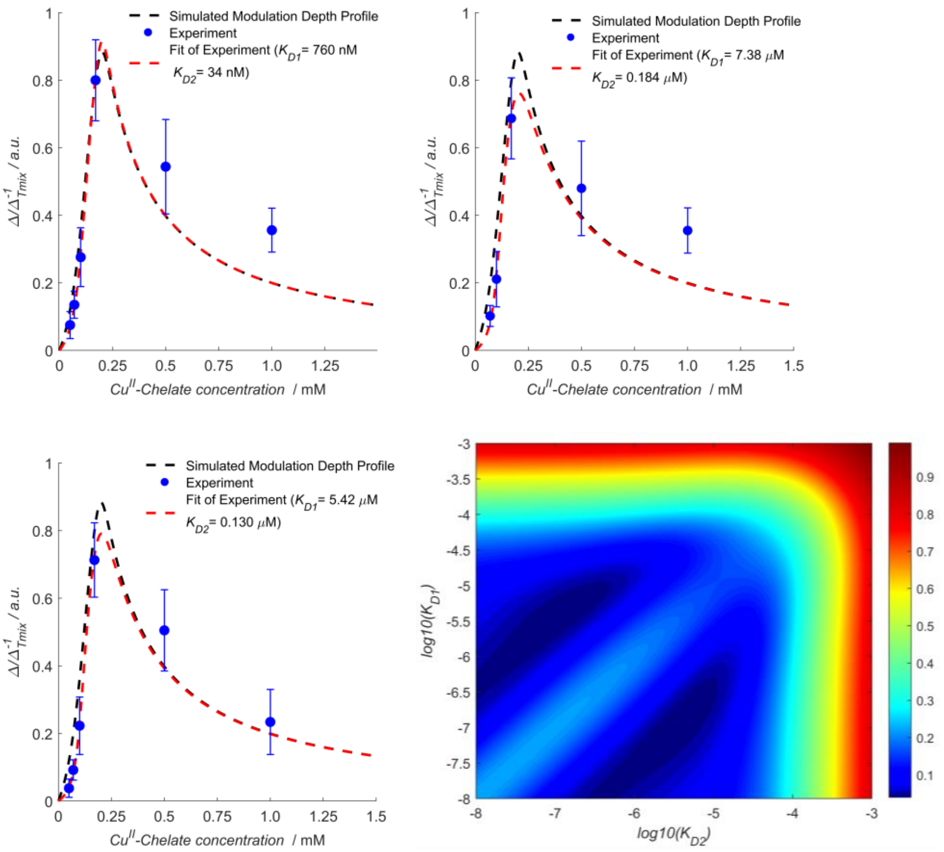

Figure 4.3.4.1. The experimental modulation depth quotients calculated using a stretched exponential background function (blue scatter), overlaid with the predicted modulation depth profile from Cu^{II}-nitroxide RIDME data (black dashes) and the associated bivariate fit (red dashes) recorded with a mixing time of top-row left panel) 0.7 × T_1, top-row right panel) 1.3 × T_1, and bottom-row left panel) 1.9 × T_1. bottom-row right panel) An error surface of the bivariate fitting of each dissociation constant to the experimental data. The colour bar indicates the normalised RMSD. Each dissociation constant varies 5 orders of magnitude from 10 nM to 1 mM.

However, the error in the absolute K_D estimation will be large, since measurements at protein concentrations in the same range as the K_D value afford higher measurement accuracy. Owing to sensitivity limitations associated with detection of small modulation depth changes in intentionally under-labelled samples, an empirical protein concentration of 100 μM was chosen. In the limiting case of high affinity, the simulated profiles are largely identical, and the discerning feature becomes the maximum modulation depth quotient (see figure 4.3.4.2 magenta trace). In this case, moving into a lower protein concentration regime would be desirable, and would improve precision of K_D determination. From figure 4.3.4.1 it is evident that the experimental data (red scatter) yields fitted K_D values of ~100 nM and ~5 μM, since observed values largely sit between the black and the blue simulated curves.

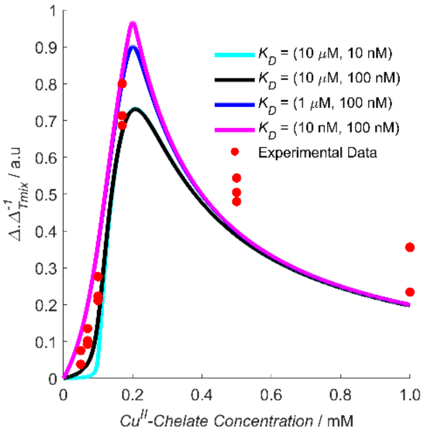

Figure 4.3.4.2: An overlay of simulated profiles with experimental data. Note that these profiles are simulations rather than fits to the corresponding experimental data.

The fitted K_D estimates are within the troughs of the error surface for all mixing time ratios. Comparison with values previously determined by ITC extrapolated to 239 K (220 and 750 nM) indicate they are at the periphery of the ridge, likely because the current protein concentration does not facilitate precise determination of K_Ds significantly below the low μM concentration regime. The ITC data showed exothermic binding, predicting higher affinity at lower temperature. The EPR data of samples snap-frozen in liquid nitrogen was consistent with the binding equilibrium freezing out at 235-240 K. Comparison of the K_Ds determined by Cu^{II}-nitroxide RIDME further supports this assumption, being consistent with the error surface troughs. Recent UV-vis data suggested an arithmetic average K_D across both double-histidine sites of 6 μM in phosphate buffer, comparing favourably with previous ITC measurements extrapolated to 281 K (16 and 2 μM for β-sheet and α-helical double-histidine motif, respectively), which is consistent with the upper limits of the Cu^{II}-Cu^{II} RIDME error surface troughs (~10 μM and ~1 μM) (figure 4.3.4.1 bottom-right panel).

The lack of exact numerical agreement between the Cu^{II}-Cu^{II} RIDME and UV-vis data is unsurprising since measurements were performed with different temperatures and cryoprotectant. As expected from the temperature dependence of the binding event, the K_D estimates from UV-vis and ITC at 281 K represent the upper-bound of the Cu^{II}-Cu^{II} RIDME estimates. The agreement between the Cu^{II}-nitroxide and Cu^{II}-Cu^{II} RIDME is greater, likely because the K_D values are reflective of similar temperature regimes, and buffer composition was nominally identical. The buffer conditions can have a significant effect on affinity. Furthermore, the cooling rate would be expected to influence the measured K_D value, as the equilibrium will freeze out somewhere between room-temperature and the glass transition temperature. Using freeze-quench techniques or alteration of the matrix composition are potential avenues of investigation in future work, to provide snapshots of the equilibrium at different temperatures using this approach.

All data shown in figure 4.3.4.1 were also fitted globally (for all ratios of T_{mix} and T_1) and K_D values were consistent, particularly with the T_{mix} to T_1 ratio of 1.9 (see section 4.3.6). The global fitting approach of both Cu^{II}-Cu^{II} and low concentration Cu^{II}-nitroxide RIDME shows an improved agreement with ITC predictions (see figure 4.3.6.5). Taken together, this suggests that accurate information regarding binding equilibria can be extracted from double dH systems, in a single measurement series. However, where available Cu^{II}-nitroxide and Cu^{II}-Cu^{II} RIDME pseudo-titrations can be combined, to independently validate binding affinities. It should also be noted that Cu^{II}-Cu^{II} RIDME pseudo-titrations are likely to be of greater diagnostic value in systems where binding sites differ by an order of magnitude or greater in their respective affinities.

The error associated with modulation depth quotients (Q_{exp}) quantified *via* Cu^{II}-Cu^{II} RIDME will tend to be larger than those quantified *via* Cu^{II}-nitroxide RIDME. However, the error in modulation depths (Δ) was more comparable with Cu^{II}-nitroxide RIDME, within ±0.03. Additionally, the relative error in the modulation depth quotients generally reduces at longer mixing time and was found to be ±25% for a T_{mix} and T_1 ratio of 1.9. Only for the series recorded with the highest ratio (figure 4.3.4.1 bottom-left panel) do all experimental data points lie on the fitted curve (within error), and the original simulated modulation depth profile, indicating it is the most consistent with previous ITC and Cu^{II}-nitroxide RIDME data. The fit quality improves at longer mixing times.

The series measured with a ratio of 0.7 overestimates Δ, and so yields the highest affinity estimates and gives a bad fit of points away from the curve. These manifest because a fast component in T_1 is not treated by the mono-exponential approximation. While all mixing time ratios reproduce the trend in K_D estimates, the longer mixing times provide greater accuracy because deviations of T_1 from mono-exponential behaviour will not manifest as severely. Indeed, analysis of the RIDME modulation depths using a bi-exponential approximation of T_1 behaviour results in K_D estimates that are more stable for different T_{mix} and T_1 ratios (see section 4.3.7). Interestingly, the error surface also reveals that the shape of the modulation depth profile is highly sensitive to the magnitude of the individual K_D values, and not simply their product. Indeed, simulation with K_D values of i) 100 nM and 1 μM, and ii) 10 nM and 10 μM (where individual K_D values are increased and decreased respectively, by an order of magnitude, but their product remains unchanged) show that the agreement between simulation and experiment is poorer in the latter case (see figure 4.3.4.2). However, this approach cannot assign the K_D values to each disparate site without additional information.

The observation that the K_D values are not ‘compensatory’ has important implications for the robustness of the model. It allows one to ‘compartmentalise’ the profile into the initial flank, maximum and the region to the right of the maximum, in discussions regarding the higher- and lower-affinity K_D values. The region to the right of the maximum is independent of either K_D and only dependent upon the ratio of tetra-histidine protein and total Cu^{II}-chelate concentrations, since in this regime all additional ligand will be unbound, and thus dilute the bound component which contributes to modulation depth. Therefore, this region of the profile can be used as an internal control, to assess the concentration accuracy of the pseudo-titration series.

4.3.5 Factors Influencing the Accuracy of K_D Determination by Cu^{II}-Cu^{II} RIDME Measurements

The accurate determination of K_D values using this approach is clearly dependent on the accurate quantitation of the modulation depths associated with the RIDME measurements. In this purview, there are several factors which need to be characterised before the approach can be considered robust.

4.3.5.1 Differential Relaxation Behaviour

One point of interest of using a coordination-based spin labelling method, is that relaxation behaviour may differ between the free and bound components. This means that under conditions of partial loading, the relative contributions of free and dH-bound Cu^{II}-chelate to the detected echo could be different. To demonstrate this, 2-pulse electron-spin echo decay traces (figure 4.3.5.1.1-2), and inversion recovery traces (figure 4.3.5.1.4-5) for quantitatively free and dH-bound Cu^{II}-IDA and Cu^{II}-NTA were recorded, respectively. Measurements were performed for 1, 10 and 100 μM Cu^{II}-IDA and Cu^{II}-NTA alone, and 1 and 10 μM in presence of 100 μM I6R1/K28H/Q32H GB1. Corresponding T_m and T_1 estimates under the stretched, mono- and bi-exponential approximations, and reciprocal e-times are given in tables 4.3.5.1.1-2 and 4.3.5.1.3-4, respectively, for Cu^{II}-IDA and Cu^{II}-NTA.

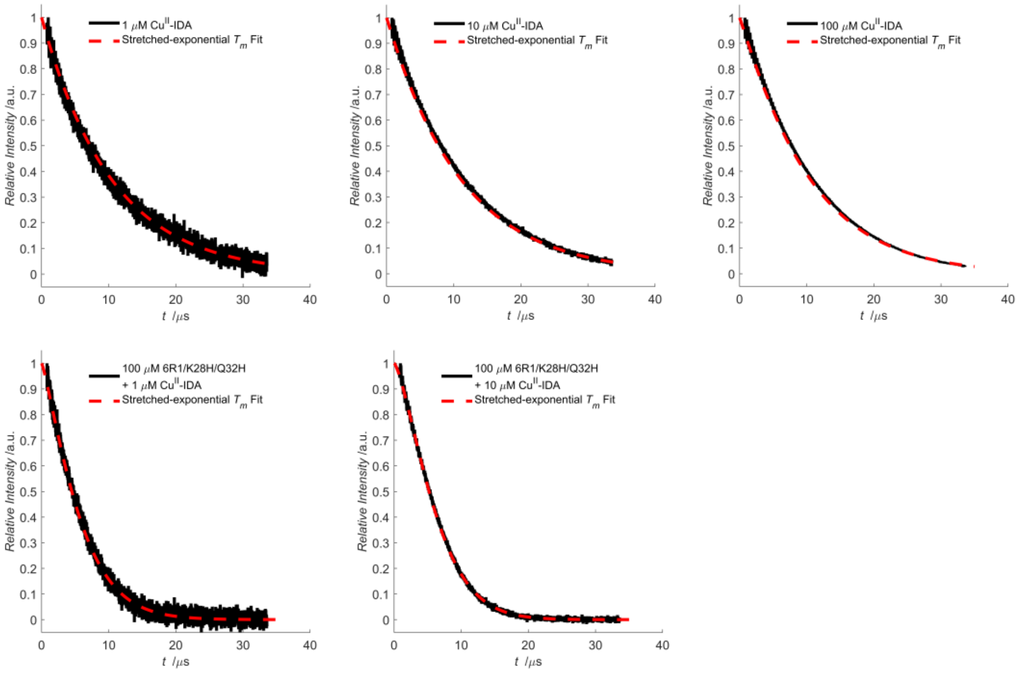

Figure 4.3.5.1.1. Two-pulse electron spin echo decay data for 1, 10 and 100 μM Cu^{II}-IDA (top row), and 1 and 10 μM Cu^{II}-IDA in presence of 100 μM I6R1/K28H/Q32H GB1 shown left-to-right, respectively. The experimental data is shown in black, with the fitted stretched exponential functions shown as red dotted lines.

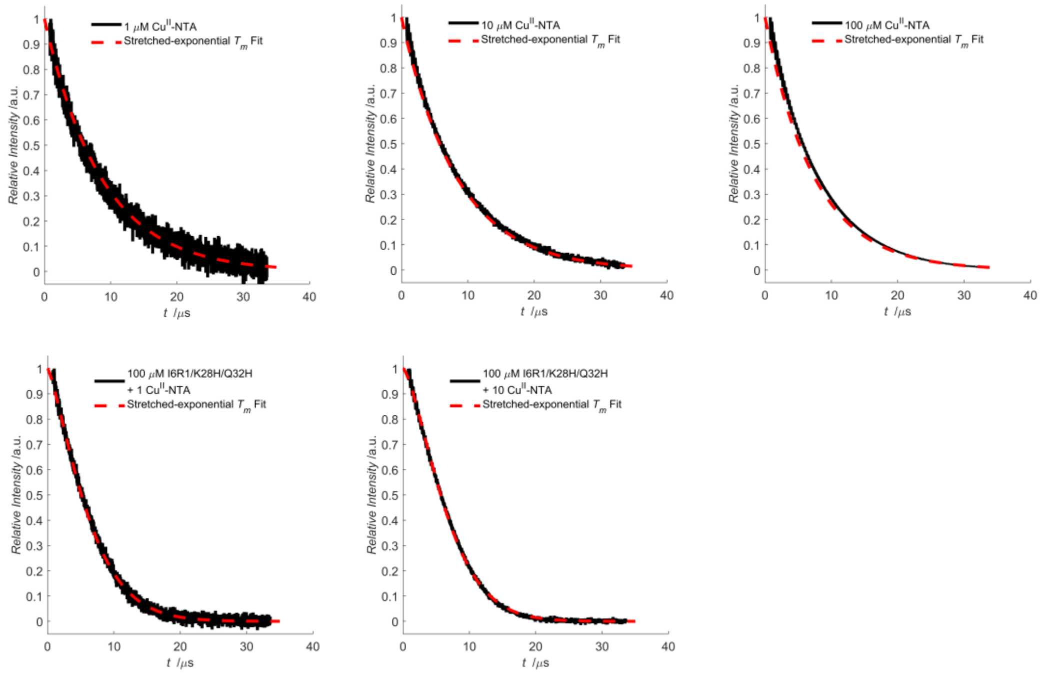

Figure 4.3.5.1.2. Two-pulse electron spin echo decay data for 1, 10 and 100 µM $\mathrm{Cu^{II}}$-NTA (top row), and 1 and 10 µM $\mathrm{Cu^{II}}$-NTA in presence of 100 µM I6R1/K28H/Q32H GB1 shown left-to-right, respectively. The experimental data is shown in black, with the fitted stretched exponential functions shown as red dotted lines.

Sample	T_m Estimate [µs]	Stretch Exponent	1/e time [µs]	0.5 × $(1/e)^2$ time [µs]
1.0 µM $\mathrm{Cu^{II}}$-IDA	10.5	1.00	11.6	11.4
10 µM $\mathrm{Cu^{II}}$-IDA	11.1	1.02	11.8	11.1
100 µM $\mathrm{Cu^{II}}$-IDA	10.6	1.07	11.0	10.4
100 µM I6R1/K28H/Q32H + 1.0 µM $\mathrm{Cu^{II}}$-IDA	6.1	1.23	6.6	5.6
100 µM I6R1/K28H/Q32H + 10 µM $\mathrm{Cu^{II}}$-IDA	6.8	1.41	7.1	5.6

Table 4.3.5.1.1: Stretched exponential T_m estimates for the $\mathrm{Cu^{II}}$-IDA control series shown in figure 4.3.5.1.1.

Sample	T_m Estimate [µs]	Stretch Exponent	1/e time [µs]	0.5 × $(1/e)^2$ time [µs]
1.0 µM $\mathrm{Cu^{II}}$-NTA	8.6	1.00	8.2	11.1
10 µM $\mathrm{Cu^{II}}$-NTA	8.3	1.00	8.6	8.7
100 µM $\mathrm{Cu^{II}}$-NTA	7.4	1.00	8.0	7.8
100 µM I6R1/K28H/Q32H + 1.0 µM $\mathrm{Cu^{II}}$-NTA	6.8	1.30	7.1	5.7
100 µM I6R1/K28H/Q32H + 10 µM $\mathrm{Cu^{II}}$-NTA	7.3	1.43	7.5	5.9

Table 4.3.5.1.2: Stretched exponential T_m estimates for the $\mathrm{Cu^{II}}$-NTA control series shown in figure 4.3.5.1.2.

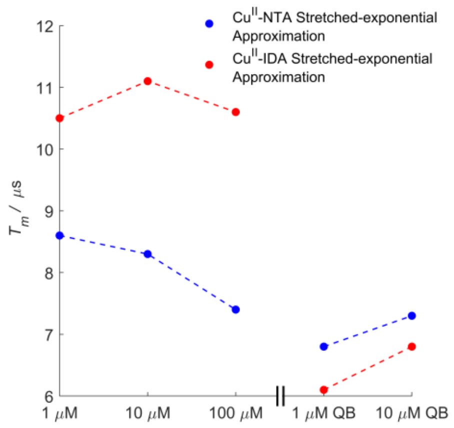

Figure 4.3.5.1.3. An overlay of the approximations of T_m from the 2-pulse electron spin-echo data shown in figures 4.3.5.1.1-2. The Cu^{II}-NTA and Cu^{II}-IDA series are shown in blue and red, respectively. QB indicates the Cu^{II}-chelate is quantitatively double-histidine bound.

Differences in T_m between free and dH bound Cu^{II}-NTA were found to be negligible, (figure 4.5.3.1.3 blue trace) while T_m of free and dH bound Cu^{II}-IDA varied by approximately 2-fold (figure 4.3.5.1.3 red trace). Free Cu^{II}-chelate has a slower rate of transverse dephasing (T_m) compared to double-histidine bound Cu^{II}-chelate. This difference in phase memory time may be explained by considering that the double-histidine bound component has greater connectivity to the protonated protein framework, and thus dephasing through proton-driven spin-diffusion will be more severe. Conversely, free component is surrounded by the deuterated solvent bath, extending the relative lifetime of electron coherence. Even so, modulation depths were approximated to be independent of transverse relaxation, which is justified by considering that RIDME experiments were performed using a total dipolar evolution time of 3.8 μs, and this time window is sufficiently short to approximate the transverse relaxation behaviour of free and double-histidine bound Cu^{II}-chelate to be largely identical. However, results indicate that this approximation is unlikely to apply for all dipolar evolution times.

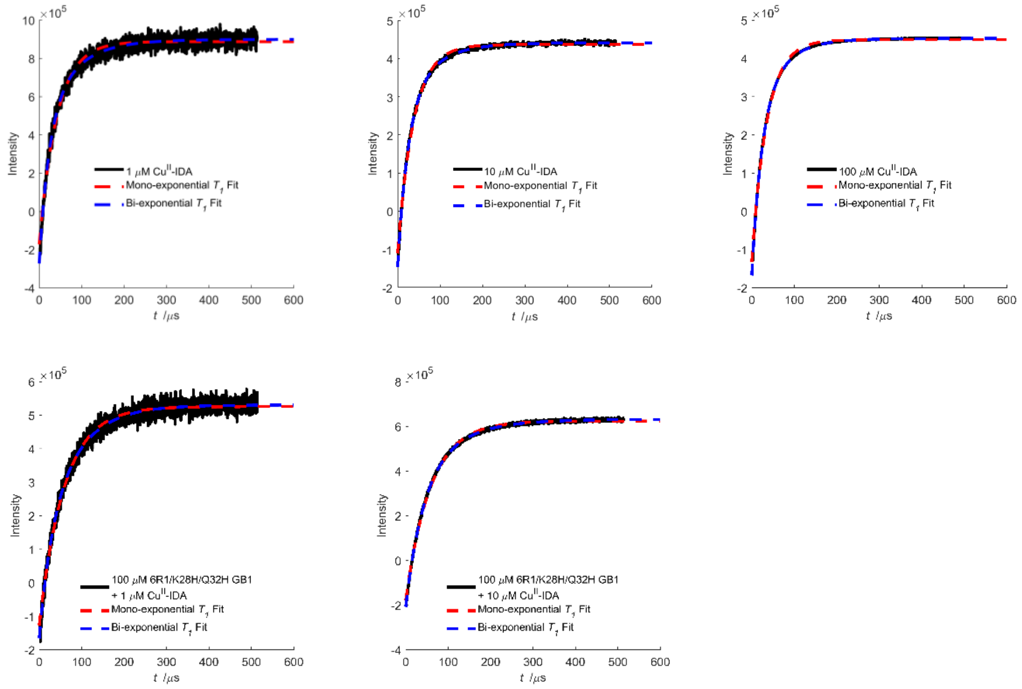

Figure 4.3.5.1.4. Inversion recovery data for 1, 10 and 100 µM Cu^{II}-IDA (top row), and 1 and 10 µM Cu^{II}-IDA in presence of 100 µM I6R1/K28H/Q32H GB1 shown left-to-right, respectively. The experimental data is shown in black, with the fitted mono-exponential and bi-exponential functions shown as red and blue dotted lines, respectively.

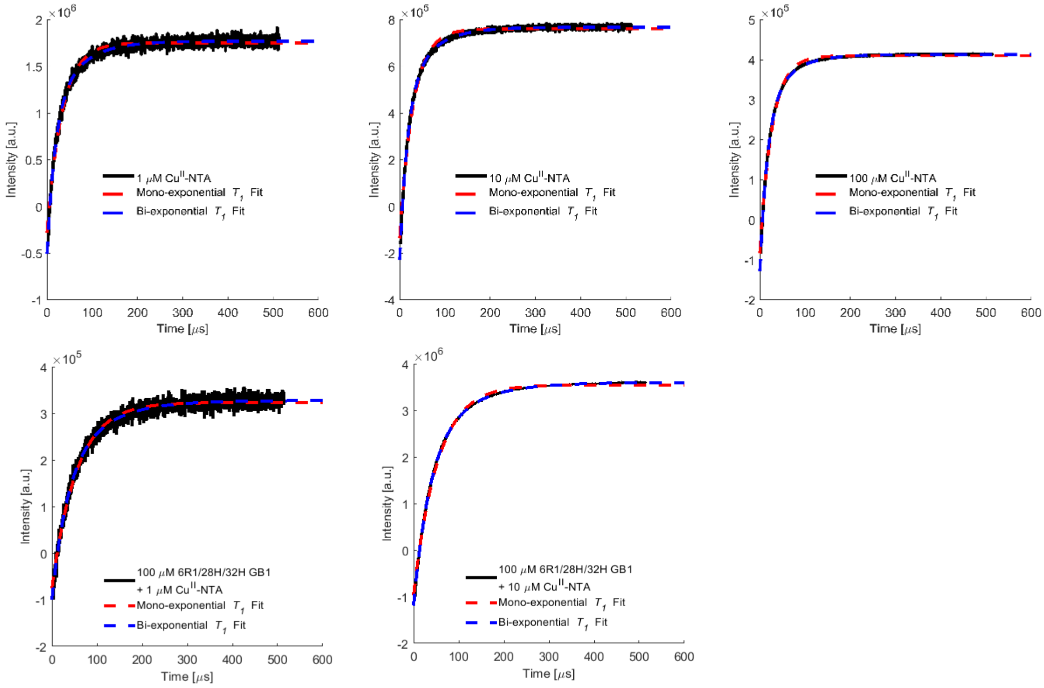

Figure 4.3.5.1.5. Inversion recovery data for 1, 10 and 100 µM Cu^{II}-NTA (top row), and 1 and 10 µM Cu^{II}-NTA in presence of 100 µM I6R1/K28H/Q32H GB1 shown left-to-right, respectively. The experimental data is shown in black, with the fitted mono-exponential and bi-exponential functions shown as red and blue dotted lines, respectively.

Sample	Mono-exponential T_1 [μs]	Bi-exponential T_{1A} / T_{1B} [μs]	Relative Contribution	1/e time [μs]	$0.5 \times (1/e)^2$ time [μs]
1.0 μM Cu^{II}-IDA	41.8 (0.977)	23.2 / 75.0 (0.983)	0.62 : 0.38	50.4	55.2
10 μM Cu^{II}-IDA	37.6 (0.995)	25.0 / 71.6 (0.998)	0.70 : 0.30	46.4	44.6
100 μM Cu^{II}-IDA	35.5 (0.997)	24.0 / 64.3 (1.00)	0.69 : 0.31	44.6	43.8
100 μM I6R1/K28H/Q32H + 1.0 μM Cu^{II}-IDA	59.2 (0.985)	28.1 / 76.8 (0.987)	0.36 : 0.64	67.2	61.2
100 μM I6R1/K28H/Q32H + 10 μM Cu^{II}-IDA	58.6 (0.998)	42.1 / 99.6 (1.00)	0.67 : 0.33	72.4	69.7

Table 4.3.5.1.3. Mono- and bi-exponential T_1 estimates, and 1/e time for each sample of the series shown in figure 4.3.5.1.4. R^2 values of each model are indicated in parentheses.

Sample	Mono-exponential T_1 [μs]	Bi-exponential T_{1A} / T_{1B} [μs]	Relative Contributions	1/e time [μs]	$0.5 \times (1/e)^2$ time [μs]
1.0 μM Cu^{II}-NTA	33.2 (0.980)	18.3 / 63.3 (0.987)	0.65 : 0.35	42.8	42.7
10 μM Cu^{II}-NTA	29.6 (0.991)	17.7 / 60.4 (0.998)	0.70 : 0.30	32.0	34.3
100 μM Cu^{II}-NTA	26.8 (0.994)	16.8 / 54.2 (1.00)	0.72 : 0.28	30.6	32.0
100 μM I6R1/K28H/Q32H + 1.0 μM Cu^{II}-NTA	54.9 (0.979)	32.6 / 87.2 (0.982)	0.56 : 0.44	68.8	66.6
100 μM I6R1/K28H/Q32H + 10 μM Cu^{II}-NTA	52.9 (0.998)	36.7 / 97.4 (1.00)	0.68 : 0.32	65.4	65.8

Table 4.3.5.1.4. Mono- and bi-exponential T_1 estimates, and 1/e time for each sample of the series shown in figure 4.3.5.1.5. R^2 values of each model are indicated in parentheses.

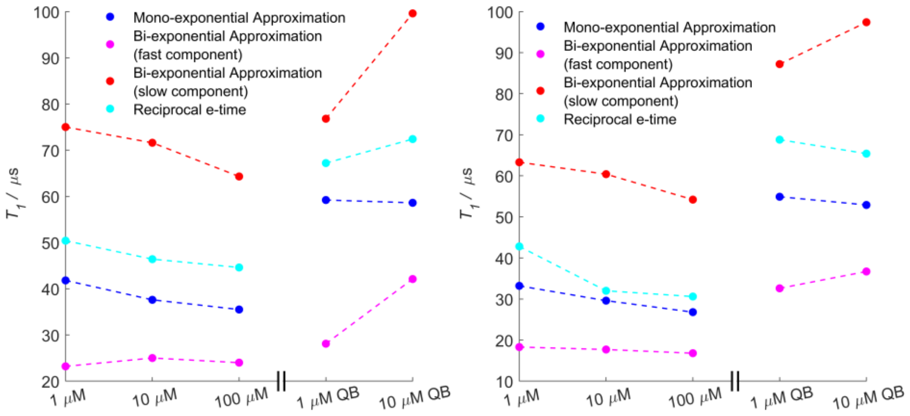

Figure 4.3.5.1.6. An overlay of the approximations of T_1 from the inversion recovery data shown in figures 4.3.5.1.4-5, for the Cu^{II}-IDA and Cu^{II}-NTA series in the left and right panels, respectively. QB indicates the Cu^{II}-chelate is quantitatively double-histidine bound.

Differential longitudinal relaxation behaviour between free and double-histidine bound Cu^{II}-chelate will more significantly impact accurate modulation depth quantitation, because a fast T_1 component can cause modulation depths at shorter mixing times to be over representative of the extent of double-histidine loading. For both chelates the longitudinal relaxation time of the bound Cu^{II}-chelate is slower than the free component (figure 4.3.5.1.6). At temperatures below 50 K diffusion processes and librational motion freeze out, however a free Cu^{II}-chelate interacting with the solvent lattice may experience a greater degree of vibrational perturbation, perhaps through breaking and reformation of co-ordinating hydrogen-bonds. A lattice in which thermal and vibrational motion is minimised leads to a reduced lattice-field, and should in principle give a longer T_1. Even at reasonably low concentrations of 10 µM Cu^{II}-chelate, upon quantitative double-histidine motif loading, the T_1 approximately doubles. Perhaps this phenomenon is attributable to a different composition of the surrounding lattice at the protein-solvent interface, compared to bulk solvent.

These differences in T_1 behaviour are partially addressed by varying mixing time length with respect to T_1, although sensitivity becomes limiting at sufficiently long mixing time intervals. Nevertheless, for all mixing times the trend in Δ was found to be consistent, without further treatment. Furthermore, the deviations of empirical T_1 values from the mono-exponential approximation were quantified by the deviation from the 1/e time by half of the $(1/e)^2$ time (table 4.3.5.4-5) and indicate that the mono-exponential condition is largely fulfilled for most cases.

4.3.5.2 Differential EPR Spectra

Whilst all nitroxides will to good approximation have identical EPR spectra and relaxation behaviour whether they are tethered to a protein with a free or occupied double-histidine motif this approximation is not well met for the Cu^{II}-based spins, as demonstrated in section 4.3.5.1 above. This means that in Cu^{II}-detected PD-EPR the ratio of free and double-histidine bound Cu^{II} does not only depend on their stoichiometric factors but also the exact position in the EPR spectrum that is detected, (i.e., if bound and free Cu^{II}-NTA differ in their EPR spectra, their contribution might not reflect their stoichiometry). Indeed, Cu^{II}-nitroxide PELDOR measurements were performed for both I6R1/K28H/Q32H and I6H/N8H/K28R1 GB1 in presence of 1.5 equivalents of Cu^{II}-IDA and Cu^{II}-NTA (figure 4.3.5.2.1-4). Associated background correction parameters are given overleaf in table 4.3.5.2.1. Detecting the maximum of the Cu^{II} spectrum (at 300 MHz higher frequency than the maximum of the NO spectrum) systematically yields a lower modulation depth than detecting the high field edge of the Cu^{II} spectrum (at 150 MHz higher frequency than the maximum of the nitroxide spectrum). This is attributed to different spectra and maxima of the two species.

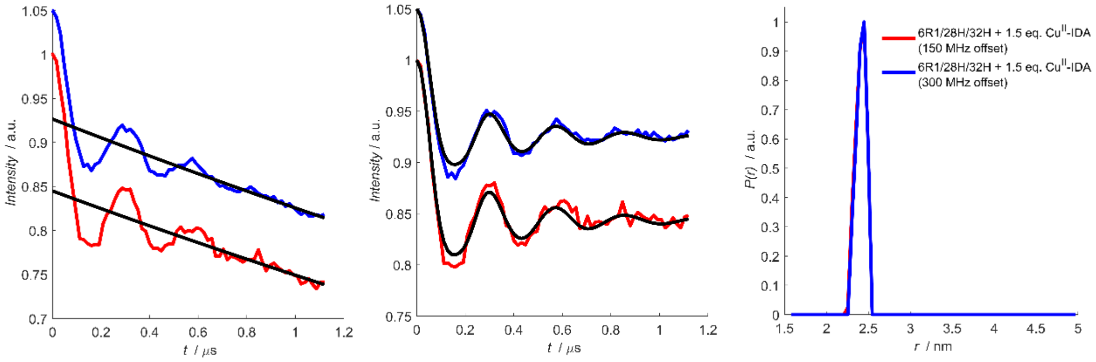

Figure 4.3.5.2.1: Plot of 6R1/28H/32H GB1 in presence of 1.5 equivalents of Cu^{II}-IDA measured with 150 and 300 MHz frequency offset, are shown as red and blue traces, respectively. The experimental trace, background corrected data, and distance distribution are shown left-to-right, respectively.

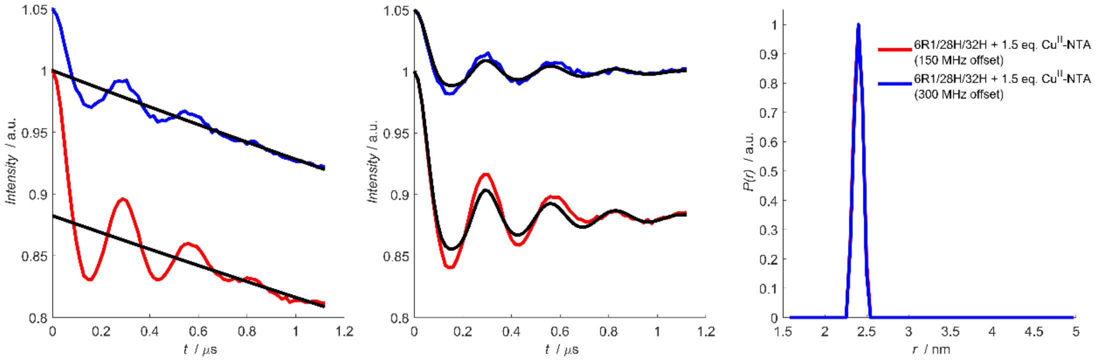

Figure 4.3.5.2.2: Plot of 6R1/28H/32H GB1 in presence of 1.5 equivalents of Cu^{II}-NTA measured with 150 and 300 MHz frequency offset, are shown as red and blue traces, respectively. The experimental trace, background corrected data, and distance distribution are shown left-to-right, respectively.

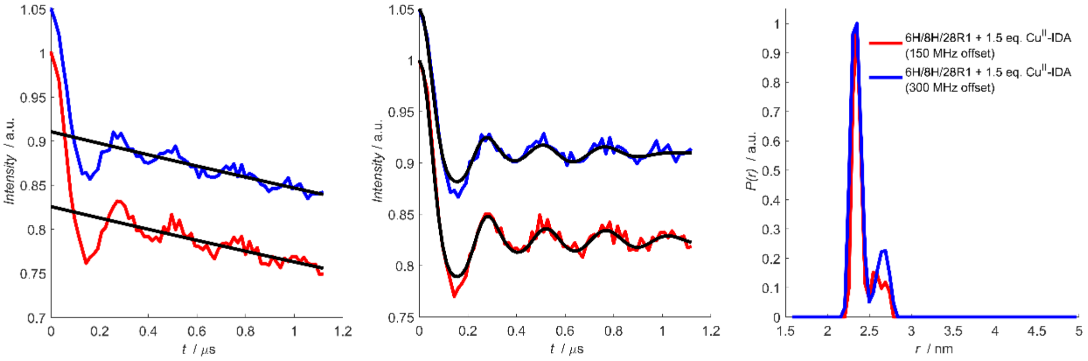

Figure 4.3.5.2.3: Plot of I6H/N8H/K28R1 GB1 in presence of 1.5 equivalents of Cu^{II}-IDA measured with 150 and 300 MHz frequency offset, are shown as red and blue traces, respectively. The experimental trace, background corrected data, and distance distribution are shown left-to-right, respectively.

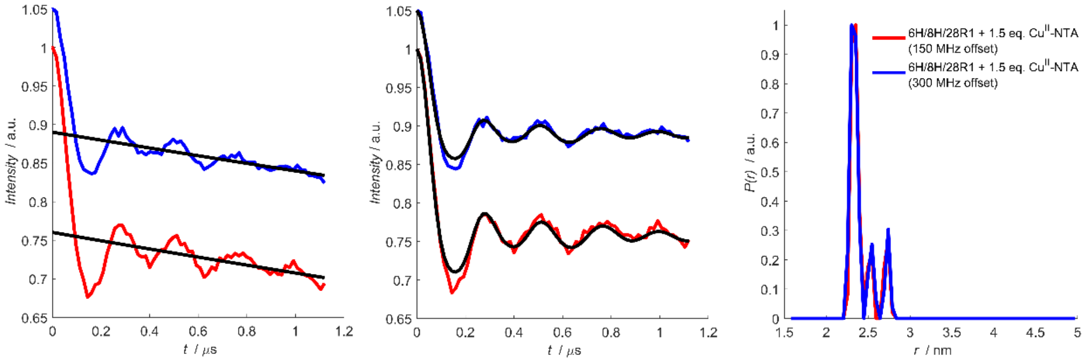

Figure 4.3.5.2.4: Plot of I6H/N8H/K28R1 GB1 in presence of 1.5 equivalents of Cu^{II}-NTA measured with 150 and 300 MHz frequency offset, are shown as red and blue traces, respectively. The experimental trace, background corrected data, and distance distribution are shown left-to-right respectively.

Sample	Zero-time (ns)	Background start (ns)	Background Cut-off (ns)	Δ
6R1/28H/32H GB1 + Cu^{II}-NTA (150 MHz offset)	341	328	1120	0.118
6R1/28H/32H GB1 + Cu^{II}-NTA (300 MHz offset)	341	328	1120	0.050
6R1/28H/32H GB1 + Cu^{II}-IDA (150 MHz offset)	339	328	1120	0.155
6R1/28H/32H GB1 + Cu^{II}-IDA (300 MHz offset)	339	328	1120	0.124
6H/8H/28R1 GB1 + Cu^{II}-NTA (150 MHz offset)	339	328	1120	0.240
6H/8H/28R1 GB1 + Cu^{II}-NTA (300 MHz offset)	340	328	1120	0.160
6H/8H/28R1 GB1 + Cu^{II}-IDA (150 MHz offset)	340	328	1120	0.174
6H/8H/28R1 GB1 + Cu^{II}-IDA (300 MHz offset)	338	328	1120	0.139

Table 4.3.5.2.1: Comparison of background correction parameters and modulation depths for the PELDOR traces shown in figures 4.3.5.2.1-4.

Previous literature values[30] and simulation of free and dH-bound Cu^{II}-chelate using Easyspin,[341] indicated g_{II} is smaller for the double-histidine bound, relative to the free component, resulting in greater excitation at lower offset, consistent with the observed trend in modulation depth. This is attributed to a higher spectral intensity of free relative to double-histidine bound Cu^{II} at the larger offset compared to the smaller offset, confounding quantification from Cu^{II}-detected PD-EPR. Easyspin simulations of the free- and dH-bound Cu^{II}-chelate component spectra at Q-band frequency (figure 4.3.3.2.5) were performed and simulation parameters are given in table 4.3.3.2.2. It is important to note that while the broad feature at low field in the free Cu^{II}-NTA absorbance spectrum is likely to be underdetermined, for qualitative support of the observed trend in modulation depth, the simulation is sufficient.

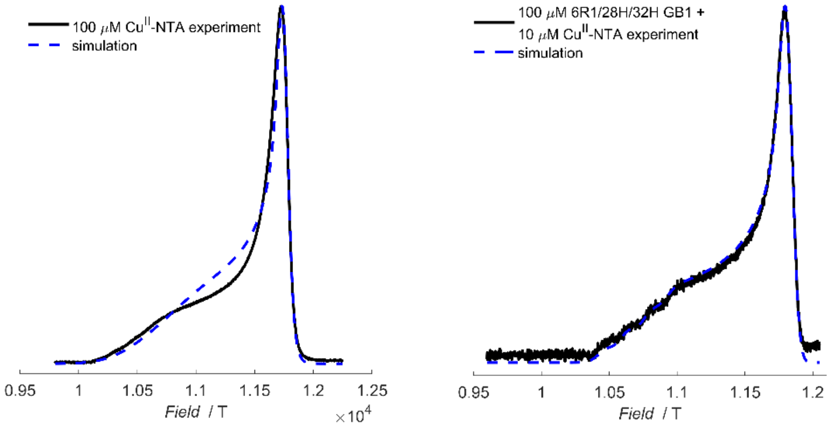

Figure 4.3.5.2.5: Absorbance spectra (echo-detected field sweep, EDFS) of 100 µM Cu^{II}-NTA (left panel) and 100 µM 6R1/28H/32H GB1 in presence of 10 µM Cu^{II}-NTA chelate (right panel), with experimental and simulated traces in black (solid) and blue (dotted), respectively.

Sample	g⊥	g‖	A‖ [MHz]	A⊥ [MHz]	A‖ strain [MHz]	A⊥ strain [MHz]	H‖ strain [MHz]	H⊥ strain [MHz]	Gaussian Linewidth [mT]	Simulation RMSD [a.u.]
100 µM Cu^{II}-NTA	2.0679	2.2867	27.932	570.00	-	-	20.436	1600	6.7800	3.00×10^{-2}
100 µM 6R1/28H/32H + 10 µM Cu^{II}-NTA	2.0216	2.2365	27.934	522.71	93.053	194.44	-	-	8.7129	1.94×10^{-2}

Table 4.3.5.2.2: Parameters of the simulated absorbance spectra shown in figure 4.3.5.2.5.

Since Cu^{II}-Cu^{II} RIDME also relies on detection of a Cu^{II}-chelate species, this could be problematic because measurement at two distinct field positions could yield different affinity estimates, and therefore not be robust. However, all RIDME measurements were performed using the maximum of the Cu^{II}-chelate spectrum as the detection position, which would commonly be the most desirable position (ignoring effects from angular correlations and orientation selection) to ensure a high SNR. Furthermore, we find that the affinities estimated from the Cu^{II}-Cu^{II} RIDME measurements closely align with previous estimates stated above. In our hands, detecting at the maximum of the Cu^{II}-chelate spectrum does not cause significant deviations in the apparent K_D, however this is not necessarily satisfied for all field positions.

4.3.5.3 Length of the Mixing Block Interval

Perhaps the furthest reaching implication of determining K_D via pulse EPR is that it allows the coupling of structural and binding equilibria information. Therefore, the aim should be to find a compromise wherein both modulation depth information and structural information can be reliably extracted. Here, using longer mixing times (i.e., 1.9 × T_1 as T_{mix}) yielded the best agreement of K_D estimates with previous Cu^{II}-nitroxide RIDME measurements, while still allowing reliable extraction of distance information. Taken together, this suggests that Cu^{II}-Cu^{II} RIDME measurements with longer mixing times (in the regime ~2 x T_1 as T_{mix}) allow for greater accuracy in K_D determination, despite the associated loss of a factor 2 in measurement sensitivity, and without compromising the reliability of the distance information extracted.

4.3.6 Error Analysis of RIDME Pseudo-Titrations and Modulation Depth Profiles

To check the reliability of the modulation depth profiles and K_D information extracted, error analysis of the RIDME pseudo-titrations was performed (as described in section 4.2.6). The previously reported Cu^{II}-NTA/nitroxide RIDME pseudo-titration series was taken as a benchmark. Modulation depth quotients were replotted as a function of Cu^{II}-NTA concentration, while indicating the ± 2σ error bars, and the corresponding weighted fitted value of K_D (figure 4.3.6.1 left panel). Importantly, the weighted fitted value of K_D is highly consistent with the value previously reported, within a factor 2; the gaussian approximation of the fitted one-dimensional inverse error surface as a function of K_D (figure 4.3.6.1 right panel) indicates a K_D value of 232 ± 130 nM. Applying this treatment to the tetra-histidine Cu^{II}-Cu^{II} RIDME pseudo-titrations is of interest, because relatively small errors in the estimation of T_1 can propagate a significant error in the calculation of Δ_{Tmix} for short mixing times.

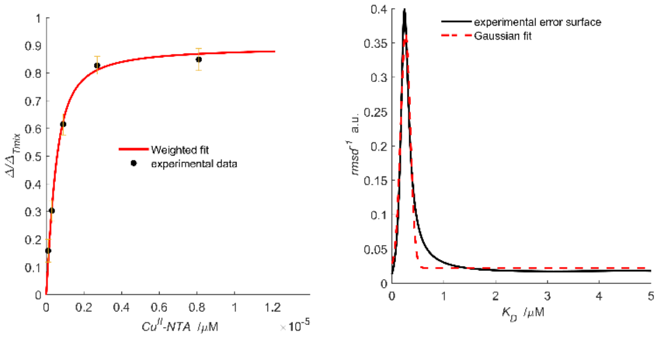

Figure 4.3.6.1: A weighted fitting of K_D, incorporating error bars for each experimental point. The weighted fitting is shown in the red trace, and the experimental data is shown in the black scatter (left). The reciprocal of the calculated root mean square deviation is shown as the black trace, and a fitted Gaussian of the data is shown in dotted red (right).

The Cu^{II}-Cu^{II} RIDME modulation depth quotients and errors for each T_{mix}-to-T_1 ratio are given below in tables 4.3.6.1-2, for stretched exponential and second-order polynomial background-correction models, respectively. Errors are relatively consistent, and typically reduce at longer mixing times, particularly at lower loading where sensitivity is limiting. Each series was fitted individually to determine the stability of the K_D values; weighted fittings were also performed for comparison. Results are summarily shown below in figures 4.3.6.2-4.3.6.3 for stretched exponential and second-order polynomial background-correction models, respectively. The unweighted- and weighted-fitted K_D values are given in tables 4.3.6.3-4, for stretched exponential and second-order polynomial background-correction models, respectively. It is observed that the K_D values differ by at least an order of magnitude in all cases, and only significantly deviate from expectation for the series recorded using a ratio of T_{mix} and T_1 of 0.7 This is expected since errors in modulation depth quotient are typically higher for these series.

Sample	Mixing time [μs]			$\Delta \times {\Delta_{Tmix}}^{-1}$		
100 μM 6H/8H/28H/32H + 50 μM Cu^{II}-NTA	35	65	95	0.075 ± 4.0 x 10^{-2}	-	0.038 ± 2.7 x 10^{-2}
100 μM 6H/8H/28H/32H + 70 μM Cu^{II}-NTA	33	61	89	0.135 ± 4.0 x 10^{-2}	0.102 ± 3.1 x 10^{-2}	0.092 ± 3.0 x 10^{-2}
100 μM 6H/8H/28H/32H + 100 μM Cu^{II}-NTA	35	65	95	0.276 ± 8.7 x 10^{-2}	0.211 ± 8.2 x 10^{-2}	0.223 ± 8.5 x 10^{-2}
100 μM 6H/8H/28H/32H + 170 μM Cu^{II}-NTA	32	59	86	0.800 ± 1.2 x 10^{-1}	0.687 ± 1.2 x 10^{-1}	0.713 ± 1.1 x 10^{-1}
100 μM 6H/8H/28H/32H + 500 μM Cu^{II}-NTA	29	53	77	0.544 ± 1.4 x 10^{-1}	0.480 ± 1.4 x 10^{-1}	0.505 ± 1.2 x 10^{-1}
100 μM 6H/8H/28H/32H + 1000 μM Cu^{II}-NTA	24	43	62	0.356 ± 6.5 x 10^{-2}	0.355 ± 6.7 x 10^{-2}	0.234 ± 9.6 x 10^{-2}

Table 4.3.6.1: Comparison of modulation depth quotients for series treated using a stretched exponential background function. The errors given in modulation depth quotient are ± 2σ.

Sample	Mixing time [μs]			$\Delta \times {\Delta_{Tmix}}^{-1}$		
100 μM 6H/8H/28H/32H + 50 μM Cu^{II}-NTA	35	65	95	0.052 ± 3.8 x 10^{-2}	-	0.024 ± 2.8 x 10^{-2}
100 μM 6H/8H/28H/32H + 70 μM Cu^{II}-NTA	33	61	89	0.107 ± 4.3 x 10^{-2}	0.085 ± 3.9 x 10^{-2}	0.073 ± 3.0 x 10^{-2}
100 μM 6H/8H/28H/32H + 100 μM Cu^{II}-NTA	35	65	95	0.269 ± 1.3 x 10^{-1}	0.165 ± 1.1 x 10^{-1}	0.190 ± 9.4 x 10^{-2}
100 μM 6H/8H/28H/32H + 170 μM Cu^{II}-NTA	32	59	86	0.796 ± 1.9 x 10^{-1}	0.679 ± 1.4 x 10^{-1}	0.668 ± 1.6 x 10^{-1}
100 μM 6H/8H/28H/32H + 500 μM Cu^{II}-NTA	29	53	77	0.481 ± 1.2 x 10^{-1}	0.422 ± 1.2 x 10^{-1}	0.479 ± 1.0 x 10^{-1}
100 μM 6H/8H/28H/32H + 1000 μM Cu^{II}-NTA	24	43	62	0.261 ± 6.2 x 10^{-2}	0.276 ± 6.1 x 10^{-2}	0.220 ± 6.7 x 10^{-2}

Table 4.3.6.2: Comparison of modulation depth quotients for series treated using a second-order polynomial background function. The errors given in modulation depth quotient are ± 2σ.

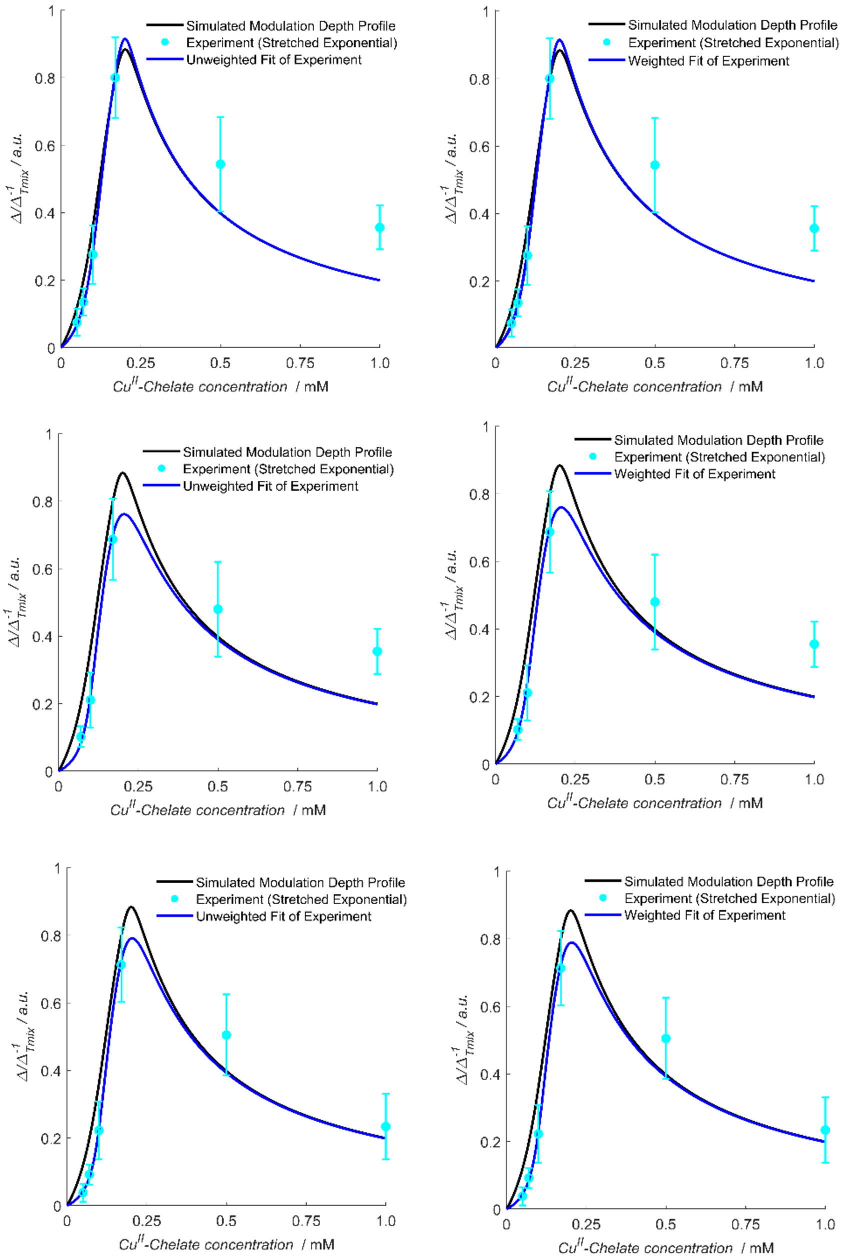

Figure 4.3.6.2: A comparative plot of the simulated modulation depth profile (black trace) and the corresponding unweighted (left) and weighted (right) fitted modulation depth profiles (blue traces) for each pseudo-titration series (background corrected using a stretched exponential function); ratios of 0.7, 1.3 and 1.9 between T_{mix} and T_1 are shown in the top, middle, and bottom rows respectively. Experimental data is also overlaid (cyan scatter), with the associated error bars.

Pseudo-titration Series	Ratio of T_{mix} and T_1 [a.u.]	K_D Values [μM]
Stretched Exponential Weighted Fit	0.7	0.76 ± 3.1, 0.037 ± 0 .036
Stretched Exponential Unweighted Fit	0.7	0.76 ± 3.1, 0.034 ± 0.035
Stretched Exponential Weighted Fit	1.3	7.46 ± 11.7, 0.229 ± 0.198
Stretched Exponential Unweighted Fit	1.3	7.38 ± 11.5, 0.184 ± 0.227
Stretched Exponential Weighted Fit	1.9	5.56 ± 7.6, 0.145 ± 0.123
Stretched Exponential Unweighted Fit	1.9	5.42 ± 7.6, 0.130 ± 0.107

Table 4.3.6.3: Comparison of weighted and unweighted fitted K_D values estimated from pseudo-titration series treated using a stretched-exponential background function.

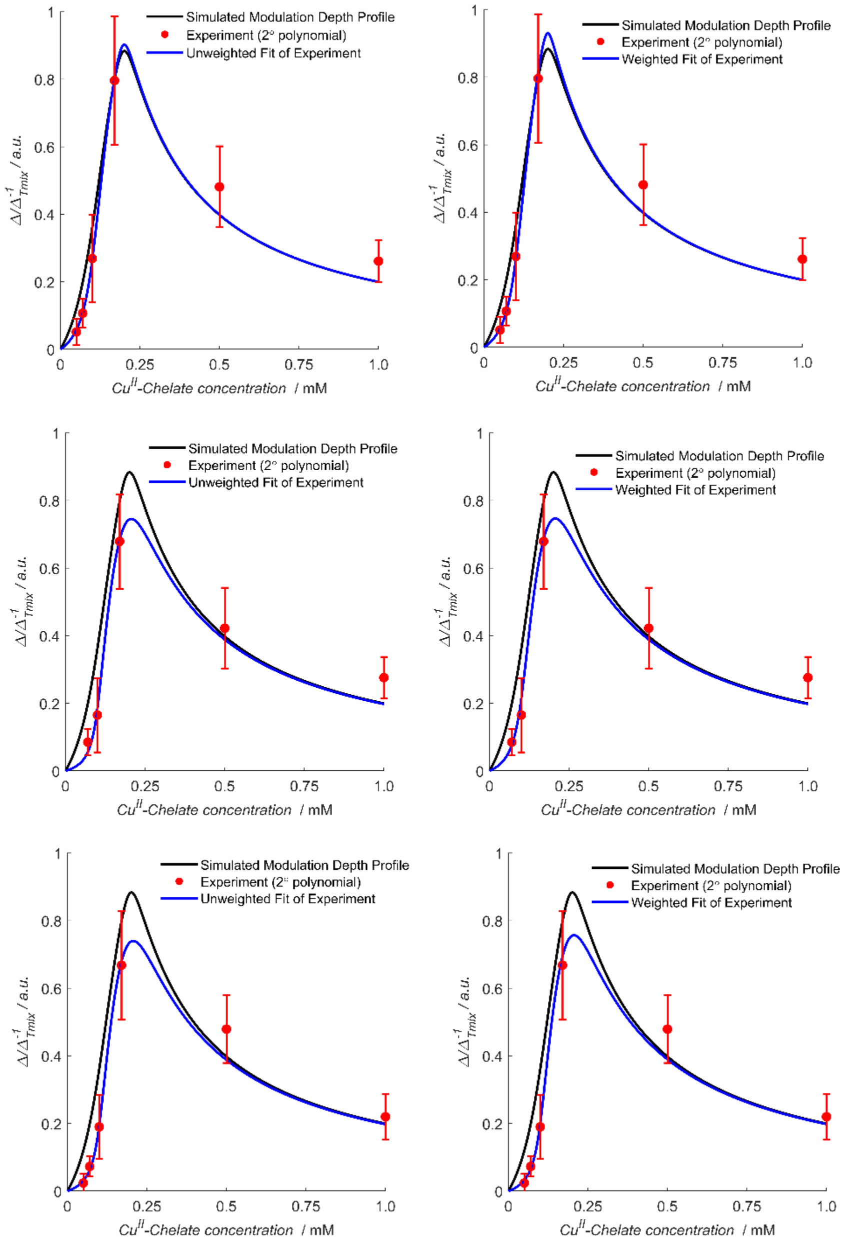

Figure 4.3.6.3: A comparative plot of the simulated modulation depth profile (black trace) and the corresponding unweighted (left) and weighted (right) fitted modulation depth profiles (blue traces) for each pseudo-titration series (background corrected using a second order polynomial function); ratios of 0.7, 1.3 and 1.9 between T_{mix} and T_1 are shown in the top, middle, and bottom rows respectively. Experimental data is also overlaid (red scatter), with the associated error bars.

Pseudo-titration Series	Ratio of T_{mix} and T_1 [a.u.]	K_D Values [μM]
Second Order Polynomial Weighted Fit	0.7	0.52 ± 4.7, 0.018 ± 0.053
Second Order Polynomial Unweighted Fit	0.7	1.0 ± 1.6, 0.038 ± 0.050
Second Order Polynomial Weighted Fit	1.3	8.5 ± 6.6, 0.191 ± 0.087
Second Order Polynomial Unweighted Fit	1.3	8.7 ± 6.6, 0.130 ± 0.092
Second Order Polynomial Weighted Fit	1.9	7.9 ± 6.5, 0.145 ± 0.139
Second Order Polynomial Unweighted Fit	1.9	9.1 ± 6.5, 0.157 ± 0.107

Table 4.3.6.4: Comparison of weighted and unweighted fitted K_D values estimated pseudo-titration series treated using a second-order polynomial background function.

Upon comparison of tables 4.3.6.3-4, it becomes apparent that the fitted pair of K_D values does not significantly change upon applying a weighting penalty to the experimental points. This is because the experimental points do not evenly influence the shape of the modulation depth profile, and this is especially true to the right of the maximum (see section 4.3.1 for discussion). While the K_D values determined for the lowest ratio of T_{mix} and T_1 (0.7) are consistently lower than the expected K_D values, the pseudo-titration series recorded with higher ratios of T_{mix} and T_1 yield values that are largely consistent with expectation from previous work, and are in-line with the simultaneous fitting of all series; indicating an order of magnitude difference in relative affinities, with low μM and high nM affinities respectively. This was also reflected by the 2D error contours for each series (data shown overleaf in figures 4.3.6.4-5).

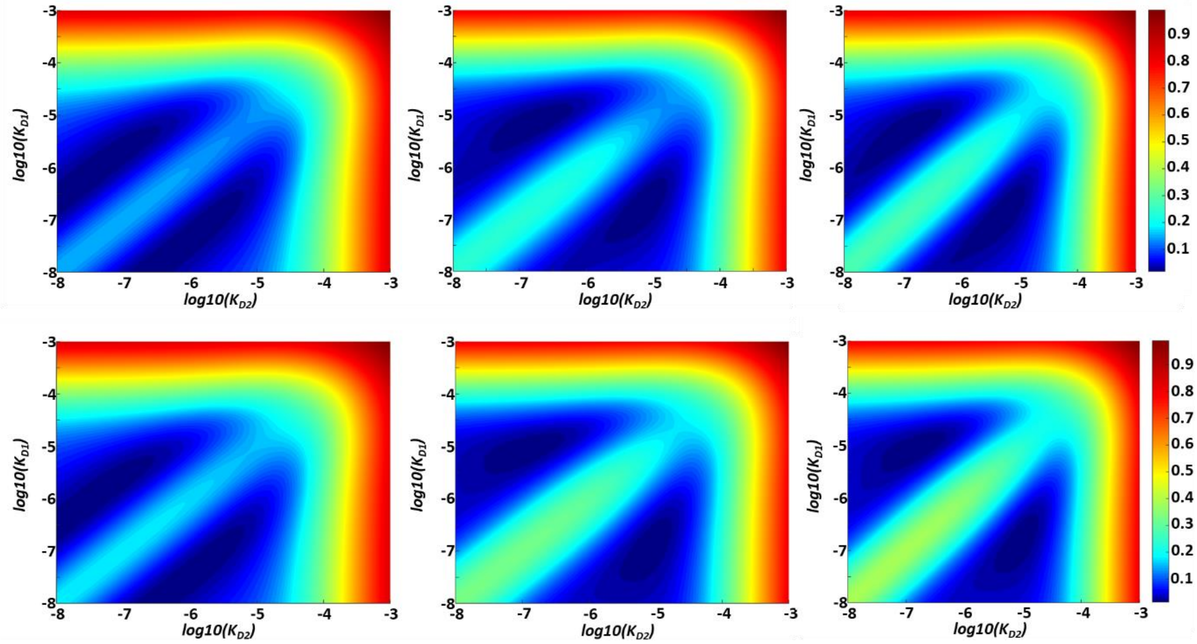

Figure 4.3.6.4: 2D unweighted error surfaces for the pseudo-titration series, using a stretched exponential background function (top row) or a second order polynomial background function (bottom row) and recorded with mixing times of 0.7, 1.3 and 1.9 × T_1 (left to right).

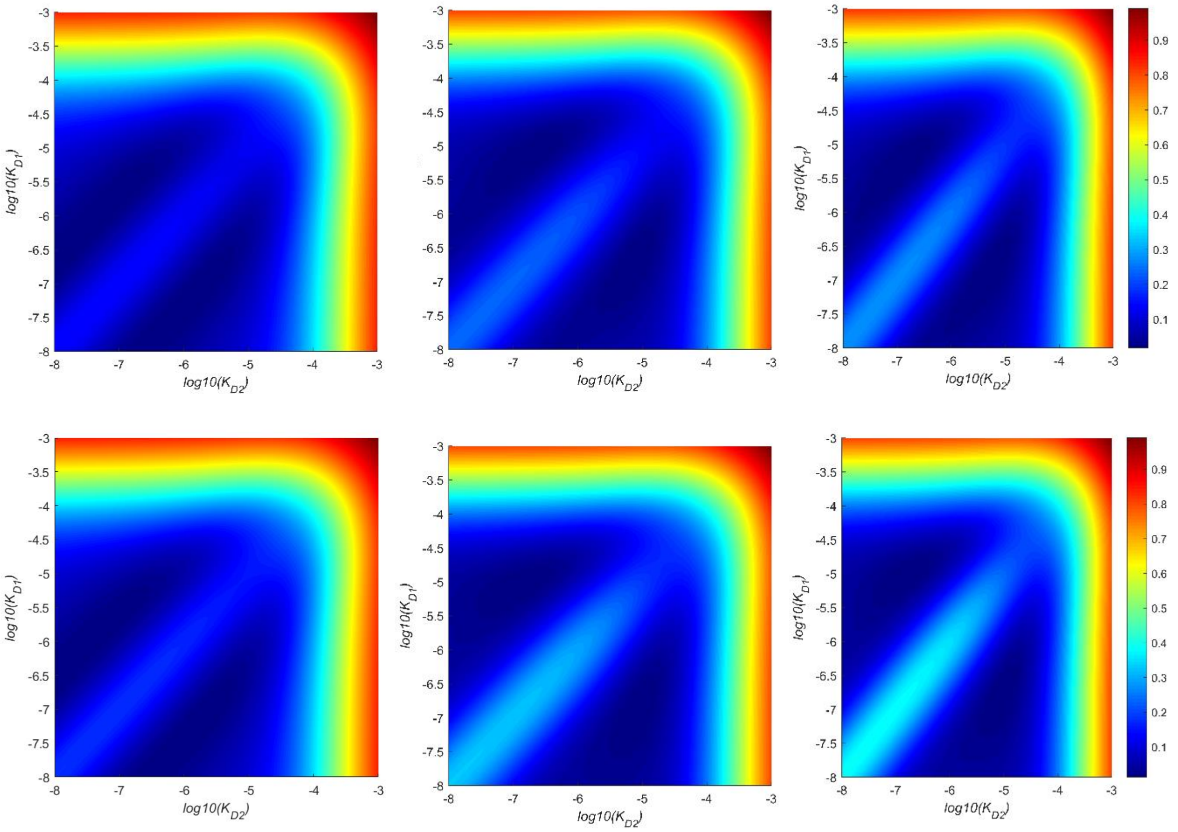

Figure 4.3.6.5: 2D weighted error surfaces for the pseudo-titration series, using a stretched exponential background function (top row) or a second order polynomial background function (bottom row) and recorded with mixing times of 0.7, 1.3 and 1.9 × T_1 (left to right).

Additionally, a global fitting approach was applied where individual mixing time series were fitted together, to check the stability of the K_D estimates. The expectation was that the fitted K_D values would be reflective of the series recorded with the highest T_{mix} to T_1 ratio since this should give the highest accuracy for K_D determination. Indeed, the global fitting (figure 4.3.3.6) leads to K_D estimates which are closely aligned with those fitted from the individual series, recorded with a mixing time of 1.9 × T_1. Estimates of K_D from the global fitting are given below in table 4.3.3.5, and the Gaussian fits of the corresponding error surfaces are given in appendix B. Furthermore, it was necessary to determine if Cu^{II}-nitroxide and Cu^{II}-Cu^{II} RIDME data could be used in concert, therefore a global fitting was performed of all Cu^{II}-Cu^{II} RIDME pseudo-titration data and previously obtained 500 nM Cu^{II}-nitroxide RIDME pseudo-titration data. Results of this combined fitting approach (figure 4.3.3.7) indicate that there are minimal changes to the fitted values from the Cu^{II}-Cu^{II} RIDME alone. This could lead to suggestion that using Cu^{II}-Cu^{II} RIDME is preferable to Cu^{II}-nitroxide RIDME, as it accesses more information than the latter approach, with respect to binding equilibria studies. However, the consistency of the global fitting across all series instils some faith as to the reliability of the K_D estimates.

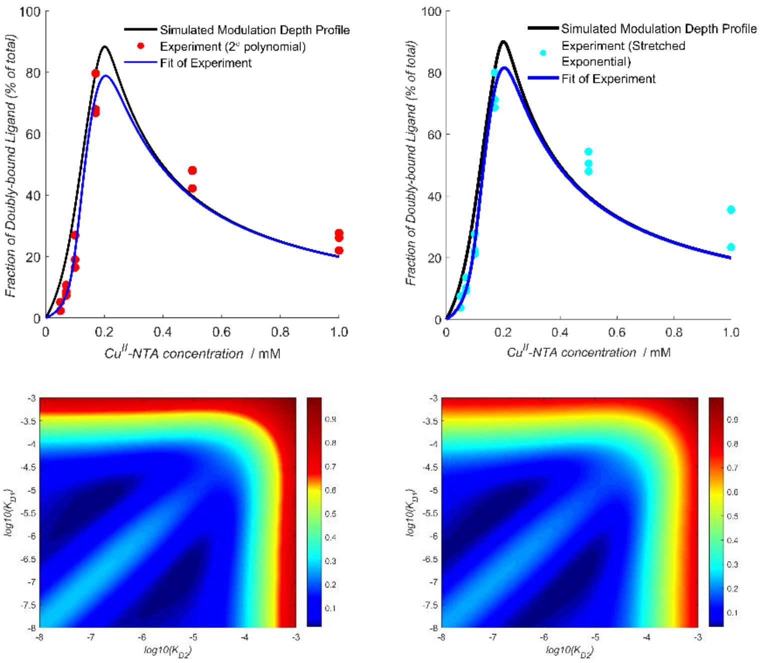

Figure 4.3.6.6. Top left) The experimental modulation depth quotients calculated using a second order polynomial background correction (red scatter), overlaid with the predicted modulation depth profile (black trace) and the associated fitted bivariate error function (blue trace). Top right) The experimental modulation depth quotients calculated using a stretched exponential background correction (cyan scatter), overlaid with the predicted modulation depth profile (black trace) and the associated fitted bivariate error function (blue trace). Bottom left) An error contour of the bivariate fitting of each dissociation constant to the experimental data shown in top left. Each dissociation constant varies 5 orders of magnitude from 10 nM to 1 mM. Bottom right) An error contour of the bivariate fitting of each dissociation constant to the experimental data shown in top right.

Pseudo-titration Series	K_D Values [μM]
Second Order Polynomial Background Model	0.126 ± 6.9 × 10^{-2}, 5.6 ± 7.6
Stretched Exponential Background Model	0.127 ± 6.6 × 10^{-2}, 4.0 ± 6.1

Table 4.3.6.5: Comparison of fitted K_D values estimated from pseudo-titration series treated using a second-order polynomial, and stretched exponential background function, respectively.

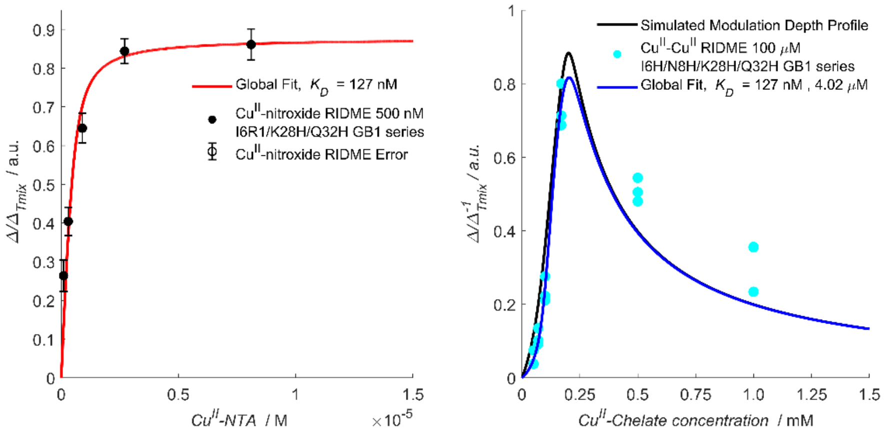

Figure 4.3.6.7: A global fit of both Cu^{II}-nitroxide and Cu^{II}-Cu^{II} RIDME pseudo-titrations shown in the left and right panels, respectively.

The pseudo-titrations performed at 25 and 75 µM protein concentration in the previous work were not included in the globally fitted K_D values. Rationale for omission of these series is provided in figure 3.3.12, as comparison of the error surfaces as a function of K_D showcases that only the 500 nM protein concentration series gives an unambiguous global minimum. The steepness of the error surface can be further contextualised as the resolution of the fitted hyperbolic function curvature, for a one-site Langmuir isotherm. Indeed, it was noted in the previous work that at all higher protein concentrations, the hyperbolic function behaved as a step function, making unambiguous estimation of the K_D difficult.

4.3.7 Influence of a Bi-exponential Approximation of T_1 on Modulation Depth Quotients:

As described in section 2.8, under the mono-exponential approximation of T_1, the asymptotic limit of modulation depth for a given ratio of mixing time (T_{mix}) and T_1, Δ_{Tmix} is defined as:

$$\Delta_{Tmix} = \left(\frac{\left(1 - exp\left(\frac{-T_{mix}}{T_1}\right)\right)}{2} \right) \tag{4.3.7.1}$$

Under the bi-exponential approximation of T_1 this can be rewritten as:

$$\Delta_{Tmix} = \left(\frac{\left(1 - \left[b \times exp\left(\frac{-T_{mix}}{T_1{}^{fast}}\right) + (1-b) \times exp\left(\frac{-T_{mix}}{T_1{}^{slow}}\right)\right]\right)}{2} \right) \tag{4.3.7.2}$$

where: $T_1{}^{fast}$ and $T_1{}^{slow}$ are the fast and slow components of the bi-exponential, and b is the weighted contribution of the fast component. Therefore, the bi-exponential approximation of T_1 influences the modulation depth quotient, and results are given for quotients of the 6H/8H/28H/32H GB1 pseudo-titration series under the mono- and bi-exponential approximations of Δ_{Tmix}, in tables 4.3.7.1 and 4.3.7.2, respectively. It is observed that the modulation depth quotients appear relatively stable regardless of the model used to approximate the T_1. This is consistent with strongly mono-exponential longitudinal relaxation behaviour across the pseudo-titration series, and is further confirmed upon comparison of the 1/e and 1/e^2 times, (in section 4.3.5.1). However, under the mono-exponential approximation of T_1 the modulation depth quotients are typically higher, particularly for shorter mixing times, primarily because the fast component is overfitted under this approximation. When the fast component is appropriately weighted under the bi-exponential approximation, the modulation depth quotient reduces.

Sample	Mixing time [μs]			$\Delta\times\,\Delta_{Tmix}{}^{-1}$ (mono-exponential)		
100 μM 6H/8H/28H/32H + 50 μM Cu^{II}-NTA	35	65	95	0.075	-	0.038
100 μM 6H/8H/28H/32H + 70 μM Cu^{II}-NTA	33	61	89	0.135	0.102	0.092
100 μM 6H/8H/28H/32H + 100 μM Cu^{II}-NTA	35	65	95	0.276	0.211	0.223
100 μM 6H/8H/28H/32H + 170 μM Cu^{II}-NTA	32	59	86	0.800	0.687	0.713
100 μM 6H/8H/28H/32H + 500 μM Cu^{II}-NTA	29	53	77	0.544	0.480	0.505
100 μM 6H/8H/28H/32H + 1000 μM Cu^{II}-NTA	24	43	62	0.356	0.355	0.234

Table 4.3.7.1: Modulation depth quotients for 6H/8H/28H/32H GB1 pseudo-titration series treated using a stretched exponential background function, and assuming a mono-exponential treatment of T_1 and Δ_{Tmix}.

Sample	Mixing time [μs]			$\Delta\times\,\Delta_{Tmix}{}^{-1}$ (bi-exponential)		
100 μM 6H/8H/28H/32H + 50 μM Cu^{II}-NTA	35	65	95	0.072	-	0.038
100 μM 6H/8H/28H/32H + 70 μM Cu^{II}-NTA	33	61	89	0.129	0.101	0.093
100 μM 6H/8H/28H/32H + 100 μM Cu^{II}-NTA	35	65	95	0.264	0.210	0.226
100 μM 6H/8H/28H/32H + 170 μM Cu^{II}-NTA	32	59	86	0.764	0.705	0.691
100 μM 6H/8H/28H/32H + 500 μM Cu^{II}-NTA	29	53	77	0.500	0.469	0.509
100 μM 6H/8H/28H/32H + 1000 μM Cu^{II}-NTA	24	43	62	0.322	0.343	0.234

Table 4.3.7.2: Modulation depth quotients for 6H/8H/28H/32H GB1 pseudo-titration series treated using a stretched exponential background function, and assuming a bi-exponential treatment of T_1 and Δ_{Tmix}.

For completeness, calculated modulation depth quotients, under the bi-exponential approximation of T_1, were fitted to a pair of dissociation constants and the results were compared with the values determined under the mono-exponential approximation (figure 4.3.7.1). K_D values determined under the mono- and bi-exponential approximation of T_1, are given in columns 2 and 3 of table 4.3.7.3, respectively. Comparison shows that the variability of K_D values across the different ratios of T_{mix} to T_1 is lower when using the bi-exponential approximation.

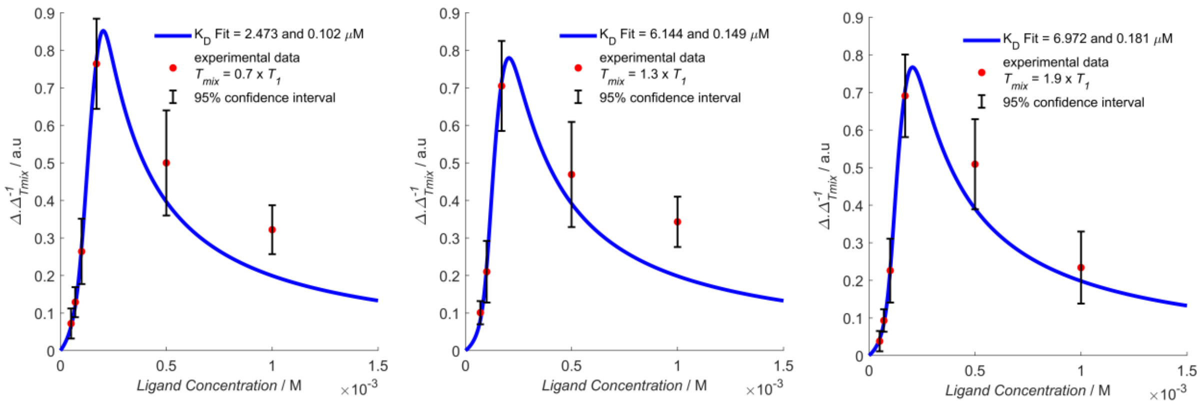

Figure 4.3.7.1: Fits of the experimental pseudo-titrations under the bi-exponential approximation of T_1 for different ratios of mixing time and T_1.

Ratio of T_{mix} and T_1 [a.u.]	Fit K_D values (mono-exponential) [μM]	Fit K_D values (bi-exponential) [μM]
0.7	0.76, 0.034	2.47, 0.102
1.3	7.38, 0.184	6.14, 0.149
1.9	5.42, 0.130	6.97, 0.181

Table 4.3.7.3: K_D values estimated from modulation depth quotients for different ratios of mixing time and T_1 calculated using a mono- and bi-exponential treatment of T_1, in the second and third columns, respectively.

4.4 Conclusion and Outlook

Our findings demonstrate that modulation depth quantitation in a Cu^{II} homo-spin system *via* 5-pulse RIDME is feasible; binding equilibria information can be reliably obtained, and empirical observation agrees nicely with prediction from theory and the general multi-site binding model developed herein. Results indicate that while there is a reasonable uncertainty in the absolute affinities, their relative difference is pronounced, even at protein concentrations >2 orders of magnitude above K_D. Furthermore, the previously benchmarked method of K_D determination *via* 5-pulse RIDME can be extended to an analytical two-site independent binding model. Potential empirical considerations for modulation depth quantitation in double dH constructs have also been discussed. Even so, for future work a systematic treatment of how to optimise modulation depth quantitation and K_D determination from Cu^{II}-nitroxide and Cu^{II}-Cu^{II} 5-pulse RIDME pseudo-titrations is desirable.

Additionally, the results presented herein also showcase that dissociation constants can be investigated and derived for systems which are not amenable to thiol-based site-directed spin labelling with an organic radical spin label. This is significant because it expands the utility of this approach to proteins containing essential cysteine residues. However, it should be acknowledged that this approach cannot assign affinities to individual sites. Nonetheless, the further confirmation of high nM and low μM affinities of α-helical and β-sheet dH motif sites for Cu^{II}-NTA, respectively, holds promise for their future widespread application in the field of PD-EPR. The mathematical model derived above can be appropriated to solve sensitivity optima and maximise labelling efficiency for coordination-based spin labelling strategies, governed by binding equilibria. This may be especially useful in cases where binding affinity or protein concentration is limiting.

Finally, while the mathematical description of optimising double-histidine motif loading and sensitivity for a given K_D pair and protein concentration is important, the model does not address how to optimise sample conditions to afford the highest binding affinity in the first place. While buffer conditions were recently optimised for double-histidine motif labelling, and the influence of pH upon formation of Cu^{II}-chelates has been characterized by CW-EPR previously, current literature has not shown how pH variations influence binding at double-histidine motif sites, particularly under cryogenic temperatures. Similarly, current literature has not addressed competition for double-histidine motifs by adventitious divalent metal ions, and so warrants investigation to inform the robustness of the spin labelling strategy. These considerations form the motivation for the next results chapter.

CHAPTER 5: Influence of Competitor Ions and pH on Cu^{II} Labelling of Double Histidine Motifs

This chapter has the following contributions. Dr Katrin Ackermann purified and labelled the model protein for EPR measurements. JLW expressed and purified the model protein for ITC measurements, prepared the EPR samples, performed the EPR measurements, processed the data, and performed UV-vis measurements. Dr Swati Arya and Dr Alan Stewart assisted with ITC measurements. Dr Bela Bode designed the experiments and assisted with the data analysis. The results of this chapter have been peer reviewed, and published online in similar form: J. L., Wort, S., Arya, K. Ackermann, A. J., Stewart, and B. E., Bode, *J. Phys. Chem. Lett.,* **12**, 2815-2819, DOI: https://pubs.acs.org/doi/full/10.1021/acs.jpclett.1c00211.

5.1 Introduction

PD-EPR is a powerful tool that complements X-ray crystallography, NMR, cryo-EM and FRET data by providing structural insight outwith crystallization, size-limitation, or structurally perturbative labels. Hence, it has been applied to characterise conformational equilibria,[61] oligomerisation state,[76,181] complexation and binding events,[67–70] and competing structural models.[62] Cysteine residues are typically covalently modified,[12] as for MTSL and the R1 sidechain,[9] though this strategy is suboptimal in systems containing essential cysteine residues, non-permissive to post-translational reduction. In this purview, Cu^{II}-based genetically-encodable self-assembling spin labels using double-histidine motifs have emerged as an alternative labelling strategy.[148,241] Additionally, the bipedal mode of Cu^{II}-chelate attachment at the double-histidine motif results in significantly improved precision and accuracy in the distance domain. Cu^{II}-NTA spin labelling of double histidine motifs for PD-EPR has been applied successfully to enzymes,[242] metalloproteins,[326] and nucleoprotein complexes.[237]

Recent studies to optimise spin labelling efficiency using double-histidine motifs in conjunction with Cu^{II}-based spin labels have proven fruitful.[73,243] However, optimization of the spin labelling approach remains non-trivial, because the non-covalency of the interaction predisposes sensitivity to variations in binding affinity. For instance, phosphate buffer was recently shown to enhance double-histidine motif labelling efficiency with Cu^{II}-NTA, while tris buffer was shown to degrade labelling efficiency. Furthermore, while the influence of pH upon formation of Cu^{II}-chelates has been characterized by CW-EPR previously, current literature has not shown how pH variations influence binding at the double-histidine motif, particularly under cryogenic temperatures. This is an important distinction, since the protonation equilibrium may be sensitive to temperature, and thus vary considerably when compared with room-temperature measurements. Similarly, current literature has not addressed competition for double-histidine motif sites by adventitious divalent metal ions in a systematic fashion, and so warrants investigation.

In the current study, GB1 constructs (I6R1/K28H/Q32H (figure 5.2.1.1. left) and K28H/Q32H (figure 5.2.1.1. right)) were used as biological model systems, in Cu^{II}-nitroxide RIDME pseudo-titrations, and

ITC measurements, respectively. Results demonstrate double-histidine motif spin labelling using Cu^{II}-NTA is robust against the competitor ligand Zn^{II}-NTA at >1000-fold molar excess, and that a dissociation constant for the competitor ligand determined by RIDME shows excellent agreement with ITC measurements. Additionally, high nM binding affinity is surprisingly retained under acidic and basic conditions even though room temperature affinity shows a stronger pH dependence. This indicates the strategy is well-suited for diverse biological applications, particularly metalloproteins with divalent metal ion cofactors. Lastly, we use UV-vis measurements of Cu^{II}-IDA spin label prepared under different conditions, including in presence of imidazole, to optimise this spin label for quantitative pulse dipolar EPR applications.

5.2 Materials and Methods

5.2.1 Construct Design, Expression and Purification

Constructs of GB1 were designed, expressed and purified as previously described.[70,170] For completeness, the protein sequences for the K28H/Q32H and I6C/K28H/Q32H GB1 constructs are given below in figures 5.2.1.1 and 5.2.1.2, respectively. The positions of the cysteine and double-histidine motif are indicated in cyan and green, respectively.

K28H/Q32H GB1 Protein Sequence:

28 32

MQYKLILNGKTLKGETTTEAVDAATAEHVFKHYANDNGVDGEWTYDDATKTFTVTE

Figure 5.2.1.1. Full amino-acid sequence for the K28H/Q32H GB1 construct used in this work, with each histidine residue of the double-histidine motif shown in green; and residue number indicated above the sequence.

I6C/K28H/Q32H GB1 Protein Sequence:

6 28 32

MQYKLCLNGKTLKGETTTEAVDAATAEHVFKHYANDNGVDGEWTYDDATKTFTVTE

Figure 5.2.1.2. Full amino-acid sequence for the I6C/K28H/Q32H GB1 construct used in this work, with the cysteine residue shown in cyan and each histidine residue of the double-histidine motif shown in green; and residue numbers indicated above the sequence.

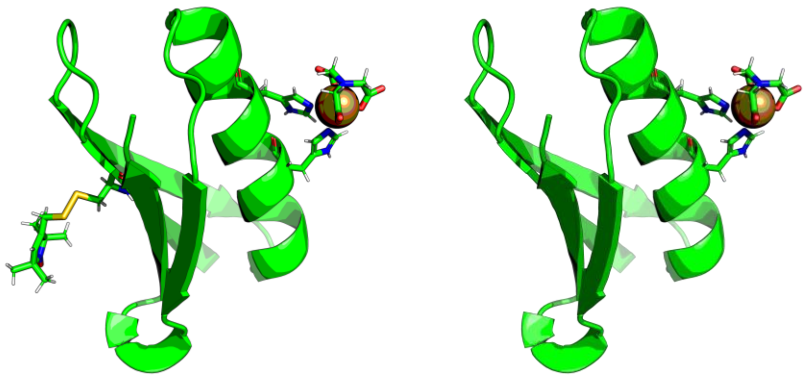

Figure 5.2.1.3. left panel) Cartoon representation of the I6R1/K28H/Q32H GB1 construct, with the R1 nitroxide and Cu^{II}-NTA spin labels shown in stick representation. right panel) Cartoon representation of the K28H/Q32H GB1 construct, with the Cu^{II}-NTA shown in stick representation.

5.2.2 Pulse EPR Sample Preparation

All material was exchanged into pH-adjusted deuterated buffer A (42.4 mM Na$_2$HPO$_4$, 7.6 mM KH$_2$PO$_4$, 150 mM NaCl) by first freeze-drying and then re-dissolving in D$_2$O. For Q-band RIDME samples of 6R1/28H/32H GB1, a total volume of 70 μL was used, with protein concentrations of 1, 2, or 5 μM as stated. All EPR samples were frozen by direct immersion into liquid nitrogen. Zn^{II}-NTA and Cu^{II}-NTA stock solutions were prepared as previously described; and for labelling, Zn^{II}-NTA and Cu^{II}-NTA stock solutions with nominal concentrations of 100 and 10 mM were used, respectively.

5.2.3 Metal Chelate Spin Label Preparation

For preparation of all metal-NTA labels: Cu^{II}-NTA, Ni^{II}-NTA and Zn^{II}-NTA, $NiCl_2$, $ZnCl_2$, $CuCl_2$ and NTA were weighed in a glove-box and aliquoted into 1.5 mL reaction tubes. Stock solutions of 100 mM were prepared as previously described.[297] Complete dissolution was ensured by vortexing until solutions were clear of precipitate. For the optimisation of Cu^{II}-IDA preparation, solutions of Cu^{II}-IDA spin labels were prepared *via* three distinct methods, i) mixed in a 1:1 equivalence, producing a solution of Cu^{II}-IDA with nominal concentration of 50 mM, before being diluted in milliQ H_2O, ii) mixed in a 1:1 equivalence before dilution with buffer A (150 mM NaCl, 42.4 mM Na_2HPO_4, 7.6 mM KH_2PO_4, pH 7.4), and iii) IDA stock solution was added in 1:8 equivalence with buffer, before addition of 1 equivalent of $CuCl_2$. A dilution series of 20, 10, 5, 2.5 and 1 mM Cu^{II}-IDA was prepared. To simulate spin label loading of protein double-histidine motifs, absorbance spectra were also recorded for the Cu^{II}-IDA dilution series in presence of two equivalents of imidazole. A stock solution of 200 mM imidazole was prepared in buffer A and subsequently diluted upon addition to pre-neutralised 50 mM Cu^{II}-IDA stock solution to 100 mM. Further dilution with buffer yielded the nominal concentrations given above.

5.2.4 Mass Spectrometry

Mass spectrometry data was collected in-house using a Sciex MALDI TOF/TOF 4800 mass-spectrometer, with samples crystallised using a matrix of α-cyano-4-hydroxycinnamic acid. I6R1/K28H/Q32H and K28H/Q32H GB1 samples were both prepared at 20 μM concentration in buffer A (42.4 mM Na_2HPO_4, 7.6 mM KH_2PO_4, 150 mM NaCl, pH 7.4), and mass spectra were recorded in the absence of Cu^{II}-chelate.

5.2.5 Pulse EPR Measurements

All pulse EPR experiments were performed using a Bruker ELEXSYS 580 pulse EPR spectrometer. Temperatures were maintained using a cryogen-free variable temperature cryostat (Cryogenic Ltd) operating in the 1.8-300 K temperature range. All measurements of the electron spin longitudinal relaxation times (T_1) of Cu^{II}-NTA, and all 5-pulse dead-time free RIDME measurements were performed at 30 K, using a high-power 150 W travelling-wave tube (TWT; Applied Systems Engineering) at Q-band (34 GHz) in a critically coupled 3 mm cylindrical resonator (Bruker ER 5106QT-2w in TE012 mode).

All RIDME measurements were performed as 6-point pseudo-titration series. Detection pulse lengths of 12 and 24 ns (π/2 and π) and a detection position at the maximum of the nitroxide spectrum. Unless otherwise stated, each trace was acquired using an SRT of 30 ms, a tau of 400 ns, with 122 points, 2 shots-per-point, and varying number of scans, as stated. Deuterium ESEEM was suppressed using a 16-step tau-averaging cycle,[298] and unwanted echoes were suppressed using an 8-step phase cycle, for a total of 128 steps per scan. Each measurement was acquired with a short (T_{ref}) and long (T_{mix})

mixing time, of 5 and 200 μs to allow suppression and observation of the dipolar coupling, respectively. Deconvoluted RIDME data was background corrected assuming a stretched exponential background function, with dimension 3-6. Data was processed and validations were performed using DeerAnalysis2018.[215] Background dimension and start-time parameters for data processing were determined by an initial validation, consisting of 56 trials; 8 iterations of background start position (between 5-30% of the total RIDME trace length), and 7 iterations of background dimension (between 3-6 in increments of 0.5). Subsequently, a second round of validations was performed. A total of 896 trials were performed for the second validation round, consisting of 16 white noise iterations (noise level of 1.5), 8 iterations of background start position (between 5-30% of the total RIDME trace length), and 7 iterations of background dimension (between 3-6 in increments of 0.5). These validation trials were also pruned, where trials exceeding the RMSD of the global minimum by ≥15% were discarded.

All inversion recovery measurements were performed using detection pulse lengths of 16 and 32 ns (π/2 and π), and an inversion π-pulse length of 32 ns. The detection position was consistently placed at the maximum of the Cu^{II}-NTA spectrum. Unless otherwise stated, each trace was acquired using an SRT of 2 ms, with 2560 points, 25 shots-per-point, and 1-5 scans, as stated. A τ of 800 ns was used, with an approximate time-window length of 500 μs, incremented in steps of 200 ns.

5.2.6 Isothermal Titration Calorimetry Measurements

All isothermal titration calorimetry experiments used a Malvern MicroCal ITC200 instrument, and were optimised and performed over 19 injections of 2 μL titrant, with an equilibration time of 120 seconds between injections, at 298 K. All samples were centrifuged immediately before measurement for degassing. For the Zn^{II}-NTA and Ni^{II}-NTA measurements, K28H/Q32H GB1 concentration was 800 μM, and titrant concentration was 12 mM. For the variable pH measurements, K28H/Q32H GB1 concentration was 75 μM and titrant concentration was 2.5 mM. Blank conditions of either buffer A (42.4 mM Na_2HPO_4, 7.6 mM KH_2PO_4, 150 mM NaCl, pH 7.4) titrated against addition of 12 mM titrant, or pH adjusted buffer A titrated against addition of 1.0 or 2.0 mM titrant, were recorded for the competitor and variable pH ITC measurements, respectively. Subtraction of the blank measurements from the raw data mitigated the heat of dilution. All data analyses were performed in MicroCal Origin 7 (OriginLab, Northampton, MA) and thermodynamic parameters were derived using a single-site fitting model.

5.2.7 UV-Visible Spectroscopy

All UV-visible absorbance spectra were recorded using a Jenway 6^7 series UV-vis spectrophotometer, in plastic cuvettes with a path length of 10 mm, in single-beam mode. All spectra are recorded at ambient temperature, and with a wavelength resolution of 1 nm, in the wavelength range 320-800 nm. Each sample was blanked before measurement, and all were repeated in triplicate. Data was processed using the Jenway 6^7-series software suite, and were exported to ASCII format for plotting and analysis in Matlab. For quantitation of Cu^{II}-IDA and Cu^{II}-NTA concentration, molar extinction coefficients of 62 M^{-1} cm^{-1} and 59 $M^{-1}cm^{-1}$ at 726 nm, and 800 nm were used, respectively, taken from previous literature.[70,297] For quantification of Ni^{II}-NTA concentration, a molar extinction coefficient of 5.47 $M^{-1}cm^{-1}$ at A_{620nm} and pH 4.4 was used.[342]

5.2.8 Parameters for Magnetic Susceptibility NMR Measurements

A solution of Ni^{II}-NTA dissolved in D_2O with nominal concentration 25 mM, and total volume of 4 mL was prepared for calibration against D_2O alone. Evans' method NMR[343] (1D proton) was performed using a Bruker AVIII 500 NMR spectrometer, with a carrier frequency of 500.13 MHz, and at a temperature of 295 K. Briefly, the Evans' method is an NMR technique used to assess magnetic susceptibility and determine whether species are paramagnetic. This is monitored as changes in chemical shift for solvent in presence and absence of the compound of interest, which can also inform the number of unpaired electrons. The NMR spectrum was acquired for 4 scans with an acquisition period of 4.96 seconds and was processed using TopSpin (Version 4.0.7). The effective magnetic moment was corrected for diamagnetic contributions originating from the NTA ligand.

5.3 Results and Discussion

5.3.1 Rationale for Model Competitor Ligand: Zn^{II}-NTA vs Ni^{II}-NTA

The choice of model competitor ligand was informed by several considerations, addressed in this section. The competitive binding model adapted to the Cu^{II}-nitroxide RIDME pseudo-titration in competition assay format is analogous to models that use radiolabelled competitor ligand. The non-competitor ligand is not radiolabelled, and so results in eventual decay of radioactivity. Here, the detected signal (dipolar modulation between pairs of paramagnets) ideally only manifests when Cu^{II}-NTA is bound, when the competitor ligand is diamagnetic (i.e., using Ni^{II}-NTA as a model competitor is immediately complicated because it is paramagnetic and both competitor and non-competitor ligand could theoretically contribute to the detected signal).

Additionally, while it has been established that the behaviour of R1 nitroxide moieties have stable longitudinal relaxation behaviour whether double-histidine motifs are occupied by Cu^{II}-NTA, this is unclear for Ni^{II}-NTA chelate and would have significant implications for subsequent modulation depth quantification. Let us assume that a nitroxide dipolarly coupled with a double-histidine motif occupied by Ni^{II}-NTA has an enhanced rate of T_1 relaxation compared with i) nitroxide in the absence of dipolar coupling, and ii) coupled to a double-histidine motif occupied by Cu^{II}-NTA. Thus, for a fixed mixing time interval, the relative population of double-histidine motifs occupied by Ni^{II}-NTA would be over-represented. While this is not problematic for an EPR silent competitor ligand (modulation depth will be continuously decreasing), as Ni^{II}-NTA is paramagnetic (see Evan's NMR in figure 5.3.1.1), the RIDME modulation depth will be the weighted contributions of the Cu^{II}-NTA and Ni^{II}-NTA bound double-histidine motifs. Modulation depth quantification may be further complicated by two factors: i) to separate the contribution of each species to the modulation depth, the T_1 of Cu^{II}- and Ni^{II}-NTA would need to be isolated (which may be feasible using an inversion recovery-based relaxation filter), and ii) for a high-spin system ($S > 0.5$), the asymptotic limit of modulation depth for a given ratio of T_1 and mixing time (Δ_{Tmix}) is not constrained to 50%.[268]

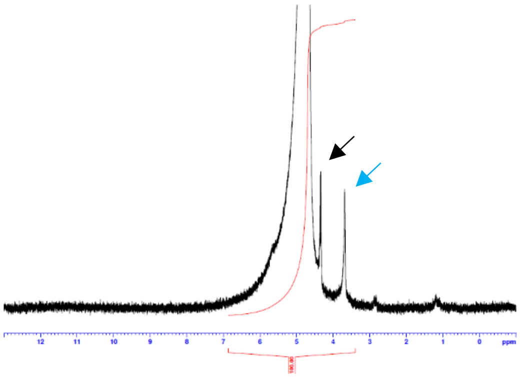

Figure 5.3.1.1: Evan's NMR spectrum of D_2O in absence and presence of 25 mM Ni^{II}-NTA, indicated in the black and blue arrows, respectively.

5.3.2 Exploratory Competitor Ligand Modulation Depth Profile Simulations

It was necessary to validate the mathematical model that would be used in the analysis and fitting of the competitor RIDME pseudo-titration data. Figure 5.3.2.1 shows various simulated modulation depth profiles in presence of diamagnetic competitor ligand with different affinities for double-histidine motifs. As expected, as the affinity of the competitor increases, the modulation depth decays more swiftly for a fixed concentration of protein and non-competitor ligand. Importantly, when the competitor ligand is diamagnetic (such as Zn^{II}-NTA used in this work), the modulation depth quotient ($\Delta \times {\Delta_{Tmix}}^{-1}$) is a continuously decreasing function with increasing competitor ligand concentration. As discussed in section 2.10.2 this is not necessarily well met in the case of a paramagnetic competitor ligand, and forms part of the rationale for selecting Zn^{II}-NTA over Ni^{II}-NTA, (see section 5.3.1). It should also be noted that competitor K_D values fitted *via* this methodology are fitted to a univariate error function (assuming a known dissociation constant of the α-helical double-histidine motif for Cu^{II}-NTA under cryogenic conditions, as discussed in chapter 3).

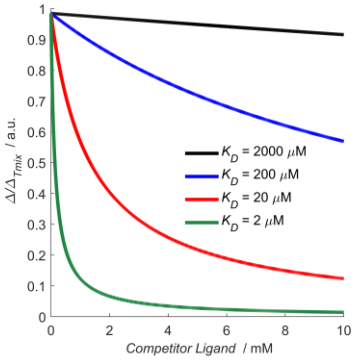

Figure 5.3.2.1. Exploratory simulations of the mathematical model used to fit competitor dissociation constants. Simulation was performed for 1 µM protein, a Cu^{II}-NTA concentration of 10 µM, and a non-competitor dissociation constant of 0.14 µM. The competitor dissociation constants are varied from 2-2000 µM as indicated in the figure legend.

5.3.3 ITC Measurements of Ni^{II}-NTA and Zn^{II}-NTA Binding at Double-Histidine Motifs

For ITC measurement of the 28H/32H GB1 construct, 12 mM Ni^{II}-NTA ligand was titrated into 800 µM protein solution, all in filtered buffer A (42.4 mM Na_2HPO_4, 7.6 mM KH_2PO_4, 150 mM NaCl, pH 7.4). The resulting isotherm, raw data and fit are shown in figure 5.3.3.1 (left panel). The calculated K_D value based on the fit is 64.8 µM. This is consistent with the literature, that Ni^{II}-chelates interact weakly with histidine motifs compared to Cu^{II}-chelates. The ΔH value is also exothermic and comparable in magnitude to previous measurements performed with Cu^{II}-NTA. Finally, the *c* value (Wiseman factor) is 12.3, consistent with literature indicating the enthalpy change can be used robustly to extrapolate the dissociation constant to low temperature.[323] Extrapolating the room-temperature K_D to 235 K[70,73] yields an expected K_D of 3 µM. The associated modulation depth profile assuming 1 µM protein and 10 µM Cu^{II}-NTA (K_D ~140 nM) is shown in figure 5.3.3.1 (right panel).

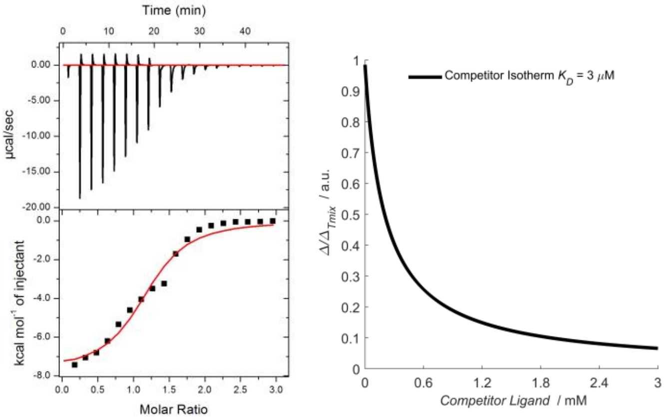

Figure 5.3.3.1. Isothermal titration calorimetry data for K28H/Q32H GB1 construct, titrated against Ni^{II}-NTA, with the raw ITC trace shown at the top, and the binding isotherm at the bottom, with the corresponding fit shown in red (left panel). Simulated modulation depth profile as a function of competitor ligand concentration (right panel).

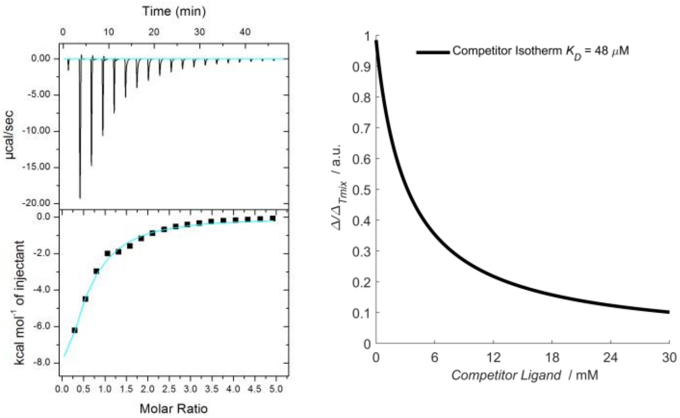

Figure 5.3.3.2. Isothermal titration calorimetry data for K28H/Q32H GB1 construct, titrated against Zn^{II}-NTA, with the raw ITC trace shown at the top, and the binding isotherm at the bottom, with the corresponding fit shown in red (left panel). Simulated modulation depth profile as a function of competitor ligand concentration (right panel).

ITC measurements were performed analogously for Zn^{II}-NTA, with the resulting isotherm, raw data and fit shown in figure 5.3.3.2 (left panel). The calculated K_D value based on the fit is 513 µM, which is consistent with Zn^{II}-NTA being a weaker competitor for double-histidine motif sites compared to Ni^{II}-NTA. Indeed, a systematic study of the propensity for divalent metal centres to bind arrays of histidine residues did not detect any binding of double-histidine motifs for Zn^{II}-NTA using ITC.[297] On this disparity with reported literature, our ITC data was performed at a significantly higher protein concentration, allowing greater sensitivity to weak interactions. Extrapolating this K_D value to 235 K reveals a predicted affinity of 48 µM, with the modulation depth profile (figure 5.3.3.2 (right panel)) forming the basis for the subsequent RIDME pseudo-titration series (section 5.3.5). Zn^{II}-NTA was a particularly appealing choice for model competitor because it is: i) diamagnetic and so does not contribute to the detected EPR signal, and ii) a sufficiently weak competitor[297] that the equilibrium concentration is adequately approximated as the total competitor concentration. This is seen by comparison of the right panels of figures 5.3.3.1-2, where even at 1 µM and ~1000-fold excess Zn^{II}-NTA, 80% of Cu^{II}-NTA is predicted to be bound, a condition less well met for Ni^{II}-NTA.

5.3.4 Influence of Differential pH upon Double-Histidine Motif Affinity:

Spin labelling with Cu^{II}-NTA and double-histidine motifs is a coordination-based approach, therefore it follows that affinity of labelling should be dependent on local pH; if the δ-nitrogen of histidine is protonated it cannot coordinate Cu^{II}-chelates effectively, and so affinity of binding should steeply decrease at pH values below the pK_A of histidine. To test this hypothesis and investigate the influence of pH upon labelling efficiency at double-histidine motifs, isothermal titration calorimetry measurements were performed at pH 5.0, 6.4, and 8.4, with results shown in figures 5.3.4.1-3, respectively. Thermodynamic parameters of each measurement are summarised in table 5.3.4.1.

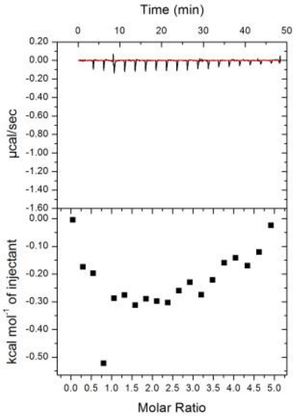

Figure 5.3.4.1: ITC data recorded for 75 µM K28H/Q32H GB1 protein in presence of 2 mM Cu^{II}-NTA at pH 5.0.

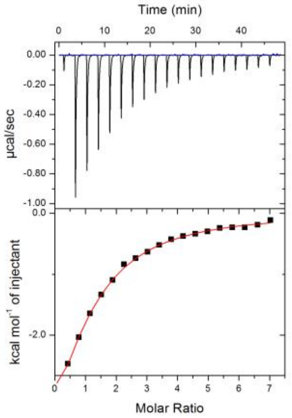

Figure 5.3.4.2: ITC data recorded for 75 µM K28H/Q32H GB1 protein in presence of 2 mM Cu^{II}-NTA at pH 6.4.

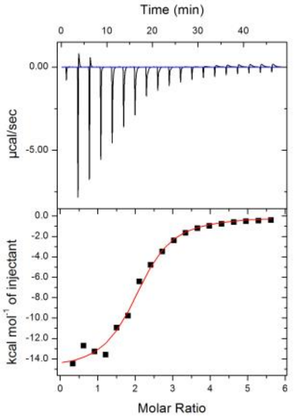

Figure 5.3.4.3: ITC data recorded for 75 µM K28H/Q32H GB1 protein in presence of 2 mM Cu^{II}-NTA at pH 8.4.

It is seen from figure 5.3.4.1 that at pH 5.0 there is negligible binding at the double histidine motif, which is consistent with the expectation that at pH < 6.0 (the approximate pK$_A$ of histidine), the binding affinity is reduced. This is likely the combination of two effects that preclude coordination of Cu^{II}-NTA at double histidine sites; first complexation of Cu^{II} with the NTA chelator will reduce with lower pH, and similarly, histidine protonation will disrupt coordination by the double histidine. Less Cu^{II}-NTA complex will be available to bind, and fewer histidine residues will be deprotonated and susceptible to coordination at the imidazole δ-nitrogen. At pH 6.4 (figure 5.3.4.2) there is a recovery of double-histidine loading, albeit with a reduced affinity, approximately an order of magnitude weaker binding than previously observed at pH 7.4. This is again in keeping with the expected trend of increasing affinity with increasing histidine deprotonation. Furthermore, it is noted that at pH 8.4 (figure 5.3.4.3), the binding affinity is approximately the same as at pH 7.4, suggesting the histidine residues are already approaching complete deprotonation at pH 7.4. If the pK_A of histidine is taken as 5.5-6.0, then this observation is consistent, since < 1% of histidine residues will be protonated at pH 7.4, and < 0.01% of neighbouring histidine pairs will be protonated.

Sample	*n*	K_D / μM	ΔH / kcal.mol^{-1}	Wiseman factor	Predicted K_D at 235 K / μM
pH 5.0	-	-	-	-	-
pH 6.4	0.97	98.6	-6.94	0.76	4.26
pH 7.4*	1.20	5.00	-7.54	15.0	1.65×10^{-1}
pH 8.4	2.04	7.96	-15.2	9.42	8.18×10^{-3}

Table 5.3.4.1: Fit parameters taken from the ITC data shown in figures 5.3.4.1-3. (*) indicates that the pH 7.4 ITC measurement was performed using 75 μM 6R1/28H/32H in presence of 2 mM Cu^{II}-NTA ligand.

As can be seen from table 5.3.4.1, there is also an apparent influence of pH on the enthalpy of binding. With increasing pH binding becomes more exothermic, and subsequently affinity increases more steeply with decreasing temperature. This is particularly relevant for pulse EPR applications since measurements are typically performed at cryogenic temperatures. There is also an increase in the stoichiometry of binding (*n*) with increasing pH, suggesting a possible role in determining the relative specificity of binding; it should be noted that WT GB1 has been observed to natively bind Cu^{II} *via* coordination to acidic residues, D40 and E56 at the C-terminal domain of the protein.[326] Propensity for this native binding event may increase as acidic residues become deprotonated at higher pH. This formed the motivation to investigate the influence of pH upon binding affinity of double-histidine motifs under cryogenic temperatures and led to the subsequent RIDME pseudo-titration series performed at pH 6.4 and 8.4, respectively (section 5.3.5).

5.3.5 Estimation of Binding Affinities from Cu^{II}-Nitroxide RIDME Measurements:

5-pulse RIDME measurements were first performed in presence of the model competitor ligand, Zn^{II}-NTA. An EPR silent competitor ligand is desirable because analysis of pseudo-titration data is simplified (see section 5.3.1 for discussion). The corresponding RIDME pseudo-titration was performed at 1 μM protein concentration in presence of 10 μM Cu^{II}-NTA (to ensure quantitative loading) and varying Zn^{II}-NTA concentrations. This allowed the influence of the competitor ligand upon double-histidine loading efficiency with Cu^{II}-NTA to be investigated under PD-EPR conditions. Importantly, the dipolar evolution functions (figure 5.3.5.1 left panel) and distance distributions (figure 5.3.5.1 centre panel) show that in all cases, the expected peak at ~2.5 nm is retrieved as the only significant feature following data validation (see section 5.3.8). The fitted competitor K_D value (32 μM) is within 2-fold of that determined from ITC when extrapolated to 235 K (48 μM) (figure 5.3.5.1 right panel). This suggests that Cu^{II}-NTA is robust against adventitious divalent metals in vast excesses, >1000-fold, even at low μM protein concentrations. Additionally, this benchmarks quantitation of Cu^{II}-nitroxide RIDME modulation depths for remotely determining binding affinities of EPR silent ligands, in a competition assay format.

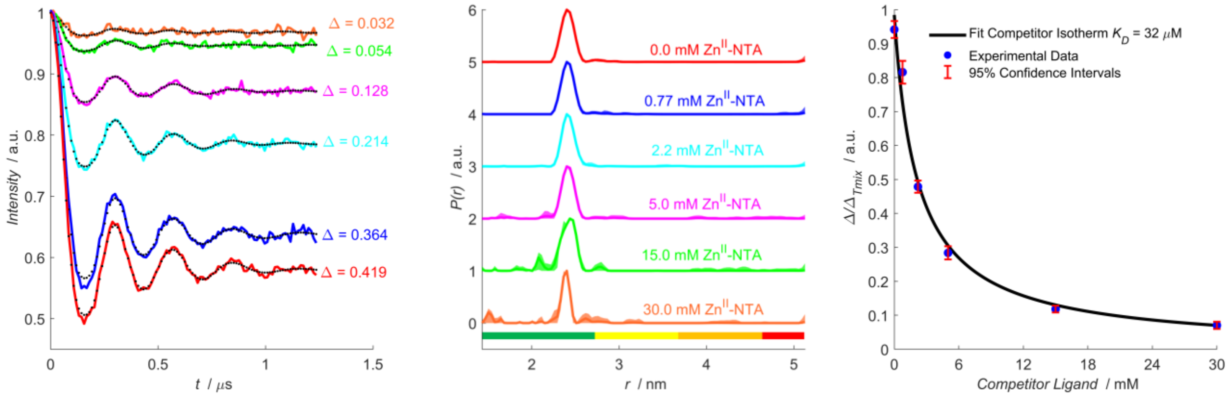

Figure 5.3.5.1: Zn^{II}-NTA competitor RIDME pseudo-titration. left panel) RIDME dipolar evolution functions, with the corresponding fits shown in dotted black. Modulation depths (Δ) are indicated. centre panel) Validated RIDME distance distributions, corresponding to the dipolar evolution functions (top-row right panel). The colour scheme is the same in each case. The concentrations of Cu^{II}-NTA are indicated. right panel) A univariate fit of the dissociation constant (32 μM) shown in solid black. Experimental points are shown as the blue scatter, and 95% confidence intervals are shown as the red error bars.

Next, the influence of pH upon double-histidine motif loading efficiency with Cu^{II}-NTA was investigated by measuring a RIDME pseudo-titration at pH 6.4. Since only deprotonated histidine residues can coordinate Cu^{II}-NTA, it follows that binding affinity should decrease under acidic conditions, as seen from negligible binding at pH 5.0, below the pK_A of solvent exposed histidine[344] (figure 5.3.4.1), and ITC measurements at pH 6.4, indicated a 20-fold reduction in affinity compared to previous work (figure 5.3.4.2). Extrapolating ΔH to 235 K suggested a binding affinity of ~4 μM.

The corresponding RIDME pseudo-titration was performed at 5 μM protein concentration. Significantly, the dipolar evolution functions (figure 5.3.5.2 left panel) show Cu^{II}-NTA binding is only marginally reduced at lower pH, with one equivalent Cu^{II}-NTA saturating ~70% of available double-histidine motifs. This is further borne out by the fitted dissociation constant (figure 5.3.5.2 right panel), 0.31 μM compared to 0.14 μM in previous work at pH 7.4. The affinity reduced by only 2-fold, indicating that the influence of pH upon double-histidine motif loading may be attenuated at lower temperatures. A possible explanation is that histidine protonation is endothermic,[345] driving the equilibrium towards the deprotonated state at lower temperatures, compensating for reduced pH and facilitating double-histidine loading. Importantly, this would also imply significantly tighter binding at higher pH, where histidine deprotonation is already favoured.

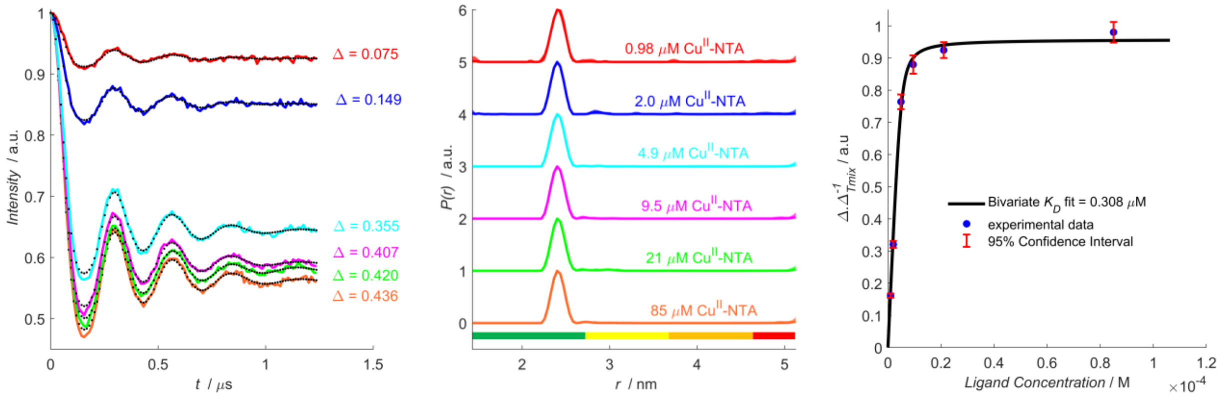

Figure 5.3.5.2: pH 6.4 RIDME pseudo-titration. left panel) RIDME dipolar evolution functions, with the corresponding fits shown in dotted black. Modulation depths (Δ) are indicated. centre panel) Validated RIDME distance distributions, corresponding to the dipolar evolution functions (left panel). The colour scheme is the same in each case. The concentrations of Cu^{II}-NTA are indicated. right panel) A bivariate fit of the dissociation constant (0.31 μM) shown in solid black. Experimental points are shown as the blue scatter, and 95% confidence intervals are shown as the red error bars.

Therefore, to investigate the influence of a higher buffer pH upon double-histidine loading efficiency under cryogenic temperatures, another RIDME pseudo-titration was performed at 2 μM protein concentration. Significantly, room-temperature ITC measurements at pH 8.4 (figure 5.3.4.3) indicated binding that could be as much as 20-fold stronger under PD-EPR conditions, (*via* improved thermodynamic favourability of binding). The corresponding dipolar evolution functions (figure 5.3.5.3 left panel) suggest modest improvement in binding affinity. The fitted dissociation constant (figure 5.3.5.3 right panel) of 0.091 μM indicates binding affinity is approximately 2-fold higher than at pH 7.4, consistent with observation at pH 6.4 that the influence of pH upon binding affinity is attenuated with decreasing temperature. While an endothermic protonation process would suggest much tighter binding is to be anticipated at pH 8.4, consider that at this pH <1% of histidine δ-nitrogen atoms should remain protonated. This may explain why the relative increase in binding affinity is smaller than expected, since the deprotonation is already driven toward completion by the high pH.

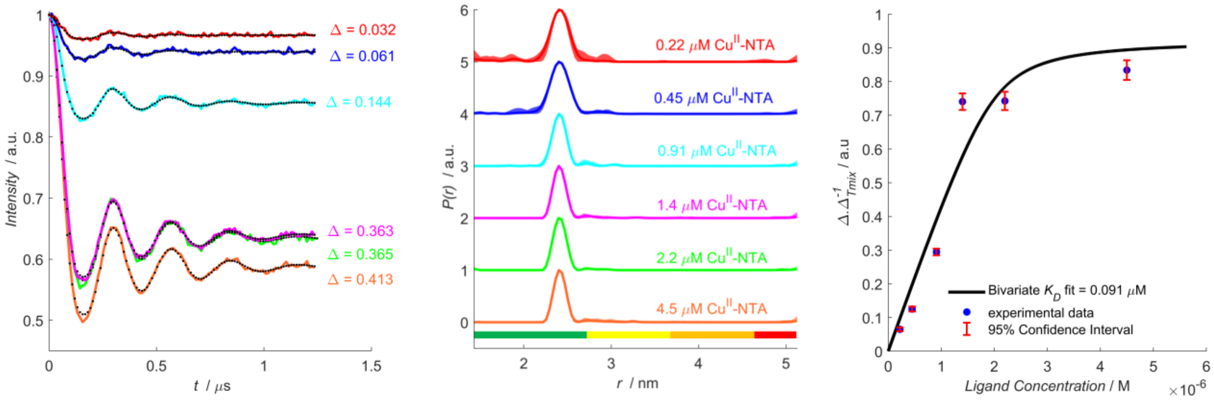

Figure 5.3.5.3: pH 8.4 RIDME pseudo-titration. left panel) RIDME dipolar evolution functions, with the corresponding fits shown in dotted black. Modulation depths (Δ) are indicated. centre panel) Validated RIDME distance distributions, corresponding to the dipolar evolution functions (left panel). The colour scheme is the same in each case. The concentrations of Cu^{II}-NTA are indicated. right panel) A bivariate fit of the dissociation constant (0.091 μM) shown in solid black. Experimental points are shown as the blue scatter, and 95% confidence intervals are shown as the red error bars.

While the data suggests that spin-labelling and measurement at pH 8.4 could afford enhanced loading and sensitivity, it should be noted that the predicted stoichiometry of binding from ITC is ~2, compared to ~1 at pH 6.4. This may arise from deprotonation of the protein surface that promotes non-specific binding. This would explain the increased exothermic nature of the binding (15.2 vs 7.5 kcal.mol^{-1} at pH 7.4), if non-specific or additional binding events contributed to the isotherm and would further inflate the binding affinity when extrapolated to cryogenic temperatures. However, the corresponding distance distributions (figure 5.3.5.3 centre panel) do not contain additional peaks to support this hypothesis, as a shorter distance peak would be expected at ~2.0 nm (i.e., between the R1 moiety and the C-terminal native Cu^{II}-centre). Perhaps most significantly, these results clearly show that Cu^{II}-NTA binding affinity for double-histidine motifs is not strongly perturbed from the high nM concentration regime by fluctuations of pH between 6.4-8.4.

5.3.6 Influence of Differential pH upon Cu^{II}-NTA Complex Formation:

Before RIDME pseudo-titration series could be performed at differential pH, it was first necessary to investigate the influence of different pH conditions upon formation of the Cu^{II}-NTA spin label, as was previously characterised by CW-EPR for Cu^{II}-IDA.[170] Importantly, these measurements ensured that Cu^{II}-NTA label concentration could still be accurately quantified.

Nominal stock solutions of 100 mM CuCl$_2$.6H$_2$O and NTA were prepared from dry weighted aliquots in 1 mL milliQ H$_2$O, and were pH adjusted to pH 2.0 and 12.0 respectively, using 2 M HCl and 5 M NaOH. Stock solutions of 10 mM Cu^{II}-NTA were prepared from these stock solutions by being mixed in a 1:1 equivalence before dilution with pH-adjusted buffer A (150 mM NaCl, 42.4 mM Na$_2$HPO$_4$, 7.6 mM KH$_2$PO$_4$). Respective dilution series were performed at pH 5.0, 6.4, 8.4 and 9.0, and were measured in triplicate, at nominal concentrations of 10, 7.5, 5.0, 2.5 and 1.0 mM Cu^{II}-NTA. Cu^{II}-NTA has an extinction coefficient of 63 M^{-1}cm^{-1} at A$_{800nm}$ at pH 7.4. Spectra are shown for series performed at pH 5.0, 6.4, 8.4

and 9.0 in figures 5.3.6.1-4. Comparison of the observed A_{800nm} values and those predicted from theory are shown in figure 5.3.6.5. Observed absorbance at 800 nm, and the calculated concentrations are given in tables 5.3.6.1-4.

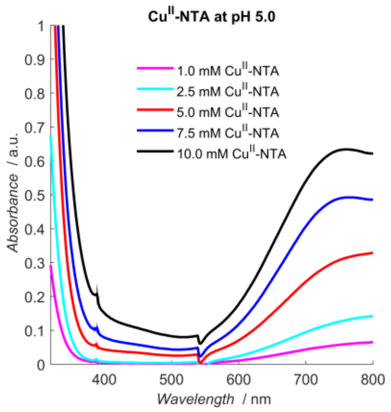

Figure 5.3.6.1: Absorbance spectra recorded for the pH 5.0 Cu^{II}-NTA dilution series, repeated in triplicate, with ± 2σ confidence intervals indicated as the shaded regions. Magenta, cyan, red, blue and black traces correspond to 1, 2.5, 5.0, 7.5, and 10.0 mM Cu^{II}-NTA concentration.

Sample	Observed A_{800nm} (a.u.)			Calculated Concentration (mM)		
Repeat	1	2	3	1	2	3
10 mM Cu^{II}-NTA	0.621	0.621	0.621	9.9	9.9	9.9
7.5 mM Cu^{II}-NTA	0.484	0.485	0.486	7.7	7.7	7.7
5.0 mM Cu^{II}-NTA	0.328	0.328	0.328	5.2	5.2	5.2
2.5 mM Cu^{II}-NTA	0.142	0.142	0.142	2.3	2.3	2.3
1.0 mM Cu^{II}-NTA	0.065	0.065	0.065	1.0	1.0	1.0

Table 5.3.6.1. The observed absorbance at 800 nm for the pH 5.0 Cu^{II}-NTA series, taken from the spectra shown in figure 5.3.6.1.

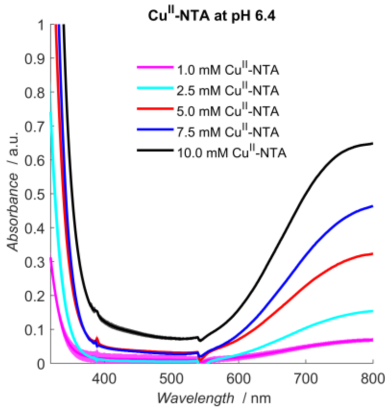

Figure 5.3.6.2: Absorbance spectra recorded for the pH 6.4 Cu^{II}-NTA dilution series, repeated in triplicate, with ± 2σ confidence intervals indicated as the shaded regions. Magenta, cyan, red, blue and black traces correspond to 1, 2.5, 5.0, 7.5, and 10.0 mM Cu^{II}-NTA concentration.

Sample	Observed A_{800nm} (a.u.)			Calculated Concentration (mM)		
Repeat	1	2	3	1	2	3
10 mM Cu^{II}-NTA	0.598	0.597	0.597	9.5	9.5	9.5
7.5 mM Cu^{II}-NTA	0.445	0.445	0.446	7.1	7.1	7.1
5.0 mM Cu^{II}-NTA	0.299	0.300	0.301	4.7	4.8	4.8
2.5 mM Cu^{II}-NTA	0.173	0.173	0.173	2.7	2.7	2.7
1.0 mM Cu^{II}-NTA	0.061	0.061	0.061	1.0	1.0	1.0

Table 5.3.6.2. The observed absorbance at 800 nm for the pH 6.4 Cu^{II}-NTA series, taken from the spectra shown in figure 5.3.6.2.

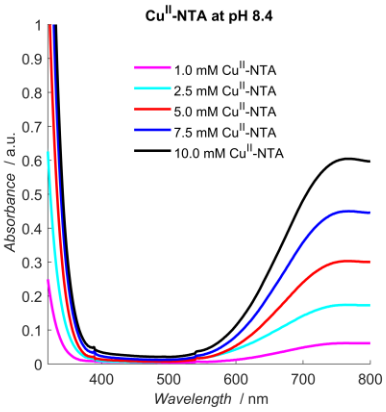

Figure 5.3.6.3: Absorbance spectra recorded for the pH 8.4 Cu^{II}-NTA dilution series, repeated in triplicate, with ± 2σ confidence intervals indicated as the shaded regions. Magenta, cyan, red, blue and black traces correspond to 1, 2.5, 5.0, 7.5, and 10.0 mM Cu^{II}-NTA concentration.

Sample	Observed A_{800nm} (a.u.)			Calculated Concentration (mM)		
Repeat	1	2	3	1	2	3
10 mM Cu^{II}-NTA	0.648	0.648	0.648	10.3	10.3	10.3
7.5 mM Cu^{II}-NTA	0.463	0.464	0.464	7.3	7.4	7.4
5.0 mM Cu^{II}-NTA	0.323	0.323	0.324	5.1	5.1	5.1
2.5 mM Cu^{II}-NTA	0.154	0.154	0.154	2.4	2.4	2.4
1.0 mM Cu^{II}-NTA	0.066	0.069	0.072	1.0	1.1	1.1

Table 5.3.6.3. The observed absorbance at 800 nm for the pH 8.4 Cu^{II}-NTA series, taken from the spectra shown in figure 5.3.6.3.

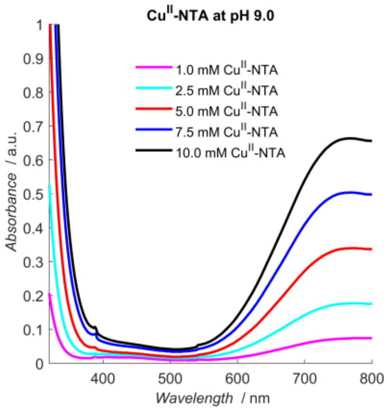

Figure 5.3.6.4. Absorbance spectra recorded for the pH 9.0 Cu^{II}-NTA dilution series, repeated in triplicate, with ± 2σ confidence intervals indicated as the shaded regions. Magenta, cyan, red, blue and black traces correspond to 1, 2.5, 5.0, 7.5, and 10.0 mM Cu^{II}-NTA concentration.

Sample	Observed A_{800nm} (a.u.)			Calculated Concentration (mM)		
Repeat	1	2	3	1	2	3
10 mM Cu^{II}-NTA	0.655	0.655	0.656	10.4	10.4	10.4
7.5 mM Cu^{II}-NTA	0.497	0.498	0.498	7.9	7.9	7.9
5.0 mM Cu^{II}-NTA	0.336	0.337	0.337	5.3	5.3	5.3
2.5 mM Cu^{II}-NTA	0.175	0.175	0.176	2.8	2.8	2.8
1.0 mM Cu^{II}-NTA	0.074	0.074	0.074	1.2	1.2	1.2

Table 5.3.6.4. The observed absorbance at 800 nm for the pH 9.0 Cu^{II}-NTA series, taken from the spectra shown in figure 5.3.6.4.

It can be seen from figures 5.3.6.1-4, that the baseline in the region 400-550 nm is not entirely flat, suggesting the presence of precipitate. Qualitatively, precipitate was not observed upon dilution in pH-adjusted buffer for any series, however for the pH 5.0 series, some precipitate was observed at the neutralisation step, suggesting the neutralisation reaction was not complete; this may have contributed to the sloping baseline in the region 400-550 nm. From figures 5.3.6.3-4 it is seen that the pH 8.4 and 9.0 absorbance series have reasonably flat baselines, and so precipitation does not appear to be problematic, even at alkaline pH. Absorbance at 800 nm seems to be consistently higher for the series recorded at pH 9.0, when compared to pH 5.0, however this does not manifest in a significant shift of the extinction coefficients, and plots in figure 5.3.6.5 show the theoretical absorbance values for an extinction coefficient of 63 $M^{-1}cm^{-1}$. When the absorbance values are linearly fit, extinction coefficients of 63 and 64 $M^{-1}cm^{-1}$ are found for Cu^{II}-NTA at pH 5.0 and 9.0, respectively.

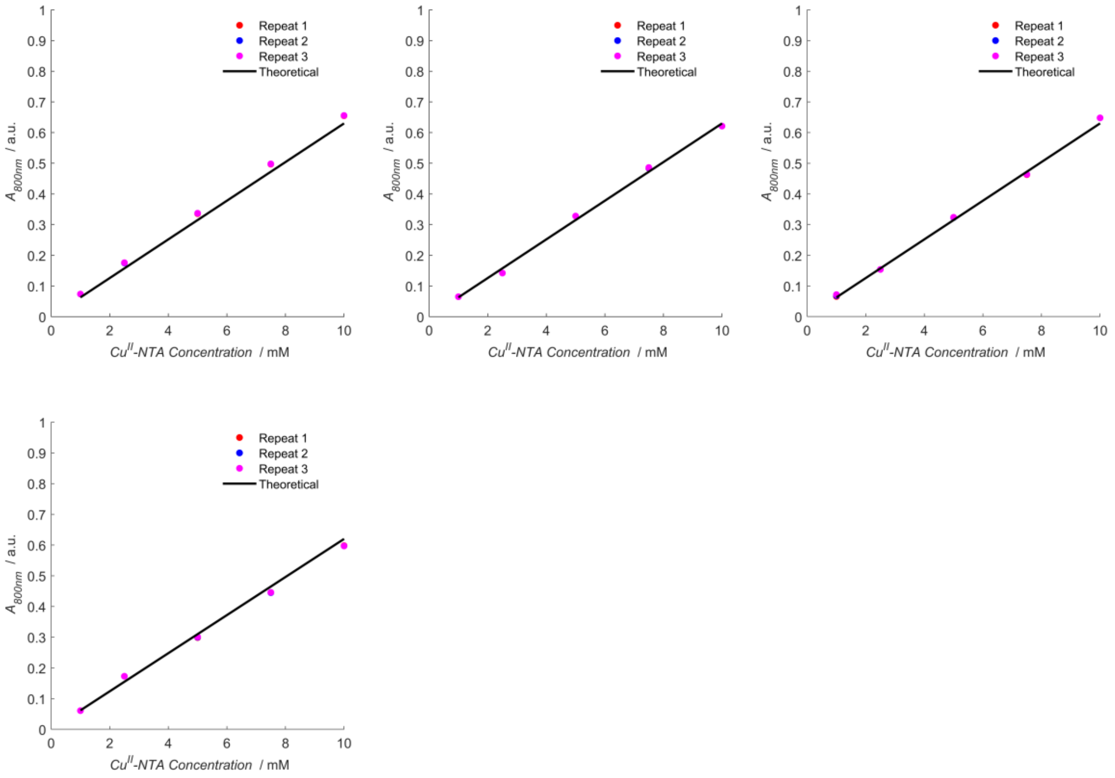

Figure 5.3.6.5: Absorbance at 800 nm as a function of Cu^{II}-NTA concentration for pH 5.0, 6.4, 8.4 and pH 9.0, from left-to-right, and top-to-bottom. Experimental data for each repeat set is shown as a red, blue or cyan scatter, with the literature value for the extinction coefficient plotted in black.

5.3.7 Inversion Recovery Measurements:

Inversion recovery measurements were performed to estimate the longitudinal relaxation time of Cu^{II}-NTA, and the raw data is shown overleaf in figures 5.3.7.1-3, for pH 6.4 and 8.4, and in presence of the competitor Zn^{II}-NTA, respectively. The corresponding mono- and bi-exponential fits are shown as red and blue traces, respectively. The estimates of T_1 fitted under the mono- and bi-exponential approximations, as well as the reciprocal e-times are given in tables 5.3.7.1-3.

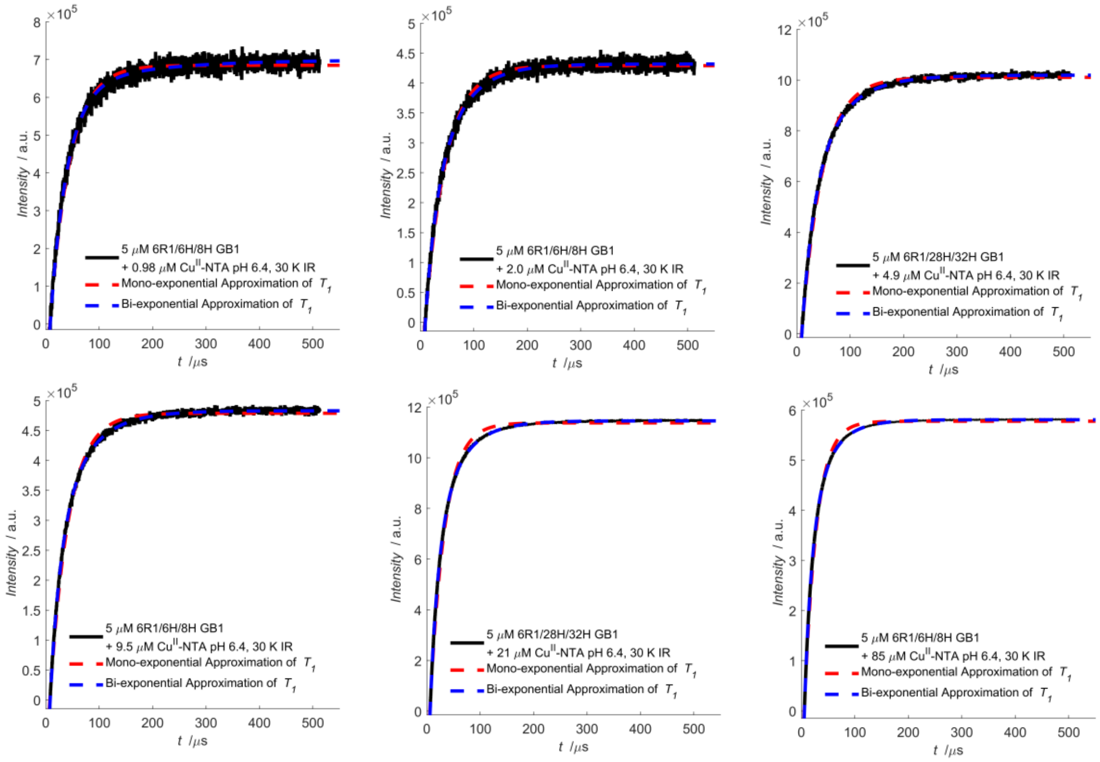

Figure 5.3.7.1. Inversion recovery data at pH 6.4 for 0.98, 2.0 and 4.9 µM Cu^{II}-NTA (top row), and 9.5, 21 and 85 µM Cu^{II}-NTA (bottom row) in presence of 5 µM I6R1/28H/32H GB1 shown left-to-right, respectively. The experimental data is shown in black, with the mono-exponential and bi-exponential fits shown as red and blue dotted lines, respectively.

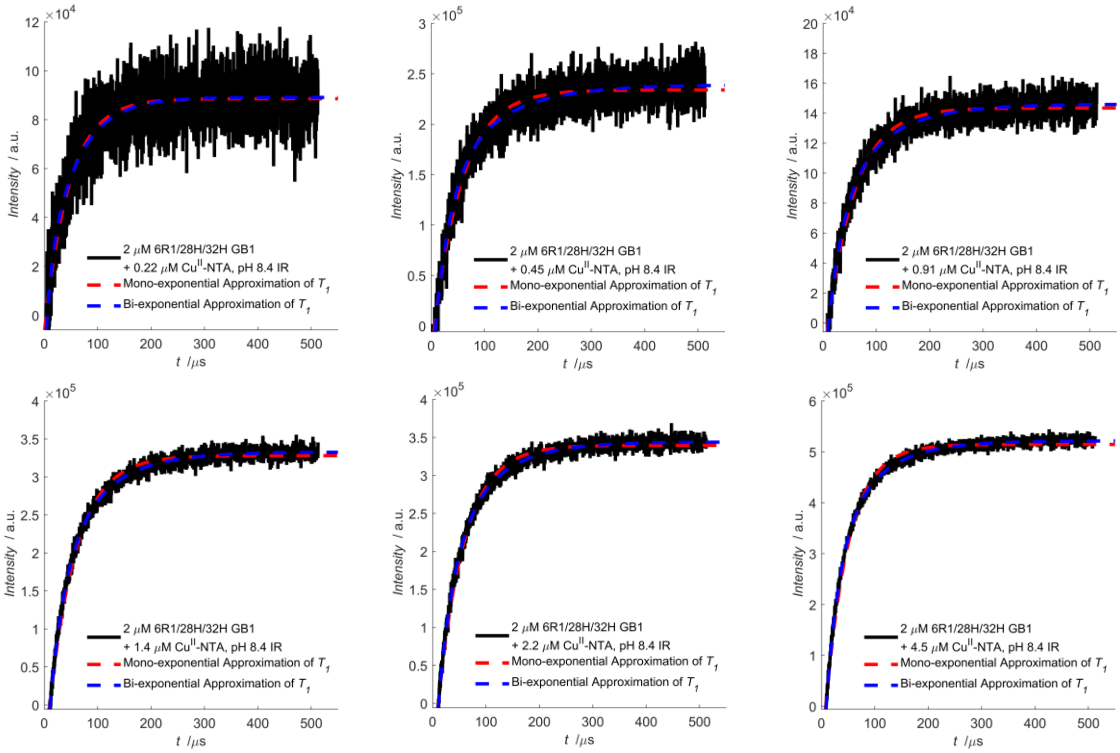

Figure 5.3.7.2. Inversion recovery data at pH 8.4 for 0.22, 0.45 and 0.91 µM Cu^{II}-NTA (top row), and 1.4, 2.2 and 4.5 µM Cu^{II}-NTA (bottom row) in presence of 2 µM I6R1/28H/32H GB1 shown left-to-right, respectively. The experimental data is shown in black, with the mono-exponential and bi-exponential fits shown as red and blue dotted lines, respectively.

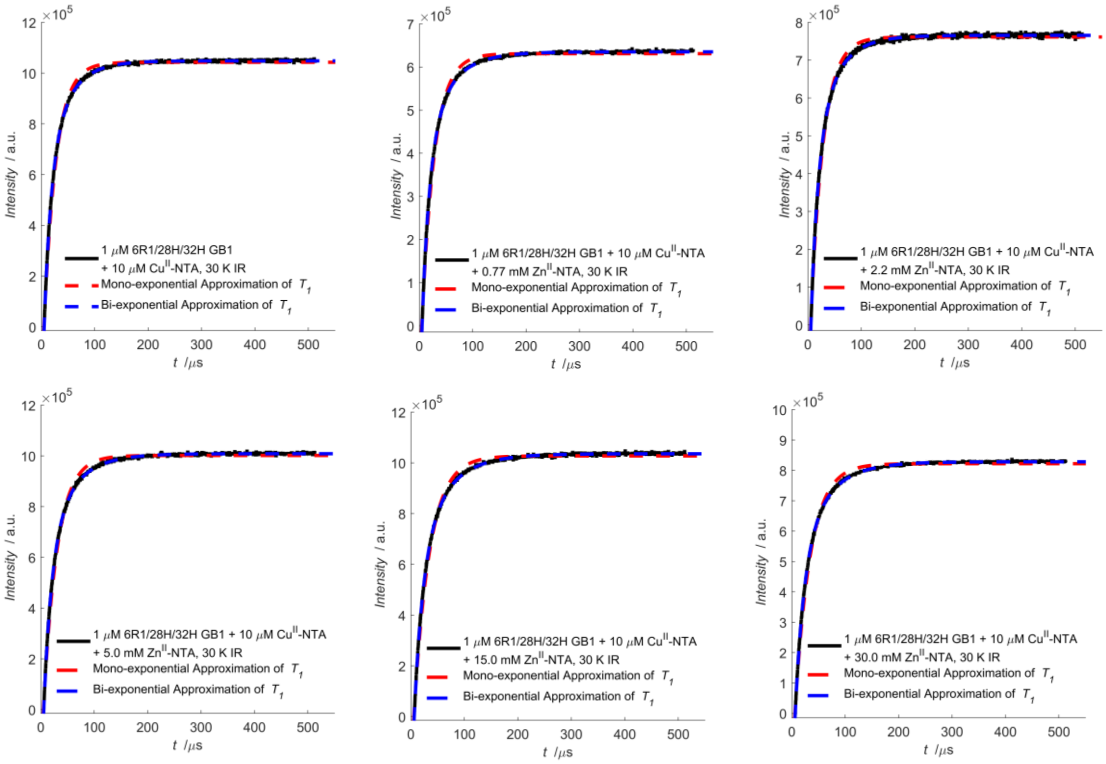

Figure 5.3.7.3. Inversion recovery data for 10 μM Cu^{II}-NTA in presence of 0, 0.77, 2.2 mM Zn^{II}-NTA (top row), and 5.0, 15 and 30 mM Zn^{II}-NTA (bottom row), in presence of 1 μM I6R1/28H/32H GB1 shown left-to-right, respectively. The experimental data is shown in black, with the mono-exponential and bi-exponential fits shown as red and blue dotted lines, respectively.

Sample	Mono-exponential T_1 [μs]	Bi-exponential T_{1A} / T_{1B} [μs]	Relative Contributions	1/e time [μs]
5 μM 6R1/28H/32H + 0.98 μM Cu^{II}-NTA	37.1 ± 0.34 (0.987)	31.6 / 159 (0.992)	0.91 : 0.09	44.6
5 μM 6R1/28H/32H + 2.0 μM Cu^{II}-NTA	38.7 ± 0.28 (0.992)	22.1 / 55.6 (0.994)	0.50 : 0.50	47.0
5 μM 6R1/28H/32H + 4.9 μM Cu^{II}-NTA	38.6 ± 0.19 (0.996)	24.2 / 63.9 (0.999)	0.61 : 0.39	46.8
5 μM 6R1/28H/32H + 9.5 μM Cu^{II}-NTA	35.0 ± 0.21 (0.995)	21.0 / 60.9 (0.999)	0.63 : 0.37	42.4
5 μM 6R1/28H/32H + 21.0 μM Cu^{II}-NTA	27.5 ± 0.16 (0.995)	16.2 / 49.5 (1.00)	0.65 : 0.35	31.6
5 μM 6R1/28H/32H + 85.0 μM Cu^{II}-NTA	22.6 ± 0.12 (0.996)	14.2 / 40.9 (1.00)	0.67 : 0.33	27.0

Table 5.3.7.1. Mono- and bi-exponential T_1 estimates, and 1/e times for the inversion recovery data shown in figure 5.3.7.1. R^2 values of each model are indicated in parentheses.

Sample	Mono-exponential T_1 [μs]	Bi-exponential T_{1A} / T_{1B} [μs]	Relative Contributions	1/e time [μs]
2 μM 6R1/28H/32H + 0.22 μM Cu^{II}-NTA	46.6 ± 2.0 (0.781)	9.57 / 56.6 (0.786)	0.30 : 0.70	41.6
2 μM 6R1/28H/32H + 0.45 μM Cu^{II}-NTA	53.6 ± 1.2 (0.924)	29.7 / 104 (0.930)	0.62 : 0.38	59.4
2 μM 6R1/28H/32H + 0.91 μM Cu^{II}-NTA	51.9 ± 0.9 (0.958)	29.2 / 92.5 (0.963)	0.60 : 0.40	56.4
2 μM 6R1/28H/32H + 1.4 μM Cu^{II}-NTA	50.9 ± 0.4 (0.989)	27.8 / 82.9 (0.993)	0.56 : 0.44	58.4
2 μM 6R1/28H/32H + 2.2 μM Cu^{II}-NTA	49.1 ± 0.4 (0.990)	28.6 / 81.0 (0.993)	0.58 : 0.42	55.4
2 μM 6R1/28H/32H + 4.5 μM Cu^{II}-NTA	43.2 ± 0.3 (0.991)	24.9 / 79.6 (0.996)	0.63 : 0.37	48.8

Table 5.3.7.2. Mono- and bi-exponential T_1 estimates, and 1/e time for the inversion recovery data shown in figure 5.3.7.2. R^2 values of each model are indicated in parentheses.

Sample	Mono-exponential T_1 [μs]	Bi-exponential T_{1A} / T_{1B} [μs]	Relative Contributions	1/e time [μs]
1 μM 6R1/28H/32H + 0 mM Zn^{II}-NTA	22.7 ± 0.14 (0.994)	13.7 / 40.9 (0.999)	0.66 : 0.34	27.0
1 μM 6R1/28H/32H + 0.77 mM Zn^{II}-NTA	23.7 ± 0.15 (0.993)	14.8 / 48.3 (0.999)	0.71 : 0.29	28.0
1 μM 6R1/28H/32H + 2.2 mM Zn^{II}-NTA	23.2 ± 0.14 (0.994)	14.4 / 43.3 (0.999)	0.68 : 0.32	27.8
1 μM 6R1/28H/32H + 5.0 mM Zn^{II}-NTA	25.7 ± 0.17 (0.993)	15.5 / 49.5 (0.999)	0.68 : 0.32	29.4
1 μM 6R1/28H/32H + 15 mM Zn^{II}-NTA	29.3 ± 0.19 (0.994)	17.5 / 55.5 (0.999)	0.67 : 0.33	33.6
1 μM 6R1/28H/32H + 30 mM Zn^{II}-NTA	28.7 ± 0.17 (0.994)	17.3 / 53.7 (1.00)	0.67 : 0.33	34.2

Table 5.3.7.3. Mono- and bi-exponential T_1 estimates, and 1/e time for the inversion recovery data shown in figure 5.3.7.3. R^2 values of each model are indicated in parentheses.

5.3.8 5-pulse RIDME Validations:

RIDME traces recorded with a mixing time interval of 200 μs were deconvoluted with traces recorded with a reference mixing time of 5 μs. This pre-processing has the benefit of suppressing artefacts arising from standing echoes, which may result in a systematic over-estimation of the modulation depth (chapter 4). Traces and corresponding validated distance distributions, with shaded regions indicating the ± 2σ confidence intervals are shown below in figures 5.3.8.1-6, 5.3.8.7-12, and 5.3.8.13-18 for pH 6.4, pH 8.4 and competitor pseudo-titration series, respectively. The colour bars represent the reliability ranges described in the DeerAnalysis manual; green indicates shape is reliable, yellow indicates mean and width are reliable, orange indicates mean is reliable, red indicates no quantification is possible. Parameters for the stretched exponential background correction are given in tables 5.3.8.1-3, respectively.

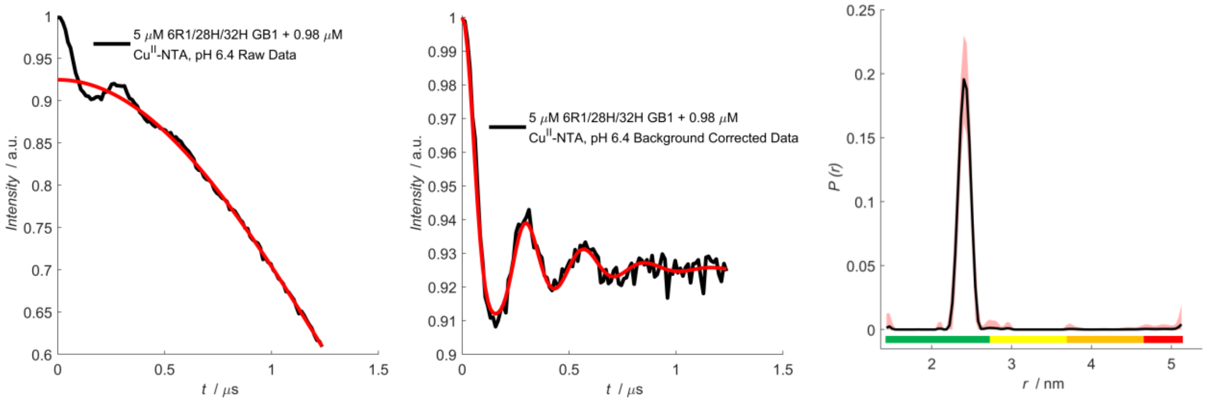

Figure 5.3.8.1: RIDME data of 5 µM 6R1/28H/32H GB1 in presence of 0.98 µM Cu^{II}-NTA. The sample pH was 6.4. The experimental trace, background corrected data, and distance distribution are shown left-to-right respectively.

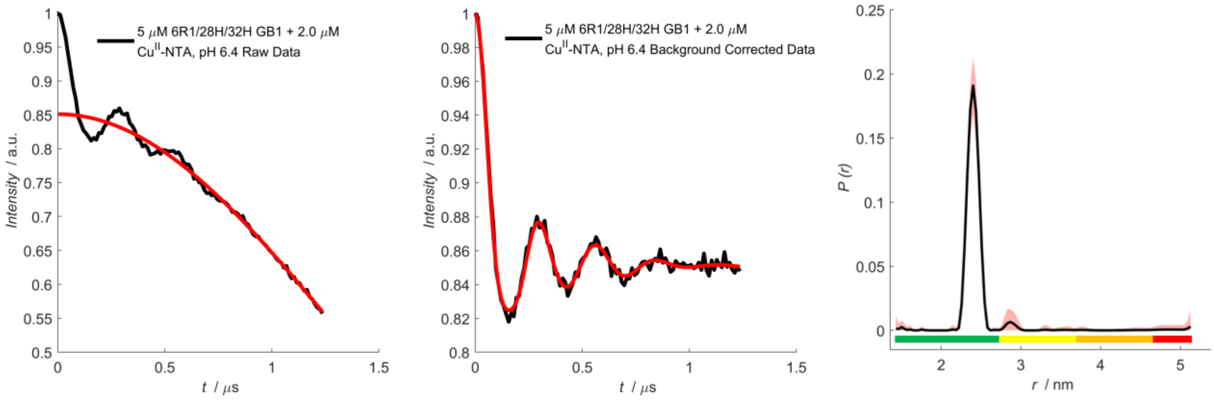

Figure 5.3.8.2: RIDME data of 5 µM 6R1/28H/32H GB1 in presence of 2.0 µM Cu^{II}-NTA. The sample pH was 6.4. The experimental trace, background corrected data, and distance distribution are shown left-to-right, respectively.

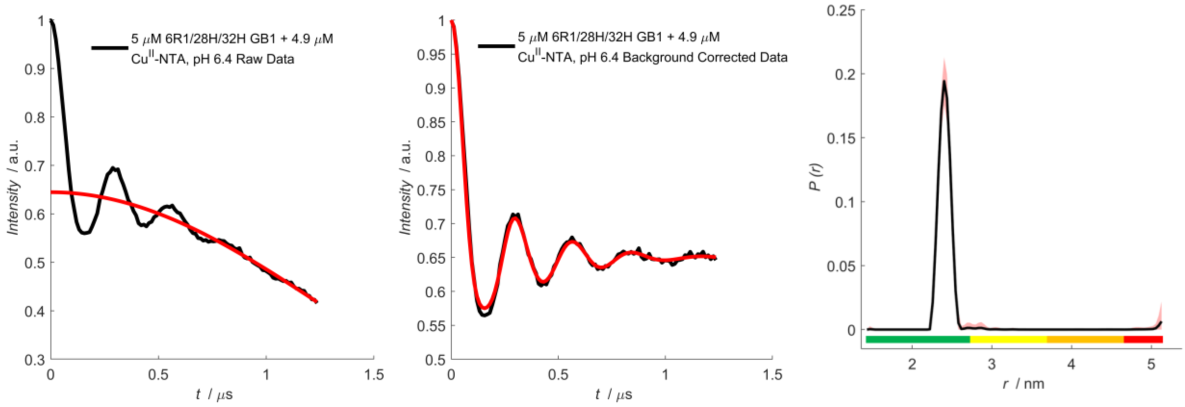

Figure 5.3.8.3: RIDME data of 5 µM 6R1/28H/32H GB1 in presence of 4.9 µM Cu^{II}-NTA. The sample pH was 6.4. The experimental trace, background corrected data, and distance distribution are shown left-to-right, respectively.

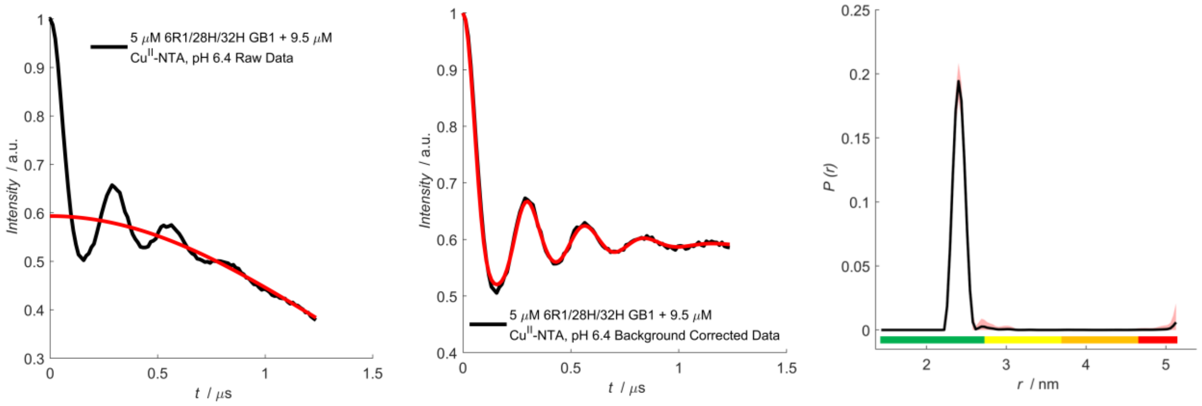

Figure 5.3.8.4: RIDME data of 5 µM 6R1/28H/32H GB1 in presence of 9.5 µM Cu^{II}-NTA. The sample pH was 6.4. The experimental trace, background corrected data, and distance distribution are shown left-to-right respectively.

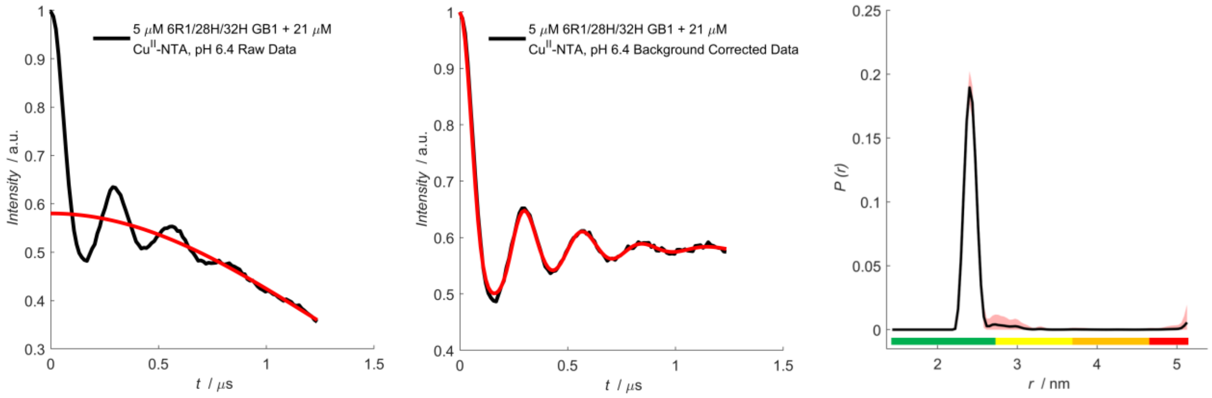

Figure 5.3.8.5: RIDME data of 5 µM 6R1/28H/32H GB1 in presence of 21 µM Cu^{II}-NTA. The sample pH was 6.4. The experimental trace, background corrected data, and distance distribution are shown left-to-right, respectively.

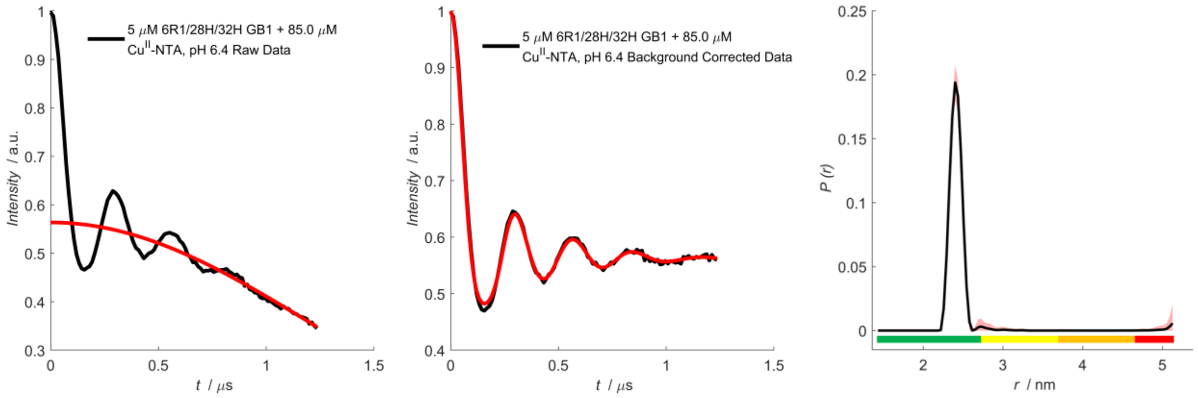

Figure 5.3.8.6: RIDME data of 5 µM 6R1/28H/32H GB1 in presence of 85 µM Cu^{II}-NTA. The sample pH was 6.4. The experimental trace, background corrected data, and distance distribution are shown left-to-right, respectively.

Sample	Zero-time [ns]	Background Start [ns]	Background Cut-off [ns]	Background Dimension	Modulation depth (Δ)
5 μM 6R1/28H/32H + 0.98 μM Cu^{II}-NTA	206	372	1236	6.00	0.075 ± 3.0 x 10^{-3}
5 μM 6R1/28H/32H + 2.0 μM Cu^{II}-NTA	206	151	1236	6.00	0.149 ± 5.0 x 10^{-3}
5 μM 6R1/28H/32H + 4.9 μM Cu^{II}-NTA	206	62	1236	6.00	0.355 ± 1.1 x 10^{-2}
5 μM 6R1/28H/32H + 9.5 μM Cu^{II}-NTA	206	151	1236	6.00	0.407 ± 1.3 x 10^{-2}
5 μM 6R1/28H/32H + 21 μM Cu^{II}-NTA	205	62	1236	6.00	0.420 ± 1.1 x 10^{-2}
5 μM 6R1/28H/32H + 85 μM Cu^{II}-NTA	205	151	1236	6.00	0.436 ± 1.4 x 10^{-2}

Table 5.3.8.1. Parameters for the stretched exponential background correction and associated modulation depths of the RIDME pseudo-titration performed at pH 6.4, shown in figures 5.3.8.1-6.

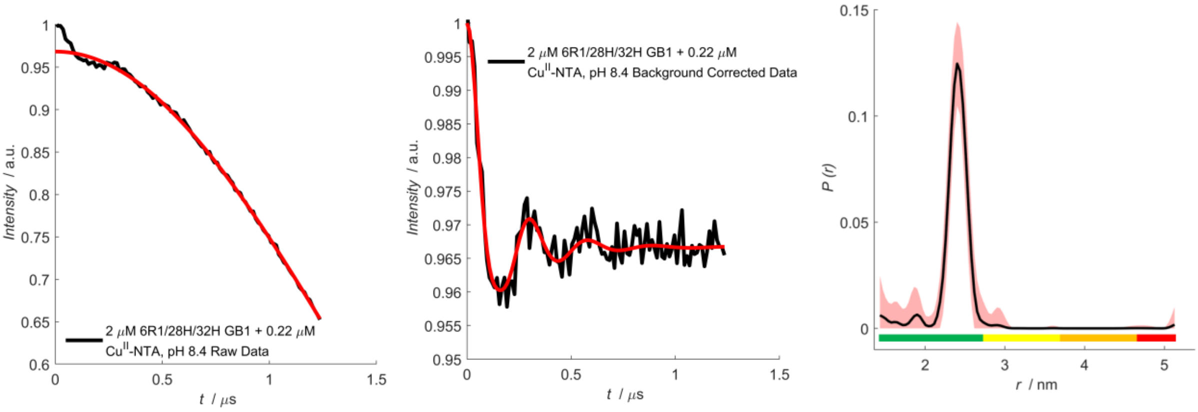

Figure 5.3.8.7: RIDME data of 2 μM 6R1/28H/32H GB1 in presence of 0.22 μM Cu^{II}-NTA. The sample pH was 8.4. The experimental trace, background corrected data, and distance distribution are shown left-to-right, respectively.

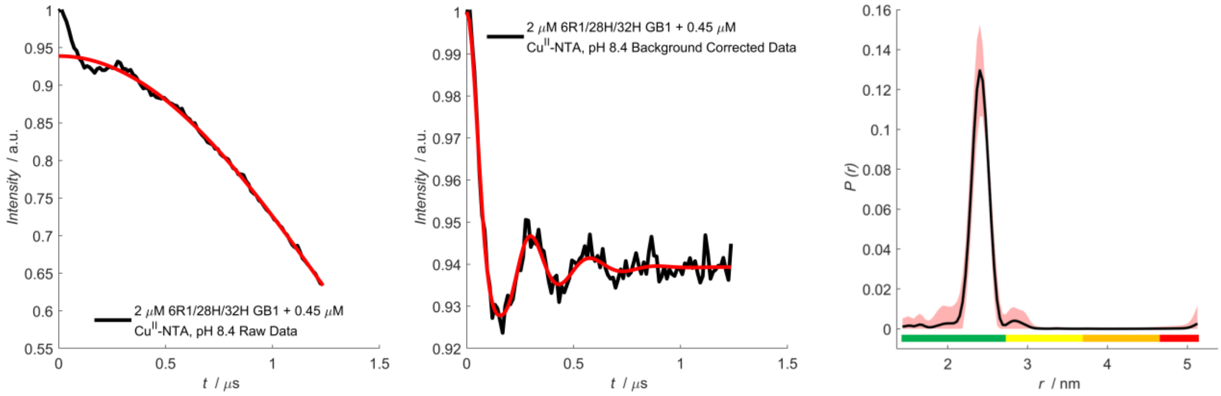

Figure 5.3.8.8: RIDME data of 2 µM 6R1/28H/32H GB1 in presence of 0.45 µM Cu^{II}-NTA. The sample pH was 8.4. The experimental trace, background corrected data, and distance distribution are shown left-to-right, respectively.

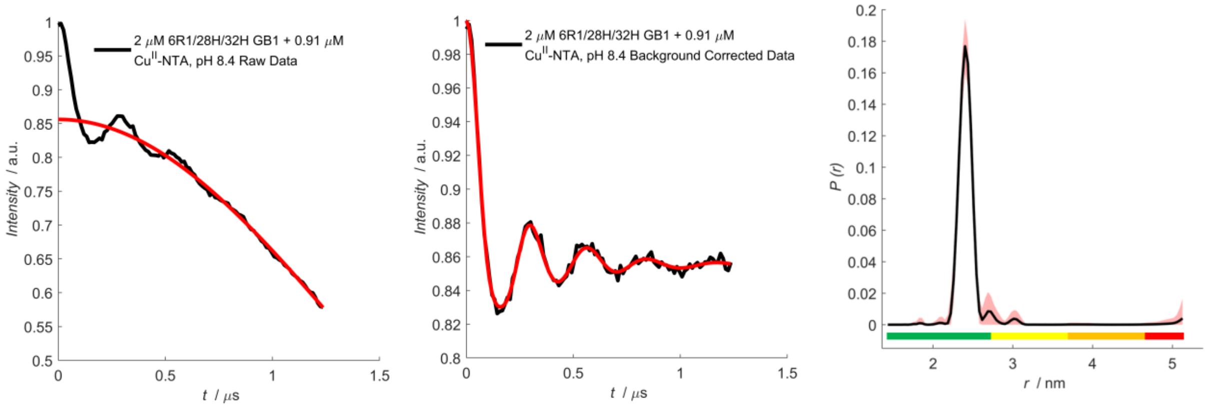

Figure 5.3.8.9: RIDME data of 2 µM 6R1/28H/32H GB1 in presence of 0.91 µM Cu^{II}-NTA. The sample pH was 8.4. The experimental trace, background corrected data, and distance distribution are shown left-to-right, respectively.

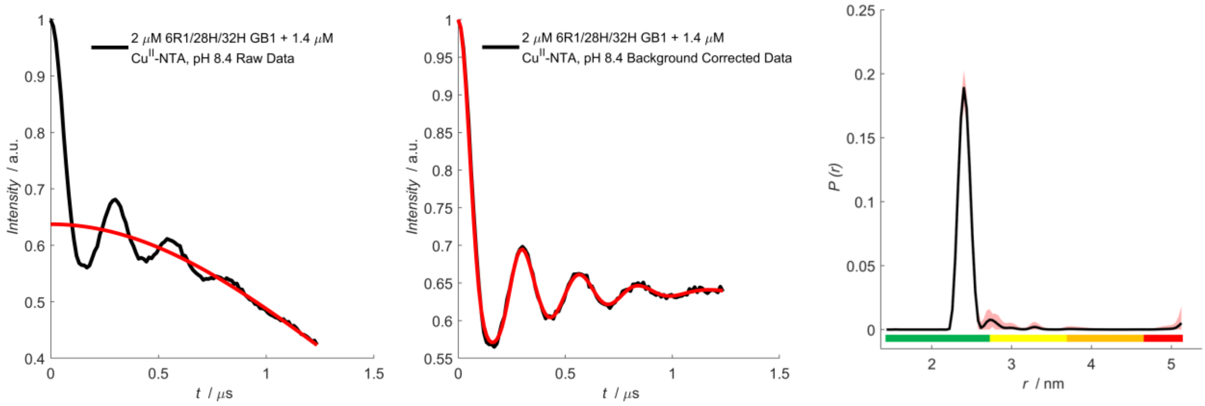

Figure 5.3.8.10: RIDME data of 2 µM 6R1/28H/32H GB1 in presence of 1.4 µM Cu^{II}-NTA. The sample pH was 8.4. The experimental trace, background corrected data, and distance distribution are shown left-to-right, respectively.

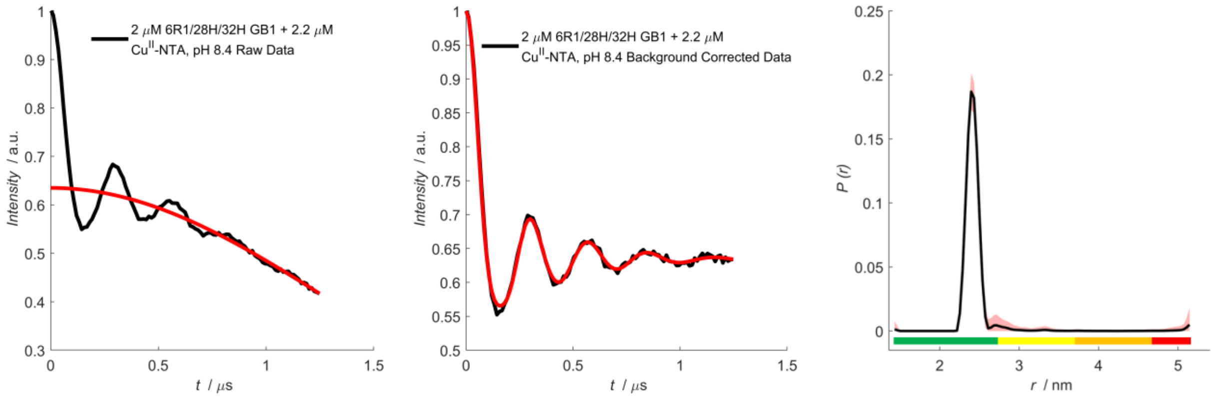

Figure 5.3.8.11: RIDME data of 2 µM 6R1/28H/32H GB1 in presence of 2.2 µM Cu^{II}-NTA. The sample pH was 8.4. The experimental trace, background corrected data, and distance distribution are shown left-to-right, respectively.

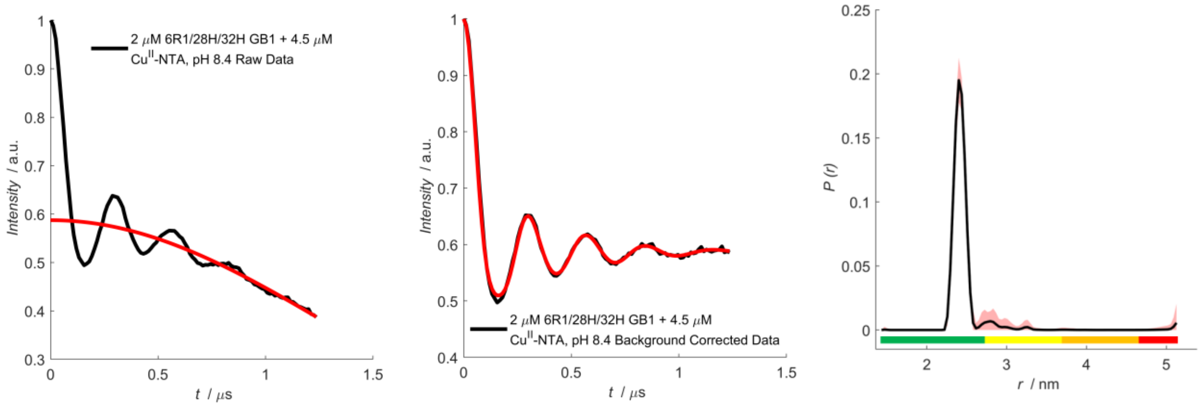

Figure 5.3.8.12: RIDME data of 2 µM 6R1/28H/32H GB1 in presence of 4.5 µM Cu^{II}-NTA. The sample pH was 8.4. The experimental trace, background corrected data, and distance distribution are shown left-to-right respectively.

Sample	Zero-time [ns]	Background Start [ns]	Background Cut-off [ns]	Background Dimension	Modulation depth (Δ)
2 μM 6R1/28H/32H + 0.22 μM Cu^{II}-NTA	206	194	1236	6.00	0.032 ± 2.8 x 10^{-3}
2 μM 6R1/28H/32H + 0.45 μM Cu^{II}-NTA	207	328	1236	6.00	0.061 ± 3.4 x 10^{-3}
2 μM 6R1/28H/32H + 0.91 μM Cu^{II}-NTA	205	151	1236	6.00	0.144 ± 4.6 x 10^{-3}
2 μM 6R1/28H/32H + 1.4 μM Cu^{II}-NTA	205	62	1236	6.00	0.363 ± 1.1 x 10^{-2}
2 μM 6R1/28H/32H + 2.2 μM Cu^{II}-NTA	204	62	1248	6.00	0.365 ± 1.3 x 10^{-2}
2 μM 6R1/28H/32H + 4.5 μM Cu^{II}-NTA	206	62	1236	6.00	0.413 ± 1.4 x 10^{-2}

Table 5.3.8.2. Parameters for the stretched exponential background correction and associated modulation depths of the RIDME pseudo-titration performed at pH 8.4, shown in figures 5.3.8.7-12.

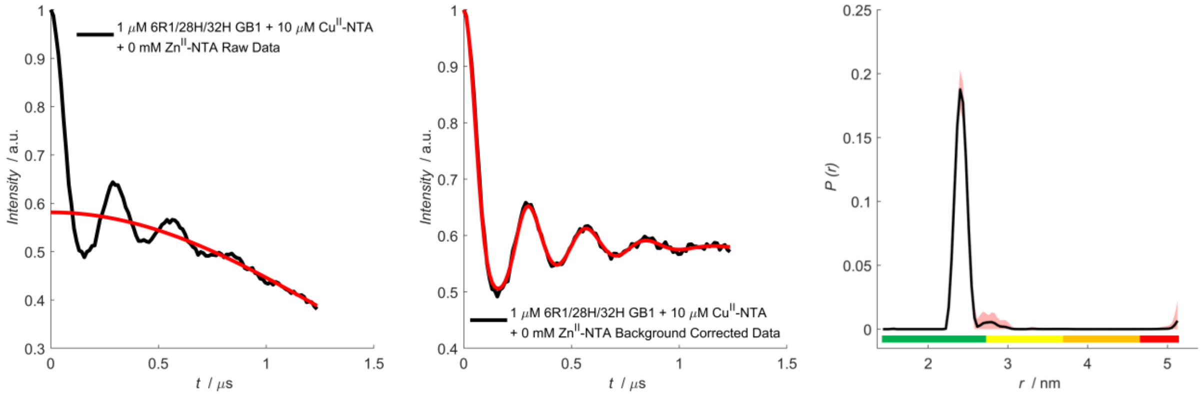

Figure 5.3.8.13: RIDME data of 1 μM 6R1/28H/32H GB1 in presence of 10 μM Cu^{II}-NTA. The sample pH was 7.4. The experimental trace, background corrected data, and distance distribution are shown left-to-right, respectively.

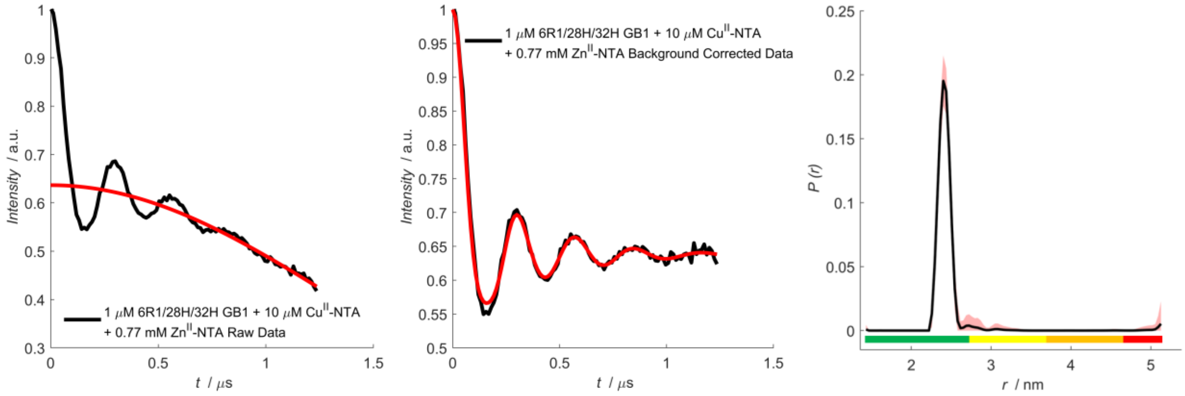

Figure 5.3.8.14: RIDME data of 1 μM 6R1/28H/32H GB1 in presence of 10 μM Cu^{II}-NTA and 0.77 mM Zn^{II}-NTA. The sample pH was 7.4. The experimental trace, background corrected data, and distance distribution are shown left-to-right, respectively.

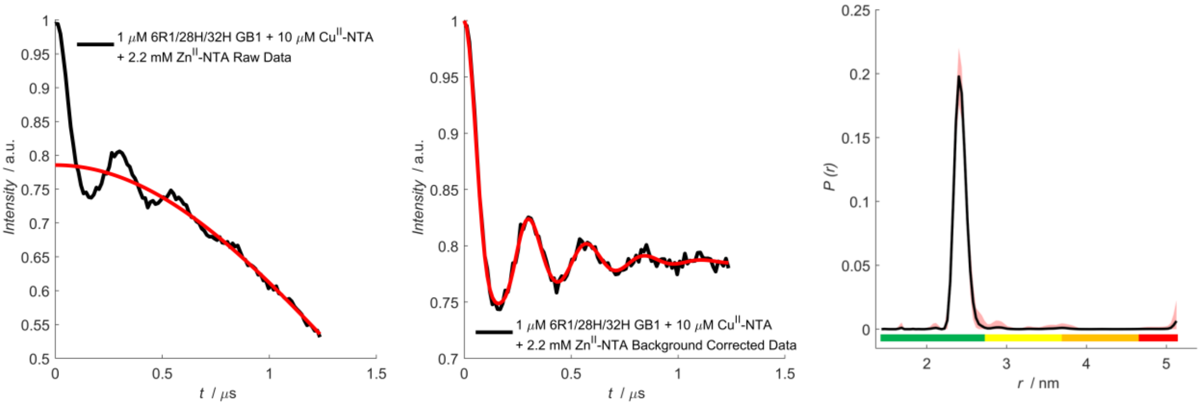

Figure 5.3.8.15: RIDME data of 1 µM 6R1/28H/32H GB1 in presence of 10 µM Cu^{II}-NTA and 2.2 mM Zn^{II}-NTA. The sample pH was 7.4. The experimental trace, background corrected data, and distance distribution are shown left-to-right, respectively.

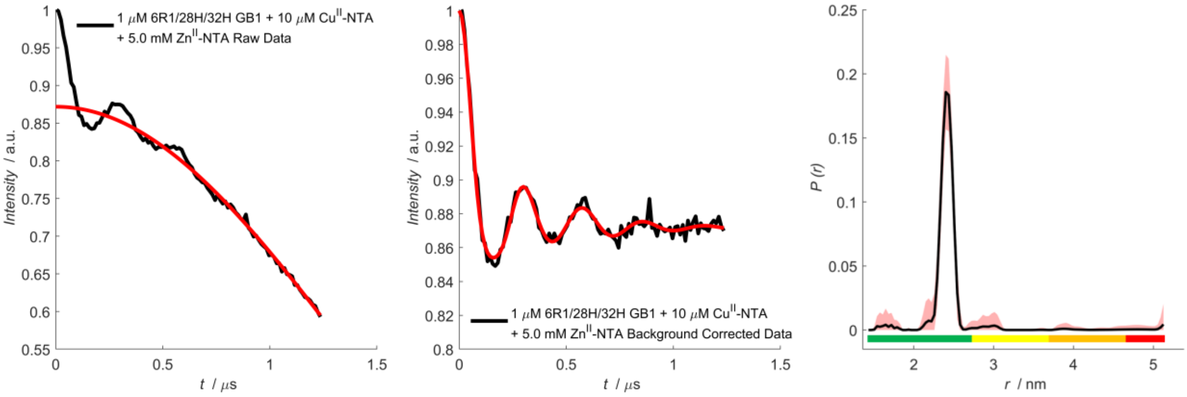

Figure 5.3.8.16: RIDME data of 1 µM 6R1/28H/32H GB1 in presence of 10 µM Cu^{II}-NTA and 5.0 mM Zn^{II}-NTA. The sample pH was 7.4. The experimental trace, background corrected data, and distance distribution are shown left-to-right, respectively.

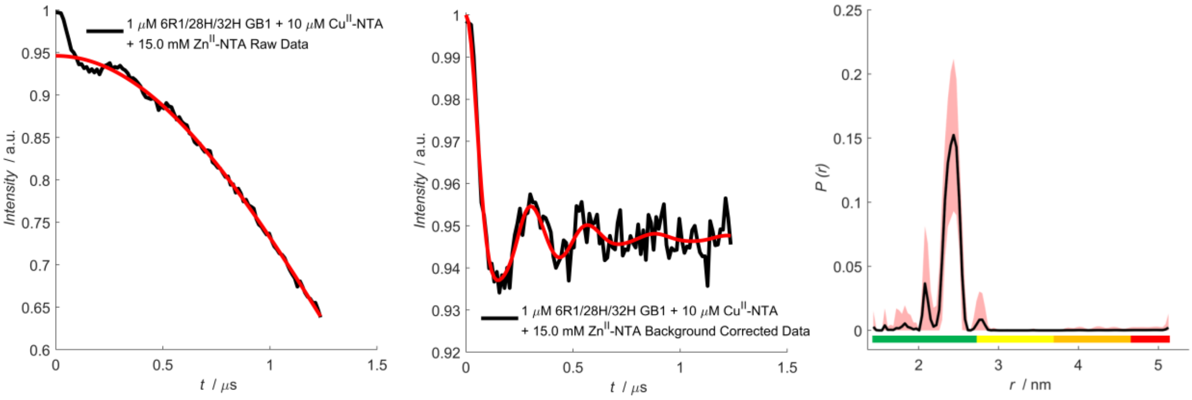

Figure 5.3.8.17: RIDME data of 1 µM 6R1/28H/32H GB1 in presence of 10 µM Cu^{II}-NTA and 15.0 mM Zn^{II}-NTA. The sample pH was 7.4. The experimental trace, background corrected data, and distance distribution are shown left-to-right, respectively.

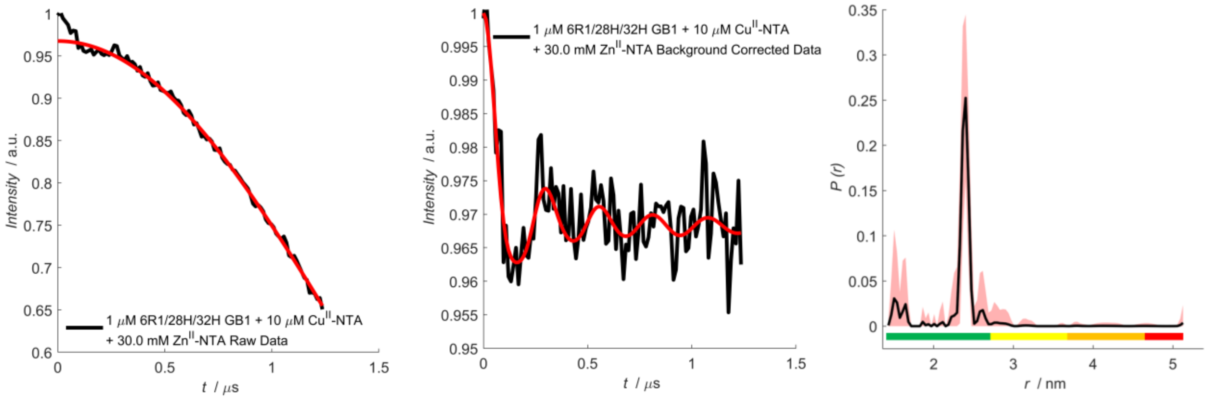

Figure 5.3.8.18: RIDME data of 1 µM 6R1/28H/32H GB1 in presence of 10 µM Cu^{II}-NTA and 30.0 mM Zn^{II}-NTA. The sample pH was 7.4. The experimental trace, background corrected data, and distance distribution are shown left-to-right, respectively.

Sample	Zero-time [ns]	Background Start [ns]	Background Cut-off [ns]	Background Dimension	Modulation depth (Δ)
1 µM 6R1/28H/32H + 0 mM Zn^{II}-NTA	206	151	1236	6.00	0.419 ± 1.1 x 10^{-2}
1 µM 6R1/28H/32H + 0.77 mM Zn^{II}-NTA	207	328	1236	6.00	0.364 ± 1.5 x 10^{-2}
1 µM 6R1/28H/32H + 2.2 mM Zn^{II}-NTA	205	151	1236	6.00	0.214 ± 8.0 x 10^{-3}
1 µM 6R1/28H/32H + 5.0 mM Zn^{II}-NTA	206	106	1236	6.00	0.128 ± 8.8 x 10^{-3}
1 µM 6R1/28H/32H + 15 mM Zn^{II}-NTA	206	62	1236	6.00	0.054 ± 4.6 x 10^{-3}
1 µM 6R1/28H/32H + 30 mM Zn^{II}-NTA	208	106	1236	6.00	0.032 ± 4.8 x 10^{-3}

Table 5.3.8.3: Parameters for the stretched exponential background correction and associated modulation depths of the RIDME pseudo-titration performed in presence of Zn^{II}-NTA and at pH 7.4, shown in figures 5.3.8.13-18.

It is seen for all validated distance distributions that the only significant peak (~2.5 nm) is within the green of the colour bar (even at vast excesses of competitor ligand Zn^{II}-NTA), indicating that distance information can still be reliably extracted under such conditions.

5.3.9 Optimisation of Cu^{II}-IDA Complex Formation

Previous literature has indicated that RIDME pseudo-titration modulation depths, particularly for the I6H/N8H/K28R1 series in presence of Cu^{II}-IDA (chapter 3.3.11) are consistently lower than anticipated. This led to speculation that the equilibrium concentration of Cu^{II}-IDA was also lower than expected, leading to a reduced availability of the chelate to coordinate the double-histidine motif. Interestingly, this effect was not observed with the Cu^{II}-NTA chelate, suggesting the problem does not stem from the protein construct, but rather is specific to the Cu^{II}-IDA label. It is known from literature that the complexation constant of Cu^{II}-NTA is approximately three orders of magnitude greater than for Cu^{II}-IDA, and it has been shown that forming the complex in presence of a tetra-histidine protein can increase PELDOR modulation depth, for otherwise identical experimental conditions.[170] Therefore, to optimise the preparation of Cu^{II}-IDA spin label, UV-visible spectroscopy measurements were performed using three different preparatory conditions, as described in section 5.2.3.

Results are shown below in figures 5.3.8.1-3 for preparation modes i), ii) and iii). Method i) corresponds to 1:1 mixing of $CuCl_2$ and IDA to produce 50 mM Cu^{II}-IDA, before diluting in milliQ H_2O, method ii) instead dilutes with buffer A (150 mM NaCl, 42.4 mM Na_2HPO_4, 7.6 mM KH_2PO_4, pH 7.4), and method iii) first dilutes the IDA buffer in 1:8 equivalence with buffer A, before addition of 1 equivalent of $CuCl_2$. Methods i), ii) and iii) are discussed subsequently as 'H_2O series', 'neutralised series' and 'buffer series', respectively, to distinguish them. Comparison of the observed A_{726nm} values and those predicted from theory are shown in figure 5.3.9.4. Observed absorbance at 726 nm, and the calculated concentrations are given in tables 5.3.9.1-3 overleaf.

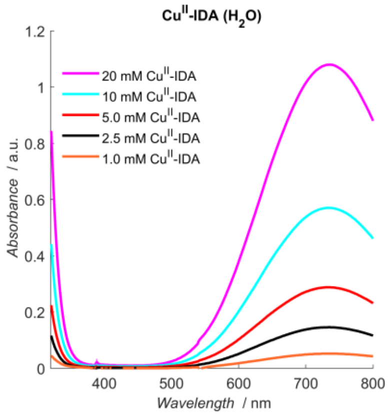

Figure 5.3.9.1. Absorbance spectra recorded for the 'H_2O' Cu^{II}-IDA dilution series (method i), repeated in triplicate, with ± 2σ confidence intervals indicated as the shaded regions. Magenta, cyan, red, black and orange traces correspond to 20, 10, 5, 2.5, and 1.0 mM Cu^{II}-IDA concentration.

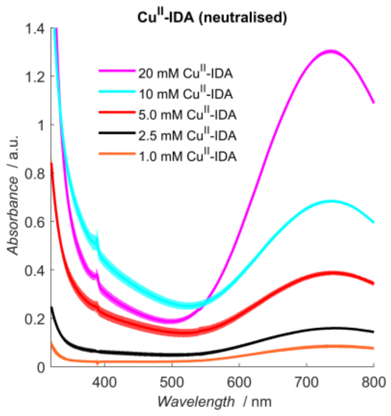

Figure 5.3.9.2. Absorbance spectra recorded for the ‘neutralized’ Cu^{II}-IDA dilution series (method ii), repeated in triplicate, with ± 2σ confidence intervals indicated as the shaded regions. Magenta, cyan, red, black and orange traces correspond to 20, 10, 5, 2.5, and 1.0 mM Cu^{II}-IDA concentration.

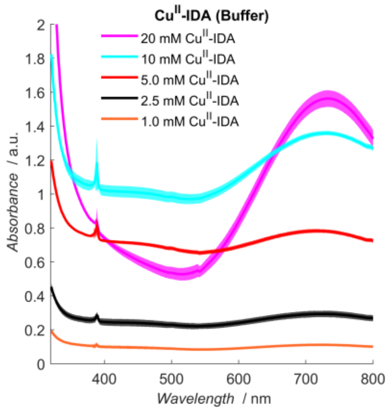

Figure 5.3.9.3. Absorbance spectra recorded for the ‘buffer’ Cu^{II}-IDA dilution series (method iii), repeated in triplicate, with ± 2σ confidence intervals indicated as the shaded regions. Magenta, cyan, red, black and orange traces correspond to 20, 10, 5, 2.5, and 1.0 mM Cu^{II}-IDA concentration.

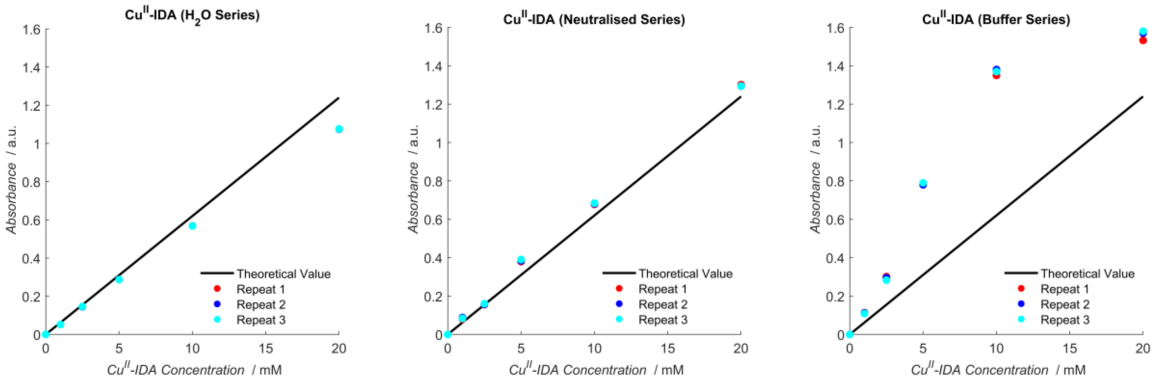

Figure 5.3.9.4. Absorbance at 726 nm as a function of Cu^{II}-IDA concentration for the ‘H_2O’, ‘neutralized’, and ‘buffer’ series, from left-to-right. Experimental data for each repeat set is shown as a red, blue or cyan scatter, with the literature value for the extinction coefficient plotted in black. For the ‘H_2O’ and ‘neutralized’ series, there is reasonable agreement (within ~20%), with the values predicted from theory.

Sample	Observed A_{726nm} (a.u.)			Calculated Concentration (mM)		
Repeat	1	2	3	1	2	3
20 mM Cu^{II}-IDA	1.075	1.075	1.075	17.3	17.3	17.4
10 mM Cu^{II}-IDA	0.569	0.569	0.568	9.2	9.2	9.2
5.0 mM Cu^{II}-IDA	0.287	0.287	0.287	4.6	4.6	4.6
2.5 mM Cu^{II}-IDA	0.145	0.145	0.145	2.3	2.3	2.4
1.0 mM Cu^{II}-IDA	0.052	0.052	0.052	0.8	0.8	0.8

Table 5.3.9.1. The observed absorbance at 726 nm for each Cu^{II}-IDA solution taken from the spectra shown in figure 5.3.9.1.

Sample	Observed A_{726nm} (a.u.)			Calculated Concentration (mM)		
Repeat	1	2	3	1	2	3
20 mM Cu^{II}-IDA	1.302	1.294	1.295	21.0	20.8	20.9
10 mM Cu^{II}-IDA	0.678	0.681	0.684	10.9	11.0	11.0
5.0 mM Cu^{II}-IDA	0.380	0.384	0.390	6.1	6.2	6.3
2.5 mM Cu^{II}-IDA	0.155	0.157	0.160	2.5	2.5	2.6
1.0 mM Cu^{II}-IDA	0.080	0.088	0.084	1.3	1.4	1.4

Table 5.3.9.2. The observed absorbance at 726 nm for each Cu^{II}-IDA solution taken from the spectra shown in figure 5.3.9.2.

Sample	Observed A_{726nm} (a.u.)			Calculated Concentration (mM)		
Repeat	1	2	3	1	2	3
20 mM Cu^{II}-IDA	1.532	1.570	1.580	24.7	25.3	25.5
10 mM Cu^{II}-IDA	1.352	1.380	1.370	21.8	22.3	22.1
5.0 mM Cu^{II}-IDA	0.780	0.780	0.790	12.6	12.6	12.7
2.5 mM Cu^{II}-IDA	0.301	0.295	0.283	4.9	4.8	4.6
1.0 mM Cu^{II}-IDA	0.113	0.112	0.109	1.8	1.8	1.8

Table 5.3.9.3. The observed absorbance at 726 nm for each Cu^{II}-IDA solution taken from the spectra shown in figure 5.3.9.3.

Figure 5.3.9.1 shows that in the absence of phosphate buffer, the region of the spectrum between 320 and ~500 nm wavelength there is minimal absorbance, regardless of the measured Cu^{II}-IDA concentration. This implies that Cu^{II}-IDA does not contribute to absorbance in this region. In figure 5.3.9.2, the baseline is no longer flat, and shows strong absorbance across a wide range of wavelengths; since the resulting solution is not black, it is possible this is instead the result of Rayleigh scattering, due to precipitation. In figure 5.3.9.3, this effect seems to be further exacerbated, with spectra also lacking the pronounced local maximum at ~750 nm. Instructively, the difference between spectra in figures 5.3.9.2 and 5.3.9.3 indicates the significance of first allowing the Cu^{II}-IDA complex to form before the addition of phosphate; this is particularly relevant since IDA is not a strong chelator of Cu^{II}, therefore the reaction equilibrium may lie on the side of unbound reactants, and result in a population of free Cu^{II}. This likely explains the emergence of the sloping baseline, since a percentage of the free Cu^{II} will precipitate through interaction with the phosphate buffer, or due to alkaline pH. In the case of figure 5.3.9.3, this may be more pronounced, since the IDA chelate is first diluted in buffer, meaning the equilibrium will shift towards the protonated state. Therefore, upon addition of the $CuCl_2$ there will be less IDA available to first form the complex, leaving free Cu^{II}, which can form copper phosphate precipitate.

Measurements were then reproduced in the presence of 2 equivalents of imidazole, to emulate conditions of forming Cu^{II}-IDA chelator in the presence of a double-histidine motif, as was performed in previous literature.[170] As above, series are distinguished in discussion as 'H_2O series' and 'buffer series' and spectra are shown respectively in figures 5.3.9.5-6. Comparison of the observed A_{726nm} values and those predicted from theory are shown in figure 5.3.9.7. Observed absorbance at 726 nm, and the calculated concentrations are given in tables 5.3.9.4 and 5.3.9.5 below. In presence of an excess of imidazole the region of the spectra between 320 and ~500 nm wavelength is similar to spectra recorded in the absence of phosphate buffer (figure 5.3.9.1). This is highly consistent with previous literature and the hypothesis that formation of the Cu^{II}-IDA complex is enhanced in presence of imidazole.

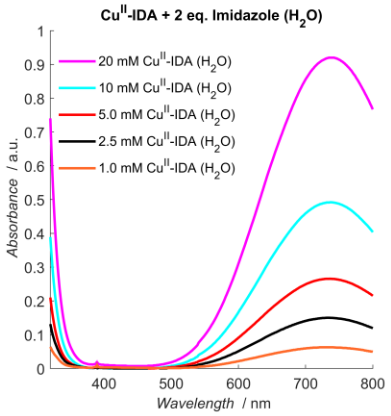

Figure 5.3.9.5. Absorbance spectra recorded for the 'H_2O' Cu^{II}-IDA + imidazole dilution series, repeated in triplicate, with ± 2σ confidence intervals indicated as the shaded regions. Magenta, cyan, red, black and orange traces correspond to 20, 10, 5, 2.5, and 1.0 mM Cu^{II}-IDA concentration (each measured in presence of 2 equivalents of imidazole).

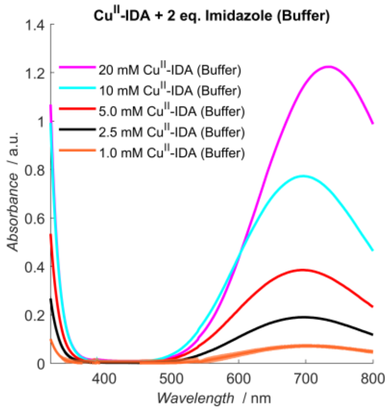

Figure 5.3.9.6. Absorbance spectra recorded for the 'buffer' Cu^{II}-IDA + imidazole dilution series, repeated in triplicate, with ± 2σ confidence intervals indicated as the shaded regions. Magenta, cyan, red, black and orange traces correspond to 20, 10, 5, 2.5, and 1.0 mM Cu^{II}-IDA concentration (each measured in presence of 2 equivalents of imidazole).

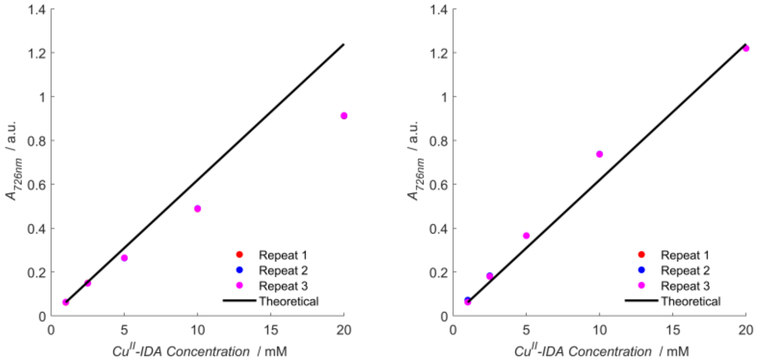

Figure 5.3.9.7. Absorbance at 726 nm as a function of Cu^{II}-IDA concentration for the 'H_2O' and 'buffer' series, from left-to-right. Experimental data for each repeat set is shown as a red, blue or magenta scatter, with the literature value for the extinction coefficient plotted in black. For the 'H_2O' series, there is a discrepancy with the values predicted from theory, particularly at higher concentrations.

Sample	Observed A_{726nm} (a.u.)			Calculated Concentration (mM)		
Repeat	1	2	3	1	2	3
20 mM Cu^{II}-IDA	0.912	0.913	0.914	14.7	14.7	14.7
10 mM Cu^{II}-IDA	0.488	0.490	0.489	7.9	7.9	7.9
5.0 mM Cu^{II}-IDA	0.264	0.264	0.265	4.3	4.3	4.3
2.5 mM Cu^{II}-IDA	0.150	0.149	0.149	2.4	2.4	2.4
1.0 mM Cu^{II}-IDA	0.062	0.063	0.063	1.0	1.0	1.0

Table 5.3.9.4. The observed absorbance at 726 nm for each Cu^{II}-IDA solution taken from the spectra shown in figure 5.3.9.5.

Sample	Observed A_{726nm} (a.u.)			Calculated Concentration (mM)		
Repeat	1	2	3	1	2	3
20 mM Cu^{II}-IDA	1.22	1.22	1.22	19.7	19.7	19.7
10 mM Cu^{II}-IDA	0.737	0.738	0.737	11.9	11.9	11.9
5.0 mM Cu^{II}-IDA	0.366	0.366	0.366	5.9	5.9	5.9
2.5 mM Cu^{II}-IDA	0.183	0.183	0.180*	3.0	3.0	2.9
1.0 mM Cu^{II}-IDA	0.065	0.072*	0.072*	1.0	1.2	1.2

Table 5.3.9.5. The observed absorbance at 726 nm for each Cu^{II}-IDA solution taken from the spectra shown in figure 5.3.9.6.

Furthermore, the presence of imidazole appears to completely remove precipitate, suggesting that free Cu^{II} forms adducts with the phosphate buffer. Imidazole co-ordinates both free Cu^{II} and likely stabilises Cu^{II}-IDA such that the equilibrium lies further to the side of the complex, leading to a reduction in the population of free Cu^{II}, as well as reducing the availability of free Cu^{II} to interact with phosphate and precipitate. To ensure that the imidazole did not contribute to absorbance in the visible range, a complete imidazole dilution series was performed, and as seen from figure 5.3.9.8, absorbance is flat in the range 550-800 nm. The λ_{max} value of the imidazole absorbance spectrum occurs at 320 nm, and values are given below in table 5.3.9.6, and plotted as a function of concentration in figure 5.3.9.9.

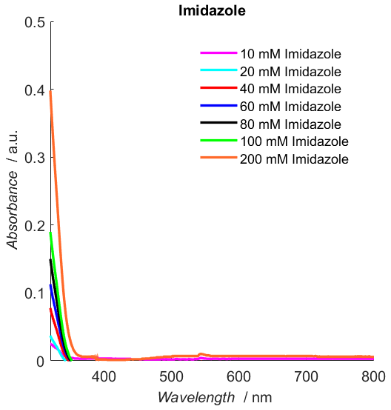

Figure 5.3.9.8. Absorbance spectra recorded for an imidazole dilution series, repeated in triplicate, with ± 2σ confidence intervals indicated as the shaded regions. Magenta, cyan, red, blue, black, red and blue traces correspond to 200, 100, 80, 60, 40, 20, and 10 mM imidazole concentration.

Sample	Observed A_{320nm} (a.u.)		
Repeat	1	2	3
200 mM Imidazole	0.399	0.398	0.397
100 mM Imidazole	0.190	0.190	0.190
80 mM Imidazole	0.150	0.150	0.150
60 mM Imidazole	0.113	0.113	0.112
40 mM Imidazole	0.078	0.078	0.077
20 mM Imidazole	0.037	0.037	0.037
10 mM Imidazole	0.026	0.024	0.024

Table 5.3.9.6. The observed absorbance at 320 nm for each imidazole solution taken from the spectra shown in figure 5.3.9.8.

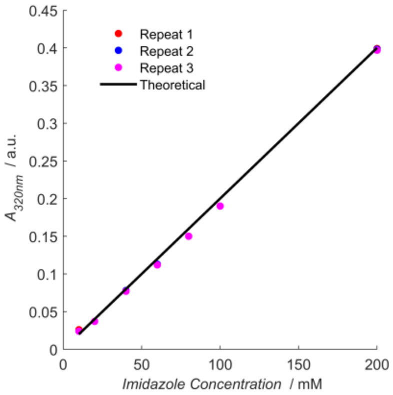

Figure 5.3.9.9. Absorbance at 320 nm as a function of imidazole concentration, the theoretical curve is given using an extinction coefficient of 2 $M^{-1}cm^{-1}$. Experimental data for each repeat set is shown as a red, blue or magenta scatter.

5.3.10 Quantification of Ni^{II}-NTA Concentration by UV-Visible Spectroscopy

Ni^{II}-NTA has an extinction coefficient of 5.47 $M^{-1}cm^{-1}$ at A_{620nm} and pH 4.4.[342] UV-visible spectra are shown in figure 5.3.10.1, and extinction coefficients of 5.2 $M^{-1}cm^{-1}$ and 5.3 $M^{-1}cm^{-1}$ are calculated from data measured at pH 4.7 shown in figure 5.3.10.2. Observed absorbance at 393, 620 and 625 nm are given in tables 5.3.10.1-3 below.

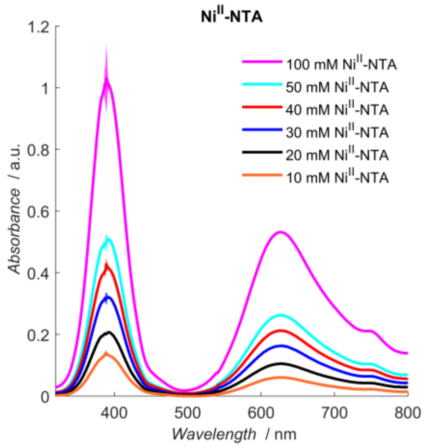

Figure 5.3.10.1. Absorbance spectra recorded for Ni^{II}-NTA dilution series, repeated in triplicate, with ± 2σ confidence intervals indicated as the shaded regions. Magenta, cyan, red, blue, black and orange correspond to 100, 50, 40, 30, 20, and 10 mM.

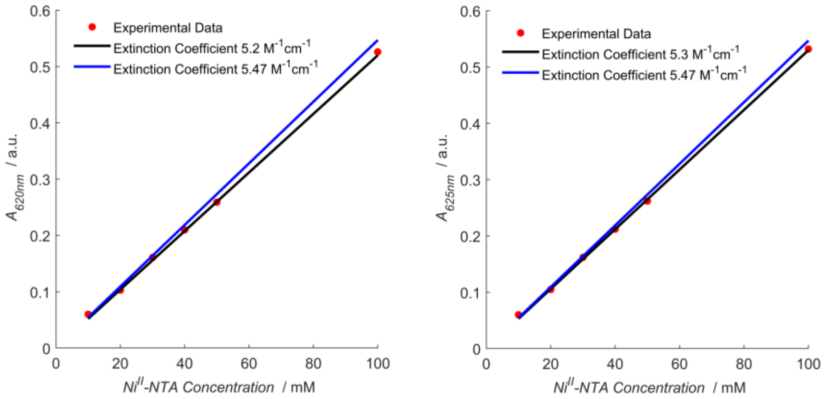

Figure 5.3.10.2. Absorbance at 620 nm (left) and 625 nm (right) as a function of Ni^{II}-NTA concentration. Experimental data is shown as a red scatter, with the literature value for the extinction coefficient shown in blue, and the empirical value (best fit of experimental data) shown in black. In both cases the experimental values for the extinction coefficient agree within 10%.

Sample	Observed A_{393nm}		
Repeat	1	2	3
100 mM Ni^{II}-NTA	1.006	1.011	1.005
50 mM Ni^{II}-NTA	0.509	0.507	0.507
40 mM Ni^{II}-NTA	0.413	0.413	0.412
30 mM Ni^{II}-NTA	0.320	0.319	-
20 mM Ni^{II}-NTA	0.207	0.207	0.207
10 mM Ni^{II}-NTA	0.131	0.060	0.060

Table 5.3.10.1. The observed absorbance at 393 nm for each Ni^{II}-NTA solution taken from the spectra shown in figure 5.3.10.1. A_{393nm} corresponds to lambda max for each spectrum.

Sample	Observed A_{620nm}		
Repeat	1	2	3
100 mM Ni^{II}-NTA	0.526	0.526	0.526
50 mM Ni^{II}-NTA	0.259	0.259	0.259
40 mM Ni^{II}-NTA	0.210	0.210	0.210
30 mM Ni^{II}-NTA	0.161	0.161	-
20 mM Ni^{II}-NTA	0.103	0.103	0.104
10 mM Ni^{II}-NTA	0.060	0.060	0.060

Table 5.3.10.2. The observed absorbance at 620 nm for each Ni^{II}-NTA solution taken from the spectra shown in figure 5.3.10.1.

Sample	Observed A_{625nm}		
Repeat	1	2	3
100 mM Ni^{II}-NTA	0.532	0.531	0.531
50 mM Ni^{II}-NTA	0.262	0.262	0.262
40 mM Ni^{II}-NTA	0.212	0.212	0.212
30 mM Ni^{II}-NTA	0.163	0.162	-
20 mM Ni^{II}-NTA	0.105	0.105	0.105
10 mM Ni^{II}-NTA	0.060	0.060	0.060

Table 5.3.10.3. The observed absorbance at 625 nm for each Ni^{II}-NTA solution taken from the spectra shown in figure 5.3.10.1.

The $NiCl_2$ dilution series at pH 4.7 of nominal concentrations of 75, 50, 40, 30, 25 and 10 mM is shown in figure 5.3.10.3 below. Each spectrum has 3 distinct bands: a global maximum at 393 nm, with local maxima at 656 nm and 720 nm. This spectrum of Ni^{II} is consistent with that reported in the literature[346,347] and the multiple absorbance peaks are attributed to multiple different electron transitions for a d^8 configuration. Extinction coefficients were determined at three wavelengths; 393, 620, and 750 nm, and were calculated as 4.2, 0.92 and 1.6 $M^{-1}cm^{-1}$, respectively, from the data shown in figure 5.3.10.4. Observed absorbance at 393, 620 and 750 nm are given in tables 5.3.10.4-6 overleaf.

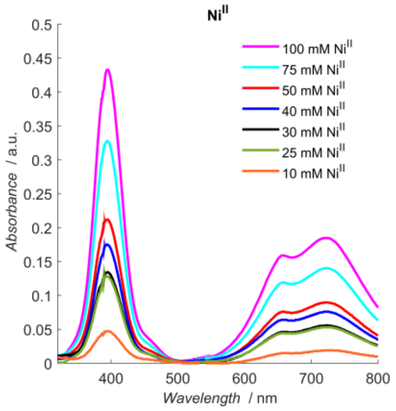

Figure 5.3.10.3. Absorbance spectra recorded for Ni^{II}.6H$_2$O dilution series, repeated in triplicate, repeated in triplicate, with ± 2σ confidence intervals indicated as the shaded regions as shown in each panel. Magenta, cyan, red, blue, black, green and orange correspond to 100, 75, 50, 40, 30, 25, and 10 mM. Note that 75 mM Ni^{II}.6H$_2$O was only repeated in duplicate.

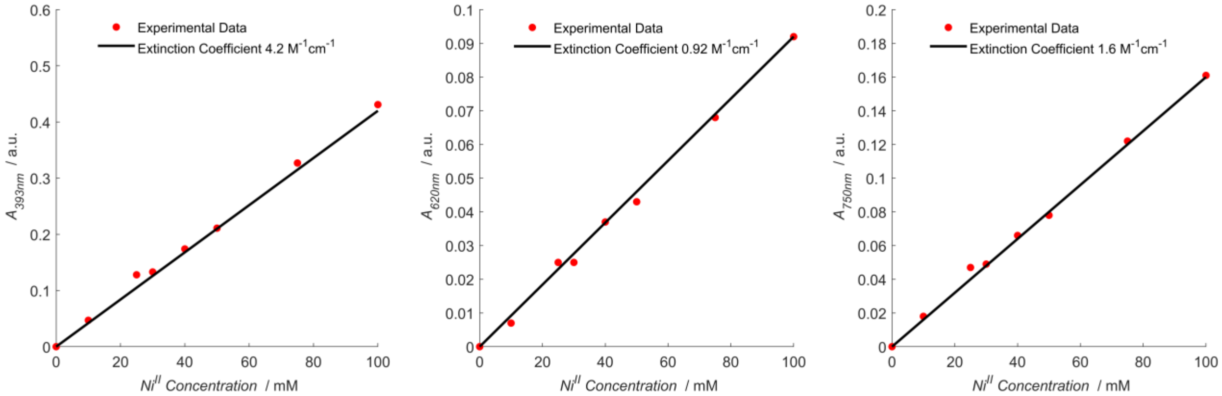

Figure 5.3.10.4. Concentration of Ni^{II} vs absorbance at 393 nm (left), 620 nm (centre) and 750 nm (right). Experimental data is shown as a red scatter, and the empirical value (best fit of experimental data) shown in black.

Sample	Observed A_{393nm}		
Repeat	1	2	3
100 mM Ni^{II}	0.431	0.431	0.432
75 mM Ni^{II}	0.327	0.327	-
50 mM Ni^{II}	0.211	0.212	0.211
40 mM Ni^{II}	0.174	0.175	0.174
30 mM Ni^{II}	0.133	0.134	0.134
25 mM Ni^{II}	0.128	0.127	0.128
10 mM Ni^{II}	0.047	0.047	0.047

Table 5.3.10.4. The observed absorbance at 393 nm for each Ni^{II} solution taken from the spectra shown in figure 5.3.10.3. A_{393nm} corresponds to lambda max for each spectrum.

Sample	Observed A_{620nm}		
Repeat	1	2	3
100 mM Ni^{II}	0.092	0.091	0.092
75 mM Ni^{II}	0.068	0.068	-
50 mM Ni^{II}	0.043	0.043	0.043
40 mM Ni^{II}	0.037	0.037	0.037
30 mM Ni^{II}	0.025	0.025	0.025
25 mM Ni^{II}	0.025	0.025	0.025
10 mM Ni^{II}	0.007	0.007	0.007

Table 5.3.10.5. The observed absorbance at 620 nm for each Ni^{II} solution taken from the spectra shown in figure 5.3.10.3.

Sample	Observed A_{750nm}		
Repeat	1	2	3
100 mM Ni^{II}	0.161	0.160	0.161
75 mM Ni^{II}	0.122	0.123	-
50 mM Ni^{II}	0.078	0.078	0.078
40 mM Ni^{II}	0.066	0.066	0.066
30 mM Ni^{II}	0.049	0.048	0.049
25 mM Ni^{II}	0.047	0.047	0.047
10 mM Ni^{II}	0.018	0.017	0.017

Table 5.3.10.6. The observed absorbance at 750 nm for each Ni^{II} solution taken from the spectra shown in figure 5.3.10.3.

5.4 Conclusion and Outlook

Our findings demonstrate that α-helical double-histidine motifs coupled with Cu^{II}-NTA is a spin labelling strategy that is highly robust against adventitious divalent metal ions, and variations in pH between 6.4 and 8.4. Results indicate that under PD-EPR measurement conditions, Cu^{II}-NTA loading of double-histidine motifs is resistant to >1000-fold molar excess Zn^{II}-NTA, as distance information could still be reliably extracted (even at 1 µM protein concentration). This is encouraging for the widespread application of double-histidine motifs in metalloproteins, or in systems where divalent metal cofactors are necessary. Additionally, the benchmarking of a competition assay using PD-EPR is particularly exciting because it allows remote detection of binding interactions with diamagnetic ligands. This will be promising in cases where paramagnetic ligand analogues are not available or cause structural perturbation.

Furthermore, measurements performed at pH 6.4 and 8.4 showcase that high nanomolar affinity is retained, and K_D estimates taken from Cu^{II}-nitroxide RIDME are consistent with the trend observed from room-temperature ITC measurements, albeit showing a reduced influence of pH at cryogenic temperatures. Importantly, our results highlight that Cu^{II}-NTA labelling of double-histidine motifs is marginally more efficient at pH 8.4 compared to pH 7.4 (91 nM vs 135 nM), and still allows reliable extraction of distance information (i.e., no additional peaks arise from off-site interactions away from the double-histidine motif). While this relative gain in binding affinity is small, it may prove important in further optimising Cu^{II}-NTA double-histidine motif spin labelling for measurements where concentration is limiting, and sensitivity is paramount. It would also be desirable in the future to understand the mechanism of how pH influences binding affinity more severely at room-temperature than under cryogenic conditions. Labelling of histidine residues with ^{15}N could allow protonation state to be followed as a function of temperature and pH *via* NMR.

Additionally, PD-EPR has greater sensitivity than ITC and the coupling of thermodynamic and structural information allows for the facile monitoring of non-specific and competitor ligand interactions.[235] Traditionally, monitoring competitive ligand binding has required expensive radio-labelling and judicious selection of appropriate isotopes.[252,348] PD-EPR may complement these strategies, while obviating potential cost and safety considerations. However, the current benchmarking work is limited in scope and in future, extension of the mathematical description applied herein beyond weak (i.e., a model with numerical solutions for the equilibrium concentrations of competitor and non-competitor ligands), and obligate diamagnetic competitor ligands is highly desirable. In this purview, ITC, UV-vis and Evan’s NMR characterisation of Ni^{II}-NTA complex suggest it could be a particularly good candidate competitor ligand for such future methodology work.

Chapter 6: Conclusions and Outlook

This chapter is intended to summarise the conclusions drawn from each of the results chapters, as well as contextualise these results in the scope of future applications and outlook. Application of modulation depth quantitation to study complex binding equilibria is discussed, through combination of different experiments.

This thesis provides an in-depth benchmarking study of applications of RIDME modulation depth quantitation to investigate non-covalent binding equilibria. As a tractile model system, various constructs of the GB1 protein were used in conjunction with pairs of histidine residues in different configurations to facilitate coordination of Cu^{II}-chelates. Investigating the affinity and robustness of these coordination interactions under PD-EPR conditions was also especially appealing, as double-histidine motif non-covalent spin labelling with Cu^{II}-chelates can provide exquisite precision and accuracy in the distance domain and present an alternative to nitroxide-based spin labels, with chemical orthogonality to thiol-directed labelling reactions. Therefore, it is hoped that the results presented herein will assist with widespread adoption of double-histidine motif spin labelling.

Briefly, chapter 3 demonstrates determination of binding constants (K_D) from Cu^{II}-nitroxide RIDME modulation depths. The RIDME pseudo-titrations, in conjunction with room-temperature ITC measurements, allow K_D values to be fitted, showcasing the high nM binding affinity of the α-helical motif for Cu^{II}-NTA. Chapter 4 demonstrates simultaneous determination of pairs of K_D values from Cu^{II}-Cu^{II} RIDME modulation depths. A general speciation model is also derived that facilitates determination of sensitivity optima of Cu^{II}-Cu^{II} RIDME measurements in dependence of K_D values, protein concentration, and label concentration. Chapter 5 demonstrates determination of diamagnetic competitor K_D values from Cu^{II}-nitroxide RIDME modulation depths, in a competitive binding-assay format. The influence of adventitious metal ions and different pH conditions upon double-histidine motif affinity is investigated using RIDME pseudo-titrations and ITC measurements.

One of the most significant findings is that double-histidine motif labelling *via* Cu^{II}-chelates is well suited for PD-EPR applications, with affinities in the high-nM and low-µM concentration regimes under cryogenic conditions. It is important to note at the end of this work that K_D estimates from PD-EPR data are likely to be upper-bounds in many cases, with the main error contributions arising from i) measurements at protein concentrations above K_D, such that the binding isotherm is closer to a step function and resolving low K_D values (i.e., high affinities) with sufficient accuracy becomes difficult and ii) mono-exponential approximation of T_1 relaxation behaviour, which can lead to over-estimation of binding affinity at short mixing times (chapter 4). In this spirit, relatively broad intervals for consensus K_D values are assigned at each double histidine motif.

When taken together, the error analysis in chapters 3 and 4 indicate that the α-helical double-histidine motif has a consensus upper-bound K_D value for Cu^{II}-NTA in the range ~0.1-1.0 µM at 235 K, (i.e., estimates lie within this range within error) which is borne-out by both Cu^{II}-nitroxide and Cu^{II}-Cu^{II} RIDME (discounting the series recorded at T_{mix}= 0.7 × T_1) pseudo-titrations. Indeed, assuming a K_D value of 0.14 µM for Cu^{II}-NTA binding in the Zn^{II}-NTA competition assay also yielded excellent agreement of the K_D values for Zn^{II}-NTA binding from ITC and PD-EPR data (chapter 5). Additionally, the α-helical double-histidine motif has a consensus upper-bound K_D value for Cu^{II}-IDA in the range ~1-10 µM at 235 K, determined from Cu^{II}-nitroxide RIDME pseudo-titration data at 75 µM protein concentration. For the β-sheet double-histidine motif, the consensus upper-bound K_D value for Cu^{II}-NTA is in the range ~1-10 µM at 235 K, approximately an order of magnitude lower binding affinity compared to the α-helical double-histidine motif (chapter 4). Similarly, the β-sheet double-histidine motif has a consensus upper-bound K_D value for Cu^{II}-IDA in the range ~1-10 µM at 235 K.

The approximation of cryogenic PD-EPR conditions to the temperature of 235 K comes from the strong empirical agreement between ITC and EPR determined K_D values at this temperature, rather than interpretation as the freezing point temperature of a 50% (v/v) mixture of water and ethylene glycol. While this temperature works, it is not clear why empirical agreement is observed (i.e., ideally one would need to know the exact temperature diffusion freezes out). However, even this very crude approximation of thermodynamic data from ITC works better than assuming thermodynamics do not contribute, in which case a disparity of 1-2 orders of magnitude in affinity estimates is observed. This is despite the concentration differences between measured ITC and PD-EPR data, as well as the absence of cryoprotectant for ITC measurements. Furthermore, as discussed in chapter 3, the binding kinetics are speculated to be sufficiently fast compared to the rate of cooling (on the order of seconds) to facilitate thermodynamic re-equilibration (i.e., if kinetics were too slow then a slower rate of cooling would yield a tighter binding, and slow kinetics could not lower the apparent K_D, rather this would yield a K_D closer to the room-temperature ITC value).

This high affinity affords quantitative labelling efficiency in cases where samples are prepared in the µM concentration regime. It should also be noted that Cu^{II}-nitroxide RIDME has phenomenal concentration sensitivity and facilitates overnight measurements at sub µM protein concentrations. Indeed, Cu^{II}-nitroxide and Cu^{II}-Cu^{II} RIDME were found to be approximately 150 and 100-fold more sensitive than Cu^{II}-Cu^{II} PELDOR, respectively. This presents a huge opportunity to access biologically relevant systems that are nonpermissive to PD-EPR measurements above a certain concentration threshold, that were perhaps previously inaccessible. The comparable sensitivity between Cu^{II}-nitroxide and Cu^{II}-Cu^{II} RIDME is also exciting for application of double histidine motif Cu^{II}-based spin labelling to systems containing essential functional or structural cysteines, nonpermissive to thiol-directed labelling procedures.

In particular, the α-helical double-histidine motif coupled with Cu^{II}-NTA is a highly robust and powerful spin labelling approach. Results demonstrate that pH fluctuations and vast excesses of adventitious metal ions do not significantly perturb the binding affinity. Indeed, this has implications for Cu^{II}-Cu^{II} distance measurements in metalloproteins with divalent metal ion cofactors, or in systems where acidic or basic pH are required, perhaps to facilitate function or native protein folding. From this perspective of high binding affinity, high concentration sensitivity, robustness to pH and competitor ions, and accurate and precise distance constraints, Cu^{II}-Cu^{II} RIDME measurements *via* this spin labelling approach are increasingly attractive. Furthermore, modulation depth quantitation in Cu^{II}-Cu^{II} RIDME measurements for K_D determination maximises the accessible thermodynamic information and extends the versatility of the methodology to systems nonpermissive to thiol-directed spin labelling.

The findings also demonstrate the experimental validation of a speciation model that facilitates prediction of Cu^{II}-labelling efficiency at double histidine motifs for systems containing two independent and non-identical binding sites. Importantly, prior to this work a general method to optimise Cu^{II}-labelling in systems containing at least pairs of double histidine motifs had not been established. Indeed, the speciation model provides a facile way to predict labelling efficiency and sensitivity optima of Cu^{II}-Cu^{II} RIDME measurements, prior to sample preparation and measurement. This is not only relevant for increasing the utility of double-histidine motif Cu^{II}-based spin labelling, (and other non-covalent spin labelling strategies) but becomes particularly significant in purview of applying these spins labels and distance measurements in challenging biomolecular systems.

Additionally, Cu^{II}-Cu^{II} RIDME modulation depth quantitation allows internal control of labelling efficiency, wherein the concentration accuracy of a pseudo-titration series can be assessed, which is useful in error analysis. Results suggest that Cu^{II}-Cu^{II} RIDME modulation depth quantitation is also useful for discriminating between binding sites of differential binding affinities. This may prove valuable in assigning different binding modalities, however this approach cannot unambiguously assign binding affinities to each site. In cases where Cu^{II}-nitroxide and Cu^{II}-Cu^{II} RIDME measurements can be performed in the same system, the corresponding distance distributions may complement thermodynamic information and allow sites to be assigned directly.

Another surprising finding is that RIDME modulation depths are reflective of the binding equilibrium in a temperature regime wherein the dynamic processes contributing to the equilibrium are frozen out. This is best illustrated by the consistent observation for all pseudo-titrations that extrapolating the ITC-determined K_D to cryogenic temperature (235 K) reconciled within a factor 2 of the value determined *via* RIDME modulation depth quantitation. This suggests the approach is robust and allows investigation of binding equilibria at much reduced material demand compared to analogous ITC measurements. This also serves to highlight the necessity for caution when comparing thermodynamic parameters under different temperature regimes. Previous studies that quantified equilibrium constants from PD-EPR distance measurements may have overlooked the influence of temperature upon the equilibrium dynamics.

The influence of temperature upon affinity has implications for the versatility of using PD-EPR to characterise binding equilibria. Notably, PD-EPR may be unsuitable to investigate endothermic binding events, wherein cryogenic temperatures drive the equilibrium to the left. However, this limitation would be ameliorated by measurements performed at higher temperatures, perhaps through use of trityl radicals, or different matrix compositions that shift the temperature where dynamic processes are frozen out. Investigating different matrix compositions to provide ‘snapshots’ of equilibria at different temperatures also presents an opportunity to extend PD-EPR to derive additional thermodynamic parameters, such as ΔH, assuming i) a large range of temperatures could be reliably sampled, and ii) ΔH is temperature independent over such a temperature range.

In the same vein, findings suggest that PD-EPR can be used to investigate competitor binding equilibria with high accuracy. Remote determination of binding affinities of diamagnetic ligands may present future opportunities to investigate systems where paramagnetic analogues are structurally perturbative, or uneconomical. Since competitive binding assays typically require radiolabelled material, and judicious selection of the appropriate isotopes, PD-EPR may provide a complementary strategy that minimises economic concerns from the perspective of i) requiring much less material, and ii) requiring only diamagnetic competitor ligands, rather than enriched radiolabelled material. This also has potential to address safety concerns synonymous with use of radioactive substances. Further, the robust application of modulation depth quantitation to describe a competitive binding equilibrium opens the possibility of applying these methods in conjunction to more sophisticated binding equilibria.

An example of a complex binding equilibrium is a metal-templated dimerisation event, in which a bivalent ligand (such as Cu^{II}) coordinates to a monomeric protein, followed by coordination of a second monomer unit to form a 'bridged' dimer structure. Such sequential binding events are notoriously difficult to analyse *via* ITC, since off-site or non-specific binding events cannot be excluded, and the potential for cooperative binding presents the risk of overfitting isotherms wherein all interactions are subsumed into a single calorimetric output signal. Furthermore, designing control experiments to deconvolute these individual contributions is often laborious and requires significant material being readily available. In this regard, PD-EPR is a facile tool to isolate individual binding events, assuming spectroscopically orthogonal spin labels are readily introduced into the system of interest.

Let us consider a system labelled with a nitroxide, wherein a Cu^{II}-templated dimer is formed at a double-histidine motif. The initial Cu^{II} binding event is followed by Cu^{II}-nitroxide RIDME, however, the second binding event will also contribute to observed modulation depth. The Cu^{II}-nitroxide RIDME modulation depth (Δ_{Cu-NO}) then reports the combined fraction of protein that is i) coordinated to Cu^{II} (PL) or ii) in a bridged dimer structure (P_2L). To disentangle these fractions, additional information is required that reports exclusively on the fraction of protein that is in the P_2L state, such as nitroxide-nitroxide PELDOR modulation depths (Δ_{NO-NO}). Finally, non-specific binding events of Cu^{II} away from the double-histidine motif can also be isolated, by quantification of Cu^{II}-Cu^{II} RIDME modulation depths (Δ_{Cu-Cu}), since only proteins that have bound additional Cu^{II} centres will contribute to the modulation of the detected echo.

As a test system, I6R1/K28H/Q32H GB1 and Cu^{II} was used. A combined bivariate fitting routine of both Cu^{II}-nitroxide RIDME and nitroxide-nitroxide PELDOR modulation depths was applied, wherein a cooperative binding model was assumed (i.e., the binding events are no longer independent, and the affinity of the second binding event is modulated by the first), with a mathematical description provided in chapter 2. The resulting fits of experimental data, and the proposed metal-templated dimer structure are shown below in figure 6.2.1.1. Significantly, a positive cooperativity factor (α) was required to adequately fit all the data, suggesting that the second binding event is thermodynamically more favourable than the first, and that perhaps the Cu^{II} ion is rigidly held in an appropriate geometry to facilitate the secondary binding event by the histidine residues. The Cu^{II}-Cu^{II} RIDME measurements indicate weak non-specific binding interactions, however this is to be expected for Cu^{II} in the absence of chelating agents that would increase specificity of binding. It should be noted that this dimerisation does not impact analysis in previous chapters, as chelated Cu^{II} (Cu^{II}-NTA/Cu^{II}-IDA) cannot coordinate pairs of double-histidine motifs simultaneously. Furthermore, the distance information from the nitroxide-nitroxide PELDOR measurements (right panel) provide a basis for validating the proposed bridged dimer structural model; the shorter experimental distance compared with *in silico* modelling suggests the coordination is not perfectly square-planar,[349] with monomers twisting towards one another.

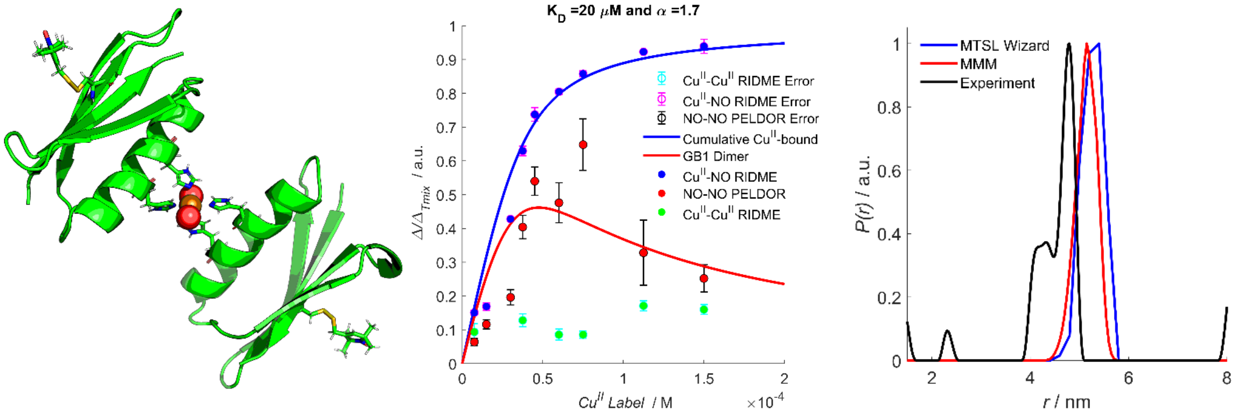

Figure 6.2.1.1: Proposed structure of the ‘bridged-dimer’ in cartoon representation (left) and a combined fitting of Cu^{II}-nitroxide RIDME (blue scatter) and nitroxide-nitroxide PELDOR (red scatter) modulation depths (centre). Corresponding experimental (black trace) and *in silico* modelled (red and blue traces) distance distributions of the ‘bridged-dimer’ GB1 structure (right). The fitted K_D and cooperativity factor are indicated in the figure title. Adapted with permission from the Doctoral thesis (Maria Oranges, Nanometre Distances, Orientation and Multimerisation Equilibria from Pulse Dipolar EPR Spectroscopy, **2020**, p155-168).[328]

This showcases the potential utility of PD-EPR to study complex binding equilibria in a modular fashion, wherein contributions can be isolated and measured independently. Importantly, it should be emphasized that these measurements were performed on a single series of pseudo-titration samples, highlighting both the amount of accessible information available, and the appeal of PD-EPR in cases where material is limiting, such that rigorous controls *via* ITC become unfeasible.

Taken together, results in this thesis suggest that PD-EPR experiments are especially well suited to couple structural and thermodynamic information. Indeed, the success of benchmarking RIDME modulation depth quantitation in biological systems sets a precedent for accessing this information content reliably and highlights the future prospect of applying such methodologies routinely to investigate more sophisticated binding or redox equilibria. This is leveraged upon the realisation that double-histidine motif Cu^{II}-based spin labelling is highly robust and efficient, and brings application to biologically relevant, complex biomolecular systems into reach.

Appendix

Abbreviations

ASR	*Anabaena* sensory Rhodopsin
AWG	Arbitrary waveform generator
BLI	Biolayer interferometry
CD	Circular dichroism
Cryo-EM	Cryo-Electron Microscopy
CW-EPR	Continuous-wave EPR
DLS	Dynamic light-scattering
DQC	Double quantum coherence
DSF	Differential scanning fluorimetry
DTT	Dithiothreitol
EDNMR	ELDOR-detected NMR
ELDOR	Electron-Electron double resonance
ENDOR	Electron-Nuclear double resonance
EPR	Electron paramagnetic resonance
ESE	Electron-spin echo
ESEEM	Electron-spin echo envelope modulation
FRET	Förster resonance energy transfer
GB1	*Streptococcus sp*. G. protein G B1 domain
HDX-MS	Hydrogen-Deuterium exchange mass-spectrometry
Hsp90	heat shock protein 90
HTA	High turning angle
HYSCORE	Hyperfine sublevel correlation
IDA	Iminodiacetic acid
IR	Inversion recovery
ITC	Isothermal titration calorimetry
IMMS	Ion-mobility mass spectrometry
LILBID	Laser-induced liquid bead ion desorption
LOX	Lysyl Oxidase
MALDI	Matrix-assisted laser desorption/ionisation

NMR	Nuclear magnetic resonance
NOE	Nuclear Overhauser effect
NTA	Nitrilotriacetic acid
PD-EPR	Pulse dipolar EPR
PELDOR	Pulse electron-electron double resonance
RIDME	Relaxation induced dipolar modulation enhancement
RMSD	Root mean square deviation
RVE	Refocused virtual echo
SAR1	Stable L-alanine radical
SAXS	Small-angle X-ray scattering
SDS-PAGE	Sodium dodecyl sulfate polyacrylamide electrophoresis
SEC-MS	Size-exclusion chromatography mass-spectrometry
SIFTER	Single-frequency technique for refocusing dipolar couplings
SNR	Signal-to-noise ratio
SPR	Surface plasmon resonance
SR	Saturation recovery
SRT	Shot-repetition time
ssNMR	Solid-state NMR
SV-AUC	Sedimentation velocity analytical ultracentrifugation
TC	Tetracycline
TMD	Transmembrane domain
TOAC	2,2,6,6-tetramethyl-N-oxyl-4-amino-4-carboxylic acid
TOF	Time-of-flight
TRAP	Tripartite ATP-independent periplasmic

Appendix A: Sub-micromolar Affinity of Cu^{II} Labelling at Double Histidine Motifs

Inversion recovery data for the 25 and 75 µM GB1 RIDME pseudo-titrations in presence of Cu^{II}-IDA and Cu^{II}-NTA have been analysed and fitted under the mono- and bi-exponential approximations (chapter 3.3.7.1.1), however the raw data and the corresponding fits were not shown, and are instead given here, in figures A1-A4.

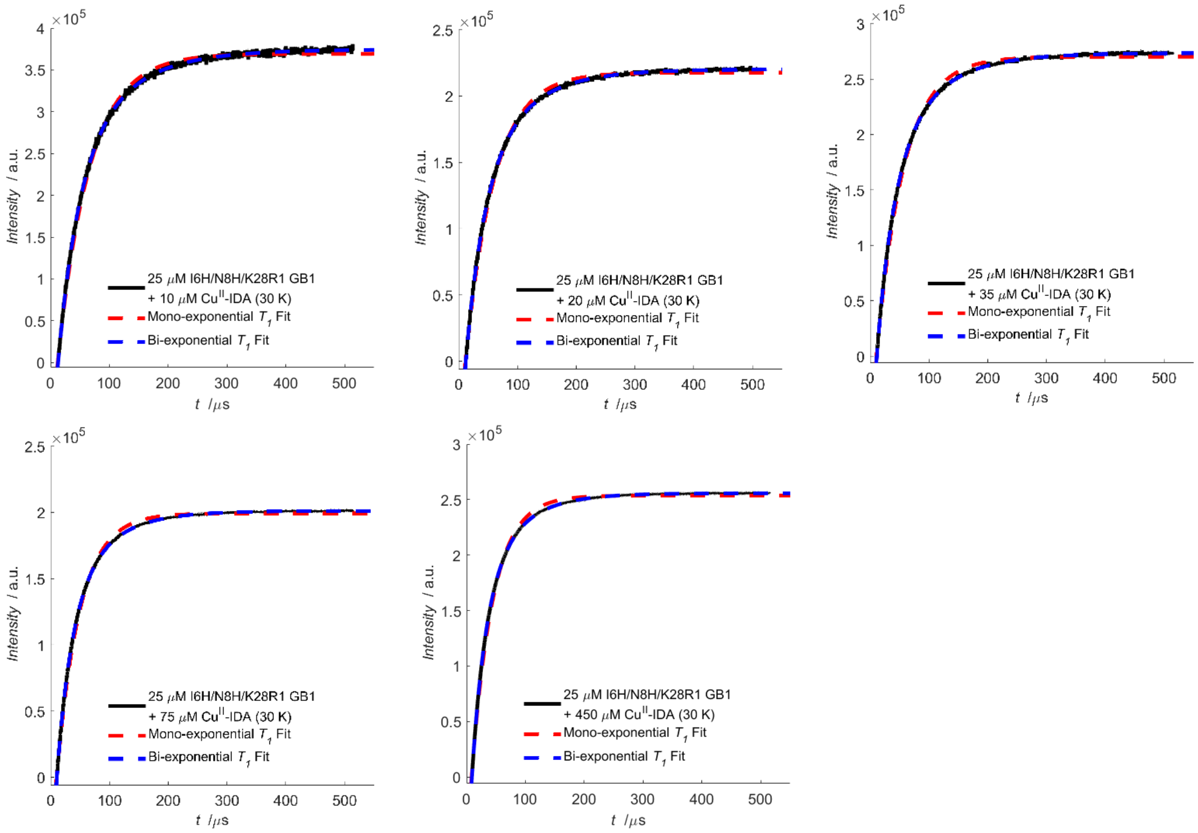

Figure A1: IR data and corresponding fits of T_1, with raw data, mono-exponential and bi-exponential approximations shown in black, red and blue traces, respectively, for the 25 µM I6H/N8H/K28R1 GB1 + Cu^{II}-IDA pseudo-titration samples.

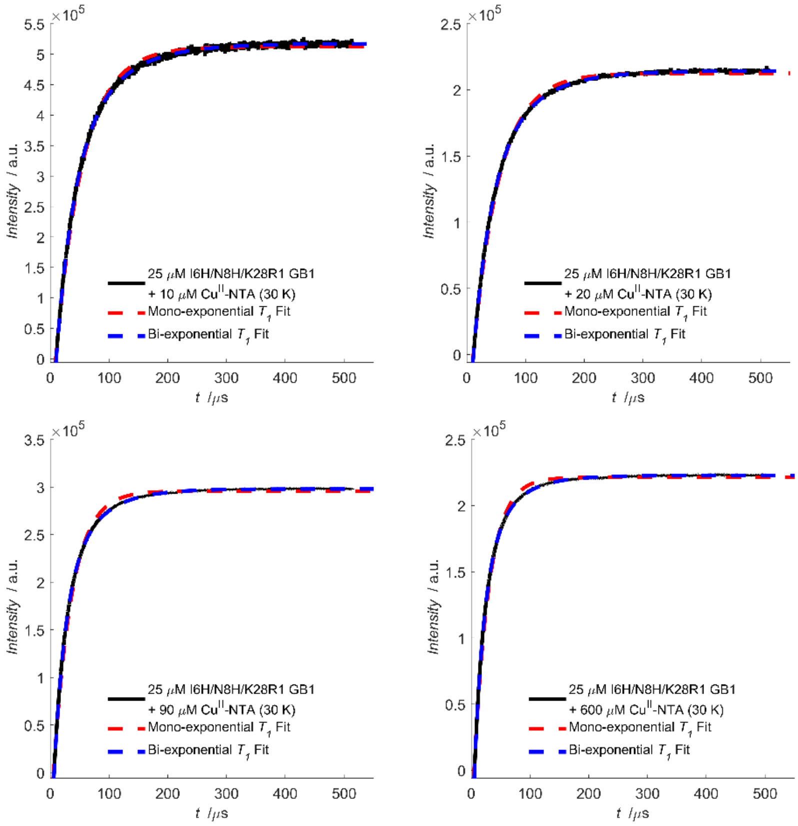

Figure A2: IR data and corresponding fits of T_1, with raw data, mono-exponential and bi-exponential approximations shown in black, red and blue traces, respectively, for the 25 µM I6H/N8H/K28R1 GB1 + Cu^{II}-NTA pseudo-titration samples.

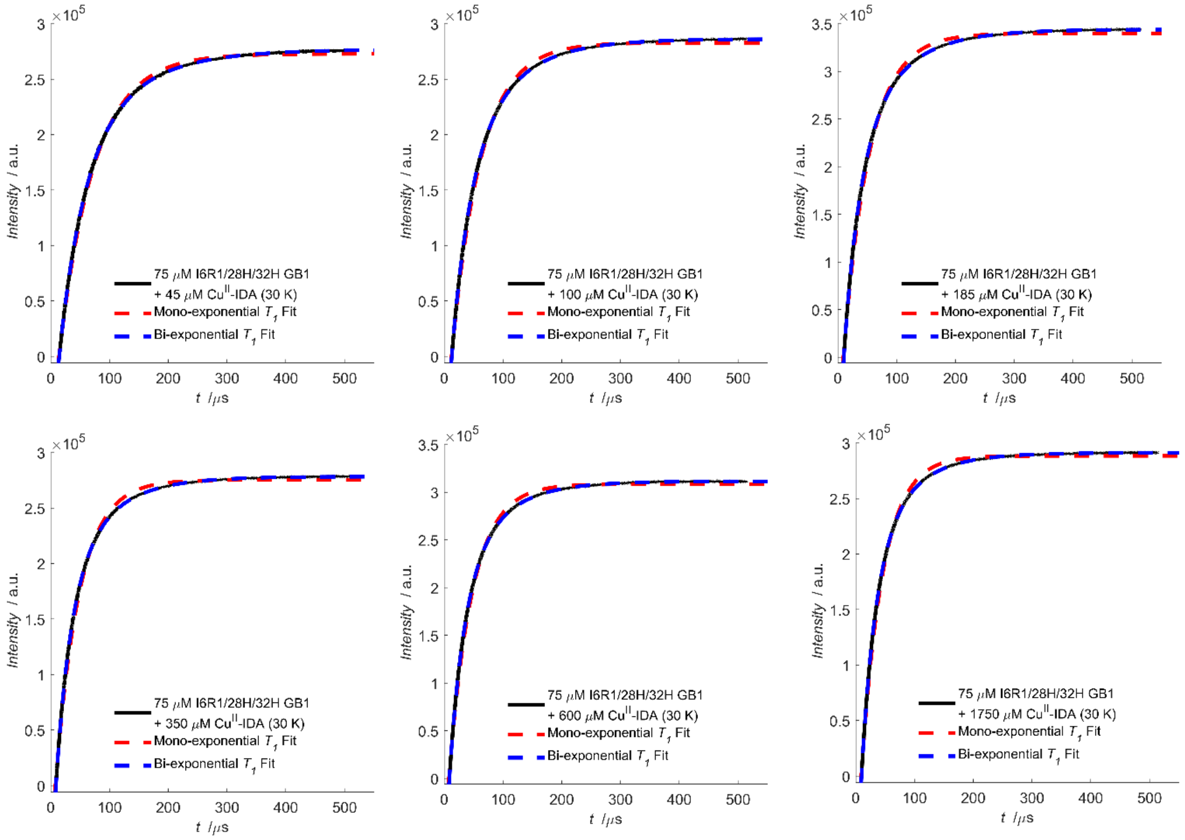

Figure A3: IR data and corresponding fits of T_1, with raw data, mono-exponential and bi-exponential approximations shown in black, red and blue traces, respectively, for the 75 µM I6R1/K28H/Q32H GB1 + Cu^{II}-IDA pseudo-titration samples.

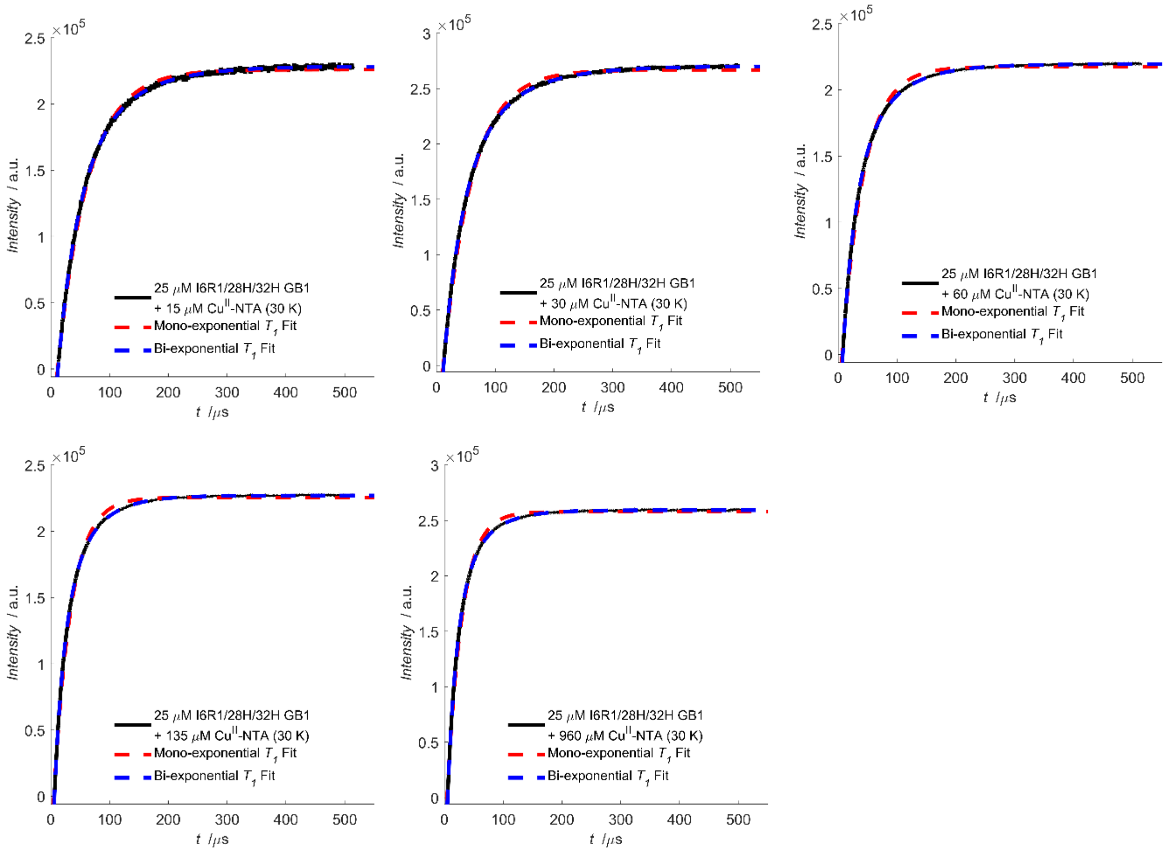

Figure A4: IR data and corresponding fits of T_1, with raw data, mono-exponential and bi-exponential approximations shown in black, red and blue traces, respectively, for the 25 µM I6R1/K28H/Q32H GB1 + Cu^{II}-NTA pseudo-titration samples.

The corresponding deconvoluted RIDME data for the 25 and 75 µM protein RIDME pseudo-titrations in presence of Cu^{II}-IDA and Cu^{II}-NTA are given in figures A5-A25 below. The corresponding background correction parameters and modulation depths are given in tables A1-A4.

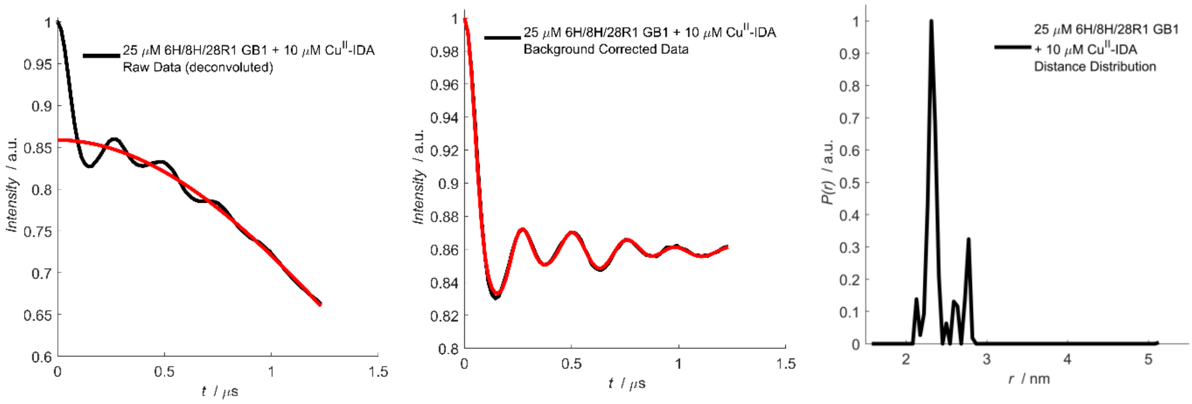

Figure A5: Deconvoluted RIDME data for 25 µM I6H/N8H/K28R1, in presence of 10 µM Cu^{II}-IDA. The raw data, dipolar evolution function, and corresponding distance distribution are shown left-to-right. The experimental data is shown in black, with the respective background correction and fit to the dipolar evolution function shown in red.

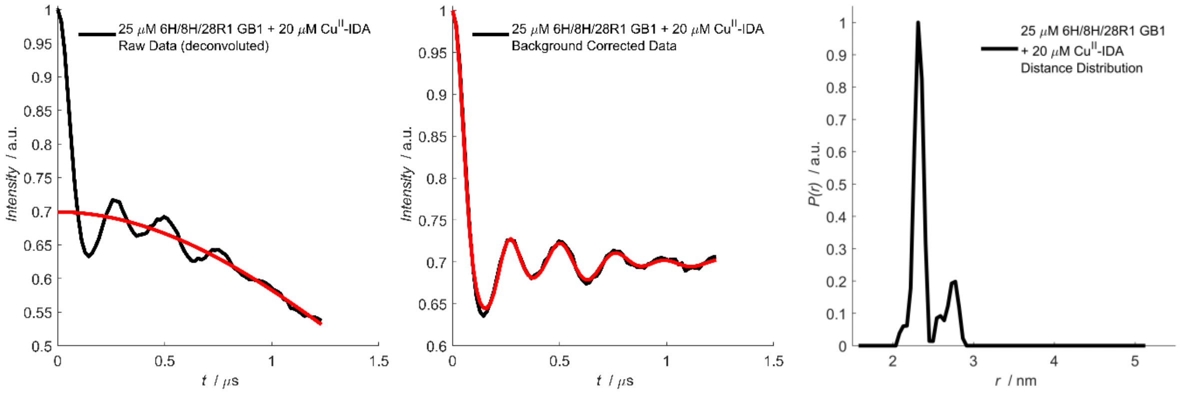

Figure A6: Deconvoluted RIDME data for 25 µM I6H/N8H/K28R1, in presence of 20 µM Cu^{II}-IDA. The raw data, dipolar evolution function, and corresponding distance distribution are shown left-to-right. The experimental data is shown in black, with the respective background correction and fit to the dipolar evolution function shown in red.

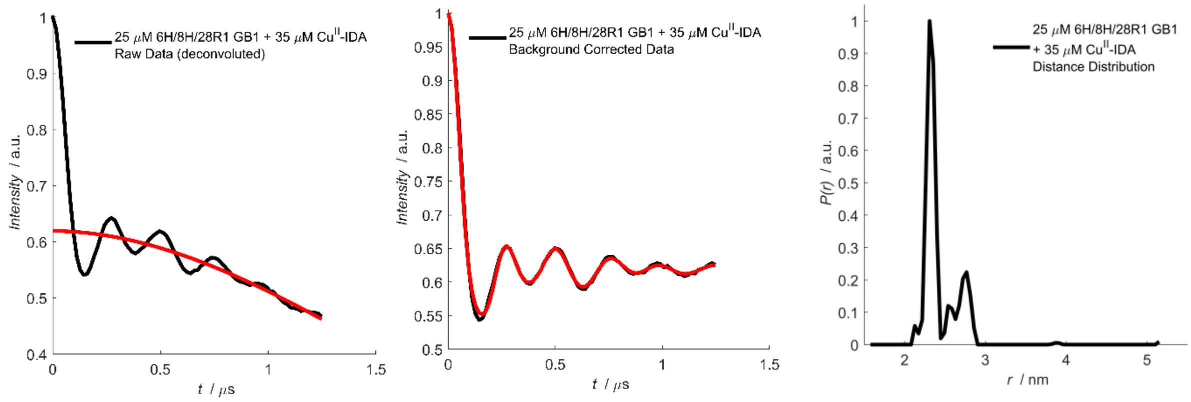

Figure A7: Deconvoluted RIDME data for 25 µM I6H/N8H/K28R1, in presence of 35 µM Cu^{II}-IDA. The raw data, dipolar evolution function, and corresponding distance distribution are shown left-to-right. The experimental data is shown in black, with the respective background correction and fit to the dipolar evolution function shown in red.

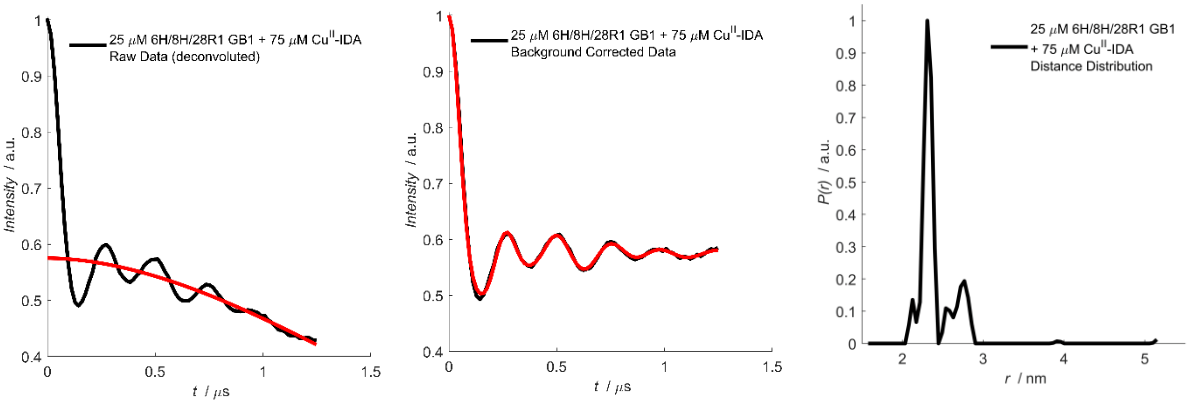

Figure A8: Deconvoluted RIDME data for 25 µM I6H/N8H/K28R1, in presence of 75 µM Cu^{II}-IDA. The raw data, dipolar evolution function, and corresponding distance distribution are shown left-to-right. The experimental data is shown in black, with the respective background correction and fit to the dipolar evolution function shown in red.

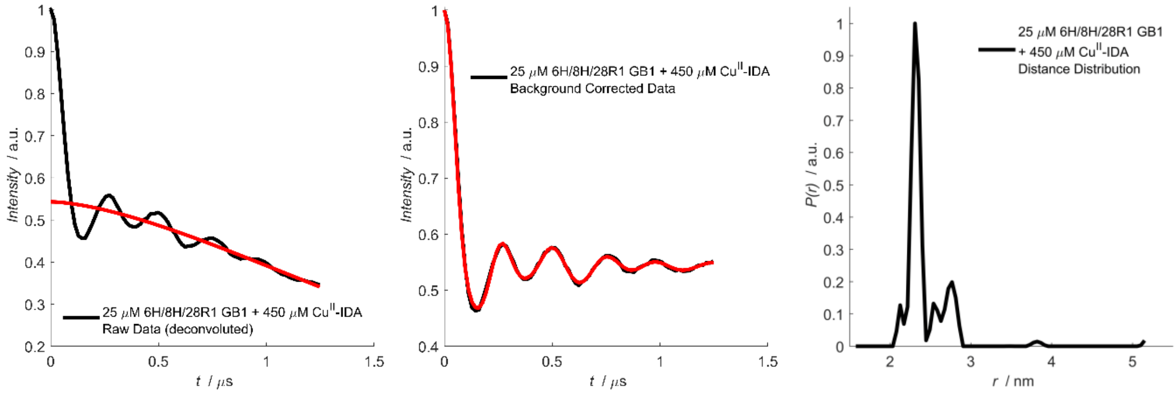

Figure A9: Deconvoluted RIDME data for 25 µM I6H/N8H/K28R1, in presence of 450 µM Cu^{II}-IDA. The raw data, dipolar evolution function, and corresponding distance distribution are shown left-to-right. The experimental data is shown in black, with the respective background correction and fit to the dipolar evolution function shown in red.

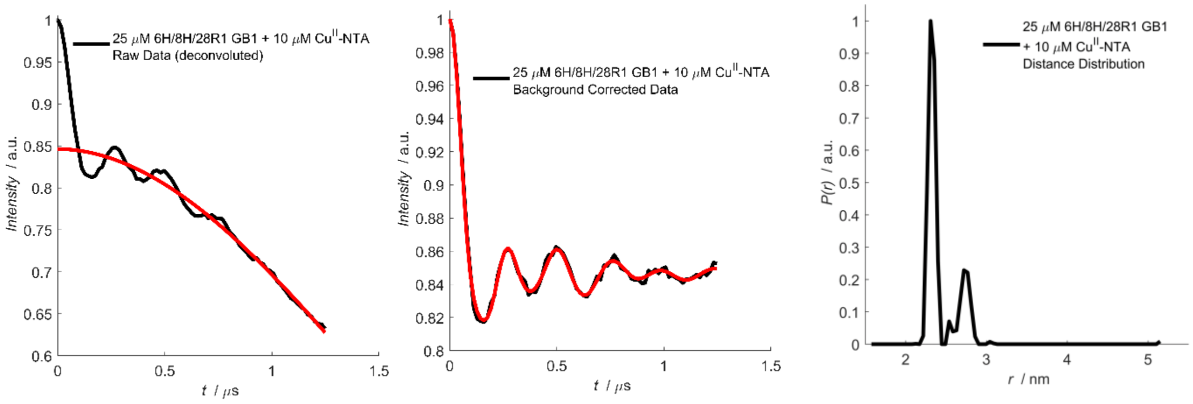

Figure A10: Deconvoluted RIDME data for 25 µM I6H/N8H/K28R1, in presence of 10 µM Cu^{II}-NTA. The raw data, dipolar evolution function, and corresponding distance distribution are shown left-to-right. The experimental data is shown in black, with the respective background correction and fit to the dipolar evolution function shown in red.

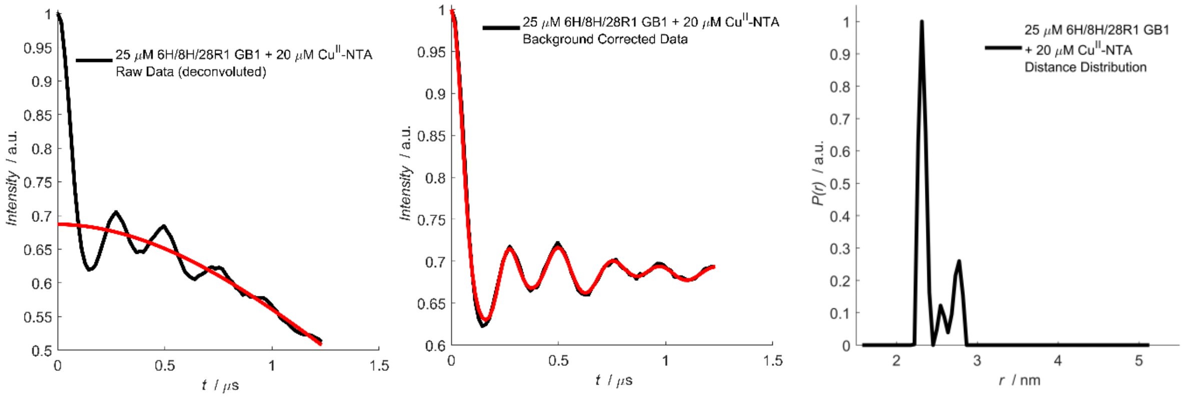

Figure A11: Deconvoluted RIDME data for 25 µM I6H/N8H/K28R1, in presence of 20 µM Cu^{II}-NTA. The raw data, dipolar evolution function, and corresponding distance distribution are shown left-to-right. The experimental data is shown in black, with the respective background correction and fit to the dipolar evolution function shown in red.

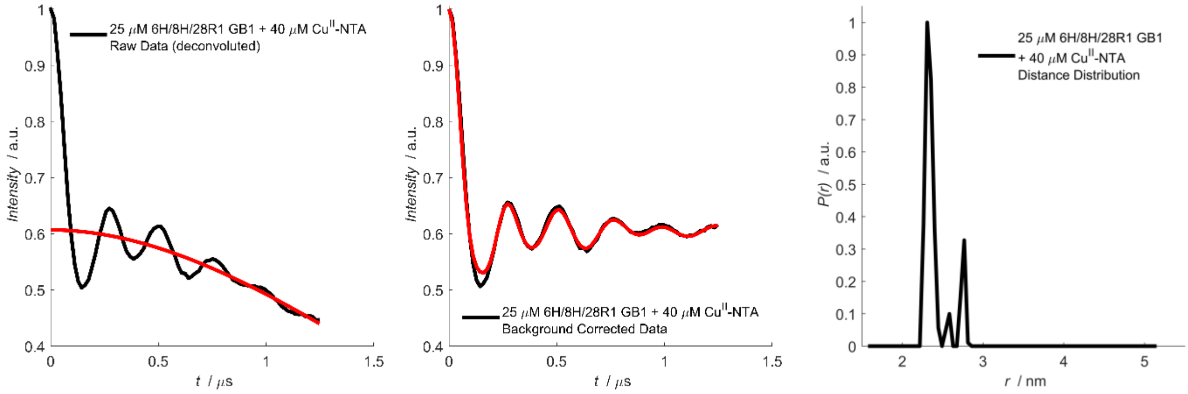

Figure A12: Deconvoluted RIDME data for 25 µM I6H/N8H/K28R1, in presence of 40 µM Cu^{II}-NTA. The raw data, dipolar evolution function, and corresponding distance distribution are shown left-to-right. The experimental data is shown in black, with the respective background correction and fit to the dipolar evolution function shown in red.

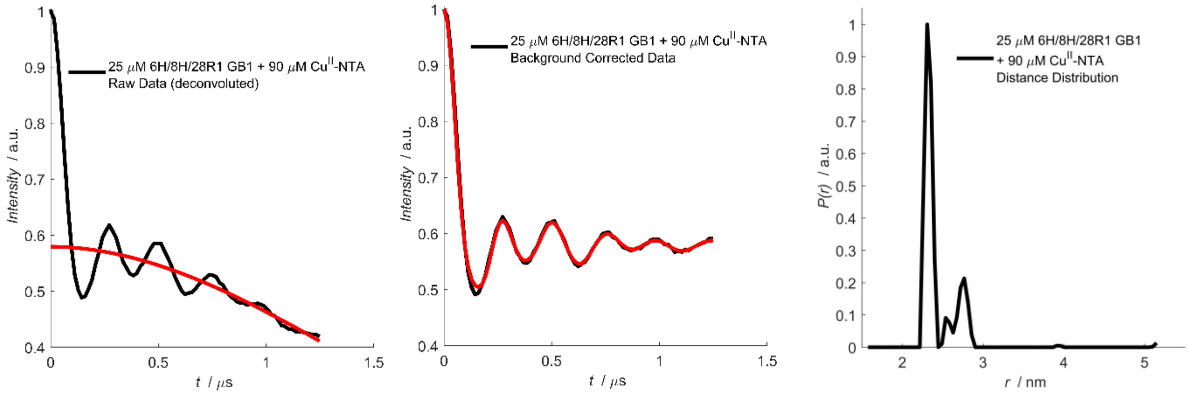

Figure A13: Deconvoluted RIDME data for 25 µM I6H/N8H/K28R1, in presence of 90 µM Cu^{II}-NTA. The raw data, dipolar evolution function, and corresponding distance distribution are shown left-to-right. The experimental data is shown in black, with the respective background correction and fit to the dipolar evolution function shown in red.

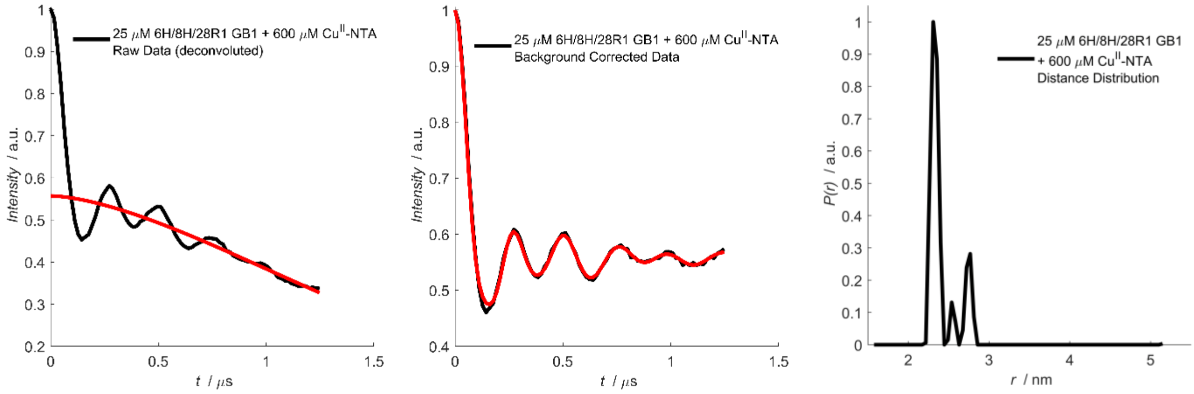

Figure A14: Deconvoluted RIDME data for 25 µM I6H/N8H/K28R1, in presence of 600 µM Cu^{II}-NTA. The raw data, dipolar evolution function, and corresponding distance distribution are shown left-to-right. The experimental data is shown in black, with the respective background correction and fit to the dipolar evolution function shown in red.

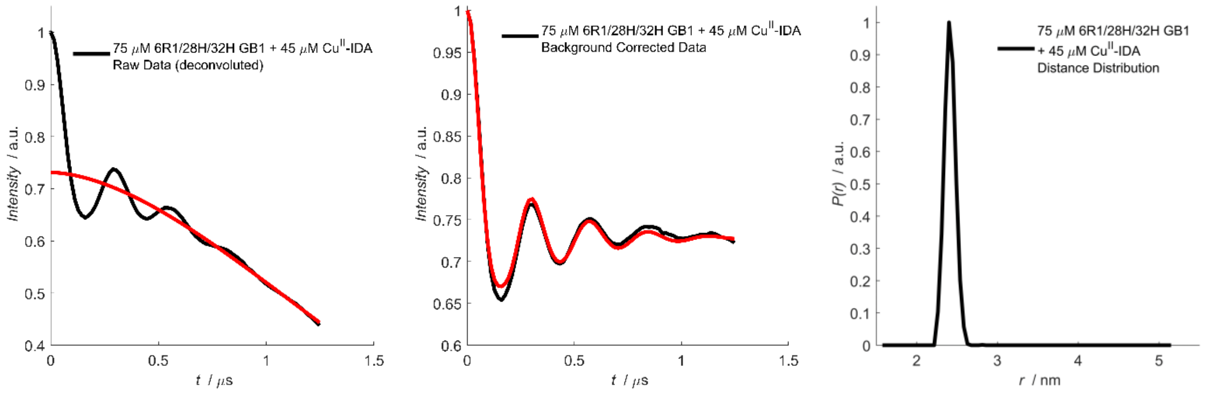

Figure A15: Deconvoluted RIDME data for 75 µM I6R1/K28H/Q32H, in presence of 45 µM Cu^{II}-IDA. The raw data, dipolar evolution function, and corresponding distance distribution are shown left-to-right. The experimental data is shown in black, with the respective background correction and fit to the dipolar evolution function shown in red.

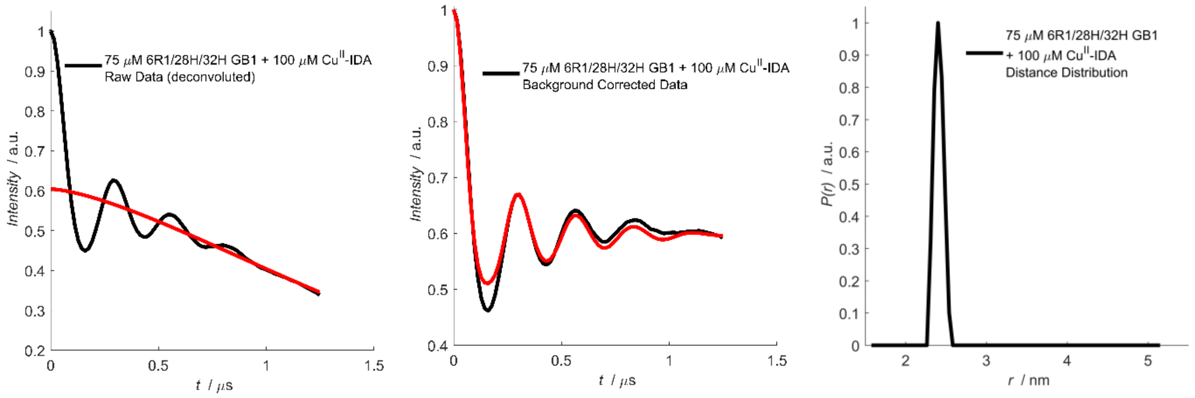

Figure A16: Deconvoluted RIDME data for 75 µM I6R1/K28H/Q32H, in presence of 100 µM Cu^{II}-IDA. The raw data, dipolar evolution function, and corresponding distance distribution are shown left-to-right. The experimental data is shown in black, with the respective background correction and fit to the dipolar evolution function shown in red.

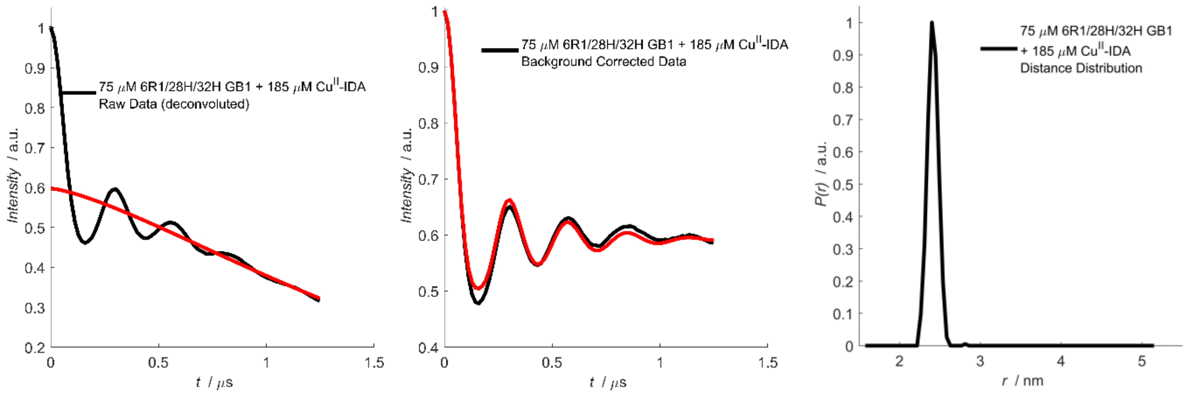

Figure A17: Deconvoluted RIDME data for 75 µM I6R1/K28H/Q32H, in presence of 185 µM Cu^{II}-IDA. The raw data, dipolar evolution function, and corresponding distance distribution are shown left-to-right. The experimental data is shown in black, with the respective background correction and fit to the dipolar evolution function shown in red.

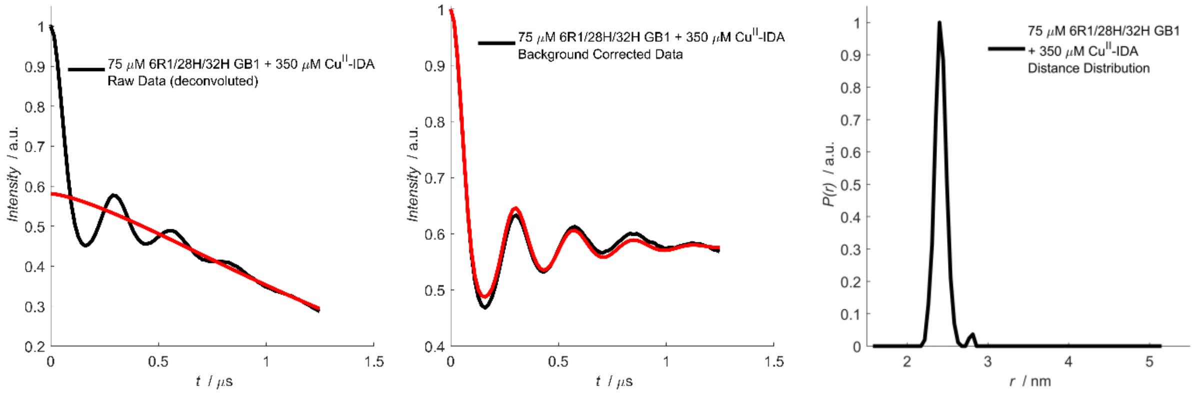

Figure A18: Deconvoluted RIDME data for 75 µM I6R1/K28H/Q32H, in presence of 350 µM Cu^{II}-IDA. The raw data, dipolar evolution function, and corresponding distance distribution are shown left-to-right. The experimental data is shown in black, with the respective background correction and fit to the dipolar evolution function shown in red.

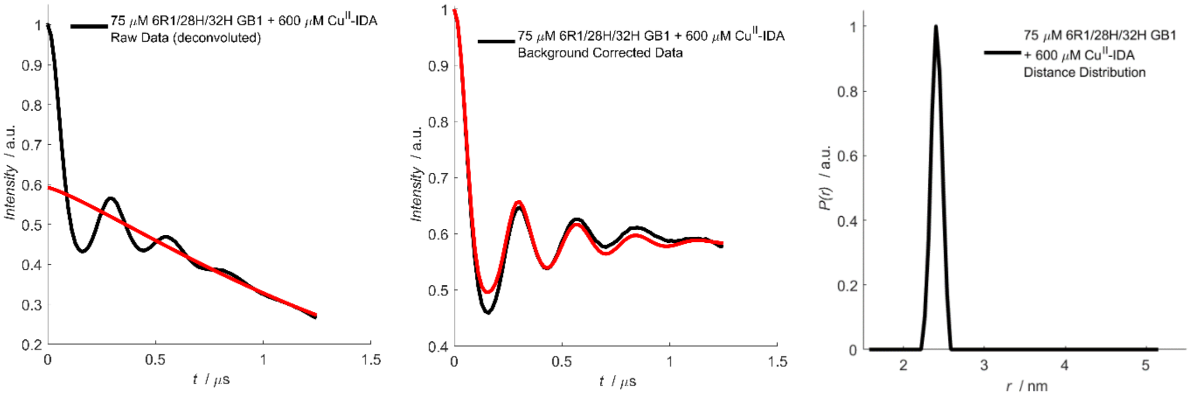

Figure A19: Deconvoluted RIDME data for 75 µM I6R1/K28H/Q32H, in presence of 600 µM Cu^{II}-IDA. The raw data, dipolar evolution function, and corresponding distance distribution are shown left-to-right. The experimental data is shown in black, with the respective background correction and fit to the dipolar evolution function shown in red.

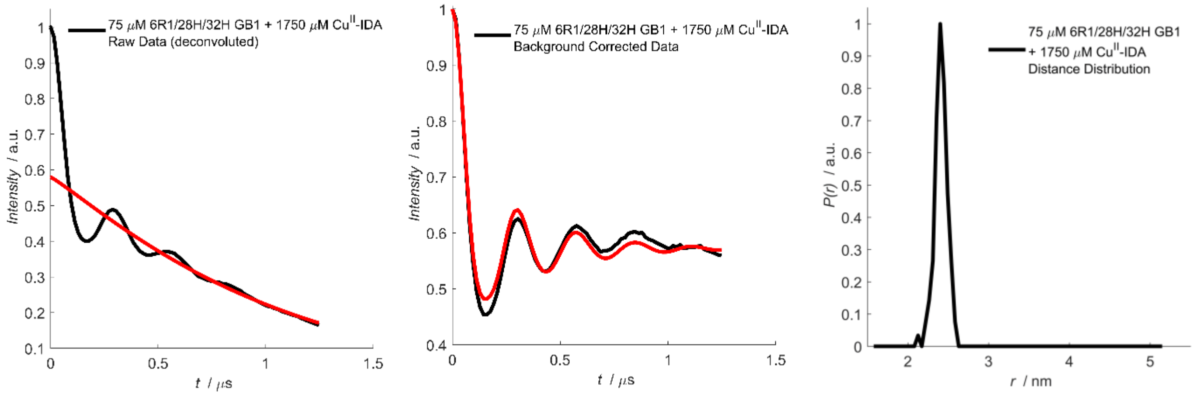

Figure A20: Deconvoluted RIDME data for 75 µM I6R1/K28H/Q32H, in presence of 1750 µM Cu^{II}-IDA. The raw data, dipolar evolution function, and corresponding distance distribution are shown left-to-right. The experimental data is shown in black, with the respective background correction and fit to the dipolar evolution function shown in red.

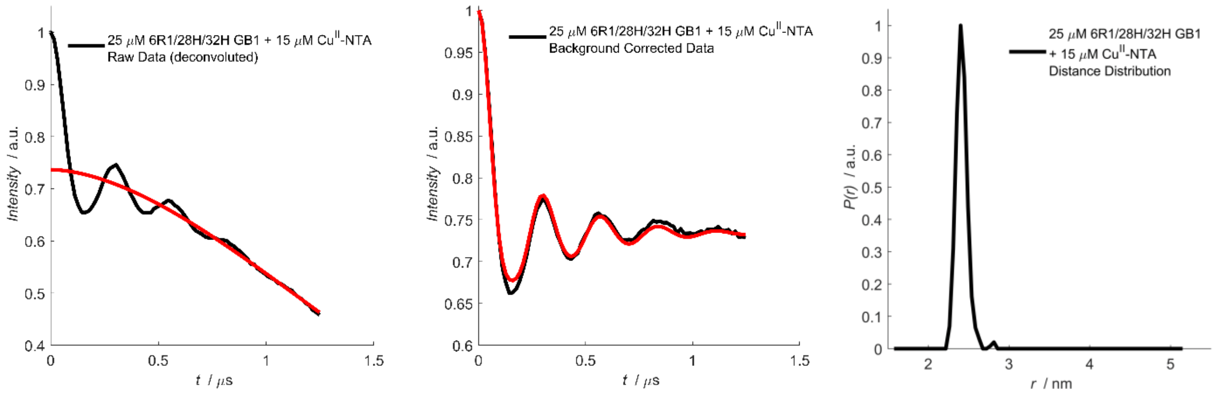

Figure A21: Deconvoluted RIDME data for 25 µM I6R1/K28H/Q32H, in presence of 15 µM Cu^{II}-NTA. The raw data, dipolar evolution function, and corresponding distance distribution are shown left-to-right. The experimental data is shown in black, with the respective background correction and fit to the dipolar evolution function shown in red.

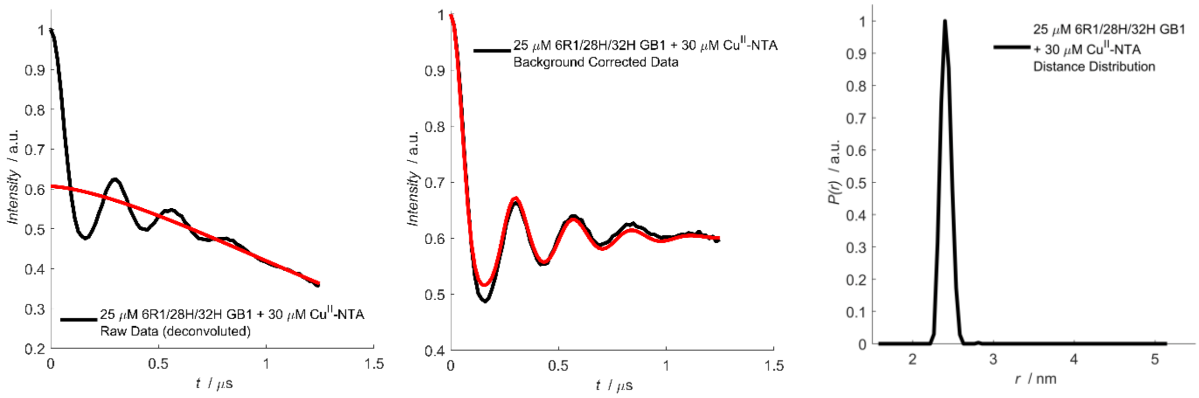

Figure A22: Deconvoluted RIDME data for 25 µM I6R1/K28H/Q32H, in presence of 30 µM Cu^{II}-NTA. The raw data, dipolar evolution function, and corresponding distance distribution are shown left-to-right. The experimental data is shown in black, with the respective background correction and fit to the dipolar evolution function shown in red.

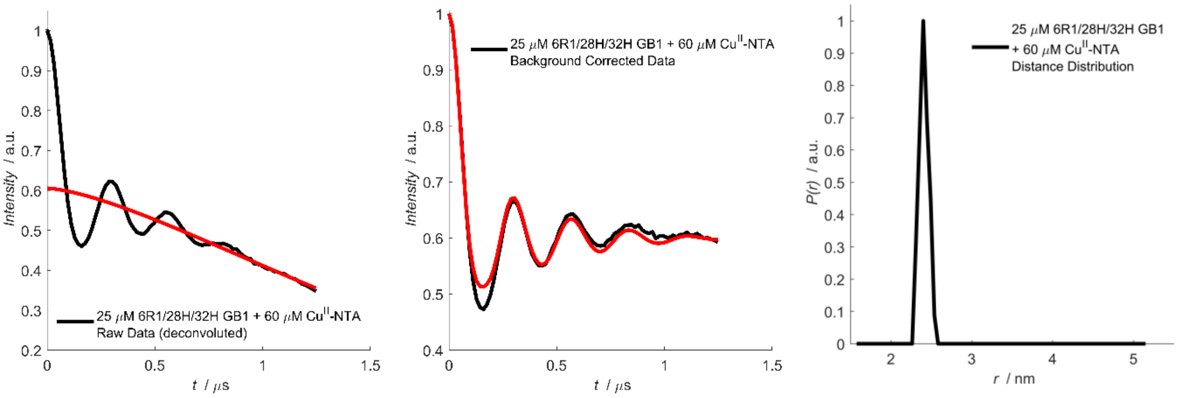

Figure A23: Deconvoluted RIDME data for 25 µM I6R1/K28H/Q32H, in presence of 60 µM Cu^{II}-NTA. The raw data, dipolar evolution function, and corresponding distance distribution are shown left-to-right. The experimental data is shown in black, with the respective background correction and fit to the dipolar evolution function shown in red.

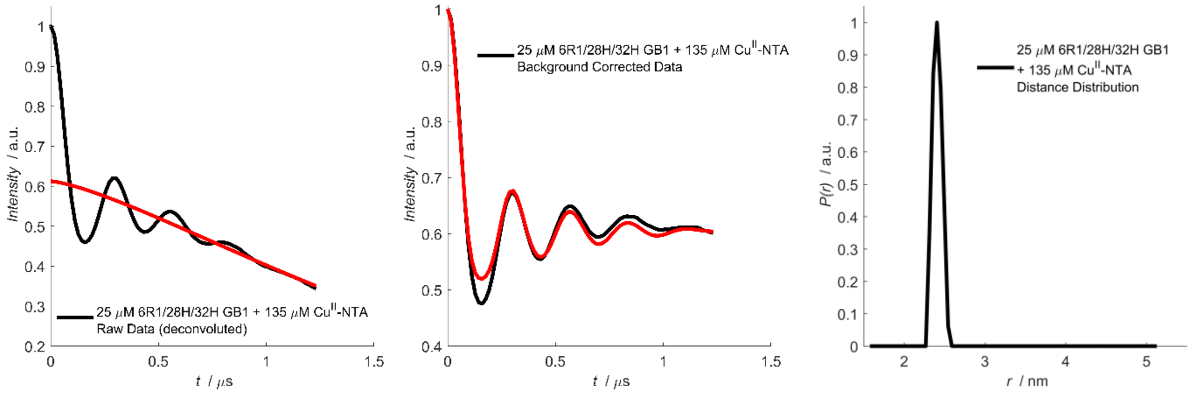

Figure A24: Deconvoluted RIDME data for 25 µM I6R1/K28H/Q32H, in presence of 135 µM Cu^{II}-NTA. The raw data, dipolar evolution function, and corresponding distance distribution are shown left-to-right. The experimental data is shown in black, with the respective background correction and fit to the dipolar evolution function shown in red.

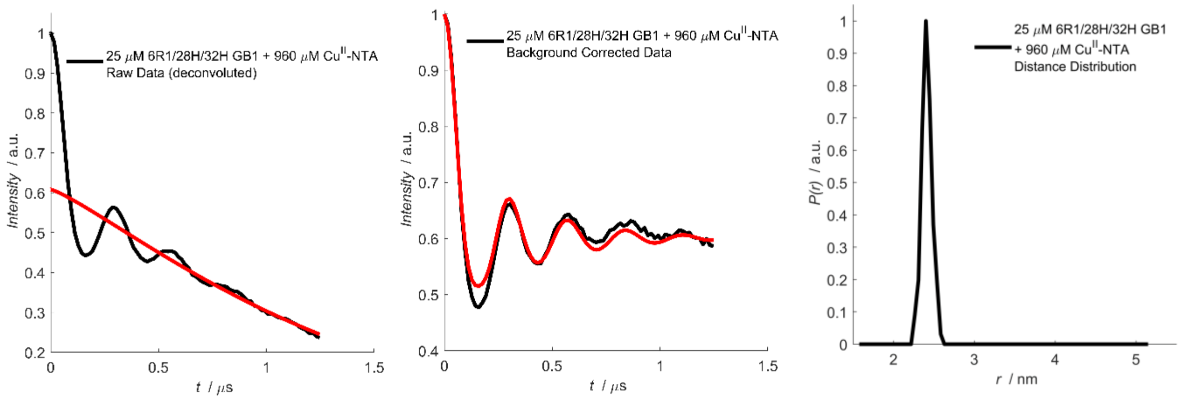

Figure A25: Deconvoluted RIDME data for 25 µM I6R1/K28H/Q32H, in presence of 960 µM Cu^{II}-NTA. The raw data, dipolar evolution function, and corresponding distance distribution are shown left-to-right. The experimental data is shown in black, with the respective background correction and fit to the dipolar evolution function shown in red.

Experiment	Zero-time [ns]	Background start [ns]	Background cut-off [ns]	Background Dimension [a.u.]
25 µM I6H/N8H/K28R1 GB1 + 10 µM Cu^{II}-IDA	206	308	1232	5.84
25 µM I6H/N8H/K28R1 GB1 + 20 µM Cu^{II}-IDA	205	308	1232	5.86
25 µM I6H/N8H/K28R1 GB1 + 35 µM Cu^{II}-IDA	202	312	1248	5.78
25 µM I6H/N8H/K28R1 GB1 + 75 µM Cu^{II}-IDA	200	312	1248	5.54
25 µM I6H/N8H/K28R1 GB1 + 450 µM Cu^{II}-IDA	203	312	1248	4.76

Table A1: The background correction parameters of the 25 µM I6H/N8H/K28R1 GB1 RIDME pseudo-titration in presence of Cu^{II}-IDA.

Experiment	Zero-time [ns]	Background start [ns]	Background cut-off [ns]	Background Dimension [a.u.]
25 µM I6H/N8H/K28R1 GB1 + 10 µM Cu^{II}-NTA	203	312	1248	5.79
25 µM I6H/N8H/K28R1 GB1 + 20 µM Cu^{II}-NTA	205	308	1232	5.72
25 µM I6H/N8H/K28R1 GB1 + 40 µM Cu^{II}-NTA	203	312	1248	5.83
25 µM I6H/N8H/K28R1 GB1 + 90 µM Cu^{II}-NTA	204	312	1248	5.77
25 µM I6H/N8H/K28R1 GB1 + 600 µM Cu^{II}-NTA	202	312	1248	4.82

Table A2: The background correction parameters of the 25 µM I6H/N8H/K28R1 GB1 RIDME pseudo-titration in presence of Cu^{II}-NTA.

Experiment	Zero-time [ns]	Background start [ns]	Background cut-off [ns]	Background Dimension [a.u.]
75 µM I6R1/K28H/Q32H GB1 + 45 µM Cu^{II}-IDA	204	312	1248	5.19
75 µM I6R1/K28H/Q32H GB1 + 100 µM Cu^{II}-IDA	203	312	1248	4.43
75 µM I6R1/K28H/Q32H GB1 + 185 µM Cu^{II}-IDA	204	312	1248	4.13
75 µM I6R1/K28H/Q32H GB1 + 350 µM Cu^{II}-IDA	203	312	1248	4.21
75 µM I6R1/K28H/Q32H GB1 + 600 µM Cu^{ii}-IDA	203	312	1248	3.67
75 µM I6R1/K28H/Q32H GB1 + 1750 µM Cu^{II}-IDA	201	312	1248	3.34

Table A3: The background correction parameters of the 75 µM I6R1/K28H/Q32H GB1 RIDME pseudo-titration in presence of Cu^{II}-IDA.

Experiment	Zero-time [ns]	Background start [ns]	Background cut-off [ns]	Background Dimension [a.u.]
25 µM I6R1/K28H/Q32H GB1 + 15 µM Cu^{II}-NTA	203	312	1248	5.25
25 µM I6R1/K28H/Q32H GB1 + 30 µM Cu^{II}-NTA	202	312	1248	4.52
25 µM I6R1/K28H/Q32H GB1 + 60 µM Cu^{II}-NTA	203	312	1248	4.40
25 µM I6R1/K28H/Q32H GB1 + 135 µM Cu^{II}-NTA	205	308	1232	4.09
25 µM I6R1/K28H/Q32H GB1 + 960 µM Cu^{ii}-NTA	203	312	1248	3.63

Table A4: The background correction parameters of the 25 µM I6R1/K28H/Q32H GB1 RIDME pseudo-titration in presence of Cu^{II}-NTA.

The Gaussian fits of the 1D error surfaces (section 3.3.12) for deconvoluted RIDME pseudo-titration series performed at 25 and 75 µM GB1 protein concentration used to approximate errors in K_D (section 3.3.10) are shown below in figure A26. Similarly, Gaussian fits of the 1D error surfaces corresponding to the different fitting methods (figure 3.3.12.1) for the RIDME pseudo-titration series performed at 500 nM GB1 protein concentration are shown overleaf in figure A27.

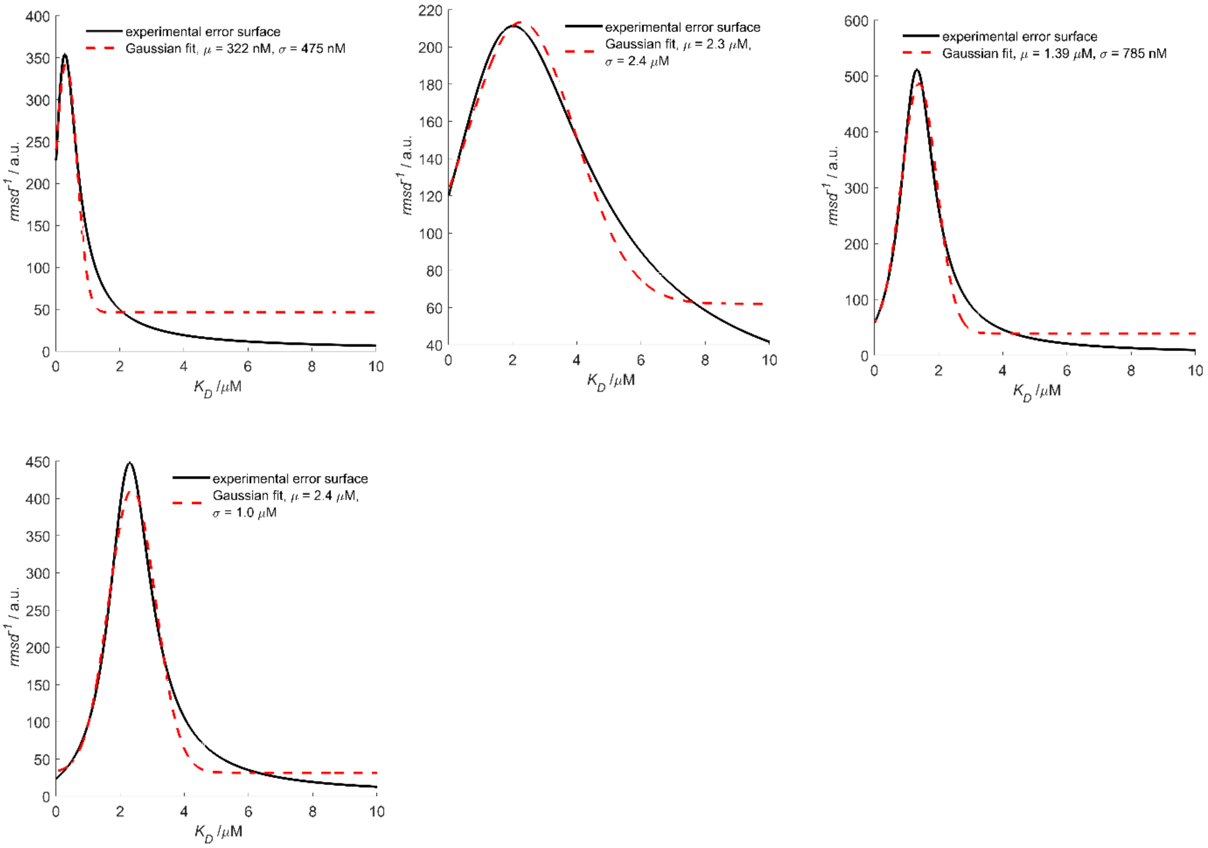

Figure A26: Gaussian fits (red traces) of the 1D error surfaces (black traces) for RIDME pseudo-titration series: 25 µM I6R1/K28H/Q32H in presence of Cu^{II}-NTA (top left), 75 µM I6R1/K28H/Q32H in presence of Cu^{II}-IDA (top centre), 25 µM I6H/N8H/K28R1 in presence of Cu^{II}-NTA (top right), and 25 µM I6H/N8H/K28R1 in presence of Cu^{II}-IDA (bottom left).

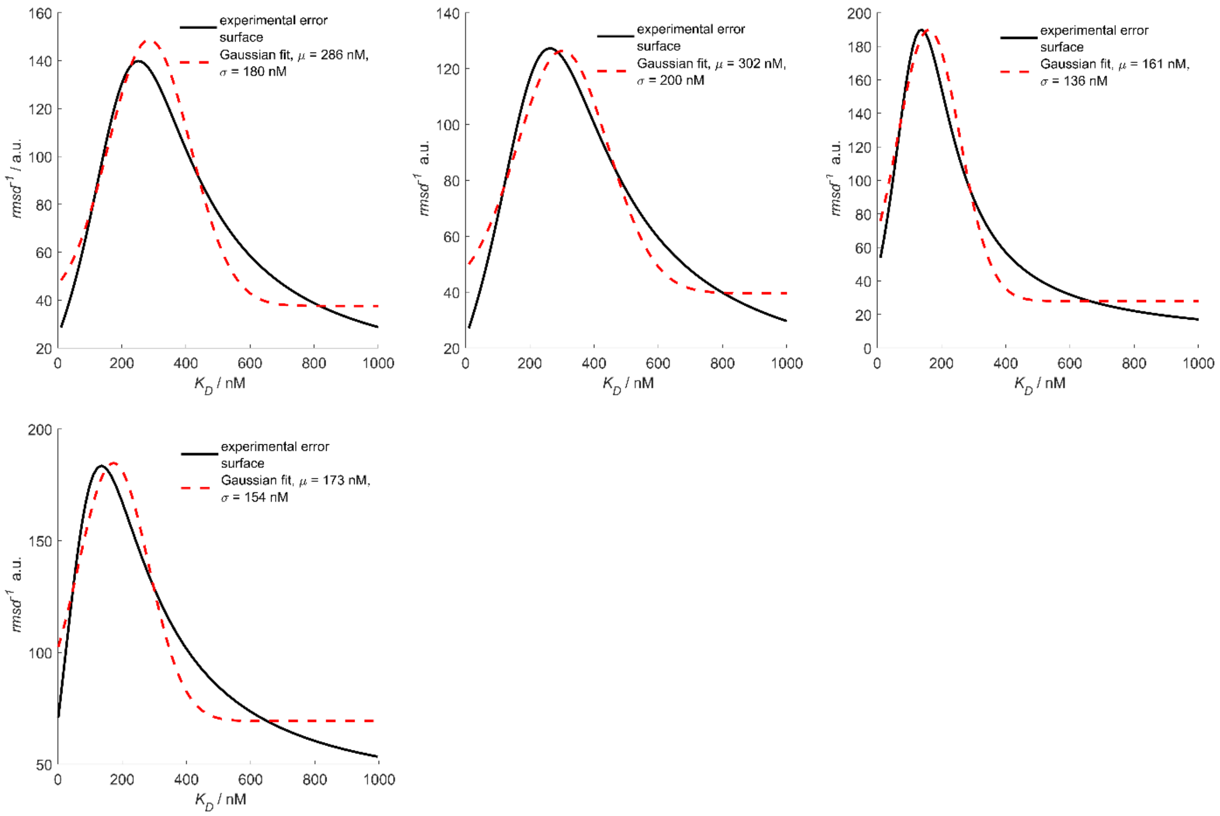

Figure A27: Gaussian fits (red traces) of the 1D error surfaces (black traces) for the 500 nM 6R1/28H/32H GB1 RIDME pseudo-titration series in presence of Cu^{II}-NTA and fitted using: a univariate fit where individual T_1 values are used (top left), a univariate fit where T_1 is assumed to be uniform (top centre), a univariate fit where T_1 is assumed to be uniform and a Δ_{Tmix} value of 0.45 is used (top right), and a bivariate fit where individual T_1 values are used, and both Δ_{Tmix} and K_D are fitted together (bottom left).

The modulation depths of the non-deconvoluted 25 µM and 75 µM RIDME pseudo-titrations are given below in tables A5-8. The corresponding bivariate fits of K_D for the deconvoluted data are shown below in figure A28, and K_D values are tabulated in table A9. Finally, the Gaussian fits of the 1D error surfaces of the non-deconvoluted RIDME pseudo-titration series performed at 25 and 75 µM GB1 protein concentration used to approximate errors in K_D are shown in figure A29.

Sample	Modulation depth (Δ)
25 µM I6H/N8H/K28R1+ 10 µM Cu^{II}-IDA	$0.18 \pm 1.3 \times 10^{-2}$
25 µM I6H/N8H/K28R1+ 20 µM Cu^{II}-IDA	$0.34 \pm 9.4 \times 10^{-3}$
25 µM I6H/N8H/K28R1+ 35 µM Cu^{II}-IDA	$0.42 \pm 2.0 \times 10^{-2}$
25 µM I6H/N8H/K28R1+ 75 µM Cu^{II}-IDA	$0.47 \pm 7.5 \times 10^{-3}$
25 µM I6H/N8H/K28R1+ 450 µM Cu^{II}-IDA	$0.49 \pm 8.3 \times 10^{-3}$

Table A5. The modulation depths of the non-deconvoluted 25 µM I6H/N8H/K28R1 RIDME pseudo-titration in presence of Cu^{II}-IDA.

Sample	Modulation depth (Δ)
25 µM I6H/N8H/K28R1+ 10 µM Cu^{II}-NTA	$0.19 \pm 7.8 \times 10^{-3}$
25 µM I6H/N8H/K28R1+ 20 µM Cu^{II}-NTA	$0.36 \pm 1.3 \times 10^{-2}$
25 µM I6H/N8H/K28R1+ 40 µM Cu^{II}-NTA	$0.44 \pm 1.1 \times 10^{-2}$
25 µM I6H/N8H/K28R1+ 90 µM Cu^{II}-NTA	$0.46 \pm 8.2 \times 10^{-3}$
25 µM I6H/N8H/K28R1+ 600 µM Cu^{II}-NTA	$0.49 \pm 4.3 \times 10^{-3}$

Table A6. The modulation depths of the non-deconvoluted 25 µM I6H/N8H/K28R1 RIDME pseudo-titration in presence of Cu^{II}-NTA.

Sample	Modulation depth (Δ)
75 µM I6H/N8H/K28R1+ 45 µM Cu^{II}-IDA	$0.31 \pm 9.3 \times 10^{-3}$
75 µM I6H/N8H/K28R1+ 100 µM Cu^{II}-IDA	$0.45 \pm 8.7 \times 10^{-3}$
75 µM I6H/N8H/K28R1+ 185 µM Cu^{II}-IDA	$0.46 \pm 4.5 \times 10^{-3}$
75 µM I6H/N8H/K28R1+ 350 µM Cu^{II}-IDA	$0.47 \pm 2.5 \times 10^{-3}$
75 µM I6H/N8H/K28R1+ 600 µM Cu^{II}-IDA	$0.47 \pm 1.4 \times 10^{-2}$
75 µM I6H/N8H/K28R1+ 1750 µM Cu^{II}-IDA	$0.50 \pm 1.8 \times 10^{-2}$

Table A7. The modulation depths of the non-deconvoluted 75 µM I6H/N8H/K28R1 RIDME pseudo-titration in presence of Cu^{II}-IDA.

Sample	Modulation depth (Δ)
25 µM I6R1/K28H/Q32H + 15 µM Cu^{II}-NTA	$0.28 \pm 1.1 \times 10^{-2}$
25 µM I6R1/K28H/Q32H + 30 µM Cu^{II}-NTA	$0.44 \pm 7.1 \times 10^{-3}$
25 µM I6R1/K28H/Q32H + 60 µM Cu^{II}-NTA	$0.43 \pm 8.6 \times 10^{-3}$
25 µM I6R1/K28H/Q32H + 135 µM Cu^{II}-NTA	$0.43 \pm 8.4 \times 10^{-3}$
25 µM I6R1/K28H/Q32H + 960 µM Cu^{II}-NTA	$0.45 \pm 2.0 \times 10^{-2}$

Table A8. The modulation depths of the non-deconvoluted 25 µM I6R1/K28H/Q32H RIDME pseudo-titration in presence of Cu^{II}-NTA.

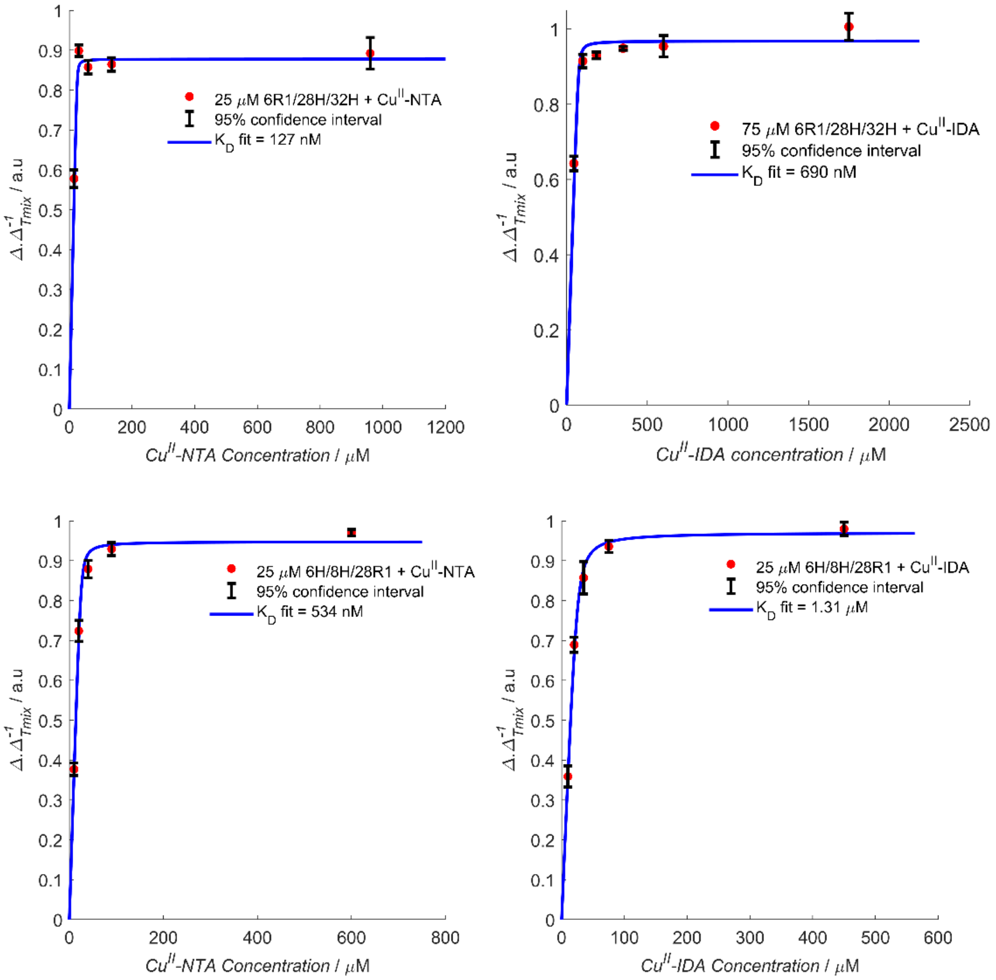

Figure A28: Binding isotherms of the non-deconvoluted RIDME pseudo-titrations, for 25 µM and 75 µM 6R1/28H/32H GB1 + Cu^{II}-NTA and Cu^{II}-IDA, (top right and left), respectively, and 25 µM 6H/8H/28R1 GB1 + Cu^{II}-NTA and Cu^{II}-IDA (bottom right and left), respectively. K_D values are given in table A9.

Pseudo-titration Series	Predicted K_D [nM]
25 µM I6R1/K28H/Q32H GB1 + Cu^{II}-NTA	127 ± 221
75 µM I6R1/K28H/Q32H GB1 + Cu^{II}-IDA	690 ± 1930
25 µM I6H/N8H/K28R1 GB1 + Cu^{II}-NTA	534 ± 1100
25 µM I6H/N8H/K28R1 GB1 + Cu^{II}-IDA	1310 ± 784

Table A9. K_D values estimated from the non-deconvoluted RIDME pseudo-titrations shown in figure A29.

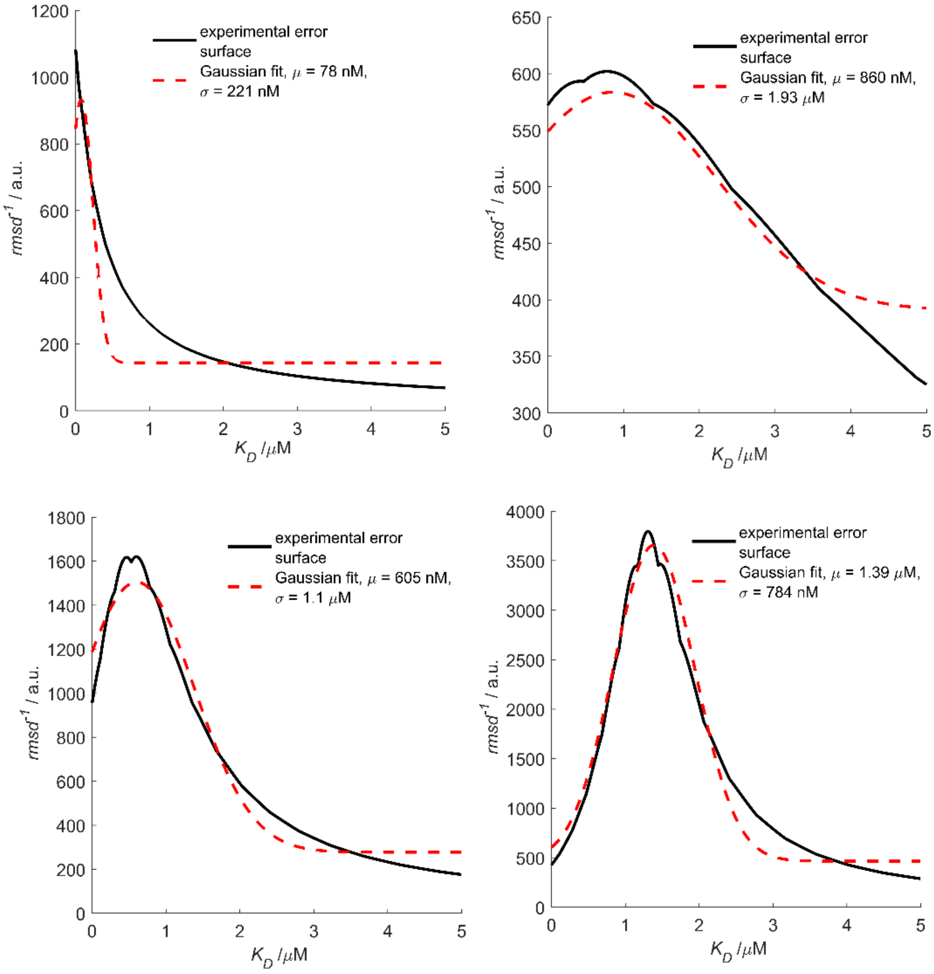

Figure A29: Gaussian fits (red traces) of the 1D error surfaces (black traces) for non-deconvoluted RIDME pseudo-titration series: 25 µM I6R1/K28H/Q32H in presence of Cu^{II}-NTA (top left), 75 µM I6R1/K28H/Q32H in presence of Cu^{II}-IDA (top centre), 25 µM I6H/N8H/K28R1 in presence of Cu^{II}-NTA (top right), and 25 µM I6H/N8H/K28R1 in presence of Cu^{II}-IDA (bottom left).

Exemplary pseudo-code used to run the simplified molecular dynamics simulations in XPLOR-NIH is also given below. To ensure the simulations are reproducible, the parent files will be given in the underpinning data. For brevity in the appendix, only the parameters and topology of the patch residue (HIC) built are given here, and dynamics input file. The parameters (parent file: parallhdg.pro) are given (pg.240-243):

```
!----------------------- HIC begin
 BOND NLA  HLA    $KBON  0.98  ! DGN ED
 bond NLA  CL2    $kbon  1.469 ! DGN ED
 bond NLA  CL4    $kbon  1.469 ! DGN ED
 bond CL2 CL1     $kbon  1.507 !
 bond CL2 HL21    $kbon  1.090 !
 bond CL2 HL22    $kbon  1.090 !
 bond CL1  OL2    $kbon  1.2 !
 bond CL1  MO1    $kbon  1.3 !
 BOND CU+2 NLA    $kbon  2.0  ! DGN ED
 BOND CU+2 MO1    $kbon  2.2  ! DGN ED
 bond CU+2 OW     $kbon  2.3  ! DGN ED
 BONDs OW  HW     $kbon   0.9572
 !BONDs HW  HW     $kbon   1.5174
 bond  CU+2 NB     $kbon 2.377
 bond CL4 CL3     $kbon  1.507 !
 bond CL4 HL41    $kbon  1.090 !
 bond CL4 HL42    $kbon  1.090 !
 bond CL3  OL3    $kbon  1.2 !
 bond CL3  MO2    $kbon  1.3 !
 BOND CU+2 MO2    $kbon  2.2  ! DGN ED
 !----------------------- HIC end
! ANGLES
!----------------------- HIC begin
ANGLe  HW   OW    HW    $kang   109
ANGLe  OW   HW    HW    $kang   37.74
ANGLe  MO1  CL1   OL2   $kang   117
ANGLe  MO2  CL3   CL4   $kang   120
ANGLe  OL2  CL1   CL2   $kang   120.5
ANGLe  OL3  CL3   CL4   $kang   120.5
ANGLe  HL21  CL2  HL22  $kang   108
ANGLe  HL41  CL4  HL42  $kang   108
ANGLe  CL1  CL2   NLA   $kang   112
```

```
ANGLe  CL3  CL4   NLA   $kang   112

ANGLe  HL21  CL2  NLA   $kang   110

ANGLe  HL22  CL2  NLA   $kang   110

ANGLe  HL41  CL4  NLA   $kang   110

ANGLe  HL42  CL4  NLA   $kang   110

ANGLe  HL21  CL2  CL1   $kang   110

ANGLe  HL22  CL2  CL1   $kang   110

ANGLe  HL41  CL4  CL3   $kang   110

ANGLe  HL42  CL4  CL3   $kang   110

ANGLe  CL2  NLA   CL4   $kang   112

!ANGLe  NLA  CL2   CL1   $kang   112

!ANGLe  MO1  CU+2  NLA   $kang   85

!ANGLe  MO2  CU+2  NLA   $kang   85

ANGLe  CU+2 MO1   CL1   $kang   109

ANGLe  CU+2 MO2   CL3   $kang   109

Angle  HLA  NLA   CL2   $kang   110

Angle  HLA  NLA   CL4   $kang   110

Angle  HLA  NLA  CU+2   $kang   109

!angle  NB   CU+2  MO1   $kang   90      ! NE2 CU+2 OM1, NE2 CU+2 OH2, NE2 CU+2 OM1

!angle  NB   CU+2  MO2   $kang   90      ! NE2 CU+2 OM1, NE2 CU+2 OH2, NE2 CU+2 OM1

angle  NB   CU+2  NB   $kang   90      !

!angle  NB   CU+2  NLA   $kang   90      !

angle  NB   CU+2  OW   $kang   90      !

angle  MO1  CU+2  NLA  $kang   85

angle  MO2  CU+2  NLA  $kang   85

angle  OW  CU+2  NLA  $kang   90

angle  OW  CU+2  MO1  $kang   180

angle  OW  CU+2  MO2  $kang   90

angle  MO1  CU+2  MO2  $kang   90

angle  MO1  CU+2  NB  $kang   90

angle   MO2  CL3   OL3 $kang  122

angle  CL2 NLA CU+2 $kang   109

angle  CL4 NLA CU+2 $kang   109

angle  CL2 CL1 MO1 $kang   120

angle  NLA CU+2 NB $kang    90

angle  MO2 CU+2 NB $kang   180

angle  CU+2 NB CV $kang   126

angle  CU+2 NB CR $kang   126
```

```
angle  HW OW CU+2  $kang 109
!angle
!angle
 !----------------------- HIC end
! IMPROPERS
! For dihedrals and impropers, the following convention was adopted:
! All dihedral terms maintaining planarity (esp. omega) have been
! converted into impropers. The only dihedrals left are around
! rotatable bonds.
!----------------------- HIC begin
improper  NB CV CR CU+2 $kpla 0 0
improper CU+2 NLA MO2 OW $kpla 0 60
improper CU+2 MO2 NLA MO1 $kpla 0 60
{
improper  NLA  CU+2  MO1  CL1  $kpla 0 0 ! NYA Cu+2 OM1 CJ3, NYA Cu+2 OM1 CJ1
improper  NLA  CU+2  MO2  CL3  $kpla 0 0 ! NYA Cu+2 OM1 CJ3, NYA Cu+2 OM1 CJ1
improper  OW  MO2  MO1  NB  $kpla 0 -80 !'
improper  MO1  MO2  OW  CU+2  $kpla 0 0 !!
improper  NB  MO2  NLA  CU+2  $kpla 0 0 !!
improper  NB  NB   NLA  CU+2  $kpla 0 0 !! for patch
improper  NB  NB  NLA  MO2  $kpla 0 0 !' for patch
improper  OW  NB  MO1  CU+2  $kpla 0 0 !' for patch
improper  MO1  MO2  OW  NB  $kpla 0 0 !' for patch
improper  NB  MO2  NLA  MO1  $kpla 0 -50 !'
improper  NLA  MO2  NB  MO1  $kpla 0 -50 !'
improper  OL2 CL1 CL3 OL3 $kpla 0 10 !
improper  NLA CL2 CL1 MO1 $kpla 0 -30 !  NYA CJ2 CJ1 OM1, NYA CJ4 CJ3 OM2
improper  NB CV CR CU+2 $kpla 0 0
}
!----------------------- HIC end
! DIHEDRALS
 dihedral  CA   CA   CT   CT       $kdih    3    0.0
 dihedral  CW   CX   CT   CT       $kdih    3    0.0
 dihedral  NA   CC   CT   CT       $kdih    3    0.0
 dihedral  X    NH1  CT   X        $kdih    3    0.0  ! chi1 - chi4
 dihedral  X    CT   CT   X        $kdih    3    0.0  ! chi1 - chi4
 dihedral  X    C    CT   X        $kdih    3    0.0  ! chi1 - chi4
 dihedral  X    S    CT   X        $kdih    3    0.0  ! chi1 - chi4
```

```
!Radii as in CHARMM param19x
! the radius is sigma*2^(-5/6)
!  use repel of 0.80
!                  eps     sigma       eps(1:4) sigma(1:4)
 !----------------------- HIC begin
NONBonded CL1  0.0900  3.2970  0.0900  3.2970
NONBonded CL2  0.0900  3.2970  0.0900  3.2970
NONBonded CL3  0.0900  3.2970  0.0900  3.2970
NONBonded CL4  0.0900  3.2970  0.0900  3.2970
NONBonded MO1  0.2304  2.7290  0.2304  2.7290
NONBonded MO2  0.2304  2.7290  0.2304  2.7290
NONBonded OL2  0.2304  2.7290  0.2304  2.7290
NONBonded OL3  0.2304  2.7290  0.2304  2.7290
NONBonded NLA  0.1600  2.8591  0.0900  2.8591
NONBonded HLA  0.0045  2.6160  0.0045  2.6160
NONBonded HL21 0.0045  2.6160  0.0045  2.6160
NONBonded HL22 0.0045  2.6160  0.0045  2.6160
NONBonded HL41 0.0045  2.6160  0.0045  2.6160
NONBonded HL42 0.0045  2.6160  0.0045  2.6160
NONBonded   HW           0.0045  2.6160  0.0045  2.6160
NONBonded   OW           0.2304  2.7290  0.2304  2.7290
NONBonded  CU+2          0.01  1.550     0.01  1.550
 !----------------------- HIC end
! the following nbfixes allow hydrogen bonding
! the distance used is (2A/B)^(1/6)*repel                                distances
!                       A    B   A1-4  B1-4
!----------------------- HIC begin
 NBFIx       HW  HW       0.0000    0.0000      0.0000    0.0000
NBFIx       HW  OW       0.0000    0.0000      0.0000    0.0000
NBFIx       OW  OW   582002.6616  595.0550      0.0000    0.0000
!----------------------- HIC end
```

Similarly, the topology file (parent file topallhdg.pro) for the patch residue HIC, is (pg. 243-248):

```
! for IDA and Cu
 MASS  CU+2   63.5460   ! copper 2+
 MASS  HL21   1.008
 MASS  HL22   1.008
 MASS  HLA    1.008
```

```
 MASS  CL1    12.011
 MASS  CL2    12.011
 MASS  OL2    15.999
 MASS  MO1    15.999
 MASS  NLA    14.007
 MASS    HW     1.0079                    ! TIP3P water hydrogen
 MASS    OW     15.9994                    ! TIP3P water oxygen
 mass MO1  15.9994
residue HIS
  group
    atom N   type=NH1 charge=-0.36 end
    atom HN  type=H   charge= 0.26 end
 group
    atom CA  type=CT  charge= 0.00 end
    atom HA  type=HA  charge= 0.10 end
 group
    atom CB  type=CT  charge=-0.20 end
    atom HB1 type=HA  charge= 0.10 end
    atom HB2 type=HA  charge= 0.10 end
 group
    atom CG  type=CC  charge= 0.05 end
 group
    atom ND1 type=NA  charge=-0.40 end
    atom HD1 type=H   charge= 0.40 end
 group
    atom CD2 type=CV  charge=-0.14 end
    atom HD2 type=HA  charge= 0.14 end
 group
    atom CE1 type=CR  charge=-0.14 end
    atom HE1 type=HA  charge= 0.14 end
 group
    atom NE2 type=NB  charge=-0.05 end
    ATOM HE2  TYPE=H     CHARge= 0.35   END  !#
 group
    atom C   type=C   charge= 0.48 end
    atom O   type=O   charge=-0.48 end
  bond N   HN
  bond N   CA     bond CA  HA
```

```
  bond CA  CB     bond CB  HB1     bond CB  HB2
  bond CB  CG
  bond CG  ND1    bond ND1 HD1
  bond ND1 CE1    bond CE1 HE1
  bond CG  CD2    bond CD2 HD2
  bond CD2 NE2
  bond CE1 NE2    bonds NE2 HE2
  bond CA  C
  bond C   O
  improper HA  N   C   CB  !stereo CA
  improper CG  CB  ND1 CD2
  improper ND1 CE1 CG  HD1
  improper CD2 NE2 CG  HD2
  improper CE1 ND1 NE2 HE1
  improper CG  ND1 CE1 NE2
  improper ND1 CE1 NE2 CD2
  improper CE1 NE2 CD2 CG
  improper NE2 CD2 CG  ND1
  improper CD2 CG  ND1 CE1
  improper HB1 HB2 CA CG  !stereo CB
  IMPRoper NE2  CD2  CE1  HE2 !planar NE2
dihedral CG  CB  CA  N
dihedral ND1 CG  CB  CA
end
residue HIC
group
  atom CJ1  type=CL1    charge=0.49    end ! ASP charge
  atom OJ2  type=OL2    charge=-0.62   end ! ASP charge
  atom OM1  type=MO1     charge=-0.62   end ! ASP charge
group
  atom CJ2  type=CL2    charge=-0.45   end ! ASP charge
  atom HJ21 type=HL21    charge=0.10    end ! ASP charge
  atom HJ22 type=HL22    charge=0.10    end ! ASP charge
group
 atom NYA  type=NLA    charge=-0.60   end ! Check charge!
 atom HYA  type=HLA    charge= 0.10   end  !dgn edit
group
  atom CJ3  type=CL3    charge=0.49    end ! ASP charge
```

```
  atom OJ3  type=OL3     charge=-0.62   end ! ASP charge
  atom OM2  type=MO2     charge=-0.62   end ! ASP charge
group
  atom CJ4  type=CL4    charge=-0.45   end ! ASP charge
  atom HJ41 type=HL41    charge=0.10    end ! ASP charge
  atom HJ42 type=HL42    charge=0.10    end ! ASP charge
! CU2 {copper 2+}
  GROUp
  ATOM CU+2 TYPE=CU+2 CHARge=+2.0 END
! water ligand
  group
 ATOM OH2  TYPE= OW   CHARge= -0.834  END
 ATOM H1   TYPE= HW   CHARge=  0.417  END
 ATOM H2   TYPE= HW   CHARge=  0.417  END
 BOND  HYA  NYA
 BOND  NYA  CJ2      BOND  NYA  CJ4      BOND  CJ2  CJ1      BOND  CJ2 HJ21
 BOND  CJ2 HJ22      BOND  CJ1  OJ2      BOND  CJ1  OM1      BOND  CJ4  CJ3
 BOND  CJ4 HJ41      BOND  CJ4 HJ42      BOND  CJ3  OJ3      BOND  CJ3  OM2
 BOND CU+2 NYA
 BOND CU+2 OM2
 BOND CU+2 OM1
 bond  NE2 CU+2
 BOND  H1  OH2
 BOND  H2  OH2
 bond  CU+2 OH2
!IMPR  2NE2 1NE2 1NYA 1OM2   ! to patch  0
!IMPR  1NYA 1OM2 2NE2 3NE2   ! to patch  0
!IMPR  1NE2 1NYA 1OM2 2NE2    ! to patch  0
IMPR  CU+2 NYA OM2 OH2    !60
IMPR  CU+2 OM2 NYA OM1     !60
 !IMPR  NYA Cu+2 OM1 CJ3 !
 !IMPR  NYA Cu+2 OM1 CJ1 !
!! IMPR   OM1 OM2 OH2 NE2
!IMPR   OM1 OM2 OH2 CU+2
!IMPR   NE2 OM2 NYA CU+2
 !IMPR  OH2 CU+2 OM2 OM1
 !IMPR  OJ2 CJ1 CJ3 OJ3
! IMPR  NYA CJ2 CJ1 OM1
```

```
!IMPR  NYA OM2 NE2 OM1
!IMPR  NE2 OM2 NYA OM1
 ACCE  OJ3  CJ3
 ACCE  OJ2  CJ1
 group
   atom N   type=NH1 charge=-0.36 end
   atom HN  type=H   charge= 0.26 end
group
   atom CA  type=CT  charge= 0.00 end
   atom HA  type=HA  charge= 0.10 end
group
   atom CB  type=CT  charge=-0.20 end
   atom HB1 type=HA  charge= 0.10 end
   atom HB2 type=HA  charge= 0.10 end
group
   atom CG  type=CC  charge= 0.05 end
group
   atom ND1 type=NA  charge=-0.40 end
   atom HD1 type=H   charge= 0.40 end
group
   atom CD2 type=CV  charge=-0.14 end
   atom HD2 type=HA  charge= 0.14 end
group
   atom CE1 type=CR  charge=-0.14 end
   atom HE1 type=HA  charge= 0.14 end
group
   atom NE2 type=NB  charge=-0.05 end
!    ATOM HE2  TYPE=H     CHARge= 0.35   END  !#
group
   atom C   type=C   charge= 0.48 end
   atom O   type=O   charge=-0.48 end
 bond N   HN
 bond N   CA     bond CA  HA
 bond CA  CB     bond CB  HB1     bond CB  HB2
 bond CB  CG
 bond CG  ND1    bond ND1 HD1
 bond ND1 CE1    bond CE1 HE1
 bond CG  CD2    bond CD2 HD2
```

```
  bond CD2 NE2
  bond CE1 NE2    {bonds NE2 HE2}
  bond CA  C
  bond C   O
  improper HA  N   C   CB  !stereo CA
  improper CG  CB  ND1 CD2
  improper ND1 CE1 CG  HD1
  improper CD2 NE2 CG  HD2
  improper CE1 ND1 NE2 HE1
  improper CG  ND1 CE1 NE2
  improper ND1 CE1 NE2 CD2
  improper CE1 NE2 CD2 CG
  improper NE2 CD2 CG  ND1
  improper CD2 CG  ND1 CE1
  improper HB1 HB2 CA CG  !stereo CB
  IMPRoper NE2  CD2  CE1  CU+2 !planar NE2
  dihedral CG  CB  CA  N
  dihedral ND1 CG  CB  CA
end
presidue CHIC                ! Copper IDA
  group
   delete  atom 2HE2 end
  add bond 1CU+2 2NE2
  add angle 1NE2 1CU+2 2NE2
  add angle 2NE2 1CU+2 1OM1
 ! add angle 2NE2 1CU+2 1OM2
 ! add angle 2NE2 1CU+2 1NYA
  add angle 2NE2 1CU+2 1OH2
add improper 2NE2 2CD2 2CE1 1CU+2
!add improper 1OH2 1OM2 1OM1 2NE2
!add improper 1OM1 1OM2 1OH2 2NE2
!add improper 2NE2 1NE2 1NYA 1OM2
!add improper 1NE2 2NE2 1NLA 1 CU+2
!add improper 1OH2 2NE2 1OM1 1CU+2
end
```

Finally, the dynamics input file (parent file: dynamics.inp) is: (pg. 249-251)

```
topology  @topallhdg_newx.pro  end                  {*Read topology file.*}
 parameter
@parallhdg_newx.pro                             {*Read empirical potential*}
                                                {*parameter file CHARMM19 *}
                                                {*with modifications.     *}
   nbonds                                       {*This statement specifies the  *}
      atom cdie shift eps=1.0  e14fac=0.4  {*nonbonded interaction energy  *}
      cutnb=7.5 ctonnb=6.0 ctofnb=6.5      {*options.  Note the reduced    *}
      nbxmod=5 vswitch                     {*nonbonding cutoff to save some*}
   end                                       {*CPU time.   This statement    *}
                                           {*overwrites the defaults in    *}
                                           {*the parameter file.           *}
 end
segment
   name="GB1A"
   SETUP=TRUE
   chain
       @TOPPAR:toph19.pep                  {*Read peptide bond file        *}
       coordinates @28C_MTSL_6H_8H_Cu_IDA_built.pdb                                          {*interpret coordinate file to*}
   end
   end
{*
 vector do (name="O") ( name OT1 )               {*names are used.         *}
 vector do (name="OT") ( name OT2 )
 vector do (name="CD1") ( name CD and resname ile )
 *}
!remove all hydrogens!
delete select (hydro) end
 coordinates @28C_MTSL_6H_8H_Cu_IDA_built.pdb                    {*Here we actually read the*}
                                               {*coordinates.             *}
hbuild                                         {*This statement builds       *}
    selection=( hydrogen )                    {*missing hydrogens, which are*}
    phistep=45                                {*needed for the force field. *}
 end
patch CHIC { patch to include chelated copper}
    reference=1=(segid A and resid 6 )
    reference=2=(segid A and resid 8 )
```

```
end
restraints plane {planarity constraints to fix the geometry of the copper chelate}
group
   selection=(
          ( segid GB1A and resid 6 and name OM2)
        or
           ( segid GB1A and resid 6 and name OH2 )
        or
           (segid GB1A and resid 6 and name NE2  )
        or
           ( segid GB1A and resid 6 and name OM1 )
              )
                 weight=400.0  end
   group
   selection=(
                ( segid GB1A and resid 6 and name NE2)
        or
           ( segid GB1A and resid 6 and name NYA )
        or
           ( segid GB1A and resid 6 and name OM2  )
        or
           ( segid GB1A and resid 8 and name NE2  )
              )
    weight=400.0
  end
end
                        {* The planarity energy term needs to be turned on.*}
!--------------------------------
!stop
{restraints harmonic. Used to constrain the protein backbone in its original conformation}
coordinates disposition = reference @28C_MTSL_6H_8H_Cu_IDA_built.pdb
vector do ( harmonic=20.0 ) ((name CA or name C or name N or name O))
vector do ( harmonic=0.0 )  ( not ( name CA or name C or name N or name O))
restraints harmonic exponent=2 end
flags include harm  plan end
mini powell
  drop=1e5
  nprint=1
```

```
  tolg=1e-5
  nstep=10000
end
param nbonds wmin = .00001 end end
evaluate ($init_t = 200 )    {* Initial simulated annealing temperature.*}
vector do (vx = maxwell($init_t)) (all)
vector do (vy = maxwell($init_t)) (all)
vector do (vz = maxwell($init_t)) (all)
vector do (fbeta=100. ) ( all )
  evaluate ($timestep = 0.0005)
  evaluate ($nstep = 100000)
evaluate ($n = 1)
while ($n <= 800) loop stage1
           if ($n < 10) then
               evaluate ($file = "Results/28C_6H_8H/c00" + encode($n) + ".pdb")
           elseif ($n < 100) then
               evaluate ($file = "Results/28C_6H_8H/c0" + encode($n) + ".pdb")
           else
               evaluate ($file = "Results/28C_6H_8H/c" + encode($n) + ".pdb")
           end if
           dynamics  verlet
                  nstep=$nstep   timestep=$timestep   iasvel=current
                  tcoupling=true tbath=$init_t  nprint=50  iprfrq=0
end
            write coor output = $file end
            evaluate ($n = $n + 1)
end loop stage1
stop
```

Appendix B: General Model to Optimise Cu^{II} Labeling at Double Histidine Motifs

A Cu^{II}-Cu^{II} RIDME pseudo-titration of 100 µM 6H/8H/28H/32H GB1 in presence of Cu^{II}-NTA has been analysed and pairs of K_D fitted using a bivariate error function (chapter 4.3.6), however the 1D experimental error surfaces and fitted Gaussian functions used to estimate the corresponding K_D error bars were not shown, and are instead given here, in figures B1-B5. Each Gaussian function was fitted individually and then plotted together.

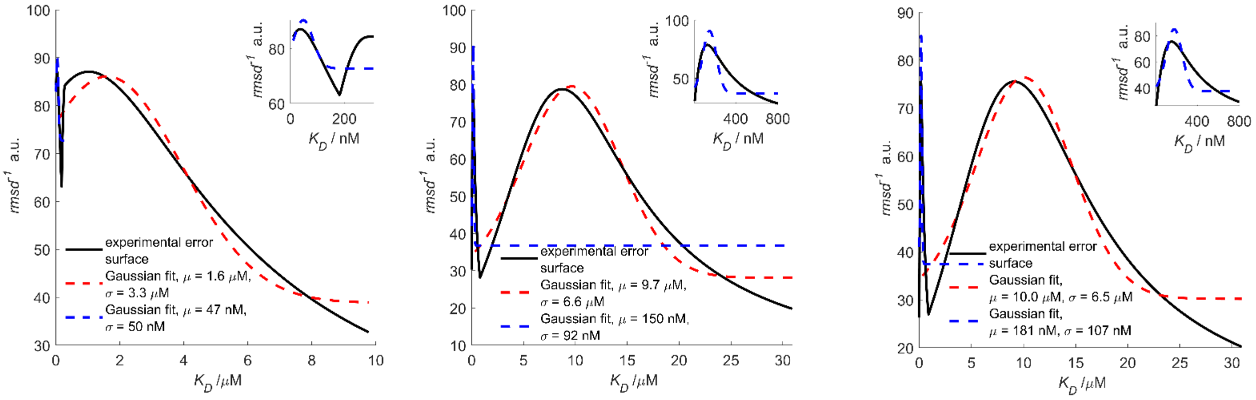

Figure B1: 1D unweighted experimental error surfaces (black traces) and corresponding Gaussian fits (blue and red dotted traces) of Cu^{II}-Cu^{II} RIDME pseudo-titration series, recorded with T_{mix} = 0.7 × T_1 (left), 1.3 × T_1 (centre) and 1.9 × T_1 (right), and background corrected using a second order polynomial background correction.

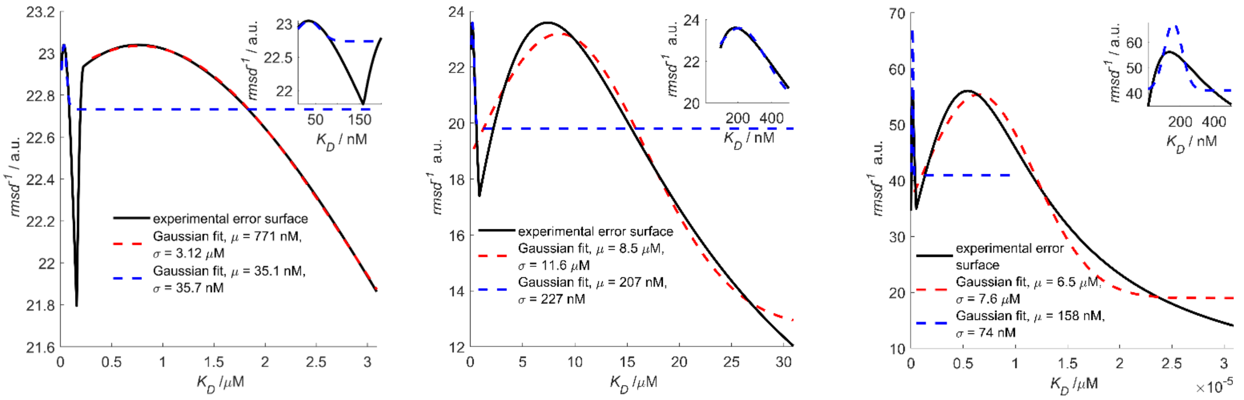

Figure B2: 1D unweighted experimental error surface (black trace) and corresponding Gaussian fits (blue and red dotted traces) of Cu^{II}-Cu^{II} RIDME pseudo-titration series, recorded with T_{mix} = 0.7 × T_1 (left), 1.3 × T_1 (centre) and 1.9 × T_1 (right), and background corrected using a stretched exponential background correction.

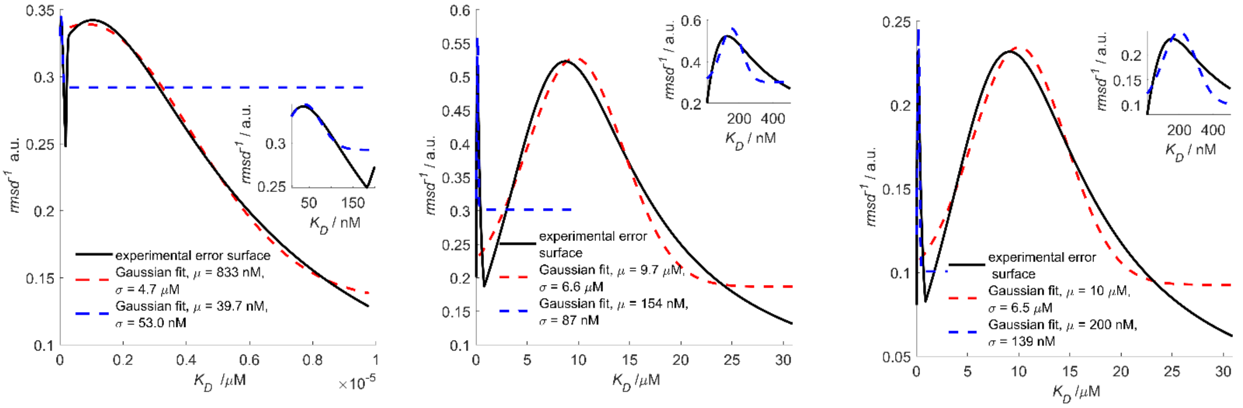

Figure B3: 1D weighted experimental error surface (black trace) and corresponding Gaussian fits (blue and red dotted traces) of Cu^{II}-Cu^{II} RIDME pseudo-titration series, recorded with $T_{mix} = 0.7 \times T_1$ (left), $1.3 \times T_1$ (centre) and $1.9 \times T_1$ (right),and background corrected using a second order polynomial background correction.

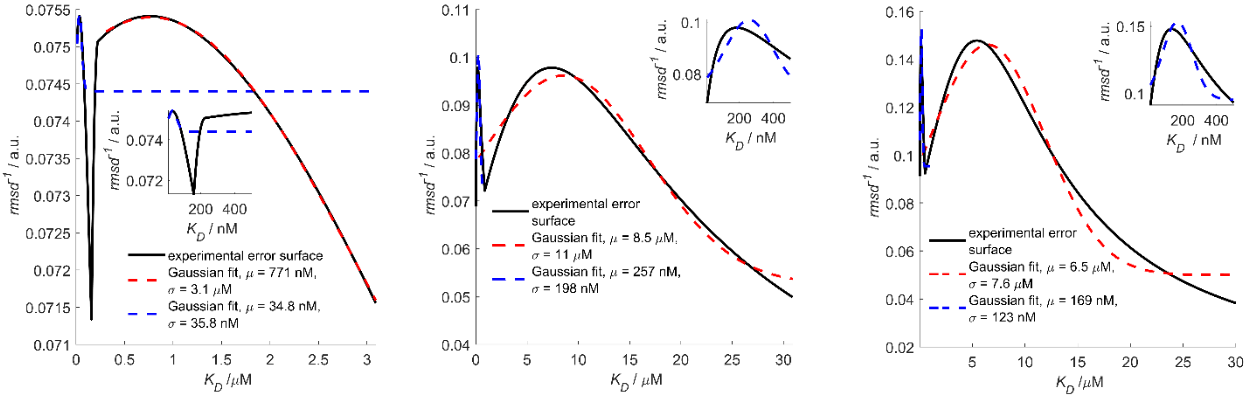

Figure B4: 1D weighted experimental error surface (black trace) and corresponding Gaussian fits (blue and red dotted traces) of Cu^{II}-Cu^{II} RIDME pseudo-titration series (recorded with $T_{mix} = 0.7 \times T_1$ (left), $1.3 \times T_1$ (centre) and $1.9 \times T_1$ (right),and background corrected using a stretched exponential background correction

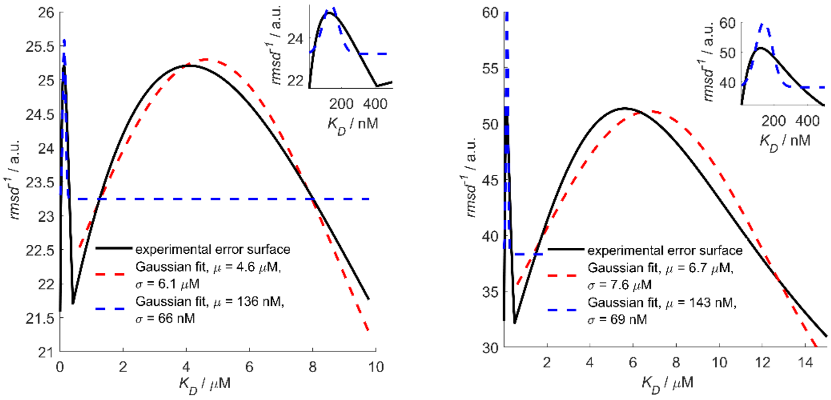

Figure B5: 1D experimental error surface (black trace) and corresponding Gaussian fits (blue and red dotted traces) of all Cu^{II}-Cu^{II} RIDME pseudo-titration series (recorded with $T_{mix} = 0.7$, 1.3 and $1.9 \times T_1$) fitted globally, and background corrected using a second order polynomial (left) and stretched exponential (right) background correction.

Bibliography

1 J. D. Watson and F. H. C. Crick, *Nature*, 1953, **171**, 737–738.

2 C. B. Anfinsen, *Science (80-.).*, 1973, **181**, 223–230.

3 H. V. Westerhoff and B. O. Palsson, *Nat. Biotechnol.*, 2004, **22**, 1249–1252.

4 D. M. Kim, X. Yao, R. P. Vanam and M. S. Marlow, *MAbs*, 2019, **11**, 1319–1330.

5 B. Commoner, J. Townsend and G. E. Pake, *Nature*, 1954, **174**, 689–691.

6 W. Gordy, W. B. Ard and H. Shields, *Proc. Natl. Acad. Sci.*, 1955, **41**, 983–996.

7 R. L. Dimmick, R. J. Heckly and D. P. Hollis, *Nature*, 1961, **192**, 776–777.

8 M. Burr and D. E. Koshland, *Proc. Natl. Acad. Sci. United States*, 1964, **52**, 1017–1024.

9 L. J. Berliner, J. Grunwald, H. O. Hankovszky and K. Hideg, *Anal. Biochem.*, 1982, **119**, 450–455.

10 V. V. Kurshev, A. M. Raitsimring and Y. D. Tsvetkov, *J. Magn. Reson.*, 1989, **81**, 441–454.

11 A. D. Milov, K. M. Salikov and M. D. Shchirov, *Sov. Phys. Solid State*, 1981, **23**, 565–569.

12 W. L. Hubbell and C. Altenbach, *Curr. Opin. Struct. Biol.*, 1994, **4**, 566–573.

13 C. Altenbach, S. L. Flitsch, H. G. Khorana and W. L. Hubbell, *Biochemistry*, 1989, **28**, 7806–7812.

14 A. P. Todd, J. Cong, F. Levinthal, C. Levinthal and W. L. Hubell, *Proteins Struct. Funct. Bioinforma.*, 1989, **6**, 294–305.

15 C. Altenbach, T. Marti, H. G. Khorana and W. L. Hubbell, *Science (80-.).*, 1990, **248**, 1088–1092.

16 R. E. Martin, M. Pannier, F. Diederich, V. Gramlich, M. Hubrich and H. W. Spiess, *Angew. Chemie Int. Ed.*, 1998, **37**, 2833–2837.

17 M. Pannier, S. Veit, A. Godt, G. Jeschke and H. W. Spiess, *J. Magn. Reson.*, 2000, **142**, 331–340.

18 P. P. Borbat and J. H. Freed, *Chem. Phys. Lett.*, 1999, **313**, 145–154.

19 G. Jeschke, M. Pannier, A. Godt and H. W. Spiess, *Chem. Phys. Lett.*, 2000, **331**, 243–252.

20 Y. W. Chiang, P. P. Borbat and J. H. Freed, *J. Magn. Reson.*, 2005, **172**, 279–295.

21 G. Jeschke, V. Chechik, P. Ionita, A. Godt, H. Zimmermann, J. Banham, C. R. Timmel, D. Hilger and H. Jung, *Appl. Magn. Reson.*, 2006, **30**, 473–498.

22 G. Jeschke, G. Panek, A. Godt, A. Bender and H. Paulsen, *Appl. Magn. Reson.*, 2004, **26**, 223.

23 G. Jeschke, A. Bender, T. Schweikardt, G. Panek, H. Decker and H. Paulsen, *J. Biol. Chem.*, 2005, **280**, 18623–18630.

24 I. D. Sahu, A. F. Craig, M. M. Dunagan, K. R. Troxel, R. Zhang, A. G. Meiberg, C. N. Harmon, R. M. McCarrick, B. M. Kroncke, C. R. Sanders and G. A. Lorigan, *Biochemistry*, 2015, **54**, 6402–6412.

25 L. G. Cuello, D. M. Cortes and E. Perozo, *Science (80-.).*, 2004, **306**, 491–495.

26 Q. Li, R. Shen, J. S. Treger, S. S. Wanderling, W. Milewski, K. Siwowska, F. Bezanilla and E. Perozo, *Proc. Natl. Acad. Sci. U. S. A.*, 2015, **112**, E5926–E5935.

27 A. R. Balo, J. Lee and O. P. Ernst, *Anal. Chem.*, 2019, **91**, 1071–1079.

28 C. Arrigoni, A. Rohaim, D. Shaya, F. Findeisen, R. A. Stein, S. R. Nurva, S. Mishra, H. S. McHaourab and D. L. Minor, *Cell*, 2016, **164**, 922–936.

29 W. R. Lindemann, E. D. Evans, A. J. Mijalis, O. M. Saouaf, B. L. Pentelute and J. H. Ortony, *Sci. Rep.*, 2020, **10**, 2597.

30 K. Singewald, X. Bogetti, K. Sinha, G. S. Rule and S. Saxena, *Angew. Chemie - Int. Ed.*, 2020, **59**, 23040–23044.

31 N. L. Pirman, E. Milshteyn, L. Galiano, J. C. Hewlett and G. E. Fanucci, *Protein Sci.*, 2011, **20**, 150–159.

32 L. Galazzo, L. Maso, E. De Rosa, M. Bortolus, D. Doni, L. Acquasaliente, V. De Filippis, P. Costantini and D. Carbonera, *Sci. Rep.*, 2017, **7**, 1714.

33 T. Ahammad, D. L. Drew, I. D. Sahu, R. A. Serafin, K. R. Clowes and G. A. Lorigan, *J. Phys. Chem. B*, 2019, **123**, 8048–8056.

34 J. J. Wright, E. Salvadori, H. R. Bridges, J. Hirst and M. M. Roessler, *J. Inorg. Biochem.*, 2016, **162**, 201–206.

35 K. Abdiaziz, E. Salvadori, K. P. Sokol, E. Reisner and M. M. Roessler, *Chem. Commun.*, 2019, **55**, 8840–8843.

36 J. H. Artz, D. W. Mulder, M. W. Ratzloff, C. E. Lubner, O. A. Zadvornyy, A. X. Levan, S. G. Williams, M. W. W. Adams, A. K. Jones, P. W. King and J. W. Peters, *J. Am. Chem. Soc.*, 2017, **139**, 9544–9550.

37 S. A. Cervantes, T. H. Bajakian, M. A. Soria, A. S. Falk, R. J. Service, R. Langen and A. B. Siemer, *Sci. Rep.*, 2016, **6**, 38265.

38 M. Tao, J. M. Isas and R. Langen, *Sci. Rep.*, 2020, **10**, 5301.

39 M. D. Rabenstein and Y. K. Shin, *Proc. Natl. Acad. Sci. U. S. A.*, 1995, **92**, 8239–8243.

40 T. Prisner, M. Rohrer and F. MacMillan, *Annu. Rev. Phys. Chem.*, 2001, **52**, 279–313.

41 O. Schiemann and T. F. Prisner, *Q. Rev. Biophys.*, 2007, **40**, 1–53.

42 B. L. Eggimann, V. V. Vostrikov, G. Veglia and J. I. Siepmann, *Theor. Chem. Acc.*, 2013, **132**, 1388.

43 O. Duss, M. Yulikov, G. Jeschke and F. H. T. Allain, *Nat. Commun.*, 2014, **5**, 3669.

44 O. Duss, E. Michel, M. Yulikov, M. Schubert, G. Jeschke and F. H. T. Allain, *Nature*, 2014, **509**, 588–592.

45 Y. Yang, T. A. Ramelot, R. M. McCarrick, S. Ni, E. A. Feldmann, J. R. Cort, H. Wang, C. Ciccosanti, M. Jiang, H. Janjua, T. B. Acton, R. Xiao, J. K. Everett, G. T. Montelione and M. A. Kennedy, *J. Am. Chem. Soc.*, 2010, **132**, 11910–11913.

46 T. Vöpel, C. S. Hengstenberg, T. O. Peulen, Y. Ajaj, C. A. M. Seidel, C. Herrmann and J. P. Klare, *Biochemistry*, 2014, **53**, 4590–4600.

47 R. V. Agafonov, I. V. Negrashov, Y. V. Tkachev, S. E. Blakely, M. A. Titus, D. D. Thomas and Y. E. Nesmelov, *Proc. Natl. Acad. Sci. U. S. A.*, 2009, **106**, 21625–21630.

48 M. Burger, S. Rein, S. Weber, P. Gräber and S. Kacprzak, *Eur. Biophys. J.*, 2020, **49**, 1–10.

49 E. H. Yardeni, T. Bahrenberg, R. A. Stein, S. Mishra, E. Zomot, B. Graham, K. L. Tuck, T. Huber, E. Bibi, H. S. Mchaourab and D. Goldfarb, *Sci. Rep.*, 2019, **9**, 12528.

50 T. Strohäker, B. C. Jung, S. H. Liou, C. O. Fernandez, D. Riedel, S. Becker, G. M. Halliday, M. Bennati, W. S. Kim, S. J. Lee and M. Zweckstetter, *Nat. Commun.*, 2019, **10**, 5535.

51 S. W. Chuo, S. H. Liou, L. P. Wang, R. D. Britt, T. L. Poulos, I. F. Sevrioukova and D. B. Goodin, *Biochemistry*, 2019, **58**, 3903–3910.

52 G. Bollag, P. Hirth, J. Tsai, J. Zhang, P. N. Ibrahim, H. Cho, W. Spevak, C. Zhang, Y. Zhang, G. Habets, E. A. Burton, B. Wong, G. Tsang, B. L. West, B. Powell, R. Shellooe, A. Marimuthu, H. Nguyen, K. Y. J. Zhang, D. R. Artis, J. Schlessinger, F. Su, B. Higgins, R. Iyer, K. D'Andrea, A. Koehler, M. Stumm, P. S. Lin, R. J. Lee, J. Grippo, I. Puzanov, K. B. Kim, A. Ribas, G. A. McArthur, J. A. Sosman, P. B. Chapman, K. T. Flaherty, X. Xu, K. L. Nathanson and K. Nolop, *Nature*, 2010, **467**, 596–599.

53 M. Kim, S. A. Vishnivetskiy, N. Van Eps, N. S. Alexander, W. M. Cleghorn, X. Zhan, S. M. Hanson, T. Morizumi, O. P. Ernst, J. Meiler, V. V. Gurevich and W. L. Hubbell, *Proc. Natl. Acad. Sci. U. S. A.*, 2012, **109**, 18407–18412.

54 D. T. Edwards, T. Huber, S. Hussain, K. M. Stone, M. Kinnebrew, I. Kaminker, E. Matalon, M. S. Sherwin, D. Goldfarb and S. Han, *Structure*, 2014, **22**, 1677–1686.

55 B. Verhalen, R. Dastvan, S. Thangapandian, Y. Peskova, H. A. Koteiche, R. K. Nakamoto, E. Tajkhorshid and H. S. McHaourab, *Nature*, 2017, **543**, 738–741.

56 O. Schiemann, N. Piton, Y. Mu, G. Stock, J. W. Engels and T. F. Prisner, *J. Am. Chem. Soc.*, 2004, **126**, 5722–5729.

57 C. Wuebben, S. Blume, D. Abdullin, D. Brajtenbach, F. Haege, S. Kath-Schorr and O. Schiemann, *Molecules*, 2019, **24**, 4482.

58 E. S. Babaylova, A. A. Malygin, A. A. Lomzov, D. V. Pyshnyi, M. Yulikov, G. Jeschke, O. A. Krumkacheva, M. V. Fedin, G. G. Karpova and E. G. Bagryanskaya, *Nucleic Acids Res.*, 2016, **44**, 7935–7943.

59 H. Sameach, A. Narunsky, S. Azoulay-Ginsburg, L. Gevorkyan-Aiapetov, Y. Zehavi, Y. Moskovitz, T. Juven-Gershon, N. Ben-Tal and S. Ruthstein, *Structure*, 2017, **25**, 988–996.

60 A. Dalaloyan, A. Martorana, Y. Barak, D. Gataulin, E. Reuveny, A. Howe, M. Elbaum, S. Albeck, T. Unger, V. Frydman, E. H. Abdelkader, G. Otting and D. Goldfarb, *ChemPhysChem*, 2019, **20**, 1860–1868.

61 B. Joseph, A. Sikora and D. S. Cafiso, *J. Am. Chem. Soc.*, 2016, **138**, 1844–1847.

62 F. X. Theillet, A. Binolfi, B. Bekei, A. Martorana, H. M. Rose, M. Stuiver, S. Verzini, D. Lorenz, M. Van Rossum, D. Goldfarb and P. Selenko, *Nature*, 2016, **530**, 45–50.

63 P. S. Kerry, H. L. Turkington, K. Ackermann, S. A. Jameison and B. E. Bode, *J. Phys. Chem. B*, 2014, **118**, 10882–10888.

64 C. A. J. Hutter, M. H. Timachi, L. M. Hürlimann, I. Zimmermann, P. Egloff, H. Göddeke, S. Kucher, S. Štefanić, M. Karttunen, L. V. Schäfer, E. Bordignon and M. A. Seeger, *Nat. Commun.*, 2019, **10**, 2260.

65 C. Kapsalis, B. Wang, H. El Mkami, S. J. Pitt, J. R. Schnell, T. K. Smith, J. D. Lippiat, B. E. Bode and C. Pliotas, *Nat. Commun.*, 2019, **10**, 4619.

66 D. Constantinescu-Aruxandei, B. Petrovic-Stojanovska, O. Schiemann, J. H. Naismith and M. F. White, *Nucleic Acids Res.*, 2016, **44**, 954–968.

67 A. Giannoulis, M. Oranges and B. E. Bode, *ChemPhysChem*, 2017, **18**, 2318–2321.

68 K. Ackermann, A. Giannoulis, D. B. Cordes, A. M. Z. Slawin and B. E. Bode, *Chem. Commun.*, 2015, **51**, 5257–5260.

69 A. Giannoulis, K. Ackermann, P. E. Spindler, C. Higgins, D. B. Cordes, A. M. Z. Slawin, T. F. Prisner and B. E. Bode, *Phys. Chem. Chem. Phys.*, 2018, **20**, 11196–11205.

70 J. L. Wort, K. Ackermann, A. Giannoulis, A. J. Stewart, D. G. Norman and B. E. Bode, *Angew.*

Chemie - Int. Ed., 2019, **58**, 11681–11685.

71 J. Glaenzer, M. F. Peter, G. H. Thomas and G. Hagelueken, *Biophys. J.*, 2017, **112**, 109–120.

72 A. Collauto, H. A. Deberg, R. Kaufmann, W. N. Zagotta, S. Stoll and D. Goldfarb, *Phys. Chem. Chem. Phys.*, 2017, **19**, 15324–15334.

73 J. L. Wort, K. Ackermann, D. G. Norman and B. E. Bode, *Phys. Chem. Chem. Phys.*, 2021, **23**, 3810–3819.

74 E. A. Riederer, P. J. Focke, E. R. Georgieva, N. Akyuz, K. Matulef, P. P. Borbat, J. H. Freed, S. C. Blanchard, O. Boudker and F. I. Valiyaveetil, *Elife*, 2018, **7**, e36478.

75 A. Giannoulis, R. Ward, E. Branigan, J. H. Naismith and B. E. Bode, *Mol. Phys.*, 2013, **111**, 2845–2854.

76 G. Hagelueken, W. J. Ingledew, H. Huang, B. Petrovic-Stojanovska, C. Whitfield, H. ElMkami, O. Schiemann and J. H. Naismith, *Angew. Chemie - Int. Ed.*, 2009, **48**, 2904–2906.

77 T. Schmidt, R. Ghirlando, J. Baber and G. M. Clore, *ChemPhysChem*, 2016, **17**, 2987–2991.

78 N. Fleck, C. A. Heubach, T. Hett, F. R. Haege, P. P. Bawol, H. Baltruschat and O. Schiemann, *Angew. Chemie - Int. Ed.*, 2020, **59**, 9767–9772.

79 Y. Yang, F. Yang, Y. J. Gong, J. L. Chen, D. Goldfarb and X. C. Su, *Angew. Chemie - Int. Ed.*, 2017, **56**, 2914–2918.

80 J. J. Jassoy, A. Berndhäuser, F. Duthie, S. P. Kühn, G. Hagelueken and O. Schiemann, *Angew. Chemie - Int. Ed.*, 2017, **56**, 177–181.

81 P. Widder, J. Schuck, D. Summerer and M. Drescher, *Phys. Chem. Chem. Phys.*, 2020, **22**, 4875–4879.

82 Y. Yang, F. Yang, X. Y. Li, X. C. Su and D. Goldfarb, *J. Phys. Chem. B*, 2019, **123**, 1050–1059.

83 D. Abdullin and O. Schiemann, *Chempluschem*, 2020, **85**, 353–372.

84 G. Jeschke, *Annu. Rev. Phys. Chem.*, 2012, **63**, 419–446.

85 A. D. Milov, A. G. Maryasov and Y. D. Tsvetkov, *Appl. Magn. Reson.*, 1998, **15**, 107–143.

86 I. Ritsch, D. Klose, H. Hintz, A. Godt, G. Jeschke and M. Yulikov, *Chimia (Aarau).*, 2019, **74**, 268–276.

87 I. D. Sahu and G. A. Lorigan, *J. Phys. Chem. Biophys.*, 2015, **5**, 188.

88 M. F. Perutz, M. G. Rossmann, A. F. Cullis, H. Muirhead, G. Will and A. C. T. North, *Nature*, 1960, **185**, 416–422.

89 J. Pujols, S. Peña-Díaz, D. F. Lázaro, F. Peccati, F. Pinheiro, D. González, A. Carija, S. Navarro, M. Conde-Giménez, J. García, S. Guardiola, E. Giralt, X. Salvatella, J. Sancho, M. Sodupe, T. F. Outeiro, E. Dalfó and S. Ventura, *Proc. Natl. Acad. Sci. U. S. A.*, 2018, **115**, 10481–10486.

90 F. Panza, M. Lozupone, G. Logroscino and B. P. Imbimbo, *Nat. Rev. Neurol.*, 2019, **15**, 73–88.

91 S. Tomoshige, S. Nomura, K. Ohgane, Y. Hashimoto and M. Ishikawa, *Angew. Chemie - Int. Ed.*, 2017, **56**, 11530–11533.

92 C. A. Brautigam, H. Zhao, C. Vargas, S. Keller and P. Schuck, *Nat. Protoc.*, 2016, **11**, 882–894.

93 D. Capelli, C. Parravicini, G. Pochetti, R. Montanari, C. Temporini, M. Rabuffetti, M. L. Trincavelli, S. Daniele, M. Fumagalli, S. Saporiti, E. Bonfanti, M. P. Abbracchio, I. Eberini, S. Ceruti, E. Calleri and S. Capaldi, *Front. Chem.*, 2020, **7**, 910.

94 G. Dal Cortivo, V. Marino, C. Iacobucci, R. Vallone, C. Arlt, A. Rehkamp, A. Sinz and D. Dell'Orco, *Sci. Rep.*, 2019, **9**, 15058.

95 M. G. Koliopoulos, M. Lethier, A. G. Van Der Veen, K. Haubrich, J. Hennig, E. Kowalinski, R. V. Stevens, S. R. Martin, C. Reis E Sousa, S. Cusack and K. Rittinger, *Nat. Commun.*, 2018, **9**, 1820.

96 D. Yang, A. Singh, H. Wu and R. Kroe-Barrett, *Anal. Biochem.*, 2016, **508**, 78–96.

97 C. Ren, A. O. Bailey, E. Vanderporten, A. Oh, W. Phung, M. M. Mulvihill, S. F. Harris, Y. Liu, G. Han and W. Sandoval, *Anal. Chem.*, 2019, **91**, 903–911.

98 J. Seo, W. Hoffmann, S. Warnke, X. Huang, S. Gewinner, W. Schöllkopf, M. T. Bowers, G. von Helden and K. Pagel, *Nat. Chem.*, 2017, **9**, 39–44.

99 T. D. Do, W. M. Kincannon and M. T. Bowers, *J. Am. Chem. Soc.*, 2015, **137**, 10080–10083.

100 M. J. Chalmers, S. A. Busby, B. D. Pascal, G. M. West and P. R. Griffin, *Expert Rev. Proteomics*, 2011, **8**, 43–59.

101 O. Vadas, M. L. Jenkins, G. L. Dornan and J. E. Burke, *Methods Enzymol.*, 2017, **583**, 143–172.

102 I. M. S. de Vera, J. Zheng, S. Novick, J. Shang, T. S. Hughes, R. Brust, P. Munoz-Tello, W. J. Gardner, D. P. Marciano, X. Kong, P. R. Griffin and D. J. Kojetin, *Structure*, 2017, **25**, 1506-1518.e4.

103 R. Adams, R. J. Burnley, C. R. Valenzano, O. Qureshi, C. Doyle, S. Lumb, M. Del Carmen Lopez, R. Griffin, D. McMillan, R. D. Taylor, C. Meier, P. Mori, L. M. Griffin, U. Wernery, J. Kinne, S. Rapecki, T. S. Baker, A. D. G. Lawson, M. Wright and A. Ettorre, *Sci. Rep.*, 2017, **7**, 37716.

104 N. Morgner, T. Kleinschroth, H. D. Barth, B. Ludwig and B. Brutschy, *J. Am. Soc. Mass Spectrom.*, 2007, **18**, 1429–1438.

105 O. Peetz, N. Hellwig, E. Henrich, J. Mezhyrova, V. Dötsch, F. Bernhard and N. Morgner, *J. Am. Soc. Mass Spectrom.*, 2019, **30**, 181–191.

106 N. Hellwig, O. Peetz, Z. Ahdash, I. Tascón, P. J. Booth, V. Mikusevic, M. Diskowski, A. Politis, Y. Hellmich, I. Hänelt, E. Reading and N. Morgner, *Chem. Commun.*, 2018, **54**, 13702–13705.

107 D. A. Korasick and J. J. Tanner, *Protein Sci.*, 2018, **27**, 814–824.

108 J. B. Bailey, R. H. Subramanian, L. A. Churchfield and F. A. Tezcan, *Methods Enzymol.*, 2016, **580**, 233–250.

109 A. D. Hanlon, M. I. Larkin and R. M. Reddick, *Biophys. J.*, 2010, **98**, 297–304.

110 N. J. Greenfield, *Methods Mol. Biol.*, 2004, **261**, 55–77.

111 M. Hoarau, K. J. Koebke, Z. Chen and E. N. G. Marsh, *Front. Mol. Biosci.*, 2019, **6**, 73.

112 J. H. Viles, F. E. Cohen, S. B. Prusiner, D. B. Goodin, P. E. Wright and H. J. Dyson, *Proc. Natl. Acad. Sci.*, 1999, **96**, 2042–2047.

113 A. P. Garnett and J. H. Viles, *J. Biol. Chem.*, 2003, **278**, 6795–6802.

114 E. Aronoff-Spencer, C. S. Burns, N. I. Avdievich, G. J. Gerfen, J. Peisach, W. E. Antholine, H. L. Ball, F. E. Cohen, S. B. Prusiner and G. L. Millhauser, *Biochemistry*, 2000, **39**, 13760–13771.

115 N. Bai, H. Roder, A. Dickson and J. Karanicolas, *Sci. Rep.*, 2019, **9**, 2650.

116 K. Gao, R. Oerlemans and M. R. Groves, *Biophys. Rev.*, 2020, **12**, 85–104.

117 P. C. A. van der Wel, *Emerg. Top. Life Sci.*, 2018, **2**, 57–67.

118 J. P. Renaud, A. Chari, C. Ciferri, W. T. Liu, H. W. Rémigy, H. Stark and C. Wiesmann, *Nat. Rev. Drug Discov.*, 2018, **17**, 471–492.

119 D. W. Piston and G. J. Kremers, *Trends Biochem. Sci.*, 2007, **32**, 407–414.

120 S. Q. Xiang, U. B. le Paige, V. Horn, K. Houben, M. Baldus and H. van Ingen, *Angew. Chemie - Int. Ed.*, 2018, **57**, 4571–4575.

121 D. J. Wright, K. J. Simmons, R. M. Johnson, D. J. Beech, S. P. Muench and R. S. Bon, *Commun. Biol.*, 2020, **3**, 704.

122 L. Jiang, Z. Xiong, Y. Song, Y. Lu, Y. Chen, J. S. Schultz, J. Li and J. Liao, *Sci. Rep.*, 2019, **9**, 2050.

123 R. Huang, A. Bonnichon, T. D. W. Claridge and I. K. H. Leung, *Sci. Rep.*, 2017, **7**, 43727.

124 A. Zawadzka-Kazimierczuk, M. Somlyay, H. Kaehlig, G. Iakobson, P. Beier and R. Konrat, *RSC Adv.*, 2018, **8**, 40687–40692.

125 G. Kang, A. T. Taguchi, J. A. Stubbe and C. L. Drennan, *Science (80-.).*, 2020, **368**, 424–427.

126 H. Sanabria, D. Rodnin, K. Hemmen, T. O. Peulen, S. Felekyan, M. R. Fleissner, M. Dimura, F. Koberling, R. Kühnemuth, W. Hubbell, H. Gohlke and C. A. M. Seidel, *Nat. Commun.*, 2020, **11**, 1231.

127 M. J. Borgnia, S. Banerjee, A. Merk, D. Matthies, A. Bartesaghi, P. Rao, J. Pierson, L. A. Earl, V. Falconieri, S. Subramaniam and J. L. S. Milne, *Mol. Pharmacol.*, 2016, **89**, 645–651.

128 I. Sengupta and J. Udgaonkar, *Elife*, 2019, **8**, e44698.

129 Ö. Poyraz, H. Schmidt, K. Seidel, F. Delissen, C. Ader, H. Tenenboim, C. Goosmann, B. Laube, A. F. Thünemann, A. Zychlinsky, M. Baldus, A. Lange, C. Griesinger and M. Kolbe, *Nat. Struct. Mol. Biol.*, 2010, **17**, 788–792.

130 Q. Z. Ni, E. Daviso, T. V. Can, E. Markhasin, S. K. Jawla, T. M. Swager, R. J. Temkin, J. Herzfeld and R. G. Griffin, *Acc. Chem. Res.*, 2013, **46**, 1933–1941.

131 A. Holoubek, P. Herman, J. Sýkora, B. Brodská, J. Humpolíčková, M. Kráčmarová, D. Gášková, M. Hof and K. Kuželová, *Methods Appl. Fluoresc.*, 2018, **6**, 035016.

132 B. Hochreiter, M. Kunze, B. Moser and J. A. Schmid, *Sci. Rep.*, 2019, **9**, 8233.

133 T. Schmidt, M. A. Wälti, J. L. Baber, E. J. Hustedt and G. M. Clore, *Angew. Chemie - Int. Ed.*, 2016, **55**, 15905–15909.

134 L. Yu, W. Wang, S. Ling, S. Liu, L. Xiao, Y. Xin, C. Lai, Y. Xiong, L. Zhang and C. Tian, *Sci. Rep.*, 2015, **5**, 7848.

135 M. A. Ehrenberger, A. Vieyra, J. M. Esquiaqui and G. E. Fanucci, *Biochem. Biophys. Res. Commun.*, 2019, **516**, 839–844.

136 J. M. Esquiaqui, E. M. Sherman, J. D. Ye and G. E. Fanucci, *Biochemistry*, 2016, **55**, 4295–4305.

137 H. H. Haeri, B. Schunk, J. Tomaszewski, H. Schimm, M. J. Gelos and D. Hinderberger, *ChemistryOpen*, 2019, **8**, 650–656.

138 S. Dunkel, L. P. Pulagam, H. J. Steinhoff and J. P. Klare, *Phys. Chem. Chem. Phys.*, 2015, **17**, 4875–4878.

139 D. Tatlidil, M. Ucuncu and Y. Akdogan, *Phys. Chem. Chem. Phys.*, 2015, **17**, 22678–22685.

140 Y. Lin, J. McCarty, J. N. Rauch, K. T. Delaney, K. S. Kosik, G. H. Fredrickson, J. E. Shea and S. Han, *Elife*, 2019, **8**, e42571.

141 G. K. Chow, A. G. Chavan, J. C. Heisler, Y. G. Chang, A. Liwang and R. D. Britt, *Biochemistry*, 2020, **59**, 2387–2400.

142 M. H. Tessmer, D. M. Anderson, A. M. Pickrum, M. O. Riegert, R. Moretti, J. Meiler, J. B. Feix and D. W. Frank, *Proc. Natl. Acad. Sci. U. S. A.*, 2018, **115**, 525–530.

143 E. Zurlo, I. Gorroño Bikandi, N. J. Meeuwenoord, D. V. Filippov and M. Huber, *Phys. Chem. Chem. Phys.*, 2019, **21**, 25187–25195.

144 Z. Liang and J. H. Freed, *J. Phys. Chem. B*, 1999, **103**, 6384–6396.

145 E. Perozo, D. Marien Cortes and L. G. Cuello, *Nat. Struct. Biol.*, 1998, **5**, 459–469.

146 A. Pavlova, C. Y. Cheng, M. Kinnebrew, J. Lew, F. W. Dahlquist and S. Han, *Proc. Natl. Acad. Sci. U. S. A.*, 2016, **113**, E127–E136.

147 M. Aitha, T. K. Richmond, Z. Hu, A. Hetrick, R. Reese, A. Gunther, R. McCarrick, B. Bennett and M. W. Crowder, *J. Inorg. Biochem.*, 2014, **136**, 40–46.

148 S. Ghosh, M. J. Lawless, G. S. Rule and S. Saxena, *J. Magn. Reson.*, 2018, **286**, 163–171.

149 P. D. Martin, Z. M. James and D. D. Thomas, *Biophys. J.*, 2018, **114**, 2573–2583.

150 K. M. Schultz, T. J. Lundquist and C. S. Klug, *Protein Sci.*, 2017, **26**, 1517–1523.

151 L. Tao, T. A. Stich, C. N. Butterfield, C. A. Romano, T. G. Spiro, B. M. Tebo, W. H. Casey and R. D. Britt, *J. Am. Chem. Soc.*, 2015, **137**, 10563–10575.

152 G. F. White, L. Ottignon, T. Georgiou, C. Kleanthous, G. R. Moore, A. J. Thomson and V. S. Oganesyan, *J. Magn. Reson.*, 2007, **185**, 191–203.

153 Y. Fichou, Z. R. Oberholtzer, H. Ngo, C. Y. Cheng, T. J. Keller, N. A. Eschmann and S. Han, *Front. Neurosci.*, 2019, **13**, 1339.

154 M. A. Ali, A. Hassan, G. C. Sedenho, R. V. Gonçalves, D. R. Cardoso and F. N. Crespilho, *J. Phys. Chem. C*, 2019, **123**, 16058–16064.

155 T. M. Hedison, D. J. Heyes, M. Shanmugam, A. I. Iorgu and N. S. Scrutton, *Chem. Commun.*, 2019, **55**, 5863–5866.

156 W. B. Mims, *Phys. Rev. B*, 1972, **5**, 2409.

157 S. Van Doorslaer, *eMagRes*, 2017, **6**, 51–70.

158 H. Kurreck, B. Kirste and W. Lubitz, *Angew. Chemie Int. Ed.*, 1984, **23**, 173.

159 N. Cox, A. Nalepa, W. Lubitz and A. Savitsky, *J. Magn. Reson.*, 2017, **280**, 63–78.

160 G. Feher, *Phys. Rev.*, 1956, **103**, 834.

161 P. Schosseler, T. Wacker and A. Schweiger, *Chem. Phys. Lett.*, 1994, **224**, 319–324.

162 D. Goldfarb, *eMagRes*, 2017, **6**, 101–104.

163 M. Chattopadhyay, E. D. Walter, D. J. Newell, P. J. Jackson, E. Aronoff-Spencer, J. Peisach, G. J. Gerfen, B. Bennett, W. E. Antholine and G. L. Millhauser, *J. Am. Chem. Soc.*, 2005, **127**, 12647–12656.

164 C. S. Burns, E. Aronoff-Spencer, C. M. Dunham, P. Lario, N. I. Avdievich, W. E. Antholine, M. M. Olmstead, A. Vrielink, G. J. Gerfen, J. Peisach, W. G. Scott and G. L. Millhauser, *Biochemistry*, 2002, **41**, 3991–4001.

165 B. K. Shin and S. Saxena, *J. Phys. Chem. A*, 2011, **115**, 9590–9602.

166 B. K. Shin and S. Saxena, *Biochemistry*, 2008, **47**, 9117–9123.

167 J. Hernández-Guzmán, L. Sun, A. K. Mehta, J. Dong, D. G. Lynn and K. Warncke, *ChemBioChem*, 2013, **14**, 1762–1771.

168 K. I. Silva, B. C. Michael, S. J. Geib and S. Saxena, *J. Phys. Chem. B*, 2014, **118**, 8935–8944.

169 Y. Shenberger, O. Marciano, H. E. Gottlieb and S. Ruthstein, *J. Coord. Chem.*, 2018, **71**, 1985–

2002.

170 M. J. Lawless, S. Ghosh, T. F. Cunningham, A. Shimshi and S. Saxena, *Phys. Chem. Chem. Phys.*, 2017, **19**, 20959–20967.

171 G. Rao, S. Bansal, W. X. Law, B. O'Dowd, S. A. Dikanov and E. Oldfield, *Biochemistry*, 2017, **56**, 3770–3779.

172 D. M. Gagnon, M. B. Brophy, S. E. J. Bowman, T. A. Stich, C. L. Drennan, R. D. Britt and E. M. Nolan, *J. Am. Chem. Soc.*, 2015, **138**, 3004–3016.

173 H. Y. V. Ching, F. C. Mascali, H. C. Bertrand, E. M. Bruch, P. Demay-Drouhard, R. M. Rasia, C. Policar, L. C. Tabares and S. Un, *J. Phys. Chem. Lett.*, 2016, **7**, 1072–1076.

174 A. Giannoulis, A. Feintuch, Y. Barak, H. Mazal, S. Albeck, T. Unger, F. Yang, X.-C. Su and D. Goldfarb, *Proc. Natl. Acad. Sci.*, 2020, **117**, 395–404.

175 A. Collauto, S. Mishra, A. Litvinov, H. S. Mchaourab and D. Goldfarb, *Structure*, 2017, **25**, 1264-1274.e3.

176 T. Hetzke, M. Vogel, D. B. Gophane, J. E. Weigand, B. Suess, S. T. H. Sigurdsson and T. F. Prisner, *RNA*, 2019, **25**, 158–167.

177 A. D. Milov, A. B. Ponomarev and Y. D. Tsvetkov, *Chem. Phys. Lett.*, 1984, **110**, 67–72.

178 A. D. Milov, A. B. Ponomarev and Y. D. Tsvetkov, *J. Struct. Chem.*, 1985, **25**, 710–713.

179 L. V. Kulik, S. A. Dzuba, I. A. Grigoryev and Y. D. Tsvetkov, *Chem. Phys. Lett.*, 2001, **343**, 315–324.

180 S. Milikisyants, F. Scarpelli, M. G. Finiguerra, M. Ubbink and M. Huber, *J. Magn. Reson.*, 2009, **201**, 48–56.

181 B. E. Bode, D. Margraf, J. Plackmeyer, G. Dürner, T. F. Prisner and O. Schiemann, *J. Am. Chem. Soc.*, 2007, **129**, 6736–6745.

182 M. Stevens, B. Franke, K. A. Skorupka, D. S. Cafiso, O. Pornillos, O. Mayans and D. G. Norman, *J. Mol. Biol.*, 2019, **431**, 2900–2909.

183 S. A. Kotler, V. Tugarinov, T. Schmidt, A. Ceccon, D. S. Libich, R. Ghirlando, C. D. Schwieters and G. M. Clore, *Proc. Natl. Acad. Sci.*, 2019, **116**, 3562–3571.

184 E. R. Georgieva, P. P. Borbat, H. D. Norman and J. H. Freed, *Sci. Rep.*, 2015, **5**, 11757.

185 Y. Yang, S.-N. Chen, F. Yang, X.-Y. Li, A. Feintuch, X.-C. Su and D. Goldfarb, *Proc. Natl. Acad. Sci.*, 2020, **117**, 20566–20575.

186 A. Ceccon, T. Schmidt, V. Tugarinov, S. A. Kotler, C. D. Schwieters and G. M. Clore, *J. Am. Chem. Soc.*, 2018, **140**, 6199–6202.

187 M. J. Morten, J. R. Peregrina, M. Figueira-Gonzalez, K. Ackermann, B. E. Bode, M. F. White and J. C. Penedo, *Nucleic Acids Res.*, 2015, **43**, 10907–10924.

188 O. A. Krumkacheva, G. Y. Shevelev, A. A. Lomzov, N. S. Dyrkheeva, A. A. Kuzhelev, V. V. Koval, V. M. Tormyshev, Y. F. Polienko, M. V. Fedin, D. V. Pyshnyi, O. I. Lavrik and E. G. Bagryanskaya, *Nucleic Acids Res.*, 2019, **47**, 7767–7780.

189 S. Barber-Zucker, J. Hall, S. V. Mangapuram, I. Kass, S. Kolusheva, F. MacMillan, R. Zarivach and A. Henn, *FEBS J.*, 2019, **286**, 2193–2215.

190 N. Erlenbach, C. Grünewald, B. Krstic, A. Heckel and T. F. Prisner, *RNA*, 2019, **25**, 239–246.

191 P. E. Spindler, S. J. Glaser, T. E. Skinner and T. F. Prisner, *Angew. Chemie Int. Ed.*, 2013, **52**, 3425–3429.

192 A. Doll, S. Pribitzer, R. Tschaggelar and G. Jeschke, *J. Magn. Reson.*, 2013, **230**, 27–39.

193 K. Ackermann and B. E. Bode, *Mol. Phys.*, 2018, **116**, 1513–1521.

194 V. P. Denysenkov, T. F. Prisner, J. Stubbe and M. Bennati, *Proc. Natl. Acad. Sci.*, 2006, **103**, 13386–13390.

195 A. Giannoulis, C. L. Motion, M. Oranges, M. Bühl, G. M. Smith and B. E. Bode, *Phys. Chem. Chem. Phys.*, 2018, **20**, 2151–2154.

196 S. Richert, J. Cremers, H. L. Anderson and C. R. Timmel, *Chem. Sci.*, 2016, **7**, 6952–6960.

197 T. Schmidt, L. Tian and G. M. Clore, *Biochemistry*, 2018, **57**, 489–493.

198 K. Barth, S. Hank, P. E. Spindler, T. F. Prisner, R. Tampé and B. Joseph, *J. Am. Chem. Soc.*, 2018, **140**, 4527–4533.

199 M. H. Timachi, C. A. J. Hutter, M. Hohl, T. Assafa, S. Böhm, A. Mittal, M. A. Seeger and E. Bordignon, *Elife*, 2017, **6**, e20236.

200 N. Van Eps, L. N. Caro, T. Morizumi, A. K. Kusnetzow, M. Szczepek, K. P. Hofmann, T. H. Bayburt, S. G. Sligar, O. P. Ernst and W. L. Hubbell, *Proc. Natl. Acad. Sci.*, 2017, **114**, E3268–E3275.

201 B. Carrington, W. K. Myers, P. Horanyi, M. Calmiano and A. D. G. Lawson, *Biophys. J.*, 2017, **113**, 371–380.

202 G. Jeschke, M. Sajid, M. Schulte and A. Godt, *Phys. Chem. Chem. Phys.*, 2009, **11**, 6580.

203 T. von Hagens, Y. Polyhach, M. Sajid, A. Godt and G. Jeschke, *Phys. Chem. Chem. Phys.*, 2013, **15**, 5854.

204 K. Ackermann, C. Pliotas, S. Valera, J. H. Naismith and B. E. Bode, *Biophys. J.*, 2017, **113**, 1968–1978.

205 S. Pribitzer, L. Fábregas Ibáñez, C. Gmeiner, I. Ritsch, D. Klose, M. Sajid, M. Hülsmann, A. Godt and G. Jeschke, *Appl. Magn. Reson.*, 2018, **49**, 1253–1279.

206 S. Pribitzer, M. Sajid, M. Hülsmann, A. Godt and G. Jeschke, *J. Magn. Reson.*, 2017, **282**, 119–128.

207 S. Valera, K. Ackermann, C. Pliotas, H. Huang, J. H. Naismith and B. E. Bode, *Chem. - A Eur. J.*, 2016, **22**, 4700–4703.

208 S. Milikisiyants, S. Wang, R. A. Munro, M. Donohue, M. E. Ward, D. Bolton, L. S. Brown, T. I. Smirnova, V. Ladizhansky and A. I. Smirnov, *J. Mol. Biol.*, 2017, **429**, 1903–1920.

209 M. Bretschneider, P. E. Spindler, O. Y. Rogozhnikova, D. V Trukhin, B. Endeward, A. A. Kuzhelev, E. Bagryanskaya, V. M. Tormyshev and T. F. Prisner, *J. Phys. Chem. Lett.*, 2020, **11**, 6286–6290.

210 C. Her, A. R. Thompson, C. B. Karim and D. D. Thomas, *Sci. Rep.*, 2018, **8**, 10681.

211 A. A. Kuznetsova, A. G. Matveeva, A. D. Milov, Y. N. Vorobjev, S. A. Dzuba, O. S. Fedorova and N. A. Kuznetsov, *Nucleic Acids Res.*, 2018, **46**, 11454–11465.

212 C. J. Lopez, Z. Yang, C. Altenbach and W. L. Hubbell, *Proc. Natl. Acad. Sci.*, 2013, **110**, E4306–E4315.

213 R. A. Stein, A. H. Beth and E. J. Hustedt, *Methods Enzymol.*, 2015, **563**, 531–567.

214 T. H. Edwards and S. Stoll, *J. Magn. Reson.*, 2018, **288**, 58–68.

215 S. G. Worswick, J. A. Spencer, G. Jeschke and I. Kuprov, *Sci. Adv.*, 2018, **4**, eaat5218.

216 L. F. Ibáñez, G. Jeschke and S. Stoll, *Magn. Reson.*, 2020, **1**, 209–220.

217 M. H. Shabestari, N. J. Meeuwenoord, D. V. Filippov and M. Huber, *J. Biol. Phys.*, 2016, **42**, 299–315.

218 J. Voss, L. Salwinski, H. R. Kaback and W. L. Hubbell, *Proc. Natl. Acad. Sci.*, 1995, **92**, 12295–12299.

219 J. Voss, W. L. Hubbell and H. R. Kaback, *Biochemistry*, 1998, **37**, 211–216.

220 R. C. Hadley, D. M. Gagnon, M. B. Brophy, Y. Gu, T. G. Nakashige, R. D. Britt and E. M. Nolan, *J. Am. Chem. Soc.*, 2018, **140**, 110–113.

221 I. Duttagupta, N. Jugniot, G. Audran, J.-M. Franconi, S. R. A. Marque, P. Massot, P. Mellet, E. Parzy, E. Thiaudière and N. Vanthuyne, *Chem. - A Eur. J.*, 2018, **24**, 7615–7619.

222 M. A. Hollas, S. J. Webb, S. L. Flitsch and A. J. Fielding, *Angew. Chemie Int. Ed.*, 2017, **56**, 9449–9453.

223 A. J. Fielding, K. Dornevil, L. Ma, I. Davis and A. Liu, *J. Am. Chem. Soc.*, 2017, **139**, 17484–17499.

224 S. Melnikov, A. Ben-Shem, N. Garreau de Loubresse, L. Jenner, G. Yusupova and M. Yusupov, *Nat. Struct. Mol. Biol.*, 2012, **19**, 560–567.

225 C. J. Lim, A. J. Zaug, H. J. Kim and T. R. Cech, *Nat. Commun.*, 2017, **8**, 1075.

226 X. Huang, B. Luan, J. Wu and Y. Shi, *Nat. Struct. Mol. Biol.*, 2016, **23**, 778–785.

227 H. Yin and A. D. Flynn, *Annu. Rev. Biomed. Eng.*, 2016, **18**, 51–76.

228 V. N. Syryamina, M. De Zotti, C. Toniolo, F. Formaggio and S. A. Dzuba, *Phys. Chem. Chem. Phys.*, 2018, **20**, 3592–3601.

229 D. M. Yin, J. S. Hannam, A. Schmitz, O. Schiemann, G. Hagelueken and M. Famulok, *Angew. Chemie - Int. Ed.*, 2017, **56**, 8417–8421.

230 S. Weickert, M. Wawrzyniuk, L. H. John, S. G. D. Rüdiger and M. Drescher, *Sci. Adv.*, 2020, **6**, eaax6999.

231 L. Galazzo, G. Meier, M. H. Timachi, C. A. J. Hutter, M. A. Seeger and E. Bordignon, *Proc. Natl. Acad. Sci.*, 2020, **117**, 2441–2448.

232 X. Shi, S.-W. Chuo, S.-H. Liou and D. B. Goodin, *Biochemistry*, 2020, **59**, 1823–1831.

233 C. M. Grytz, A. Marko, P. Cekan, S. T. Sigurdsson and T. F. Prisner, *Phys. Chem. Chem. Phys.*, 2016, **18**, 2993–3002.

234 M. Teucher, H. Zhang, V. Bader, K. F. Winklhofer, A. J. García-Sáez, A. Rajca, S. Bleicken and E. Bordignon, *Sci. Rep.*, 2019, **9**, 13013.

235 J. R. Bankston, H. A. DeBerg, S. Stoll and W. N. Zagotta, *J. Biol. Chem.*, 2017, **292**, 17794–17803.

236 T. Morizumi, W.-L. Ou, N. Van Eps, K. Inoue, H. Kandori, L. S. Brown and O. P. Ernst, *Sci. Rep.*, 2019, **9**, 11283.

237 H. Sameach, S. Ghosh, L. Gevorkyan-Airapetov, S. Saxena and S. Ruthstein, *Angew. Chemie Int. Ed.*, 2019, **58**, 3053–3056.

238 A. A. Malygin, D. M. Graifer, M. I. Meschaninova, A. G. Venyaminova, I. O. Timofeev, A. A. Kuzhelev, O. A. Krumkacheva, M. V. Fedin, G. G. Karpova and E. G. Bagryanskaya, *Nucleic Acids Res.*, 2018, **46**, 897–904.

239 A. A. Malygin, O. A. Krumkacheva, D. M. Graifer, I. O. Timofeev, A. S. Ochkasova, M. I. Meschaninova, A. G. Venyaminova, M. V. Fedin, M. Bowman, G. G. Karpova and E. G. Bagryanskaya, *Nucleic Acids Res.*, 2019, **47**, 11850–11860.

240 M. Kerzhner, H. Matsuoka, C. Wuebben, M. Famulok and O. Schiemann, *Biochemistry*, 2018, **57**, 2923–2931.

241 T. F. Cunningham, M. R. Putterman, A. Desai, W. S. Horne and S. Saxena, *Angew. Chemie Int. Ed.*, 2015, **54**, 6330–6334.

242 M. J. Lawless, J. R. Pettersson, G. S. Rule, F. Lanni and S. Saxena, *Biophys. J.*, 2018, **114**, 592–601.

243 A. Gamble Jarvi, J. Casto and S. Saxena, *J. Magn. Reson.*, 2020, **320**, 106848.

244 A. Schweiger and G. Jeschke, *Oxford Univ. Press.*, 2001.

245 M. H. Levitt, *Spin Dynamics: Basics of Nuclear Magnetic Resonance*, 2002.

246 J. W. Robinson, *Practical Handbook of Spectroscopy*, Routledge, 2017.

247 G. Jeschke and Y. Polyhach, *Phys. Chem. Chem. Phys.*, 2007, **9**, 1895–1910.

248 D. Goldfarb, *J. Magn. Reson.*, 2019, **306**, 102–108.

249 J. J. Wyman, *Adv. Protein Chem.*, 1964, **19**, 223–286.

250 Z. X. Wang and R. F. Jiang, *FEBS Lett.*, 1996, **392**, 245–249.

251 Z.-X. Wang, *FEBS Lett.*, 1995, **360**, 111–114.

252 E. C. Hulme and M. A. Trevethick, *Br. J. Pharmacol.*, 2010, **161**, 1219–1237.

253 E. Freire, A. Schön and A. Velazquez-Campoy, in *Methods in Enzymology*, 2009, pp. 127–155.

254 E. T. Mack, R. Perez-Castillejos, Z. Suo and G. M. Whitesides, *Anal. Chem.*, 2008, **80**, 5550–5555.

255 W. Gerlach and O. Stern, *Z. Phys.*, 1922, **9**, 353–355.

256 W. Gerlach and O. Stern, *Z. Phys.*, 1922, **9**, 349–352.

257 E. Zavoisky, *Zhur. Eksp. i Theor. Fiz.,* 1945, **15**, 344–350.

258 W. B. Mims, K. Nassau and J. D. McGee, *Phys. Rev.*, 1961, **123**, 2059–2069.

259 R. J. Blume, *Phys. Rev.*, 1958, **109**, 1867–1873.

260 L. G. Rowan, E. L. Hahn and W. B. Mims, *Phys. Rev.*, 1965, **137**, A61–A71.

261 J. S. Hyde and K. V. . Rao, *J. Magn. Reson.*, 1978, **29**, 509–516.

262 N. Sannikova, I. Timofeev, E. Bagryanskaya, M. Bowman, M. Fedin and O. Krumkacheva, *Molecules*, 2020, **25**, 2677.

263 A. Zecevic, G. R. Eaton, S. S. Eaton and M. Lindgren, *Mol. Phys.*, 1998, **95**, 1255–1263.

264 J. L. Du, G. R. Eaton and S. S. Eaton, *J. Magn. Reson. Ser. A*, 1995, **115**, 213–221.

265 B. Rakvin, N. Maltar-Strmečki, P. Cevc and D. Arčon, *J. Magn. Reson.*, 2001, **152**, 149–155.

266 A. Abragam and M. H. L. Pryce, *Proc. Phys. Soc. Sect. A*, 1950, **63**, 409–411.

267 K. Keller, V. Mertens, M. Qi, A. I. Nalepa, A. Godt, A. Savitsky, G. Jeschke and M. Yulikov, *Phys. Chem. Chem. Phys.*, 2017, **19**, 17856–17876.

268 S. Razzaghi, M. Qi, A. I. Nalepa, A. Godt, G. Jeschke, A. Savitsky and M. Yulikov, *J. Phys. Chem. Lett.*, 2014, **5**, 3970–3975.

269 K. Keller, M. Qi, C. Gmeiner, I. Ritsch, A. Godt, G. Jeschke, A. Savitsky and M. Yulikov, *Phys. Chem. Chem. Phys.*, 2019, **21**, 8228–8245.

270 A. Meyer and O. Schiemann, *J. Phys. Chem. A*, 2016, **120**, 3463–3472.

271 P. Hu and S. R. Hartmann, *Phys. Rev. B*, 1974, **9**, 1–13.

272 A. Savitsky, A. A. Dubinskii, M. Flores, W. Lubitz and K. Möbius, *J. Phys. Chem. B*, 2007, **111**, 6245–6262.

273 I. Ritsch, H. Hintz, G. Jeschke, A. Godt and M. Yulikov, *Phys. Chem. Chem. Phys.*, 2019, **21**, 9810–9830.

274 D. Abdullin, *Appl. Magn. Reson.*, 2020, **51**, 725–748.

275 A. N. Tikhonov, *Dokl. Akad. Nauk SSSR*, 1963, **151**, 501–504.

276 A. G. Matveeva, V. M. Nekrasov and A. G. Maryasov, *Phys. Chem. Chem. Phys.*, 2017, **19**, 32381–32388.

277 Y. W. Chiang, P. P. Borbat and J. H. Freed, *J. Magn. Reson.*, 2005, **177**, 184–196.

278 L. Fábregas Ibáñez and G. Jeschke, *J. Magn. Reson.*, 2019, **300**, 28–40.

279 R. Ward, A. Bowman, E. Sozudogru, H. El-Mkami, T. Owen-Hughes and D. G. Norman, *J. Magn. Reson.*, 2010, **207**, 164–167.

280 B. Joseph, A. Sikora, E. Bordignon, G. Jeschke, D. S. Cafiso and T. F. Prisner, *Angew. Chemie Int. Ed.*, 2015, **54**, 6196–6199.

281 C. Pliotas, R. Ward, E. Branigan, A. Rasmussen, G. Hagelueken, H. Huang, S. S. Black, I. R. Booth, O. Schiemann and J. H. Naismith, *Proc. Natl. Acad. Sci.*, 2012, **109**, E2675–E2682.

282 H. Celia, N. Noinaj, S. D. Zakharov, E. Bordignon, I. Botos, M. Santamaria, T. J. Barnard, W. A. Cramer, R. Lloubes and S. K. Buchanan, *Nature*, 2016, **538**, 60–65.

283 D. Hilger, Y. Polyhach, E. Padan, H. Jung and G. Jeschke, *Biophys. J.*, 2007, **93**, 3675–3683.

284 B. E. Bode, J. Plackmeyer, T. F. Prisner and O. Schiemann, *J. Phys. Chem. A*, 2008, **112**, 5064–5073.

285 E. Narr, A. Godt and G. Jeschke, *Angew. Chemie Int. Ed.*, 2002, **41**, 3907–3910.

286 Z. Wu, A. Feintuch, A. Collauto, L. A. Adams, L. Aurelio, B. Graham, G. Otting and D. Goldfarb, *J. Phys. Chem. Lett.*, 2017, **8**, 5277–5282.

287 L. Garbuio, E. Bordignon, E. K. Brooks, W. L. Hubbell, G. Jeschke and M. Yulikov, *J. Phys. Chem. B*, 2013, **117**, 3145–3153.

288 G. Prokopiou, M. D. Lee, A. Collauto, E. H. Abdelkader, T. Bahrenberg, A. Feintuch, M. Ramirez-Cohen, J. Clayton, J. D. Swarbrick, B. Graham, G. Otting and D. Goldfarb, *Inorg. Chem.*, 2018, **57**, 5048–5059.

289 H. Jäger, A. Koch, V. Maus, H. W. Spiess and G. Jeschke, *J. Magn. Reson.*, 2008, **194**, 254–263.

290 M. C. Mahawaththa, M. D. Lee, A. Giannoulis, L. A. Adams, A. Feintuch, J. D. Swarbrick, B. Graham, C. Nitsche, D. Goldfarb and G. Otting, *Phys. Chem. Chem. Phys.*, 2018, **20**, 23535–23545.

291 A. A. Kuzhelev, O. A. Krumkacheva, G. Y. Shevelev, M. Yulikov, M. V. Fedin and E. G. Bagryanskaya, *Phys. Chem. Chem. Phys.*, 2018, **20**, 10224–10230.

292 G. W. Reginsson, N. C. Kunjir, S. T. Sigurdsson and O. Schiemann, *Chem. - A Eur. J.*, 2012, **18**, 13580–13584.

293 A. Fielding, M. Concilio, G. Heaven and M. Hollas, *Molecules*, 2014, **19**, 16998–17025.

294 G. E. Merz, P. P. Borbat, A. R. Muok, M. Srivastava, D. N. Bunck, J. H. Freed and B. R. Crane,

J. Phys. Chem. B, 2018, **122**, 9443–9451.

295 E. G. B. Evans and G. L. Millhauser, in *Methods in Enzymology*, 2015, pp. 503–527.

296 M. J. Schmidt, J. Borbas, M. Drescher and D. Summerer, *J. Am. Chem. Soc.*, 2014, **136**, 1238–1241.

297 M. R. Mehlenbacher, F. Bou-Abdallah, X. X. Liu and A. Melman, *Inorganica Chim. Acta*, 2015, **437**, 152–158.

298 K. Keller, A. Doll, M. Qi, A. Godt, G. Jeschke and M. Yulikov, *J. Magn. Reson.*, 2016, **272**, 108–113.

299 D. Abdullin, M. Suchatzki and O. Schiemann, *Appl. Magn. Reson.*, , DOI:10.1007/s00723-021-01326-1.

300 X. Bogetti, S. Ghosh, A. Gamble Jarvi, J. Wang and S. Saxena, *J. Phys. Chem. B*, 2020, **124**, 2788–2797.

301 A. Gamble Jarvi, A. Sargun, X. Bogetti, J. Wang, C. Achim and S. Saxena, *J. Phys. Chem. B*, 2020, **124**, 7544–7556.

302 C. D. Schwieters, J. J. Kuszewski, N. Tjandra and G. M. Clore, *J. Magn. Reson.*, 2003, **160**, 65–73.

303 G. Hagelueken, R. Ward, J. H. Naismith and O. Schiemann, *Appl. Magn. Reson.*, 2012, **42**, 377–391.

304 M. J. D. Powell, *Comput. J.*, 1964, **7**, 155–162.

305 L. Verlet, *Phys. Rev.*, 1967, **159**, 98–103.

306 S. Ghosh, S. Saxena and G. Jeschke, *Appl. Magn. Reson.*, 2018, **49**, 1281–1298.

307 Y. Polyhach, E. Bordignon and G. Jeschke, *Phys. Chem. Chem. Phys.*, 2011, **13**, 2356–2366.

308 G. Jeschke, *Protein Sci.*, 2018, **27**, 76–85.

309 M. Schlenkrich, J. Brichmann, A. MacKerell and M. Karplus, *Biological Membranes: A Molecular Prospective from Computation and Experiment*, Birkhauser, Boston, 1996.

310 D. Sezer, J. H. Freed and B. Roux, *J. Phys. Chem. B*, 2008, **112**, 5755–5767.

311 W. Clark Still, A. Tempczyk, R. C. Hawley and T. Hendrickson, *J. Am. Chem. Soc.*, 1990, **112**, 6127–6129.

312 J. Gao, F. Xing, Y. Bai and S. Zhu, *Dalt. Trans.*, 2014, **43**, 7964.

313 J. T. Kellis, R. J. Todd and F. H. Arnold, *Bio/Technology*, 1991, **9**, 994–995.

314 F. H. Arnold and B. L. Haymore, *Science*, 1991, **252**, 1796–1797.

315 T. Abudiab and R. R. Beitle, *J. Chromatogr. A*, 1998, **795**, 211–217.

316 E. Norkus and A. Vaškelis, *Polyhedron*, 1994, **13**, 3041–3044.

317 C. Park and R. T. Raines, *J. Am. Chem. Soc.*, 2001, **123**, 11472–11479.

318 A. V. Korennykh, J. A. Piccirilli and C. C. Correll, *Nat. Struct. Mol. Biol.*, 2006, **13**, 436–443.

319 T. D. Pollard, W. C. Earnshaw, J. Lippincott-Schwartz and G. T. Johnson, *Cell Biology: Third Edition*, 2016.

320 G. Schreiber, G. Haran and H. X. Zhou, *Chem. Rev.*, 2009, **109**, 839–860.

321 F. G. M. Wiertz, O. M. H. Richter, A. V. Cherepanov, F. MacMillan, B. Ludwig and S. De Vries, *FEBS Lett.*, 2004, **575**, 127–130.

322 S. Rebsdat and D. Mayer, in *Ullmann's Encyclopedia of Industrial Chemistry*, Wiley-VCH Verlag GmbH & Co. KGaA, Weinheim, Germany, 2000.

323 W. B. Turnbull and A. H. Daranas, *J. Am. Chem. Soc.*, 2003, **125**, 14859–14866.

324 A. P. Behera, P. Naskar, S. Agarwal, P. A. Banka, A. Poddar and A. B. Datta, *Biochem. J.*, 2018, **475**, 1569–1582.

325 A. Zubriene, J. Matuliene, L. Baranauskiene, J. Jachno, J. Torresan, V. Michailoviene, P. Cimmperman and D. Matulis, *Int. J. Mol. Sci.*, 2009, **10**, 2662–2680.

326 A. Gamble Jarvi, T. F. Cunningham and S. Saxena, *Phys. Chem. Chem. Phys.*, 2019, **21**, 10238–10243.

327 A. Gamble Jarvi, K. Ranguelova, S. Ghosh, R. T. Weber and S. Saxena, *J. Phys. Chem. B*, 2018, **122**, 10669–10677.

328 M. Oranges, 2020, 'Nanometre Distances, Orientation and Multimerisation Equilibria from Pulse Dipolar EPR', *PhD Thesis*, University of St Andrews, St Andrews, pp155-168.

329 S. Saha, T. Hetzke, T. F. Prisner and S. T. Sigurdsson, *Chem. Commun.*, 2018, **54**, 11749–11752.

330 N. Kamble, M. Wolfrum, T. Halbritter, S. T. Sigurdsson and C. Richert, *Chem. Biodivers.*, 2020, **17**, e1900676.

331 A. Bahramzadeh, H. Jiang, T. Huber and G. Otting, *Angew. Chemie - Int. Ed.*, 2018, **57**, 6226–6229.

332 N. Fleck, C. Heubach, T. Hett, S. Spicher, S. Grimme and O. Schiemann, *Chem. – A Eur. J.*, 2021, **27**, 5292–5297.

333 D. F. Senear and M. Brenowitz, *J. Biol. Chem.*, 1991, **266**, 13661–13671.

334 K. Ackermann, J. L. Wort and B. E. Bode, *ChemRxiv. Prepr.*

335 H. H. Ku, *J. Res. Natl. Bur. Stand. Sect. C Eng. Instrum.*, 1966, **70C**, 263.

336 J. R. Horn, D. Russell, E. A. Lewis and K. P. Murphy, *Biochemistry*, 2001, **40**, 1774–1778.

337 S. A. Kantonen, N. M. Henriksen and M. K. Gilson, *Biochim. Biophys. Acta - Gen. Subj.*, 2017, **1861**, 485–498.

338 L. Baranauskienė, V. Petrikaitė, J. Matulienė and D. Matulis, *Int. J. Mol. Sci.*, 2009, **10**, 2752–2762.

339 D. Abdullin, F. Duthie, A. Meyer, E. S. Müller, G. Hagelueken and O. Schiemann, *J. Phys. Chem. B*, 2015, **119**, 13539–13542.

340 D. Abdullin, H. Matsuoka, M. Yulikov, N. Fleck, C. Klein, S. Spicher, G. Hagelueken, S. Grimme, A. Lützen and O. Schiemann, *Chem. – A Eur. J.*, 2019, **25**, 8820–8828.

341 S. Stoll and A. Schweiger, *J. Magn. Reson.*, 2006, **178**, 42–55.

342 P. Laine and R. Matilainen, *Anal. Bioanal. Chem.*, 2005, **382**, 1601–1609.

343 D. F. Evans, *J. Chem. Soc.*, 1959, 2003–2005.

344 J. S. Cohen, J. H. Griffin and A. N. Schechter, *J. Biol. Chem.*, 1973, **248**, 4305–10.

345 M. Tanokura, M. Tasumi and T. Miyazawa, *Chem. Lett.*, 1978, **7**, 739–742.

346 S. Mathpal and N. D. Kandpal, *E-Journal Chem.*, 2009, **6**, 445–448.

347 N. Zhang, J. Brugger, B. Etschmann, Y. Ngothai and D. Zeng, *PLoS One*, 2015, **10**, e0119805.

348 J. J. Maguire, R. E. Kuc and A. P. Davenport, *Methods Mol. Biol.*, 2012, **897**, 31–77.

349 E. N. Salgado, R. A. Lewis, S. Mossin, A. L. Rheingold and F. A. Tezcan, *Inorg. Chem.*, 2009, **48**, 2726–2728.

List of Figures and Tables